RAL-82-039

Science and Engineering Research Council
Rutherford Appleton Laboratory
CHILTON, DIDCOT, OXON, OX11 0QX

Science and Engineering Research Council Central Laser Facility

Annual Report to the Laser Facility Committee 1982

Laser Division
Rutherford Appleton Laboratory

RAL-82-039

SCIENCE AND ENGINEERING RESEARCH COUNCIL

CENTRAL LASER FACILITY

ANNUAL REPORT TO THE LASER FACILITY COMMITTEE, 1982

CONTENTS

SCIENCE AND ENGINEERING RESEARCH COUNCIL

CENTRAL LASER FACILITY

ANNUAL REPORT TO THE LASER FACILITY COMMITTEE, 1982

Preface

The report covers the work done at, or in association with, the Central Laser Facility during the year April 1981 to March 1982. It follows the same format as last years report and is arranged in seven chapters reflecting the six groups of the Glass Laser Scientific Programme and Scheduling Committee (GLSPSC) together with the gas laser development group. An appendix at the end of the report lists the publications based on the work of the facility which have either appeared or been accepted for publication during the year.

The scientific groups using the glass laser are listed in the accompanying table together with the names of their chairmen and secretaries and the experimental time allocated to them. The total of the latter exceeds 52 weeks because of parallel operation in the single and six beam target areas.

The most important new facility available during the year under review was the ability to irradiate spherical targets with six beams at the second harmonic of the glass laser frequency. Mass ablation rates and ablation pressures have been measured at two frequencies in spherical geometry and at three freqencies in planar geometry. This work, which shows a $\lambda^{-2.3}$ scaling of ablation pressure with wavelength, was followed up by major experimental runs on ablative implosions driven by 0.53 μm radiation, as described in Chapter 5. The main limitation to the achievement of high densities appears, not surprisingly, to be the symmetry of compression. Some experimental and theoretical work has been done during the year on sources of shell instability and thermal smoothing (see Chapters 4 and 7) but more is required. In the modelling of these phenomena the 2D code developed at the University of Hull has been invaluable.

Work on filamentation and harmonic generation in laser-plasma interactions has continued and is described in Chapter 3. The availability of radiation at the harmonics of the glass laser has again been valuable here, for example for the study of $\omega_o/2$ radiation from plasmons at the quarter critical density of the plasma. By using the third harmonic as the driving frequency the generated $\omega/2$ radiation is emitted at an experimentally convenient wavelength. The phenomena contributin to filamentation, jet formation and self focusing in a laser generated plasma are not yet fully understood but progress in this direction is being made.

One of the interesting and internationally topical research areas being studied by and in association with the gas laser group is that of phase conjugation. Phase conjugation has been obtained in the ultraviolet for the first time, using both four-wave mixing and stimulated Brillouin scattering. The phase correcting properties of a phase conjugate reflector should allow the use of poor quality (and hence cheap) optics in a high power KrF system and possibly correct for phase abberations due to air turbulence in the long paths required for multiplexing. This work, together with other applications of UV radiation and progress in the construction of Sprite is described in Chapter 2.

Compared with 1980/81, the effort devoted to upgrading Vulcan has been relatively small. The most important single improvement was the installation of a new oscillator system (see Chapter 1). Other smaller, but significant improvements have been made to beam quality, power output and computer control, as described in Chapter 1.

Finally the theory and computation chapter, Chapter 7, is the largest of all. Many of the subjects referred to above reappear in this chapter and the instabilities occuring in laser generated plasmas receive particular attention. Energy transport remains an important and topical issue though considerable progress in understanding of energy transport inhibition has been made in recent years.

A F Gibson
31 March 1982

GLASS LASER SCIENTIFIC PROGRAMME AND SCHEDULING COMMITTEE

SCIENTIFIC GROUPS

GROUP TITLE	CHAIRMAN	SECRETARY	TIME ALLOCATED DURING YEAR (WEEKS)
Laser Plasma Interactions	Professor T J M Boyd University College of North Wales	Dr R G Evans	14.5
Transport and Particle Emission	Dr J Kilkenny Imperial College	Mr W T Toner	10.75
Spectroscopy and XUV lasers	Dr G Pert Hull University	Dr I N Ross	11.25
Ablative Compression	Dr T A Hall Essex University	Dr P T Rumsby	24.5
Facility Development	Dr A F Gibson R.A.L	Mr J Boon	for development 12.5 for maintenance 9
Theory and Computational Modelling	Professor M G Haines Imperial College	Dr A Bell	-

CHAPTER 1 GLASS LASER FACILITY DEVELOPMENT

INDEX

CHAPTER EDITOR: J E Boon

CHAPTER 1 GLASS LASER FACILITY DEVELOPMENT

1.1 Introduction

Though two target areas were in use last year, a large fraction of the year was taken up with laser development so that the number of laser shots provided for users was not much greater than the year before.

During the year under review, however the laser has produced a record number of target shots; about 1600, almost twice as many as in any previous year. This illustrates the improved reliability of the "Vulcan" structure. On the other hand there is no justification for complacency and further improvements are planned or in progress. In particular the degree of computer control can be further improved and as a consequence of the versitility of Vulcan an output prediction routine is seen as essential. Work towards this is discussed below.

The largest single improvement to Vulcan made during the past year was the installation of a new oscillator system (see Section 1.3.2). This allows the synchronous generation of long and short pulses which may be used together in, for example, ablative compresion of microballoons with short pulse X-ray backlighting. Installation necessitated a five week shut down of the facility in February/March and at the same time additional capacitors were installed to drive the additional disc amplifiers expected to be available before the end of 1982. The separation of the latter two events is necessitated by financial limitations but it is, nevertheless, frustrating to have 600kJ of stored energy capacity lying idle!

Some improvements in beam quality have been made during the year but more are needed. More generally, significant improvements in target illumination uniformity are required to obtain good implosions. Some pertinent calculations are described in this Chapter, which look forward to the proposed increase in beam number from 6 to 12. To fully exploit the power capability of Vulcan it will also be necessary to use lenses of larger diameter than at present so the steady development of lens fabrication techniques described below is also important. Fully automatic lens

production has not yet, and may never, be achieved but manual polishing is becoming less and less necessary.

While the laser was shut down in February/March, as recorded above, the target preparation group took the opportunity of reduced demand to move into a newly reconstructed laboratory. Target production must obviously grow to meet the growing laser shot rate and target requirements are becoming progressively more sophisticated. A significant step forward, reported below, has been the production of pure polymer shell targets which facilitate the use of X-ray diagnostic techniques. The area vacated by the target preparation group has been refurbished and added to the laser cleaning area, expansion being required to deal with the increased number of disc amplifiers to be serviced after installation next year.

A F Gibson (RAL)

1.2 Glass Laser Operations

This year has seen a busy operational schedule for the glass laser which has been aimed at maximising the available experimental time and bringing the system performance up to the design energy of 200 J per beam. During the year, 33 weeks have been available to the target areas, 8 weeks for laser maintenance, 6 weeks for the synchronised oscillator and capacitor bank installation (Sections 1.3.1 and 1.3.2) and 3 weeks for laser development. A total of 811 disc amplifier shots were fired into TA1 and 835 to TA2 with shot failures on 20 and 23 shots respectively due to computer crashes, switchout failure etc.

Early problems with damage to the output polarisers to the disc amplifiers lead to a study of beam quality. Air turbulence from the air conditioning system and cooling fans in various equipment racks was found to be the major problem. Careful screening of equipment racks plus a routine shutdown of the air conditioning fans prior to a shot has resulted in a significant improvement to the beam quality (Figure 1.01). Some residual turbulence is still visible and it is proposed to enclose the beam lines as far as possible to remove this. As a result of these improvements target areas shots have

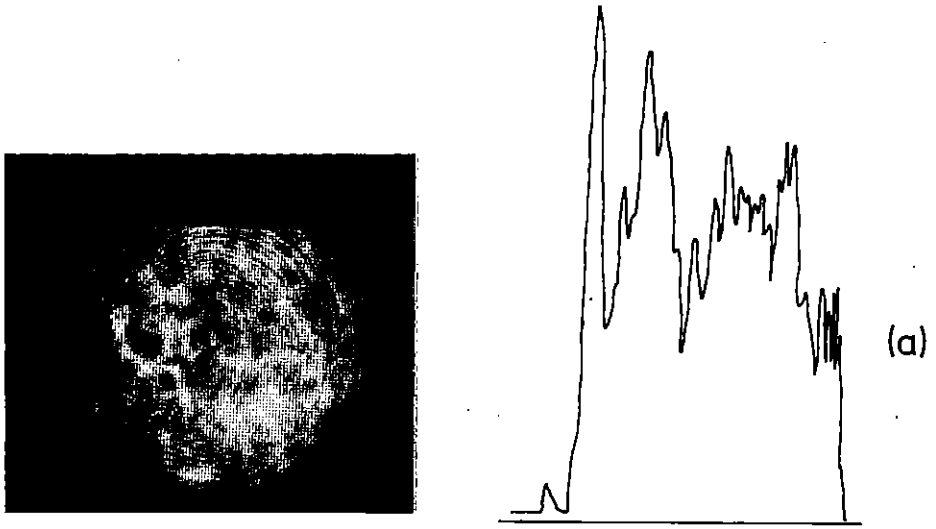

Figure 1.01 Single beam output profile before (a) and after (b) removal of air turbulance effects.

been fired at 150 J/beam, 50% up on the previous level at which damage occurred to the polarisers, and a single beam has been fired successfully above the 200 J level with no damage problems.

During the year, extensive use has been made of the synchronised short and "stacked" long pulse for time resolved X-ray and optical measurements, and lead to the installation of a synchronised long and short pulse oscillator system in February which is covered in Section 1.3.2. This system is now in routine and regular use adding further to the flexibility and capability of the laser system.

Additional diagnostics have been introduced in the form of the video disc system for output beam monitoring and further energy monitoring. A careful survey of all losses and amplifier gains in the system has been made and a very simple axial gain/loss computer programme has proved to be remarkably accurate in predicting the chain output from the sampled oscillator energy and amplifier settings. This will be shortly introduced as a routine operational aid together with the control development covered in Section 1.3.3.

N Allen, E Hodgson, A Raven, I N Ross and D Vigar (RAL)

1.3 Glass Laser Development

1.3.1 Glass Laser Enhancement

Following implementation of the major part of the laser enhancement programme towards the end of the previous annual report period, the only enhancement work on the laser has taken place with the pulse generator and this is reported in the following section of this report. The final phase of the current enhancement programme will be implemented in September of this year. This phase will add three disc amplifiers, bringing the number of output amplifiers driving the six beam experiments to the full complement of six. Preparations for this installation have been in progress during this year with the acquisition of components for the three 108mm diameter disc amplifiers (to be almost identical to those in current use) and with the

construction of capacitor banks to drive these amplifiers.

I N Ross (RAL)

1.3.2 Pulse Generator Enhancement

The highlight of the year's pulse generator development has been the installation of a new synchronized oscillator front end for the Vulcan glass laser facility. This timely refinement was added to the facility during a five week shutdown (shared with a capacitor bank upgrade) around February 1982. After an initial debugging period of 1 - 2 weeks, the system has been running routinely and reliably since early March.

The system employs two oscillators - one mode locked, the other single longitudinal mode (SLM) Q switched - and a single master synchronized switchout driven by a photoconductive silicon switch. Both oscillators run with 'prelase', allowing the ~25 ns (fwhm) smooth pulse from the SLM oscillator and the train of mode locked pulses to be temporally overlapped with ~nanosecond precision. A single mode locked pulse illuminates the silicon switch to produce a ~1 nanosecond electrical pulse which has essentially zero jitter wrt the mode locked train, because of the photoconductive nature of the switching. This single high voltage pulse is used to drive both the short and long pulse switchouts in tandem, such that the selected mode locked pulse is accompanied by a temporally corresponding nanosecond slice from the quasi-CW background provided by the 25 ns smooth pulse. The relative timing of the short and sliced long pulse is jitter-free and drift-free because it is fixed only by a cable length.

The details of the oscillators and associated control electronics are shown in Figure 1.02. Figure 1.03 shows the switchout arrangement and the interfacing with the amplifier chains and Figure 1.04 is a photograph of the components, with their covers removed, for illustration.

Both oscillators use Nd:YLF as the active medium, for compatibility with the phosphate glass of the amplifier chains.

The mode locked oscillator is conceptually similiar to those developed by Kuizenga (1.01) except that it uses electro-optic Q switching. The flashlamp power supply, produced by J K Lasers LTD (who also contributed a great deal to the development of this oscillator under an R&D contract) gives a feedback controlled 7 ms current pulse of variable slope, allowing several milliseconds of quasi-CW oscillation after all relaxation oscillations have decayed away. During this prelase a DC bias voltage of 0.7 $V_{\lambda/4}$ is applied to the intra cavity Pockels cell, allowing enough breakthrough for low level oscillation. Stable mode locking is established during the prelase by acousto-optic modulation. At a predetermined time, in phase synchronization with the RF driver, the Pockels cell bias is switched to zero by a krytron switch (common to both oscillators) to produce the Q switched output train of mode locked pulses. Pulse durations varying from 65 ps to 850 ps have so far been achieved from this oscillator. Whereas the upper figure was restricted only by available etalons, the lower limit seems to be the best figure achievable with the present modulator and drive electronics.

The long pulse oscillator derives its prelase, of up to ~ 200 μs, from an electro-optic negative feedback loop modulating the intra-cavity Pockels cell transmission. The scheme is somewhat similar to one previously described by Luther Davies (1.02). The flash lamp is driven by a conventional capacitor discharge network, with a current pulse duration of 280 μs (fwhm). The DC bias on the Pockels cell of 0.7 $V_{\lambda/4}$ allows laser oscillation to breakthrough before peak inversion on the rising gain edge. A photodiode senses the oscillation and applies, via a two stage transistor amplifier, a proportional negative feedback to the Pockels cell, which clamps the oscillation at a quasi CW level. Up to 200 μs of continuous prelase (pump level dependent) can be achieved in place of the normal relaxation oscillations. However since only a few microseconds are needed to establish good single axial mode selection with the resonant reflector designs used, typically only 5 μs of prelase is used prior to Q switching. This miminizes the tendency for thermal, mechanical or spatial hole burning effects to spoil the single mode selection by mode hopping. For this ability to run with a short prelase, for the reasons stated, the feedback stabilisation technique has advantages over the long pulse excitations techniques where prelases $\geq$ 0.5ms have to be used to allow relaxation oscillations to die away.

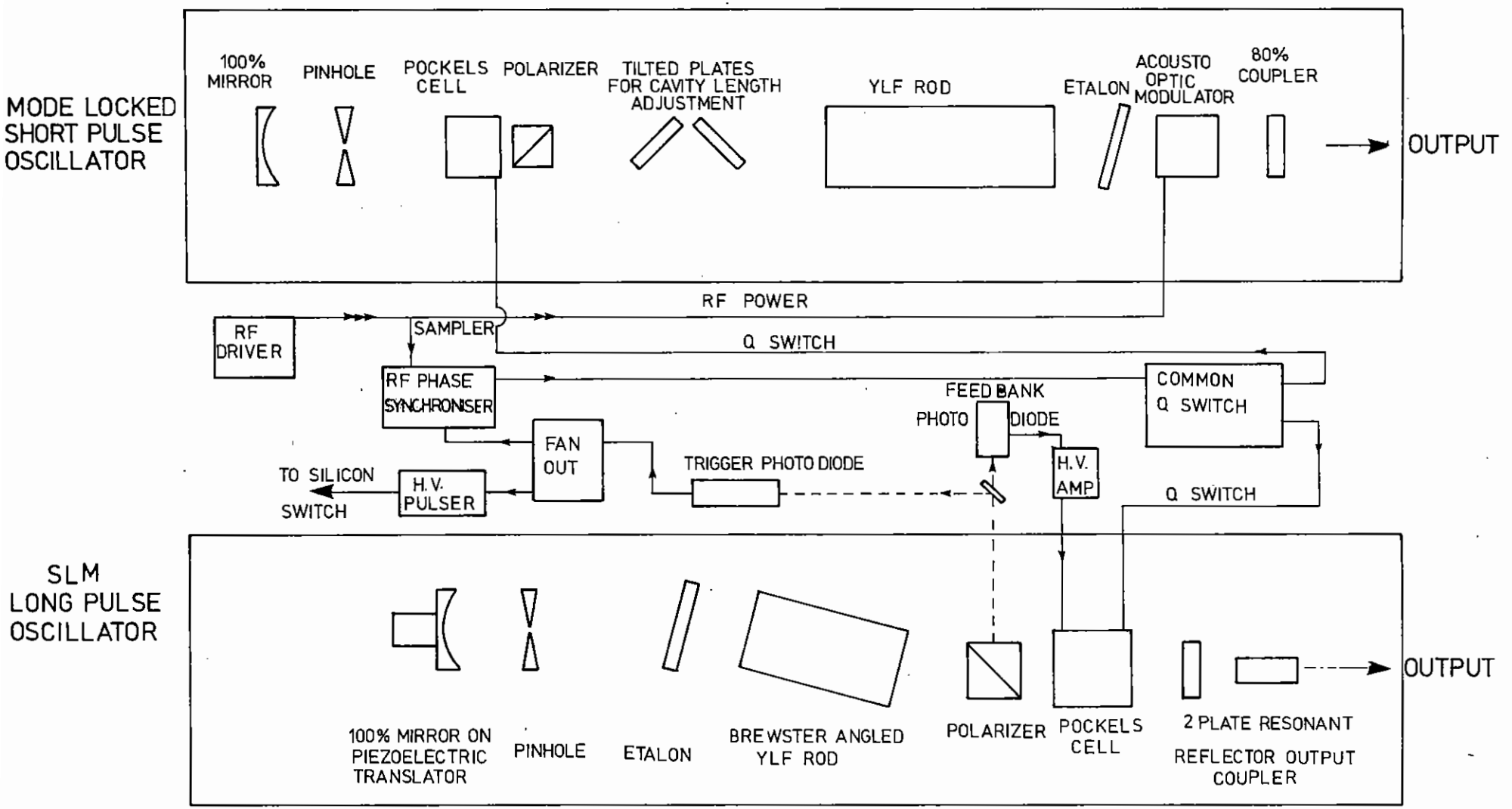

FIG. 1·02 OSCILLATORS AND CENTRAL ELECTRONICS.

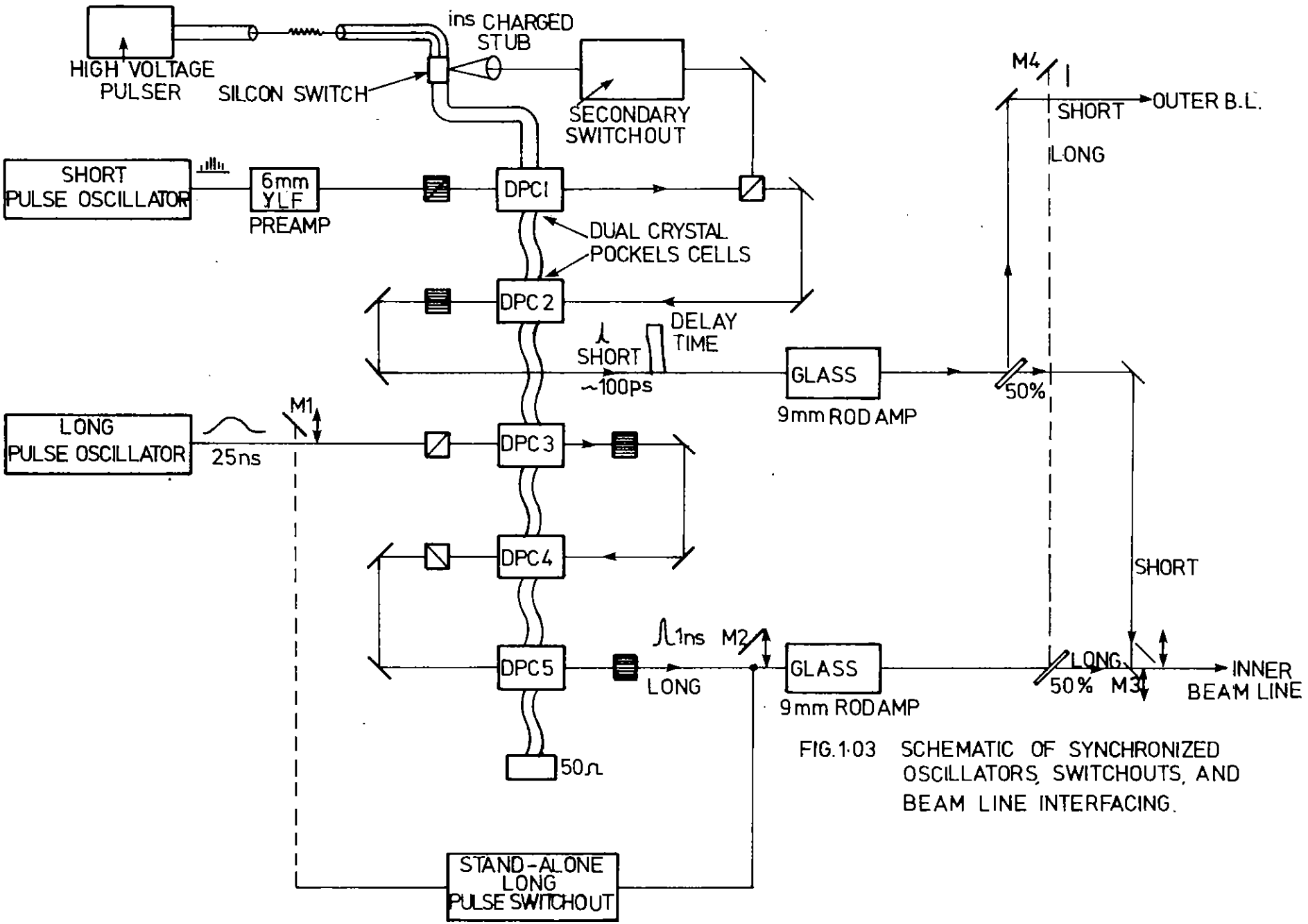

FIG. 1·03 SCHEMATIC OF SYNCHRONIZED OSCILLATORS, SWITCHOUTS, AND BEAM LINE INTERFACING.

The use of a single krytron to Q switch both oscillators means that any electronic jitter is common, and does not produced relative jitter in the timing of the two Q switched envelopes. Different cable lengths from the krytron to each Pockels cell allow the envelopes to be timed appropriately for the switchout, taking account of the different build-up times.

The master synchronized switchout utilizes five high speed dual crystal Pockels cells (DPC) produced by Electro Optic Developments Ltd. Dual crystal cells are used to halve the voltage hold off requirements on the silicon switch. The complete mode locked train passes through DPC, and is initially reflected out from the second (crossed) polarizer. The secondary switchout - an avalanche transistor unit made by Quantel - selects a single member of the mode locked train to illuminate the photoconductive silicon switch. [The silicon switch technology is similar to that devised by Mourou et al (1.03) and was described in the 1980 Annual Report.] A 3.5 kV pulse is generated with a duration (~1 ns here) fixed by the double transit time of the charged stub. This voltage pulse travels through the pair of Pockels cells DPC_1 DPC_2 and is timed to transmit a subsequent pulse from the train through to the amplifiers with a power contrast ratio of~10^7. The quality of the Pockels cells is such that, even after passage over DPC_1 and DPC_2, the nanosecond high voltage pulse is still clean enough to slice a good quality optical pulse from the 25 ns long pulse envelope in the three stage slicer made up from DPC_3 to DPC_5 The power contrast ratio for the long pulse is better than 10^{10}.

Figure 1.05 displays some waveforms illustrative of the oscillator and switchout performance. All traces were recorded using a vacuum photodiode feeding a direct access transient digitizer, with a time resolution of 350 ps. In Figure 1.05(a) the sliced long pulse is shown on 0.5 ns/division. It is seen to be clean, with a ~0.5 ns rise and fall time. The slight 'tail' on the pulse is due to electrical reflections from the Pockels cells, and should be eliminated in a second generation design of these units already underway. Figure 1.05(b) shows a twelve shot overlay of the sliced long pulse at 1 ns/division. The digitizer was triggered from the "command to Q switch" signal so that the good overlay illustrates not only good pulse height reproducibility (short term variance $\leq$ 5%) but also the

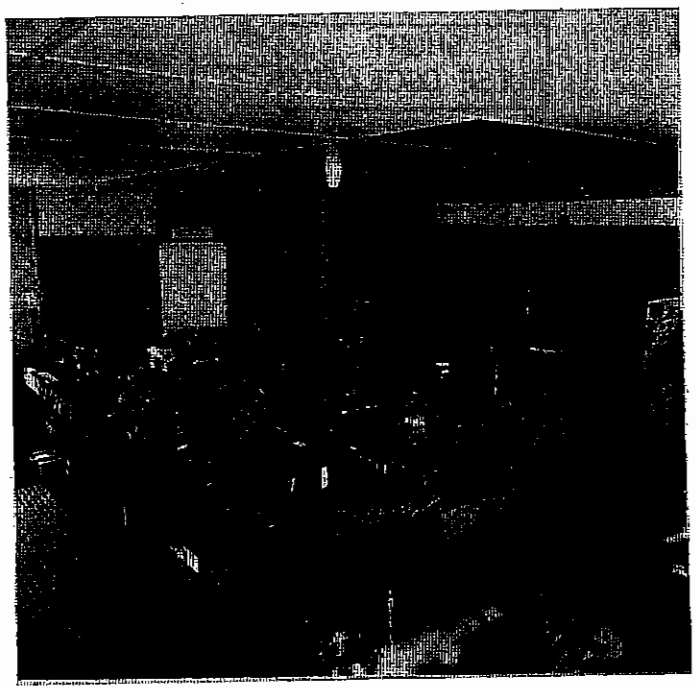

FIG. 1.04 PHOTOGRAPH OF SYNCHRONISED OSCILLATOR, SWITCHOUT AND PRE AMPLIFIERS WITH COVERS REMOVED.

very low jitter of the pulse timing. The mode locked pulse train, as seen at the second polarizer of the auxiliary switchout, is shown in Figure 1.05(c). The first of the missing pulses is that transmitted by the secondary switchout and the second is that selected by the main switchout.

After the switchout stages, and preamplification, the short and long pulses can be injected in any combination into the two beam lines of Vulcan, to service the wide range of experimental requirements. The beams are directed by fixed splitters and selected by the remotely controlled kinematically relocating mirrors M3 and M4 (see Figure 1.03). Other kinematic mirrors (M1 and M2) can select a separate "stand alone" long pulse slicer for use when experiments require extended periods of long pulse only operations (when it would be inefficient to have to run the short pulse oscillator merely to drive the long pulse switchout). The stand alone unit is driven by a laser triggered spark gap, and produces nanosecond pulses with a contrast ratio 10^8 from two tandem stages. Careful design of all optical path lengths maintains a fixed pulse timing in all options.

The simple but effective synchronized pulse scheme described here has several advantages over other techniques - such as synchronized mode locked oscillators or regenerative amplifiers.

(i) The relative pulse timing is drift-free and essentially jitter-free, because it is fixed only by a cable length, and it is not dependent on oscillators nor switchouts staying finely tuned during long periods of routine operations.

(ii) Reduced complexity.

(iii) The duration of the long pulse is much more flexible than would be the case if two mode locked oscillators were used. Here the ability to provide pulses of several (or even many) nanoseconds is retained, whereas a mode locked long pulse oscillator would be limited at a little over 1 ns. Pulse duration versatility is extremely important when servicing a user facility. During the past year pulse durations varying over three orders of magnitude have been used in different experiments! (50 ps - 40 ns).

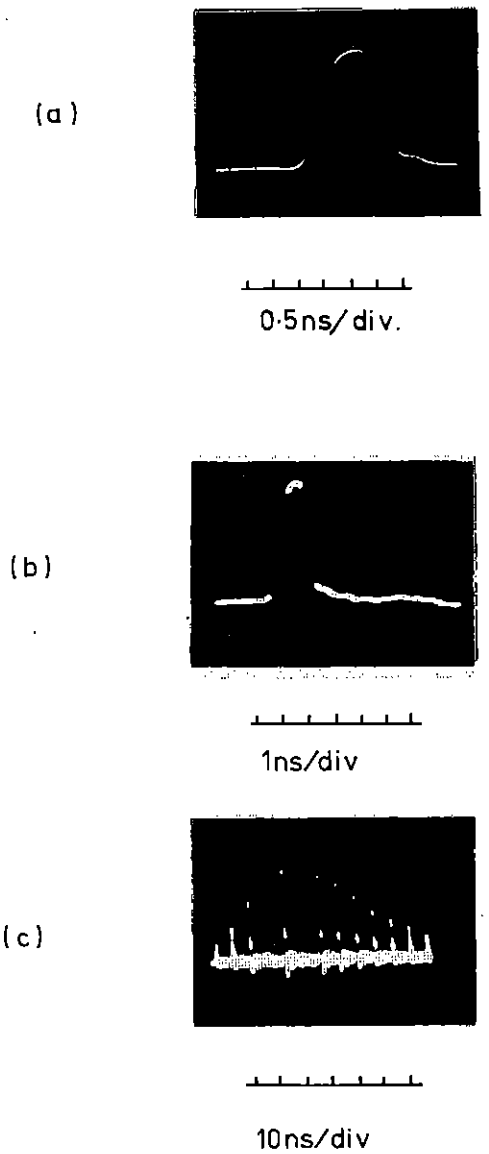

Figure 1.05 Pulse waveforms from synchronised oscillators.

(iv) The non-linear disadvantages of regenerative amplifiers - in grossly enhancing oscillator and switchout variations - are avoided.

(v) The use of organic dyes, common in the regenerative amplifier approach, is avoided. Since these dyes tend to be chemically unstable, their elimination reduces maintenance and improves reliability.

(vi) The possibility exists of performing rudimentary pulse shaping with this system, either by adding the short and long pulses or by inserting electrical filters between the short and long pulse slicers to modify the pulse shape.

M S White, A Damerell, I N Ross, R W Wyatt, E Hodgson (RAL), C L M Ireland, J K Wright (J K Laser Ltd)(Short pulse oscillator development)

1.3.3 Computer Control and Data Acquisition

1.3.3(a) General Development

The computer based control system has been updated in line with the laser enhancement programme. The colour graphics mimic diagram now includes the latest oscillator modifications and also shows the beam path in different colours depending on the type of beam in use. Modifications to the colour hardware have brought the colour palette under computer control. Any 16 colours may be selected for a display from the full range available. This new feature has been particularly useful for production of colour coded intensity images.

The use of the computer has been extended. It now monitors the second harmonic conversion efficiency and also produces a daily summary showing amplifier voltages and energies associated with each shot. A data base to facilitate target stock keeping is available and this may be operated from a terminal in the target manufacturing laboratory.

An Apple microcomputer has been linked to the GEC 4080 using a V.24 interface to give the Apple access to the graphics output and other facilities of the

main computer. The Apple will be used to monitor a flash lamp test facility now under construction.

M Forster (RAL)

1.3.3(b) Predicting the Output Energy of the Laser

The need to change the laser configuration from one shot to the next, depending on the target chamber in use, has increased the possibility of errors in setting the amplifier gains in the system. This could lead to damage of the optical components if the gain is too high. It was therefore decided that the computer should be able to predict the energy of the shot as part of the initial checks thus allowing the operator to tune the laser to the required energy. Should the energy at any part of the amplifier chain be above the optical damage threshold, the computer will stop the shot until the settings were reduced.

To predict the output energy to the required accuracy, three things need to be known:

(i) The formula relating amplifier gain to small signal gain.

(ii) The variation of small signal gain with amplifier voltage setting for each amplifier in the system.

(iii) The losses at each stage in the system.

The first two are known or easily determined, but the latter is difficult to quantify and may vary dramatically with changes in the alignment of the beam (eg, through pinholes etc). It may well be necessary to normalise the results of a prediction to the measurements made on the previous shot by including variable 'lumped losses' in the beam.

The program presently used operates in 'stand alone' mode in which the operator defines the laser configuration and settings from the oscillator to the output. He receives a printout of the energy at each point in the chain.

The results compare closely with actual conditions when the laser beam is well aligned.

A routine has been written to be included in the laser control program 'LASR', to model the whole chain from oscillator settings to output energy. This reads the settings of each element automatically, thus giving a prediction for the current system. It will be installed when a complete set of readings are available to the computer.

A development of the prediction routine is planned in which the predictions and the results of the shot will be displayed graphically and recorded to give the operator a clearer indication of where any discrepancies occur.

C J Reason and D Vigar (RAL)

1.3.3(c) Beam Profile

The video recording system for acquiring beam intensity profiles has been used in the near field and has given useful results. The system is based on a video disc recorder capable of recording six simultaneous images eight times. (The system can be extended to eight images making a total of 64 recorded images.) The cameras used incorporate IR sensitive tubes (Siemens XQ1112 or equivalent) which have a good response at 1.05 μm and do not suffer from the interference patterns typical of silicon vidicons when subjected to coherent laser light in the near IR. Over-illumination can, however, easily damage the IR sensitive tubes by burning a permanent image into the target.

The recorded data can be viewed immediately using the video output from the disc and can also be acquired by the computer, using a Lecroy 2256 A/D converter which digitizes the image line by line. The data can then be presented using standard contouring routines, in colour if desired, or as a probability density function (PDF). A PDF is a histogram of the number of data points at a particular intensity plotted against the intensity. An ideal super-gaussian beam profile represented as a PDF shows a peak corresponding to the plateau and another peak corresponding to the base at zero intensity. In practice the peak corresponding to the plateau tends to

flatten out and its width indicates the amplitude of the superimposed spatial noise. In the case of a very poor beam this peak may disappear altogether. A typical PDF together with the corresponding grey level representation is shown in Figure 1.06.

If the data points are summed starting from the maximum value and working downwards then the level at which the total number of points defining the beam area is reached can be taken as the background level and subtracted from the data. The fill factor can then be estimated by dividing the mean intensity over the beam area by the peak intensity. Alternatively the mean intensity over the beam plateau may be determined from the PDF and this used to estimate the fill factor instead of the peak intensity; clearly this will give a more optimistic result. All this information together with the ratio of the peak intensity to the mean plateau intensity is extracted from the data by the computer and printed out together with the PDF. An unfortunate aspect of using a PDF is that it it extremely sensitive to deficiencies in the ADC and can indeed be used as a means for testing an ADC. Any missing codes for instance will show up as zeros in the PDF. The Lecroy 2256 has been characterised by anlysing a triangular waveform which should give a horizontal line PDF. It showed several discontinuities, the major one being where the output changes from 00001111 to 00010000. Steps have been taken to minimise these effects by digital filtering and other techniques.

While very little running experience has been gained with this system it is felt that the PDF will give a more objective view of the state of the beam than a single line cross-section since the PDF does represent all the digitized data. It is also more amenable to analysis than a 2D grey scale representation of the beam. However, an operator may prefer the latter but these take a long time to produce using the computer and are impractical for routine use on a six beam system. The direct output from the video disc is, of course, available and may be used to supplement the PDF.

There are inadequacies in the system due to noise, non linearity in the camera and spurious background signals. The use of solid state cameras with fibre optic plates to de-cohere the laser light and prevent fringing effects should overcome some of these problems. At present, however, the video disc

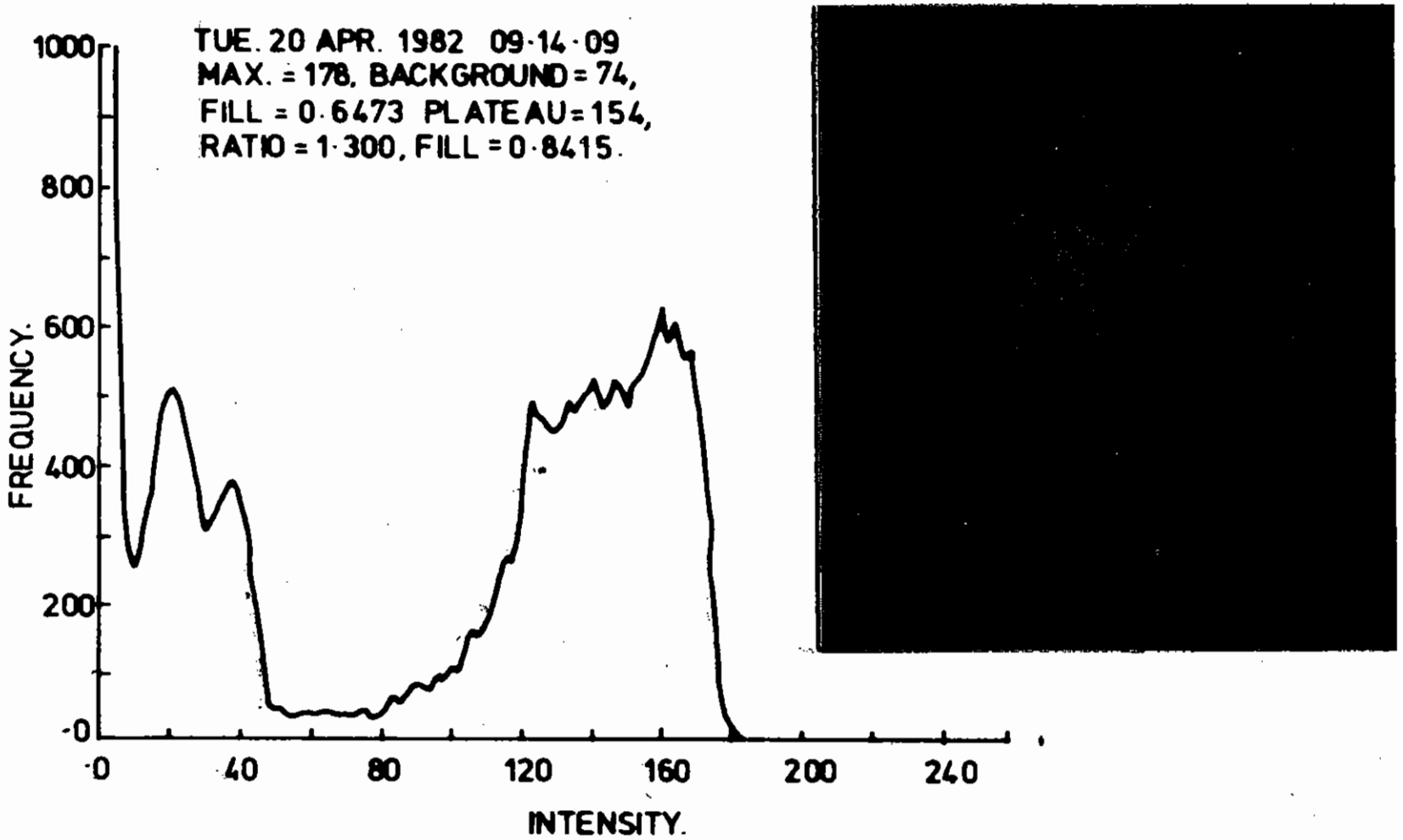

Figure 1.06 Beam profile, probability density function and corresponding intensity display.

recorder seems the only economical solution for 2-dimensional data recording for a multibeam laser.

P Gottfeldt and C J Reason (RAL)

1.4 Target Areas

1.4.1 Target Area TA1

The 6 beam compression facility has operated very successfully with green beam irradiation of targets almost exclusively over the last year. Initial experiments were performed using one 15mm thick KDP harmonic generator crystal for each of the incoming 6 infra-red beams. Due to laser output limitations, however, with this system infra-red power densities at the crystals were low ($\sim$1GW/cm^2) leading to low conversion effiencies ($\sim$30%). Total green energies in 6 beams entering the target chamber were only about 100 Joules in 1ns in this mode of operation. To overcome this problem major modifications were made to the splitting and conversion optics at the end of the laser system in the middle of the year. Rather than dividing the infra-red output from each of the 3 final disc amplifiers before conversion, one harmonic crystal was placed after each disc (so doubling the power density on the crystal) and splitting from 3 to 6 beams is now performed in the green in the target area. This modification enabled the green energy routinely delivered to the target chamber to be increased to the 200 Joule level (in 1 ns) with conversion eficiencies (including reflection losses) of $\sim$ 60%. During February 1982 the 6 beam alignment and beam reference optics were once again converted so that compression experiments driven by 6 infra-red beams could commence in March 1982.

Throughout the year several major diagnostic improvements have been introduced. A second vacuum air-lock was installed on the chamber thus enabling both microballoon and backlighting targets to be introduced. With this air-lock system all types of X-radiography and emission experiments using the X-ray streak camera can now be performed without letting the target chamber up to air. New miniature zone plate and pinhole cameras have been built and used during pulsed X-radiography

experiments performed when the synchronised stacked driving pulse and short X-ray backlighting pulse became available from the laser system in the middle of the year. Equivalent plane cameras were installed and used routinely on 4 of the 6 green beams. As well as for target diagnostics these cameras were used to monitor improvements in beam quality achieved by reducing air turbulence at various points in both the laser and target areas.

Compression experiments diagnosed by X-radiography using short pulse backlighting allowed 2-d pictures of the core at peak compression to be obtained for the first time. During these experiments the focusing of the 6 f/1 lenses with respect to the target was varied in order to produce the most spherical compressed core. The optimum focal condition was determined empirically by observation of the radiographs to be with $d/R = 3.5$, where d is distance of the lens focus beyond target centre and R is the radius of the target.

The majority of experiments carried out during the year used 6 beams for compression of spherical targets but in addition the versatility of the 6 beam facility was exploited by using either 1, 2 or 3 beams to irradiate many microdisc or foil targets. These experiments used X-radiographic and optical probe techniques to study thermal smoothing (Section 4.4), target stability during ablative acceleration (Section 5.4) and coronal plasma uniformity (Section 3.7)

C Hooker, S Knight and P Rumsby (RAL)

1.4.2 Target Area 2

Beam was routinely available throughout the year at ω_o, $2\omega_o$ and $3\omega_o$. Changeover time can be as little as two hours. The argon ion laser was upgraded to work at 351 nm to aid focusing at the third harmonic. Using the expanded beam from this laser it was found that the spherical aberrations of the f2.5 fused silica (spherical) doublet produced unacceptably large intensity variations when the lens was used to produce large area spots by defocusing. An f1.5 aspheric doublet in fused silica

was commissioned and is now available. The design and manufacture of this doublet is described in Section 1.4.3. This lens should be capable of spanning the range between ω_o and $4\omega_o$ by adjustment of the element spacing.

Some experimenters have found it advantageous to work with their own purpose-built target chambers so that related experiments can be performed elsewhere with other lasers. The simultaneous electron-photon excitation experiment described in 6.3 is one example. Another is the X-ray spectroscopic survey work discussed in 6.5 for which a small chamber containing only a simple target mount was built. This chamber can be mounted on any of the spectrographs and the spectrographs can be set up in any convenient place in the target area. It was found to be easy to bring a beam to the spectrograph and to focus it. During the spectrographic run, another experiment was in progress in the main TA2 target chamber and beam was switched from one experiment to the other with a moveable mirror. This experiment used the fundamental whereas the spectroscopists were using $2\omega_o$. A further experiment was being run in TA1 at the same time.

1.4.3 Aspheric Lens Design and Production

The extension of VULCAN's wavelength range into the blue by third harmonic conversion has brought with it the need for a suitable focusing lens. The present f/1 doublets, manufactured from BK7, whilst suitable for operation at the 1.054 μm and 0.527 μm are strongly absorbing at 0.351 μm. It was therefore decided to design a new lens from vitreous silica for operation in the single beam target area, capable of handling ~50 J at the third harmonic in the long pulse >500ps mode. With the experiments currently under consideration a lens with an f number around 1.5 seems to be the most useful. It was also decided that it would be worth designing a lens that would cover the entire wavelength range from the fourth harmonic to the fundamental.

The design finally adopted considered many factors. The ratio of the radii of curvature of the two components dictated the spectral coverage of the lens as well as power sharing between components which reduces the asphericity of first component and hence the ease of manufacture. The separation of the components is dictated by the exclusion of third order and lower-order ghosts at λ = 0.351 μm. The power handling at the fourth harmonic is therefore $\leq$ 20 J and hence the minimum B integral criterion is not operative in the design.

The final lens, based on these criteria turns out to be fairly reasonable (Figure 1.07) in terms of manufacturing difficulty the radii of curvature being within the standard range of optical tools and the maximum departure of the aspheric form from the best-fit-sphere being only 0.02mm.

A lens based on this design satisfies our design criterion (that the blur-circle minimum should be limited only to the uncorrectable divergences in the laser beam) over its entire operational wavelength range (0.351 μm to 1.054 μm).

1.4.3(a) Manufacture

The aspheric component of the lens was manufactured by CNC machining of a blank initially prepared by grinding to its best-fit-sphere. By suitable choice of machine and head speeds, grinding wheel grit-size and angular rotation speed of the stock, a finish could be obtained that was smooth and fine enough for the component to have an overall transmission of around 50%, sufficient for the lens to be viewed through a Twyman and Green interferometer without further polishing. At this stage the lens turned out to have roughly four fringes of residual spherical aberration at a wavelength of 0.5 μm. Figure 1.08a. The final polishing of the lens from this state proved to be a relatively trivial operation giving a lens with a final residual of less than one wavelength Figure 1.08b. It is fairly easy to compute from this stage that such a lens would meet its wavelength performance requirement.

D J Nicholas and J E Boon (RAL)

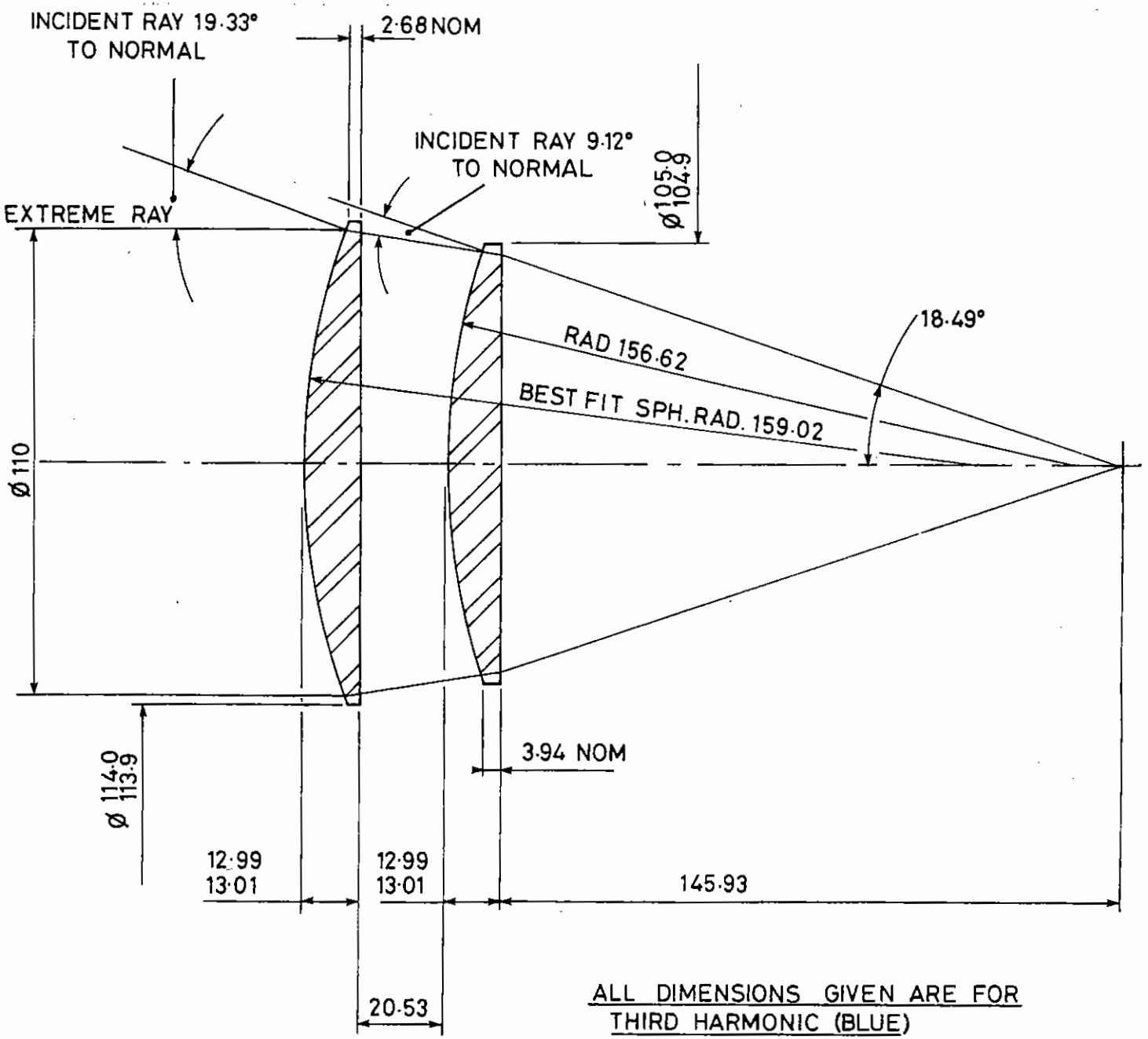

FIG. 1.07 NEW F.1.5 ASPHERIC DOUBLET LENS DESIGN IN VITREOUS SILICA.

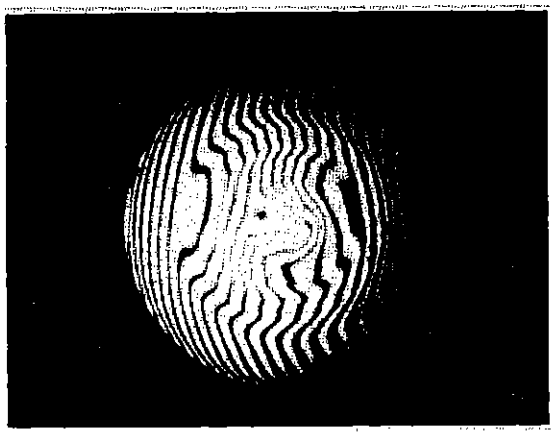

1.08 (a) INTERFEROGRAM PICTURE OF LENS TAKEN WITH A ZYGO INTERFEROMETER USING He Ne (0·632 μm) AFTER A LIGHT HAND POLISH.

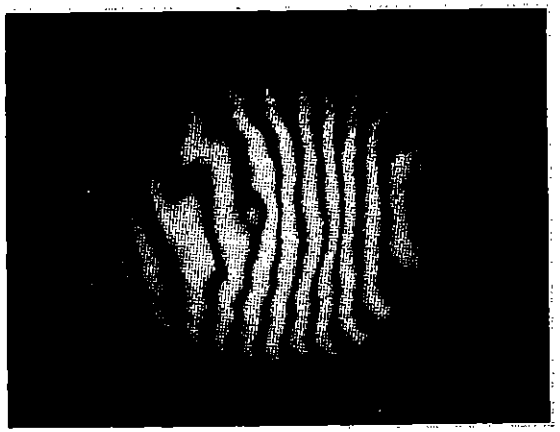

1·08 (b) PICTURE OF SAME LENS AFTER FINAL POLISHING IN SAME INTERFEROMETER AND AT THE SAME WAVELENGTH.

1.5 Computational Studies

1.5.1 Uniformity of Illumination

An efficient ablative spherical implosion is only possible if the driving pressure is uniform to a few per cent (1.04). In a multibeam irradiation system the required pressure uniformity can be attained by shaping the beams and making use of smoothing mechanisms within the target to redistribute the incident energy. We have investigated the illumination uniformity given by various laser beam characteristics and also the effect of varying amounts of smoothing. Previous studies of illumination uniformity have been made by Nicholas and Evans (1.05) and Howard.(1.06).

Firstly we consider the case of six laser beams focused by ideal lenses. The distribution of energy in each beam is assumed to be super-Gaussian with power p such that the intensity at the final lens is given by $I(y) = \exp - [y/(aY)]^p$ where y is the distance from the axis of the lens, and Y is the radius of the lens. The degree to which the lens is filled by the beam is determined by the parameter 'a'. The beam is focused onto a spherical target of radius R a distance sR beyond the centre of the target. The energy deposited by the six beams is summed at each point giving the distribution of energy over the whole target. The surface of the target is then searched for the maximum Emax and minimum Emin levels of energy deposition and the ratio of these Emax/Emin is taken as a measure of the degree of uniformity. The calculations were checked against similar calculations made by Howard (1.06) and were found to agree to the accuracy with which his published graphs could be read. Figure1.09(a) is a plot of the percentage non-uniformity $100 \times (Emax/Emin - 1)$ for six f/1 lenses and various beam shapes. Refraction in the expanding plasma is neglected and absorption is assumed to be independent of the angle of incidence. The ray from the extreme edge of an f/1 lens grazes the surface of the spherical target when $s = 2.236$. For larger values of s the outer rays miss the sphere completely and energy is wasted. Of the cases considered the Gaussian ($p = 2$) gives the greatest uniformity, giving approximately 10 per cent

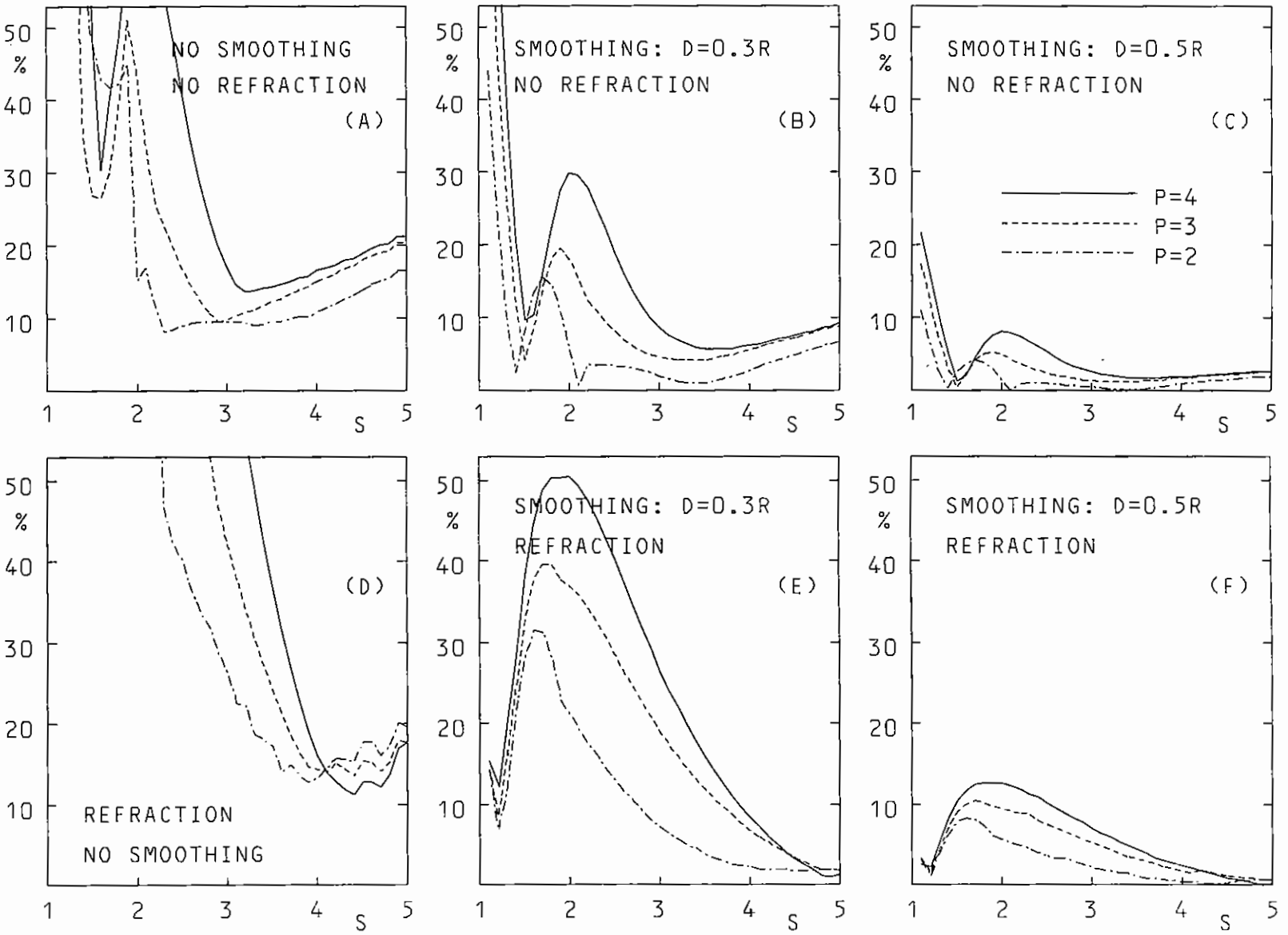

Figure 1.09 Percentage uniformity given by 6 f/1 ideal lenses with and without refraction and with different amounts of smooting within the target characterised by the half-width D of the smoothing function relative to the target radius R. For each case the uniformity is drawn for beam profiles which are super-Guassian with different powers p = 2,3,4 (legend in Fig 1.09c).

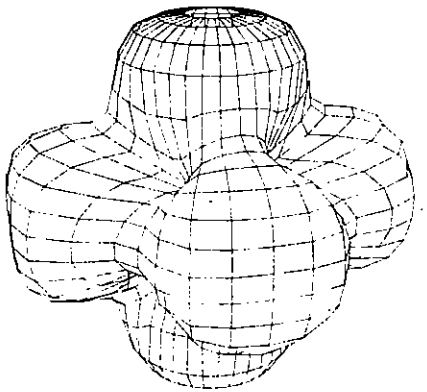

$s = 1.2$

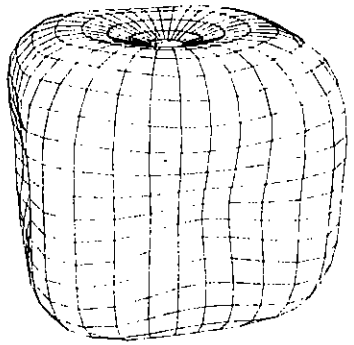

$s = \sqrt{5}$

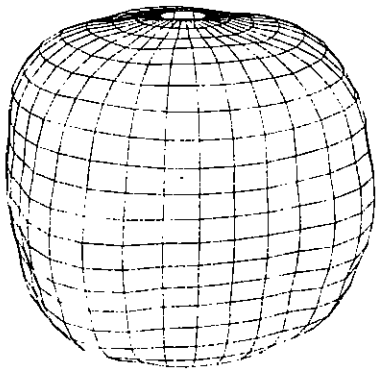

$s = 3$

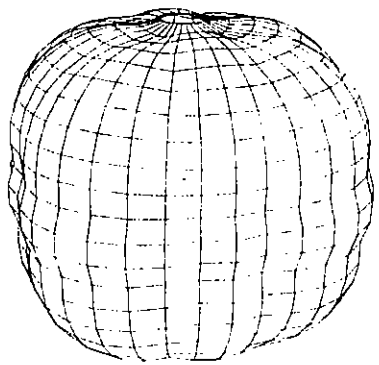

$s = 4.5$

Figure 1.10 3-D representations of the uniformity given by fourth-power super-Guassian beams focussed by 6 f/1 lenses at a position 5 times the target radius beyond the target centre.

non-uniformity when s >2.2. The cases considered here are a small representative subset of the many ways of illuminating a target with six beams, and greater uniformity may be possible for a specially designed combination of lens, beam profile and target size (1.07). To be of practical use, the calculated uniformities must be relatively undisturbed by changes in size of target, refraction, and angular dependence of absorption which will inevitably take place during an implosion. The cases considered here show what can be achieved without 'trying too hard'. A system carefully designed for a higher degree of uniformity is more likely to be sensitive to refraction etc. In Figure 1.09(a) the uniformity is relatively insensitive to changes in the target size (changes in s) provided s does not fall below some value s_o, where $2 < s_o < 3$, at which the nonuniformity increases drastically. The effect of refraction is discussed below. A further constraint is the need to extract energy from the laser efficiently, and a high power super-Gaussian with a large fill factor, a, is optimum. In this respect, a fourth power super-Gaussian is prefereable to a Gaussian profile.

The case of a fourth power super-Gaussian (p = 4) with a = 0.7 is depicted in Figure 1.10. The diagram is a spherical equivalent of a polar diagram in which the distance of the surface from the centre at a particular angle is proportional to the energy deposition at that angle. Two beams are directed at the target from above and below, and the other four beams are arranged around the equator. At low values of s (eg, s = 1.2) each beam only illuminates a small area of the sphere and energy maxima occur in the direction of each of the six lenses. At the condition for grazing incidence of the outer rays, s = 2.236, the position of maximum energy deposition occurs in the beam overlap region and there are minima in the direction of each lens. At large s (eg, s = 3) the angle of beam overlap is large and is sufficient to reduce the minima in the direction of each lens because each beam contributes to the energy deposition at an angle of 90° to the beam axis. When strongly defocused (eg, s = 4.5) much of the beam misses the targetand only energy passing through the centre of the focusing lens hits the target. Consequently, the strongly defocused cases are equivalent to cases in which slower lenses and larger fill factors, a, are used.

Refraction and absorption are ignored in Figure 1.09(a). A full treatment of these factors is not attempted here and the results obtained would vary considerably with temperature, density, irradiance, pulse length, wavelength etc. A simplified treatment is given to produce a measure of the importance of thes effects. It is assumed that the plasma is steadily ablating with constant velocity in the underdense region, leading to a density profile proportional to $1/r^2$. The ray paths can be calculated analytically in such a plasma. It is assumed that the energy in each ray is absorbed at the point of closest approach to the critical surface with an absorption factor which is proportional to the square of the cosine of the angle of incidence. The results in Figure 1.09(a) are repeated in figure 1.09(d) with these assumptions about refraction and absorption, and the energy depositon is found to be considerably less uniform. The assumptions about refraction and absorption will be unrealistic in many cases and the inverse square density profile may lead to an overestimate of refractive effects, but Figure 1.09(d) shows that these factors are important and may result in less uniform energy deposition than would otherwise be expected. The differences between Figure 1.09(a) and Figure 1.09(d) cannot be attributed mainly to the reduced absorption at large angles of incidence because the tendency of refraction to move the point of incidence of a ray is also important. In fact, absorption and refraction tend to work in opposite directions as regards the pattern of energy deposition on the target. For the cases plotted in Figure 1.09(d) the best uniformity is about 15% and this can only be obtained by focusing a large distance beyond the target (s >4).

Thermal conduction is an important mechanism for smoothing non-uniformities in energy deposition. Thermal smoothing is more effective over relatively short distances and we model its effect by convolving the incident energy distribution with a smoothing function. We assume that the energy smoothing is diffusive, in which case energy input at one point on the surface, when allowed to diffuse for some characteristic time, will have an energy distribution which might be expected to be roughly Gaussian. We choose the smoothing function

$$f(\mu) = \exp\left[-\left(\frac{2}{\mu_o}\right)^2 \sin^2\frac{\mu}{2}\right]$$

where μ is the angle through which energy diffuses on the surface of the sphere. For $\mu c \frac{\pi}{2}$, $\sin\frac{\mu}{2}$ is approximately equal to $\frac{\mu}{2}$ with an error of about 10% at most, and consequently $f(\mu)$ is a good approximation to a Gaussian in the cases of interest. This form for $f(\mu)$ is chosen because the convolution integral is analytically integrable in one dimension leaving only integration in the second dimension to be caluclated numerically. The energy deposited $E_c(\phi)$ by one beam at an angle ϕ on the sphere with respect to the axis of the lens is given by

$$E_c(\phi) = 2\pi \int_0^{\pi} E\left(\psi I_o\left(\frac{2}{\mu_0^2}\ \mathrm{Sin}\phi\ \mathrm{Sin}\psi\right)\right) \exp\left(\frac{2}{\mu_0^2}\ (\cos\phi\cos\psi - 1)\right) \sin\psi = d\psi$$

where $E(\psi)$ is the distribution before convolution and I_o is a zeroth order Bessel function. In Figure 1.09(b) the half-height half-width $D(D = \mu_o \quad (1n2)^{\frac{1}{2}})$ of the convolving Gaussian is equal to 0.3 times the target radius (D = 0.3 R), and refraction and angular variation of absorption are ignored as in Figure 1.09(a). Figure 1.09(c) is for a similar case except that the smoothing is stronger, D = 0.5 R, and here the uniformity is better than 10% for all cases when $s > 1.5$. As expected, the Gaussian (p = 2) gives greatest uniformity at a level around 1-2%. Comparing Figure 1.09(b) and 1.09(c) it appears that, in the case of a six beam laser, thermal smoothing will only be effective if the distance over which energy is smoothed is approaching half the target radius. In the case of smoothing by thermal transport this suggest that the absorption region must stand-off from the ablation region by a substantial fraction of the target radius, although determination of the exact stand-off distance requires an improved treatment of thermal transport in the ablating plasma. Figures 1.09(e) and 1.09(f) show the effect of including refraction and absorption (in the sam way as in Figure 1.09(b)) when there is smoothing with D = 0.3 R and 0.5 R respectively. Once again, refraction increases the non-uniformity, but the smoothing is sufficient to keep it to around 10% or less when D = 0.5 R.

Only a small part of the parameter space has been searched and important effects such as refraction and absorption have been inadequately treated, but the following tentative conclusions can be drawn for a six beam system:

(i) Uniformities better than 10% require substantial smoothing within the target.

(ii) A Gaussian beam profile gives better uniformity than a high-power super-Gaussian.

(iii) Refraction can increase the non-uniformity substantially.

(iv) To be effective, a smoothing mechanism must spread energy over distances equal to about half the target radius.

(v) In many cases, strong defocusing (s ≈ 4) improves the uniformity.

Calculations for a 12 beam laser system with f/1.5 lenses are presented in Figure 1.11. The conditions are the same as in Figure 1.09 except that there are 12 f/1.5 instead of six f/1 lenses and the amount of smoothing is different in those cases where smoothing is included. Figure 1.11(b) shows that, without smoothing or refraction, the 12 beam system gives uniformities better than 10%. In the cases where smoothing is included, note that D=0.1 R. and 0.3 R in Figures 1.11(b) and 1.11(c) respectively, instead of 0.3 R and 0.5 R in Figures 1.09(b) and 1.09(c). D = 0.1 R does not give sufficient smoothing to cause a noticeable improvement in uniformity. However, smoothing with D = 0.3 R does have a large effect, and a 12 beam system with D = 0.3 R gives better uniformity than a six beam system with D = 0.5 R. This is to be expected because there is a smaller angular distance between beams in a 12 beam system than in a six beam system, and this reduces the distance over which the deposited energy must be spread by smoothing. Figures 1.11(d), 1.11(e) and 1.11(f) show that refraction has a deleterious effect on a 12 beam system, but for the case considered, a 12 beam system with D = 0.3 R gives a non-uniformity well below 10%.

We thank Drs R G Evans, A Raven and I N Ross for illuminating discussions.

A R Bell and D J Nicholas (RAL)

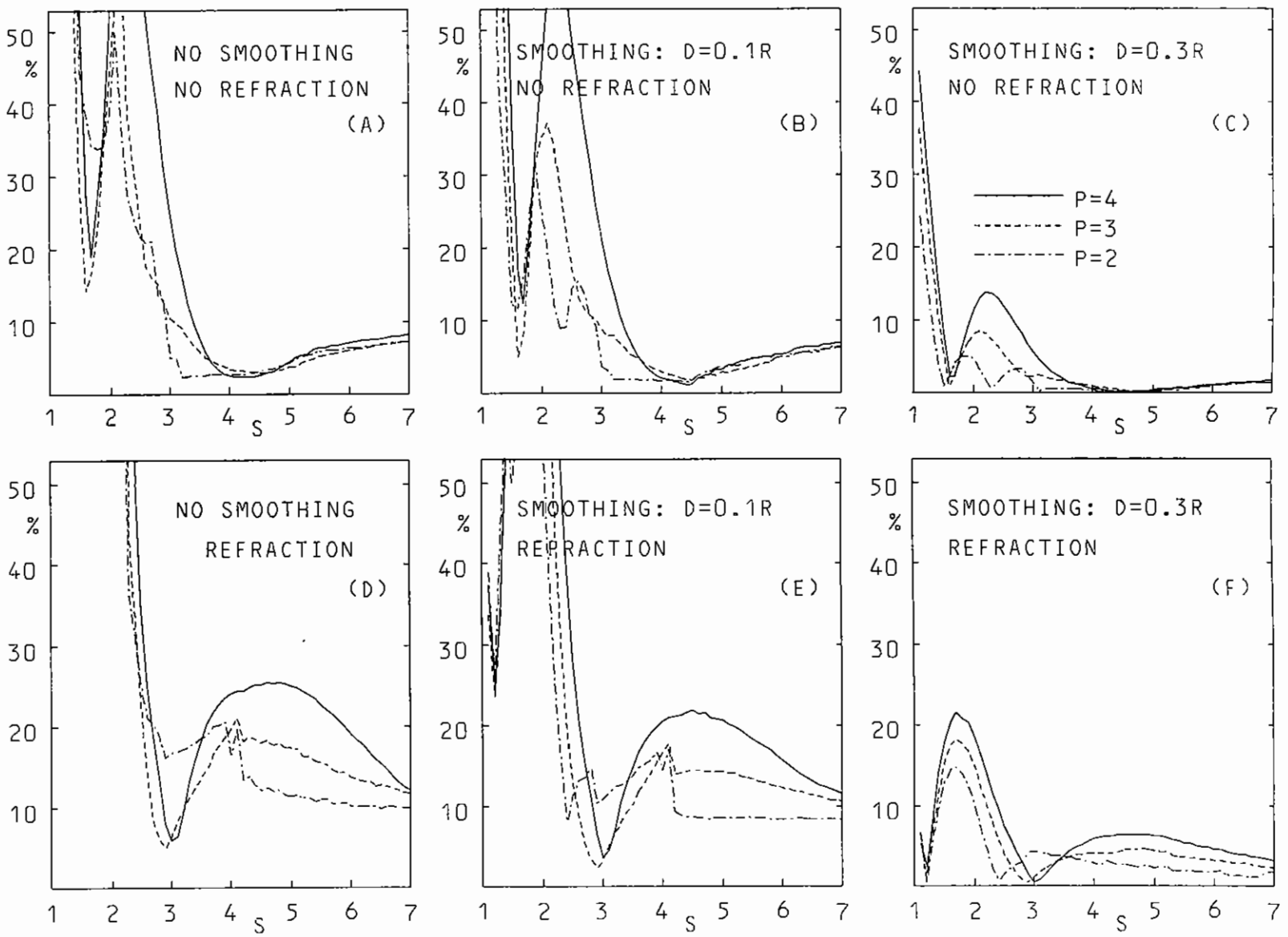

Figure 1.11 Percentage uniformity given by 12 f/1.5 ideal lenses with and without refraction and with different amounts of smoothing within the target characterised by the half-width D of the smoothing function relative to the target radius R. For each case the uniformity is drawn for beam profiles which are super-Guassian with different powers p=2,3,4 (legend in Fig. 1.11c). This figure differs from figure 1.09 in the number of beams and the amount of smoothing in Fig. 1.11b,c,e and f.

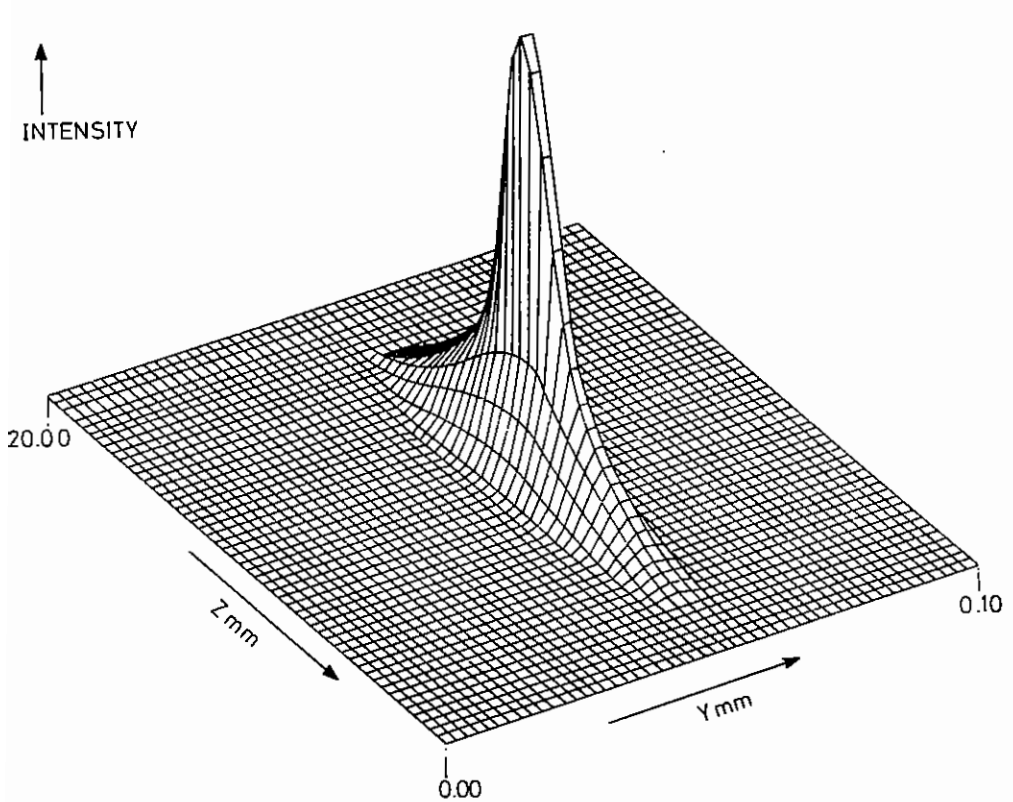

(a)

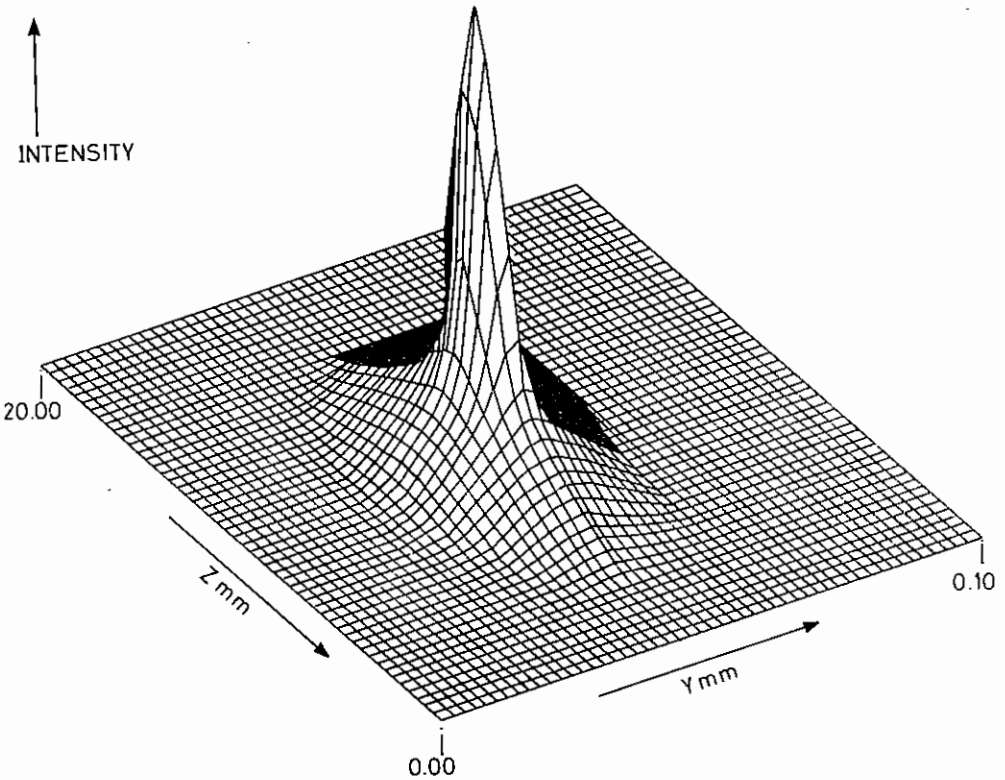

(b)

Figure 1.12 Intensity profiles within the line focus at two image screens placed at the optimal stigmatic focus in both planes.

1.5.2 Line Images

In the preliminary experiments carried out on suitable materials for demonstrating the feasibility of VUV and XUV lasers CVI appears to be a possible choice. The CVI takes the form of a carbon fibre approximately 10 mm long by 15 μm in diameter onto which the laser beam has to be focused. The experimental set-up dictates a fairly uniform energy deposition along the length of the fibre and hence a uniform intensity slit focus for the laser beam.

In the initial experiments this was fairly trivial mearly comprising of a long focal length cylindrical lens placed in front of the f/1 aspheric. To make a qualitative assessment of the performance of the focusing optics in providing a constant intensity line focus the present optical codes were modified to enable a calculation of the intensity within the line focus to be made. Figures 1.12(a) and 1.12(b) show the intensity profiles within the line focus at two image screens placed at the optimal stigmatic focus in both planes. Figure 1.12(a) which represents the line focus shows such a focus of approximately the right aspect ratio in length $\sim$ 1.2 mm and with (HWHM) $\sim$ 15μm. However the intensity changes quickly across its length indicating a non-optimal system, a factor which no doubt contributed to the negative results obtained from the experiment.

Currently computational work is in progress designing a more optimal system based on a system of cylindrical spherical lenses and on a spherico-cylindrical approach. Preliminary results are quite encouraging.

D J Nicholas (RAL)

1.5.3 Beam Transport Studies

Beam transport studies have been carried out recently using the RAL diffraction propogation code. As an illustrative example of the use of the code the high power laser was modelled in its two beam configuration just prior to the present six beam update. The driver stage is the

Quantel system modified to EV-2 phosphate glass and has a series of rod amplifiers up to 76 mm diameter (Figure 1.13) followed by a spatial filter and single ILC disc amplifier used in double pass. There is a choice of target chambers placed 30 m and 50 m downstream of the disc amplifier and the beam is finally focused onto the target by means of an f/1 doublet lens. The following beam propagation studies attempt to model the laser in its short pulse mode. In this mode, the oscillator produces a 100 ps, 0.15 GW output pulse Gaussian in space and time. The first studies were therefore concerned with propagating such a pulse, without diffraction in order to check the amplifier gain, radial profiles and general energy conservation within the numerical schemes. Figure 1.14 shows the laser pulse at the four places marked on Figure 1.13. The output pulse has a well preserved Gaussian profile of 780 GW as expected from a knowledge of the gain in the system. This shows that the FFT, inverse transforms and numerical schemes are operating correctly.

The apodiser is used to modify the beam profile to super-Gaussian. The gain at each state in the system is optimised for maximum output energy. It is then found necessary to take into account gain saturation, and this was based on the treatment by Frantz and Nordwick. In order to extract the maximum energy at peak efficiency the order of the super-Gaussian has to be around 4. The result from such an optimised system is illustrated in Figure 1.15 showing that it is possible under ideal conditions to extract some 908 GW of power from the system. This is without exceeding the damage threshold of any optical component: in particular the multilayer dielectric coatings on the final turning mirrors which are critical components. However with diffraction and filamentation included (Figure 1.16) peak intensities $\sim$ 15 GW/cm^2 occur at these turning mirrors with an input spatial noise intensity $\varepsilon = (I_{max} - I_{min})/I_{max}$ of 10^{-3}. This is well above the damage threshold for dielectric coated surfaces. The gain in the system has therefore to be reduced so that the peak intensities fall within safe working limits. This drops the possible output power of the laser, in the present case by around 20%. In order to recover the full output power the high spatial frequencies have to be removed from the beam. This requires the introduction of additional spatial filters into the system. An

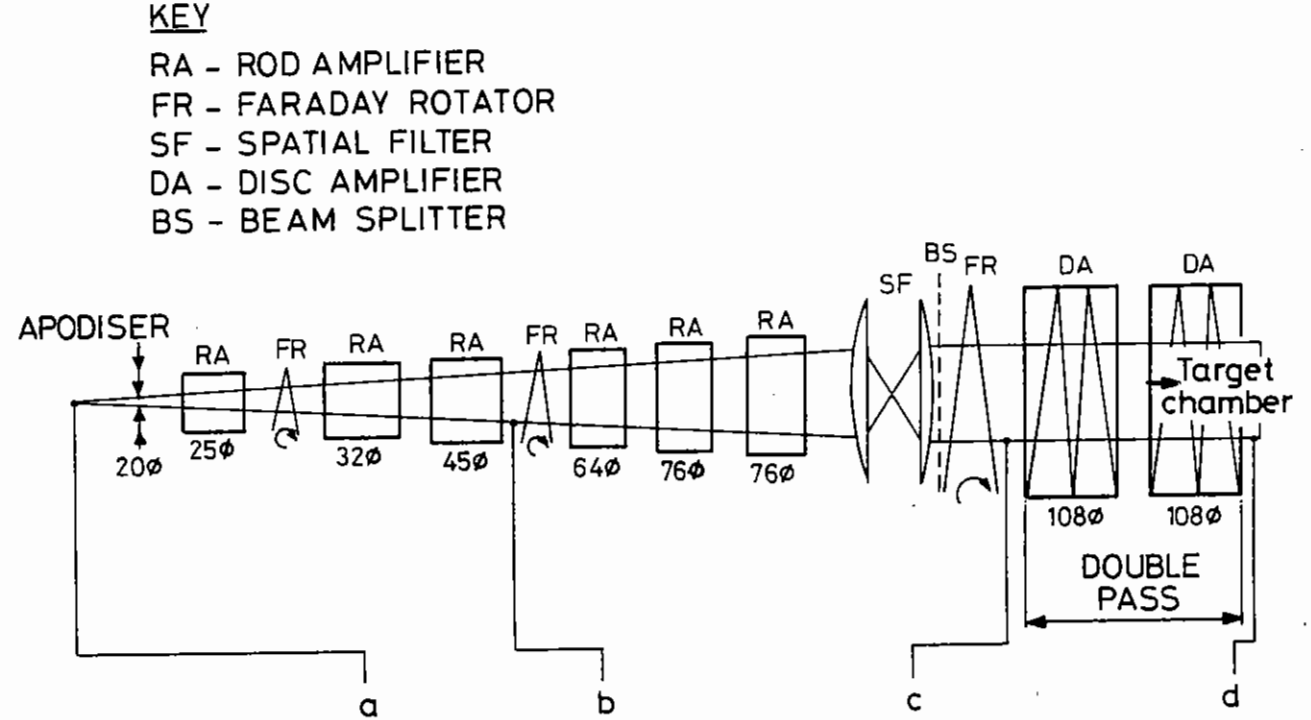

	a	b	c	d
POWER GW	0.15	13.2	10.2	946
ENERGY J	10.8×10^{-3}	0.95	7.9	73.7
ΔB NEP	0	.38	4.6	6.5
B_{TOT} RAD	0	.98	5.4	8.7

Figure 1.13 The configuration of laser components considered. The positions indicated by letters a-d are the positions for the beam profile shown in Figure 1.14 to Figure 1.16. The figures in the table refer to Figure 1.16, Pulse Length ∿100ps.

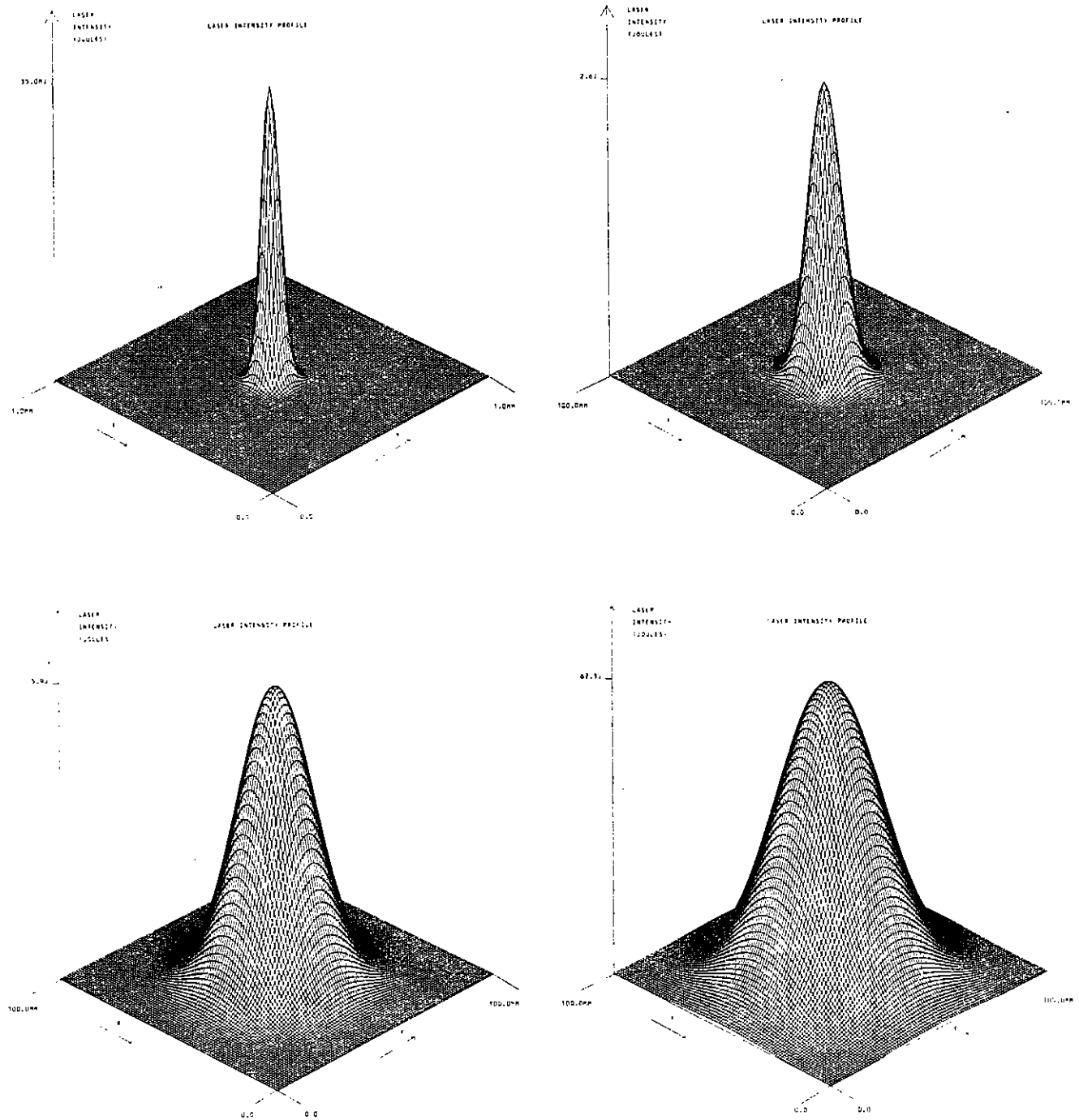

Figure 1.14 The propagation of a Guassian pulse with zero spatial noise through the system. The four positions of the intensity profiles are as shown in Figure 1.13. The propagation of an initially Guassian pulse as a perfect Guassian is one of the numerical checks made on the model.

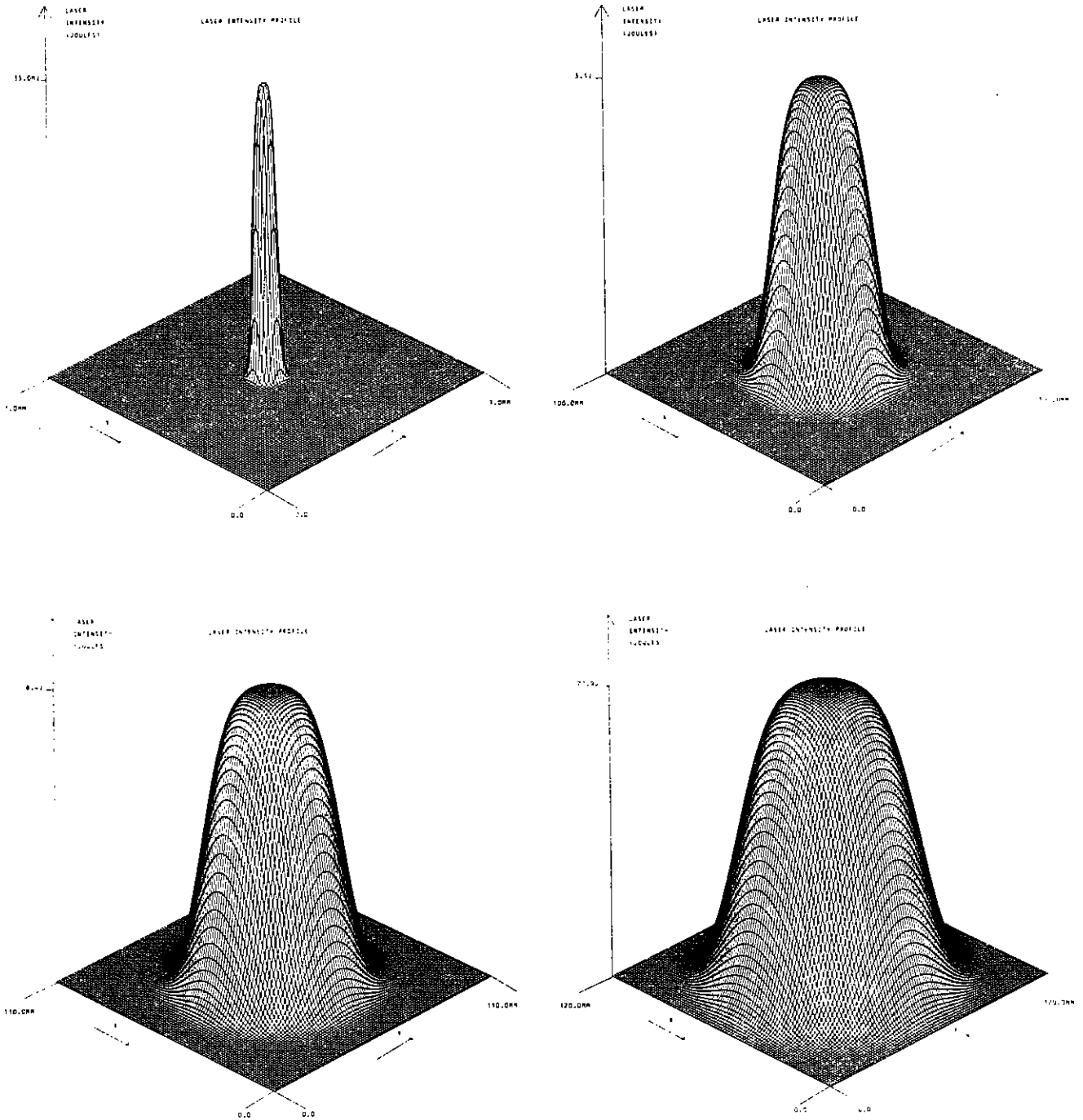

Figure 1.15 The propagation of a super-Guassian pulse $\sim e^{-(r/ro)^4}$ with zero spatial noise through the system optimised for peak extraction efficiency. The letters again refer to the positions shown in Figure 1.13 except for 1.15(a) which is immediately after the apodiser.

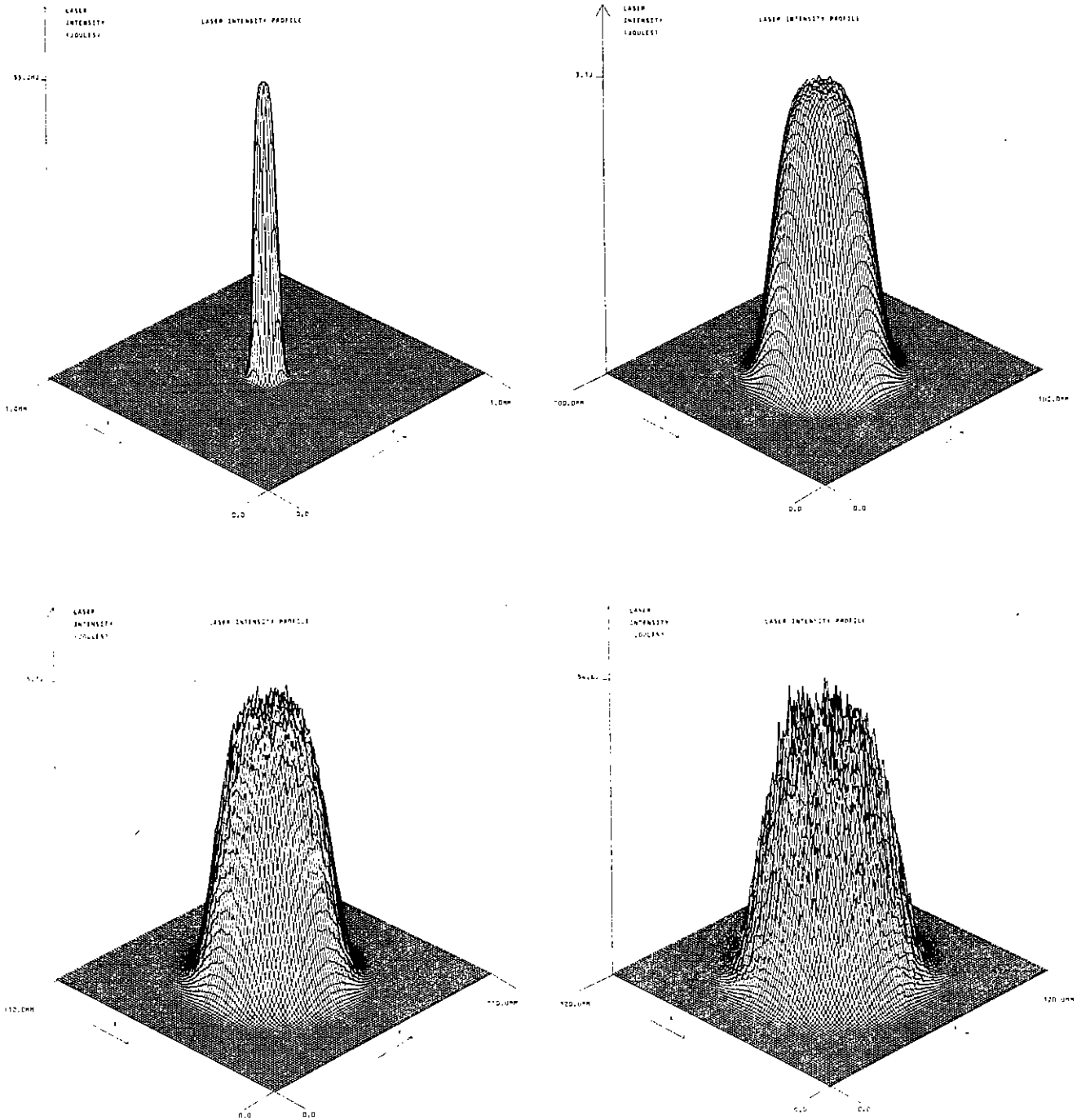

Figure 1.16 As for Figure 1.15 but with a spatially noise input $\varepsilon = 10^{-3}$ (see text). Note that the optimised output energy has dropped to 700GW compared with maximum output of 900GW (Figure 1.15(d)).

investigation of this problem with the present model indicates that it is possible to recover 70% of this lost energy by introducing an additional spatial filter between the double pass of the final amplifiers.

1.5.3(a) The Treatment of Filamentation

Coupled with the breakup of the beam, as described above, is the fact that the high intensity regions so produced can also self focus and filament often within an optical component.

The critical power P_{cr} at which the focusing due to the non-linear refractive index coefficient n_2 overcomes the diffraction spread is given by

$$P_{cr} = \frac{c\lambda^2}{32\pi^2 n^2} \quad \text{esu}$$

Such filaments, initially of radius r_o and power $P > P_{cr}$ will focus down to spot sizes of a few free space wavelengths in a distance z given by

$$Z = \frac{r_o^2 n_o}{4} \left(\frac{c}{n_2 P_{ar}}\right)^{\frac{1}{2}} \frac{1}{\left[(P/P_{ar})^{\frac{1}{2}} - 1\right]}$$

In an axi-symmetric system such as is under discussion at present the damage takes the form of a Fresnel ring pattern at the output face of the optical component. Such damage patterns have been observed on many occasions. However when the optical power greatly exceeds the critical power for self focusing (by several orders of magnitude), a spatial instability develops which tend to make the beam break up into multiple beams, and the symmetry of the system is broken. This is also observed experimentally. This effect can be modelled in the present analysis by allowing filaments to develop in a random manner in azimuth at each spatial step in the computation. These filaments are then followed, independant of the main computation, to their final focus, and an account is kept of whether this final focus is within an optical component. An example of the growth of these filaments is shown in Figure 1.17 which is an iso-intensity plot of the output pulse of Figure 1.16(d) and shows

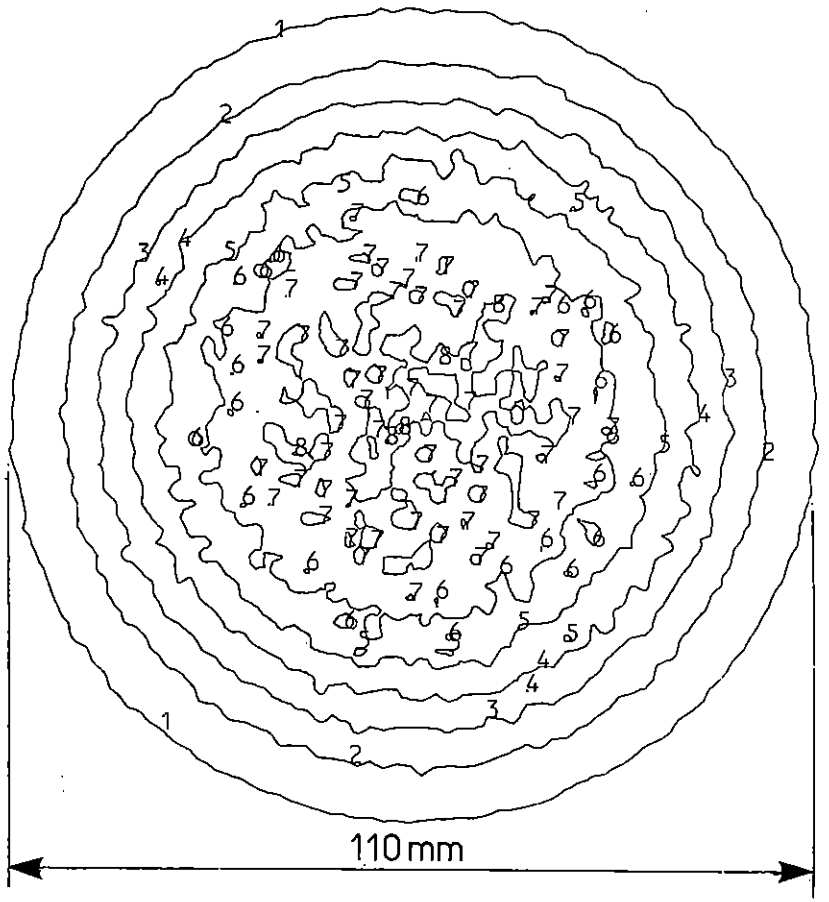

Figure 1.17 Iso-intensity contours for the beam profile Figure 1.16(d). Note the small-scale beam breakup or filamentation. The contours are at approximately decade intervals except for the very high peaks which cannot be plotted on this scale.

several well defined filamentary regions.

1.5.3(b) Beam Propagation in Air

Using the analysis developed in Section 1.53(a), beam propagation studies in air over 30 m to 50 m separating the final disc amplifiers from the target chamber were carried out. The two effects considered were linear turbulence and the combination of the non-linear part of the refractive index of air, n_2. This was taken to be two orders of magnitude less than that for Nd/glass ie $\sim 10^{-15}$ esu.

In general it was found that the output beam was effected by turbulence scale lengths L of several mm and below whilst L values of $\sim$ 2 - 10 cm such as is generally accepted for thermal temperature gradients found in temperature controlled environments proved to have an insignificant effect on the output beam. The effect of turbulence, in this linear regime scaled as $L^{-5/3}$. On the other hand n_2 contributed some 8% to the beam breakup at full power over a distance of 50 m.

It is apparent from their basic theory that what has to be avoided are regions of high shear flow in the beam line. This provides scale lengths for turbulence which is almost ideal for maximizing the perturbations on the beam output. These regions of high shear flow can readily be produced by (for example) quite modest flow rates $\sim$22 cm sec^{-1} past the end of the beam pipes (where the air inside is stagnant), placed immediately after the final amplifier. The initial input noise in this case was 10^{-4} so that most of the beam break up is due to the non-linear index in air.

1.5.3(c) Overall Laser Performance

The theoretically predicted laser output power, in short pulse mode, is shown in Figure 1.18 for a range of spatial noise $0 \leqslant \varepsilon \leqslant 10^{-1}$. Also shown is the linear small signal gain of the system. In practice, radial saturation of gain and non-uniform pumping limits the output power, even at zero spatial noise ($\varepsilon = 0$), to below this ideal limit. In practice the

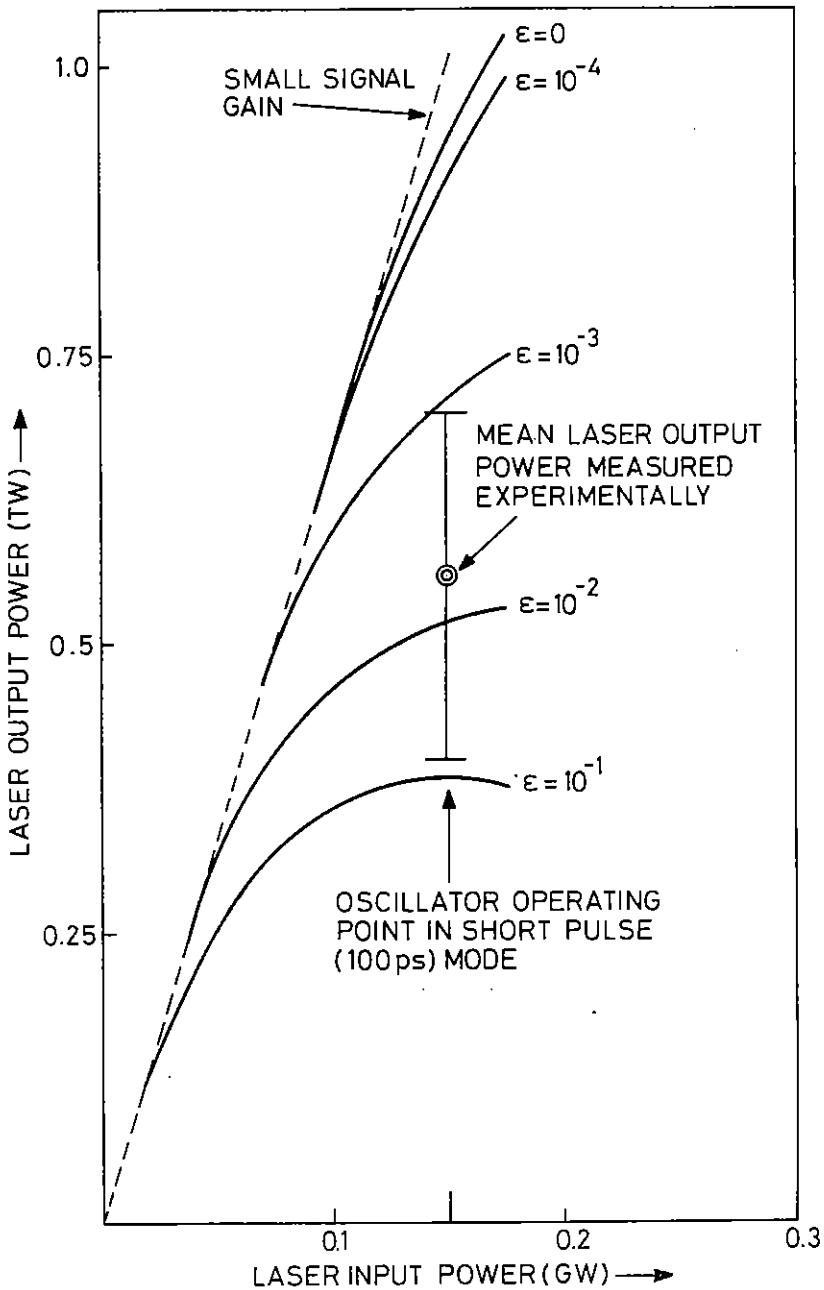

Figure 1.18 Predicted laser performance showing the effects of non-linear beam breakup on laser output power. In practice this laser configuration gave an average beam output power of around 550 GW indicating a distributive noise level $\varepsilon \sim 10^{-2}$.

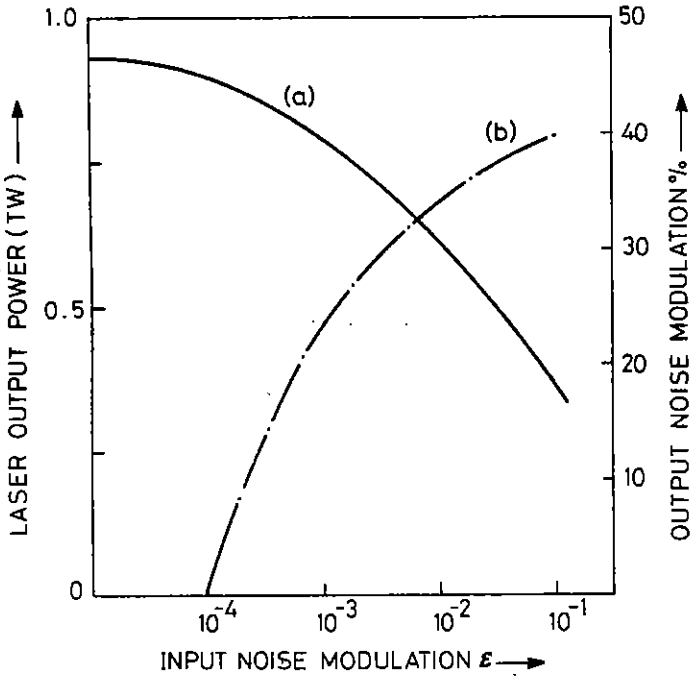

Figure 1.19 The effect of nonlinear enhancement of spatial noise intensity on the output of the laser system, (a) power, (b) spatial noise For reasonable uniformity of irradiance of a pellet the output noise modulation should not exceed ∿10%.

oscillator delivers 0.15 GW in a pulse length of 100 ps. The mean output power of the laser measurement over ∿ 200 laser shots is ∿ 550 GW. This experimentally determined point together with an error bar of one standard deviation is indicated on Figure 1.18, implying a distributed noise source $\sim 10^{-2}$, higher than the $\sim 10^{-4}$ level normally accepted for such oscillators. The output power of the laser is therefore degraded by around 30%. Only by a reduction of the growth of spatial noise, or its removal by the introduction of additional spatial filtering can the performance of this system be improved.

During a systematic analysis of the performance of this laser configuration, the effects of the introduction of additional spatial filtering and also of fully image relaying the system was considered. It is found in practice that the most cost effective improvement in laser performance could be achieved by the inclusion of either one or two additional spatial filters at strategic points in the laser chain. Around 40% of the performance loss can be recovered by inserting a spatial filter between the first and second pass of the final disc amplifier and this is the optimum position for just one additional spatial filter. Further improvement in output can only be obtained with inclusion of a progressively larger number of filters: for example a second spatial filter placed between the 64ϕ and 76ϕ rod amplifiers would recover 70% of the performance loss of the system.

Figure 1.19 demonstrates quite clearly the need for limiting the growth of noise on the beam, if only for the two primary reasons shown. The first is the obvious limitation on the beam output power of the laser. However the output pulse is finally focused onto a micro-target for laser compression and heating experiments as outlined in Section 1.53. It is found both theoretically and experimentally that the stability of the implosion is a strong function of the laser illumination uniformity. This is a combination of large scale non-uniformtiy due to beam overlap in multibeam irradiation systems and the small scale perturbations on individual beams. Currently, it is believed that illumination uniformity of around 10% will be required for volumetric implosions $\lesssim$ 500. This

would require an input noise modulation $\lesssim 10^{-4}$.

D J Nicholas (RAL)

1.6 Target Production

As in previous years, the majority of the effort of the target group has been devoted to the preparation, characterisation and mounting of microballoon targets. In addition to this however, large numbers of microdisc or lollipop type targets have been supplied for the experimental programme during the year. This situation has arisen because a short pulse backlighting beam syncronized to the main laser beam became available during the year. Using this diagnostic facility experimenters rapidly realised that lollipop type targets are ideal for carrying out experiments to study such problems as target stability during ablative acceleration and plasma thermal smoothing of laser beam non-uniformities. Suitable lollipop targets for thermal smoothing experiments have been produced relatively simply from thin (3-12μm) metal or polymer foils using high precision micro punches that have been purchased. Such punches are capable of producing high quality, burr free lollipop targets in the few 100μm diameter range from a wide range of foils. In addition mask coating techniques have been used to produce modulated or rippled lollipop targets for Rayleigh-Taylor stability experiments. Preliminary tests have also been carried out to investigate the techniques of reactive ion etching and determine whether this process can be used to fabricate modulated lollipop target. In this process polymer foils are placed behind a metallic mask and bombarded with oxygen ions of a few KeV energy produced in an ion gun. The etch (or sputtering) rate of the polymer is much higher than that of the metal mask and consequently as the process continues the shadow of the mask is imprinted in relief on the polymer foil. The tests carried out so far have shown that the polymer etch rates are relatively high and that this process has good potential for the production of modulated targets. Suitable nickel masks for the production of targets for experiments have now been specified.

For some time now the experimental ablative compression programme has had

a need for shell targets made entirely of polymer rather than the polymer coated glass shells used up to now. This is because imploded glass shells have too high an X-ray absorption at the energies (few KeV) used at present for X-radiography measurements. The lower atomic number of polymer shells, on the other hand, gives less absorption and allows transmission through the core at peak compression permitting accurate core density profile measurements to be carried out. Various unsuccessful attempts have been made in the past to obtain supplies of polymer shells produced by spraydrying techniques. Over the last year supplies of target quality polymershells have been manufactured using solvent evaporation techniques, pioneered by the Japanese at Osaka. In this process a suspension is first formed consisting of water drops in a solvent (dicloromethane) containing about 10% of dissolved polystyrene. By variation of the beating rate droplets of the required size can be formed. After this suspension is transferred to another vessel containing water, a suspension of water drops surrounded by a thin layer of polystyrene solution is formed. Heating to about 70°C while continuously beating causes the solvent to evaporate (under water) and the polystyrene shells to harden. Polystyrene has a high permeability to water and so after removal from the vessel the water inside the shells diffuses out over a few days leaving high quality hollow polymer shells.

By varying the emulsion beating rates and the polystyrene concentration it has been possible to make shells in the range 80 - 300μm diameter with wall thickness from a few to 20μm. Figure 1.20 is a scanning electron micrograph of a batch of polystyrene shells.

Gas retention lifetimes of polystyrene shells are very short even for high molecular weight gases and consequently so far it has only been possible to use empty shells in experiments. Techniques are now being developed however to use similar solvent evaporation methods to make shells from polymers with much lower permeabilities such as cellulose, polyvinyl alcohol and polyacrlonitrile. Such shells should retain gases such as argon or SF_6 for periods up to a few hours which is just long enough to be useful for experimental purposes.

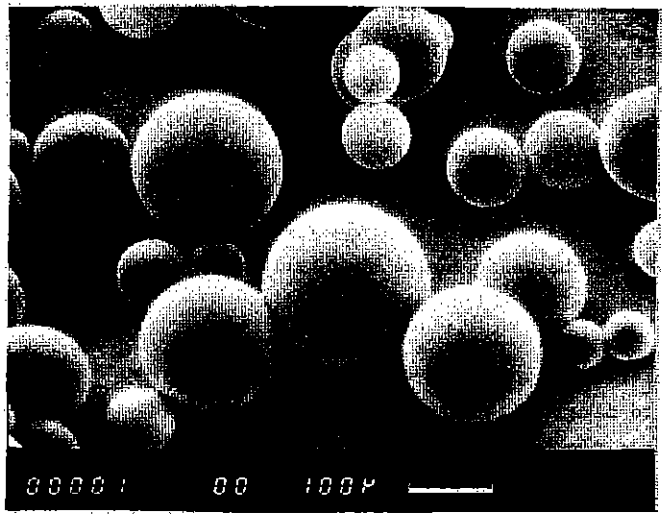

1.20. HOLLOW POLYSTYRENE SHELLS.

The target production facility has moved into a somewhat larger laboratory area during the latter part of the year. Experience with the very limited amount of air filtering equipment that was installed in 1980 over the target measuring and mounting stations has demonstrated that very clean conditions are essential for all target handling and production processes. Consequently the whole of new laboratory area is maintained under clean conditions. The area for coating operations, batch processing and other activities is maintained at class 10000 while an inner area used for all individual target handling operation is kept at class 100. Prepared targets are now stored under conditions of much greater cleanliness than previously and batches of targets for experiments are transported to the target area in sealed transfer boxes. These steps have successfully eliminated the problem of target contamination. Figure 1.21. shows a view of the target measuring and mounting area in the new laboratory.

G Arthur B C Brown B Child S Hallewell P Rumsby

1.7 Diagnostic Development

1.7.1 Curved Crystal Spectrometer

X-ray spectra emitted in the 1 - 5 keV region from laser plasmas have proved themselves a valuable source of diagnostic information (1.08). Spectra are routinely recorded using flat Bragg diffracting crystals to produce the dispersion. Time integrated spectra are obtained using minispectrometers (1.09) placed so that the entrance slit is within 6 mm of the plasma and the total separation of plasma and film is typically 6 cm. These spectrometers are thus very sensitive but their spectral resolution is limited by the plasma source size.

Time resolved X-ray spectroscopy has been performed using the same flat crystals to diffract X-rays onto the photo-cathode of an X-ray streak camera (1.10)). However constraints due to the size of the streak camera and target chamber diagnostic space mean that the separation of plasma and cathode cannot be less than $\sim$ 30 cm. Since the brightness of a spectral line varies as the square of the distance to source, for a constant

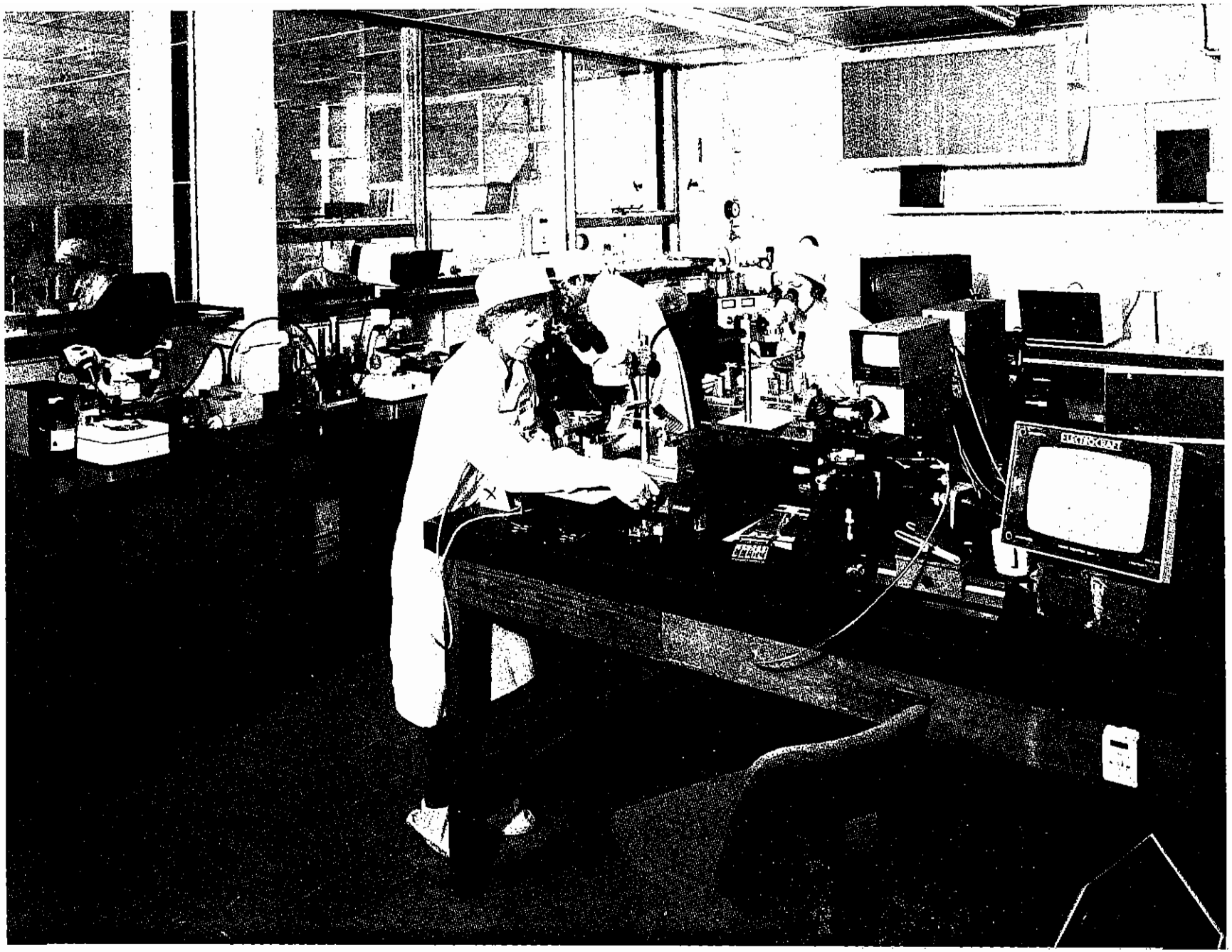

FIG.1.21. NEW TARGET MEASURING AND MOUNTING LABORATORY.

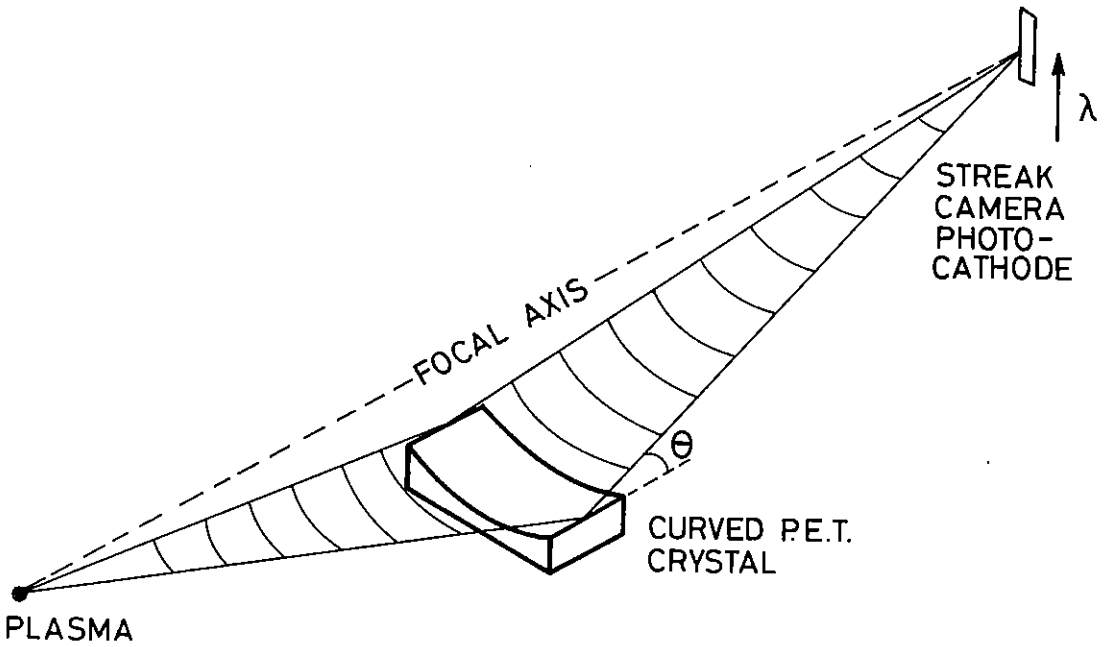

FIG. 1.22 FOCUSING GEOMETRY OF CURVED CRYSTAL

diffracting crystal, obtaining time resolution meant sacrificing sensitivity.

A method of increasing the sensitivity of time resolved spectroscopy is suggested when it is realised that most of the X-rays reflected off of the flat crystal are not admitted through the time resolving slit over the streak camera photocathode. If the spectrum is compressed, or focused, along the spectral lines, all of the X-rays reflected by the crystal can be incident on the photo-cathode without any loss of time resolution. The focusing is achieved using a curved crystal arranged in the geometry shown in Figure 1.22.

The crystal is a sector of a cylinder whose axis connects the plasma to the centre of the streak camera photocathode. X-rays are collected over the whole curved surface of the crystal and focused back onto the axis of the cylinder. The condition for focusing is simply:

$$r = \frac{\ell}{2} \tan\theta$$

where r is the radius of the cylinder and ℓ is the separation of the cathode and plasma. The Bragg angle $\theta = \sin^{-1} \frac{n.\lambda}{2d}$

The quality of the focus at right angles to the spectral direction is set by the quality of the crystal curvature and by the source size. The crystal spatially resolves along the spectral lines (1.11) in a manner analogous to a concave mirror, hence the size of the spectrum at focus is the source size. Aberrations due to poor focusing and the crystal curvature quality also limit the size of the spectrum.

The crystal only focuses at one wavelength on the cathode, at the point where the cylinder axis intersects the cathode. However the aberration for the wavelengths off focus can be kept less than 1 mm over the spectral region of interest. The aberration sets the time resolution of the streak camera and replaces a time resolving slit in performing this function.

A prototype PET curved crystal has been purchased with a radius of

curvature of 11 cm and arc length of 5 cm. Using this crystal to produce a spectrum of less than 1 mm wide in the cathode region resulted in a signal gain of ∿ x 60 over a flat crystal using a 1 mm wide time resolving slit. A spectrum obtained with this curved crystal is shown in Section 5.3.6.

B J MacGowan (Imperial College)

1.7.2 X-ray Streak Camera Developments

There are currently two X-ray streak cameras in operation and these have been used extensively in laser-plasma experiments throughout the year.

The older of these cameras, built in 1977 (1.12) is now used mainly in the single beam interaction chamber and is referred to below as the TA2 camera. The more recent miniature X-ray streak camera (1.10), (1.13) has been used exclusively in the six beam interaction chamber and is referred to as the TA1 camera. Both of these cameras have undergone modifications during the year.

The main change has been a redesign of the photocathode and grid structure used in the TA2 streak tube. Originally each of these electrodes was mounted independently on its own pair of glass pillars and an outer metal cylinder at cone potential was needed to shield the region from distorting electric fields caused by nearby objects at earth potential. The new arrangmenet is shown in Figure 1.23 and is an improved version fo that successfully used in the miniature (TA1) camera.

The outer metal body both forms a cylindrical extension to the cone electrode and acts as a support for the photocathode and grid. Insulation between the three electrodes is provided by the nylon insert and spacer rings shown. A single lock ring is used to clamp the assembly in position. This arrangment is readily demountable allowing easy replacement of the photocathode and grid.

The photocathode itself is simple in construction consisting of a brass

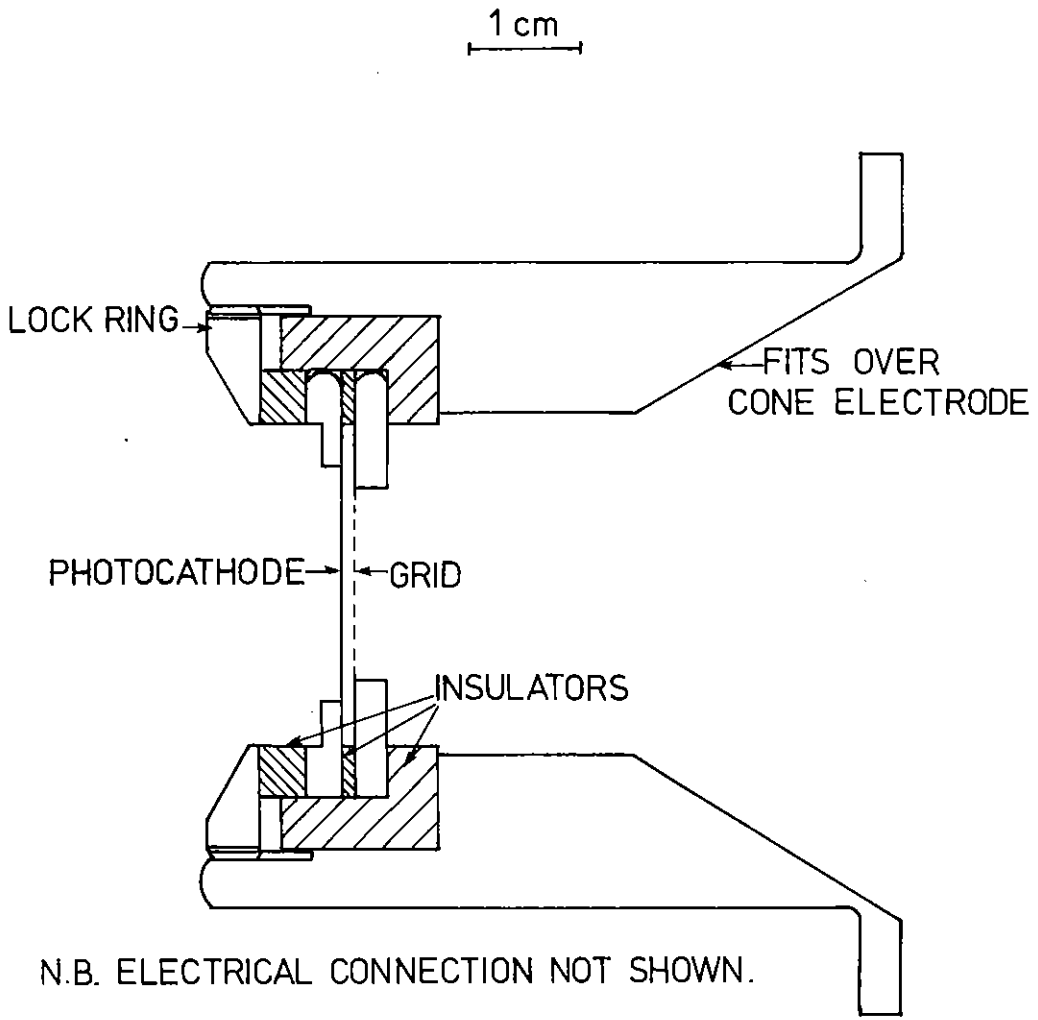

FIG. 1.23. NEW PHOTOCATHODE / GRID ASSEMBLY FOR THE TA2 X-RAY STREAK CAMERA.

disc having a central 5 mm wide slot covered by typically 15 μm thick Beryllium foil on which is deposited an X-ray photo-sensitive layer such as cesium iodide. The maximum usable length of the photocathode is 18 mm, determined by the size of the grid.

Minor changes were made to the TA1 camera to enable it to use the same photocathode design.

The microfocus X-ray source was used to check the operation and measure the static characteristics of the cameras after the changes had been made. The main advantages gained from the modifications may be summarised as follows:

(i) TA2 Camera: spatial resolution increased to 20 line pairs mm^{-1}, now equivalent to TA1.

(ii) TA1 Camera: usable photocathode length increased from 10 mm to 18 mm.

(iii) Both cameras now use identical photocathode and grid components which are easily interchanged.

M H Lamb, J M Ward (Belfast) and E Paul (Bath)

1.7.3 Probe Beams

A double pulse optical probe beam system has been developed during the last year in order to investigate the time evolution of laser beam filamentation (see Section 3.5) and plasma jetting (see Section 3.7) observed in the plasma corona. It allows to take two images separated in time on each shot.

The layout of the probe beam system is shown in Figure 1.24. A 100 ps Gaussian pulse generated by a modelocked oscillator is split into two where one fraction is used to generate a long heating pulse by means of a coherent pulse stacker and the second one is used to provide a short

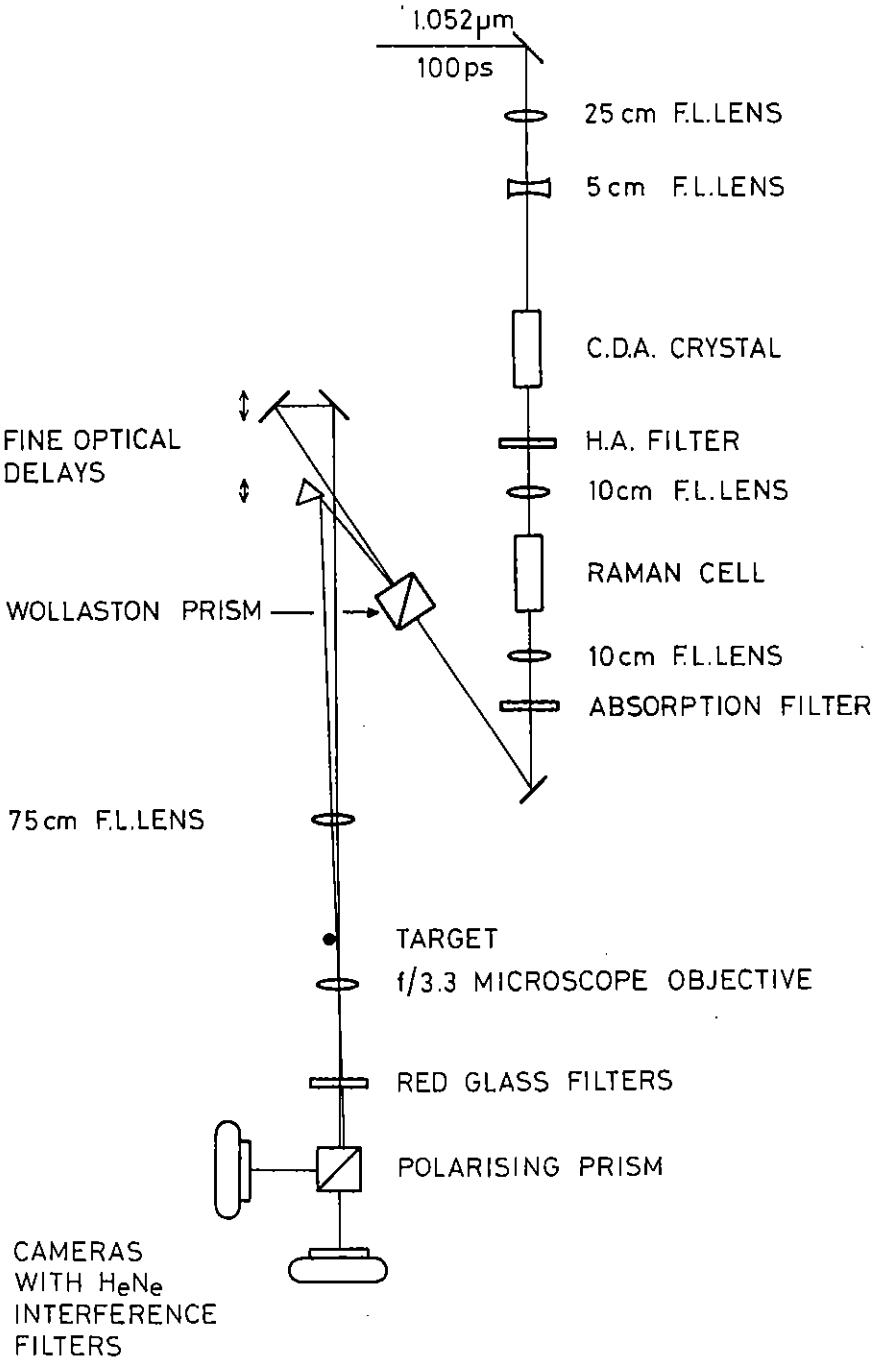

Figure 1.24 Layout of the optical probing system. The pulses seperated in time are generated.

optical probing pulse. This second portion is amplified in a high repetition rate amplifier, is frequency doubled in a CDA crystal and Raman shifted to the red ($\lambda \neq 0.62$ μm) in a cell of ethanol for the purpose of frequency discrimination against the harmonics from the heating laser beam. A detailed description of the conversion stages is given elsewhere (1.13), (1.14). The 30 to 50 ps red pulse is then split into two orthogonally polarized pulses using a Wollaston polarizer. They can be time delayed relatively to each other by adjustable units and after being recombined they are directed past the target. The target is imaged onto film by an f/3.3 microscope objective with an overall magnification of 32. The two orthogonally polarized pulses are separated again after the target with a polarizing prism giving two images at different times. The polarizing prism is protected from the laser radiation scattered off the target by a red cut-off filter when the target is heated with green light or by a HA3 filter when the target is irradiated with infrared laser light. HeNe interference filters 100 Å in bandwidth are mounted on the cameras to block radiation emitted from the plasma. The spatial resolution of the imaging system is 2 to 3 μm in the object plane.

O Willi (Oxford)

1.7.4 CR39 Technique for the Measurement of α-particle Emission from D-T Targets

In the current series of hot ablative compression experiments the energy spectrum of emitted α-particles was determined using the track detector CR-39. This plastic is the most sensitive of the nuclear track recording plastics. When a charged nuclear particle traverses this material it is delineated by a trail of chemical damage. The subsequent immersion in a suitable etchant such as NaOH results in bulk etching of the material at a characteristic rate, V_B and preferential etching at a rate V_T along the track axis. The etch pit so formed when enlarged to a size that is easily visible under an optical microscope can be measured to find the excess etch rate ratio V_T/V_B and hence the particle ionisation. CR-39 is unique among the solid state track recorders in that it is very sensitive, recording tracks of protons up to 15 MeV, and possesses a high

degree of isotropy and uniformity of response. In terms of particle nuclear charge (Z) and relativistic velocity (β) it records particles in the range $6 \lesssim Z/\beta \lesssim 100$. It is however completely insensitive to other radiations and can operate successfully against a hostile background of electrons, gamma and X-rays. The overall form of the CR-39 track response expressed as the variation of V_T/V_B with particle restricted energy loss is shown in Figure 1.25(a).

In this application we are interested in looking at thermonuclear products and knock-on ions in D-T fusion reactions, ie $_1H^1$, $_1H^2$, $_1H^3$, $_2He^3$ and $_2He^4$ particles. This means we are utilising the middle and lower half of the CR-39 response curve.

CR-39 -Response

The growth of etch pits along α-particle tracks in CR-39 is illustrated in the computer simulation shown in Figure 1.25(b). The simulation has used as its input parameters the measured relationship between V_T and α-particle range (R) at an etch temperature of 75°C in 6.25 N NaOH. The track initially grows with its familiar cone-like structure. The track walls are curved owing to the increase in V_T with decreasing R. Once track etching has reached the end of the particle range further etching enlarges the track at the bulk etching rate. The track structure has become progressively lost and once the post-etch surface is carried beyond the particle range only a spherical remnant remains.

In general, α-tracks take on a variety of appearances depending upon their dip angle, range at the plastic surface and degree of etching. These shapes owe their structure to the plastic response to α-particles, in particular to the V_T-R relationship, an example of which is shown in Figure 1.25(c). The relationship follows a familiar Bragg-type curve reaching a peak in V_T at $R \sim 2$ μm.

Etched tracks may be described by the five parameters included in Figure 1.25(d). They are: the track total depth Z, the total length X, the major

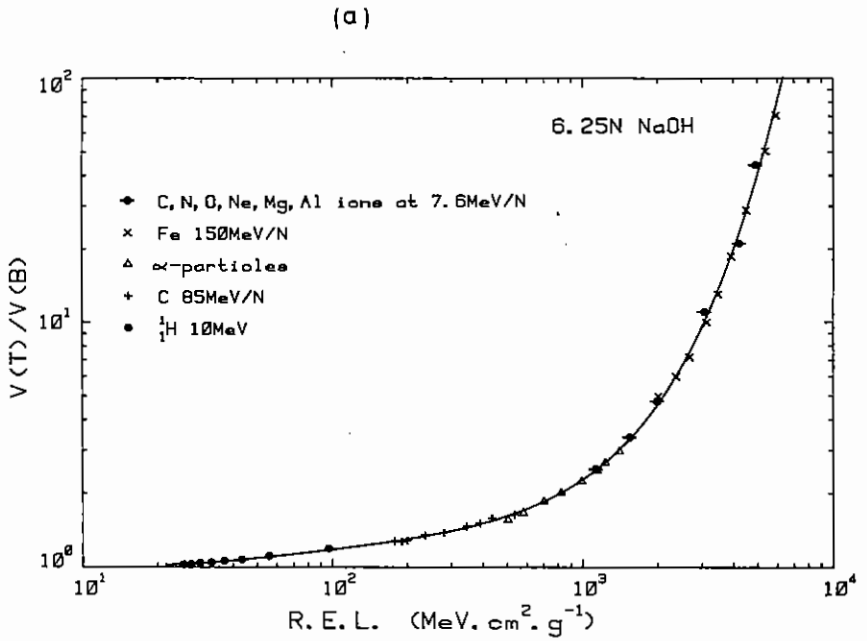

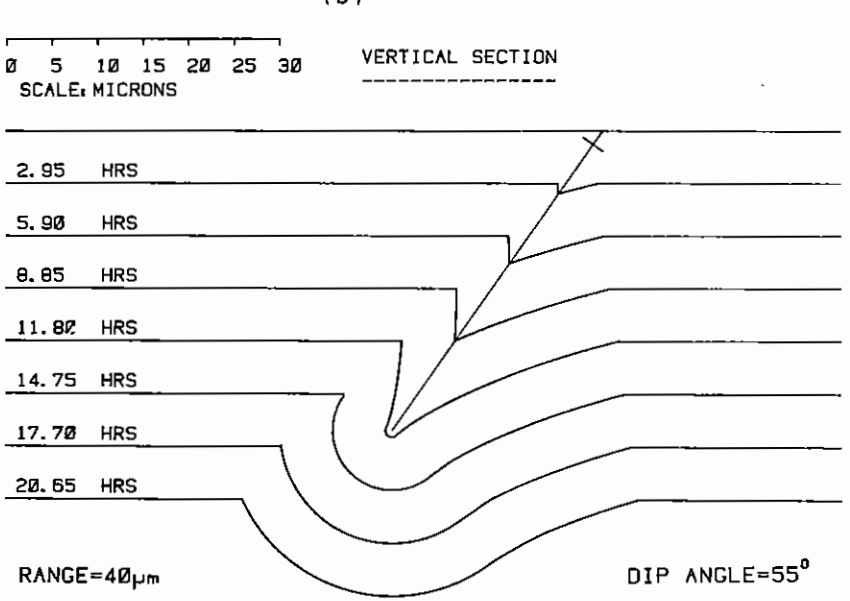

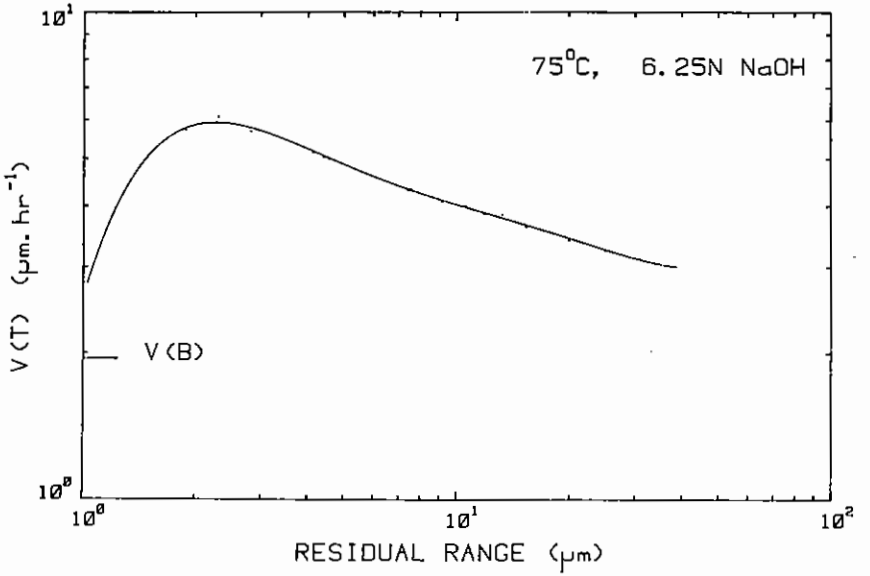

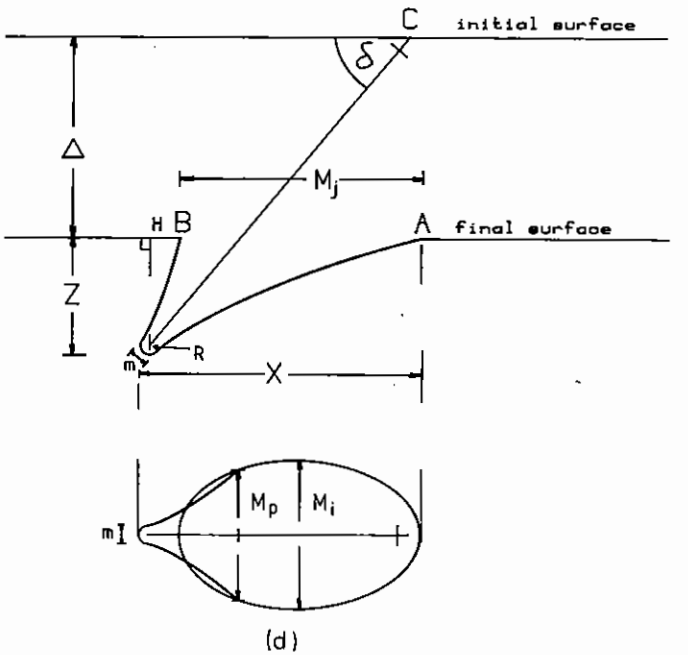

Figure 1.25 (a) CR-39 response curve using 6.25 NaOH at 70°C.
(b) Growth of etch pit along α - particle track in CR-39.
(c) V_T - Range Curve for α - particles in CR-39.
(d) The measureable etch track parameters on α particles in CR-39.

and minor axis diameters of the opening mouth M_j and M_i and the diameter of the etch out end, m, which is equal to zero if track etching has not reached the end of the particle range. However, if the track is etched well beyond its range the available measurement parameters can be severely restricted, for example to an overall track length and width.

In this experiment all the tracks were visibly etched well beyond their range. One consequence of this is that the minor axis end diameter m and the minor axis M_i take on one and the same value. Detailed examination showed that the ranges of all tracks were $\lesssim 4$ μm corresponding to energies below 1 MeV. In this situation the major contribution to track etching lies on the low energy side of the peak in the $V_T - R$ relation.

The first stage in the analysis was to construct theoretical curves of the variation of X, M_i and m with track length L (ie, particle range R) and under these etch conditions. Examples of these are shown in Figures 1.26(a), 1.26(b) and 1.26(c). These curves constitute a look up table from which the track length and hence particle energy could be determined.

The resulting α-particle spectra from a series of D-T shots are shown in Figure 5.18 (see Section 5.3.4). Shot number 1 on 14/12/81 shows the additional interesting feature of tracks recorded which are inconsistent with those from α-particles. These appear only at the end of the foil close to the target where the incident angle is 60°. Indeed the emission shows a discontinuity ~ 5 mm from the end of the foil as seen in Figure 1.26(d). On these tracks the m and X values differ, which is in contrast to the α-tracks where they are closely similar. A scatter plot of m vs X from these tracks is shown in Figure 1.27 where the crosses denote α-particle tracks and the circles proton-type tracks. The origin of these proton-type tracks is uncertain but they may represent fast ions accelerated from the target.

A P Fews and D L Henshaw (Bristol)

1.7.5 Laser produced pinholes for X-ray imaging

To give the spatial resolution required by present compression experiments X-ray pinhole cameras need pinholes with diameters as small as a few microns. In addition the pinhole substrate needs to be opaque to the hard X-rays produced and so must be made from high atomic number (gold or platinum) foils of thickness greater than about 10μm. Such pinholes, having aspect ratios (depth/diameter) greater than 2 or 3, have not been readily available up to now since commercial methods for producing pinholes using photolithography and electro-deposition are unable to produce pinholes with aspect ratios much greater than 1. To overcome this limitation laser drilling techniques have now been successfully developed and supplies of high aspect ratio, small dimater pinholes have now been manufactured.

A 1.06μm, Q-switched Nd glass laser has been used with the oscillator adjusted to give a single transverse mode. A microscope objective (with numerical aperture of 0.17) is used to focus the beam onto the surface to be drilled. Accurate positioning of the material and observation of the drilling process is possible via a filtered viewing system. Tests have shown that high aspect ratio holes with the smallest most uniform diameters are produced when the output beam is attenuated to give about 100 μJ per 20ns pulse and 10 - 20 shots are needed to penetrate foils of 10 - 20 μm thickness. Higher pulse energies drill more rapidly but conical holes are produced.

Large numbers of pinholes with diameters from 3 to 15 μm have been drilled in 3mm diameter platinum substrates with thickness of 8, 15 and 25 μm ready for plasma physics experiments. Fig (1.28) shows an example of such a pinhole, having a diameter of 10μm. A major additional advantage of the laser drilling technique is that multiple pinholes of any spacing and size can be readily produced in the same substrate.

1.7.6 Gated micro channel plate X-ray intensifier

Recently encouraging results indicating a gating time of 150 ps have been

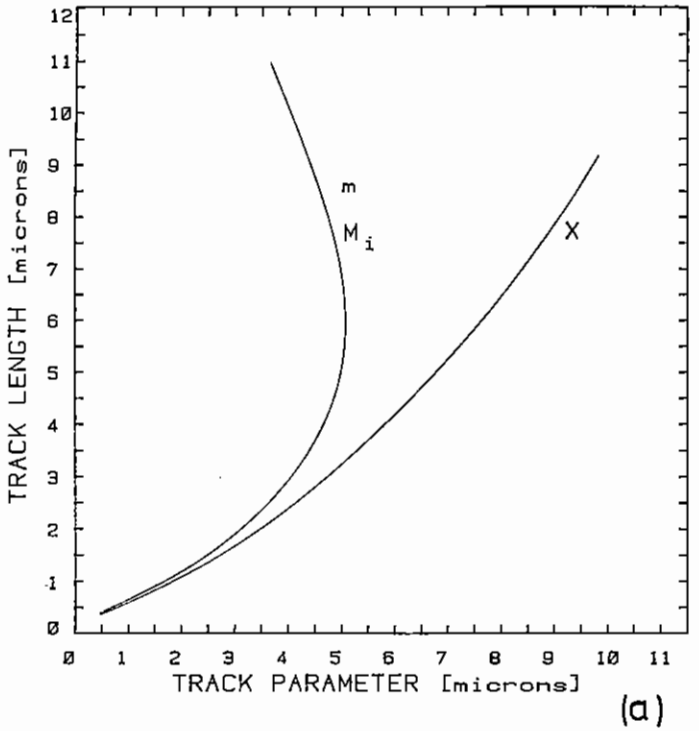

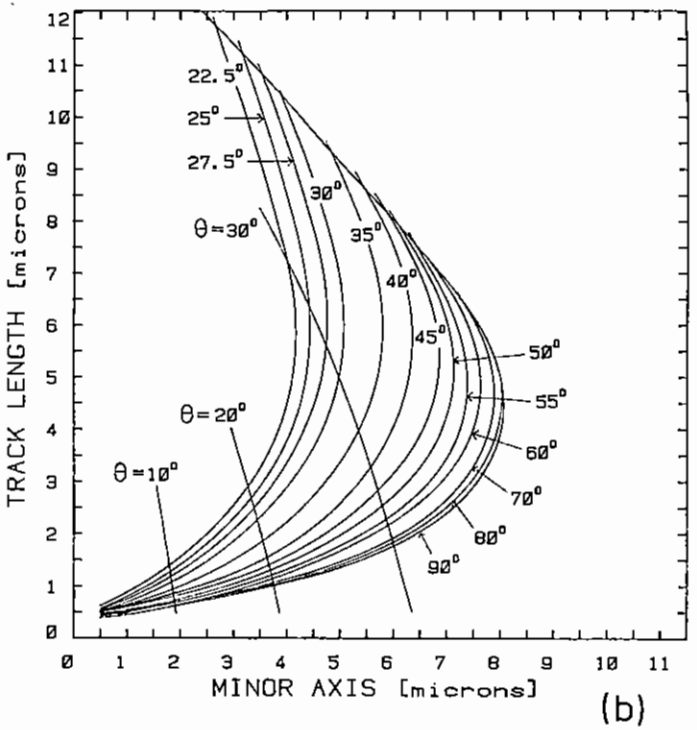

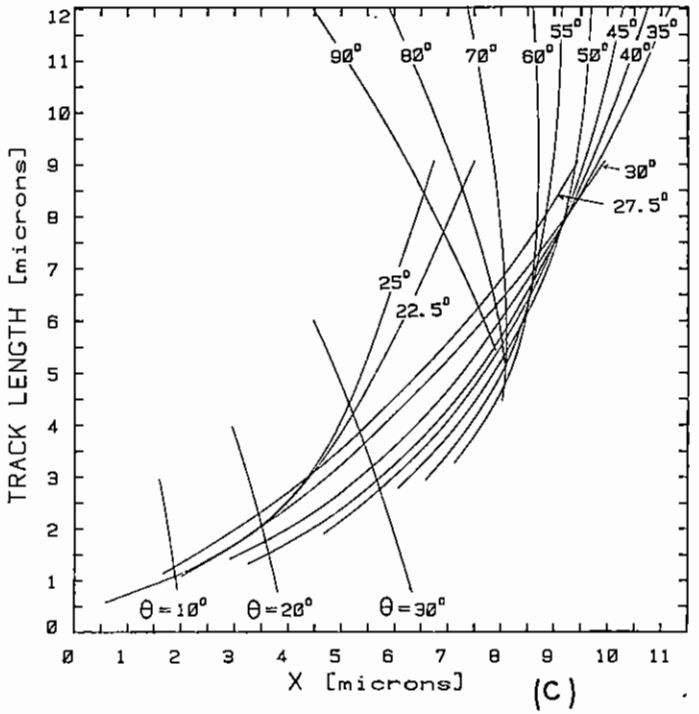

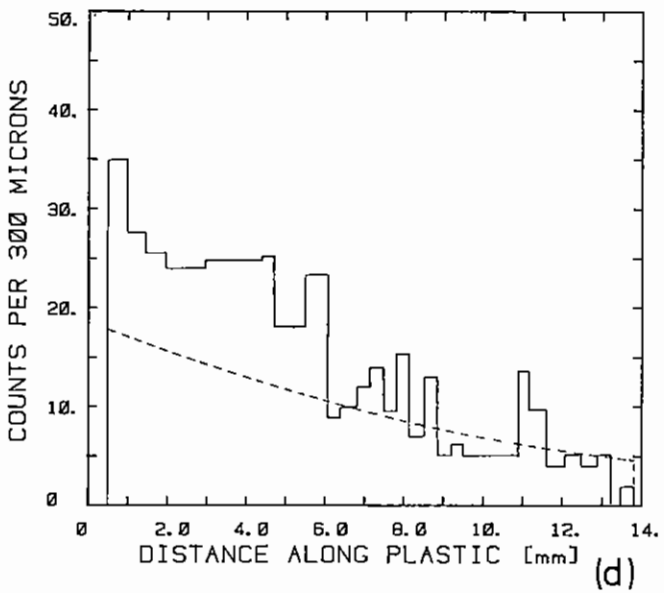

Figure 1.26 (a) Variation of Mi, m and X with track length, dip angle 30°.
(b) Variation of Mi with track length as a function of dip angle and cone parameter, θ.
(c) Variation of X with track length at various dip angles and cone parameter, θ.
(d) Variation of particle count with distance along the plate for shot 01/14/12/81.

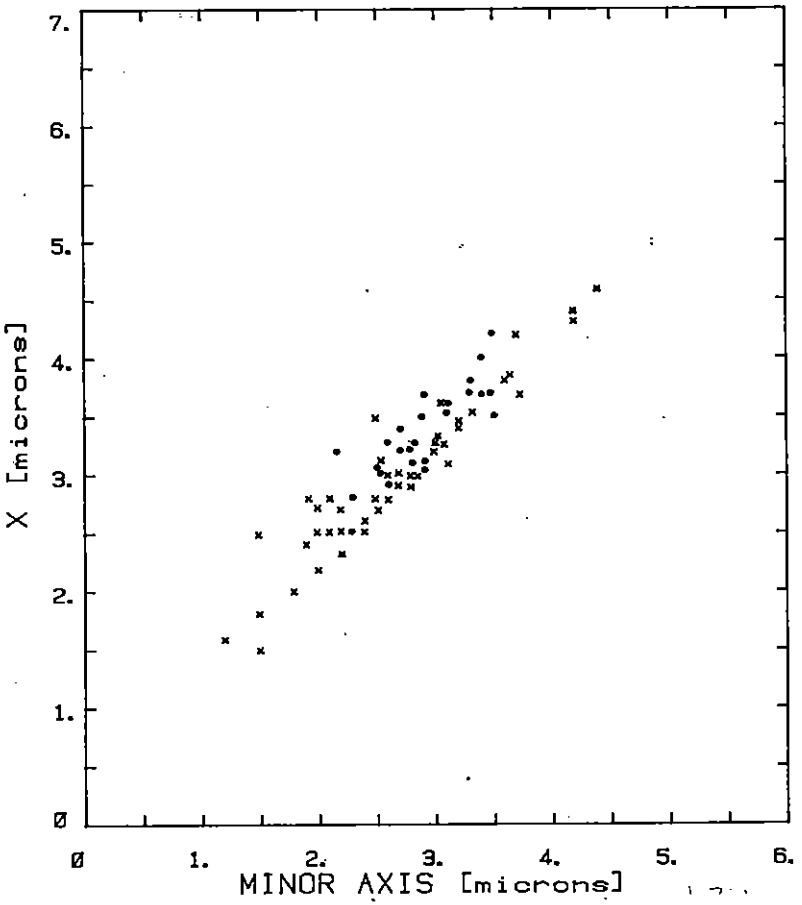

Figure 1.27 A scatter plot of m is X; crosses denote α - particle tracks and the circles proton-type tracks.

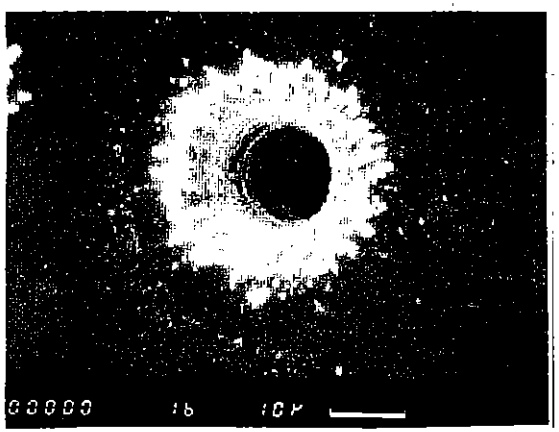

Figure 1.28 10 μm diameter laser drilled pinhole.

obtained using the gated X-ray intensifier reported last year. Subsequently design changes enabling a higher speed have been implemented.

In its original form the intensifier was demonstrated to be able to be turned on and off by a d.c. voltage across the cathode-grid. However there was considerable reliability problems in the making of the photo-cathode assembly and the risetime was not good due to uncertainty in the positioning of the photocathode holder and mismatches in the stripline geometry.

A new stripline and photocathode assembly was built. The important design criteria that have to be balanced are the transit time of the photo-electrons from the photocathode to the micro-channel plate and the gating time. The photo-electron transit time is important as resolution is lost due to lateral spreading if the transit time is too long. For a given gating pulse amplitude this puts an upper limit on the photocathode to mesh distance. In order to have a fast gating time it is desirable that the stripline impedance be maintained throughout the photocathode region, this fixes the width to separation ratio of the photocathode.

In our case the gating voltage of $\sim$100 volts from a photodiode fixed the photocathode to mesh spacing to $\sim$200μm for $\sim$50μm resolution. For a 50 ohm line impedance this requires a photocathode width of $\sim$900μm, some of which had to be support structure, giving only $\sim$300μm useful width. To increase the width to a more practical size, a lumped capacitor type photocathode was used $\sim$5mm in diameter. This gave a calculated ZC response time of $\lesssim$ 100ps.

Using this camera gating on and off was demonstrated, and the camera was found to be reliable. Speed was still a problem. Measurement on a laser produced plasma indicated that the gate time was $\sim$ 200ps.

Electrical measurements of the speed of the photodide gate pulse source performed at A.W.R.E. on a Thomson-CSF oscilloscope, showed that the rise time was 150 ps, with an oscilloscope rise time of 100ps and a laser pulse

length of 60ps FWHM. (The diode, a Motorola MRD 500 although rated at ∿60 volts has a breakdown voltage of ∿ 307 volts). In stripline geometry the indicated rise-time was ∿ 120ps with only half the voltage available.

Additionally a Gallium Arsenide photo-conducting switch (Auston switch) was tested. A 700 volt pulse with a oscilloscope limited risetime 80ps was generated using a D.C. bias of ∿2kV and 50ps pulse of 100μJ.

The availability of such high voltage fast pulses considerably simplifies the 'camera' design and a larger gap can be used. The lumped capacitor photocathode can be abolished and 50ohm impedance maintained throughout. Higher frequency response cables and connectors have been used and the assembly checked for mismatches with a faster TDR than was used previously ((30ps instead of 80 ps). The rise time of the voltage pulse at the cathode is 65 ps.

To date, turn off of the camera has been achieved by placing a short circuit across the stripline after the photocathode. This reflects the rising edge of the gate pulse, inverted. Consequently the camera remains on for two transits of the rising edge of the gate pulse from the photo-cathode to the short circuit. There are several problems with this method; firstly the short circuit has to have a low inductance and include a series capacitor so that a D.C. bias may be applied. For gate times $\lesssim$ 100ps the position of the short is very close to the photocathode making design difficult. Secondly the camera would have to be dismantled to change the gate pulse length.

An alternative approach would be to generate a pulse of the desired length and to pas this through the device. This would be highly desirable as the pulse length may be changed externally and also the scheme is adaptable to multi photocathode devices with the pulse travelling from one to another. The drawback is the difficulty in generating a pulse with a fast falling edge when the laser intensity is liable to fluctuate. To avoid this the pulse generator will be configured to generate simultaneous positive and negative step pulses. These will propogate in opposite directions across

the photocathode,their relative timing determining the gate pulse width. Gate pulse length is easily adjusted externally in this system.

With all these modifications the new camera is nearly ready for use. It is intended to measure its gating time by generating two plasmas separated in space by ∿ 500μm and in time by down to < 100ps. The ability to photograph just one of these events will demonstrate the gating time.

Several improvements are envisaged depending upon user requirements. Multi-frames are possible essentially by making several cameras but with one intensifier assembly. If pulses with fast falling edges can be generated reliably only a single driver may be required. An optical device may be possible but, due to the nature of the photocathode this would have to be sealed off from the chamber vacuum.

A Dymoke-Bradshaw (Imperial Coll)

CHAPTER 1 REFERENCES

1.01 D J Kuizenga IEEE J Quant Elect. 17 1694 (1981)

1.02 B Luther Davies and V Del Pizzo, Optics Comm, 30, 403 (1979)

1.03 G Mourou and W Knox, App Phys Lett, 35, 492 (1979)

1.04 J H Gardner and S E Bodner, Phys Rev Lett, 47, 1137 (1981)

1.05 D J Nicholas and R G Evans, Rutherford Laboratory Report RL-78-017 (1978)

1.06 J E Howard, Appl Opt, 16, 2764 (1977)

1.07 I N Ross, Private Communication

1.08 J D Kilkenny, R W Lee, M H Key and J G Lunney, Phys Rev Lett

1.09 J G Lunney, Queens Univ, Belfast, Phd Thesis (1980)

1.10 Annual Report to the CLF RL-81-040 (1981)

1.11 B Yaakobi and V Bhagavatula, Rochester Report LLE89 (1979)

1.12 Annual Report to the CLF RL-78-039 (1978)

1.13 Annual Report to the CLF RL-80-026 (1980)

1.14 O Willi, P T Rumsby and S Sartang, IEEE J Quant Elect, 17, 1909 (1981)

CHAPTER 2 GAS LASER DEVELOPMENT

INDEX

CHAPTER EDITOR: F O'Neill

CHAPTER 2 GAS LASER DEVELOPMENT

2.1 Introduction

This year most of the effort of the Gas Laser Development Group was devoted to the construction of the high power KrF laser SPRITE. By the end of the reporting period (March 1982) the machine had been fully assembled, high voltage pulses had been applied to the diodes and a considerable amount (~2 KJ) of e-beam energy had been deposited in the laser cell. The device has not yet been operated as a laser because of high voltage tracking problems in some of the pulsed power components. These problems, which are now being rectified, are occurring in the "fast" sections of the machine and are therefore not considered to be particularly serious. Some minor design changes have been carried out and laser operation of SPRITE should be accomplished early in 1982.

We have also made considerable progress on the developmeent of KrF discharge lasers capable of producing low divergence output beams of high (50 - 100 mJ) energy. One of these lasers is at present being installed on SPRITE for triggering the four PFL line output gaps in synchronism. These SF_6 gaps can be triggered with only a few millijoules of laser energy because laser breakdown can be easily obtained with the low divergence beam from the discharge laser which we have developed.

In other experiments we have aimed at obtaining narrow line output from KrF discharge lasers. Line narrowing is achieved using a grazing incidence grating in the laser cavity and linewidths ~ 0.2 cm^{-1} are easily obtained. These lasers have been used in collaborative experiments with Oxford University to demonstrate for the first time, high quality phase conjugate reflection of a KrF laser. The generation of phase conjugate reflections of high power lasers is of interest because of the potential use for correction of abberations and diffraction induced image distortion. Examples of such use include automatic target alignment in multi-beam laser compression experiments and compensation for optical distortions that occur in high gain laser media or in the propagation of laser beams over large distances.

Finally in collaboration with Bradford University we have performed some very successful laser annealing experiments using the ELF XeCl laser. The 308 nm XeCl laser has been used at an irradiation energy density of 3 J/cm^2 to anneal manganese-doped thin films of ZnS. These films are of interest for use in high efficiency large area electroluminescent displays. Previously annealing was achieved using thermal methods. We have found that the luminsecent output of laser annealed films can be considerably higher (x 4) than the output of thermally annealed samples.

2.2 SPRITE

2.2.1 Pulsed Power Design and Testing

2.2.1(a) Water Capacitor Testing

The Sprite water capacitor was fitted in August 1981 with a single pulse forming line firing into a liquid resistor load. We were pleased to find that the recirculating Elga water de-ionizer system could routinely achieve resistivities of 2 - 6 MΩ cm after several hours circulation. The alochrom (ICI) treatment of the water capacitor components seems to work well with no corrosion evident after six months operation. Initially we studiously avoided metals other than aluminium in the system but from experience have found that a considerable amount of stainless steel can be tolerated in the system without any corrosion.

The initial electrical testing involved measuring the capacitance and leakage resistance of the water capacitor, (C_s and R_w in Figure 2.01) by discharging a known capacitor into C_s and measuring the resulting decay. In this way C_s was found to be 40 nF and R_w for 2 MΩ cm deionised water was 440 Ω. This agrees well with the calculation for a leaky capacitor which gives $R_C = 0.088\ \varepsilon\rho$ (μs) where ε is the dielectric constant and ρ the resistivity of the insulator in MΩ cm. For ρ = 2 MΩ cm and C = 40 nF this gives R = 350 Ω.

Next, the voltage gain and energy transfer efficiency from the Marx

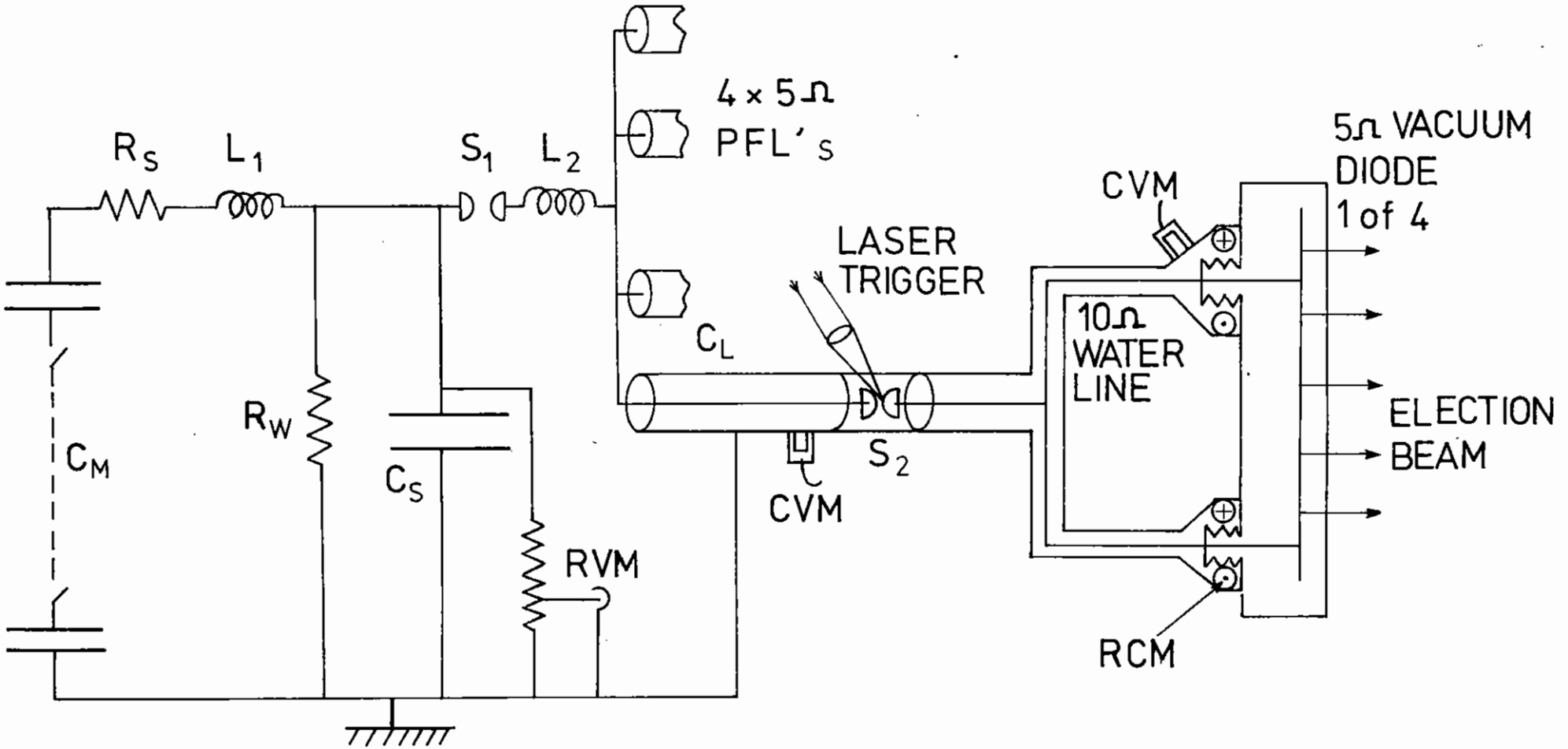

Figure 2.01 Equivalent circuit of the Sprite pulsed power system. RVM = Resistance Voltage Monitor. CVM = Capacitive Voltage Monitor. RCM = Rogowski Current Monitor.

generator to the water capacitor was determined at low voltage by over pressurizing switch S_1 so that the charge rings between the Marx and water capacitor giving a voltage waveform on the water capacitor as shown in Figure 2.02. The ringing period is $2\pi\sqrt{L_1C_1}$ where L_1 is the inductance of the Marx generator and C_1 is the capacitance of C_m and C_s in series. Since these capacitances are known (42 and 40 nF respectively) we calculate L_1 = 8.4 μH. This allows us to obtain the characteristic impedance of the water capacitor system as $Z_c = \sqrt{L_1/C_1} = 20\ \Omega$. The amplitude of the first peak V_1, gives the gain of the system $G = V_1/V_m$ where V_m is the erected Marx voltage. The gain is given theoretically by:

$$G = \frac{C_m}{C_m + C_s}\left\{ e^{-\frac{\pi}{2}\frac{R_s}{Z}} + e^{-\frac{\pi}{2}\frac{Z_c}{R_p}} \right\}$$

in which expression all of the quantities are known except R_s, the equivalent series resistance of the Marx generator. R_p is the parallel resistance of the Marx generator (~500 Ω) in parallel with the water resistance (~500 Ω). The measured gain was 0.80 which gives a series resistance of 5 Ω for the Marx generator. This gives a maximum energy transfer efficiency from the Marx to the water capacitor of 60%, the bulk of the energy loss occurring in the Marx series resistance.

2.2.1(b) The Main Gap

The main spark gap in the Sprite water capacitor system, S_1, is a self-breaking sphere gap with brass electrodes operating in pressurized SF_6 (Figure 2.03). The gap body is made from polycarbonate plastic with a tracking length of 24 cm. The hemispherical electrodes have a radius of 3.5 cm. The peak electric field at the surface of the electrodes is enhanced by a factor f over the mean field V/X where f is given by Alston (2.01) as:

$$f = \frac{\frac{X}{R} + 1 + \left\{\left(\frac{X}{R} + 1\right)^2 + 8\right\}^{1/2}}{4}$$

where X is the electrode separation and R is the radius of the sphere. For our gap X/R = 1 and f ≈ 1.37. Initially, the breakdown voltage was

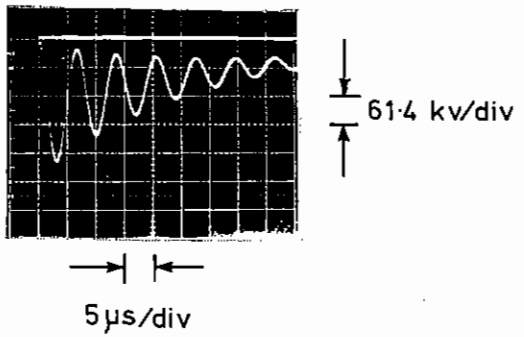

Figure 2.02 Voltage waveform on water capacitor with switch S_1 not firing to show ringing gain from the Marx to the water capacitor and damping due to R_S and R_W.

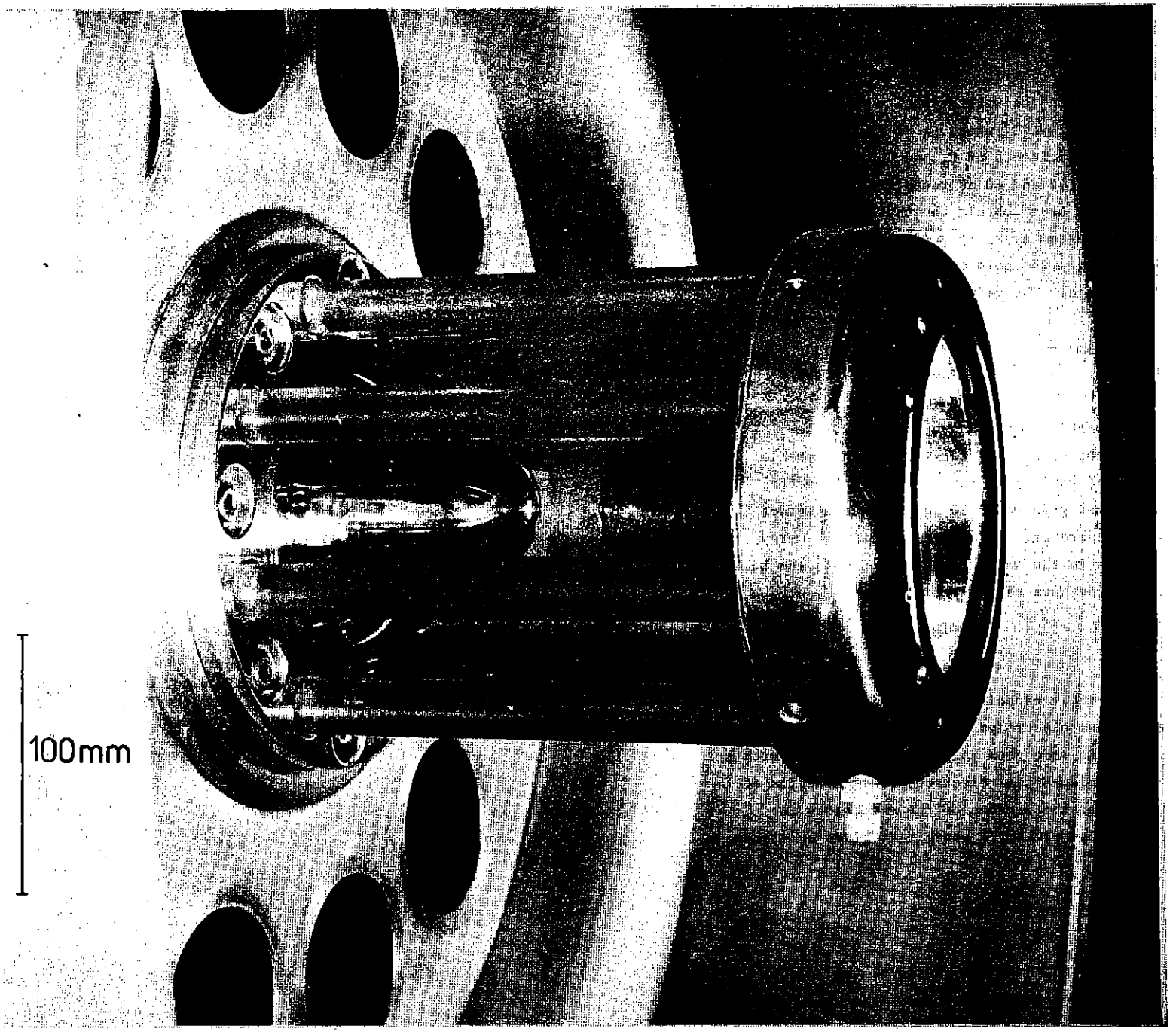

Figure 2.03 Sprite water capacitor spark gap (S_1)

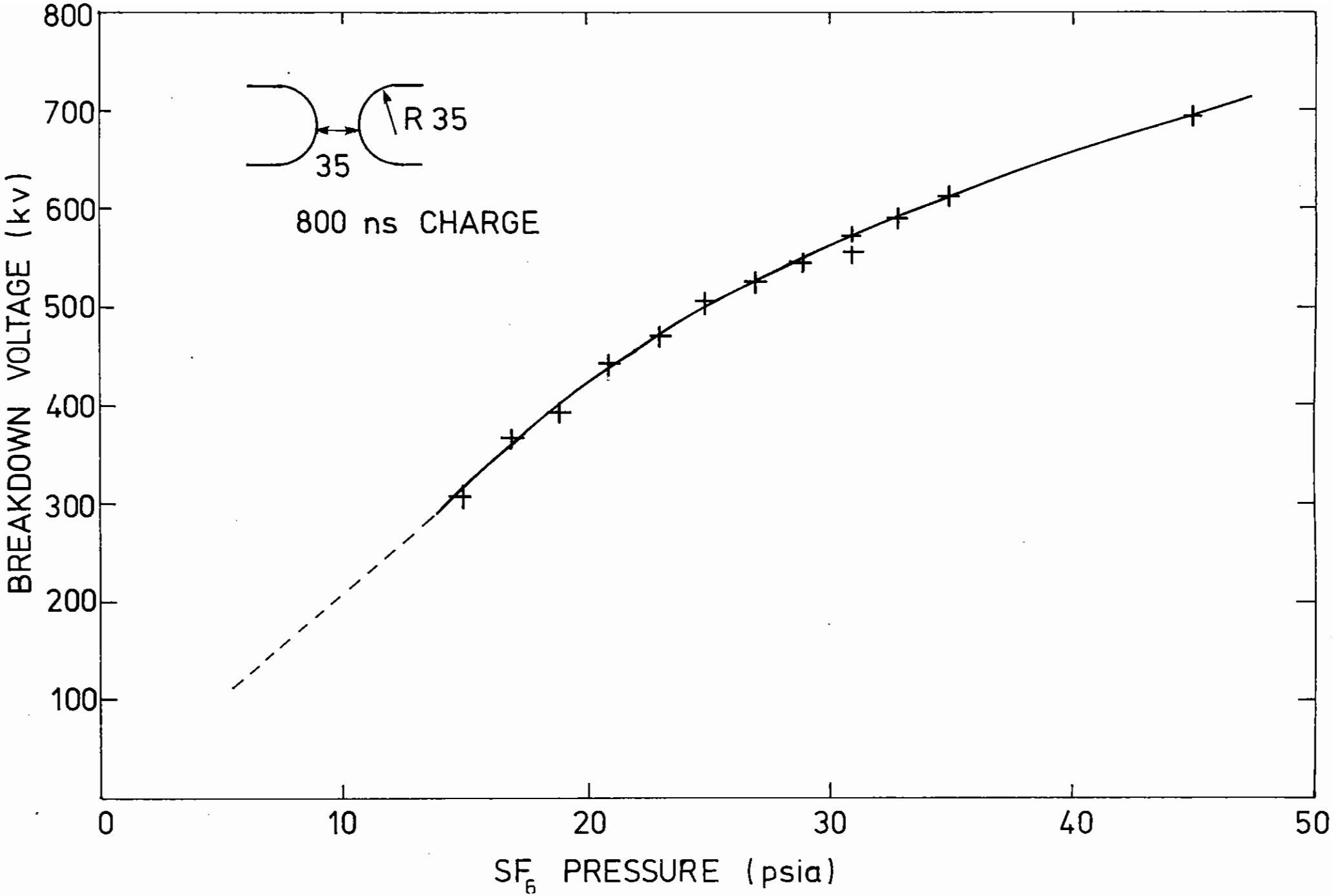

Figure 2.04 Self breakdown voltage versus SF_6 pressure for the water capacitor spark gap (S_1)

found to have a rather high jitter (standard deviation approximately 5%). At the same time inspection of the inside insulator surface revealed that partial tracking had been occuring. It is thought that the tracks produce a non-uniform potential distribution which distorts the field in the centre of the gap and results in a lower breakdown voltage. The tracks may either occur during the charge cycle or on the discharge cycle in which case they can lay down a surface charge which can persist and distort the field for the following shot. In either event this effect would be considerably reduced if the insulator surface was sufficiently resistive to either resistively grade the field along the surface or at least to leak away any static charge build-up. Two such surfaces have been tried with this gap, the first a low resistance film made from a mixture of colloidal graphite and calcium silicate which by adjusting proportions can produce a uniform film with a wide range of resistivity, and secondly a high resistivity film from an aerosol anti-static spray (Polaron 0802). In the first case the resistance across the electrodes was about 1 kΩ and in the second of the order of $10^9\Omega$. Both films were found to work well in reducing jitter and so it was concluded that the major problem was due to static charge build-up. With the high resistance film the breakdown voltage curve shown in Figure 2.04 was obtained. The non-linearity in the curve is interesting, expecially when compared with the data of Tucker (2.02) which show linear breakdown curves in this pressure range for a similar switch. Tucker's breakdown curve was linear with a slope of 60 kV cm^{-1} $atmos^{-1}$ which is the same as this data at high pressures if one assumes a linear curve above 30 psia. The low pressure part of our curve does however extrapolate to the origin, which is not the case for Tucker's curve. In the low pressure region the breakdown field increases at a rate of 120 kV cm^{-1} $atmos^{-1}$ (Note $E_b = V_b f/X$). The DC breakdown field in the pressure range 1 - 3 atmos and pX > 1 cm atmos follows Paschen's Law (E_b/p = constant) at 92 kV cm^{-1} $atmos^{-1}$ (2.03).

2.2.1(c) Charging of Pulse Forming Lines

In January 1982 the four pulse forming lines were fitted to the water capacitor for test firing into four liquid resistor loads. The connection

between S_1 and the lines was made with 35 mm dia flexible stainless steel tubing giving minimum inductance and resistance in the charging circuit. Figure 2.05(a) shows the water capacitor and PFL charging waveforms on the same time base. On this particular shot the water capacitor charges to 700 kV in about 900 ns when switch S_1 closes. The PFL's then charge as shown in the lower waveform (inverted) to 910 kV in about 180 ns at which point switch S_1 closed. Figure 2.05(b) shows the resulting output voltage waveform across a matched load. The peak voltage is 455 kV in a 65 ns FWHM pulse. The pulse rise time is about 18 ns from 10 - 90% levels. The operation of this part of the circuit is very efficient; of the 10 kJ stored on the water capacitor, 9 kJ is deposited in the load in the desired short pulse. Some of the circuit characteristics can be obtained from the waveforms. Referring to Figure 2.01 the charge time of the PFL's is $\pi(L_2\frac{C_L\ C_S}{C_L+C_S})^{\frac{1}{2}}$ where C_L is the total capacitance of the four pulse forming lines which was measured to be 29 nF. From the charge time to peak of 200 ns we get L_2 = 250 nH. The characteristic impedance of the circuit is given by $[L_2(C_L + C_S)/C_LC_S]^{\frac{1}{2}}$ and this is simultaneously much less than the parallel resistance of the water (~300 Ω) and much greater than the series resistance of S_1 and the feeds (~0.1 Ω). Thus the voltage gain into the lines is given by $G = 2C_L/(C_L + C_S)$ which gives G = 1.16. The energy transfer efficiency is then $[C_L(1.16)^2/C_S]$ = 97%.

One interesting point concerning the charge waveforms of the PFL is that the peak voltage as read on a monitor at the spark gap end of the line is greater than that given by G as calculated above - in fact typically 1.3 times the water capacitor voltage. This is a result of the rapid charging of the PFL's through the low inductance circuit. The net effect is that the voltage along the PFL is not distributed uniformly and a wave reflects up and down the line during charging. This can be seen in Figure 2.05(a) as a slightly staircase-like waveform. This resonant charging effect can be put to good use, since if the switch S_2 is triggered when excess charge is at the output end of the line, a faster risetime than normal would be obtained. This effect has been demonstrated under self-break conditions but is somewhat uncontrollable due to jitter in the self-breakdown voltage. Laser triggering of the four gaps as envisaged for the future

operation of Sprite should provide precise triggering and hence reproducible pulse shapes.

2.2.1(d) Sprite Voltage and Current Monitors

In the past we have only used resistive current and voltage monitors which have the advantage of wide bandwidth and may be calibrated under DC conditions. For Sprite we have found it necessary to develop capacitive voltage monitors and Rogowski current monitors (CVM's and RCM's). The locations of the monitors are shown in Figure 2.01. The CVM's are used to monitor the voltage on the PFL's and on the output lines as close to the diode as possible. In both cases insufficient tracking length and non-uniform voltage gradients ruled out the use of resistive dividers. The RCM's measure the current flowing to the diode through the vacuum feed-throughs. Since there are eight such feed-throughs, normal resistive current monitors would have all been in parallel (apart from some inductive isolation) and the interpretation of the current waveforms would have been complex. The Rogowski monitor has the distinct advantage that it can be electrically isolated form the rest of the system since it relies only on changing magnetic field for its operation.

The capacitive voltage monitor used on the PFL's is shown in Figure 2.06(a) and its equivalent circuit in 2.06(b). C_1 is the capacitance between the circular end of the cylindrical capacitor and the PFL line inner. This may be approximated by assuming the end of the probe to be a square of side $\sqrt{\pi}r$ in which case $C_1 = 0.555\,\epsilon\, r^2/(2b \ln b/a)$pf where the dimensions are in cm. The value of C_2 is given by $0.555\,\epsilon r1/d$ pf. For the PFL monitor C_1 = 4 pf and C_2 = 1000 pf. In addition to this capacitive divider, because the water is resistive there is a resistive divider r_1, r_2 giving an equal division ratio. The overall division ratio would be the same for the resistive as for the capacitive divider if $R_1 >> r_2$ but this is not always the case (and definitely not true for the PFL monitor). The divider will act capacitively at frequencies such that $1/\omega C_1 << r_1$ or for pulses of duration $\tau << \pi r_1 C_1$. Since r_1 and C_1 are just the resistance and capacitance of the water their product depends only on the water resistivity. Numerically the above relation is

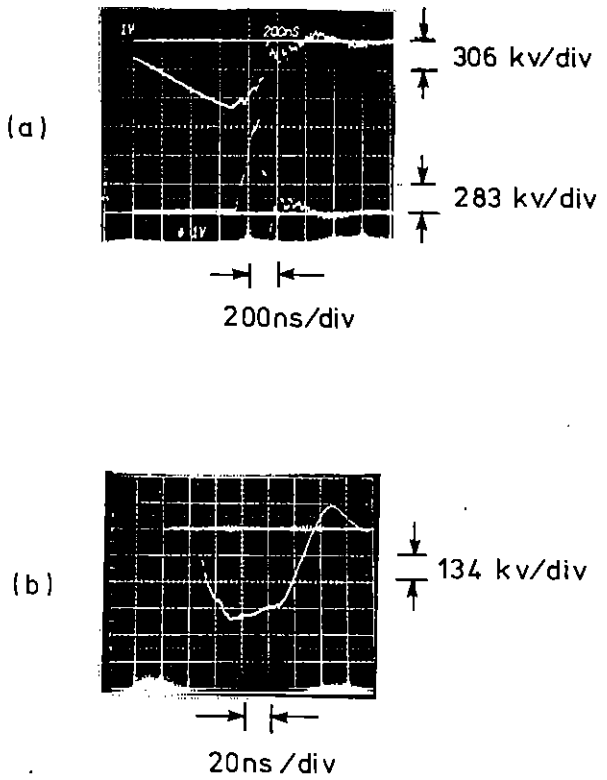

Figure 2.05 Voltage waveforms of the Sprite pulsed power system when operating with 4 PFL s firing into 4 dummy loads.

(a) Upper trace Voltage on water capacitor with main gap S_1 firing at 705 kV.

Lower trace Charging of one of the PFL s with line output gap S_2 firing at 910 kV.

(b) Resulting PFL output voltage pulse into 5 Ω liquid resistor load. V_{Max} = 455 kV

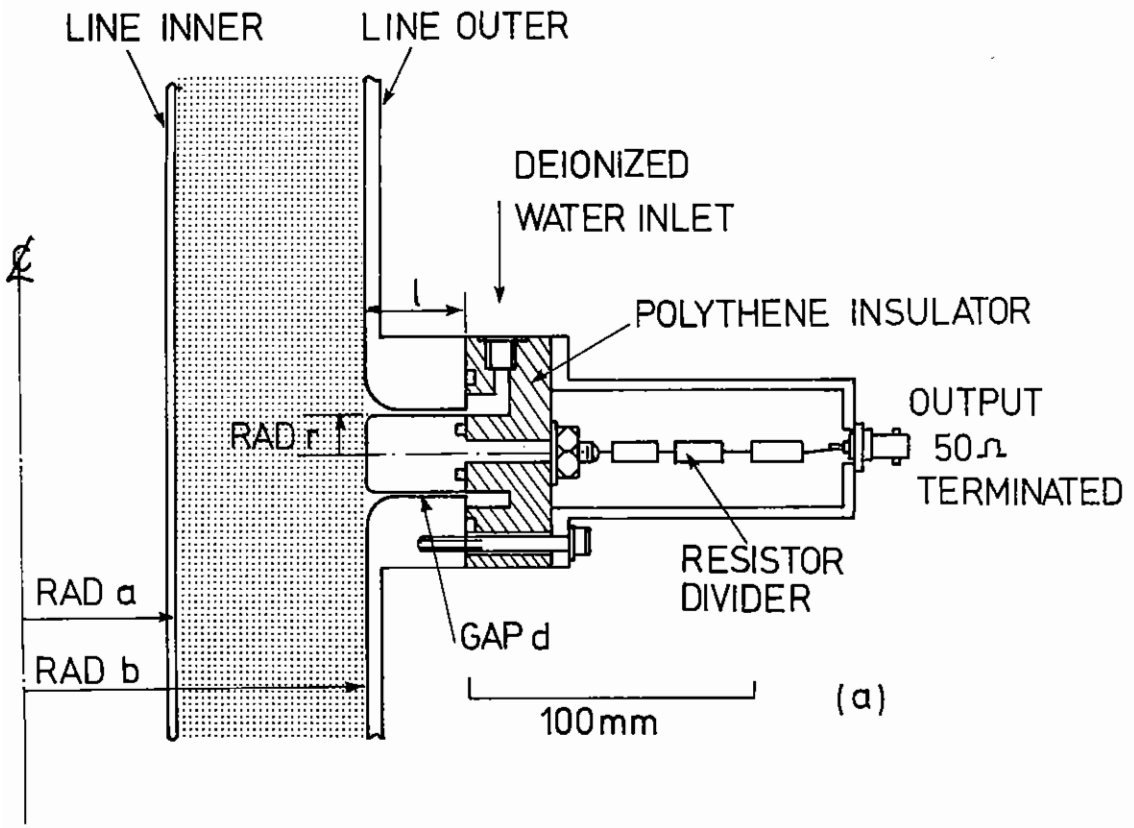

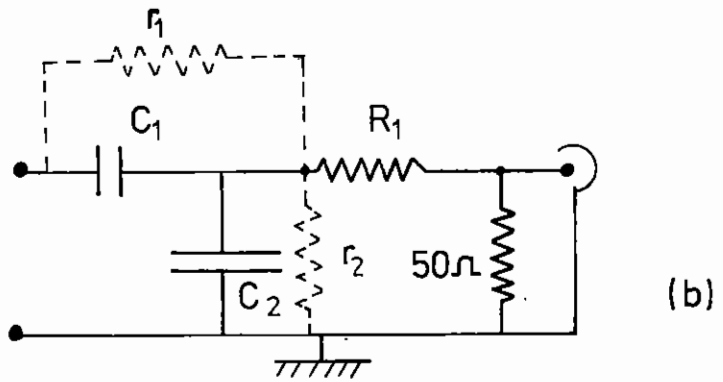

Figure 2.06 (a) Cross-section through the PFL capacitive voltage monitor

(b) Equivalent circuit.

$\tau << 22\ \rho$ (μs) where ρ is in MΩ - cm. Since ρ is typically larger than 2 MΩ - cm and the pulse lengths to be monitored are < 200 ns, these dividers are dominated by the capactive effects. The output voltage is thus given by $V_{out} = V_{line} \left(\frac{C_1}{C_1 + C_2}\right)\left(\frac{R_o}{R_o + R_1}\right)$ where R_o is the output load resistance. To minimise reflections it is useful to terminate the cable in 50 Ω at the divider and at the oscilloscope in which case $R_o = 25\Omega$. R_1 is typically 10 kΩ and since $C_2 >> C_1$ we have $V_o = V_{line} \frac{C_1 R_o}{C_2 R_1}$ or typically 1 V per 100 kV on the line. In practice the CVM's are calibrated by pulse charging the lines from a known capacitor and are found to be typically in the region 1 V per 150 kV. The time constant of the monitors is given by $C_2 R_1 r_2/(R_1 + r_2)$ and is measured during calibration to be ~ 5 μs. The rise time of the system is determined by the propagation time of the wave down the cylindrical capacitor which will act as a transmission line. The length in the case of the PFL monitor gives a rise time of the order of 1 ns. One practical point worth noting is that fresh de-ionized water should flow through the cylindrical capacitor both to prevent the water resistivity from degrading and to stop the formation of bubbles in the small gap between the inner and outer electrodes. In practice these monitors are found to be easy to install and free from pick-up of extraneous noise signals.

The Rogowski current monitors are operated in the self-integrating mode (2.04) and thus give an output proportional to the current to be measured. The basic Rogowski coil is shown in Figure 2.07(a) and is a coil of major radius, A, and minor radius, a, completely surrounding the current to be measured I. In the self integrating mode a low value resistor R shunts the coil. By Faraday's Law the voltage induced in the coil is $\frac{d\phi}{dt}$ where ϕ is the total flux linking the coil. We then have

$$\frac{d\phi}{dt} = L \frac{di}{dt} + i\,(R + r)$$

where L is the coil inductance and r is the resistance of the windings. R is chosen such that $r << R << \omega L$, ie, the measuring duration $\tau << L/R$. In this case $di/dt = \frac{1}{L}\frac{d\phi}{dt}$ and hence $i = \phi/L$. The voltage output across R is then $V = \phi R/L$. The flux ϕ is calculated from the field due to the current I at radius A from $\mu_o I = \oint \vec{B} \cdot \vec{dl}$ or $B = \mu_o I/2\pi A$. The total flux linking

n turns is thus $\phi = \mu_o a^2 \ell n/2A$. We next need to calculate the inductance of the coil. The formula for an infinite, close wound solenoid is not appropriate in this case since Rogowski coils need to be wound widely spaced to minimise interturn capacitance. Instead we use the formula given by Pellinen et al (2.04):

$$L = \mu_o a \frac{2\pi A}{P}\left[\frac{\pi a}{P} + \ln\left(\frac{2P}{d}\right) - \frac{5}{4} - \sum_{i=0}^{3} a_i \left(\ln \frac{2\pi A}{P}\right)^i\right]$$

where $a_o = 0.0007$, $a_1 = 0.1773$, $a_2 = -0.0322$, $a_3 = 0.00197$, (P is the pitch of the winding and d the wire diameter). Using this formula for the inductance and that above for the flux, the sensitivity of the coil can be calculated. The decay time of the signal is just L/R. In practice the arrangement shown in Figure 2.07(a) is not used since changing fields due to currents elsewhere would induce a large voltage across R from flux linking the major turn of radius A. In order to avoid this we have found that it is best to wind a second layer identical solenoid on top of the first to give a balanced output at one end as shown in Figure 2.07(b). In addition an electrostatic shield can be fitted to almost totally enclose the coil apart from a small slot along the meridian plane which prevents magnetic shielding of the coil. The practical winding arrangement is shown in Figure 2.07(c). Two layers of 32 turns of 0.9 mm diameter copper wire are wound on a 9 mm diameter former of major diameter 370 mm. The inductance is calculated from the above formula, assuming the two layers are equivalent to a single layer of 64 turns, to be 1.25 μH. The shunt resistor R is 0.75 Ω made from four 3 Ω carbon resistors in parallel in order to minimise inductance. Back termination with 47Ω as shown in Figure 2.07(b) is found to be useful in both preventing cable reflections and reducing high frequency ringing associated with the shunt resistor R. With these values of L and R the time constant of the coil is 1.6 μs which means that a 60 ns output pulse will only have a droop of 3% which is well within the accuracy required of the coil. The sensitivity of the coil is calculated from the flux and inductance formulae to give 1.6 V/kA into a 50 Ω load.

The coils are calibrated on a test rig which uses a spare vacuum feed through from Sprite so that the coil is calibrated with exactly the same

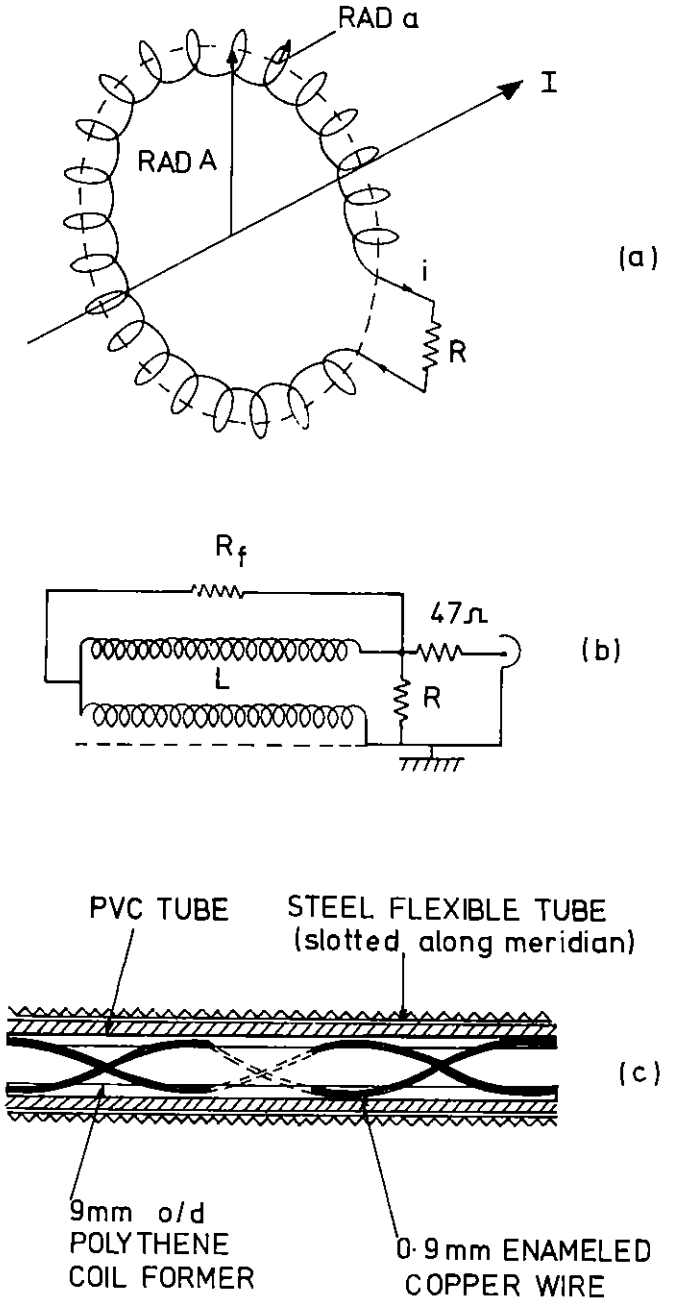

Figure 2.07 (a) A typical Rogowski coil.

(b) Equivalent circuit of the self-integrating bifilar wound coil.

(c) Cross-section through the bifilar winding and shielding for the Sprite current monitors (RCM).

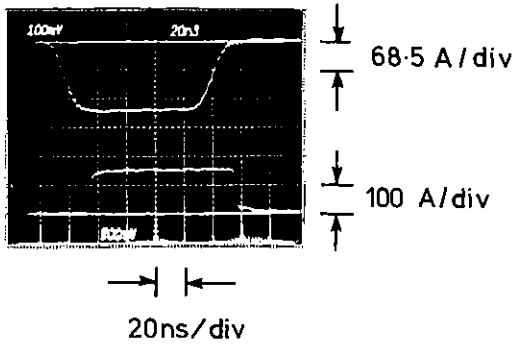

Figure 2.08 Upper trace Output from bifilar wound Rogowski coil with 25 MHz oscilloscope bandwidth.

Lower trace Actual test current pulse measured from the output voltage across the test line load resistor. Oscilloscope bandwidth 200 MHz.

current distribution as it will see when in use. A suitable current pulse is obtained by charging a length of 50Ω cable to about 20 kV and discharging it through the vacuum feedthrough into a 50 Ω load. A simple atmospheric pressure SF_6 gap is used as a switch and up to 200 A calibration pulses can be generated with approximately 2 ns rise times. This fast rising current pulse was found to excite high frequency oscillations in the coil at around 500 MHz. It is simplest to filter such oscillations out at the oscilloscope since they are not exicted by slower rising pulses. Figure 2.08 shows a typical output from the coil from a 164 A calibration pulse (lower trace). The rise time is limited by the scope bandwidth of 25 MHz to around 12 ns (10 - 90%). With a wide band amplifier the rise time from the coil is as fast as the calibration pulse (2 ns). It is thought that the maximum useful bandwidth for the coil is about 75 MHz. The calibration factor was measure to be 1.5 V/kA compared with the calculated value of 1.6 V/kA.

In some early coils a much lower oscillation frequency of around 30 MHz was obtained. This oscillation was severe in non-bifilar wound coils where one end of the solenoid was returned co-axially through the centre of the coil. It is thought that this oscillation is the fundamental frequency of the coil, the period being equal to the transit time around the circumference and back with the coil acting as a delay cable. The bifilar winding practically eliminates this effect but a small modulation persists. The addition of a feedback resistor R_f in Figure 2.07(b) of value about 100 Ω was found to eliminate this oscillation but leave the calbiration otherwise unaffected.

M J Shaw and C B Edwards (RAL)

2.2.2 Development of PFL Output Gaps

In last year's annual report we described the initial testing of the pulse forming line (PFL) laser triggered spark gaps. Whilst the laser triggering was found to work well, two major problems were discovered which has necessitated major modifications and extensive testing over the past year. The two problems were damage to the line assembly due to shock

from the spark channel being transmitted through the spark gap electrodes and jitter in the self breakdown voltage caused by partial tracking around the insulator surface. Before modifications to the original gap were made it was suggested (2.05) that we investigate the effect of diverging fields on the breakdown voltage in high pressure SF_6. This sort of data was not available for pulse-charged gaps but previous DC measurements (2.06) showed a strong polarity dependence in the breakdown field in co-axial geometry at pressures above one atmosphere. For the positive high field case, the DC breakdown field increases at a rate of 92 kV cm^{-1} atm^{-1}, but for the negative high field case the breakdown field increases at only 33 kV cm^{-1} atm^{-1}. The high pressure DC breakdown is thus controlled by cathode effects and indeed, pre-breakdown electron emission is observed from the cathode when the field exceeds about 120 kV cm^{-1}. It was interesting to see whether such effects would occur with pulse-charged gaps. To this end, two sets of brass electrodes (without laser triggering holes) were made, which when installed in the gap gave different fields on the anode and cathode. In both cases the charged electrode was negative which was dictated by considerations of water breakdown in the PFL. The fields at the anode and cathode were calculated using the PE2D computer program. For the high field negative case, the field enhancement factor (FEF) on the cathode was 1.52 and on the anode 1.03. For the high field positive case, the FEF on the cathode was 1.22 and on the anode 1.54. The results are shown in Figures 2.09 and 2.10 for an 800 ns charge time and show the same marked polarity effect as for DC charged gaps. Unfortunately this data is somewhat marred by very large jitter, particularly in the case where the high field was on the positive electrode. This is now thought to almost certainly be due to tracking along the insulator surface during the charging of the gap. Since such tracking is only likely to reduce the breakdown voltage, the true non-tracking curve is probably located fairly close to the upper points on the graphs. Using the FEF's one can relate the breakdown voltage to breakdown field at the anode and cathode. The gradients of the two curves in terms of cathode field are 38 kV cm^{-1} $atmos^{-1}$ and 43 kV cm^{-1} $atmos^{-1}$ for high negative and high positive fields respectively. The absolute cathode breakdown fields at 4 atm are 325 kV cm^{-1} and 340 kV cm^{-1}. Within the limits of the errors of these measurements it

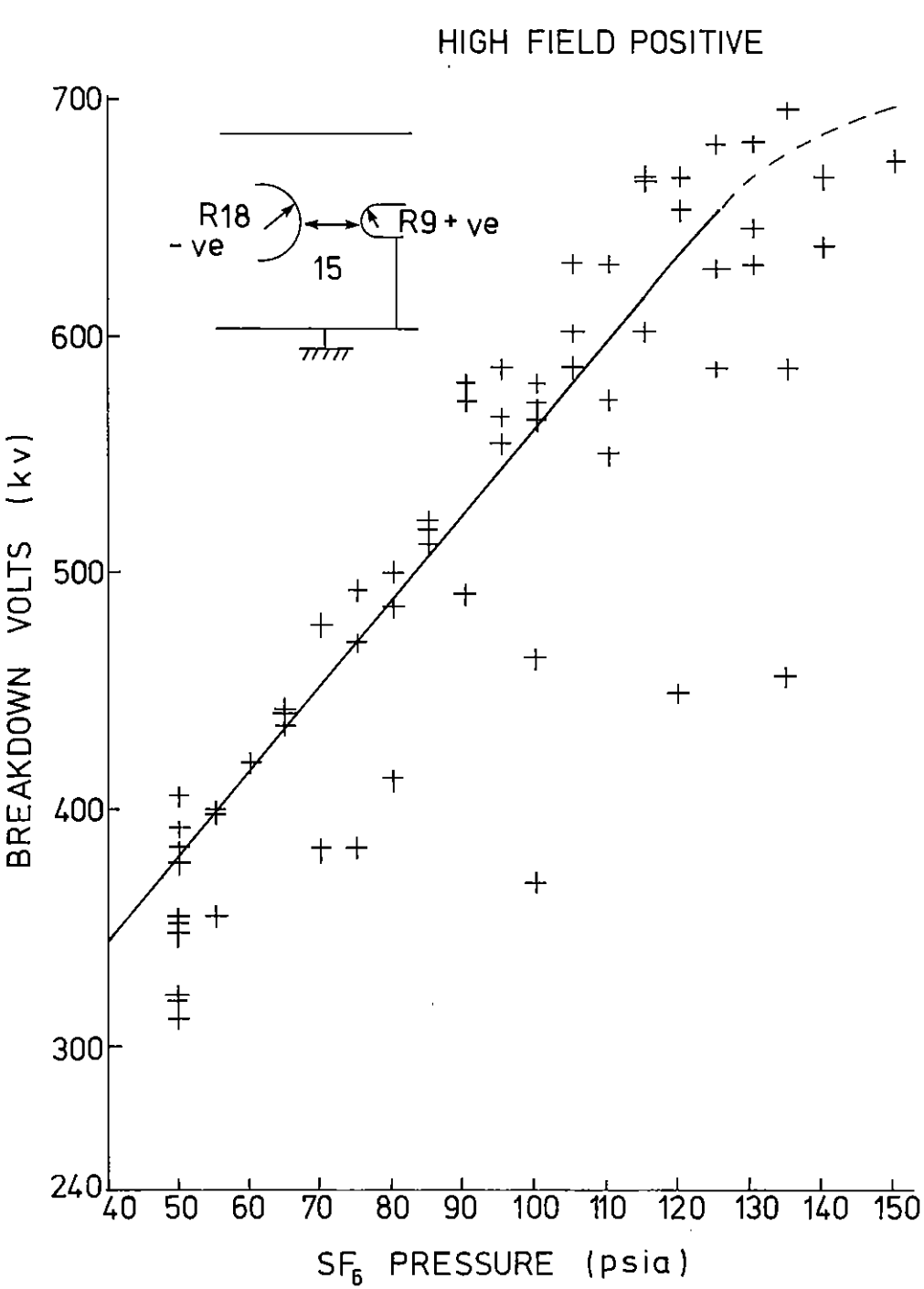

Figure 2.09 Self breakdown voltage as a function of SF_6 pressure for an assymetric high field positive gap (800 ns charge time).

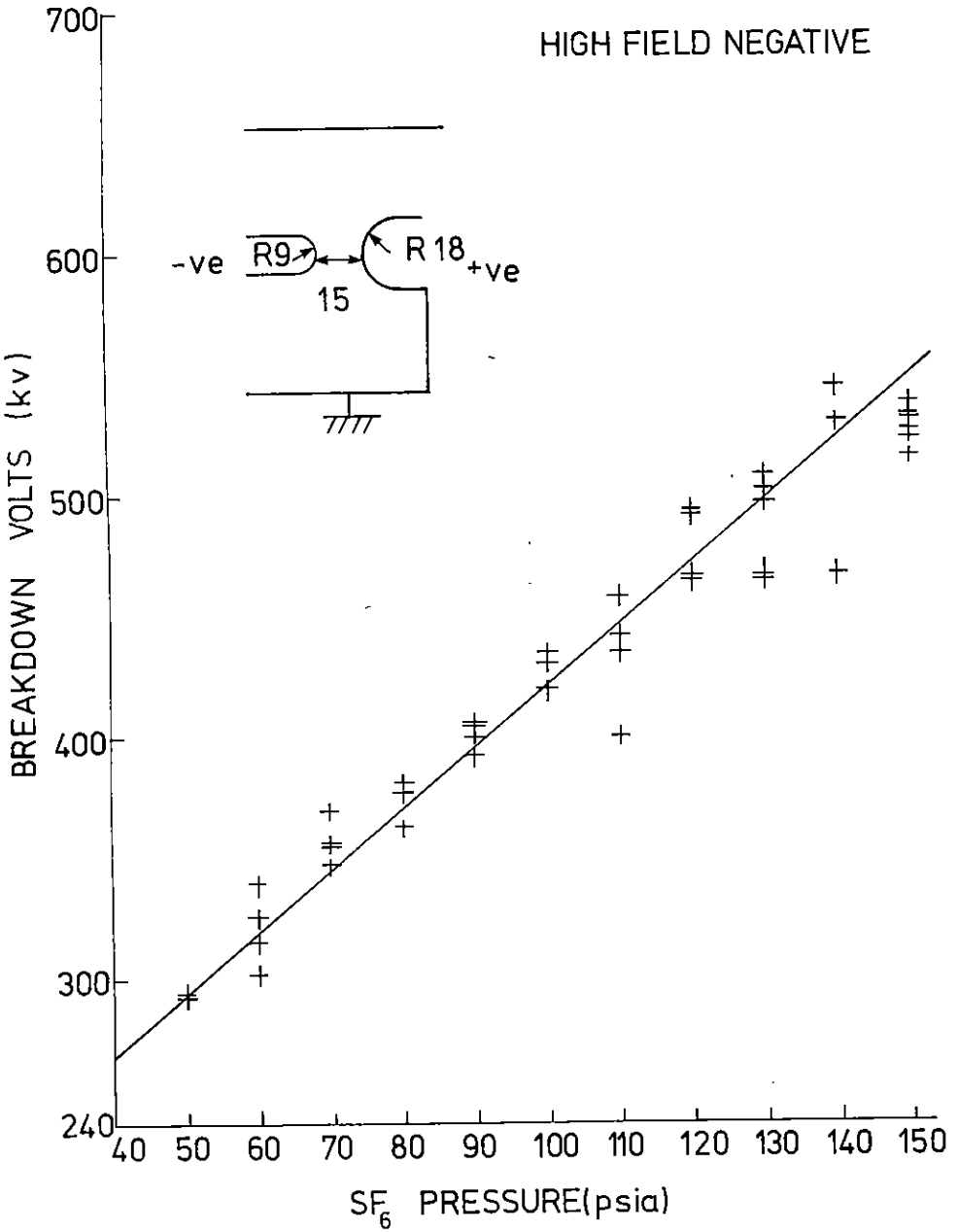

Figure 2.10 Self breakdown voltage as a function of SF_6 pressure for an assymetric high field negative gap (800 ns charge time).

is thus reasonable to conclude that in both cases breakdown was occuring at the cathode. With these electrodes the field enhancemet of the anode was insufficient over the cathode field to cause breakdown to be dominated by anode effects. There still holds out a promise of improved gap performance for sufficiently non-uniform fields in SF_6.

Unfortunately we were unable to incorporate positively enhanced fields in our gap design due to other constraints. In fact with our rather small diameter PFL's which must be charged negative the natural enhancement is on the cathode. The design finally arrived at is shown in Figure 2.11. The electrodes are made from brass and are spring loaded to absorb the shockwave from the spark channel. The outer electrode holders are also made of brass and are screwed into the expoxide resin gap body. The resin blanks are made by the Chemical Technology Group at Rutherford Appleton Laboratory from high strength mix No 222A. They are machined and pressure tested to 120 psig before use. The electrodes are deliberately set asymetrically within the pressure chamber in order to reduce the field along the insulator surface. A small garter spring is used to reduce the field on the threads of the charged electrode holder.

The equipotential distribution for the gap prior to breakdown is shown in Figure 2.12 calculated using the PE2D program. At the maximum charge voltage of 1 MV the peak field along the insulator surface is 170 kV cm^{-1}. At this field, partial tracking still occurs along the surface causing increased jitter in the breakdown voltage above 1 MV. Figure 2.13 shows the breakdown voltage versus pressure curve.

The field plot gave the enhancement factors as 1.43 on the cathode and 1.19 on the anode. The variation with pressure implies a cathode field increase at the rate of 110 kV cm^{-1} $atmos^{-1}$, a very much greater slope than for the assymetric field gaps although in this case the charge time is much less (250 ns as opposed to 800 ns) and the gap is almost twice as big. The cathode breakdown field at 4 atmos is 560 kV cm^{-1}.

The final test on the PFL gaps before the assembly of Sprite was to fire the four gaps into four dummy loads and measure the timing jitter between

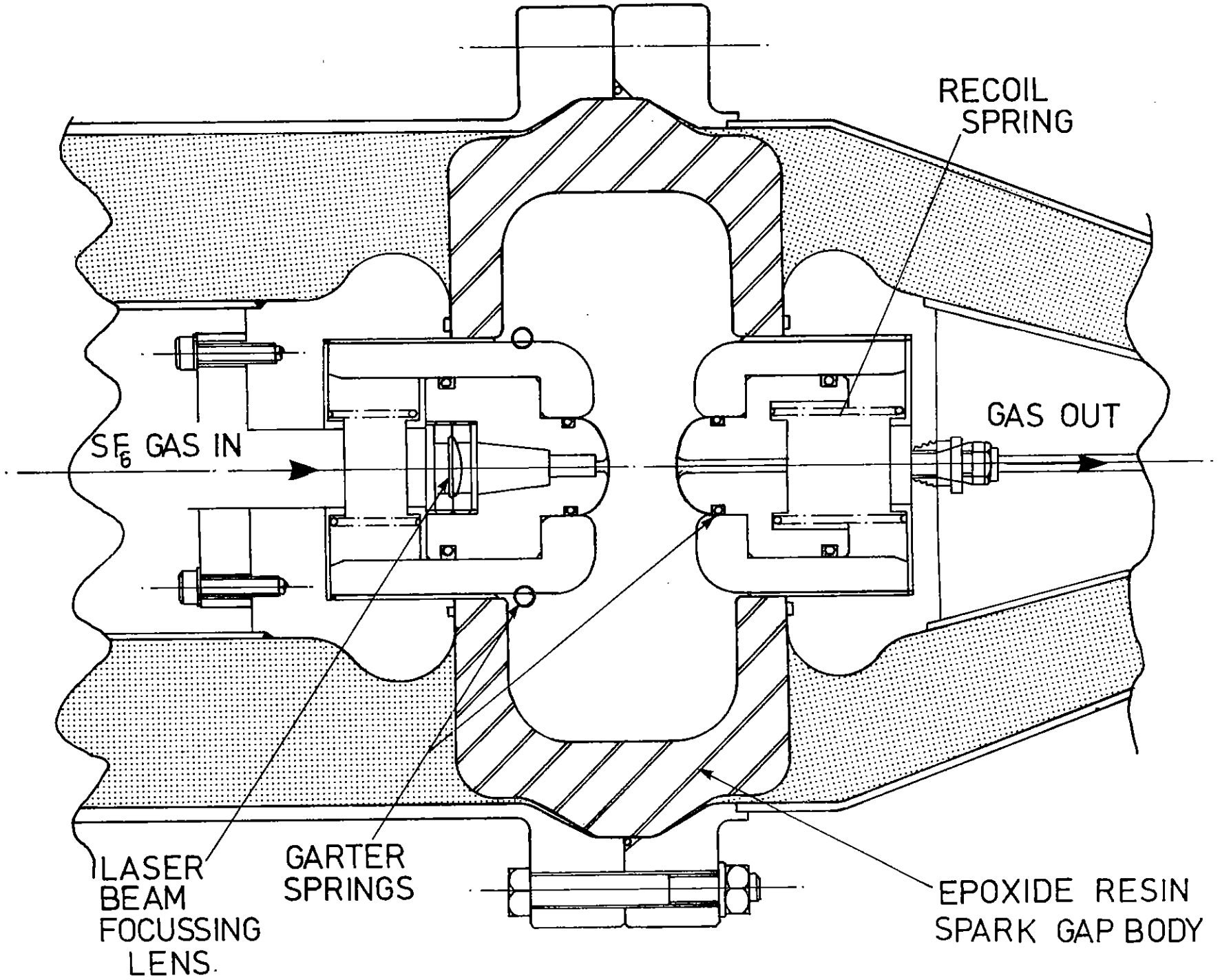

Figure 2.11 Cross-section through the PFL laser triggered switch.

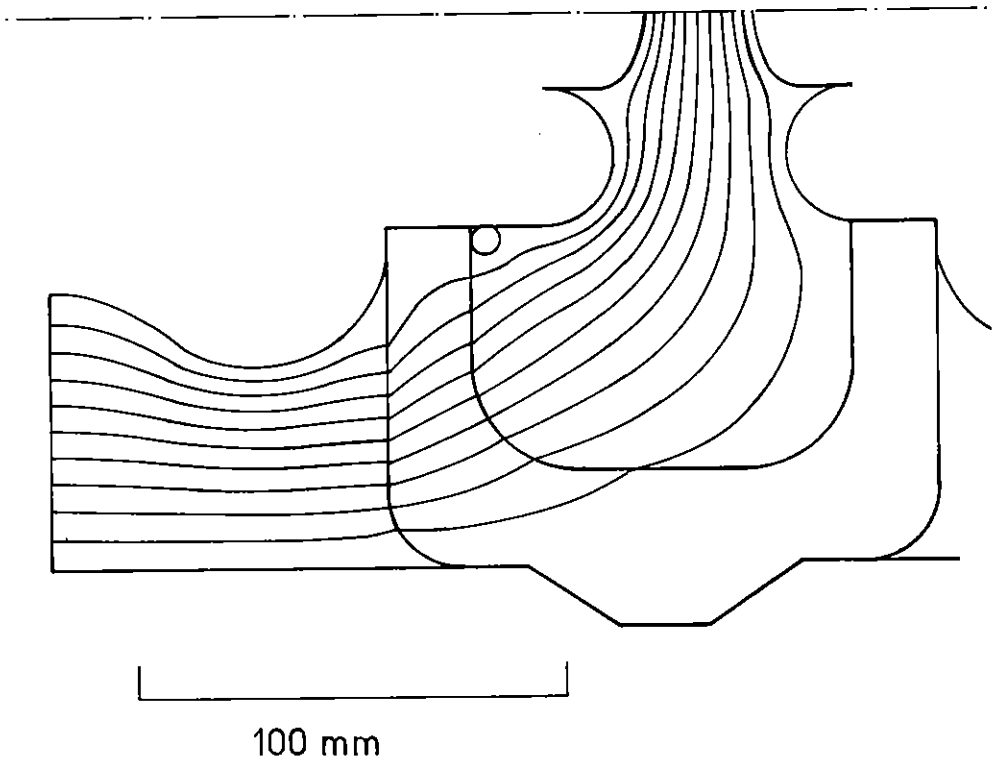

Figure 2.12 Equipotentials obtained from PE2D computer code calculations for the PFL output gap.

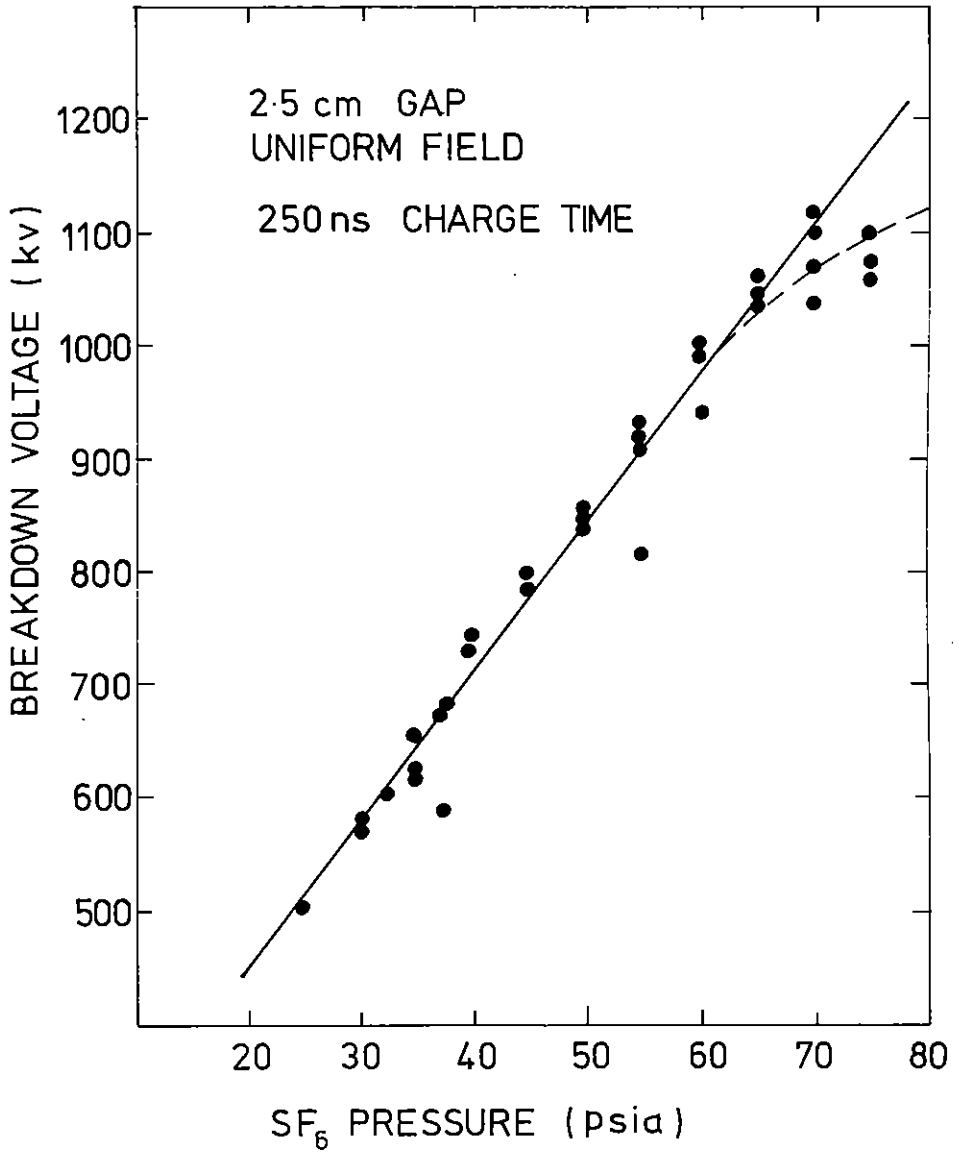

Figure 2.13 Self breakdown voltage versus SF_6 pressure for the PFL output gap.

	$\bar{t}$	σ
Line 2	+0.3ns	9.0ns
Line 3	-1.5ns	10.7ns
Line 4	-5.4ns	11.3ns
All lines	-2.0ns	10.0ns

Table 2.01 Mean and standard deviation in PFL gap self breakdown time relative to self breakdown in gap 1.

the output pulses. By using known cable delays and adding-type plug-ins on a dual beam Tektronix 7844 oscilloscope, all four pulses could be displayed on the same sweep. The gaps were all operated in self-break mode with a nominal breakdown voltage of 950 kV. The mean and standard deviations in ns of the rising edge of the output pulse relative to that of line 1 is shown in Table 2.01. The means are well within the standard deviation indicating that no one line is systematically different from the others. The standard deviation however is unacceptably large for the operation of these gaps in self break mode and these results show the necessity of laser triggering to provide reproducible pumping of the Sprite laser medium.

D Craddock, C B Edwards, F O'Neill and M J Shaw (RAL)

2.2.3 Sprite Construction and Operation

While the testing of the pulsed power components of Sprite was being performed on the ELF Marx bank (sections 2.2.1 and 2.2.2 above) a preliminary mechanical assembly of the e-beam vacuum vessel and laser cell was carried out in another laboratory on site. In this way the electrical testing and the vacuum/pressure testing of components could be accomplished in parallel. After all testing had been satisfactorily carried out the two parts of the machine were integrated into one system attached to the ELF Marx bank as shown in Figure 2.14(a). It is interesting to compare this photograph of the final system with our conception of how the device would look when it was first being planned 2½ years ago. For comparison therefore Figure 2.14(b) is an artist's impression diagram of Sprite taken from our 1980 report to the Laser Facility Committee - it can be seen that we have stayed very close to our original ideas.

In our 1981 LFC report we described some electrical tests that were carried out by running a one-eighth-sized Sprite diode on the 15Ω ELF 60 ns Blumlein. While these experiments were mainly aimed at optimising the design of the full-sized Sprite diode they also showed that the Sprite e-beams would produce copious amounts of X-rays. During the initial test

(a)

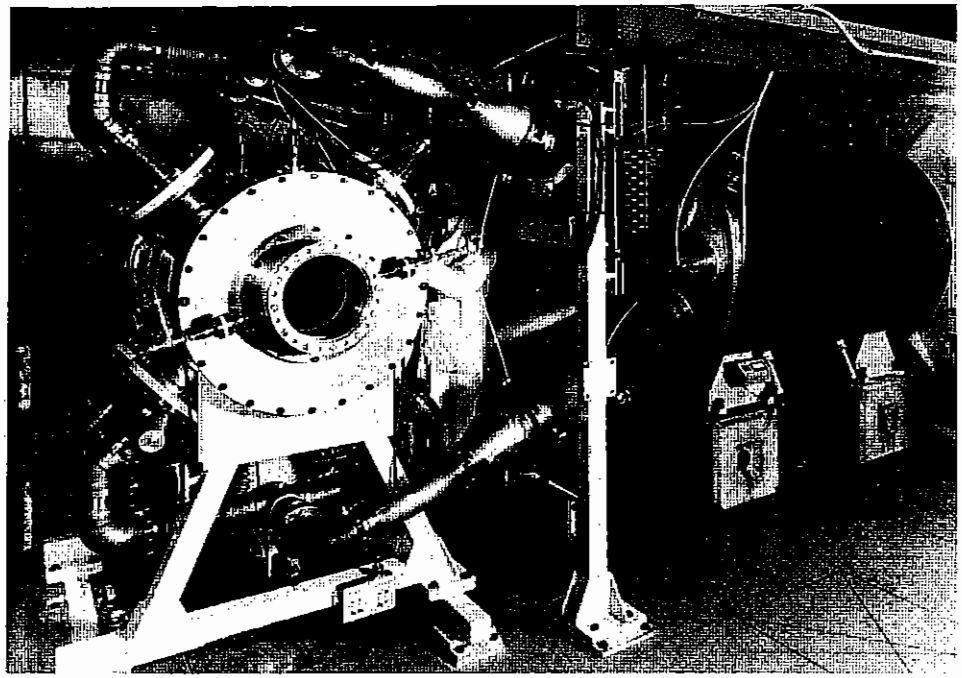

(b)

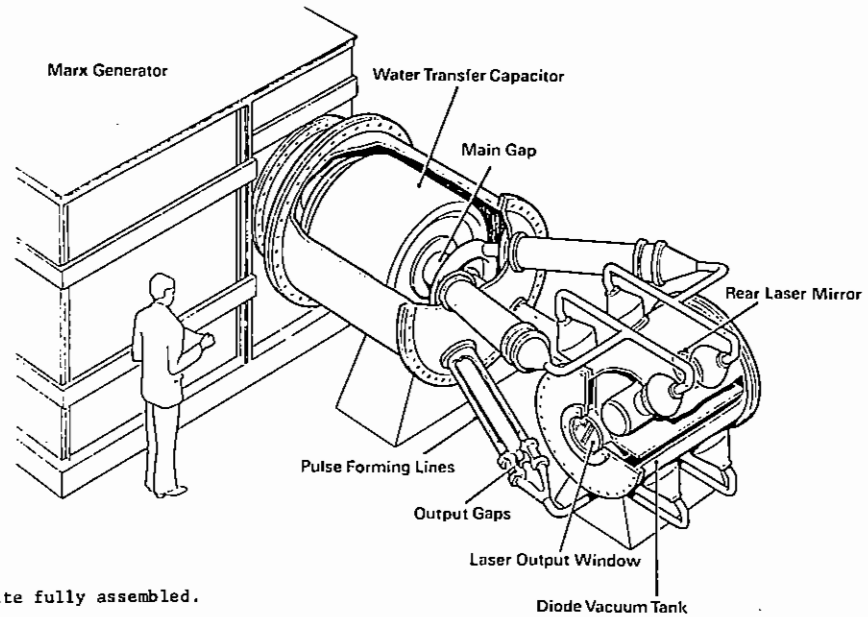

Figure 2.14 (a) Photograph of Sprite fully assembled.

(b) Artists impression of Sprite taken from 1980 report to the Laser Facility Committee. This view is from the opposite side to (a).

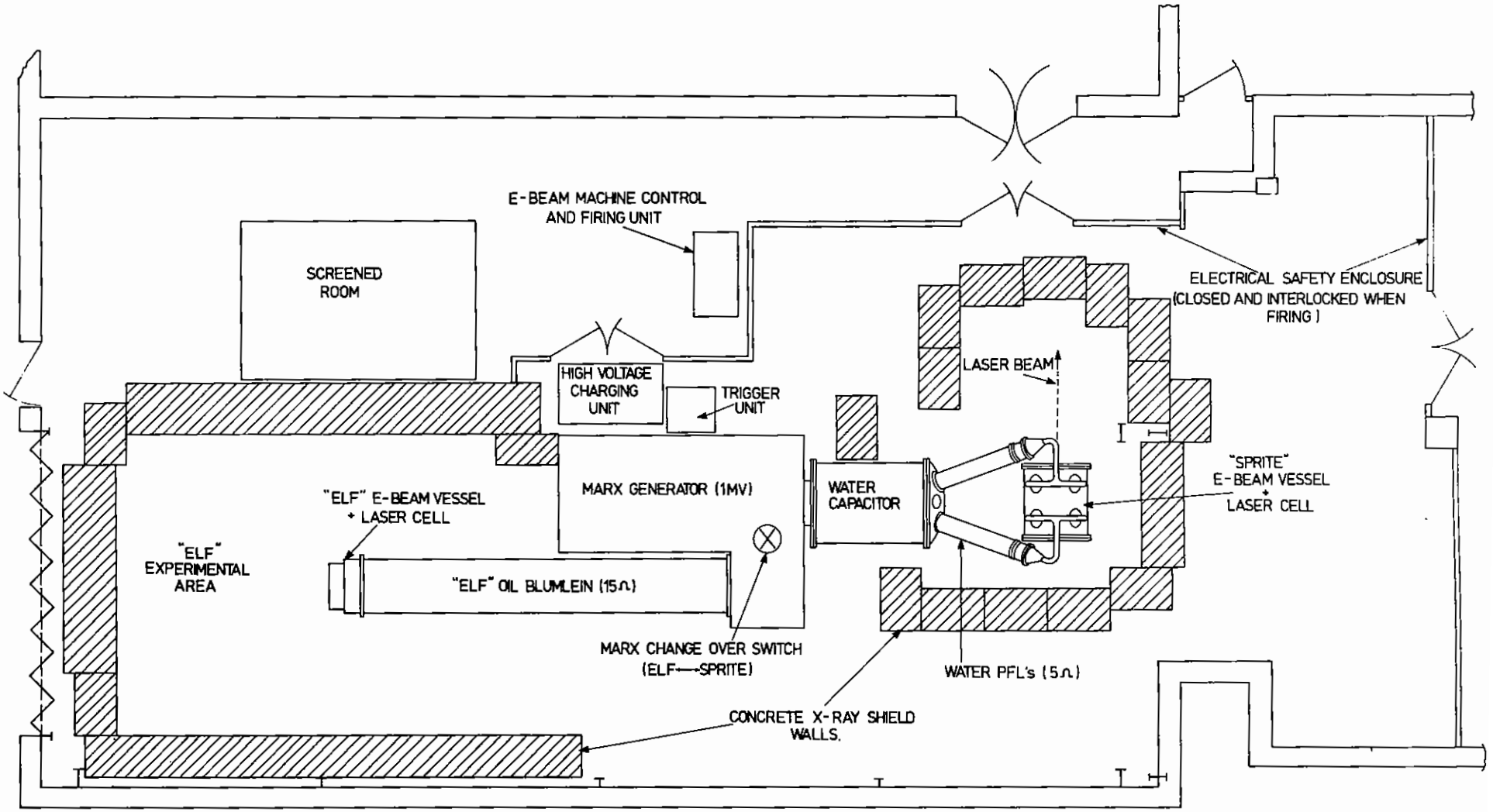

Figure 2.15 Layout of ELF/Sprite e-beam laboratory

phase with the completed laser system it has therefore been necessary to provide considerable close-in X-ray shielding around the machine. To this end we constructed a concrete block-house around Sprite and the complete laboratory area is now laid out as shown in Figure 2.15. When the machine is firing all personnel remain outside the area bounded by the electrical safety enclosure shown in this diagram. The concrete block-house is also fitted with a concrete roof and enough space has been left inside the blocks so that the laser cell and pulse forming/transmission line components can be dismantled without disturbing the concrete. There is also sufficient space to carry out basic laser beam diagnostic measurements viz. energy measurements, beam uniformity measurements, etc. It is expected however that when the machine radiation hazard has been fully assessed a less massive and more spacious shielding enclosure can be designed.

Our first shots on the machine were aimed at measuring the amount of e-beam energy deposited in the laser cell. This is a good machine diagnostic because when coupled with current and voltage measurements a considerable amount of information on diode performance is obtained. In addition of course the energy deposition measurements give a rough indication of the laser output energy that can be expected - an intrinsic efficiency ~10% can be assumed (2.07). The main constructional details of the Sprite laser system are shown in Figures 2.16 and 2.17. E-beam energy is pumped into the laser cell in a four-sided geometry and the amount of e-beam energy actually getting into the cell is determined by measuring the resultant pressure jump in the gas. The gas pressure in the laser cell has of course to be high enough so that the high energy e-beam does not penetrate right through. The details of this technique have been discussed in a previous publication (2.07). For the present measurements where e-beam voltages of < 450 kV are used we filled the laser cell with 1500 torr of pure N_2.

To date the machine has been fired 9 times and the highest performance data so far achieved is shown in the table below. Operation at present is limited to 300 kV on

12 stage ELF Marx charge voltage	65 kV
Water capacitor charge voltage	500 kV
Peak PFL charge voltages	610 kV
Diode voltage (peak)	300 kV
Individual diode current (peak)	48 kA
Energy deposited in laser cell	1.8 kJ

the diodes due to insulator tracking problems in the fast, water-filled, transmission line sections. This particular problem is not considered to be severe and is now being rectified at which time the machine will be run up to ~450 kV. Scaling from the above listed measurements, and allowing for the fact that even at 300 kV late time tracking was occurring in the feed lines to two of the diodes, operation at 450 kV should result in ~ 4 kJ e-beam energy deposited in the laser gas which would imply a laser output energy of 300 - 400 J.

D Baker, D Craddock, C B Edwards, H T Medhurst, F O'Neill and M J Shaw (RAL)

2.3 Phase Conjugation

2.3.1 Four-wave Mixing Experiments

The experimental arrangement used in the present work is shown in Figure 2.18 and is described fully in references (2.08) – (2.10). The KrF laser source (Section 2.4.2) consists of a line-narrowed master oscillator and a slaved unstable resonator oscillator. This system produced ~5MW, 10-20 ns pulses of radiation at 249 nm with a linewidth of ~ 0.3 cm^{-1} in a near diffraction limited beam. The probe wave, I_3, in the standard retroreflecting DFWM geometry shown in Figure 2.18, was focused by a 1.75m focal length lens, L, and intersected the pump waves, I_1 and I_2, at an angle of 4° at the 0.5 cm long sample cell.

The mechanism responsible for the observed phase conjugate signals in our DFWM experiments is a thermal refractive index non-linearity induced in the medium (2.08) - (2.10). In (2.08) we presented measurements which showed that, in the low reflectivity regime ($R \lesssim 1\%$), the PC reflectivity

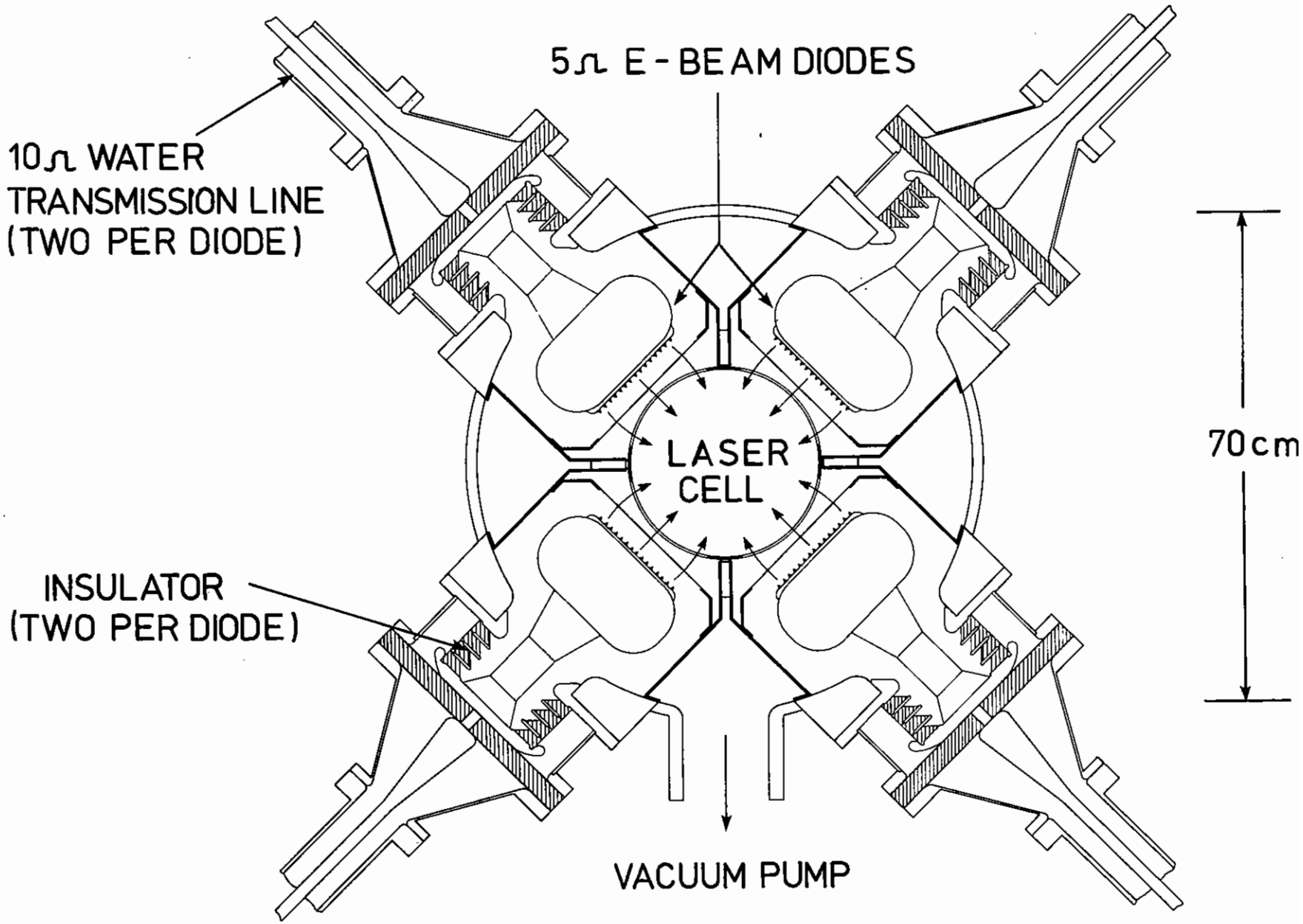

Figure 2.16 Cross-sectional diagram of Sprite.

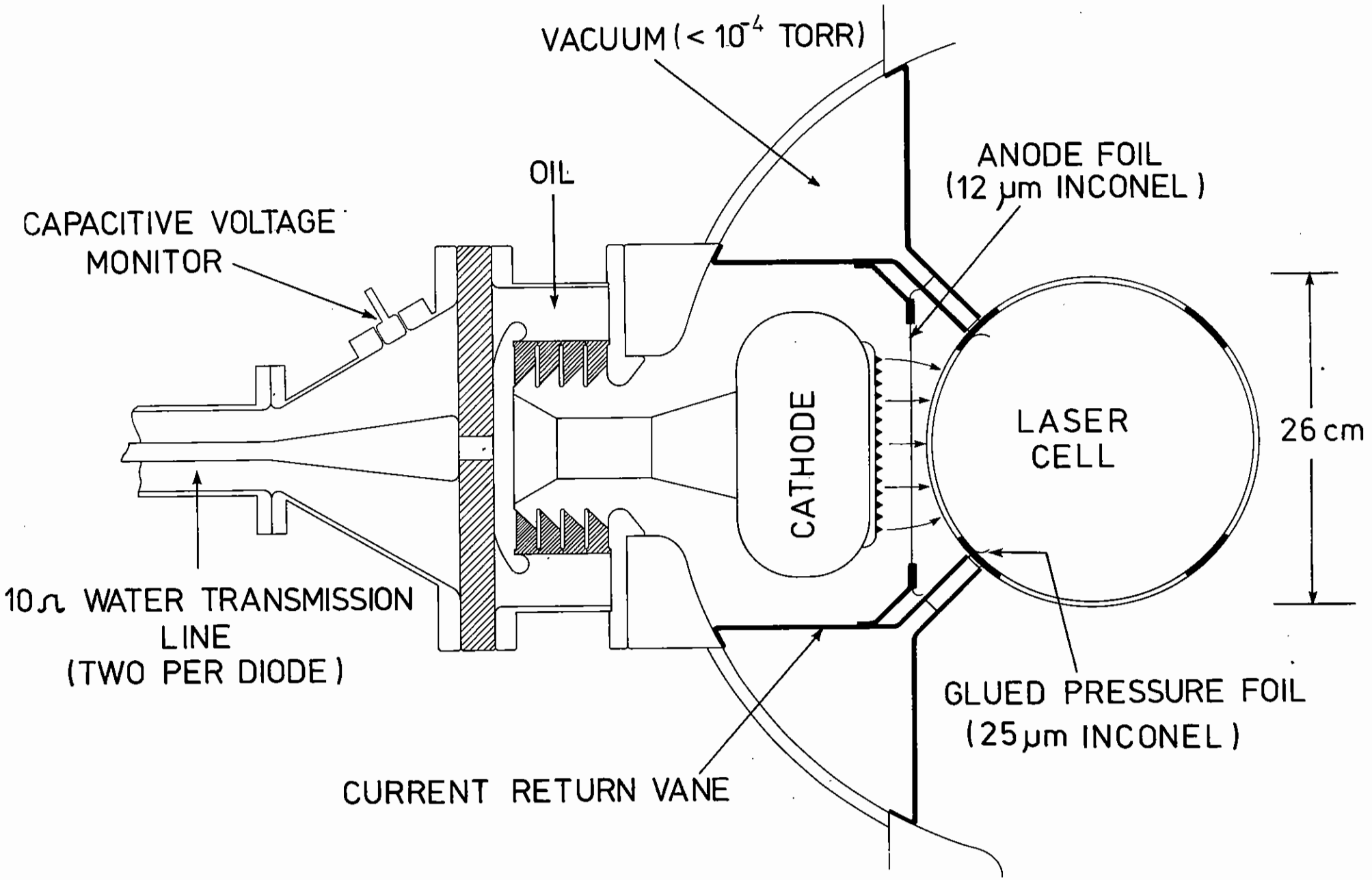

Figure 2.17 Detailed cross-section of one quadrant of Sprite

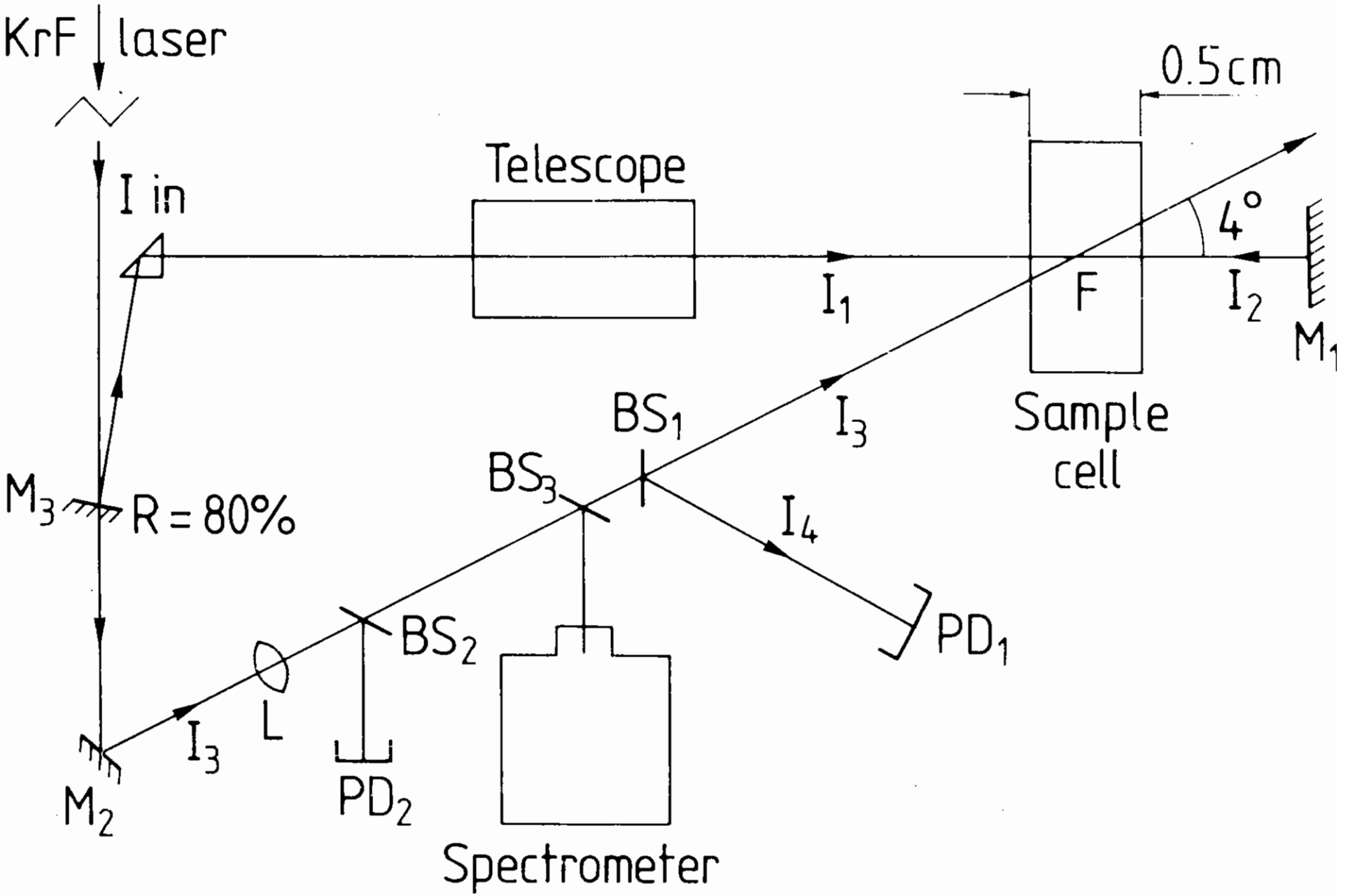

Figure 2.18 Experimental set up for PC measurements using DFWM. I_1, and I_2 are pump waves and I_4 is the phase conjugate of the probe wave I_3. BS and PD are beamsplitters and photodiodes respectively. The telescope contracts the pump waves to a 1.4 x 4.1mm beam.

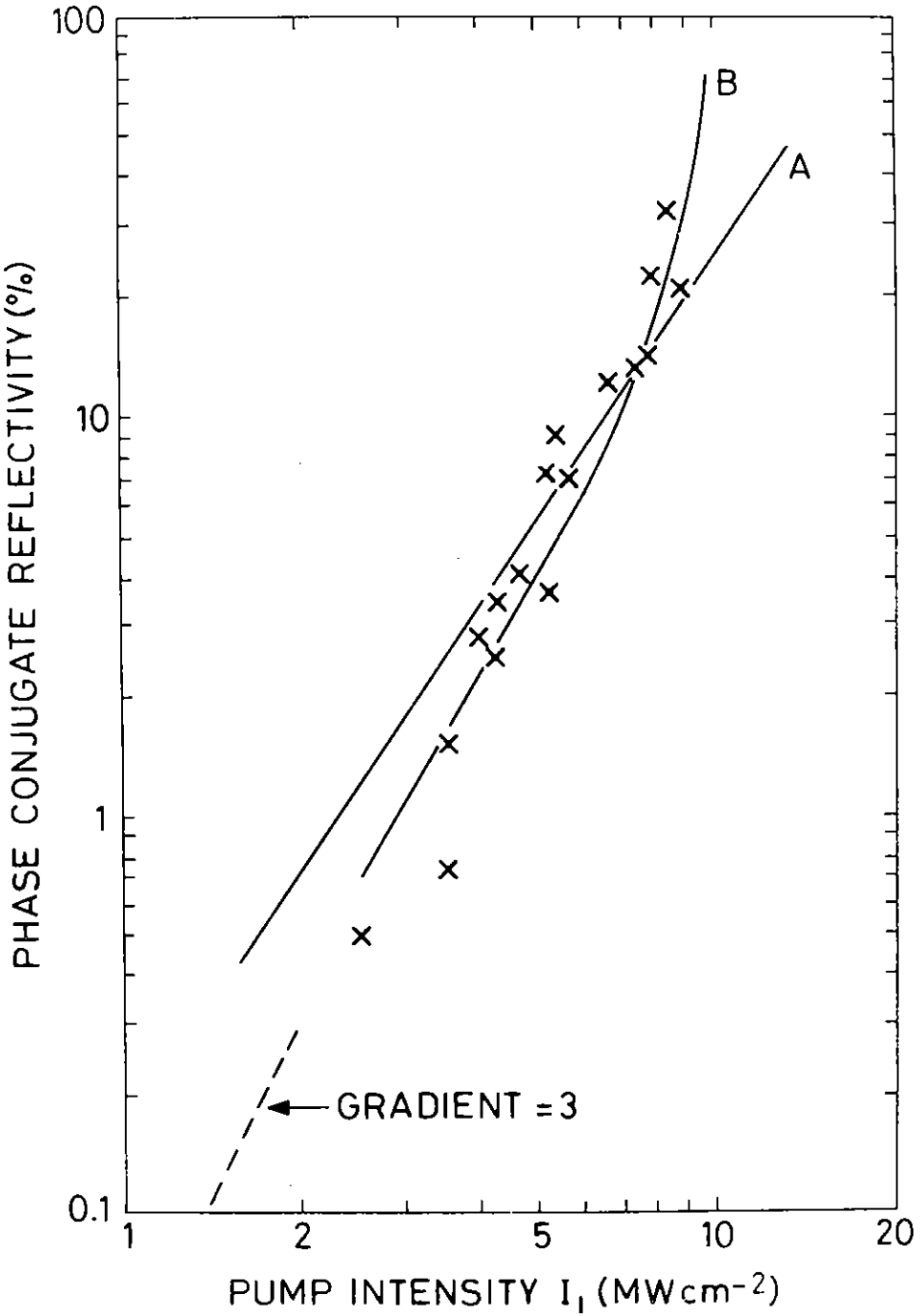

Figure 2.19 Measured PC DFWM reflectivity vs pump intensity. Curves A and B are plots of Equation (2) for values of f = 0.3 and 0.7 respectively. Curve B has been multiplied by a scaling factor of 0.1.

exhibited a quadratic dependence on the pump wave intensity, I_1, in accordance with the expression:

$$R = \left[Df\, I_1\, \tau e^{-\alpha d} \left(1 - e^{-\alpha d} \right) \right]^2 \qquad (1)$$

where f = fraction of absorbed energy converted to heat, τ = laser pulse duration, α = absorption coefficient of the medium, and d = the cell length. The thermodynamic parameter $D = \left(- \frac{\omega}{c\rho C_p} \right) \left(\frac{dn}{dT} \right)_p$ in a medium which has density ρ, and specific heat and refractive index temperature coefficient, at constant pressure, C_p and $\left(\frac{dn}{dT} \right)_p$ respectively. Equation (1) was originally derived by Martin and Hellwarth (2.11) in the low reflectivity limit. In contrast to those results, in Figure 2.19 we show measurements of R versus I_1, in the high reflectivity regime for a 2×10^{-5} M solution of rhodamine 6G (Rh6G) in ethanol (EtOH), and with $I_3/I_1 \sim 2 \times 10^{-2}$.

Clearly, for the case of high reflectivity, a quadratic dependence of R on I, is no longer observed and Equation (1) is no longer valid. Although a cubic dependence seems to be more appropriate in the regime of the data shown in Figure 2.19, we have developed a more general theory which is valid at both high and low reflectivity and includes the effects of absorption of the pump and probe waves by the medium. The results of this (coupled wave) analysis predict

$$R = \left| \frac{2Q \sin (Hd/2)}{H \cos (Hd/2) + \alpha \sin (Hd/2)} \right|^2 \qquad (2)$$

where $H = (4|Q|^2 - \alpha^2)^{\frac{1}{2}}$ and for a thermally-induced nonlinearity $|Q|^2 = [Df I_1 \tau \alpha e^{-\alpha d}]^2$.

Curves A and B in Figure 2.19 are plots of Equation (2) for values of f = 0.3 and 0.7 respectively (curve B has been multiplied by a scaling factor of 0.1). Although the choice of value for f is somewhat arbitrary since exact values are unknown, it can be seen that good agreement can be

obtained between the theory and the experimental results.

Figure 2.20 shows the effect of varying the concentration of Rh6G with either EtOH or H_2O as solvents. It is immediately apparent from these data that much lower PC reflectivities are obtained when H_2O, rather than EtOH, is used as the solvent. We believe that this provides further evidence that the mechanism producing the refractive index non-linearity is a thermal one, since, in Equations (1) and (2), the value of the thermodynamic parameter, D, for H_2O is approximately a factor of 5 less than that for EtOH (10^{-3} and 5×10^{-3} m^2/J, respectively). Other possible mechanisms which could produce PC signals in Rh6G are not expected to be as solvent sensitive as the thermal effect. Curve A in Figure 2.20 shows a plot of Equation (2) for water as the solvent and using f = 0.3. Again there appears to be good agreement between our theoretical expression (Equation 2) and the experimental data.

Similar concentration data is also shown in Figure 2.21 for the case of CS_2, with a fractional concentration ψ, diluted in hexane. The dilution of CS_2, in hexane reduces the CS_2 absorption cross-section at 249 nm (2.12). Our previous observations in CS_2 (2.10) are also consistent with a thermal mechanism producing the PC signal. In Figure 2.21, the maximum reflectivity of ~ 300% is comparable in magnitude to the amplified PC signals reported using Rh6G as the medium (2.10). The curve, which again is in good agreement with the data, is a plot of Equation (2) with f = 0.5 and $D = \psi D_{CS_2} + (1-\psi)D_{Hexane}$; ($D_{CS} = 4 \times 10^{-2}$ m^2/J and $D_{Hexane} = 8 \times 10^{-3}$ m^2/J).

2.3.2 Phase Conjugation by Stimulated Brillouin Scattering (SBS)

Although Bigio et al (2.13) first reported observation of KrF laser SBS in a variety of liquids, their scattered signal was a relatively poor phase conjugate of the incident pump radiation. We first reported high quality pulse conjugation of KrF laser radiation using SBS (2.14). We have also used this phase conjugate mirror as a resonator element in a KrF laser cavity to produce a diffraction limited output beam.

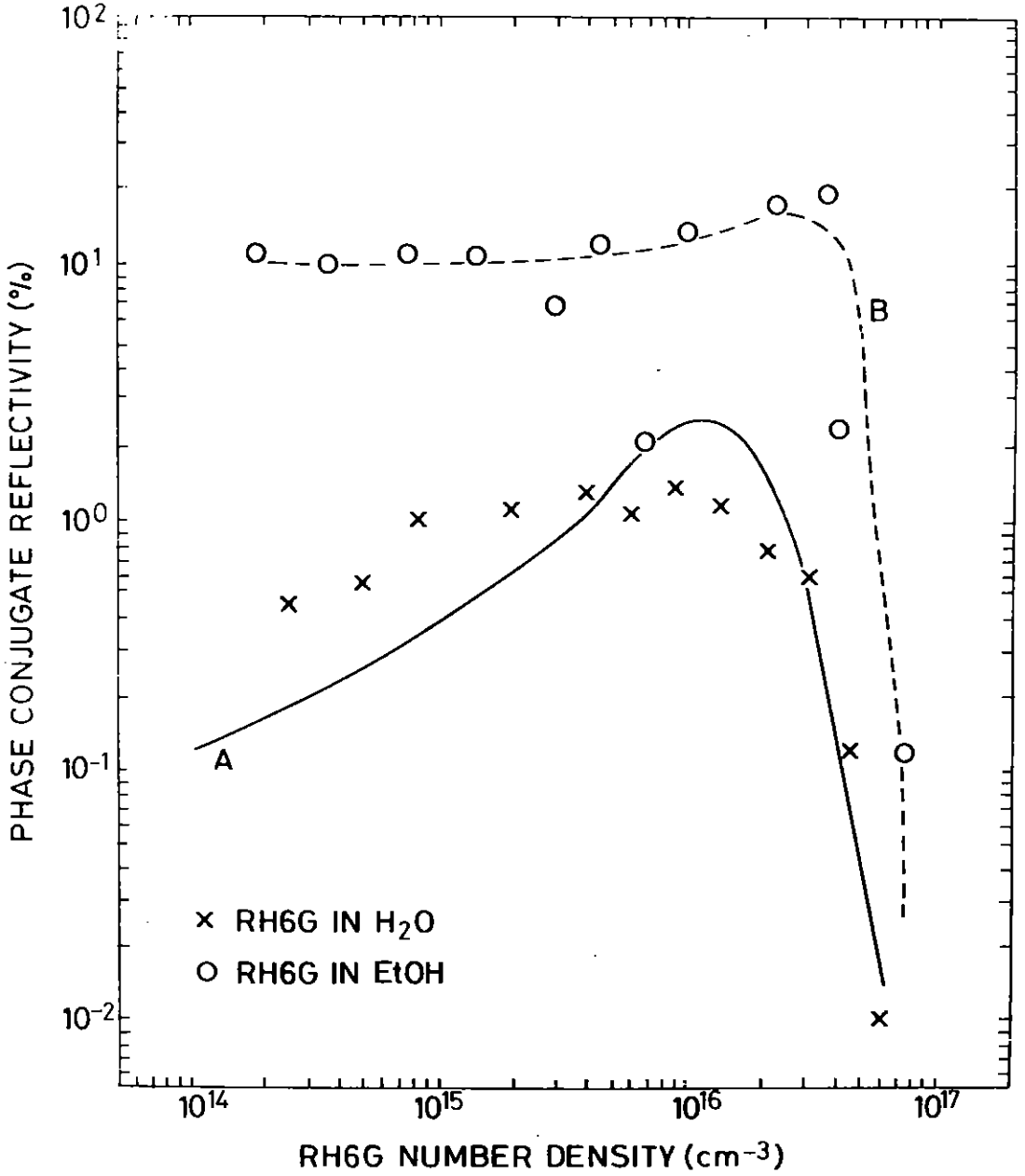

Figure 2.20 Measured PC DFWM reflectivity vs Rh6G concentration in EtOH and water. $I_1 \sim 12MW/cm^2$. $I_3 = 3MW/cm^2$. Curve A is a plot of Equation (2) with f = 0.3.

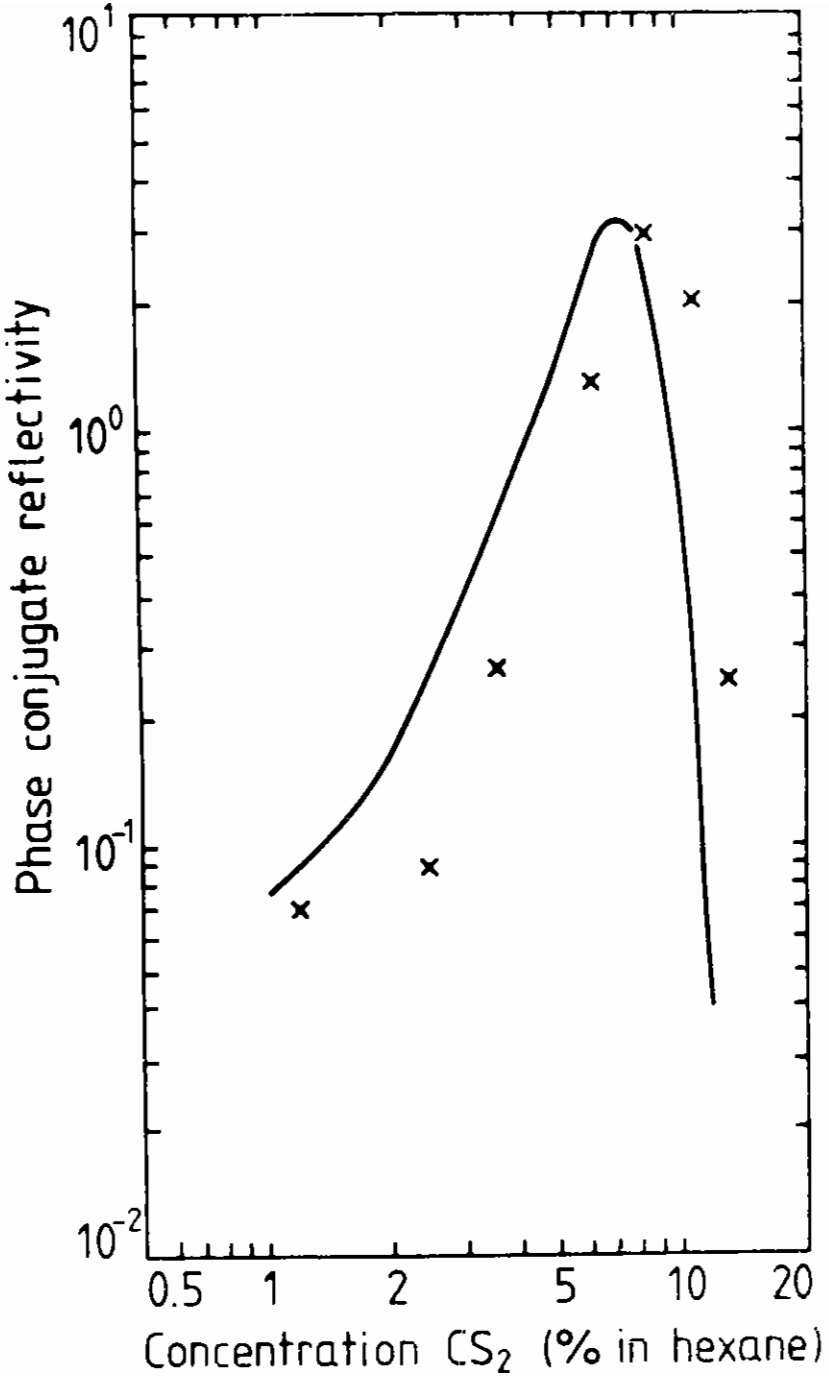

Figure 2.21 Measured PC DFWM reflectivity vs CS_2 concentration, ψ, in hexane. The curve is a plot of Equation (2) with f = 0.5.

The experimental set-up of the oscillator/amplifier configuration is shown in Figure 2.22. The KrF oscillator produced ~4μJ of energy in a diffraction limited beam of area 0.3 cm^2 and linewidth < 0.2 cm^{-1}. The temporal behaviour of the oscillator output pulse is shown in Figure 2.23(a). In order to better fill the amplifier volume, this pulse was focused by a 50 cm focal length lens, L_1, and the resulting diverging beam was passed through the amplifier which had a net gain ~ 3×10^3. The radiation emergent from the amplifier had the area of the discharge $(2 \times 0.5)cm^2$, the pulse shape shown in Figure 2.23(b), and a beam divergence measured to be ~ 5 times the diffraction limit at BS_1. It was focused by a 10 cm focal length lens, L_2, approximately 0.5 cm below the surface of the Brillouin liquid.

In the case where ethanol (EtOH), which has a Brillouin shift of 0.1 cm^{-1} (2.15) was used as the scattering medium, the stimulated backscattered pulse is depicted before entering the amplifier (reflected from BS_1) in Figure 2.23(c) and after passing through the amplifier (reflected from BS_2) in Figure 2.23(d). Without any liquid in the cell these signals were completely absent. As well as being reshaped by the amplifier, the scattered pulse was amplified by approximately a factor of 5 upon returning through the amplifier. In Figure 2.23(e) is shown the analogous signal to that of Figure 2.23(d) after the pulse had passed through a spatial filter consisting of a 100 μm diameter pinhole placed at the focus of a 2.5 m focal length lens (F = 180). The size of the aperture was such that the transmitted radiation corresponded to a diffraction limited beam. It can be seen that the stimulated backscattered signal had two components, one of which was the shorter pulse shown in Figure 2.23(e). Approximately 90% of this shorter pulse passed through the 100 μm pinhole, illustrating the diffraction limited nature of this pulse. Figure 2.23(d) shows this diffraction limited pulse together with a second more divergent stimulated pulse which had a longer duration. The longer component is not observed in Figure 2.23(c) since it is sufficiently spatially removed from the shorter component at the photodiode so as not to be detected. However, as seen in Figure 2.23(d), there is sufficient feedback into the amplifier for it to be detected from BS_2.

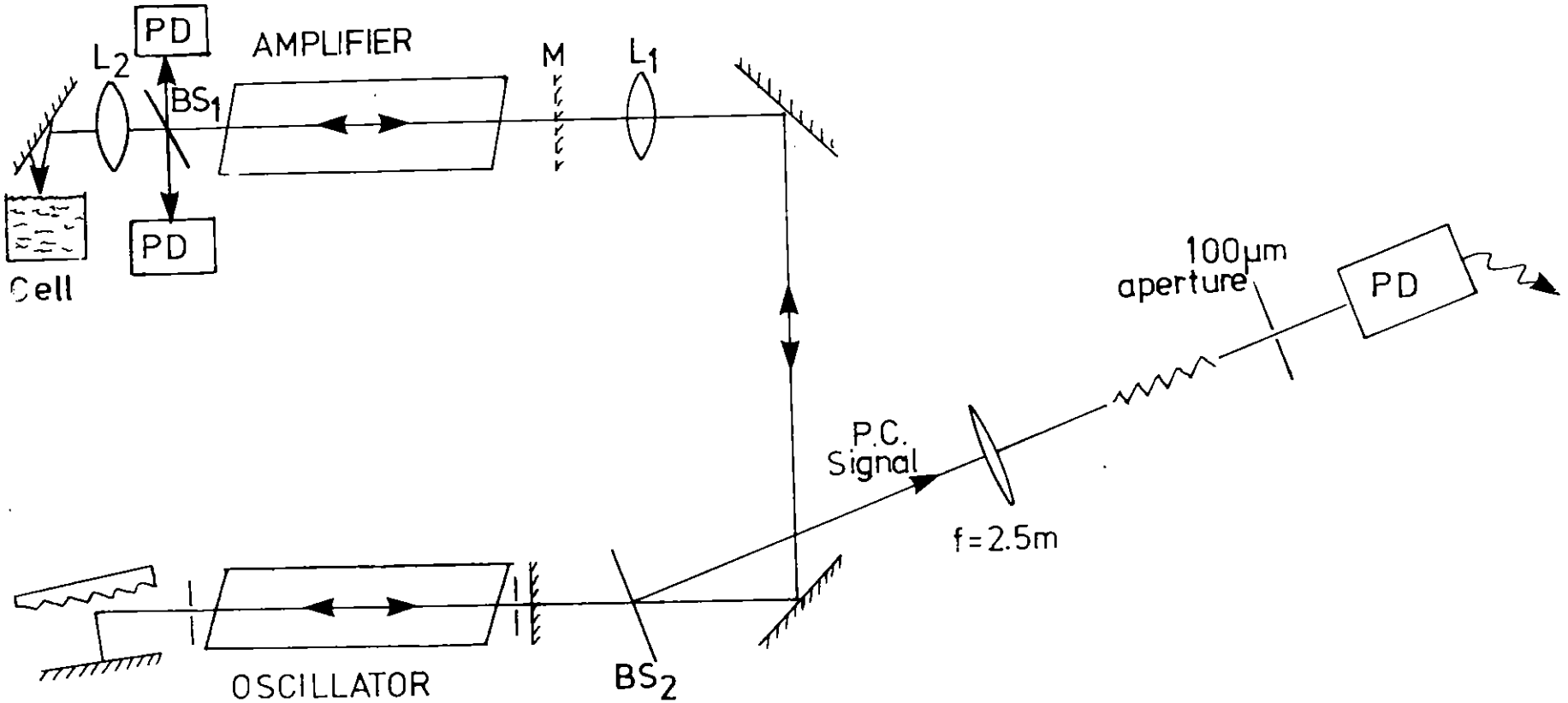

Figure 2.22 Experimental set up for PC measurements using SBS. L_1 and L_2 are 50cm and 10 cm focal length lenses L_1 was 110cm in front of the entrance plane of the amplifier, the distance of the oscillator to the amplifier was 3.2m. BS and PD are beamsplitters and photodiodes respectively.

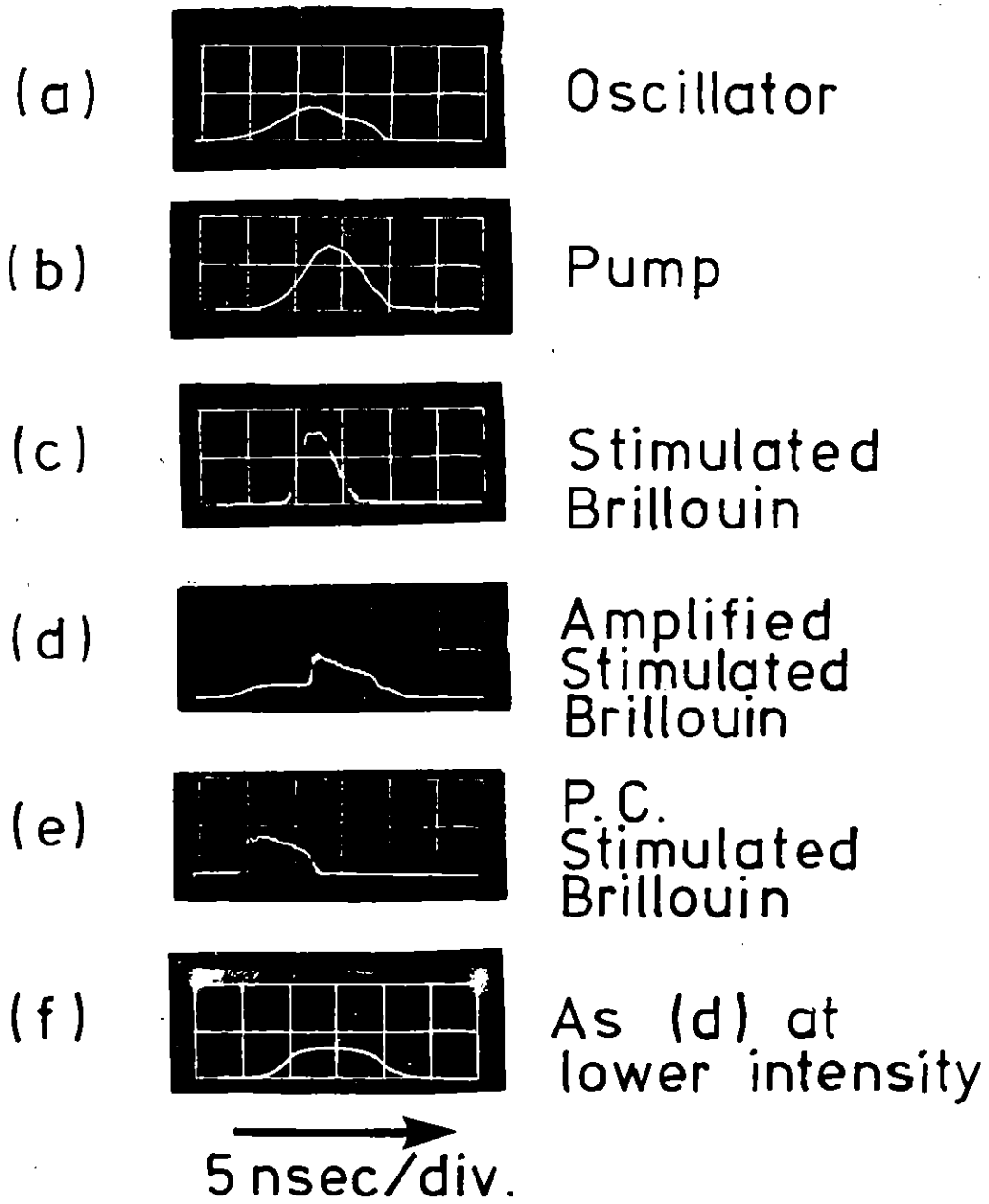

Figure 2.23 (a) Oscillator pulse
(b) Amplified oscillator (pump) pulse
(c) Backscattered signal at BS_1 (SBS PC component only)
(d) Amplified total backscattered signal at BS_2.
(e) Diffraction limited component of (d)
(f) As (d) at lower intensity.

Although the pump radiation at the sample cell had a divergence ~ 5 times the diffraction limit, after returning through the amplifier the shorter of the two stimulated backscattered pulses had the same diffraction limited divergence as the original oscillator pulse. This illustrates the phase conjugate nature of this shorter pulse, which is most likely produced by SBS, and demonstrates the use of a SBS phase conjugate mirror to compensate for the distortions to the pump wavefront which were produced by the amplifier. The phase conjugate nature of the shorter SBS pulse was further confirmed by placing a silica aberrator at M in Figure 2.22 and observing that the shorter of the two pulses in Figure 2.23(d) remained diffraction limited at BS_2. With the aberrator in place, severe distortion of the output radiation was observed when the phase conjugate mirror was replaced by a high reflectance plane mirror. Furthermore, when BS_1 was used to monitor the backscattered signal, it was found that the shorter pulse passed through a focus at the equivalent position relative to BS_1 to that at which the pump radiation was focused by L_1.

In Figure 2.23(f) we show the amplified stimulated backscattered signal at a somewhat lower pump intensity than that used to obtain the pulse shown in Figure 2.23(d). In Figure 2.23(f) the shorter PC component is completely absent which indicates that the non-PC stimulated scattering component has a lower threshold than the PC SBS component. We measured the beam divergence of this longer pulse to be ~ 10 times the diffraction limit at BS_2. We believe that the presence of this non-PC SBS component is due to incomplete line-narrowed operation of our oscillator. In more recent experiments we have found that when care was taken to fully line narrow the oscillator output. this non-PC component was completely absent. On the other hand, we have found that when the oscillator was intentionally operated broadband, the the PC SBS return was ~ 2 times less intense than the longer non-PC component.

The constraints for good SBS phase conjugation are expected to be more stringent when using broadband pump radiation (2.16). This longer component may also correspond to the KrF laser stimulated backscattered signal observed by Bigio et al (2.13) who reported poor signal

reproducibility and image reproduction (∿7 times diffraction limited stimulated backscattered signal for a diffraction limited pump wave). This hypothesis is further supported by their recent work (2.17) in which high quality SBS PC was observed using a very narrow linewidth XeF laser operating at 351 nm.

In Figure 2.24 are shown measurements of the phase conjugate reflectivity (the fraction of the pump wave reflected as the PC Brillouin component) as a function of the pump intensity times (focal length)^2 for different focal lengths of L_2. To obtain an estimate of the pump intensity, the area of the beam at the focus of L_2 was calculated using measurements of the pump beam divergence at BS_1. It can be seen that the maximum PC reflectivity observed was ∿80% and that the reflectivity was independent of the focal length, f, of the lens used (the intensity at focus, $I \propto 1/f^2$ and the interaction length $\ell \propto f^2$ so that $I\ell$ is independant of f). At higher values of If^2 a decrease in the PC reflectivity was observed which may be due to other competing nonlinear effects such as self-focusing.

In an effort to further demonstrate the utility of this Brillouin PC mirror, we placed an aligned 90% transmitting mirror 120 cm from the cell, at M in Figure 2.22, and thus obtained further feedback into the amplifier

(3 cavity round trips are possible during the amplifier gain duration). We observed that the diffraction limited PC output from the Brillouin mirror increased at BS_2. This suggests that this type of PC mirror may be extremely useful in obtaining diffraction limited output from large aperture high gain laser oscillators provided that the multiple Brillouin shifts generated by such a mirror remain within the (homogeneous) bandwidth of the gain medium. We are currently performing further experiments on this type of device.

M C Gower (RAL) and R G Caro (Oxford)

2.3.3 Pulse Compression and Phase Conjugation by SBS in a Waveguide

Rare gas halide excimer lasers have storage times of only a few

nanoseconds and, since electron-beam pumped systems have their greatest efficiences for excitation pulses ≈ 50 ns or greater, the amplification of a single nanosecond pulse is inefficient. The problem may be overcome by laser pulse compression and stimulated Raman scattering (SRS) has been shown to be an effective method for achieving this (2.18). However, stimulated Brillouin scattering (SBS) can also produce compression (2.19) when a laser pulse is injected into a convergently tapering waveguide which is filled with a Brillouin-active medium and whose length is approximately half that of the laser pulse.

The use of SBS offers several potential advantages over compressor systems based upon SRS. The production of second Stokes radiation which limits the efficiency of compression by SRS is not a serious problem, because SBS occurs only in the backward direction. Since the first Stokes pulse is of short duration, the gain length for the backward second Stokes field is small and occurs in the transient regime where the gain is reduced. In addition, the fact that the Stokes pulse propagates into an increasing area of the waveguide keeps the intensity of the first Stokes low and maintains a small second Stokes gain. The quantum efficiency of the SBS process is almost one hundred per cent since the Stokes frequency (ω_S) is approximately equal to the laser frequency (ω_L). The small frequency shift would therefore enable the Stokes pulse to be further amplified in a laser amplifier. The fact that the Brillouin process is initiated spontaneously in the medium removes the need for an injected Stokes pulse as required in an SRS compressor and therefore reduces the complexity of the system. Moreover, since the Stokes wave in SBS under appropriate conditions is a phase conjugate of the input wave (2.20), compensation for optical inhomogeneities in laser amplifiers can be made (2.21).

The basic scheme of compression by SBS involves the use of a tapered geometry which may be achieved most controllably in a convergently tapering waveguide. As with SRS, the interaction length should be approximately half that of the laser pulse. The stokes pulse is spontaneously generated in the medium by the SBS process. As the laser propagates along the waveguide into decreasing area, its intensity increases. The gain is greatest near the exit of the waveguide and, by

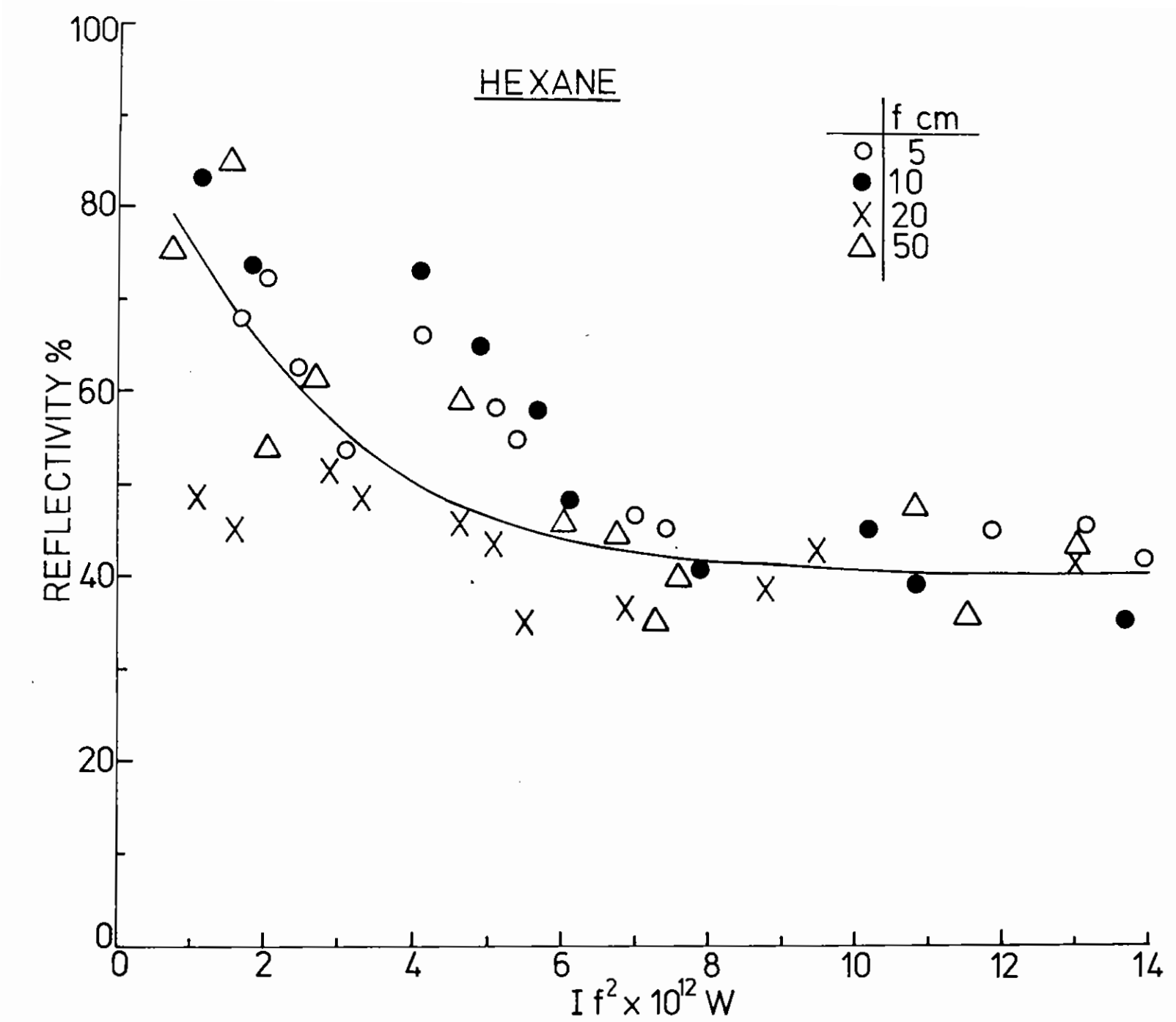

Figure 2.24 Phase conjugate stimulated Brillouin reflecticity versus If^2. Hexane was the active medium.

suitable choice of input laser intensity and waveguide taper, a Stokes pulse of short duration originates from a region near the exit. Once generated, it propagates backwards down the waveguide, receiving amplification by the incoming laser pulse. An intense Stokes pulse of short duration is produced and the laser pulse is correspondingly depleted. SBS is described by three coupled equations for the laser field (E_L), backscattered Stokes field (E_S) and the acoustic fluctuation (Q) and are taken in the following form:

$$\left(\frac{\partial}{\partial t} + \frac{c}{n}\frac{\partial}{\partial z}\right) E_L = - E_s Q \qquad (1)$$

$$\left(\frac{\partial}{\partial t} - \frac{c}{n}\frac{\partial}{\partial z}\right) E_S = E_L Q^* \qquad (2)$$

$$\left(\frac{\partial}{\partial t} + \frac{1}{2\tau_B}\right) Q = \gamma E_L E_S^* \qquad (3)$$

where τ_B is the damping time of the acoustic wave in the Brillouin-active medium and γ is a coupling constant which is proportional to g_B/τ_B where g_B is the steady state gain coefficient.

These equations are solved by a computer code which we have developed. The tapered geometry required for pulse compression is modelled in the code by making the gain term γ a function of z related to the waveguide area A(z) in the form $\gamma(z) = \gamma_o/A(z)$. This provides a simple and accurate method for handling arbitrary interaction geometries provided a plane wave or mean field analysis can be evoked.

The computation is considered for the Brillouin-active gas methane at high pressure as a representative medium exhibiting high gain (g_B) and long damping time (τ_B). Several Brillouin-active media might be considered for a compressor system and the particular choice would be dependent on factors such as gain coefficients, damping times and threshold levels for detrimental processes such as breakdown, self-focusing and forward Raman scattering.

In Figure 2.25(a) are illustrated typical computed output Stokes and laser

(a)

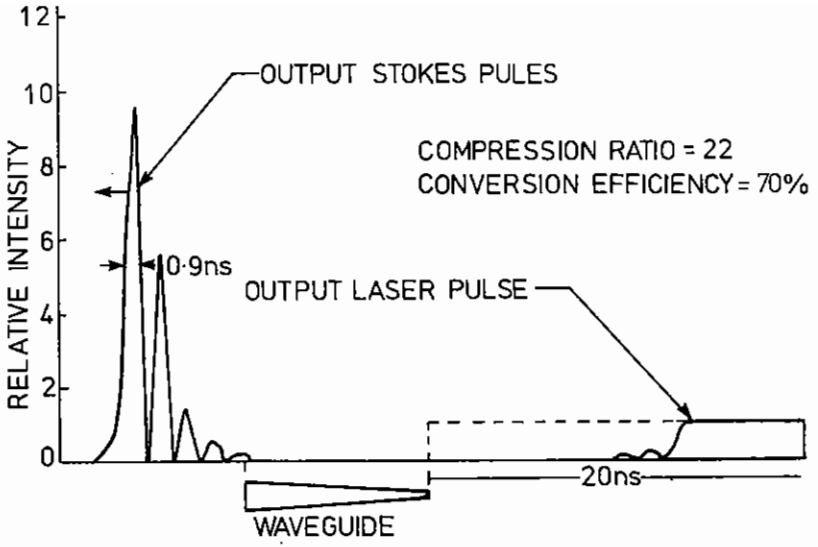

(b)

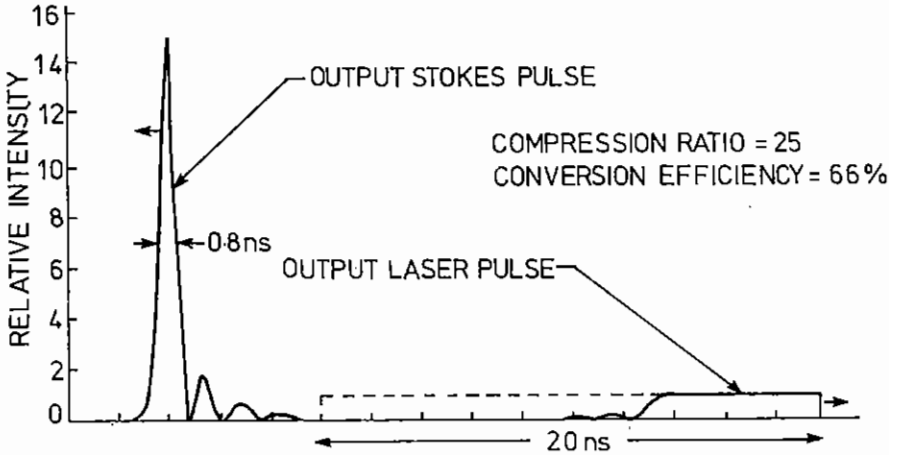

Figure 2.25 (a) Typical laser and Stokes pulses after interaction in a tapered waveguide filled with a Brillioun active medium with long acoustic decay time. The Stokes pulse exhibits pulse break-up.
(b) Pulse compression in a suitably tapered waveguide geometry to reduce Stokes pulse break-up under transient SBS conditions.

pulses from the compression process in a tapered geometry. The output Stokes pulse is of a complex nature, exhibiting pulse break-up and is a consequence of the transient nature of the SBS process and occurs when the laser pulse is depleted before the end of a counterpropagating Stokes pulse. This is detrimental to the compressor system since energy is lost from the main stokes pulse. However, the situation can be improved by the use of a more strongly damped medium and with a more suitable geometric taper, as shown in Figure 2.25(b). For high pressure gases, $\tau_B \propto \lambda_L^2$ (2.22) and damping times of 1 - 2 ns are expected for the UV excimer lasers such as KrF. Pulse break-up is therefore reduced at short wavelengths.

The limit of compression by this technique appears to be reached when the Stokes pulse is reduced to a duration comparable to the inverse of the acoustic frequency. This situation can be analysed by retaining the second time derivative of the acoustic field $\partial^2 Q/\partial t^2$ in Equation (3). For acoustic waves $\omega_Q \sim 10^{10}$ rad/S typically and this will tend to limit the Stokes pulse duration to the subnanosecond timescale. The compression of pulses of various duraitons t_L in CH_4 at different wavelengths, has been analysed and Figure 2.26 shows the variation of conversion efficiency with the power density of the laser pulse at the exit of the waveguide for compression to a 1 ns pulse. It is noteworthy that compression ratios of ~30 with > 80% efficiency at exit power densities as low as 50 MW cm^{-2} are predicted for KrF.

The compression of laser pulses by SBS has also been investigated experimentally. A 30 ns pulse from a Q-switched ruby laser operating in a single longitudinal and TEM_{oo} transverse mode was amplified and injected into a 1.5 m long waveguide containing CS_2 as the Brillouin-active medium. Waveguides were fabricated from glass tubing and had internal diameters at the entrance and exit typically of 5 mm and 1 mm respectively. The laser and compressed Stokes pulses are shown in Figure 2.27 for an input pulse power of 1 MW and indicate a compression ratio of 7. Pulses as short as 1.5 ns have been produced with compression efficiencies of 70% in good

agreement with theoretical predictions.

M D Damzen and M H R Hutchinson (Imperial College)

2.4 Development and Application of RGH Lasers

2.4.1 Gain and Absorption measurements in a Discharge Excited KrF Laser

In order to design and operate efficient, high power rare gas halide laser oscillators and amplifiers, it is necessary to achieve a large ratio of small signal gain to non-saturable/non-interceptable loss. In addition, knowledge of the saturation behaviour of both gain and loss in the laser medium enables the system to be operated at the optimum intracavity photon flux (2.23). During the past year, the techniques for measuring these parameters, described in last year's report (Section 2.2.2), have been extended to the case of discharge excited krypton fluoride (2.24).

The experimental apparatus is shown schematically in Figure 2.28. The discharge laser, similar to that described by Kearsley et al (2.25), employed automatic preionisation by disconnected door-knob capacitors pulsed from a 25 nF storage capacitor charged to 30 kV; the active discharge volume was (2 x 0.5 x 14) cm^3, and an E_2:Kr:He/3:100:1800 torr gas mixture was used for all measurements. As described previously (2.23), optical loss in the cavity was probed at 257 nm with a low divergence, C.W. beam derived from the frequency doubled 514 nm radiation from an argon ion laser, (Figure 2.28(a)), whilst optical gain was measured using the single/double pass ASE technique (2.26) (Figure 2.28(b)).

The intracavity photon flux could be varied using mirrors of different reflectivity at M_2.

The variation of peak absorption with peak intracavity laser flux is plotted in Figure 2.29; also shown is the normalised KrF B-state population obtained by observation of sidelight emission at 249 nm. It

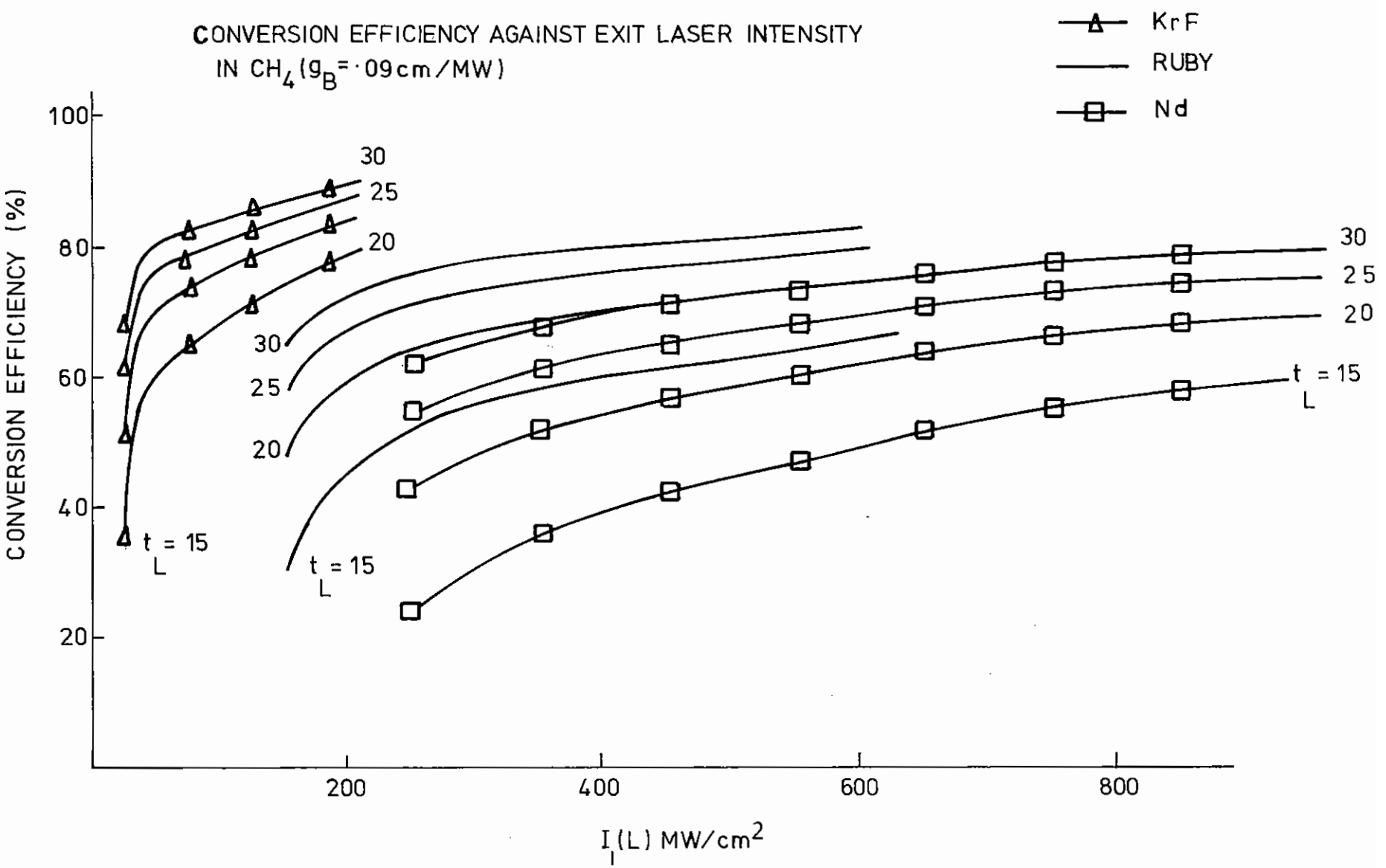

Figure 2.26 Computationally determined conversion efficiency against laser intensity at waveguide exit for various laser pulse durations (t_L in ns), and in a tapered geometry such that a Stokes pulse duration of approximately 1 ns is generated in each case (t_L therefore also represents the compression ratio in each case)

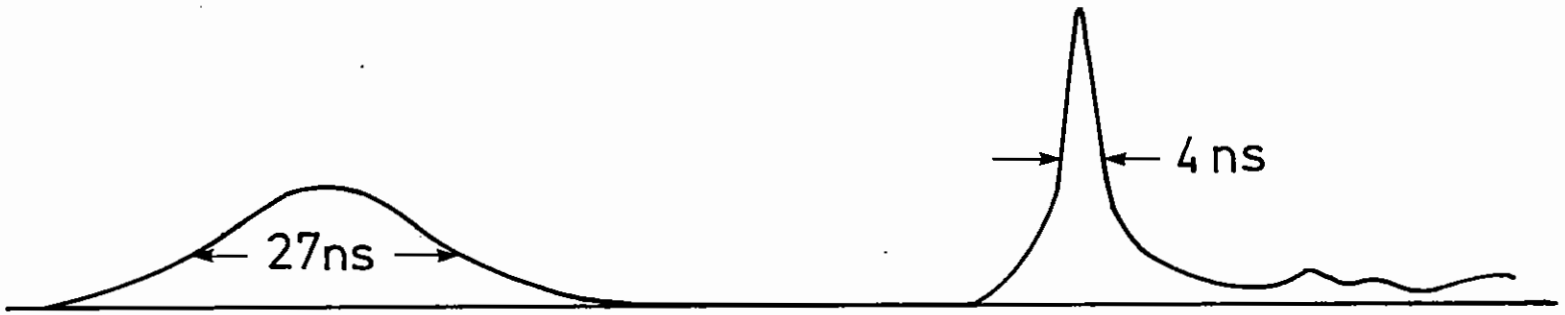

Figure 2.27 Experimental input laser pulse and compressed Stokes output pulse.

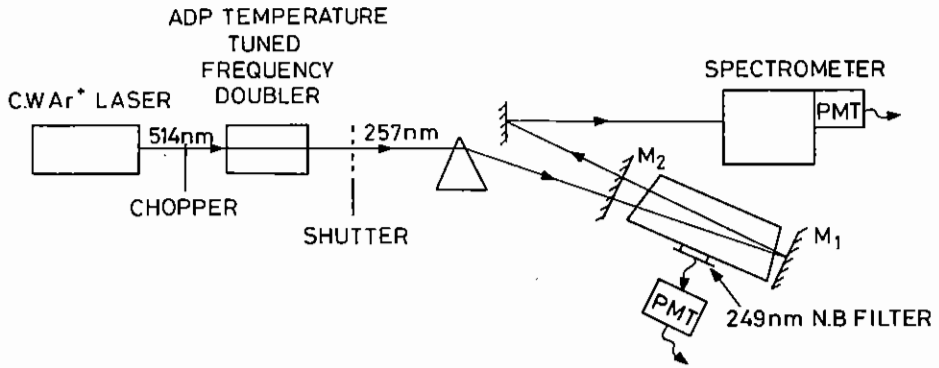

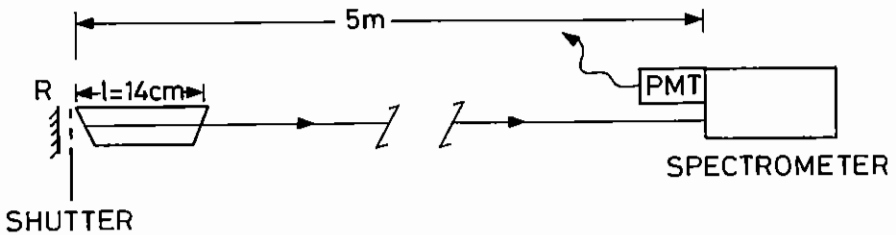

$$g_o = \frac{1}{l} \ln\left[\frac{(I_{DP}/I_{SP} - 1)}{RT^2}\right]$$

$$= 26.7\%/\text{cm for } R = 1, 0.5, 0.1$$

Figure 2.28 (a) Experimental apparatus for the measurement of loss in discharge excited KrF.

(b) Arrangement for measuring optical gain in KrF.

can be seen that there is a reduction of the loss as the intracavity flux increases, but that a non-saturable, or non-interceptable, component remains at high intracavity laser powers. It is also apparent that only approximately 50% of the B-state emission, and hence population, is depleted by the stimulating wave. This is probably due to incomplete vibrational relaxation in the B-state mainfold, leaving a population in high-lying levels inaccessible to the stimulating wave (high levels have a lower gain cross-section). If this is the case, then the remaining loss component is most probably due in part to the absorption by the trimer Kr_2F^*, formed in the reaction

$$KrF^* + Kr + He \xrightarrow{k_1} Kr_2F^* + He$$

where $k_1 = 6.5 \times 10^{-31}$ cm^6 sec^{-1}

Such a loss could be expected to exhibit similar saturation behaviour to that of the B-state population; this is supported by Figure 2.29. It is also believed that some non-saturable absorption is due to the F^- ion.

$$F^- + h\nu(249\text{ nm}) \xrightarrow{\sigma} F + e^-$$

where the F^- absorption cross-section $\sigma = 5.0 \times 10^{-18}$ cm^2 at 249 nm.

Using the experimental arrangement shown in Figure 2.28(b), the small signal gain, g_o, of the amplifier was found to be 26%/cm, obtained from the relation (2.23)

$$g_o = \frac{1}{\ell} \ln\left[\frac{I_{DP}/I_{SP} - 1}{RT^2}\right]$$

where I_{SP} and I_{DP} are the observed single and double pass ASE intensities, and R,T are the mirror reflectivity and window transmission respectively. For this relation to be valid, it is necessary for the detector - laser distance to be large compared with the gain length, ℓ, and that the single and double pass signals exhibit the same spatial propagation. This was verified since within experimental areas, the value obtained for g_o was independent of mirror reflectivity, and hence

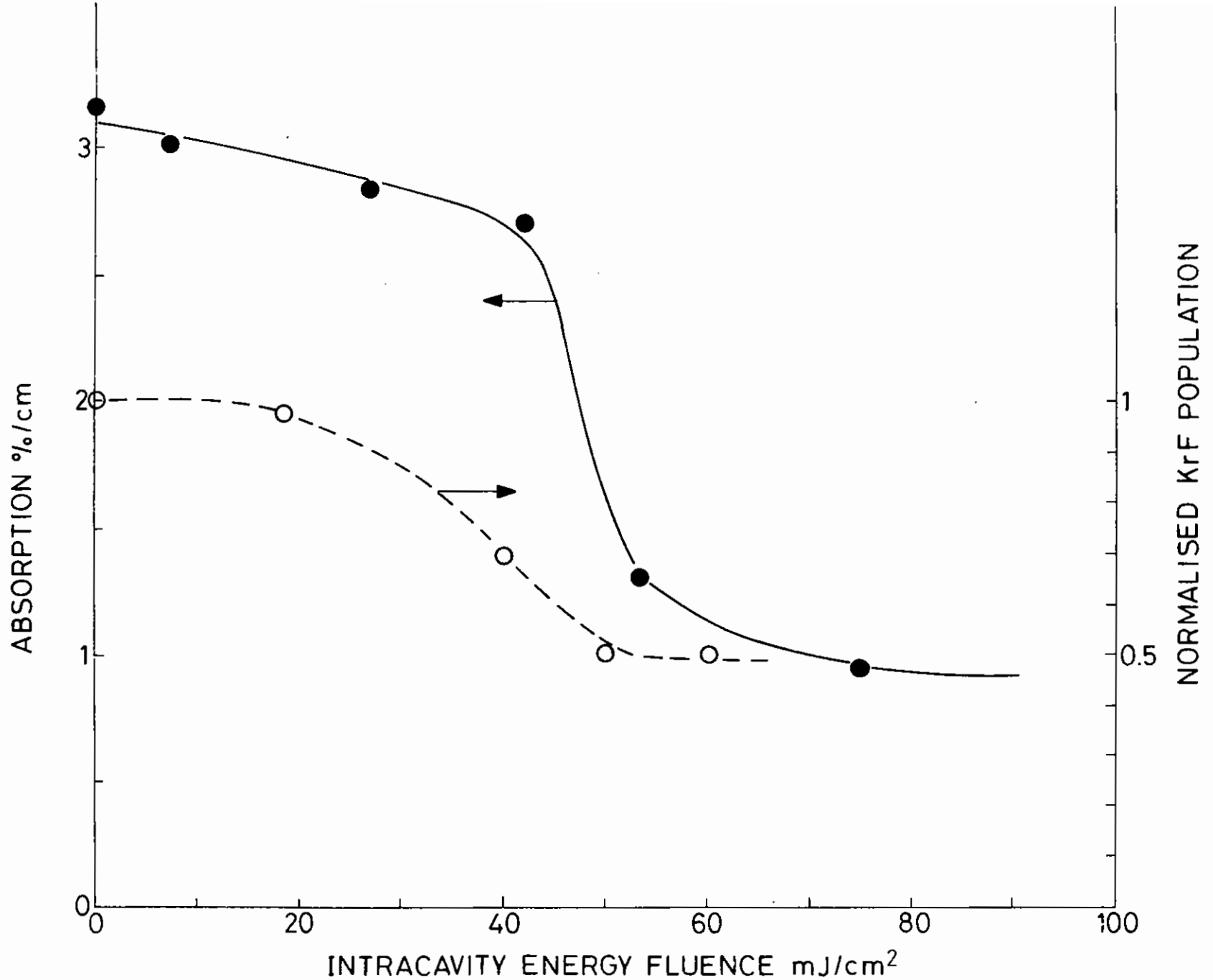

Figure 2.29 Variation of optical loss and B-state population as a function of intracacity photon flux.

intracavity flux, over a wide range.

In conclusion, we have measured a small-signal gain of 26% cm^{-1} for the KrF discharge laser described above, with a total small signal loss of 3% cm^{-1} of which 2% is saturable/interceptable; this is believed to be due to absorption by Kr_2F^*. The measured KrF saturation intensity was 2.4 MW cm^{-2}, corresponding to a radiative and collisional lifetime of 1.3 ns for the B-state population accessible to the laser radiation.

C B Edwards and M C Gower (RAL)

2.4.2 A simple tunable KrF laser system with narrow bandwidth and diffraction-limited divergence

2.4.2(a) Introduction

Discharge-excited rare gas halide lasers are now well established as important sources of high power coherent ultraviolet radiation. They are extensively used as pump sources for dye lasers and to provide high UV photon fluxes for photochemistry. A particularly interesting application of these lasers is to the investigation of a variety of nonlinear optical phenomena.

For processes such as these, as well as for many of the most promising applications of RGH lasers to photochemistry, the source of radiation must be capable of producing high spectral intensities.

Discharge-excited RGH lasers, such as 'standard' models which are commercially available, are characterised by high gains (~ 0.2 cm^{-1}) and short pulse durations ($\sim$ 10–20 ns). Typically, such lasers employ an optical resonator consisting of plane parallel mirrors in order to satisfactorily couple out the energy from the large active volume of the laser medium. As a result the output beam has a divergence of about 100 times the diffraction limit. In conjuction with the relatively large linewidth of the radiation generated by these lasers (up to 100 cm^{-1} for a KrF laser) this divergence limits the obtainable spectral intensities to

values several orders of magnitude smaller than could be obtained if the same laser energy were produced in a diffraciton limited beam of narrow linewidth.

Lasers with output beam quality approaching the fundamental limits governing spectral width and beam divergence have been demonstrated by using a RGH laser as a high-gain single pass amplifier (2.27), (2.28). The signal input to the amplifier in such a system can be derived from the high quality output of a CW dye laser which is then pulse amplified and frequency converted to match the frequency of the RGH laser amplifier. A system of this kind has the disadvantages of high cost and complexity. An alternative approach is to use a low power narrow linewidth RGH master oscillator to injection-lock an unstable resonator RGH slave oscillator (2.29). Systems of this nature have typically used multiple etalons to obtain narrow linewidths from the master oscillator and elaborate charging circuits to provide the required low jitter between the initiation of the discharges of the slave and master oscillator.

In this report we describe a simple injection-locked oscillator KrF laser system which used simple circuitry to obtain the required sub-nanosecond jitter between the two lasers. The narrow linewidth output from the system can be tuned over the entire tuning range of the master oscillator using a single micrometer adjustment. The output from the laser system is a nearly diffraction-limited beam of radiation with a linewidth less than 0.3 cm^{-1} and a power of 5 MW which is tunable between 248.1 and 248.6 nm.

2.4.2(b) Design Considerations

The laser system described in this report was designed around two discharge-excited RGH laser modules of the 'automatic' preionisation type similar to that described by Kearsley et al (2.25). For each of these modules a 70 nF charging capacitor, C_1, was first charged to 40 kV and then discharged through a spark gap switch and low inductance strip lines into the laser discharge volume via a set of thirty 625 pF parallel 'peaking' capacitors, C_2, placed inside the gas envelope of the laser.

The preionisation for the 20 mm x 5 mm cross-section discharge was automatically provided by a series of arcs that were formed, immediately preceding the main discharge, between the grounded discharge electrode and the disconnected discharge capacitor terminals. Synchronisation of the two modules was obtained, with a jitter of less than our detection limit of 1 ns, by using a single spark gap to fire both the laser discharge circuits as shown in Figure 2.30. The relative delay of the two modules could be varied by adjusting the inductance of the two discharge circuits and once this had been set no further adjustment was required to compensate for effects due to ageing of the spark gap.

Both laser modules had external mirrors and fused silica windows tilted away from the laser axis. When operated as un untuned oscillator, in a cavity consisting of a plane 80% reflector and a plane silica output coupler, each module was capable of producing energies up to 100 mJ using a gas mixture of 100 Torr Kr, 5 Torr F_2, and He to a total pressure of 2300 Torr. As reported by Goldhar and Murray (2.29), we found that the beam quality produced by our slave oscillator could be improved by decreasing the pressure of He to between 700 and 1400 Torr. At pressures greater than these the discharge showed an increased tendency to arc and this may have been the cause of the observed degradation of beam quality. With such a gas mixture and the plane-plane cavity described above, the laser produced an output energy of 65 mJ in a 12 ns FWHM pulse.

In order to obtain a nearly diffraction-limited beam from the laser system, the slave oscillator was provided with an unstable resonator cavity (2.30). Although the use of such resonators with RGH lasers had become quite widespread since the initial work of McKee et al (2.31) the choice of magnification for an unstable resonator to suit a particular RGH laser module, as described in publications to date, has been almost wholly empirical. Since RGH lasers are characterised by high gains and short pulse durations it is generally no longer relevant to consider the laser output as a quasi-CW unstable resonator mode. Instead one must consider the build up of the resonator mode from noise since, in many cases, this build up occupies a significant fraction of the time interval, τ_g, for which the RGH laser medium exhibits gain.

An extensive analysis of the build up of modes in an unstable resonator for high gain short pulse lasers has been presented in a series of papers by Zemskov et al (2.32) and Isaev et al (2.33) - (2.35). The key concepts that emerge from their analysis are that the magnification of the unstable resonator, M, must be sufficiently large to enable a diffraction-limited resonator mode to become the dominant mode in the resonator in a time which is less than τ_g, and that the gain coefficient of the laser medium must be sufficiently small so that the threshold of lasing is not reached before such a mode has had time to build up. These conditions can be summarised by requiring

$$\tau_g > \tau \tag{1}$$

and

$$\alpha < \alpha_{cr} \tag{2}$$

where τ and α_{cr} are given, for a confocal positive branch unstable resonator (2.33), by

$$\tau = (2L/c)\ (1 + \ln M_o/\ln M) \tag{3}$$

$$\alpha_{cr} = \frac{\ln M}{L_a}\left(\frac{A}{2\ \ln (MM_o)} + 1\right) \tag{4}$$

in which $M_o = 2a^2/f_1\lambda$, where a is the radius of the laser aperture, f_1 is the focal length of the less curved of the two mirrors, L is the resonator length and L_a is the length of the gain medium. The quantity A is the gain-length product (usually taken to be about 30) for which superradiance becomes observable.

Using these formulae it is a simple matter to design an unstable resonator capable of producing the optimum performance from a given RGH laser module. For the 40 cm gain length of our RGH laser modules we chose a positive branch unstable resonator with a magnification of M = 20 and a value of L = 63 cm and thus obtained $\tau \sim 9$ ns which is less than the duration of the laser pulse and thus certainly less than τ_g. Equation

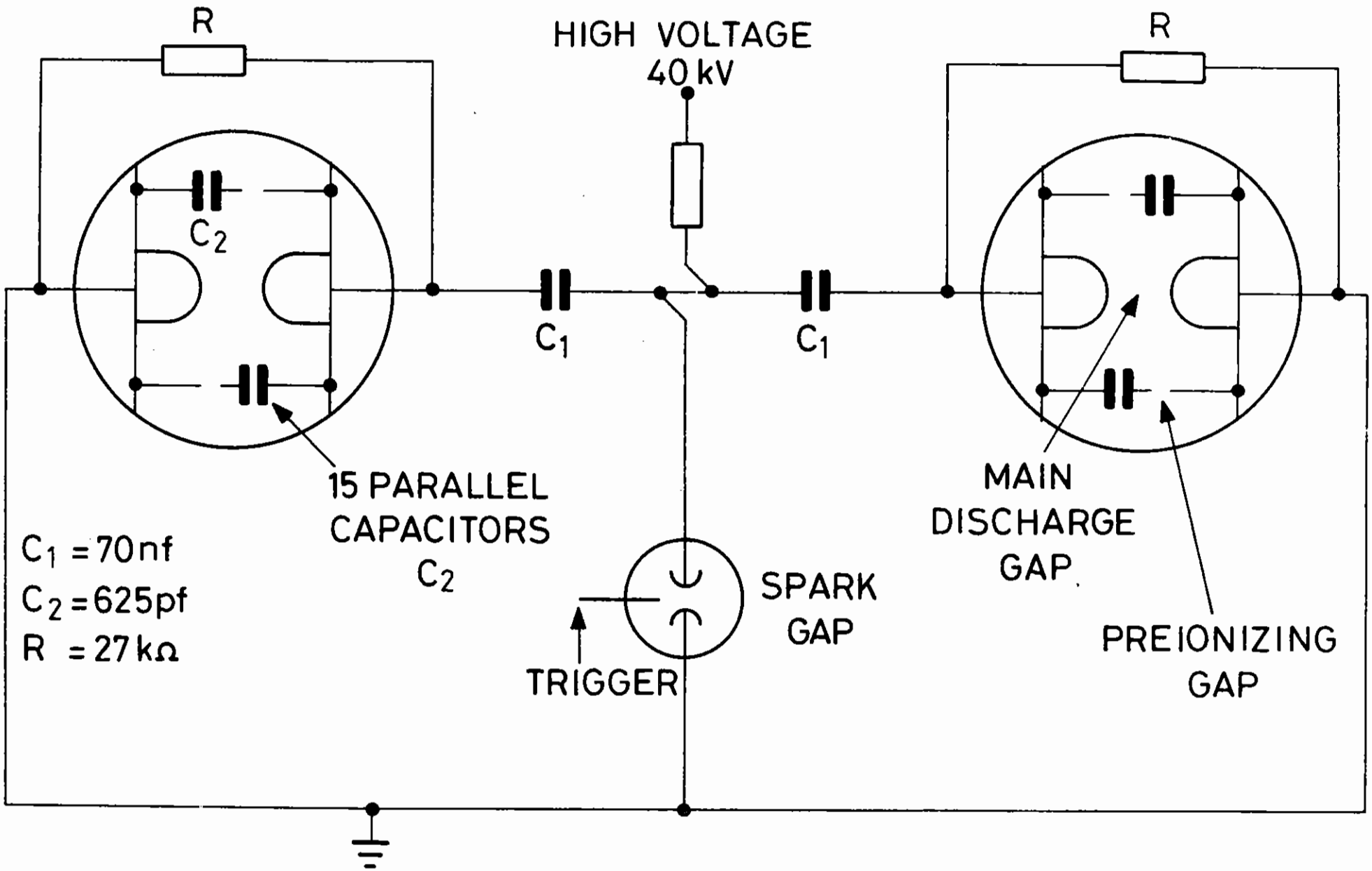

Figure 2.30 Laser system discharge circuit. C_1 = 70 nf; C_2 = 625 pf; R = 27 kΩ

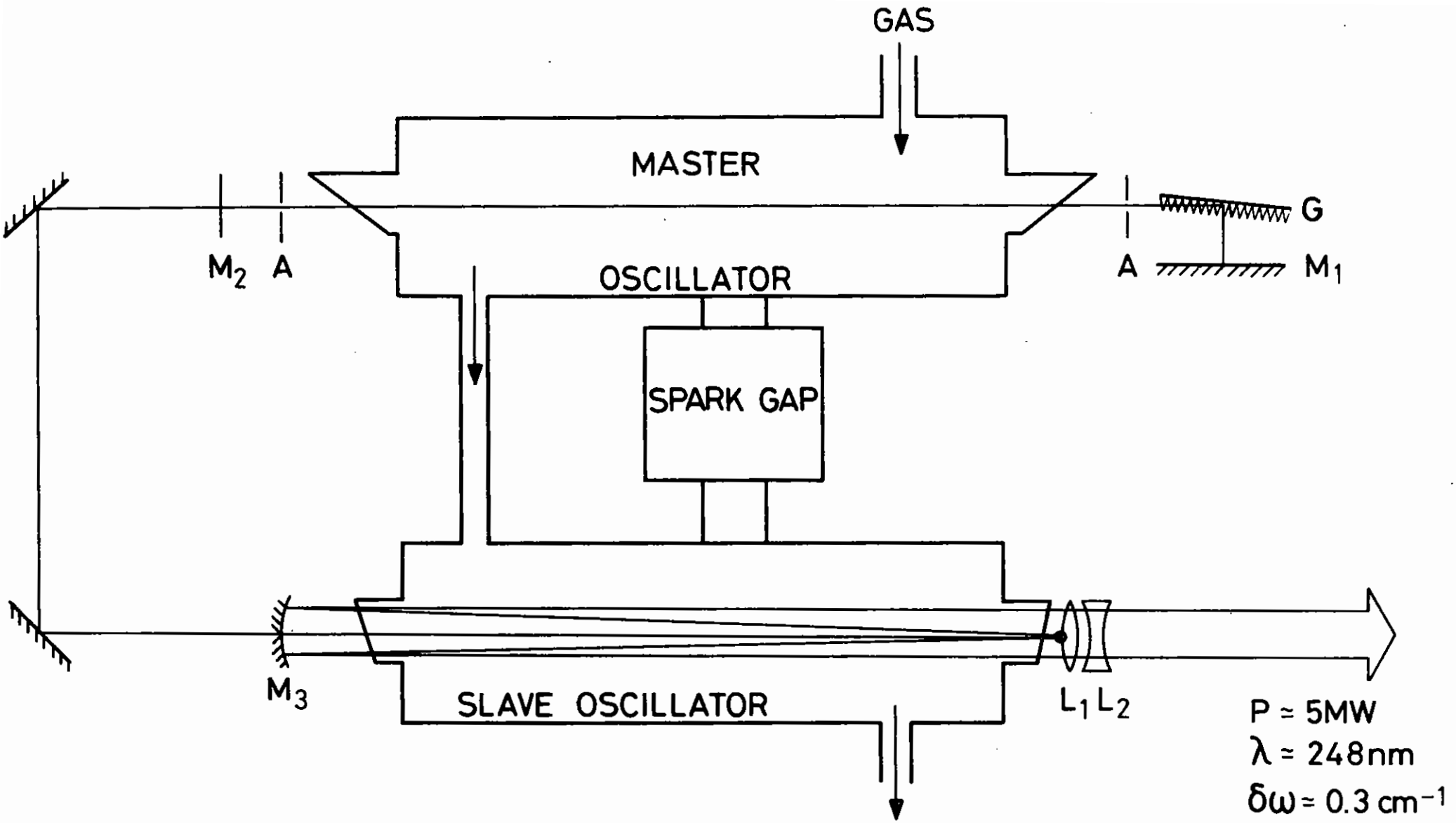

Figure 2.31 Schematic of laser system. G - 1200 lines/mm grating blazed at 7500 Å used in 3rd order; M_1 - plane mirror (R=80%); M_2 - plane silica output coupler; M_3 - concave mirror (R=93%, f=1.1m); L_1 - biconvex lens (f=10cm); L_2 - biconcave lens (f=-10cm); A - aperture (dia = 0.6 mm).

(4) gives the value $\alpha_{cr} = 0.2cm^{-1}$ which is of the order of the value of the gain coefficient recently measured for a similar laser module (2.24). The output from this unstable resonator device was measured to have the nearly diffraction-limited divergence predicted by theory and provides an illustration of the usefulness of the guidelines given by Isaev et al (2.33) - (2.35) for designing unstable resonators for use with RGH lasers.

2.4.2(c) Construction Details

Details of the optical configuration of our laser system are illustrated Figure 2.31. The windows of the master oscillator module were set at Brewster's angle so that the output radiation from this oscillator was linearly polarised. The windows on the slave oscillator were tilted at 5° from the normal to the optical axis of the system to avoid both the competing cavity effects which can be observed at normal incidence and the beam distortion which can be observed when Brewster's angle windows are used with the strongly diverging beam that is present in an unstable resonator.

The slave oscillator resonator output was coupled out of the system through the biconvex silica output coupler lens, L_1, (focal length = 10 cm) which had a spot of 2 mm diameter, dielectric coated for high reflectivity, at the centre of the face nearest the laser module. The slave resonator cavity was completed by M_3, a planoconvex lens of 2.25 m focal length, which had a dielectric coating of 93% reflectivity on its rear (plane) face. A biconcave lens, L_2, of 10 cm focal length, was used to render the emergent beam approximately parallel.

2.4.2(d) Performance

The wavelength and linewidth of the output from the slave oscillator were controlled by the signal from the master oscillator which was injected through M_3 into the slave resonator along its axis. For reliable injection-locking the relative timing of the two lasers was found to be sensitive to variations of the order of 1 ns although use of a longer

master oscillator pulse would almost certainly reduce this sensitivity.

The cavity of the master oscillator consisted of a plane silica output coupler, M_2, a grazing incidence grating, G, (2.36) and an 80% reflecting plane mirror, M_1. The narrow linewidth radiation from this oscillator could be tuned over the entire laser bandwidth by adjusting only a single micrometer which varies the horizontal tilt of M_1. This feature represents a considerable simplification over the multiple etalon systems which have been used in similar RGH laser systems in the past. The two 0.6 mm apertures, A, performed the dual functions of decreasing the linewidth of the oscillator output by aperturing down the gain region and of producing a nearly diffraction limited beam. With the grating normal at $\theta = 88.5°$ to the optical axis, the output from the oscillator was found to be less than our detection limit of 15 μJ. Although higher energies could easily be obtained, with only a slight increase in linewidth, by decreasing the value of θ, we found this unnecessary as full injection-locking could be obtained even at these low oscillator powers. Up to 90% of the slave oscillator energy was extracted in a narrow line.

In Figure 2.32 we show the spectral outputs from the injection-locked oscillator system that were measured using a 1 m spectrograph in fourth order and an optical multichannel analyser. In the absence of an injected signal, the slave oscillator output had the broad spectral form of trace B - characteristic of an untuned KrF laser. With an injected signal at line centre, the spectrally narrowed output shown as trace A was obtained. The limits of tunability over which complete injection-locking could be obtained are shown in traces C and D while traces E and F show the absolute limits of the tuning range of the system. The narrowed traces shown in Figure 2.32 are instrument-limited and have a linewidth which was measured, by use of an etalon, to be less than $0.3\ cm^{-1}$. It seems likely that this linewidth could be further improved by increasing the value of θ or by replacing the mirror, M_1, with a grating used in a Littrow configuration.

At line centre 90% of the output energy of the system could be obtained in a single narrow line while at the 'limits' C and D the narrow line

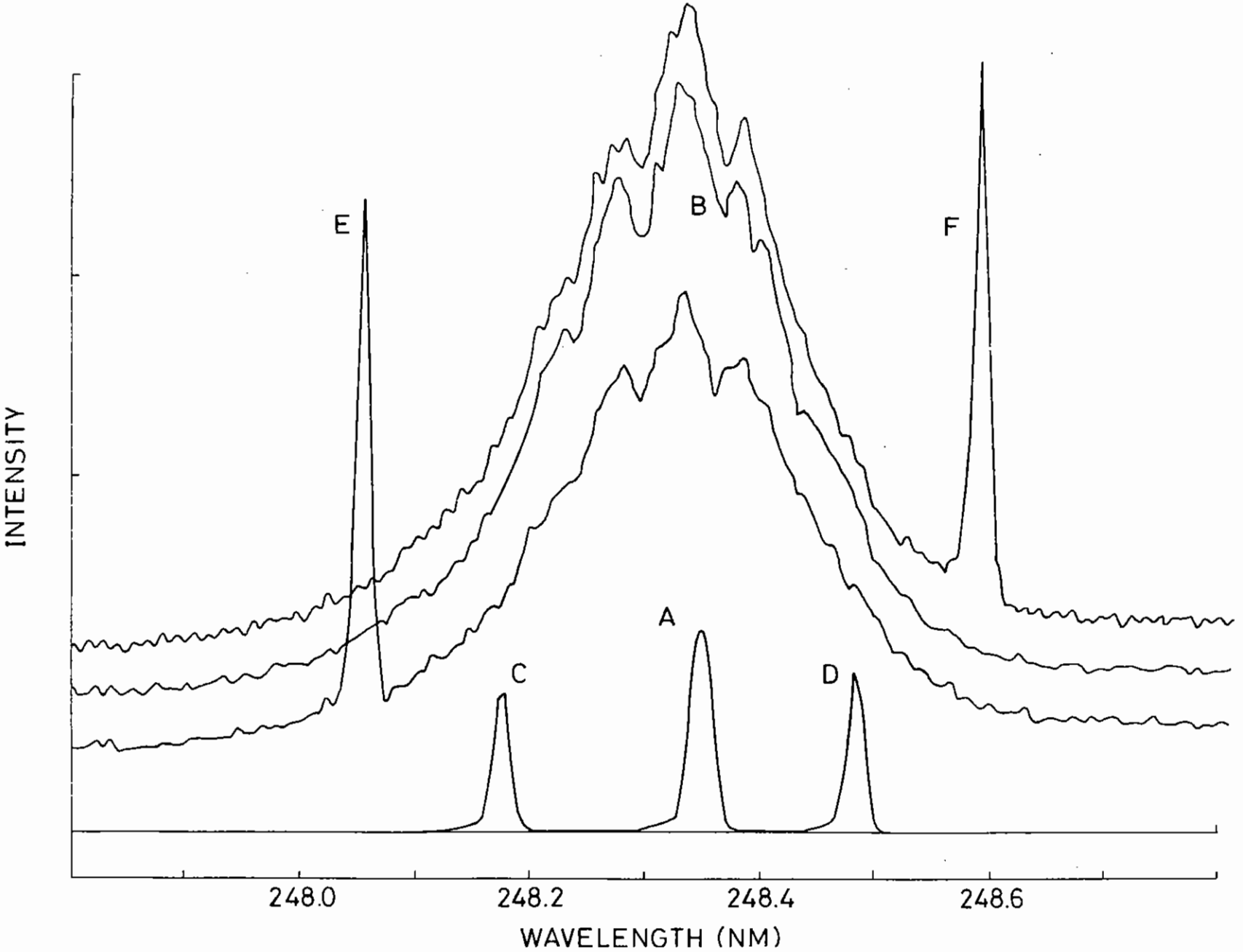

Figure 2.32 Spectral output traces from the laser system. The intensity scale is linear for each trace but varies from trace to trace. The narrow linewidth signals shown are instrument-limited and have actual linewidths ~ $0.3cm^{-1}$. A - typical line-centre output with injection locking; C,D - limits of complete injection locking; E,F - absolute limits of tunability.

contained about 60% of the total laser energy. From traces E and F it can be seen that in the wings of the laser output it was not possible to suppress completely the radiation at line centre. By changing the angle of the grating, and thus increasing the master oscillator energy, we were able to extend slightly the tuning range of the system but we did not observe an appreciable improvement in the suppression of broad bandwidth radiation when the master oscillator was tuned significantly away from line centre. This may have been due to imperfect mode matching of the two oscillator resonator modes (2.37) or to insufficient contrast ratio between the injected narrow-linewidth signal and noise at line centre either in the slave oscillator or from the master oscillator. An alternative explanation is that the KrF B-X transition is not fully homogeneous due to incomplete v-v coupling in the B state (2.24)(2.38)

To measure the divergence of the output from the laser system we used a telescope (focal length = 15 m) to focus the beam onto a screen and estimated the width of the beam profiles from their burn patterns in the focal plane. For comparison, when one of the laser modules was set up with a plane-plane resonator cavity, the spot at focus of this telescope had dimensions of 10 mm x 20 mm. This corresponds to a beam divergence of the order of 1 mrad. In contrast, the output beam from the unstable resonator laser system described here produced a focal spot of dimensions 0.2 mm x 1.2 mm, which corresponds to a beam with divergence of 15 μrad by 80 μrad and is very close to the limit for diffraction from the 20 mm x 5 mm aperture of the laser discharge.

As expected from our earlier discussion there was no detectable change in the focal spot when the master oscillator output beam was blocked. This confirms that the unstable resonator had sufficient magnification to allow a rapid build up of a diffraction limited mode from noise so that injection of the low divergence master oscillator beam resulted in little change in the spatial properties of the output from the slave resonator.

R G Caro, C E Webb (Oxford) and M C Gower (RAL)

2.4.3 XeCl Laser Annealing of ZnS Thin Films

The programme of research on annealing of implanted zinc sulphide films on silicon substrates, as first described in Section 2.3.3 of the 1981 report to the LFC, has produced some extremely encouraging results in the past year. For the first time manganese-doped films of ZnS, a promising material for the fabrication of high intensity, low voltage, large area displays, has been successfully annealed using XeCl laser radiation at 308 nm from the 'ELF' excimer laser system at RAL (2.39 , 2.40).

Previous attempts, at this and other laboratories, to laser anneal the lattice damage due to manganese implantation, and to modify the essentially gaussian implant profile to one more suited to efficient device operation, have been unsuccessful due to the relatively low damage threshold of ZnS films at the 308 nm annealing wavelength (~ 200 mJ cm^{-2}). This is believed to be due to the absence of a liquid phase in ZnS at atmospheric pressure. However, in the experiments performed here it has been found that in an inert atmosphere at high pressure (~100 psig), laser energy densities of ~ 3 J cm^{-2} may be employed without significant damage to the material.

Preliminary results of the laser annealing experiments are shown in Figure 2.33, a plot of photoluminescence at 580 nm observed from the annealed sample under UV illumination, as a function of laser anneal energy density. Samples annealed under high pressure, and at atmospheric pressure are compared with conventional thermal annealed specimens. Though this diagnostic technique is somewhat crude, a significant improvement over the thermal process is apparent with the high pressure sample. In addition electron microscopy studies suggest increased crystallinity in the laser annealed sample in comparison with a non-annealed specimen.

It is essential for the diagnostics of the annealing process, that the irradiating laser beam has a spatial uniformity of better than 10%. In experiments to date, no special measures have been taken to improve beam uniformity, other than careful alignment of all components in the optical

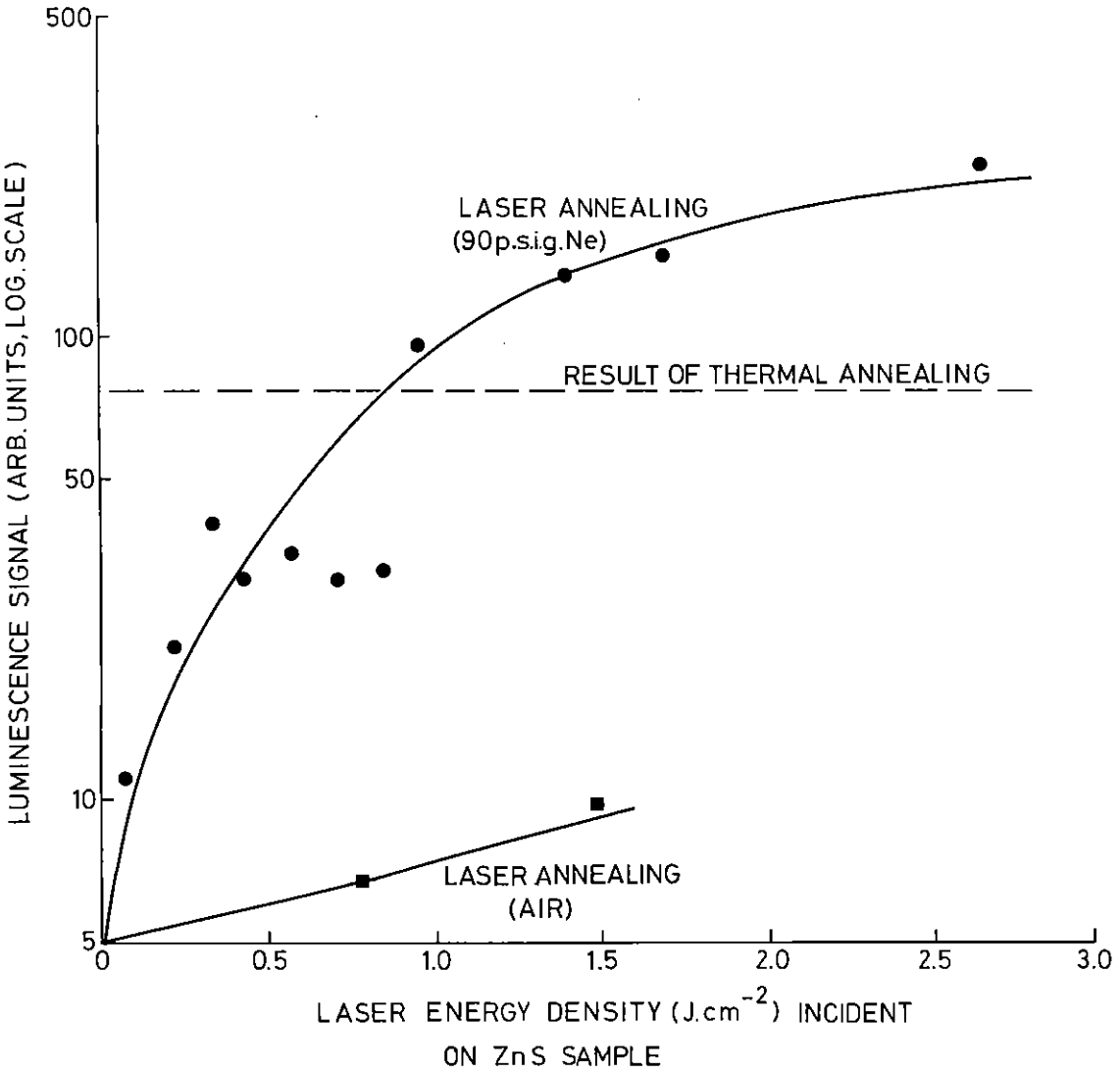

Figure 2.33 Comparison of ZnS UV-excited 580nm photolumniescence for different conditions of annealing.

system. However, the particular configuration of the ELF pumping geometry, whereby there is a signficant proportion of the pumping by retroreflected electrons within the laser cell and a relatively poor utilisation of available electron energy, produces a beam of acceptable quality, though improvements may be necessary as the diagnotics become more quantitative. A plot of the spatial characteristics of the beam is shown in Figure 2.34.

Having demonstrated the feasibility of the laser technique (2.40) recent experiments have concentrated upon a more quantitative assessment of the behaviour of ZnS films under laser irradiation. Improved facilities at Bradford University, where all samples to date have been prepared, have enabled samples of epitaxially grown ZnS on silicon substrates to be studied. The lattice mismatch between silicon and ZnS is small ($\sim 0.1\%$), and once the oxide layer which is present on raw silicon is removed, by heating under vacuum, epitaxial films of ZnS may be deposited, in which the crystalline characteristics of the silicon is preserved in the deposited layer. The latest experiments on implanted ZnS on Si, have attempted to melt the damaged region back to epitaxial material, hoping for subsequent epitaxial regrowth with manganese incorporated substitutionally in the ZnS lattics. Analysis of the crystallinity of the material is then carried out using reflection high energy electron diffraction (RHEED) at Leeds University, while secondary ion mass spectrometry (SIMS) at Imperial College, London, is used to determine dopant profile and redistribution. These experiments are at an early stage, with analysis of the first epitaxial films incomplete.

In conclusion, the programme of research will continue with effort concentrated on the study of the crystallinity of annealed samples, and associated topics including effects due to variation of film thickness etc. Since the work has now reached a quantitative stage, it is likely that improvements will be necessary to the laser spatial profile (to enable larger areas to be annealed with the available laser energy) and to the processing techniques in general.

H S Reehal, J M Gallego (Bradford University) and C B Edwards (RAL)

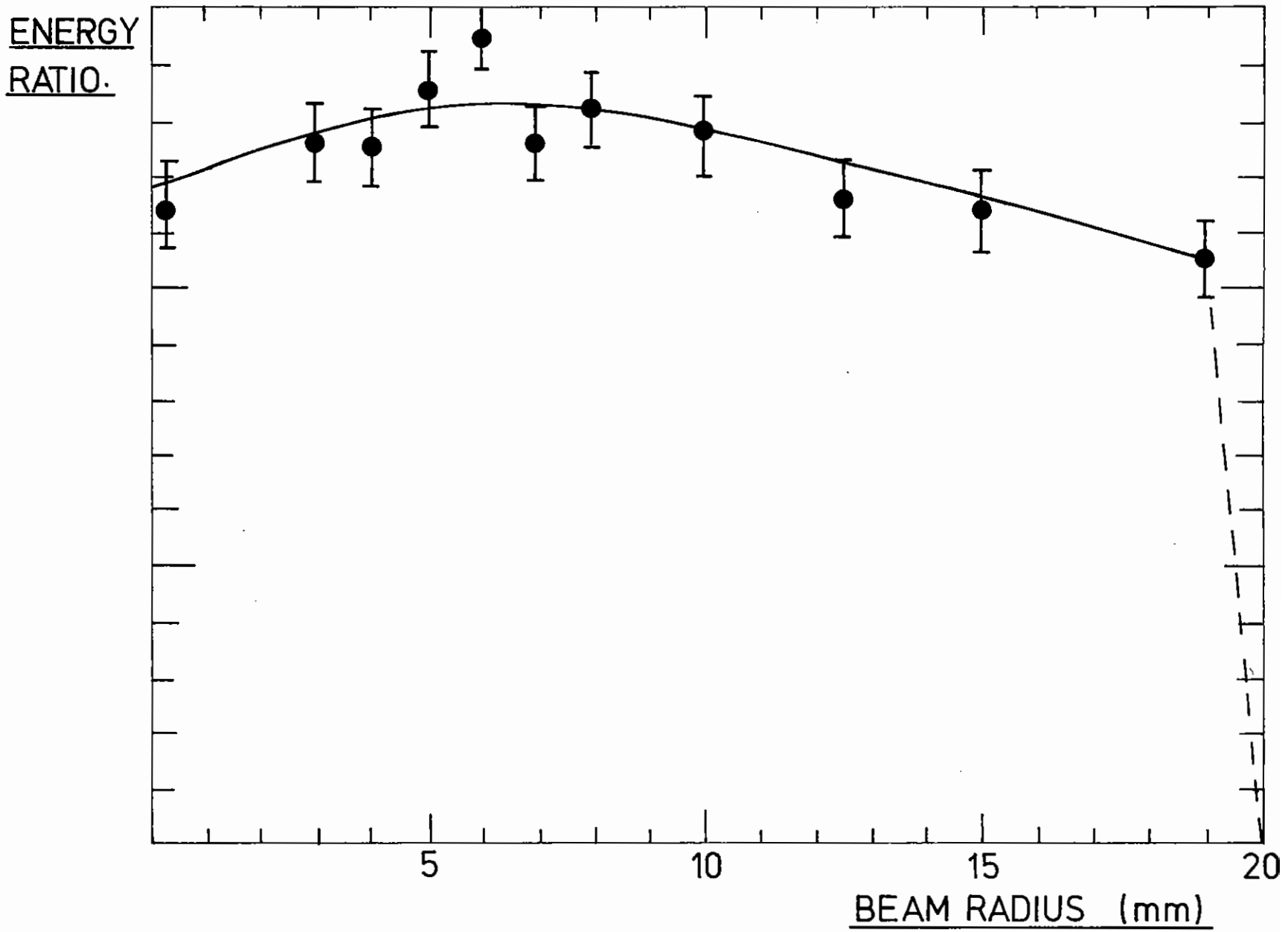

Figure 2.34 XeCl laser beam profile used for laser annealing studies.

2.4.4 UV Laser Damage Studies

One of the major limitations in the development of high energy excimer lasers is the relatively low damage threshold of the laser mirrors themselves. The damage threshold is observed to decrease as the laser wavelength is reduced. The problem of laser induced damage becomes severe in the ultra-violet where > 99% reflectivity laser mirrors are produced by multi-coated dielectric layers deposited on a suitable substrate material such as fused silica. The laser damage threshold of coated optics is always lower than that of the bare substrate material.

Generally, little work has been done on the measurement of laser damage thresholds to optics suitable for use in the ultra-violet region. The energy densities achieved with very large lasers are simulated by focusing the output from a low energy laser to a suitable spot size. If the spot size is very small, a large number of measurements must be taken to adequately cover the variations in the surface quality over a given sample (microcracks, impurities, etc), as well as variations from sample to sample. In order to cover the statistical variation in the damage threshold with fewer shots, and to simulate real large area use, a large spot size should be used. This requires a higher output energy to maintain the energy density in the partially focused beam. The two-dimensional spatial profile of each damage shot should also be monitored to detect any beam 'hot spots' in the focused radiation. A scaling law giving the damage threshold varying as the (temporal pulse-width)$^{\frac{1}{2}}$ has been observed. The temporal pulse width should therefore also be monitored.

A laser damage and diagnostic facility has been set up at Loughborough University based on a discharge pumped 1 J KrF excimer laser. A schematic diagram of the apparatus is shown in Figure 2.35. Two techniques for measuring the two dimensional spatial profile of each damage shot are being investigated, these are: multiple reflections, the intensities being recorded photographically, and photographic recording of dye fluoresence induced by the excimer laser. To date the laser has mainly been operated at the ArF excimer wavelength of 193 nm where a maximum output of about

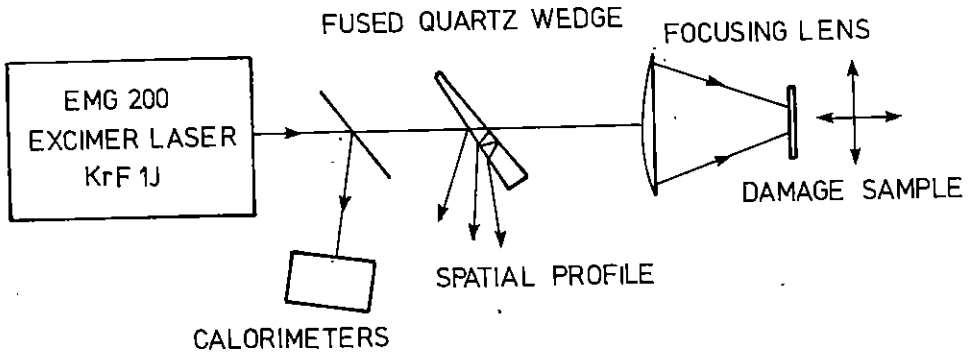

Figure 2.35 Apparatus for UV laser damage studies

0.5 J is available. Using a 50 mm diameter f-2 fused silica plano-convex lens a peak fluence of 80 J cm^{-2} was measured at the focus. This is well in excess of the damage threshold of substrate materials in the ultra-violet which is usually in the range 30 - 50 J cm^{-2}. At such fluence levels irradiation areas of 1 - 1.5 mm^2 have been used.

An experimental programme is now underway to measure the damage threshold of a range of bare substrates and coated components at the excimer wavelengths of 193 nm, 248 nm and 308 nm. The substrate materials include fused silica and most of the alkali and alkalic earth fluorides. Preliminary measurements on a cleaved sample of SrF_2 indicated that at 193 nm and an energy density < 1 J cm^{-2} the damage area was observed to grow with further subsequent laser shots. A study of the damage morphology is included in these measurements. As an example, Figure 2.36 shows an electron micrograph image of the surface of an aluminium mirror over-coated with silicon monoxide after being irradiated with three laser shots at 193 nm at an energy density of 0.2 J cm^{-2}. The undulating surface finish is attributed to a melt-resolidification process. The surface consists of a random distribution of uniform size 'globules' with a diameter of 1.25 μm and a depth of 0.3 μm. The globule size of 1.25 μm is in agreement with measurements taken of the circular diffraction pattern produced when the damage region is illuminated with a helium neon laser. The cause of the linear and concentric surface structure which is shown in Figure 2.36 and observed in several areas over the damage region (~ 2 cm^2) is uncertain.

D C Emmony and S S Wiseall (Loughborough University)

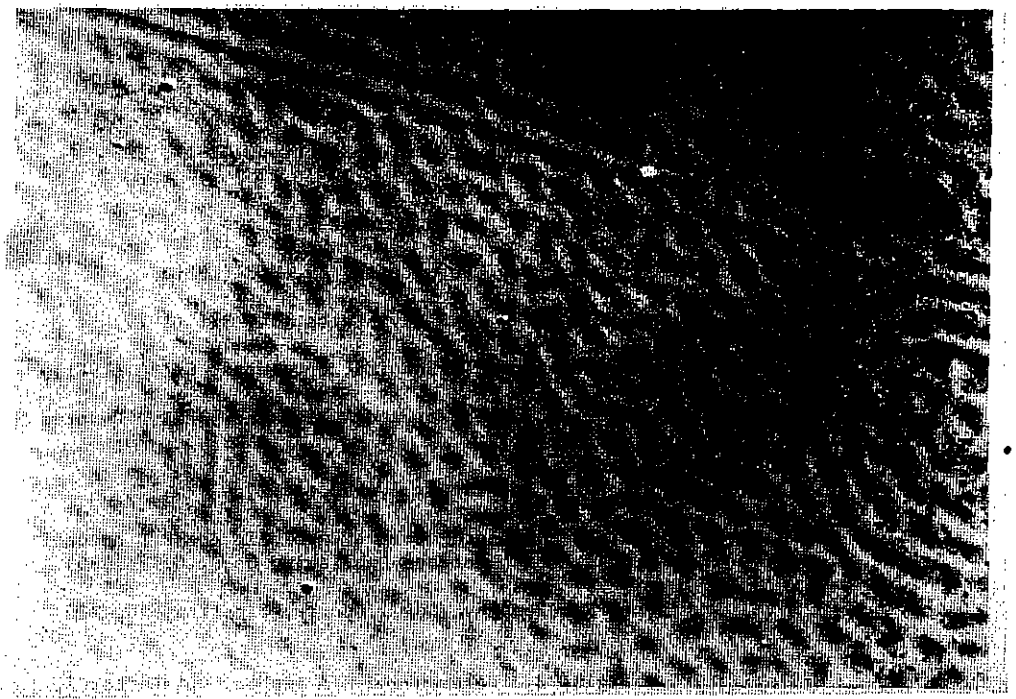

Figure 2.36 Electron micrograph image of laser damaged aluminium mirror.

CHAPTER 2 REFERENCES

2.01 L L Alston (Editor), High Voltage Technology, Oxford University Press, p6 (1968)

2.02 W K Tucker, A 3 MV SF_6 Trigatron, Sandia Labs Report No SC-DR-720506 (1972)

2.03 I D Chalmers and D J Tedford, Proc IEE, 118, 1893 (1971)

2.04 D G Pellinen, M S DiCapua, S E Sampayan, H Gerbracht and M Wang, Rev Sci Instrum, 51, 1535 (1980)

2.05 J C Martin (private communication)

2.06 M Ermel, Proc 4th Int Gas Discharge Conf, IEE Publication, No 143, (1976)

2.07 C B Edwards, F O'Neill and M J Shaw, Appl Phys Letts, 36, 617 (1980)

2.08 R G Caro and M C Gower, IEEE J Quantum Electron, QE-17, 225 (1981)

2.09 R G Caro and M C Gower, Opt Letts, 6, 557 (1981)

2.10 R G Caro and M C Gower, Appl Phys Letts, 39, 855 (1981)

2.11 G Martin and R W Hellwarth, Appl Phys Letts, 34, 371 (1979)

2.12 B J Feldman, R A Fisher and S L Shapiro, Opt Letts, 6, 84 (1981)

2.13 I J Bigio, B J Feldman, R A Fisher and M Slatkine, IEEE J Quantum Electron, QE-17, 220 (1981)

2.14 M C Gower and R G Caro, Opt Letts, 7, 162 (1982)

2.15 W Kaiser and M Maier in "Laser Handbook", Vol II, Eds F T Arecchi and E O Shulz-Dubois, North Holland Publishing Co, p1077 (1980)

2.16 I M Bel'dyugin and E M Zemskov, Sov J Quantum Electron, 10, 120 (1980)

2.17 M Slatkine, I J Bigio, B J Feldman and R A Fisher, Opt Letts, 7, 108 (1982)

2.18 J R Murray, J Goldhar, D Eimerl and A Szoke, IEEE J Quantum Electron, QE-15, 342 (1979)

2.19 D J Hon, Opt Letts, 5, (1980)

2.20 B Ya Zel'dovich, V I Popovichev, V V Ragul'skii and F S Faizullov, JETP Letts, 15, 109 (1972)

2.21 O Yu Nosach, V I Popovichev, V V Ragul'skii and F S Faizullov, JETP Letts, 16, 435 (1972)

2.22 E E Hagenlocker, R W Minck and W G Rado, Phys Rev, 154, 226 (1967)

2.23 C B Edwards, F O'Neill and M J Shaw, Appl Phys Letts, 38, 843 (1981)

2.24 M C Gower and C B Edwards, Opt Commun, 40, 369 (1982)

2.25 A J Kearsley, A J Andrews and C E Webb, Opt Commun, 31, 181 (1979)

2.26 G Marowsky, F K Tittel, W L Wilson and E Frankel, Appl Opt, 19, 138 (1980)

2.27 R T Hawkins, H Egger, J Bokor and C K Rhodes, Appl Phys Letts, 36, 391 (1980)

2.28 H Egger, T Srinivasan, K Hohla, H Scheingraber, C R Vidal, H Pummer and C K Rhodes, Appl Phys Letts, 39, 37 (1981)

2.29 J Goldhar and J R Murray, Opt Letts, 1, 199 (1977)

2.30 A E Siegman, Appl Opt, 13, 353 (1974)

2.31 T J McKee, B P Stoicheff and S C Wallace, Appl Phys Letts, 30, 278 (1977)

2.32 K I Zemskov, A A Isaav, M A Kazaryan, G G Petrash and S G Rautian, Sov J Quantum Electron, 4, 474 (1974)

2.33 A A Isaev, M A Kazaryan, G G Petrash and S G Rautian, Sov J Quantum Electron, 4, 761 (1974)

2.34 A A Isaev, M A Kazaryan, G G Petrash, S G Rautian and A M Shalagin, Sov J Quantum Electron, 5, 607 (1975)

2.35 A A Isaev, M A Kazaryan, G G Petrash, S G Rautian and A M Shalagin, Sov J Quantum Electron, 7, 746 (1977)

2.36 T J McKee, J Banic, A Jares and B P Stoicheff, IEEE J Quantum Electron, QE-15, 332 (1979)

2.37 I J Bigio and M Slatkine, Opt Letts, 6, 336 (1981)

2.38 H Pummer, K Hohla and F Rebentrost, Appl Phys, 20, 129 (1979)

2.39 H S Reehal, C B Edwards, J M Gallego and C B Thomas, Proc 5th UK Nat Quantum Electron Conf, Hull, Sept 1981

2.40 H S Reehal, J M Gallego and C B Edwards, Appl Phys Letts, 40, 258 (1982)

CHAPTER 3 LASER PLASMA INTERACTIONS

INDEX

CHAPTER EDITOR: R G Evans

3.1 Introduction

During 1982 the laser plasma interaction work has concentrated on achieving a better understanding of some physical processes in plasmas which were first described in the 1981 report to the Facility Committee. Time resolved spectra of $\omega_o/2$ and $3\omega_o/2$ emissions have been obtained over a wider range of laser parameters than hitherto and with better temporal resolution. The results have led to speculative new models for the plasma harmonic emissions and have also shown the important connection between filamentation and harmonic emission.

The optical probe observations of filamentation and plasma jets have now been performed at a variety of laser wavelengths and for different target materials and surface structures. The results show the increasing importance of thermal self-focusing for short laser wavelengths but the mechanism for the production of the spectacular plasma jets remains in doubt. An instability due to radiation cooling appears to be capable of explaining the results but it may also be necessary to invoke magneto thermal instabilities as described in Section 7.2.5.

The use of pre-formed plasmas for the study of stimulated Brillouin scattering is indicative of present trends in attempting to create long scale length plasmas, as might appear in targets for inertial confinement fusion reactors. Pre-formed plasmas also provide a more controllable way of performing interaction experiments since the plasma scale length is largely decoupled from the laser irradiance and pulse duration.

3.2 Stimulated Brillouin Scattering from Pre-formed Plasmas

The stimulated Brillouin scattering (SBS) instability poses a serious light scattering problem for large underdense plasmas (3.01). A recent experiment at the CLF investigated the backscatter from a preformed plasma

when different regions in the plasma were probed by a 1 μm beam. The geometry of the experiment ensured the beam did not penetrate to the critical density layer so that no light would be reflected from n_c.

Figure 3.01 shows the experimental layout. Six beams (λ_L = 0.53 μm; τ_L = 0.6 ns; E_L = 50 J) were used to uniformly illuminate plastic coated microballoon targets of 250 to 300 μm diameter. After a delay of 1.1 ns to allow long scale lengths to develop in the underdense plasma, a seventh beam (λ_o = 1.05 μm; τ_o = 100 ps) was focused onto a region corresponding to 0.1 n_c to probe for the Brillouin instability. Calorimeters monitored the incident and backscattered energies of the seventh beam. The light backscattered through the seventh beam focusing lens was imaged onto a Monospek grating spectrograph to obtain spectra of the backscattered emission.

Simultaneous with the arrival of the seventh beam, the density profile of the underdense plasma was recorded by interferometry performed with a Raman shifted 2ω probe (λ = 0.622 μm; τ = 100 ps). The interferometer system has been described previously (3.02).

A range of data was obtained by keeping the energy of the seventh beam constant and scanning it through the underdense plasma in the direction of increasing density. To do this, the seventh beam was focused onto the target surface, then moved to a position a known distance away which corresponded to the density region to be studied. A subsequent range of data was obtained by repeating this procedure for a different energy in the seventh beam.

Figure 3.02 shows the variation in backscatter with the position of the seventh beam relative to the original target surface. For irradiances $\sim 4 \times 10^{15}$ W cm^{-2} the backscattered energies increased as the beam was positioned closer to the target surface. For irradiances $\sim 10^{14}$ W cm^{-2}, the backscattered level remained approximately constant at around 1% of the incident energy. This low value implied the lower irradiance was below the threshold for SBS.

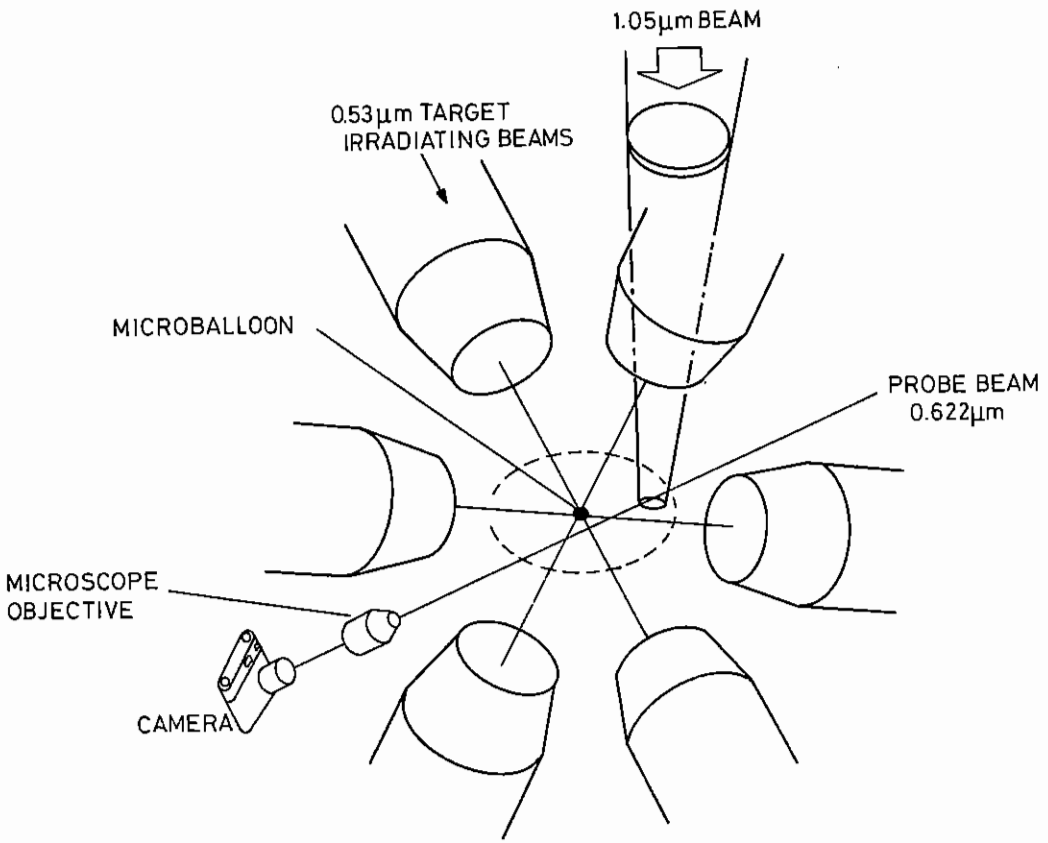

Figure 3.01 Experimental layout for Brillouin scattering from pre formed plasma.

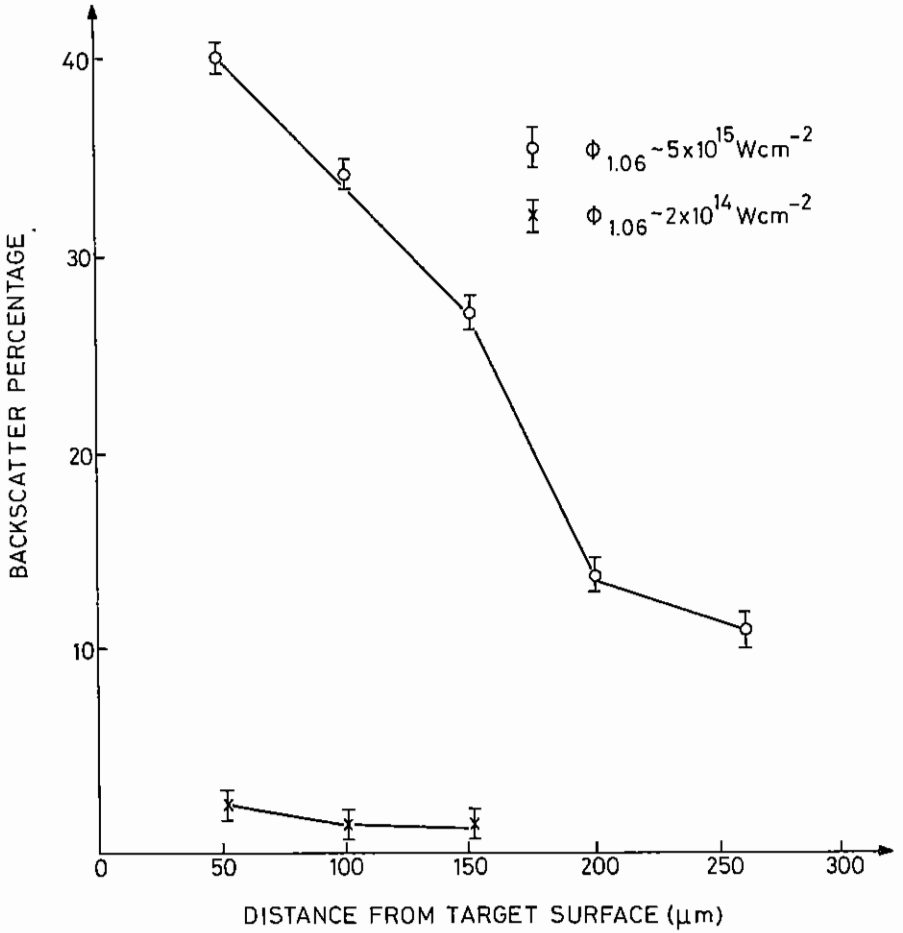

Figure 3.02 Reflectivity versus distance from target surface.

No saturation in the backscattered level was observed for the limited scan performed, nor for increasing energy in the seventh beam (see Figure 3.03).

The density profiles along the direction of the seventh beam were obtained by Abel inversions of the interferograms. Figure 3.04 shows examples of the density profiles and it can be seen that no significant profile modification at 0.1 n_c occurred when the seventh beam was incident on the underdense plasma. The average density scale length, L was $\sim$ 160 μm in the test region.

A ray tracing code developed by S Sartang (3.03) was used to simulate the refraction of the light in the plasma and as shown in Figure 3.05 only light which retraced the incident path would have been collected by the backscattered energy calorimeter.

The refraction of the light through the underdense plasma makes these results difficult to interpret. As the seventh beam is focused closer to the original target surface, several factors are expected to increase:

(i) n_c, the electron density.

(ii) The scattering volume.

(iii) The scale length L (tangential to a given density surface $L \to \infty$).

(iv) The path length through the underdense plasma.

The contribution of each of these factors to the increase in backscatter energies is not clear from the present data. The velocity gradients in the underdense plasma may also play an important role in suppressing SBS as, for SBS $k_s = 2k_o$, and the phase mismatch would increase in the more underdense regions.

However, this investigation has shown that high levels ($\sim$ 30 to 40%) of backscatter are obtained from long scale length ($\sim$ 160 μm) plasmas, even

when the maximum density encountered is $\sim$ 0.1 n_c.

T P Hughes, F McGoldrick, S M L Sim (Essex) and O Willi (Oxford)

3.3 Time Resolved Spectra of $\omega_o/2$ Emission

In the region of quarter critical density of a laser produced plasma, two parametric instabilities are thought to exist - stimulated Raman scattering (SRS) and the two plasmon decay instability (TPI). In SRS the incident electromagnetic wave (frequency ω_o) decays into a scattered electromagnetic wave of frequency $\sim \omega_o/2$ and an electron plasma wave, whereas in TPI the electromagnetic wave decays into two electron plasma waves with frequencies close to $\omega_o/2$.

Hence $\omega_o/2$ emission can be generated directly by SRS, producing an emission spectrum which is single peaked with the peak shifted to the longer wavelength side (3.04). Alternatively, the emission may be produced from the plasmons created by TPI either by Stokes Raman scattering or possibly by linear mode conversion (3.05). In this case the spectrum should be double peaked with the peaks lying on either side of the nominal $\omega_o/2$ value, similar to the $3\omega_o/2$ emission spectrum (3.06)(3.07).

In this experiment backscattered emission at $\omega_o/2$ was observed when foils of plastic, aluminium, and gold were irradiated by the third harmonic (ω_o = 0.35 μm) of Neodymium laser light ($E_{LAS} \sim$ 10 J; FWHM $\sim$ 340 ps) using the same method reported in earlier work (3.08).

Figure 3.06 shows the experimental layout. The 1.05 μm light pulse, produced with a pulse stacker, was converted(3.09) to 0.35 μm by two KDP crystals and focused onto target by an F/2.5 fused silica doublet lens. The backscattered $\omega_o/2$ emission was diverted and imaged onto the slit of a spectrograph (F = 0.5 m, 1200 lpmm grating) and the output of the spectrograph coupled to an S20 Imacon streak camera as shown. This arrangement gave a spectral window at the streak camera of 230 Å, with spectral and temporal resolutions of 8 Å and 20 ps respectively.

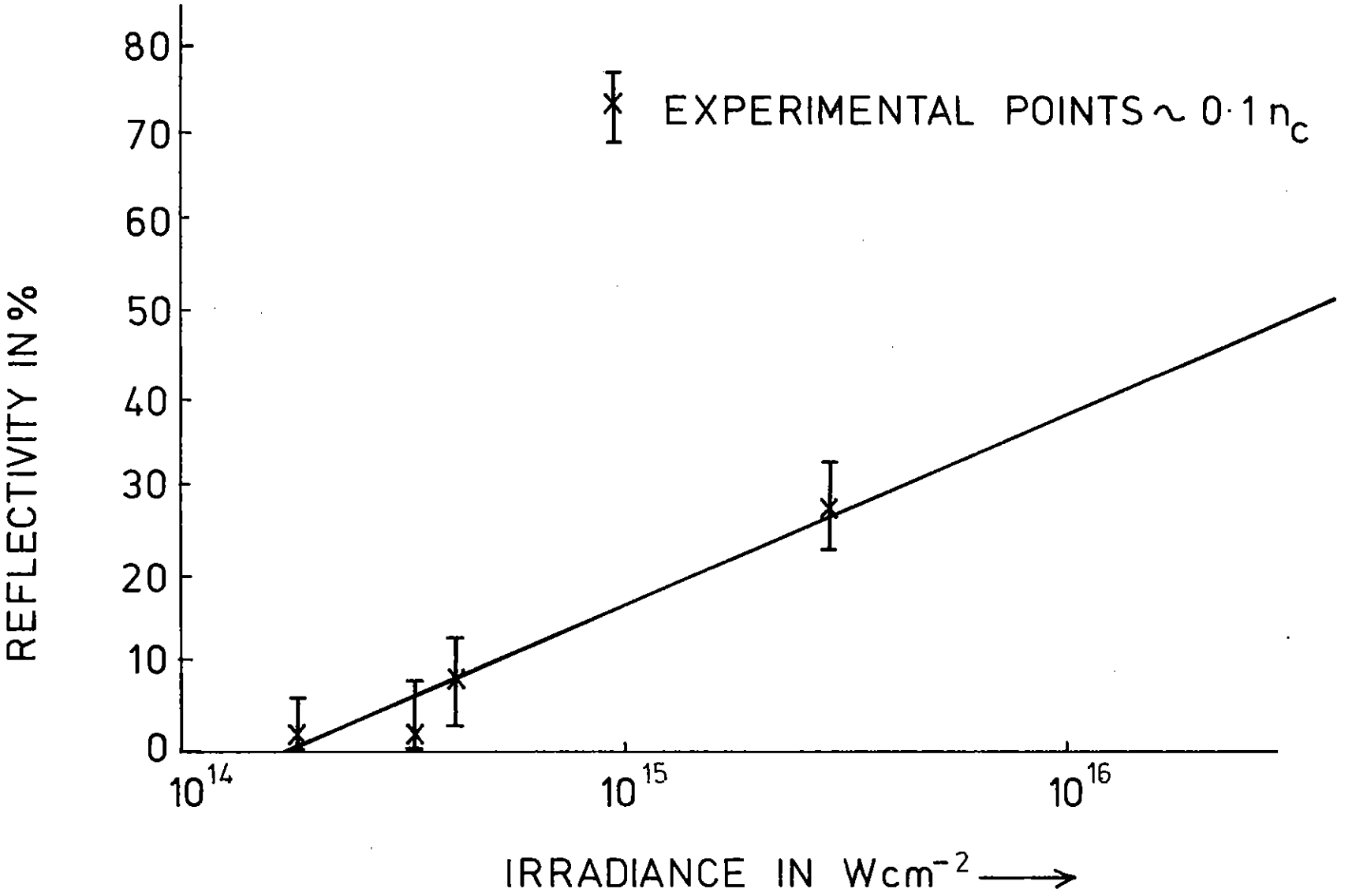

Figure 3.03 Reflectivity versus irradiance.

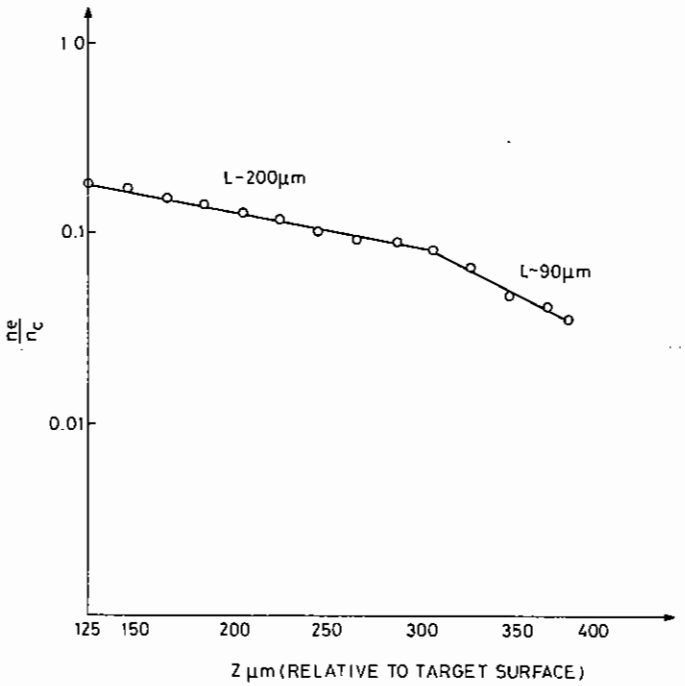

No 1.06μm BEAM

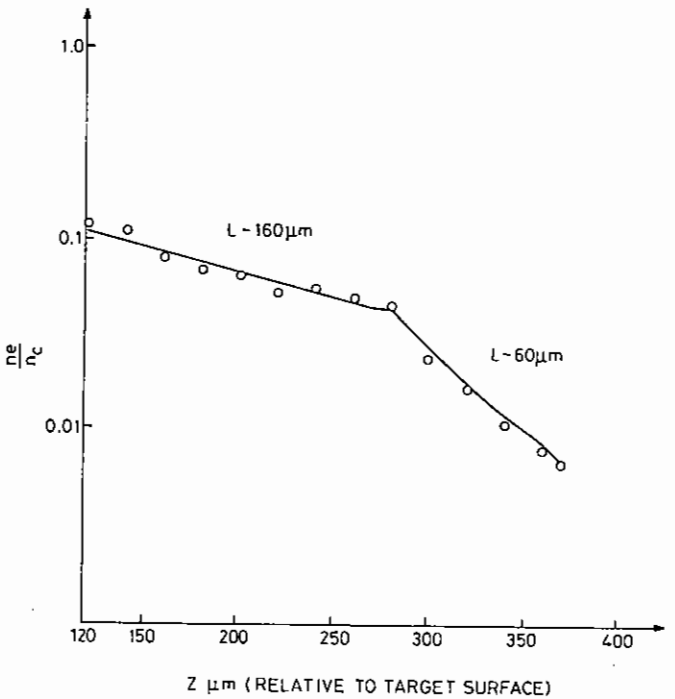

1.06μm BEAM POSITIONED 100μm FROM TARGET SURFACE

Figure 3.04 (b)

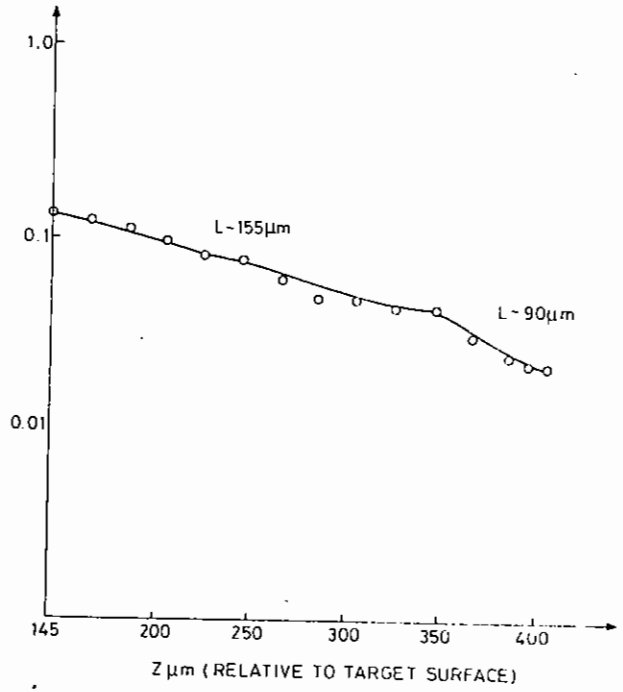

1.06μm BEAM POSITIONED 200μm FROM TARGET SURFACE

Figure 3.04 (c)

Figure 3.04 Density profiles (a) no seventh beam (b) seventh beam positioned 100μm from target surface (c) seventh beam positioned 200μm from target surface.

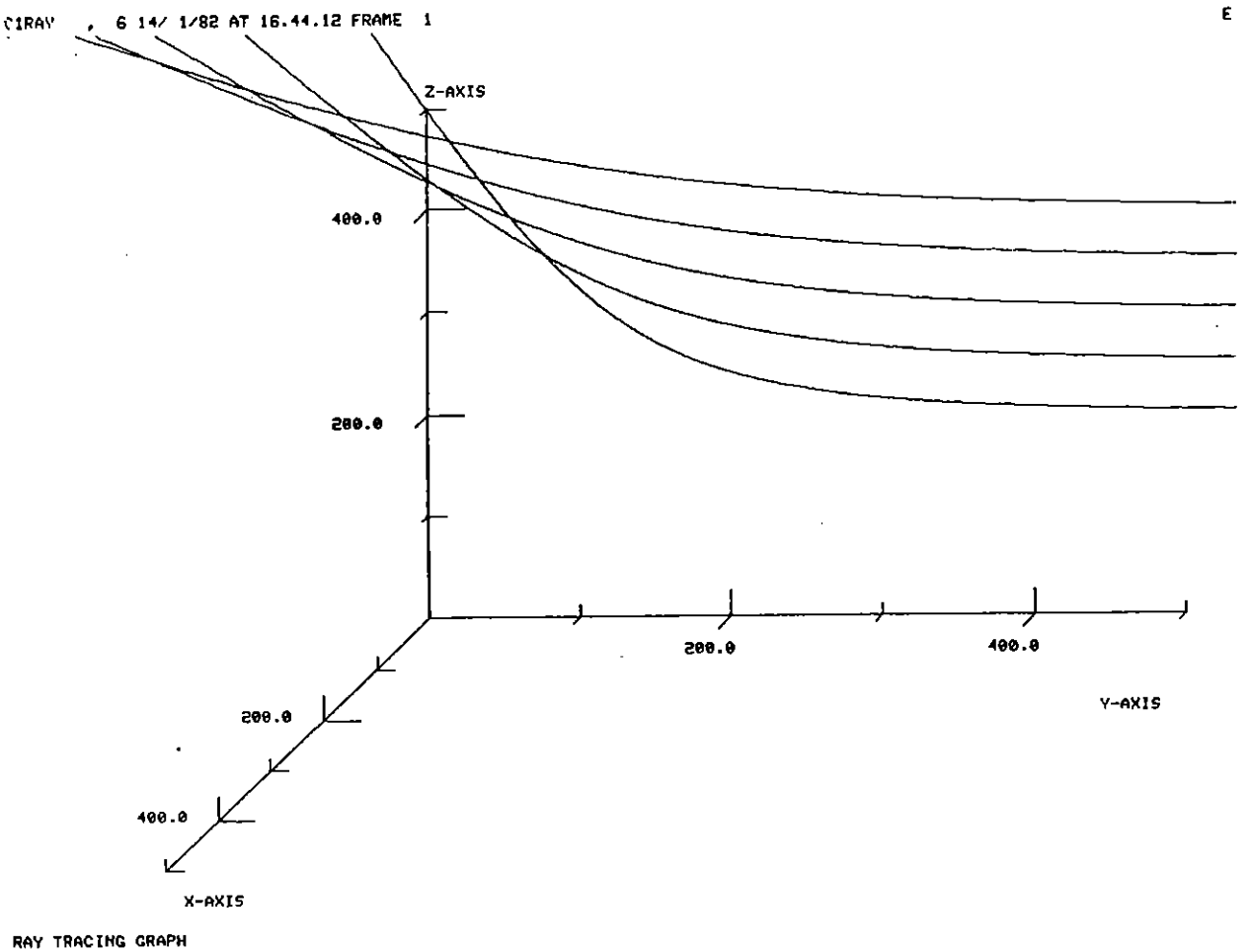

Figure 3.05 Raytracing simulation for scalelength of 160μm.

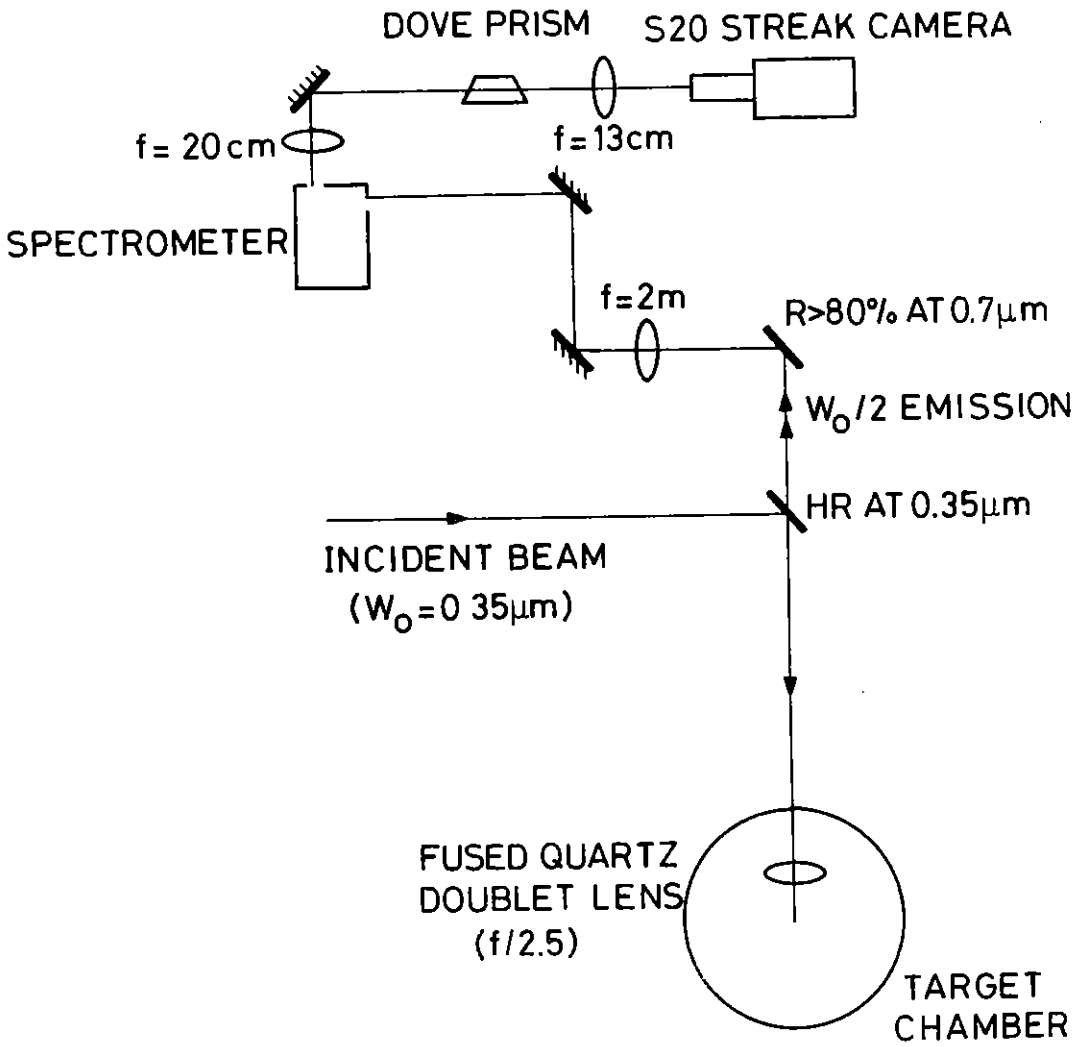

Figure 3.06 Schematic diagram of the experimental arrangements for observing backscattered emission at $\omega_o/2$.

Calibration marks were obtained after every shot by streaking part of the second harmonic emission produced by a subsequent low energy shot with suitable adjustments to the spectrograph wavelength setting and camera trigger delay.

Figure 3.07 shows the emission at two irradiances observed with plastic foils. It can be seen that both spectra are single peaked, broad and lying mainly to the blue side of $\omega_o/2$. The FWHM of the spectra were found to depend on the irradiance.

With gold targets the emission spectrum is entirely different - Figure 3.08. Here a double peak structure is found and the blue peak is shifted farther from the nominal value than the red. The whole spectrum is not observed due to the limited spectral window at the streak camera.

For an intermediate Z plasma, a transition between these two spectra may be observed. Figure 3.09 shows the $\omega_o/2$ emission spectra obtained from aluminium targets. It can be seen that with a high irradiance the spectrum appears to be double peaked, whereas at a lower irradiance, produced by increasing the focal spot size, the spectrum resembles that obtained with plastic targets.

All the $\omega_o/2$ emission spectra show temporal structure. This is due mainly to the fact that the incident pulse is shaped using a pulse stacker.

The double peak structure observed is attributed to the existence of the two plasmon decay instability as already discussed. The single peak structure however cannot be explained on this basis. It is possible that in this case it is due to stimulated Raman scattering, although this is expected to produce a peak shifted more towards longer wavelengths than observed.

The threshold for these instabilities are (3.10)(3.01)

$$\text{TPI} \qquad \frac{1}{3}\left[\frac{v_o}{v_{th}}\right]^2 k_o L > 1$$

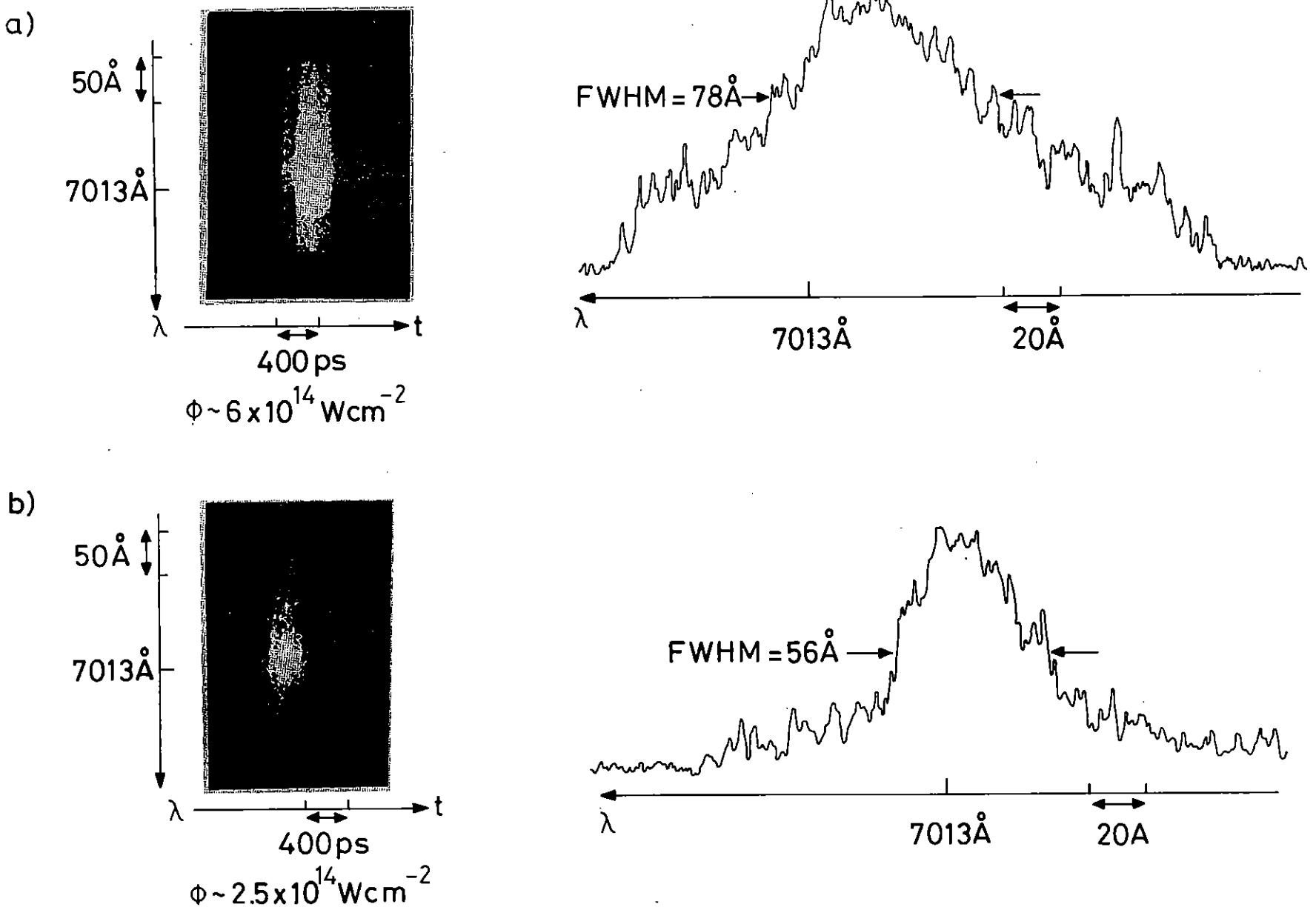

Figure 3.07 Time-resolved spectrum of $\omega_o/2$ harmonic emission from 0.35μm laser irradiated plastic foils.

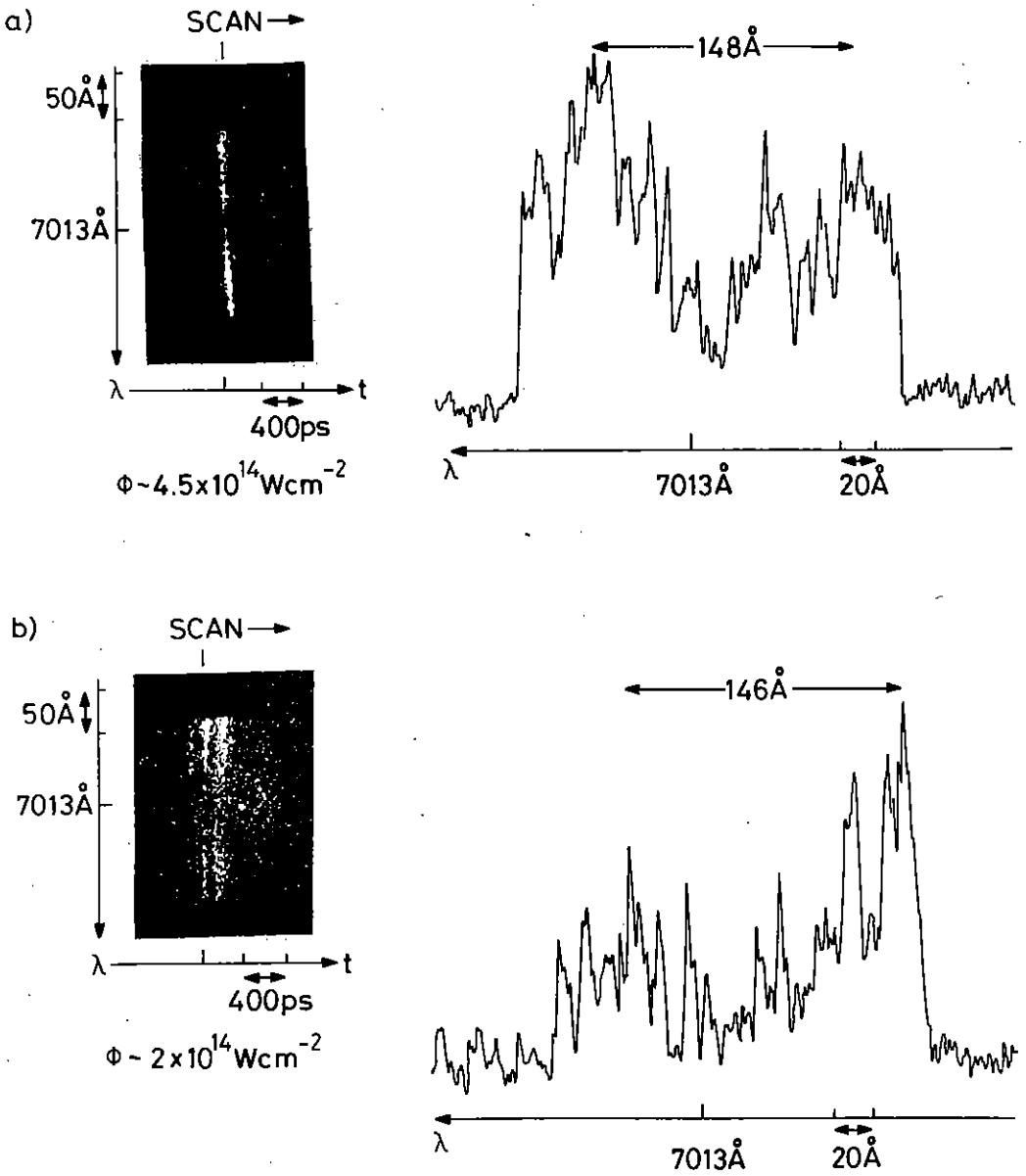

Figure 3.08 Time-resolved spectrum of $\omega_0/2$ harmonic emission from 0.35 m laser irradiated gold foils.

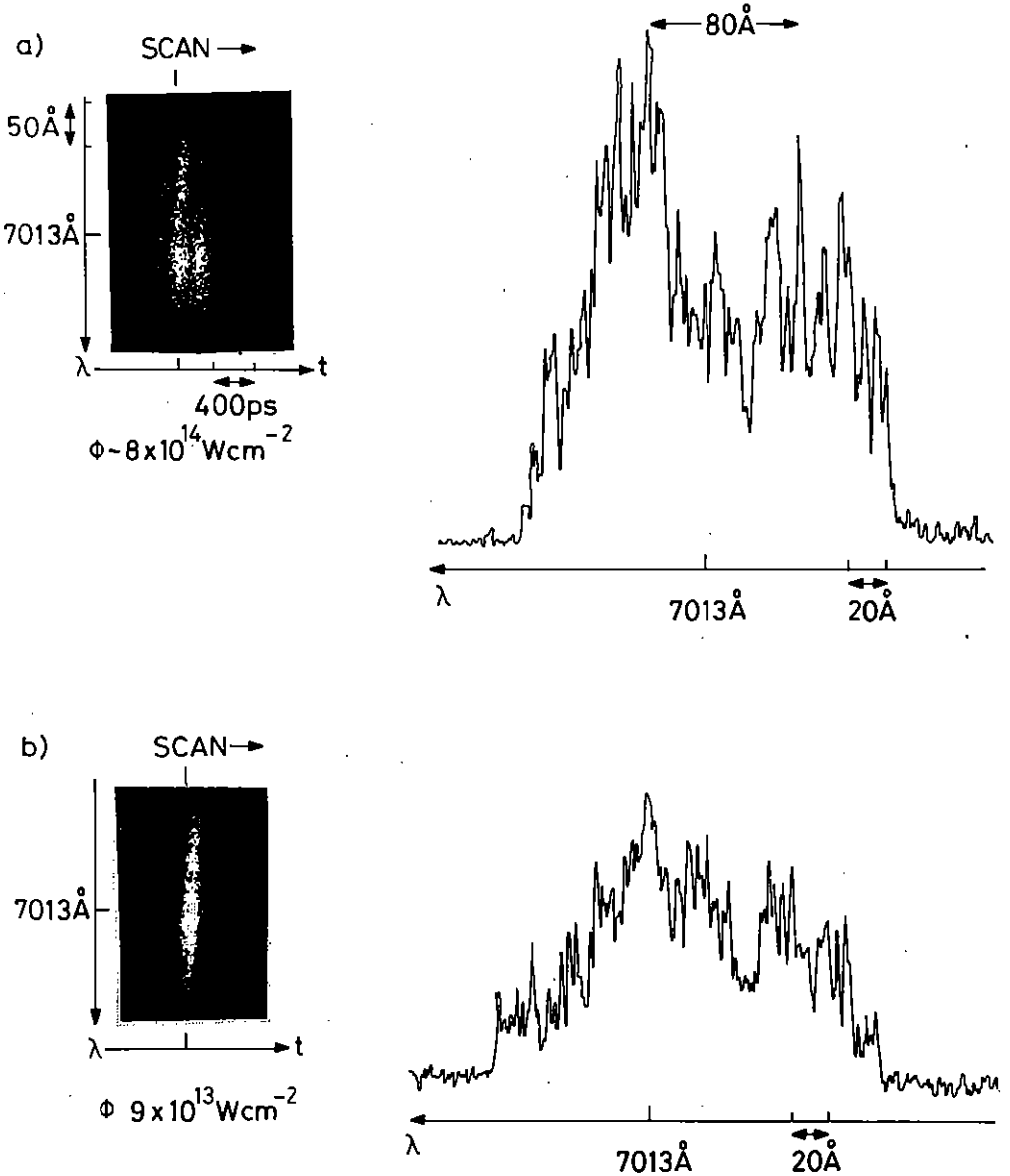

Figure 3.09 Time-resolved spectrum of $\omega_0/2$ harmonic emission from 0.35 m laser irradiated aluminium foil.

$$\text{SRS} \quad \left[\frac{v_o}{C}\right]^2 (k_o L)^{4/3} > 1$$

where k_o is the wave number of the pump laser, L is the plasma density scale length, v_o is the electron quiver velocity and v_e the electron thermal velocity. Hence it can be seen that for long enough scale lengths Raman scattering may dominate.

Studies of laser produced plasmas have shown that low Z plasmas expand more rapidly than higher Z ones (3.11), and so the scale lengths associated with a plastic target should be greater, and may be sufficient to reach the SRS threshold. However, this needs to be investigated more thoroughly.

E McGoldrick and S M L Sim (Essex)

3.4 Time Resolved Spectra of $3\omega_o/2$ Emission

3.4.1 Introduction

High resolution time-resolved spectra of the $3\omega_o/2$ emission have been obtained and investigated in order to explore the physical mechanism responsible for the rapid pulsing of the spectrum which has been interpreted as density profile modification at the subcritical density region caused by the ponderomotive force of the plasma waves (3.07). By considering the filamentary structures and other features (3.12) seen in the $3\omega_o/2$ harmonic emission an alternative explanation can be proposed which connects the $3\omega_o/2$ harmonic emission with the growth and collapse of filaments. The $3\omega_o/2$ emission is assumed to come from the quarter critical density contour within a filament. This moves, firstly in the direction of the incident laser light, during the formation and growth of the filament, and then in the opposite direction during the collapse of the filament.

According to this model the temporal pulsations of the $3\omega_o/2$ spectrum should be composed of an early red shifted component and a later blue one with a few or several tens of picoseconds time difference, which depends

on the emitting time of the $3\omega_o/2$ emission.

Several improvements to the time resolution of the spectrum were carried out and special techniques were adopted to offset the time distortion of the spectrum by the pin-cushion distortion of the streak camera, giving a time resolution of about 5 ps.

A prepulse was utilised to preform a long scale length plasma. Thus a longer $3\omega_o/2$ emission time of a single fine structure can be obtained, and so it is easier to identify the time difference of the red and blue components.

3.4.2 Experimental Arrangement

The experimental arrangement is shown in Figure 3.10. The output of the 0.5 m, 1200 line/mm grating spectrograph was relayed to the 100 μm input slit of an IMACON 675 streak camera using an f = 200 mm achromatic lens. A narrow (∿ 0.5 mm) slit was located inside the spectrograph in front of the grating in order to improve the temporal resolution.

The streak camera body was turned 90° to match the vertical slit image of the spectrograph. This simplified the coupling optics. A 40 mm iris was put in the collecting optics to improve the target image on the entrance slit of the spectrograph.

Several factors which might influence the time measurements along the spectral direction are shown in Table 3.01. The overall time resolution was estimated to be ∿ 5 ps including all these effects. Spectral resolution was estimated to be ∿ 3 Å by using the uncertainty relation $\Delta\omega\Delta t \geq 2\pi$.

To confirm the time dependent fine structure on the screen of the streak camera a special bi-wedge element was occasionally introduced into the coupling optics to split the time resolved spectrum into an identical pair on the screen of the streak camera (3.10). The image of the spectrum is thus split into an identical pair along the horizontal direction both of

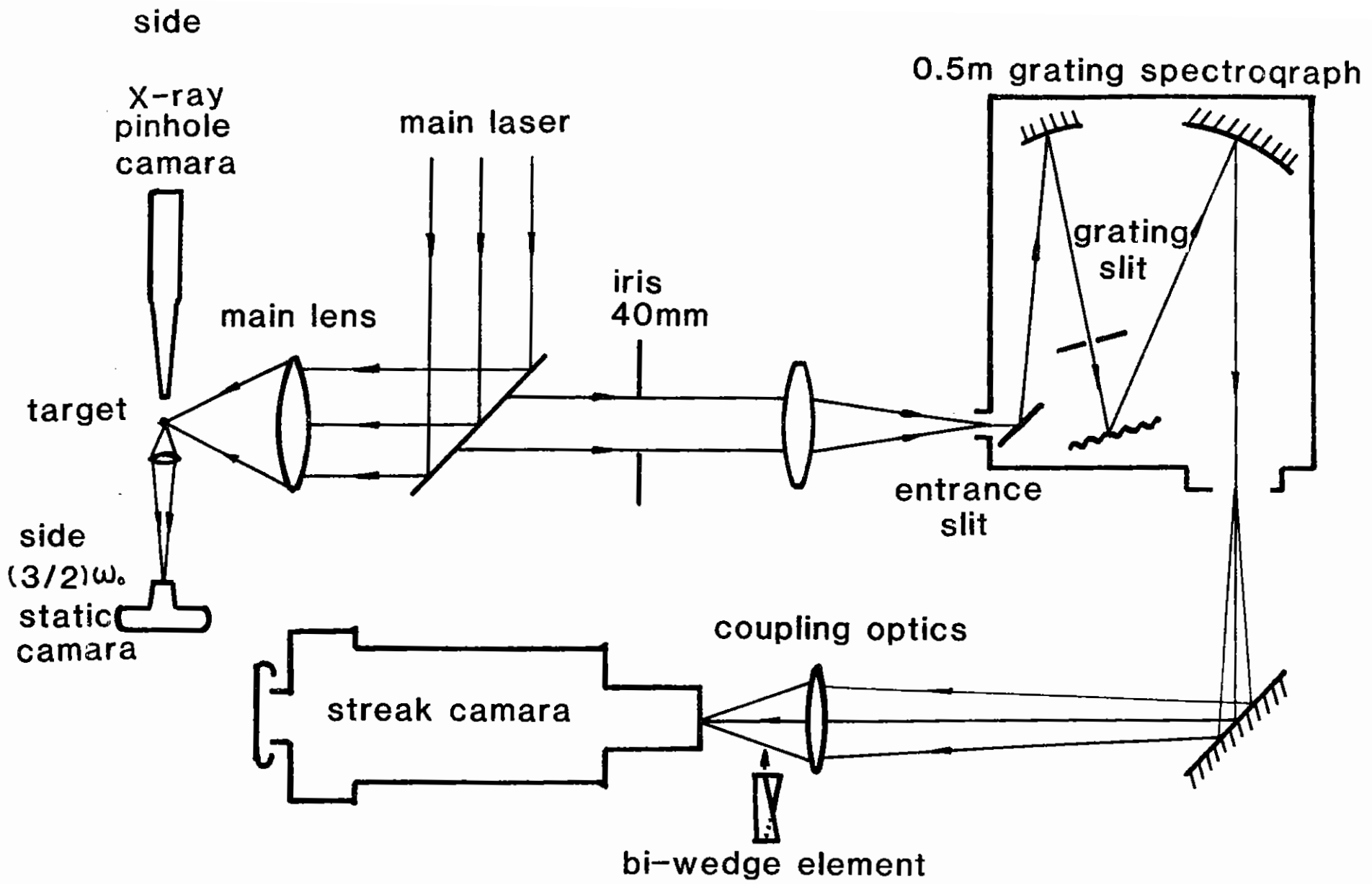

Figure 3.10 EXPERIMENTAL SET-UP

Fig.1.

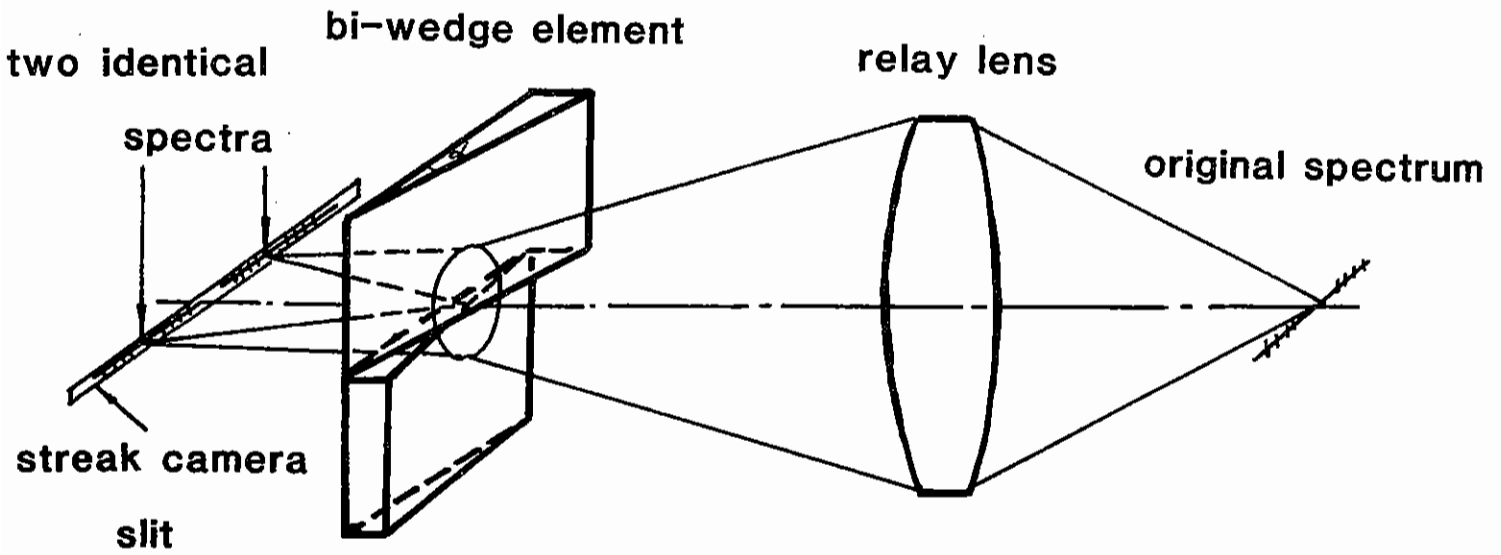

Figure 3.11 Layout of the bi-wedge element.

SEVERAL IMPORTANT FACTORS WHICH MIGHT INFLUENCE THE TIME MEASUREMENTS

factors	conditions	time delay relative to $t_{3/2}=0$		image distortion
		for red shifted wavelength ($\lambda_{3/2}$+200Å)	for blue shifted wavelength ($\lambda_{3/2}$-200Å)	
refractive index	the thickness of the BK 7 glass is less than 100 mm	<-0.07 ps	<+0.07 ps	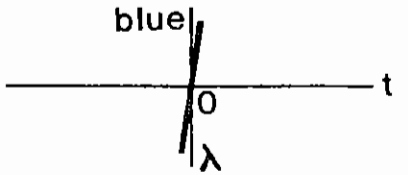
coupling optics imaging system	f= 8 inch S_0= 1020 mm G = 3.7	+0.7 ps	+0.7 ps	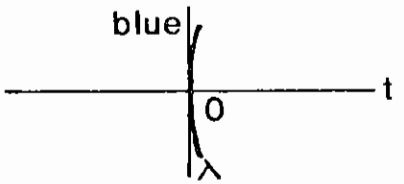
the broadenning due to the width of grating	unmasked area 0.6 mm	~3ps broadening	~3ps broadening	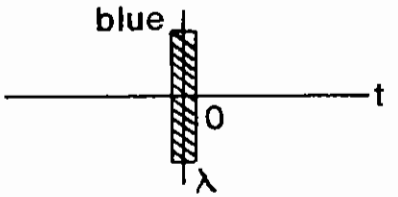
pincushion distortion- the traveling delay of electrons	IMACON 675	average +5ps	average +4ps	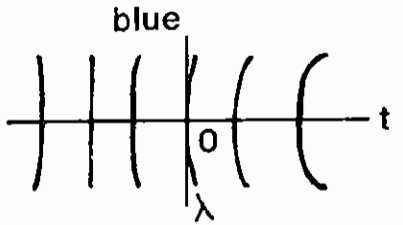

Table 3.01

which are sampled by the streak camera slit when the bi-wedge element is used. The wedge angles were 0.7° and 1.4° respectively.

3.4.3 Experimental Results

The intensity of the heating laser beam was varied from 2.5×10^{13} W cm^{-2} to 10^{16} W cm^{-2} both by changing laser energy between 3 and 50 Joules and by adjusting the defocusing of the f/1 main lens. A 500 ps (FWHM) stacked pulse was used as the main pulse. On most of the shots a 10% prepulse preceded the main pulse by 1 to 4 ns in order to preform a long scale length plasma.

It was found that all the $3\omega_o/2$ emission consisted of very fine time modulated structures with red and blue shifted components for laser intensities from 2.5×10^{13} W cm^{-2} to 10^{16} W cm^{-2}. Figure 3.12 shows a time resolved backscattered spectrum of the $3\omega_o/2$ harmonic emission produced from a planar tungsten target. The laser energy was 56.9 Joules in a focal spot of 67 μm, giving an irradiance of 0.92×10^{15} W cm^{-2}. A ~10% prepulse, 2 ns before the main pulse was used to preform the plasma. A time integrated $3\omega_o/2$ picture was taken at 90° to the beam direction for the same shot. In Figure 3.12 filament No 1 and No 2 represent the time burst signals originating from two different filaments.

Figure 3.13 shows another time resolved spectrum of $3\omega_o/2$ harmonic emission together with a side scattered $3\omega_o/2$ static picture and side scattered X-ray pinhole photograph. "Filament a" on the picture represents one of the sinusoidal shaped fine structures along the time axis, which is schematically plotted in Figure 3.14(a). On the assumption of the Doppler shift model Figure 3.14(b) gives the bottom contour phase velocity at ¼-critical surface within "filament a" against time. Integration of Figure 3.14(b) gives the position of the $n_c/4$ contours with time in Figure 3.14(c). The calculated length of "filament a" is 28 μm, consistent with the filament length data (32 – 40 μm) from the spatially resolved side scattered $3\omega_o/2$ emission picture for the same shot (Figure 3.13, upper left). In a number of shots it is found that either the red shifted tail of the fine structure curves to the right hand

side while the blue one curves to the left or the time burst structure is tilted in the same way. These regular time differences were further confirmed during experiments when the bi-wedge element was utilised. Both time resolved spectra on the streak camera screen showed the same time dependence of the spectra. This excludes the possibility that the time dependence was caused by streak camera distortion. These phenomena seem to support the Doppler shift model.

Two comparatively "clear" fine structures, filaments No 1 and No 2, which have less interference from other fine structures, are densitometered along the spectrum direction. The results are shown in Figure 3.15(a) and (b) respectively. It is found that for each modulated single peak or double peak on the red shifted hump (marked A^+, B^+ ... etc) there exists an equivalent modulated one on the blue shifted hump (marked A^-, B^- ... etc). If the quasi-symmetrical axis is chosen at the central dip position of the spectrum or in some cases at the central modulated peak (which are not necessarily at the exact $3\omega_o/2$ frequency), a nearly linear relation of frequencies about the chosen axis can be found as shown in Figure 3.16.

3.4.4 Discussion

It is pointed out that the nonlinear formation theories of filamentation fall into two contrasting categories (3.13). Simply speaking, they are stable and unstable filamentation theories. It seems that our experimental results are in favour of the unstable filamentation model. When the optical refraction effect in a focused channel (3.14) and filamentation modulation effect (3.15) were considered, the time dependence of the fine structure and the quasi-symmetrical features of the spectrum can be explained (3.14) in terms of the unstable filamentation model. But the original broadening mechanism (3.16) of the $3\omega_o/2$ emission has to be reconsidered.

If we base on the recent theory (3.16) about the $3\omega_o/2$ broadening and the theory of stable filamentation, the spectrum modulation of the $3\omega_o/2$ emission may presumably be interpreted as a result of an assumed

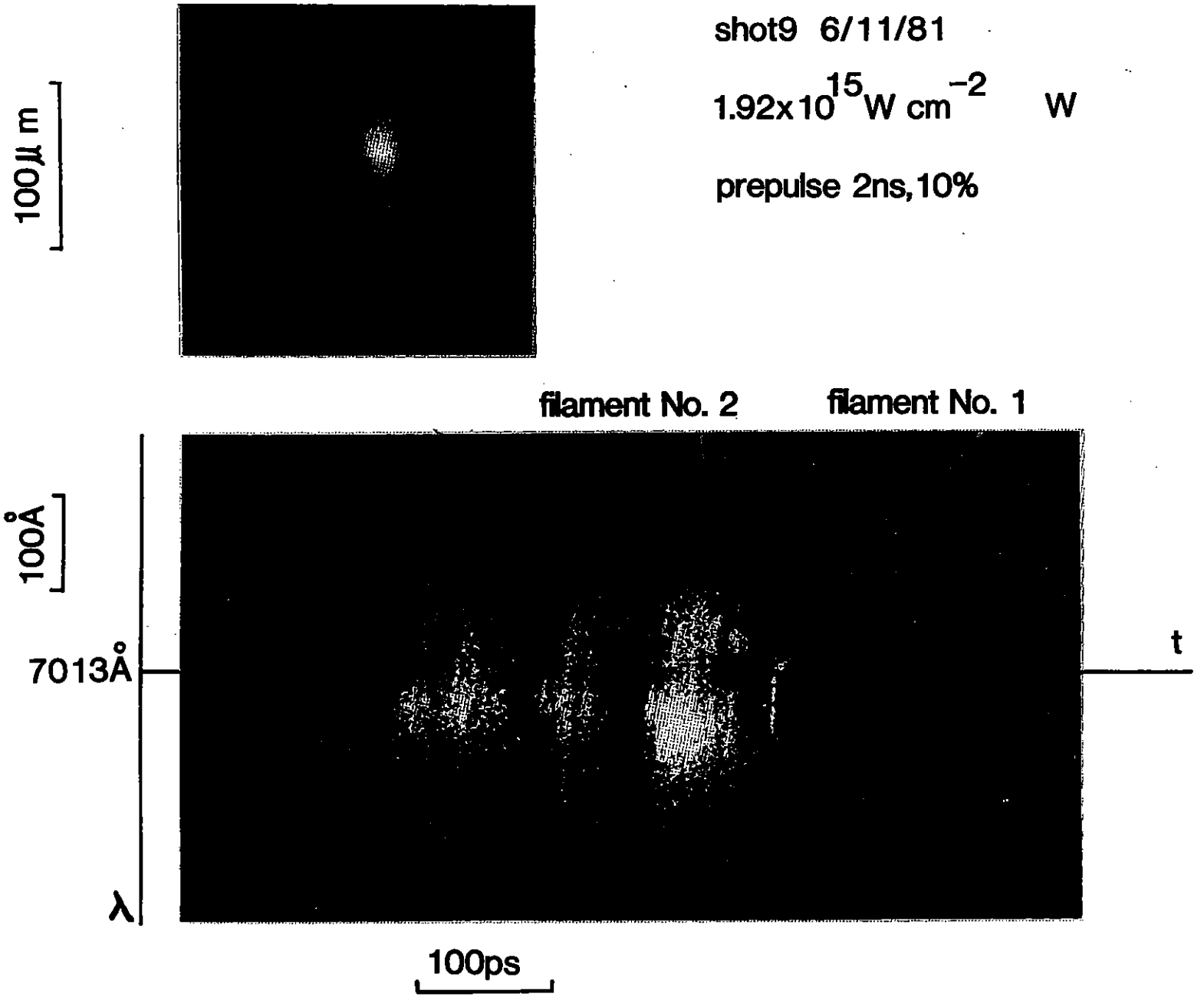

Figure 3.12 Back reflected temporally resolved spectrum of $(^3/_2)\omega_0$ harmonic emission, with laser irradiance of 1.92×10^{15}w cm^{-2} on a tungsten planar target.

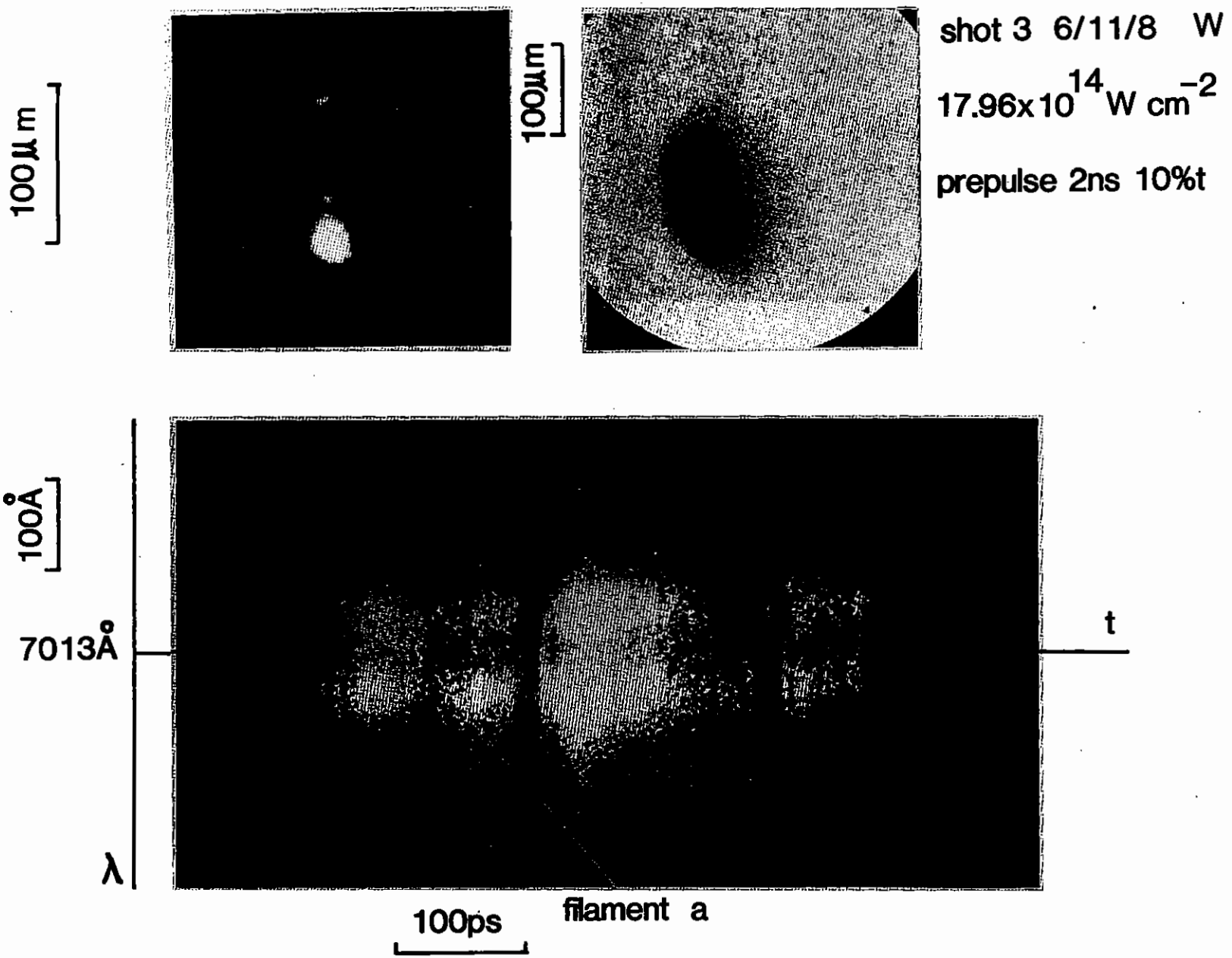

Figure 3.13 Back reflected temporally resolved spectrum of $(^3/_2)\omega_o$ harmonic emission with laser irradiance of 7.96×10^{14}w cm^{-2} on a tungsten planar target.

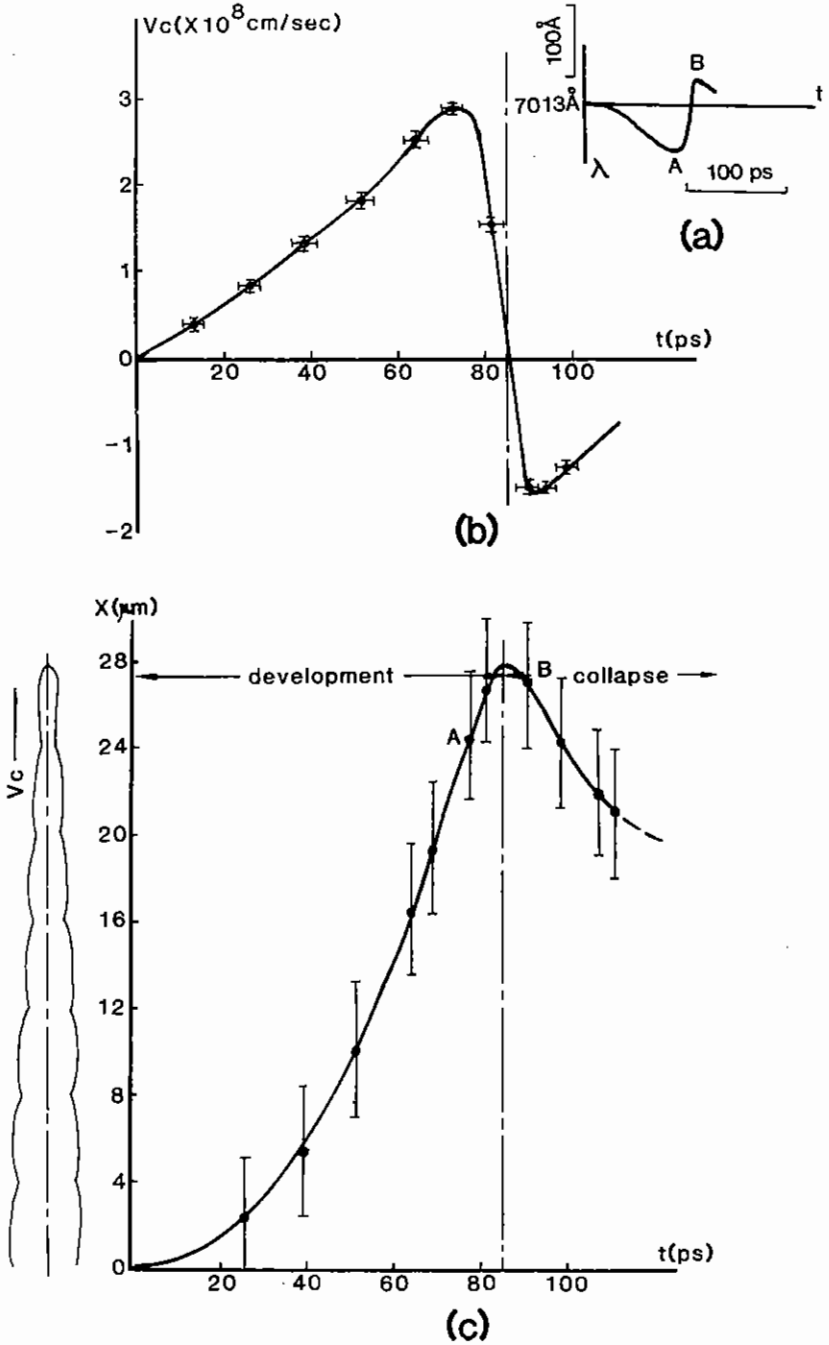

Figure 3.14 (a) Schematic plot of filament a of Fig 3.13. (b) The calculated Doppler velocity of the sample which refer to the contour velocity. (c) The calculated time dependence of the position of the filament bottom.

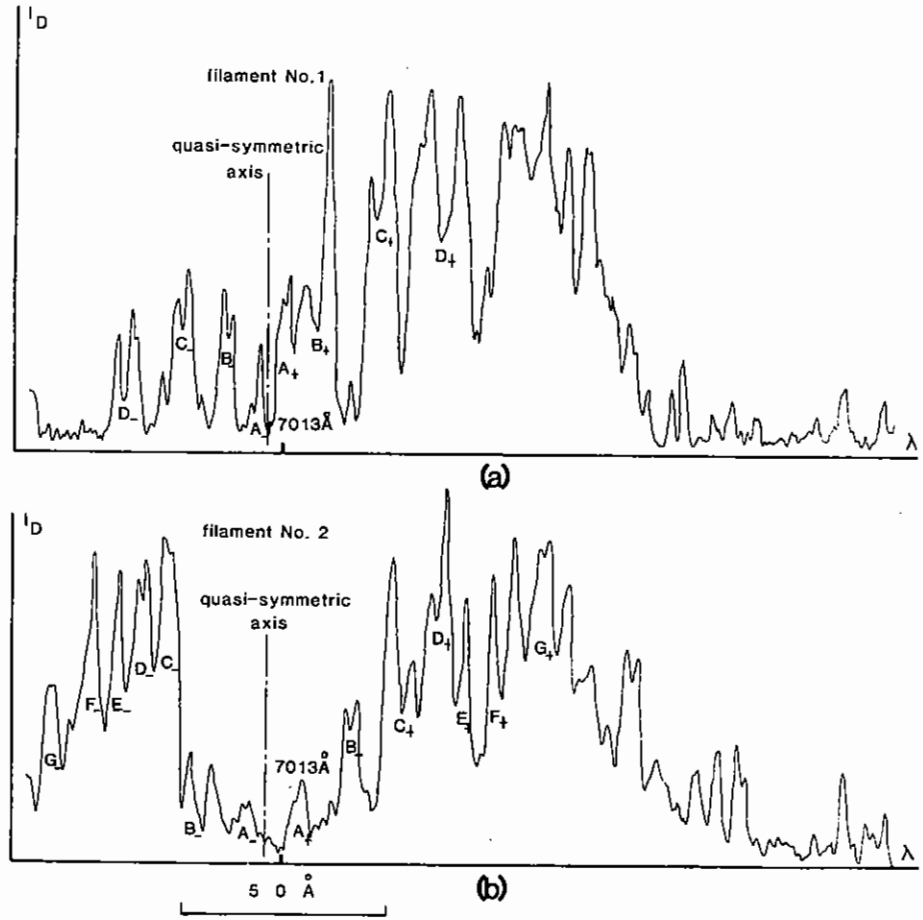

Figure 3.15 Two densitometer traces from Figure 3.12 showing show spectral modulation for a single fine structure. The modulated peaks on the red shifted side labelled A^+, B^+... have guasi symmetrical features on the blue labelled A^-, B^- ...

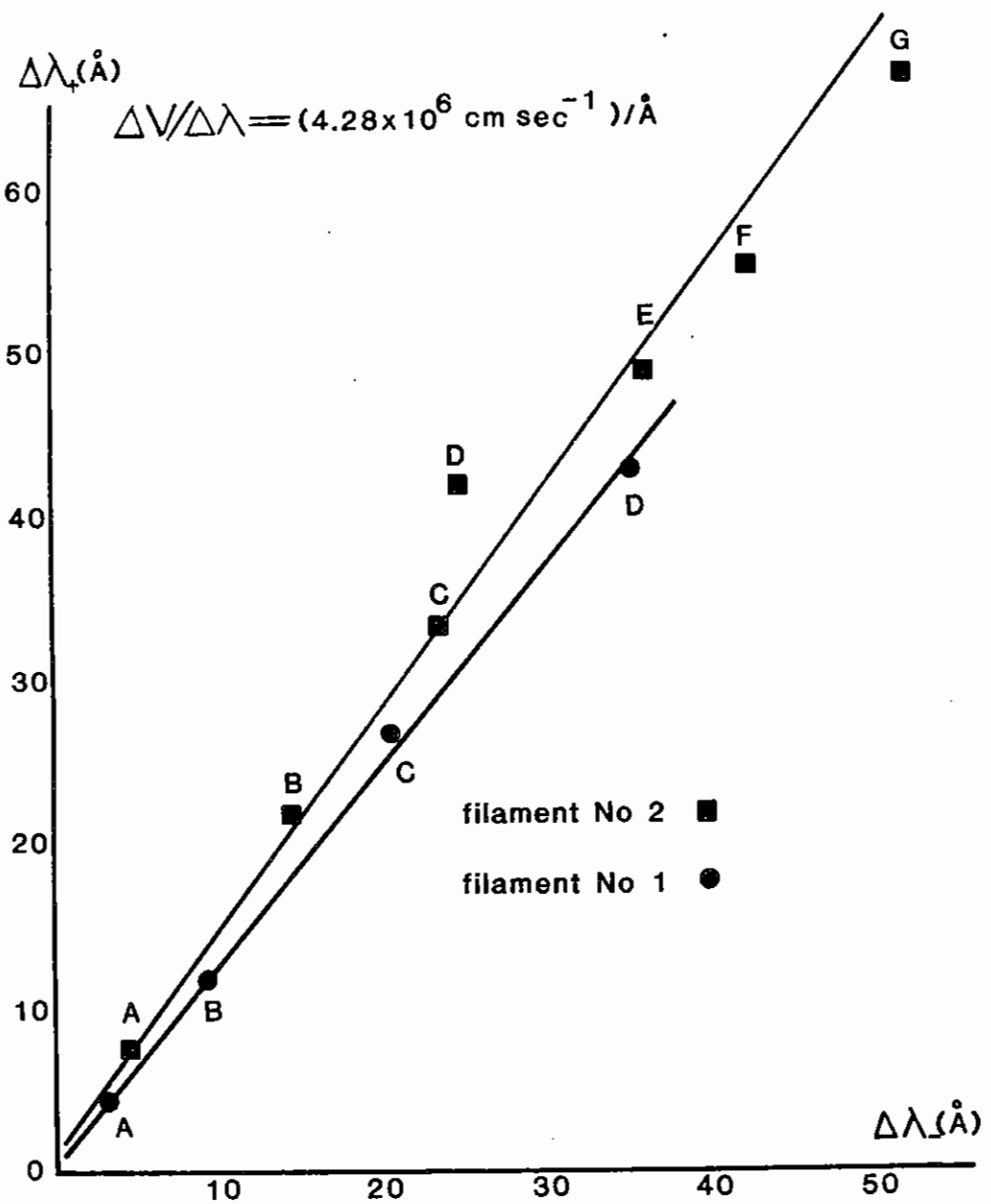

Figure 3.16 Frequency shift relation of the modulated peaks between the red and the blue from the fine structure of $(^3/_2)\omega_0$ spectra.

plasma wave travelling or standing along a stable filament wall. But the cause of the time dependence of the $3\omega_0/2$ fine structure will remain unknown, and the explanation of the time burst structure of the $3\omega_0/2$ emission is still unclear.

Finally, the time dependence of the fine structure of the spectrum should be confirmed further.

Z Q Lin (Shanghai)

3.5 Laser Beam Filamentation

3.5.1 Introduction

Several experiments at various laser wavelengths (λ = 1.05 μm, 0.53 μm and 0.35 μm) have been carried out during the last year to study laser beam filamentation and self-focusing. Filamentary structures aligned along the laser beams have recently been observed in harmonic emission images (3.17) in optical shadowgrams and in Schlieren images (3.18) in the plasma corona of targets irradiated with infrared laser beams. The distribution of the filaments however appeared to be rather random and the filaments may have grown from initial small perturbations on the laser beams. Two mechanisms namely thermal expansion and ponderomotive force effects can give rise to density depletions in the plasma leading to a focusing of either the whole or part of the laser beam due to the changes in the refractive index. The thermal effects are more likely to occur in collisional plasmas whereas the ponderomotive force processes may initiate self-focusing in collisionless plasmas. Laser beam filamentation may be particularly detrimental at shorter laser wavelengths where thermal smoothing effects become inefficient arising from the short distance between the absorption and ablation regions and consequently any non-uniformities generated by filamentation may be imprinted on the imploding shell.

3.5.2 Experimental Arrangement

3.5.2(a) Laser System

A short (100 ps) Gaussian pulse was generated by a mode locked oscillator and the output was split into two portions using a 50% beam splitter. One of the fractions was passed through a coherent pulse stacker which combined several pulses to produce a relatively long heating pulse of approximately 430 ps (FWHM) in duration. Figure 3.17 shows the temporal profile of the pulse after frequency doubling, obtained from a streak camera. Most of the energy is concentrated in the central pulse with smaller pulses before and after it. For experiments with green laser light six green beams were generated by splitting the amplifier output into six and frequency doubling them with type 1 KDP crystals. The beams were focused onto target using f/1 doublet aspheric lenses. The conversion efficiency was about 50%. The unconverted 1.05 μm laser radiation in each beam was less than 10^{-3}% due to four dielectric mirrors coated for λ = 0.53 μm light following the crystals, and due to the chromatic aberration in the lenses. Due to the conversion to the green the diameter of the green beams was about two thirds of the infrared beams giving an effective lens aperture of f/1.7. Green light energies up to 10 Joules per beam were used resulting in target irradiances of between 2×10^{13} and 6×10^{14} W cm^{-2}. If targets were irradiated with ultraviolet light (λ = 0.35 μm) the infrared beam was converted to the ultraviolet with two type II KDP crystals using the polarisation mismatch scheme proposed by Craxton (3.19), overall conversion efficiency was about 25%. The laser beam was focused onto the target using an f/2.5 fused silica spherical doublet lens. Due to the conversion to the UV the diameter of the UV laser beam was about 60% of the size of the original infrared beam giving an effective lens aperture of f/3.5. The residual 1.05 μm and 0.53 μm radiation in the laser beam hitting the target was less than 10^{-3}% due to four dielectric mirrors coated for 0.35 μm radiation following the conversion crystals. In addition the 1.05 μm and 0.53 μm laser intensities at the target surface were reduced by chromatic aberration in the lens to less than 10^{-5}%. When the target was displaced from the best focus of the lens a ring structure appeared on the

target surface arising from the spherical aberration in the lens.

3.5.2(b) Diagnostics

Shadowgrams and Schlieren images were recorded using a Raman shifted second harmonic probing beam (λ = 0.62 μm) (see Section 1.7.3). In addition X-ray images were taken using a pinhole camera equipped with two pinholes 5 μm and 12.5 μm in diameter which were filtered with 15 μm and 40 μm Beryllium respectively giving an e^{-1} transmission of $h\nu$ = 1.2 keV and 1.6 keV respectively. The temporal profile of the laser pulse was recorded with an EPL streak camera. Laser beam profiles were taken in an equivalent target plane.

3.5.3 Experimental Results

Figure 3.18 shows two shadowgrams recorded on a polystyrene target. The target was irradiated with a green laser beam which was incident at 45° to the target normal. The irradiance on target was 2.5×10^{14} W cm^{-2}. The image taken during the laser pulse clearly shows bright striations aligned along the direction of the laser beam whereas no irregularities are observed in the second image which was recorded after the laser pulse. Similar observations were also made on high atomic number targets. Figure 3.19 shows a shadowgram taken on a tungsten wire target which was irradiated at an intensity of 9×10^{13} W cm^{-2}. The laser beam again was incident at 45° to the target normal. However in addition to the bright striations along the direction of the laser beam small jets issuing normally from the target surface are observed on high Z targets indicating the presence of small scale instabilities (see Section 3.7).

The filamentary structures aligned along the laser beam may have grown from the hot spots in the laser beam since the lateral scalelength which is between 30 - 50 μm is in good agreement with the separation of the spots in the laser beam observed in the equivalent target plane.

A periodic break-up of the laser beam was however observed on targets irradiated with 0.35 μm laser radiation when the target was displaced from

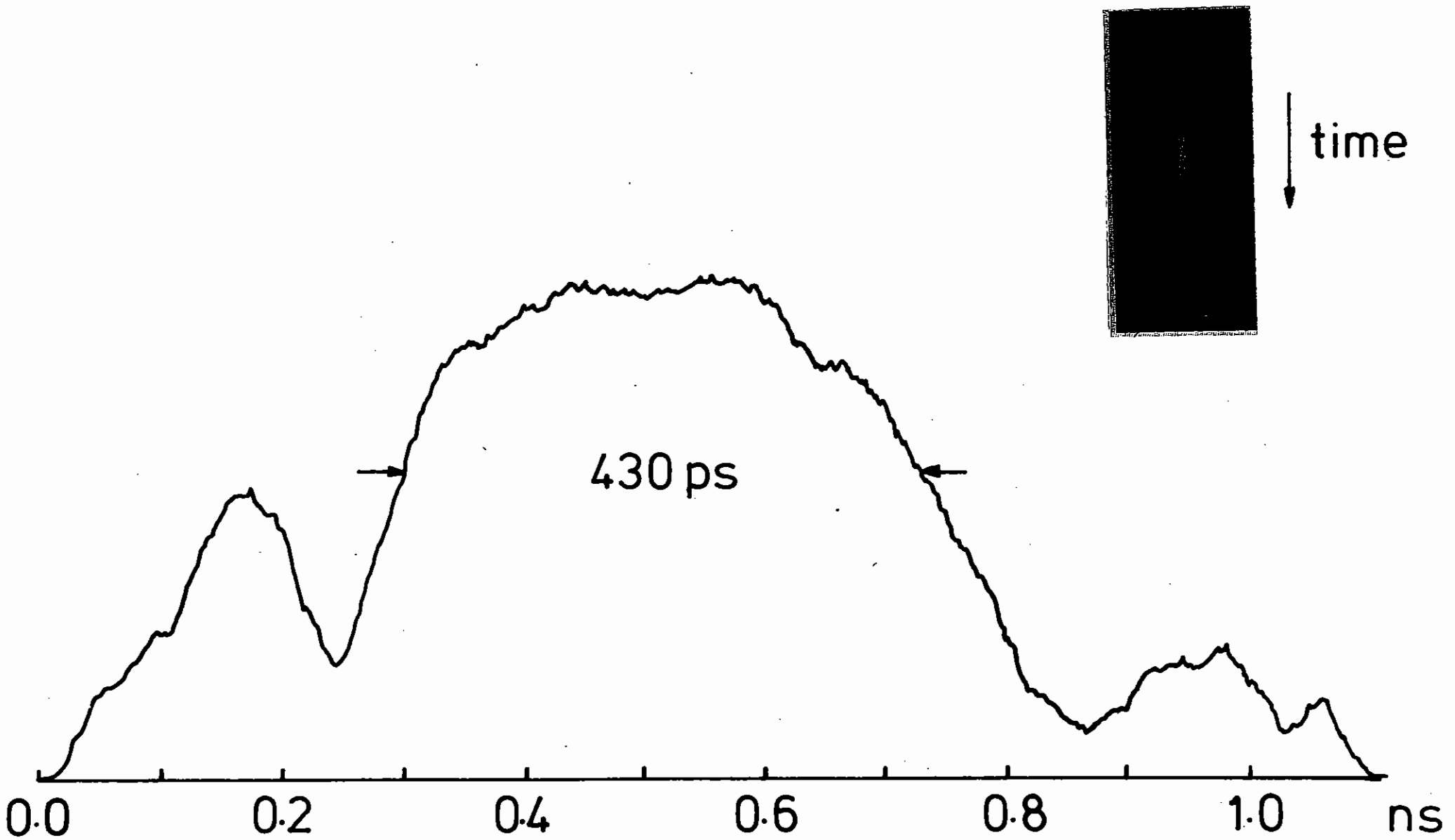

Figure 3.17 Temporal profile of the green laser pulse.

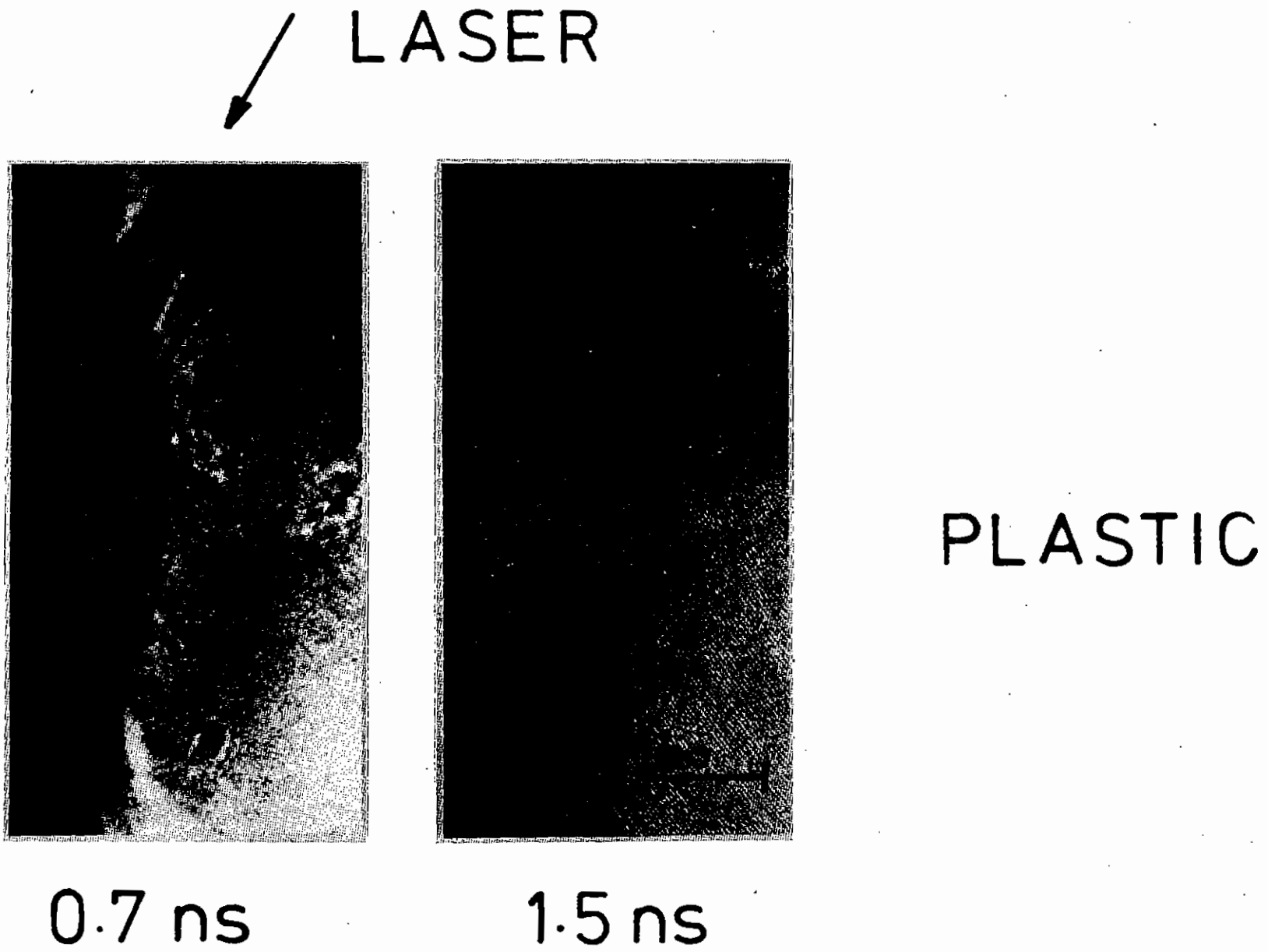

Figure 3.18 Shadowgrams recorded on a polystyrene target 0.7 ns and 1.5 ns after the beginning of the laser pulse showing filamentary structures along the laser beam during the laser pulse.

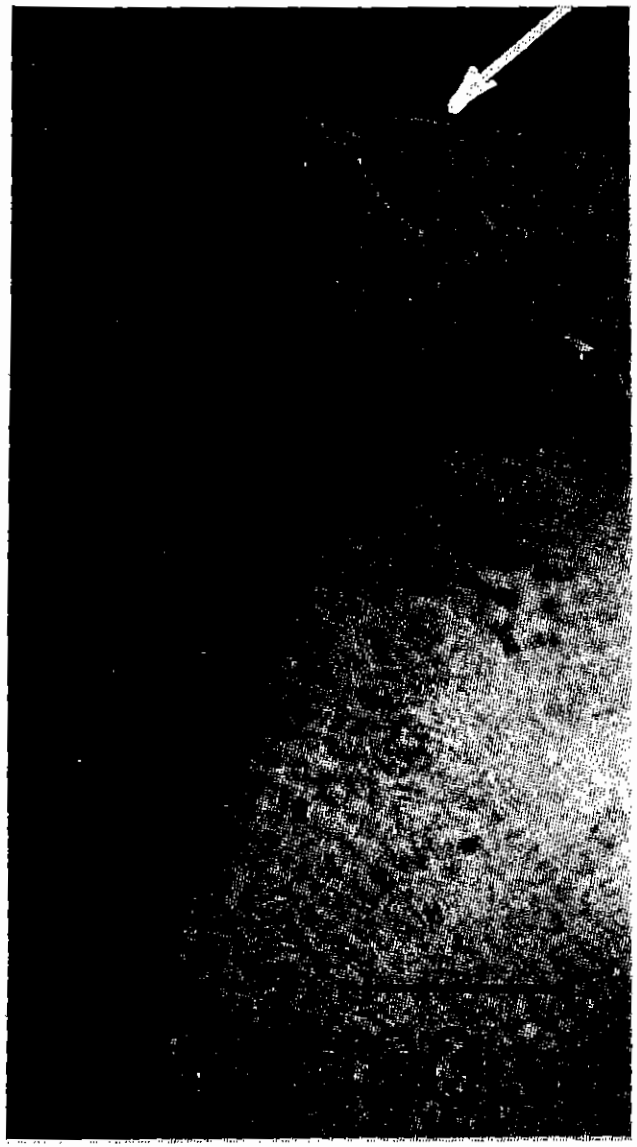

Figure 3.19 Shadowgrams taken on a tungsten target showing filaments along the laser beam. In addition jets normal to the target surface are observed.

the best focus of the main focusing lens. Since the main focusing lens was not corrected for spherical aberrations the laser energy was deposited in an annular ring structure on the target surface. Figure 3.20 shows an X-ray image recorded on a tungsten target. The laser beam was normally incident on the target which was displaced 600 μm from the best focus of the lens.

The incident irradiance was derived from the measured annular cross section of the X-ray image. The energy on target was 3.7 Joules in a cross section of 180 μm in diameter and 25 μm in thickness giving an average irradiance of 5.9×10^{13} W cm^{-2}. The ring in the X-ray image appears elliptical as the pinhole camera viewed the focal spot at 60°. As can be seen in Figure 3.20 and all the other images the ring is broken up into a number of tiny spots. The striking feature of the images is the regularity of the spacing between the spots around the ring. The images reveal a remarkable similarity to the observations made in a cell of CS_2 where an annular laser beam broke up periodically (3.20). As the irradiance increases the transverse scale length between the spots decreases. By dividing 2π by the spacing between the spots, the wave number is obtained and is plotted versus the irradiance in Figure 3.21. A curve can be drawn through the measurements and error bars are drawn on the points resulting from uncertainties of the measured cross sections. An analysis of the experimental observations is presently in progress.

O Willi (Oxford), P T Rumsby (RAL) and Z Q Lin (Shanghai)

3.6 Scaling of Ponderomotive and Thermal Self-Focusing

Experimentally observed self focusing in laser plasmas (3.5 ibid) originates from expulsion of plasma from a local region of high irradiance where the associated increase in refractive index n focuses the laser light and enhances the irradiance.

$$n = (1 - \rho/\rho_c)^{\frac{1}{2}} \qquad (1)$$

The mechanism for the expulsion of plasma can be either the ponderomotive

force or thermal pressure due to inverse Bremsstrahlung absorption and heating. A simple appreciation of the scaling behaviour of these pressures can be obtained from the well known non linear optics formulation of self-focusing in which the refractive index is

$$n = n_o + n_2 E^2 = n_o + \gamma I \qquad (2)$$

where E is the electric field strength and I the irradiance, and $\gamma/n_2 = 3.16 \times 10^{-3}$.

The spatial growth α of an irradiance perturbation of wavenumber k_p is then (3.21)

$$\alpha = k_p (n_2 E^2/n - k_p/4k^2)^{\frac{1}{2}} \text{ cm}^{-1} \qquad (3)$$

with the greatest growth when $k_p = k_m$ where,

$$k_m = \frac{2\pi}{\lambda} (2n_2 E^2/n)^{\frac{1}{2}} \text{ cm}^{-1} \qquad (4)$$

and k and λ are the laser wave number and wavelength respectively.

The growth exponent for the most unstable case $k_p = k_m$ is the well known 'B integral',

$$B = \frac{2\pi}{\lambda} \int_0^L \gamma I \, d\ell \qquad (5)$$

Alternatively the self-focusing of the whole beam of radius 'a' can be described by (3.22) a critical power

$$P_c = \frac{(1.22\ \lambda)\ c}{256\ n_2} \text{ esu}$$

and a self focusing length Z_f where

$$Z_f = \frac{a^2}{4} \left(\frac{c}{n_2}\right)^{\frac{1}{2}} (\sqrt{P} - \sqrt{P_c})^{-1} \text{ cm} \qquad (6)$$

The above results are applicable when the laser pulse duration is long

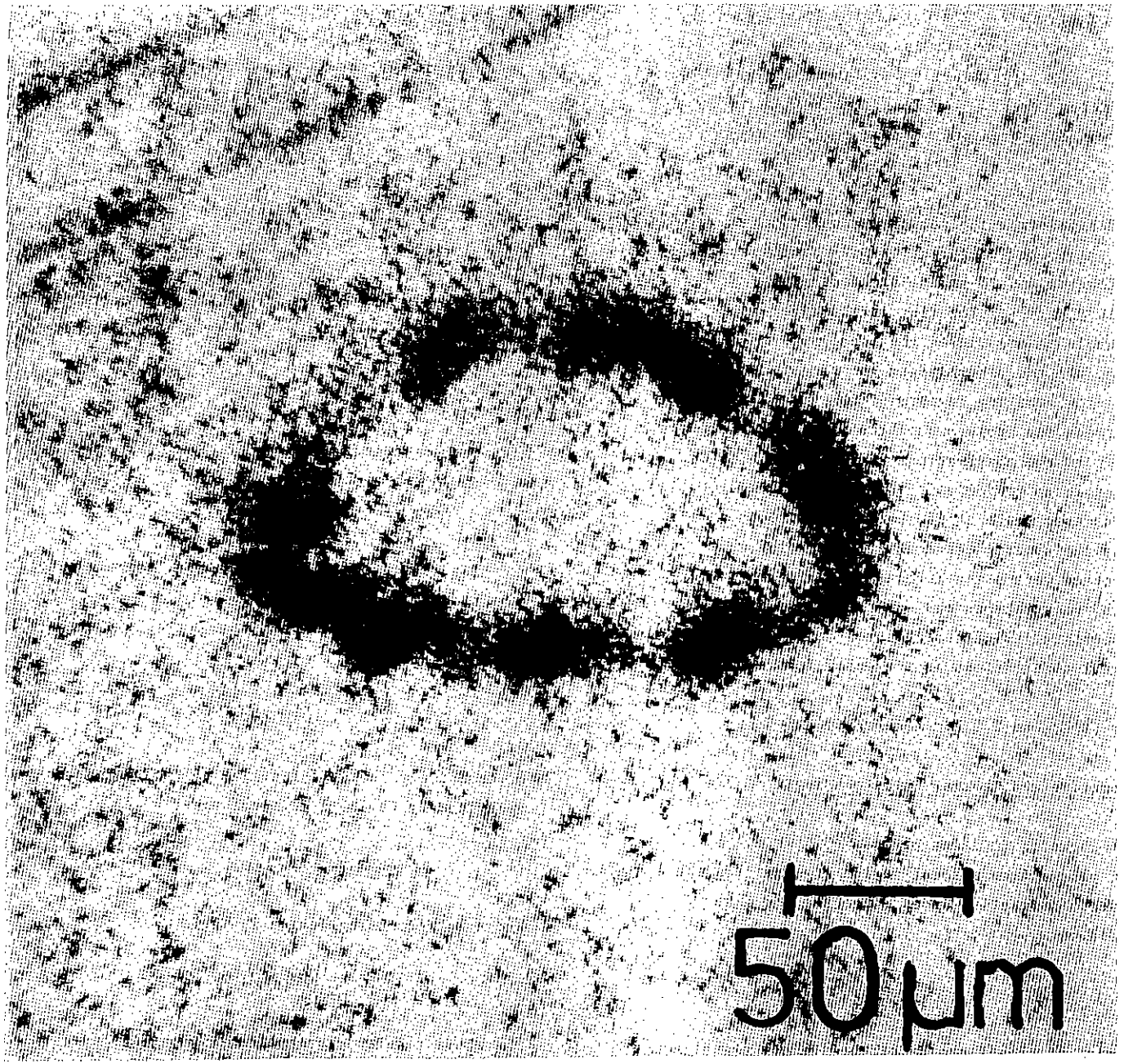

Figure 3.20 X-ray pinhole camera image in the 1 keV energy band showing that an annular ring is broken up periodically into a number of tiny spots

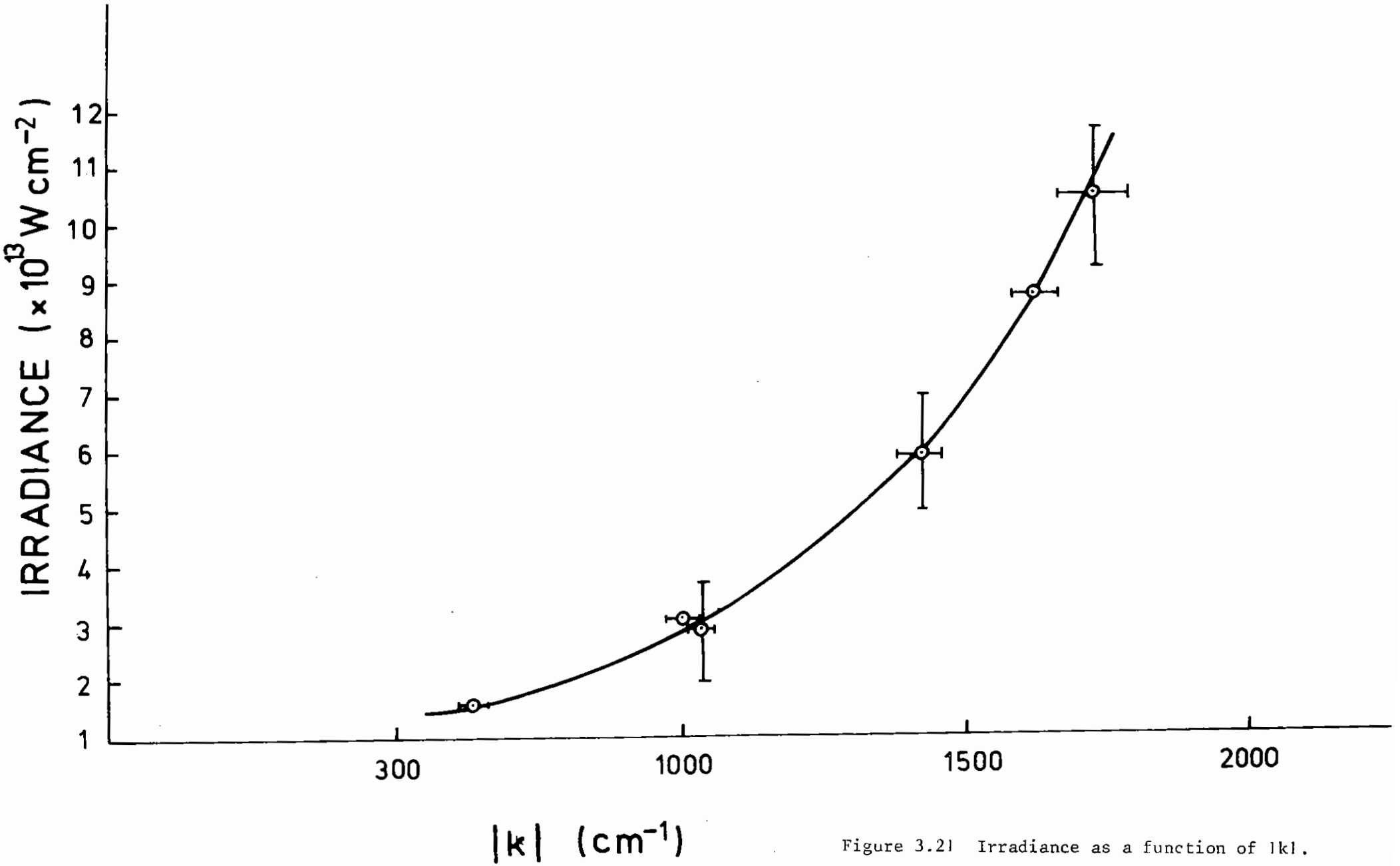

Figure 3.21 Irradiance as a function of |k|.

compared to the response time of the non linearity. This is generally true for the microscopic non linear polarizability of molecules. For the macroscopic expulsion of plasma from the beam it is true only if the pulse duration is much greater than the acoustic transit time $\tau_a = 2\pi/k_p v_a$, where

$$v_a = 2.2 \times 10^7 \ (kT)^{\frac{1}{2}}; \text{ with } kT \text{ in keV} \tag{7}$$

is the acoustic velocity. (For a distance of 20 μm and a temperature of 1 keV. $\tau_a \sim 90$ ps suggesting that the approximation will be valid in experimental cases of interest (3.5 ibid).

The effective n_2 due to the ponderomotive force can be estimated by equating the thermal pressure gradient to the ponderomotive force,

$$\nabla p_e = \frac{\nabla \langle E \rangle^2}{8\pi} \cdot \rho/\rho_c \tag{8}$$

whence

$$n_2 \simeq 2 \times 10^{13} \frac{\lambda^2}{kT} \cdot \rho/\rho_c; \text{ with } \lambda \text{ in } \mu m \tag{9}$$

The various self-focusing characteristics (eqs 3 to 6) can then be evaluated using n_2 from equation 9. For example a condition for instability due to self-focusing is a large growth exponent ($B \gtrsim 10$) for the fastest growing perturbation and this can be expressed from equations (9) and (5) as

$$I \gtrsim 2 \times 10^{15} \frac{kT}{L\lambda} \cdot \frac{\rho_c}{\rho} \text{ W cm}^{-2} \tag{10}$$

where L is the axial scale length of plasma density . This is in close agreement with the results of a more rigorous calculation (3.23).

A similar approach may be adopted with the thermal self-focusing mechanism, in which a local temperature rise is caused by a local irradiance peak which, after acoustic response to balance the pressure, gives a density decrease. The unperturbed situation is a plasma

temperature T heated by inverse Bremsstrahlung absorption with axial flow balancing the absorbed irradiance I_o.

The heating and cooling time constants τ_h and τ_c and the acoustic response time τ_a for a local hot spot of additional intensity I are the time scales of interest.

The additional rate of heating is

$$\frac{dT}{dt} = \left(\frac{I\beta}{\rho}\right)\left(\frac{4m_p}{3k_B}\right) \tag{11}$$

where β, the inverse Bremsstrahlung absorption coefficient, is approximately

$$\beta = 10^6 \ \rho^2 \ Z \ \lambda^2 \ (kT)^{-3/2} \left(1 - \frac{\rho}{\rho_c}\right)^{\frac{1}{2}} \tag{12}$$

giving a time constant for heating $\tau_h = \frac{1}{T}\frac{dT}{dt}$ which can be written as,

$$\tau_h = 2.2 \times 10^{-9} \ kT^{5/2} \ (I/10^{13} \text{ W cm}^{-2})^{-1} \ \frac{\rho_c}{\rho Z} \tag{13}$$

The time constant for cooling by thermal conduction for a perturbation of wavelength L_p can be estimated from

$$L_p = (4\varkappa \tau_c)^{\frac{1}{2}}$$

where L_p is the thermal conduction length in time τ_c for a plasma of thermal diffusivity ϰ. With the Spitzer thermal diffusivity the cooling time can be written as,

$$\tau_c = 1.4 \times 10^{-17} \ L_p^2 \ Z \ \ln\Lambda (kT)^{5/2} \ \rho/\rho_c; \text{ with } L_p \text{ in } \mu m \tag{14}$$

with L_p in μm.

The heating and cooling times for a typical case [Z = 6, ρ/ρ_c = 0.25, kT = 0.5 keV, $I = 5 \times 10^{13}$ W cm^{-2}, L_p = 10 μm] are $\tau_c \simeq 0.25$ ps, $\tau_h \simeq 50$ ps. The acoustic response time discussed

earlier is $\tau_a \simeq 63$ ps.

When $\tau_c \ll \tau_h$ equilibrium is reached in a time τ_c at which point the temperature rise is given by

$$\frac{\Delta T}{T} \simeq \tau_c/\tau_h \qquad (15)$$

(It is assumed that only lateral thermal conduction and local additional heating are relevant on this time scale. The response time for a change in the overall ablation process would be much longer, moreover the ablation flow need not be along the axis of the filament so the ablation response can be decoupled from the filamentation process.)

The maximum density change is that given by pressure balance on a time scale of the order of τ_a, viz,

$$-\frac{\Delta\rho}{\rho} = \frac{\Delta T}{T} = \frac{\tau_c}{\tau_h} \qquad (16)$$

The change in refractive index and hence n_2 can then be calculated with the result.

$$n_2 = 3.8 \times 10^{-20}\, L_p^{\,2}\, Z^2\, \ell n\Lambda\, (kT)^{-5}\, (\rho/\rho_c)^2 \qquad (17)$$

This result is valid only when $\tau_c \ll \tau_h$, moreover the fact that n_2 is a function of the spatial scale L_p of the perturbations makes equations 4 and 5 inapplicable. Nevertheless useful estimates of the relative importance of the thermal and ponderomotive mechanisms can be made.

For example the ratio ε of n_2 for the ponderomotive and thermal processes is

$$\varepsilon = 10^6 \left(\frac{\lambda}{L_p}\right)^2 (kT)^4 \left(\frac{\rho_c}{\rho}\right) Z^{-2} \qquad (17)$$

indicating increased importance for the thermal process at short wavelength λ, large scale length L_p, low temperature kT, high density ρ/ρ_c, and high Z, but dominance of the ponderomotive mechanism for

typical situations. (Eg, for $\lambda = 0.5\ \mu m$, $L_p = 10\ \mu m$, kT = 1keV, $\rho/\rho_c = 0.2$, Z = 10; $\varepsilon = 125$)

The self-focusing threshold equation 10 is a relevant constraint for compression experiments where (see Section 7.2.3) it is found that there are advantages in working at shorter laser wavelength provided the irradiance is scaled up to conserve thermal smoothing. (Eg, $I/10^{13}\ W\ cm^{-2} = 3(\lambda/1\ \mu m)^{-3\cdot8}$, equation 17 in Section 7.2.3.)

The ratio of the lower bound irradiance for smoothing to the upper bound for ponderomotive self-focusing is thus

$$I_{\text{self focus}}/I_{\text{smoothing}} = 66\ (kT)\lambda^{2\cdot8}\, L^{-1}\, \frac{\rho_c}{\rho}$$

indicating a growing problem for larger targets and shorter wavelengths. A rough estimate of the short wavelength limit arising in this way is obtained by assuming $L \simeq 0.3\ R$ where R is the target radius and L is assumed to be of the same order as the absorption to ablation front scale length used in deriving equation 17 as discussed in section 7.2.3. With kT = 1 keV and $\rho/\rho_c = 0.2$ it follows that the minimum value of λ is about 0.5 μm. The numerical value should not be taken too seriously but clearly the problem increases at reduced wavelengths.

M H Key (RAL)

3.7 Plasma Jet Formation

3.7.1 Introduction

Recent optical probe observations (3.18), (3.24), (3.25) have shown strong plasma jetting in the corona plasma of laser irradiated targets. Several experiments have been carried out during the last year to establish which generation mechanism may be responsible for the jet formation. Jets may be produced by higher mass ablation rates due to the hot spots in the laser beam which may be enhanced by self-focusing. Secondly superthermal electrons generated in the high intensity light filaments may produce

localised plasma jets. Imperfections or impurities on the target surface could give rise to non-uniformities. In addition, interaction of plasma clouds ablating from the stalk and pellet, for example, may generate jet-like structures. Finally, several instabilities such as hydrodynamic, heat-flow (Section 7.2.5), magnetothermal (3.26), radiative cooling (Section 3.8) or Weibel instabilities (3.27) may produce regions of high density in the plasma. Here the effects of initial beam non-uniformities and irregularities of the target surface on the jet-formation have been studied. Further the dependence on the atomic number of the target material, the time evolution and the dependence on the laser wavelength were investigated.

3.7.2 Experimental Arrangement

Experiments have been carried out at three different laser wavelengths (λ = 1.05 μm, 0.53 μm and 0.35 μm). The laser configuration, the laser beam characteristics and the arrangement of the diagnostics are described in Section 3.5.

3.7.3 Experimental Results

3.7.3(a) Effects of Beam Non-uniformities and Laser Beam Filamentation on the Jet Production

Figure 3.22(a) shows a shadowgram taken on a glass target recorded 1 nsec after the beginning of the laser pulse. A green laser beam was incident normally on the target with an average irradiance of 3.3×10^{13} W cm^{-2} in a focal spot of 250 μm in diameter. The image clearly shows pronounced jets stretching far into the underdense plasma corona with a transverse spatial scalelength of 7 - 18 μm. Figure 3.22(b) shows the laser beam profile recorded in the equivalent target plane. The separation of the hot spots in the laser beam is between 30 and 50 μm with a maximum peak to valley intensity ratio of 3:1. These intense laser spots may be further enhanced due to self-focusing in the plasma. A spotty structure of similar scalelength was observed in X-ray pinhole camera images in the 1.5 keV energy band as shown in Figure 3.22(c). It seems that the X-ray

spots originate from denser regions of the expanding plasma with similar temperature as the background plasma (deduced from a pair of pinholes with different transmission filters) and are caused by higher ablation rates in the more intense spots of the laser beam. Consequently, as there is a significant difference in scalelength between laser hot spots and plasma jets, and as jets are visible well outside the focal spot region, it may be concluded that the plasma jets seen in Figure 3.22(a) are not generated directly by the laser hot spots.

As described in Section 3.5 the laser beam may break up into tiny spots due to laser beam filamentation. Figure 3.23(a) shows an X-ray image recorded on a tungsten wire target which was irradiated with a normally incident 0.35 μm laser beam. The pinhole camera was situated perpendicular to the laser symmetry axis and the X-ray image clearly shows localised X-ray emitting regions. Figure 3.23(b) shows an optical shadowgram recorded transversely to the target normal at 1.05 ns after the beginning of the laser pulse. The irradiance on target was 8.8×10^{13} W cm^{-2}. As can be seen in Figure 3.23(b) the underdense plasma expands grossly non-uniformly with a similar pattern as observed in the X-ray image. However distinct jets with a different transverse scale length as the global structure are also observed indicating the presence of a small scale instability.

Part of the laser beam was obscured with a 2 cm bar across the centre of the focusing lens blocking the central part of the focal spot from direct illumination in order to investigate whether plasma jetting also occurs in the unirradiated region. Figure 3.24 shows two shadowgrams taken on the same shot at 0.9 ns and 1.4 ns after the beginning of the laser pulse. The inset shows the laser beam profile recorded in an equivalent target plane. The average irradiance was 5.7×10^{13} W cm^{-2} in a focal spot of 150 μm in diameter. As can be seen in Figure 3.24 jetting is visible over the whole focal spot region, ie also in the unirradiated part of the expanding plasma. It is however possible that some laser light may have reached this central unirradiated region due to refraction in the outer portions of the laser beam.

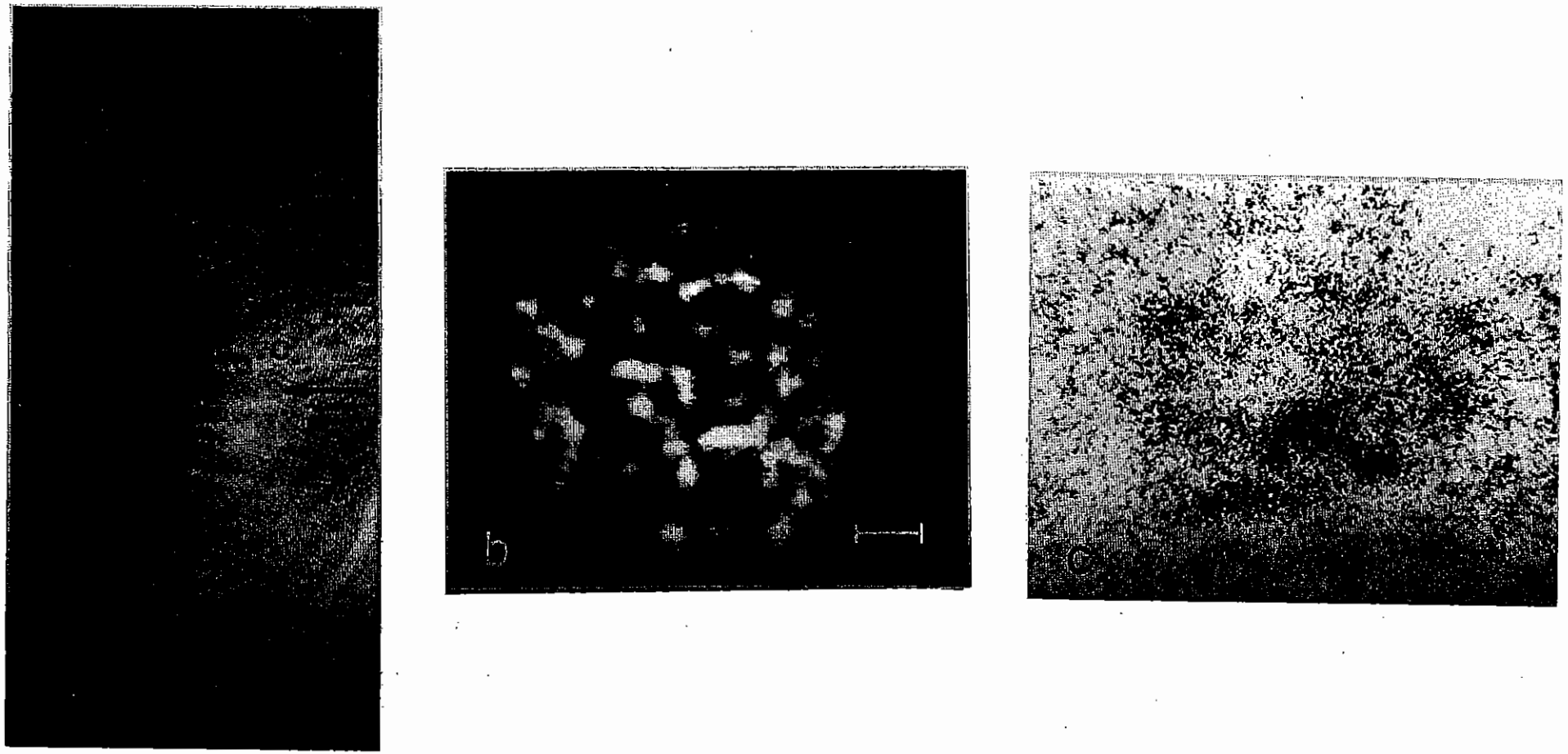

Figure 3.22 (a) A shadowgram recorded on a glass target 1 ns after the beginning of the laser pulse showing pronounced plasma jets.

(b) Laser beam profile taken in the equivalent target plane.

(c) X-ray pinhole camera image in the 1.5 keV energy band (12.5 μm diameter pinhole filtered with 40 μm of beryllium).

The scale on all the images is 50 μm.

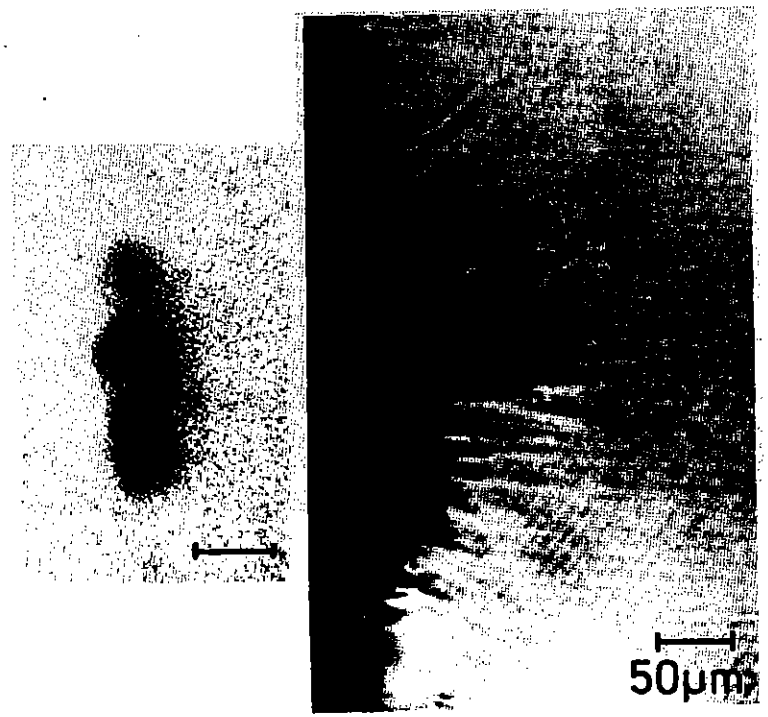

Figure 3.23 (a) X-ray pinhole camera image taken perpendicularly to the laser symmetry axis.

(b) A shadowgram recorded on a tungsten target at 1.05 ns which was irradiated with a UV laser beam.

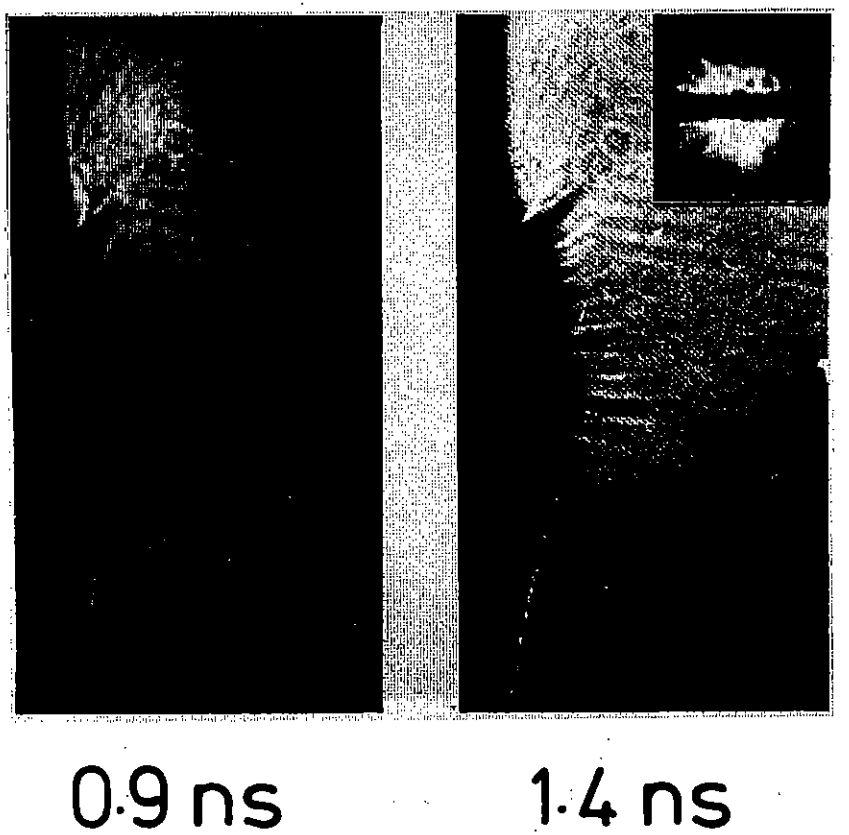

Figure 3.24 Two shadowgrams recorded on a tungsten target illuminated at an average irradiance of 5.7×10^{13} W cm^{-2}. The centre part of the laser beam was blocked with a 2 cm bar.

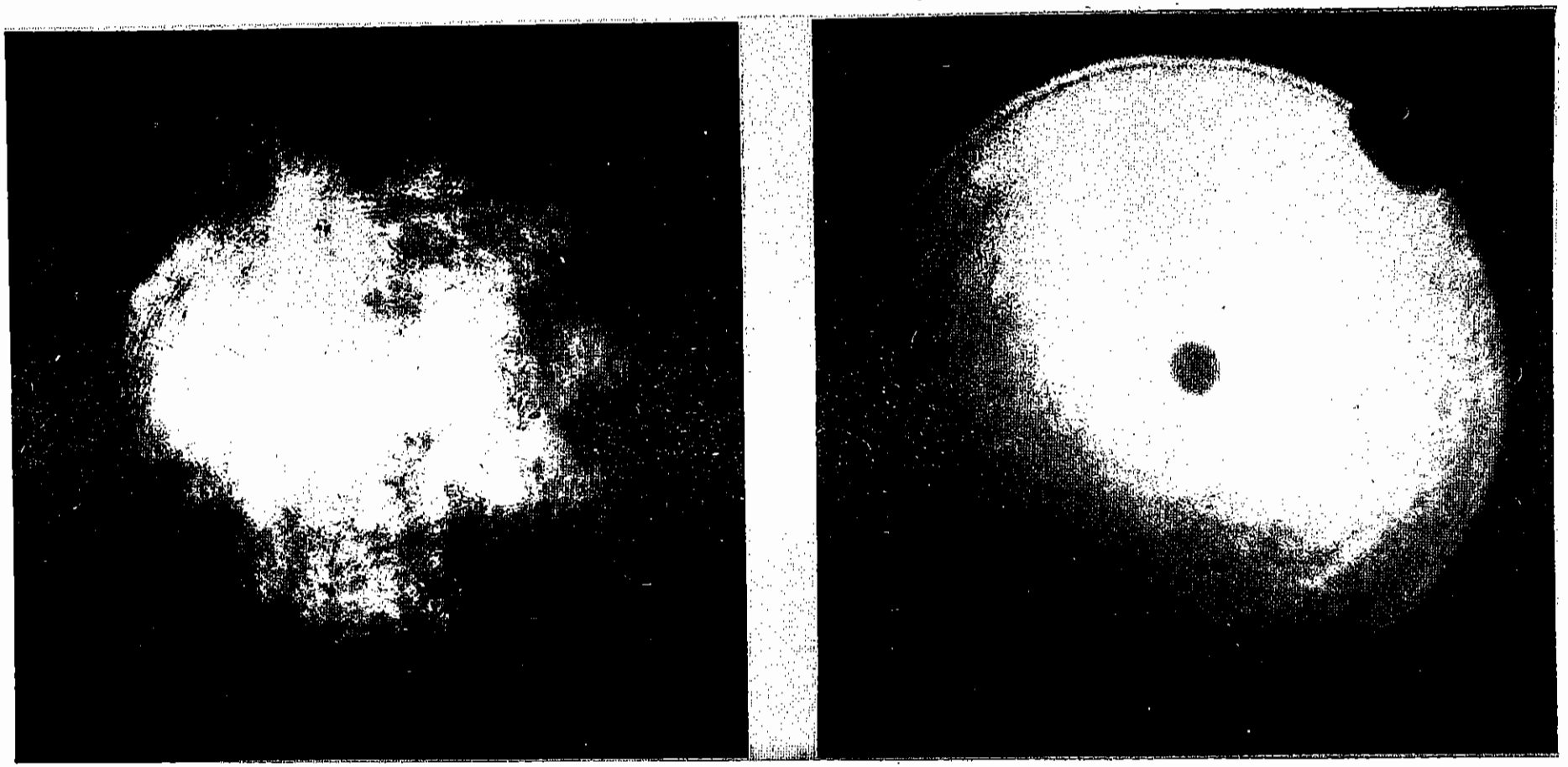

Figure 3.25 Profiles taken in the near field of an incident green laser beam and of a laser beam which was specularly scattered off a plastic target showing smoothing due to scattering.

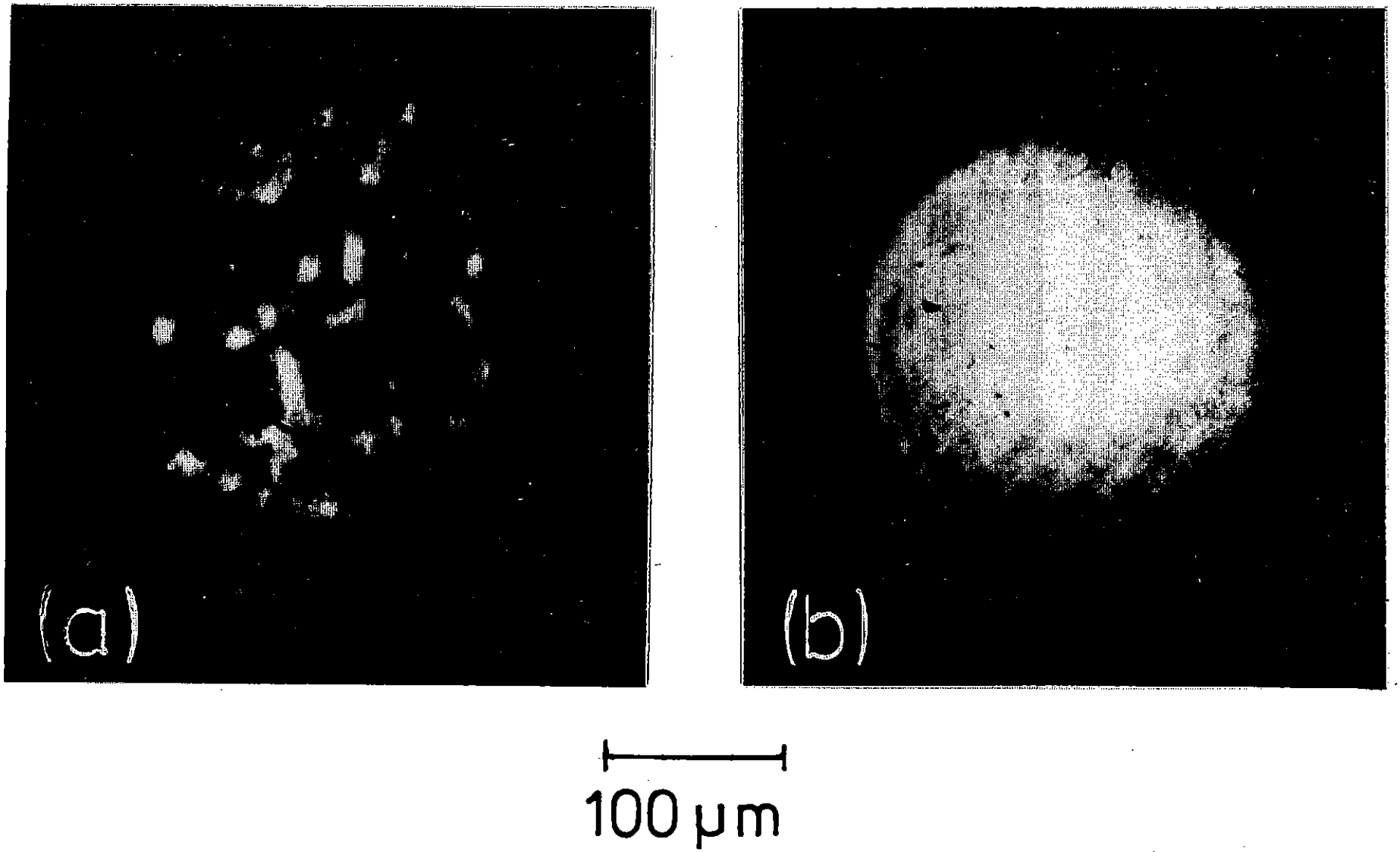

Figure 3.26 Profiles taken in an equivalent target plane of 300 µm in diameter of an incident laser beam (a) and specularly scattered off a plastic target, (b) .

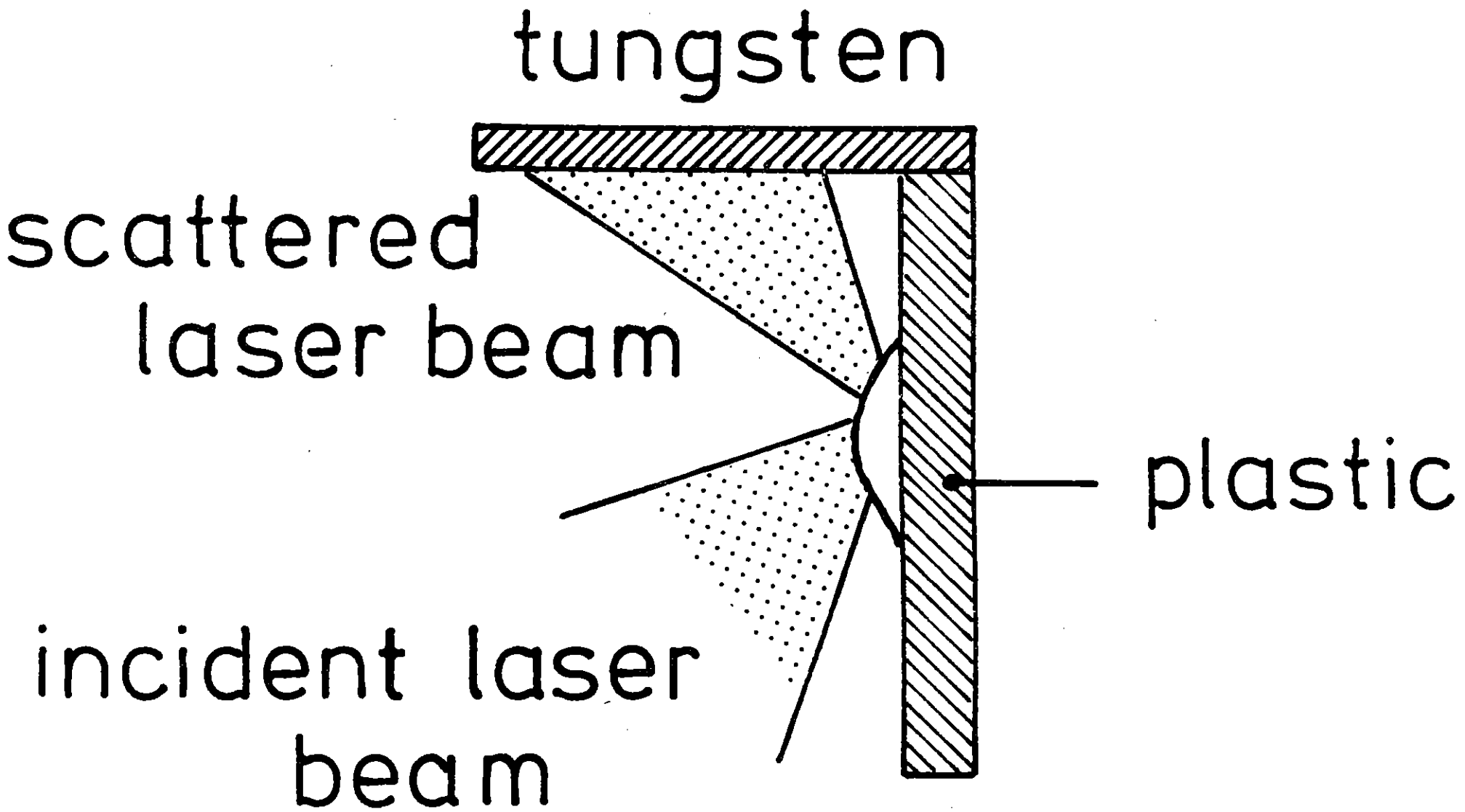

Figure 3.27 Geometry of the target arrangement to generate a more uniform laser beam. The incident beam was scattered specularly off a plastic target and used to illuminate a tungsten target.

In order to positively eliminate the possibility that non-uniformities in the laser beam were causing the plasma jets, tests were carried out to try to produce a spatially more uniform beam by specular reflection. A plastic target was irradiated at 45° to the target normal and it was found that the light scattered specularly off the plasma and collected with another f/1 lens at 90° to the main focusing lens and in the lens-target plane was much more uniform than the incident radiation. Figure 3.25(a) and 3.25(b) show the laser profiles of the incident and the scattered laser beams recorded in the near field and Figure 3.26(a) and 3.26(b) show the laser beam profiles taken in a plane corresponding to a target plane of 300 μm in diameter. 40% of the energy of the incident beam was collected by the f/1 lens. The specularly scattered beam was of considerably greater uniformity and was used to irradiate a tungsten target. Figure 3.27 shows the geometry of the target arrangement. Figure 3.28 shows a shadowgram of such a target recorded 0.7 ns after the beginning of the laser pulse. The irradiance on the tungsten foil was estimated to be 4×10^{12} W cm^{-2}. Plasma jetting from the tungsten surface similar to that shown in Figure 3.22(a) is observed with a scale length of 5 to 15 μm. Consequently the jetting phenomenon does not seem to be a function of the uniformity of laser radiation.

3.7.3(b) Imperfections on the Target Surface

Small imperfections on the target surface may initiate the growth of jets. Observations were therefore carried out on targets with stripes separated by 20 to 50 μm and 0.5 μm in depth. Figure 3.29 shows two shadowgrams recorded on an aluminium disc target. The target was coated with 250 nm of gold and was corrugated on the front surface with the stripes separated by 20 μm and 0.5 μm in depth and was irradiated with two green laser beams which were situated at 45° to the target normal and were perpendicular to each other. The average irradiance on target was 5×10^{13} W cm^{-2}. As can be seen in Figure 3.29(a) jets with a similar transverse scale length as the imposed perturbations are observed. However in the second image 0.75 ns after the beginning of the laser pulse where a relatively large plasma cloud has developed the spacing of the jets is about 10 μm, ie is independent of the separation of the perturbations.

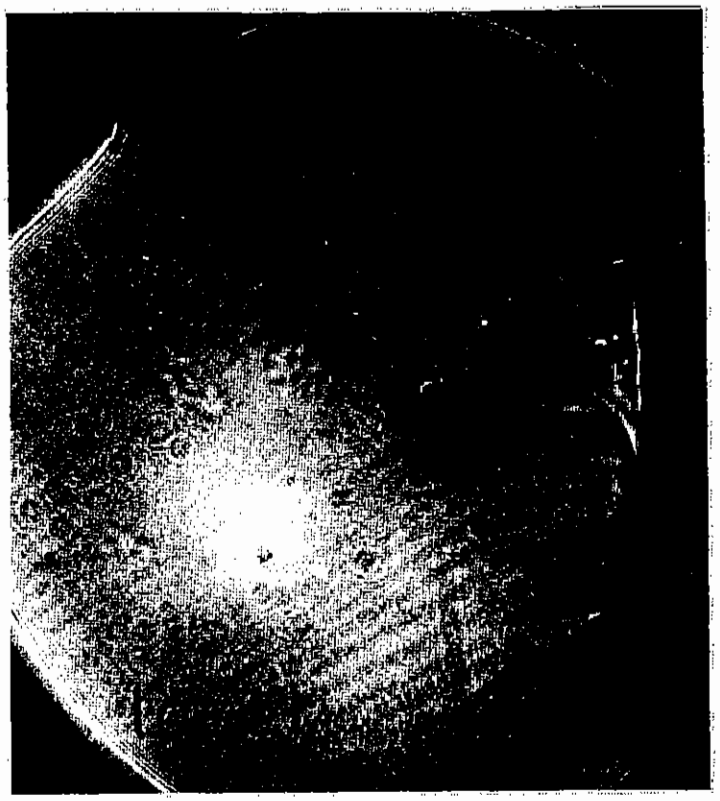

Figure 3.28 Shadowgram taken at 0.7 ns after the beginning of the laser pulse.

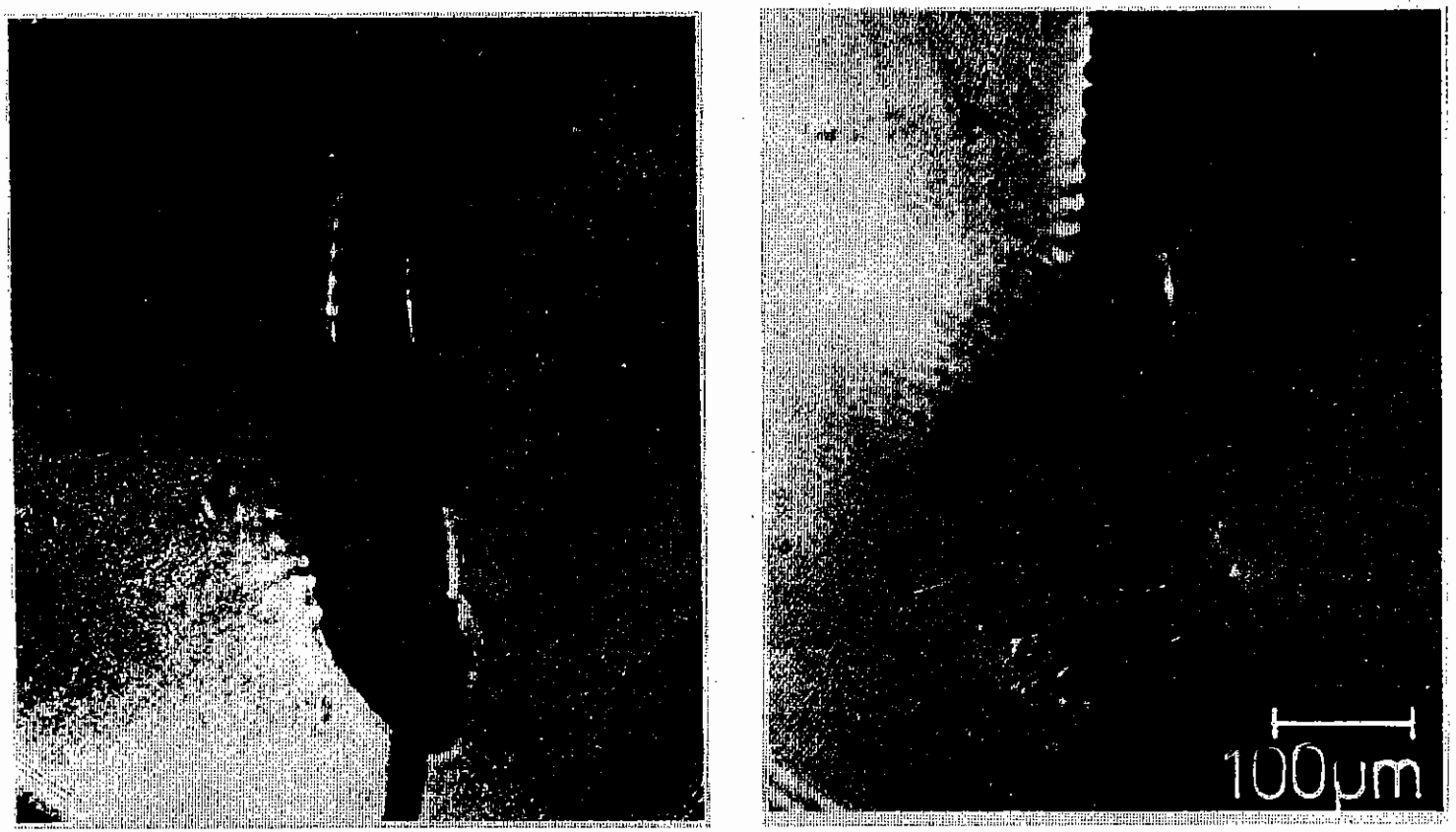

Figure 3.29 Shadowgrams taken on a corrugated disc target with stripes on the front surface separated by 20 μm and 0.5 μm in depth, taken 0.3 ns and 0.75 ns after the beginning of the laser pulse. The lateral scale length of the jets seen in the second image is smaller than that of the perturbations.

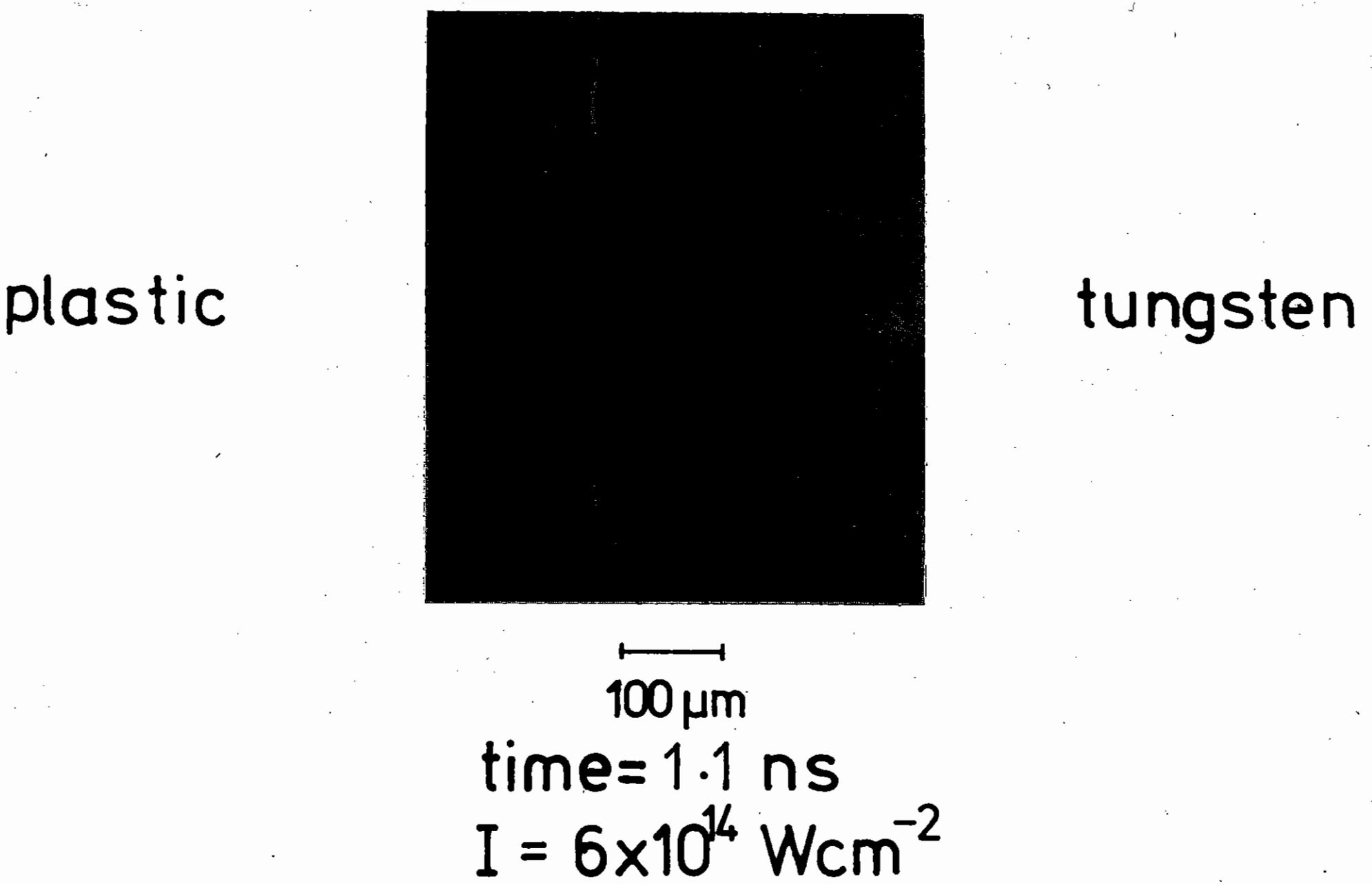

Figure 3.30 Shadowgram of a target consisting of plastic on one side and tungsten on the other irradiated with opposing laser beams. The average irradiance was 6 x 10^{14} W cm^{-2} on both sides. The probe timing was 1.1 ns after the beginning of the laser pulse.

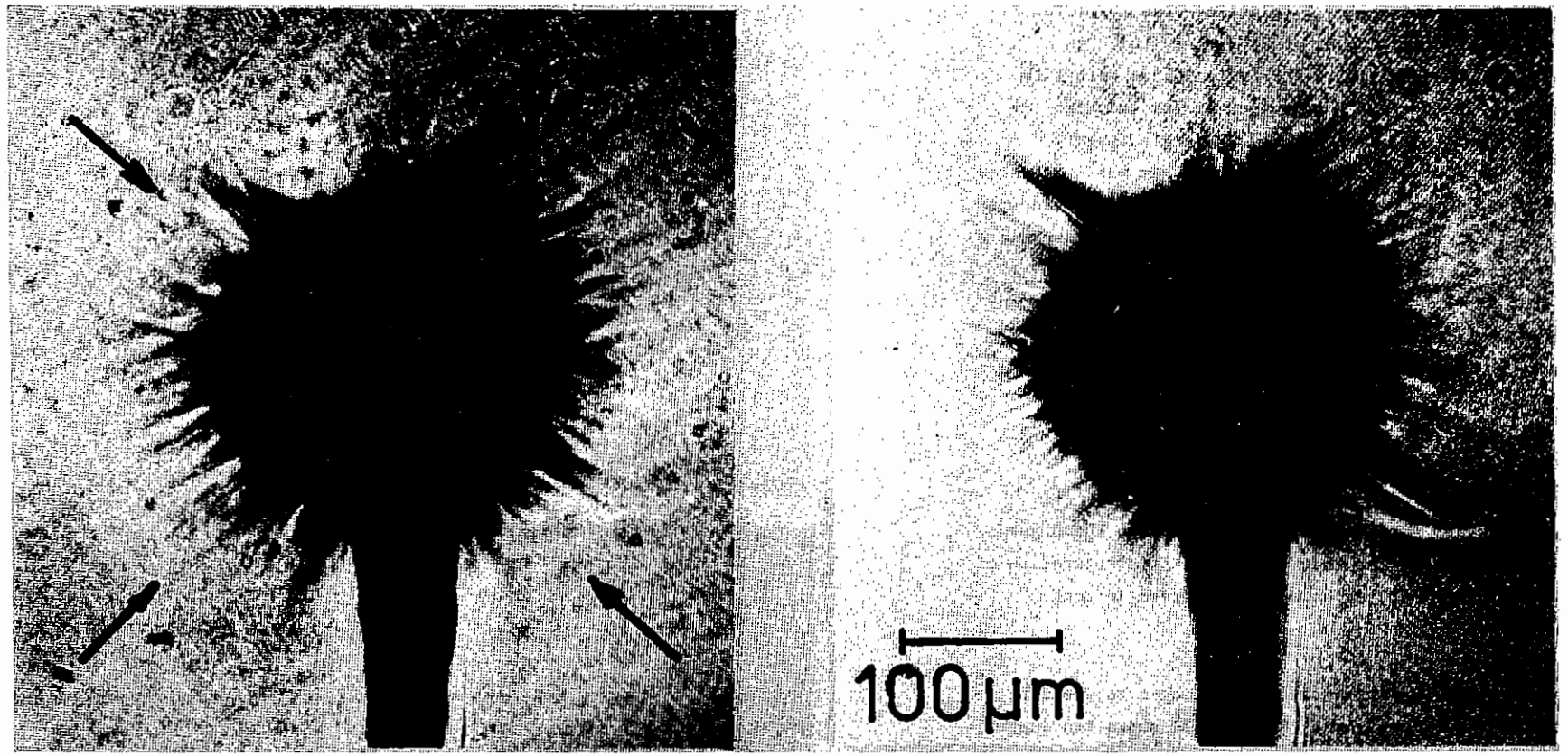

Figure 3.31 Shadowgrams of a gold coated microballoon showing the time evolution of the jets.

3.7.3(c) Atomic Number Dependence

The jetting is much less pronounced on low Z (plastic) than on medium Z (glass) and high atomic number (tungsten or gold) targets which is consistent with the observations made on targets illuminated with 1 μm laser light (3.24) (3.25). The different behaviour of low and high atomic number targets is illustrated in Figure 3.30 where a target consisting of plastic on one side and tungsten on the other was irradiated normally with opposing green laser beams. Both sides were irradiated with an energy of 5 Joules in focal spots of 50 μm diameter giving an average irradiance of 6×10^{14} W cm^{-2}. Figure 3.30 clearly shows pronounced jets on the tungsten side whereas no jet-like structure is observable on the plastic side. Jet-like structures are observed on medium and high atomic number targets in the investigated intensity range of 4×10^{12} to 6×10^{14} W cm^{-2}.

3.7.3(d) Time evolution

In order to investigate the time evolution of the jetting two shadowgrams separated in time were taken on all the shots. Up to a time separation of about 200 ps similar jet-like structures have been observed in both images.

However by increasing the time separation of the two images to greater than 0.5 ns the jetting is more pronounced. Figure 3.31 shows two images taken on a gold coated microballoon 155 μm in diameter and illuminated with four green laser beams which were situated normal to each other in a plane. The energy on target was 10.5 Joules giving an irradiance of 4.9×10^{13} W cm^{-2}. Figure 3.32 shows two shadowgrams taken on a tungsten wire target at 0.9 and 1.4 ns after the beginning of the laser pulse. The target was irradiated with two green laser beams with an energy of 16 Joules in a focal spot of 230 μm in diameter giving an irradiance of 9.3×10^{13} W cm^{-2}. As can be seen in Figure 3.32 the jetting is more distinct in the second image.

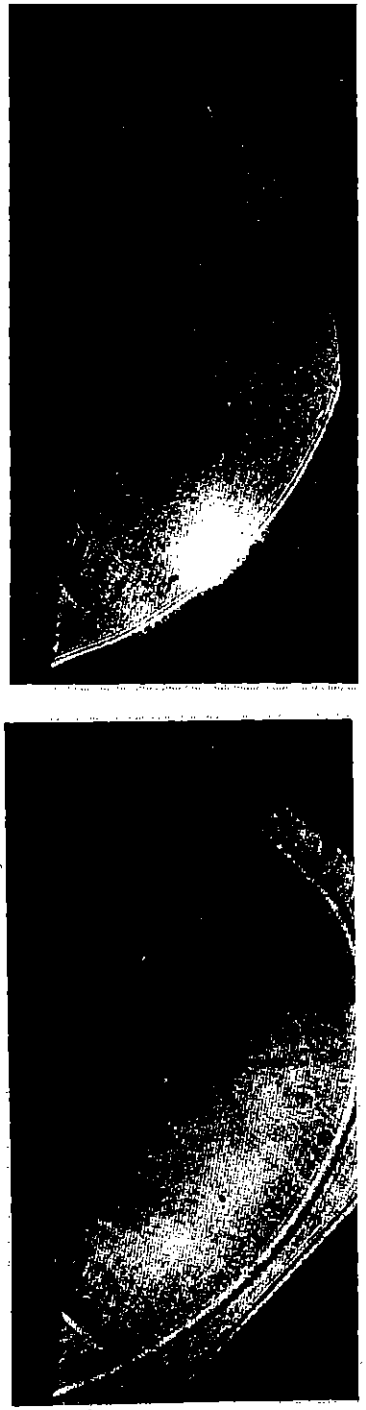

Figure 3.32 Shadowgrams taken on a tungsten wire target, recorded at 0.9ns and 1.4ns after the beginning of the pulse. The second image clearly shows that the jetting is more pronounced at later times.

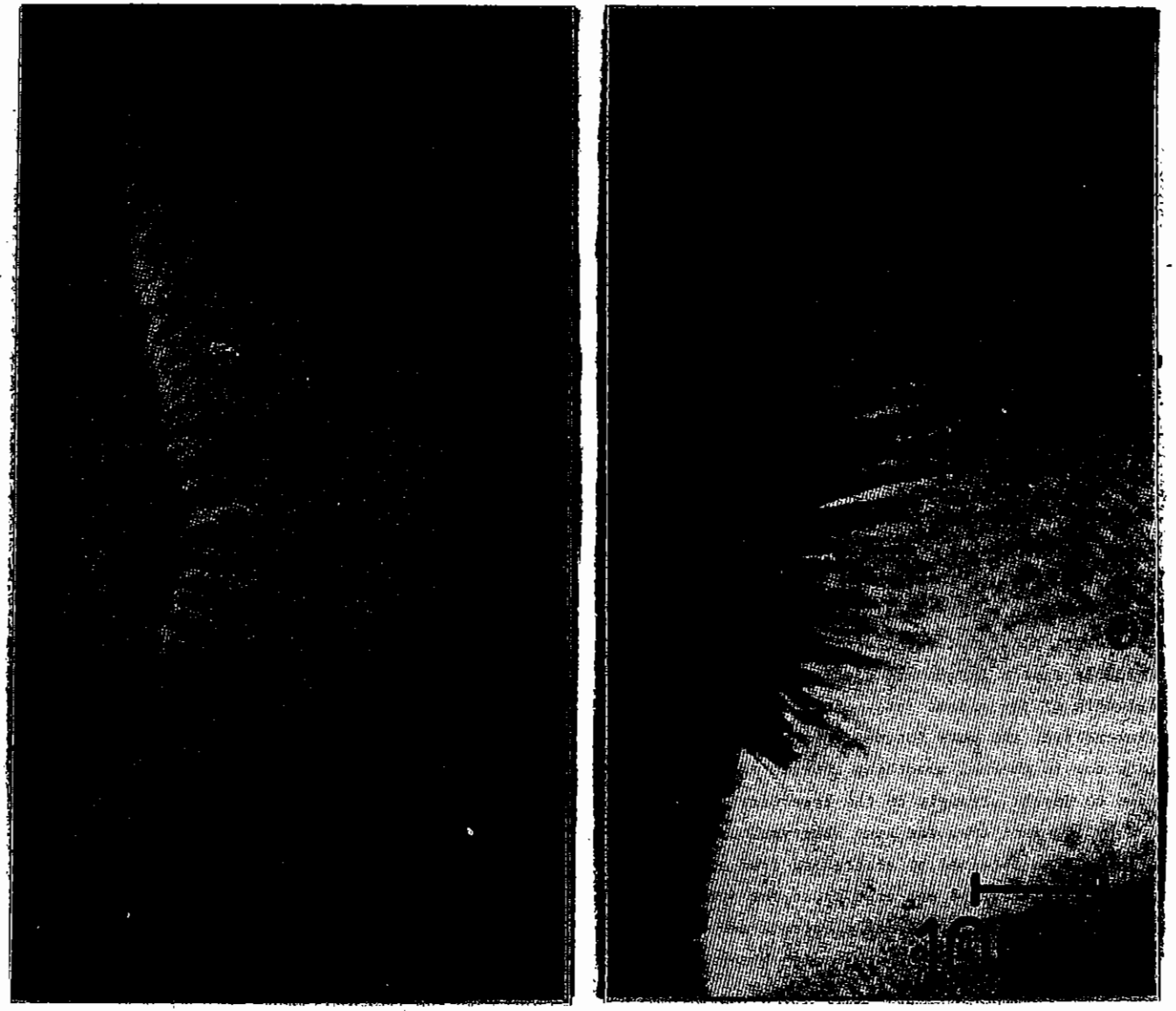

Figure 3.33 Shadowgrams taken on tungsten wire targets which were irradiated either with infra-red radiation or with UV laser light showing that the jet formation is more pronounced at shorter wavelengths.

3.7.3(e) Dependence on the Laser Wavelength

Observations made at several wavelengths (1.05, 0.53 and 0.35 μm) clearly showed that the jetting is more pronounced at shorter wavelengths.

Figure 3.33(a) shows a shadowgram taken on a tungsten wire which was irradiated with a normally incident infrared beam (λ = 1.05μm). The energy on target was 22 Joules in a focal spot of 200 μm in diameter giving an irradiance of 1.5×10^{14} W cm^{-2}. Figure 3.33(b) shows a shadowgram recorded again on a tungsten wire which was however irradiated with a UV laser beam (λ = 0.35 μm). The average irradiance was 2.5×10^{14} W cm^{-2}. As can be seen the jetting is much more pronounced in the second image, ie at shorter laser wavelengths.

3.7.4 Discussions

The plasma jets in the coronal plasma seen in optical shadowgraphy indicate in several ways that they are caused by small scale instabilities. Higher ablation rates caused by the hot spots of the laser beam can be excluded as a generation mechanism because the spatial scalelength of the hot spots recorded in the equivalent target plane and the transverse scalelength of the X-ray spots seen in pinhole camera images are distinctly different from the transverse scalelength of the plasma jets. In addition, it may be assumed that at high intensities the more intense regions are washed out at the ablation surface due to thermal smoothing whereas the jet-formation does not seem to depend strongly on the laser intensity. This is further underlined by the fact that the same observations are made even with a more uniform laser beam obtained by scattering from a plastic target. Hot electrons may equally be ruled out as a cause for jet formation since significant numbers of superthermal electrons are not expected to occur at intensities as low as 10^{13} W cm^{-2} with green irradiation ($I\lambda^2 = 2.5 \times 10^{12}$ W cm^{-2} μm^2).

In addition the observed jetting does not seem to be caused by imperfections on the target surface because similar observations were made on flat targets as well as on targets with stripes separated by 20 μm and

0.5 μm in depth.

Several theoretical models predict small scale instabilities which may produce plasma jets in the corona of laser heated targets. An electro-thermal instability, for example may grow in plasmas where a large heat flow is present (see Section 7.2.5). This instability can develop only above critical density, but the density perturbations may convect outwards into the underdense plasma. On the other hand a magneto-thermal instability has been predicted (3.26). This instability can only start to grow in the underdense plasma because the temperature and density gradients have to be in the same direction. In addition another instability due to radiation cooling has been proposed (Section 3.8). The conditions necessary for the growth of this instability are that the plasma be in a state where the local heating rate is a weak function of local density and temperature and is balanced by optically thin radiative losses. There are two regions where this instability can grow namely between the critical density surface and the ablation front and after the laser pulse in the underdense plasma.

Although the experimental observations clearly indicate that the jetting is caused by one or other of these instabilities, calculations of the maximum growth rates and spatial scalelengths for all three models using typical parameters for a laser produced plasma do not allow one to determine which instability is responsible for the occurrence of the jets. Radiation may however play a part in the jetting because of the strong dependence on the atomic number of the targets. In order to positively identify the responsible mechanism further experiments have to be carried out.

The jetting may be closely associated with the generation of magnetic fields and though self-generated magnetic fields were detected in earlier observations (3.24) (3.25) further studies have to be made.

Although on most of the shots X-ray pinhole camera images were taken no definite conclusion can be drawn that the jetting also exists in the ablation region because no spotty structure with a scalelength of about

10 μm was observed. The images were however time-integrated and consequently the spottiness may have been washed out.

O Willi (Oxford), P T Rumsby, W D Luckin, C Hooker, A Raven (RAL) and Z Q Lin (Shanghai)

3.8 Radiation Cooling Instabilities

Recent experiments (3.28) (3.24) have shown evidence for small scale density modulations in laser-heated plasmas from solid surfaces at irradiances of 10^{13} W cm^{-2} - 10^{14} W cm^{-2}. The features appear in X-ray emission and in optical shadowgraphy and Schlieren imaging and it has been inferred that the observed features represent local enhancements of density, with scalelengths typically 10 μm - 20 μm. Explanations of these features have been in terms of self-focusing and filamentation of the laser light producing local hot spots on the target surface and a magneto-thermal heat flow instability has been proposed by Haines (3.29).

There is another contributory process relying on an instability associated with optically thin radiative losses which has been applied to solar physics (3.30 and references therein) but does not appear to have been applied to laser-produced plasmas. The conditions necessary for this instability are that the plasma be in a state where the local heating rate is a weak function of local density and temperature and is balanced by optically thin radiative losses. A local enhancement of density then leads to an increase in the radiative losses. In the unstable regime this leads to a reduction in temperature, then to a reduction in pressure and finally to a further enhancement in density due to the action of the surrounding material.

In order to develop these ideas quantitatively we consider an equilibrium in which there is a source of energy S W kg^{-1} balanced by a radiative loss term R W kg^{-1}. S and R are assumed to vary with density and temperature as

$$S = S_o \, (\rho/\rho_o)^{\alpha_1} \, (T/T_o)^{\beta_1}$$

$$R = R_o \, (\rho/\rho_o)^{\alpha_2} \, (T/T_o)^{\beta_2}$$

where ρ_o and T_o are the equilibrium values, so that $S_o = R_o$. The system is assumed to vary only in the y direction leading to a heat flow

$$Q = - \kappa \frac{\partial T}{\partial Y}$$

where κ is the Spitzer thermal conductivity.

The energy, momentum and continuity equations are

$$\frac{\partial}{\partial t}\left(\frac{U}{\rho}\right) - \frac{p}{\rho^2} \frac{\partial \rho}{\partial t} = S - R + \frac{1}{\rho} \frac{\partial}{\partial y}\left(\kappa \frac{\partial T}{\partial y}\right)$$

$$\rho \frac{\partial v}{\partial t} = - \frac{\partial p}{\partial y}$$

$$\frac{\partial \rho}{\partial t} + \frac{\partial}{\partial y}(\rho v) = 0$$

The plasma is assumed to obey a perfect gas equation of state so that

$$U = \tfrac{3}{2}(Z+1)\, n_i \, k_B \, T$$

$$p = (Z+1)\, n_i \, k_B \, T$$

$$\rho = n_i \, m_i$$

where k_B is Boltzmann's constant, Z is the degree of ionisation and n_i is the number density of ions of mass m_i.

These equations are linearised and a solution is sought of the form

$$\left.\begin{matrix} \hat{\rho} \\ \hat{p} \\ \hat{v} \\ \hat{u} \end{matrix}\right\} \quad \alpha \quad \exp(iky + \gamma t)$$

where the caret denotes a perturbed quantity. The condition for a nontrivial solution to the set of linearised equations then leads to the dispersion relation $D(k, \gamma) = 0$, which is third-order in γ and fourth-order in k:

$$\gamma^3 \frac{U}{\rho} + \gamma^2 \left(\frac{k^2 \kappa T}{\rho} + (\beta_2 - \alpha_2) R_o\right) + \left(\gamma \frac{5}{2} \frac{k^2 p^2}{\rho^2}\right) + \ldots\ldots$$

$$+ \frac{k^4 k_B T}{\rho^2} + \left[(\beta_2 - \alpha_2) - (\beta_1 - \alpha_1)\right] R_o = 0$$

From this we can identify the three characteristic timescales of the system.

$\tau = \frac{U}{R_o \rho}$ the cooling time

$\tau_{th} = \left(\frac{k^2 k_o}{u}\right)^{T-1}$ the thermal conduction time

$\tau_s = \left(\frac{k^2 p}{\rho}\right)^{-1/2} = \frac{1}{k c_s}$ the sound transit time

The dispersion relation is then given conveniently in terms of these timescales.

$$\gamma^3 \tau_c + \gamma^2 \left(\frac{\tau_c}{\tau_{th}} + (\beta_2 - \alpha_2)\right) + \gamma\left(\frac{5}{3} \frac{\tau_c}{\tau_s^2}\right) + \frac{1}{\tau_s^2}\left(\frac{\tau_c}{\tau_{th}} + (\beta_2 - \alpha_2) - (\beta_1 - \alpha_1)\right) = 0$$

The behaviour of this equation is determined mainly by the constant $q = (\beta_2 - \alpha_2) - (\beta_1 - \alpha_1)$, since $\tau_c / \tau_{th} \to 0$ as $k \to 0$. If $q > 0$ there are no unstable modes, ie all the roots have negative real parts. If $q < 0$ there is a range of unstable modes for small k before thermal conduction damps out modes of large k. There is also a qualitative difference according to the sign of $(\beta_2 - \alpha_2)$. If $(\beta_2 - \alpha_2) < 0$ the instability remains with a finite growth rate down to $k = 0$ and the eigenmode in this limit is a pure cooling mode with no hydrodynamic motion, the growth rate being set by the cooling time τ_c. For $(\beta_2 - \alpha_2) > 0$ the growth rate becomes vanishingly small for small k and the corresponding eigenmode may be called a purely growing acoustic mode with growth rate proportional to kc_s. For the case $\alpha_1 = \alpha_2 = 0$, $\beta_1 = 1$, $\beta_2 = \frac{1}{2}$ (corresponding to free-free Bremsstrahlung) the full behaviour of the roots is shown in Figure 3.34. For all cases studied the convective modes are damped and are not considered further. In Figure 3.35 we show the behaviour of the real root for different values of β_2 in order to illustrate the point made earlier in this paragraph.

It is worth noting that the same dispersion relation may be obtained for a plasma with no heating source (ie $S_o = 0$, $\alpha_1 = \alpha_2 = 0$) if the

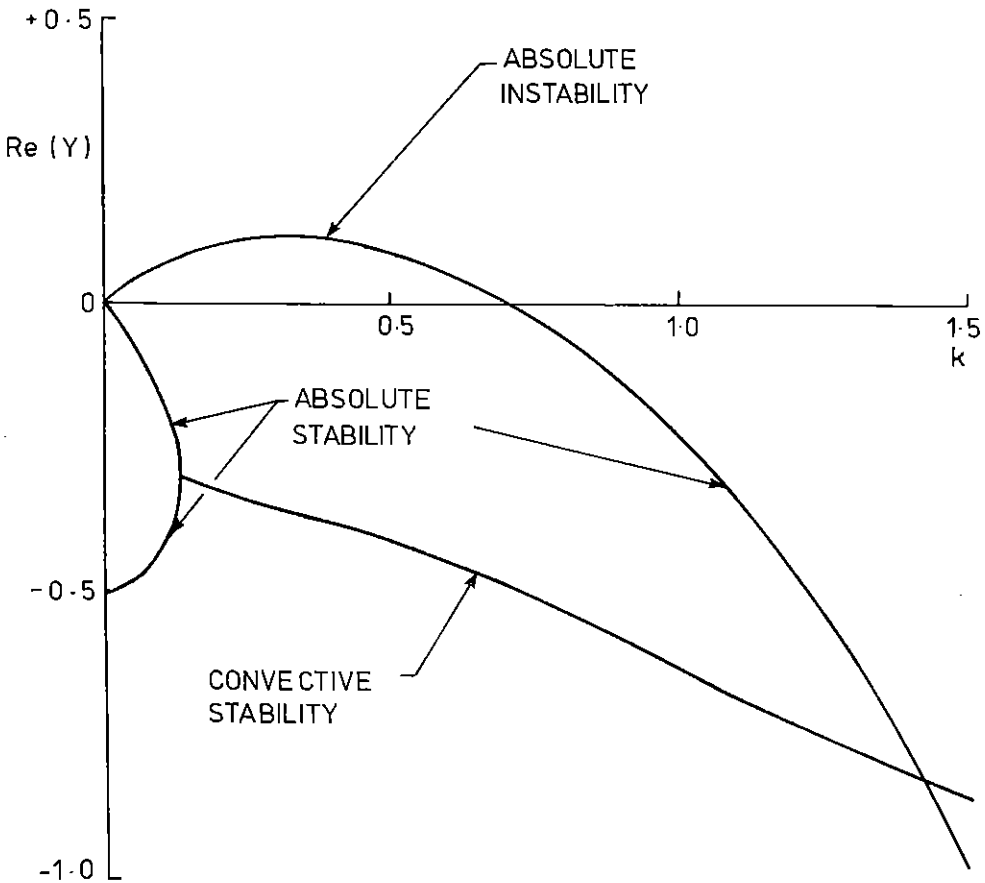

Figure 3.34 The behaviour of the roots of the dispersion relation for $\alpha_1 = \alpha_2 = 0$, $\beta_2 = 1$, $\beta_2 = \frac{1}{2}$

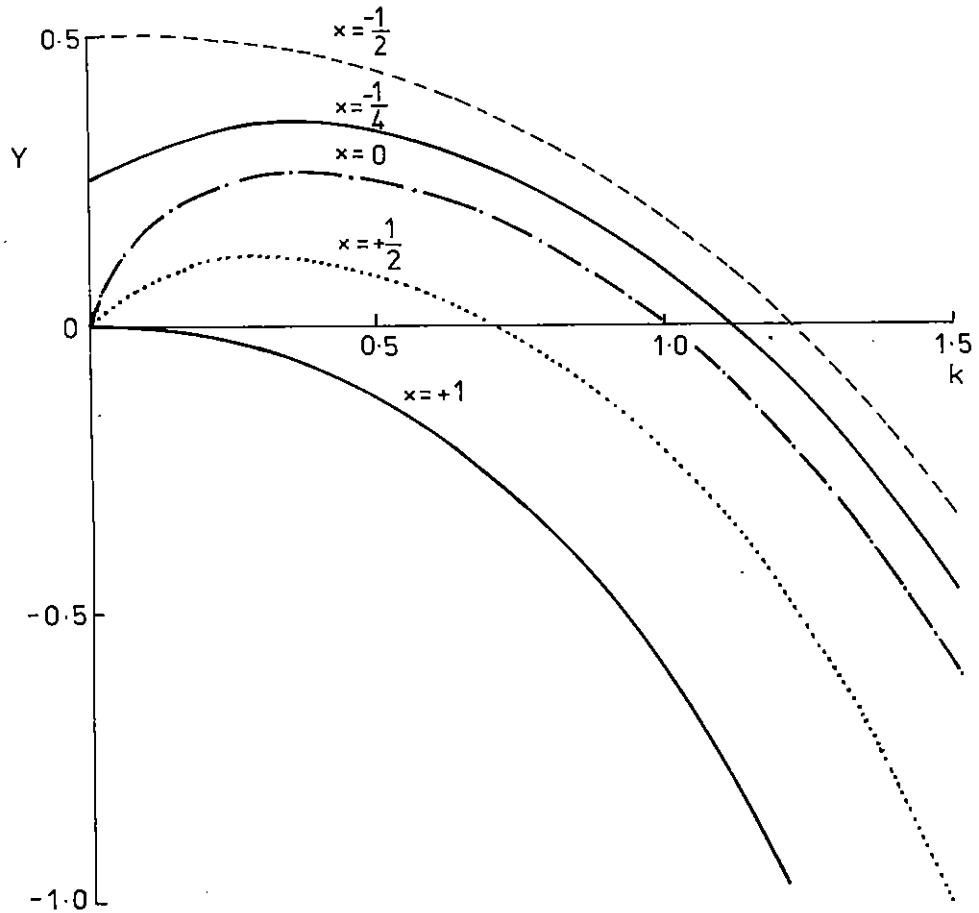

Figure 3.35 The real root of the dispersion relation for different values of $x = (\beta_2 - \alpha_2)$, with $(\beta_1 - \alpha_1) = 1$

perturbations are taken not from the equilibrium solution but from the constant density solution to $d/dt(U/\rho) = -R$. The instability then implies accelerated cooling of parts of the plasma.

A discussion of the conditions in laser heated plasmas which might allow this instability to grow is given in (3.31). Since the radiative losses are so much larger in high Z materials than in low Z materials it appears that even though the instability may exist in low Z (eg plastic) targets the growth rate is sufficiently small that little growth occurs on a period of 10^{-9} s. In materials such as Gold however the growth rate is typically 5×10^{10} s^{-1}, and the fastest growing mode has a wavelength of 5 - 10 μm.

It appears that this radiative cooling instability may explain the filament and jet-like structures recently observed in laser produced plasmas.

R G Evans (RAL)

CHAPTER 3 REFERENCES

3.01 C S Liu, M N Rosenbluth and R B White, Phys Fluid, 17, 1211 (1974)

3.02 Rutherford Laboratory Annual Report to the Laser Facility Committee, RL-80-026, Section 1.6.1 (1980)

3.03 S Sartang, PhD Thesis, Westfield College, University of London (1982)

3.04 W L Kruer et al, Phys Fluid, 23, 1232 (1980)

3.05 V L Ginzburg, "The propagation of electromagnetic waves in plasmas", publ Pergamon Press, Oxford, p27 (1970)

3.06 A I Avrov et al, Soviet Phys JETP, 45, 507 (1977)

3.07 P D Carter et al, Phys Rev Lett, 44, 1407 (1980)

3.08 E McGoldrick and S M L Sim, Opt Comm, 39, 172 (1981)

3.09 Rutherford Laboratory Annual Report to the Laser Facility Committee, RL-81-040, Chapter 1 (1981)

3.10 C S Liu and M N Rosenbluth, Phys Fluid, 19, 976 (1976)

3.11 Rutherford Laboratory Annual Report to the Laser Facility Committee, RL-81-040, Chapter 4 (1981)

3.12 Z Q Lin, O Willi and P T Rumsby, Rutherford Laboratory Report, RL-82-010 (1982)

3.13 C E Max, "The physics of laser fusion", Vol I, University of California Report, UCRL 53107 (1981)

3.14 Z Q Lin, Rutherford Laboratory Report, RL-82-012 (1982)

3.15 C E Max, Phys Fluid, 19, 74 (1976)

3.16 A I Avrov et al (Reference 3.06), also Rutherford Laboratory Annual Report to the Laser Facility Committee, RL-79-036, H C Barr, p8.12 (1979)

3.17 Z Q Lin, O Willi and P T Rumsby, J Phys D, 14, L35 (1981)

3.18 O Willi and P T Rumsby, Opt Comm, 37, 45 (1981) also O Willi, P T Rumsby and S Sartang, IEEE, Journal Quant Electronics, 17, 1909 (1981)

3.19 R S Craxton, Opt Comm, 34, 474 (1980)

3.20 A J Campillo, S L Shapiro and B R Suydam, Appl Phys Lett, 23, 628 (1973)

3.21 E S Bliss, D R Speck, J E Holtzrichter, J M Erkilla and A J Glass, Appl Phys Lett, 25, 448 (1974)

3.22 P L Kelley, Phys Rev Lett, 15, 1005 (1965)

3.23 C E Max, K G Estabrook, Comments on Plasma Phys Contr Fusion, 5, 237 (1980)

3.24 O Willi, P T Rumsby, Z Q Lin and S Sartang, Rutherford Laboratory Report, RL-81-015 (1981)

3.25 O Willi, P T Rumsby, C Hooker, A Raven and Z Q Lin, Opt Comm, 41, 110 (1982)

3.26 D A Tidman and R A Shanney, Phys Fluid, 17, 207 (1974)

3.27 E S Weibel, Phys Rev Lett, 2, 83 (1953) also A Ramani and G Laval, Phys Fluid, 21, 980 (1978)

3.28 M J Herbst, J A Stamper, R R Whitlock, R H Lehmberg and B H Ripin, Phys Rev Lett, 46, 328 (1981)

3.29 M G Haines, Inst Phys Conf on Laser Plasma Interactions and ICF, April 1981 (unpublished paper)

3.30 I S Shklovskii, "Physics of the Solar Corona", Pergamon Press, Oxford (1956)

3.31 R G Evans, J Phys D, 14, L173 (1981)

CHAPTER 4 TRANSPORT AND PARTICLE EMISSION STUDIES

INDEX

CHAPTER EDITOR: W T Toner

CHAPTER 4 TRANSPORT AND PARTICLE EMISSION STUDIES

4.1 Introduction

The experimental work of the group in the past year was devoted to two aspects of lateral transport, radial spreading associated with fast electrons and the smoothing of ablation pressure by lateral conduction. It is very pleasing that one of the experiments (Sec 4.2) was performed by a joint Imperial College -Garching group who took data with the same equipment at both RAL and Garching.

Experiments on plane targets continue to be attractive because of the experimental flexibility they allow despite the presence of edge effects which make interpretation difficult. A proper understanding of lateral transport is therefore necessary. The experiment described in section 4.2 is the first quantitative study at short wavelength of lateral spreading associated with hot electrons and shows that remote energy deposition can easily exceed local deposition, particularly for long pulses. Qualitative confirmation from ion data is discussed in Section 4.3.

At shorter wavelengths where there are few hot electrons thermal smoothing should be much reduced and some of the advantage to compression experiments to be gained from increased absorption at short wavelengths may be lost due to the greater difficulty of producing uniform compression. The first direct experimental comparison of thermal smoothing at two wavelengths is described in Section 4.3. The experimental data show the combined effect of thermal conduction and decompression to vary as $I\lambda^{1.5}$ in this experiment. Analysis suggests that thermal conduction smoothing alone should have a substantially greater wavelength dependence. A simple analytical model of thermal smoothing which takes transient effects into account is given in Section 4.5.

Very detailed model simulations of the spherical mass ablation rate experiment presented in last year's report have now been made and are discussed in Section 4.6. The most important result of this further analysis is the high value of the flux limit ($f \sim 0.1$) needed to fit the

data in contrast to the low values ($f \sim 0.03$) required by most previous experiments using plane geometry. This result is in agreement with recent theoretical work.

4.2 Preheat and Lateral Spreading

When an intense laser beam is incident on a solid target a fraction of its energy is absorbed in the dense plasma cloud which is produced during the interaction. At the high irradiance of interest to laser fusion the subsequent transport of energy away from the absorption region is complicated by the coupling of a major fraction of the absorbed energy into very fast, so-called suprathermal electrons. These high energy electrons are nearly collisionless in the plasma cloud which expands at velocities up to several 10^8 cm sec^{-1}. After reflection at the plasma cloud boundary, instead of entering the solid target under the small focal spot, they may deposit their energy many millimetres away, leading to a very high rate of lateral spreading of energy. The trajectories may be further complicated by intense electric and magnetic fields existing in the plasma. Investigation of such effects is of interest for laser fusion as they affect the uniformity of energy deposition in laser fusion targets. Furthermore they complicate the interpretation of model experiments, in particular those using planar targets, which might become two dimensional in nature in the presence of strong lateral spreading.

Recently sideways spreading of energy has been observed, albeit semi-qualitatively, for 10.6 μm irradiation (4.01)(4.02). In this paper we present the first quantitative experiments in which the amount and rate of sideways energy spreading in 1.05 μm and 1.3 μm irradiation experiments are measured. We show that the radially spread energy, or remote deposition, can exceed the energy deposition beneath the focal spot. The results were obtained in a collaboration between British and German groups using the Rutherford Laboratory Central Laser Facility (λ = 1.05 μm) and the Asterix III iodine laser (λ = 1.3 μm) at Garching.

The two laser facilities enabled single beam experiments to be performed over a wide range of illumination conditions as listed in Table 4.01.

TABLE 4.01 SUMMARY OF THE RADIAL TRANSPORT MEASUREMENTS

Laser parameters:					
Irradiance (10^{15} W cm^{-2})	18 ± 6	2.0 ± 0.5	2.6 ± 0.5	6.0 ± 2.0	1.5 ± 0.5
Wavelength (μm)	1.05	1.05	1.05	1.3	1.3
Pulse length (psec)	80	1300	80	300	300
Fractional absorption	.3	.3	.3	0.4	0.4
Local deposition E_L/E_{INC} (%)	7 ± 1	< 0.3	7 ± 1	1 ± 0.2	1 ± 0.2
Remote depositions E_R/E_{INC} (%)	10 ± 2	5 ± 1	1 ± 0.5	6 ± 1	6 ± 1
Spreading rates (10^8 cm sec^{-1})	20 ± 10	2.5 ± 1	20 ± 10	3.5 ± 1.5	–

Planar targets of various shapes and materials were used in all experiments at near normal incidence ($\theta \leq 10°$). The diagnostics used were high speed photography with a synchronised 10 ps dye laser pulse, multiple X-ray pinhole camera arrays, filtered for target K_α emission, an X-ray streak camera for time and space resolution of the K_α emission and a time integrating crystal spectrometer to measure the K_α emission from the focal area (4.03).

Two-dimensional, time-resolved information (though qualitative with respect to energy deposition) on lateral spreading of energy is obtained from high-speed photography. Figure 4.01 shows a shadowgram, taken 2.2 ns after the 300 ps laser pulse, of a 2 μm thick plastic foil ribbon (~ 0.5 mm wide) irradiated from the left. It is seen to explode over the whole field of view (~ 3 mm in diameter). The relatively small size of the focal region is indicated by the bright spot in the centre of the photograph produced by the second harmonic of the laser light generated in the plasma. The time delay before the foil starts to explode was determined in a separate experiment using a streak camera whose slit was displaced laterally a distance δ as shown in Figure 4.01. In this case the dye laser was operated in a long pulse mode. The streak photographs showed a sudden onset of foil expansion corresponding to a spreading velocity of 3.5×10^8 cm s^{-1} for $\delta \approx 2$ mm. Quantitative measurements of the fast electron energy deposition were made using X-ray pinhole cameras and calibrated film. Images of the X-ray emission from these experiments taken with large ($\gtrsim$ 200 μm diameter) pinholes are shown in Figure 4.02. In each case there is a shadow of the pinhole formed by emission from the intense focal spot and a spatially resolved image of emission remote (> 200 μm) from the focal spot. Pairs of pinholes were used with the filtering chosen such that the difference between the two images was due to emission in the region of the K_α line of the target material.

In Figure 4.02(a), for which a 1 mm wide V strip was irradiated at $5 \pm 2 \times 10^{15}$ W cm^{-2}, there is a clear difference in the images of the spread emission through these two filters. The filters were chosen such that V K_α emission produces a large difference in the brightness of the recorded images whereas a continuum of the form $I_o \exp(-h\nu/kT)$ only

produces a small difference. This difference is a factor of 1.5 for a typical fast electron continuum temperature of 10 keV. Plasma line emission such as V XXII $1s^2$ - 1s 2p is strongly attenuated by both filters. The spread emission in the top image is ~ 8 times brighter than the lower image and is attributable to V K_α emission. A continuum cannot produce such a large difference.

The K_α emission is due to electron K shell ionisation and not K shell photoionisation. In Figure 4.02(a) this is clear from the asymmetry; also sprectra show that the main plasma emission from the central spot is the V XXII $1s^2$ - 1s 2p transition which cannot cause K shell photoionisation. Thus Figure 4.02(a) shows that for a 300 ps pulse electrons are depositing energy some millimetres away from the focal spot with enhanced deposition at the edge of the target.

For Figure 4.02(b) to 4.02(e) the fainter images through the K_α attenuating filter (not included) showed that the spread emission was dominantly $K_{\tilde{\alpha}}$, as in Figure 4.02(a). Figure 4.02(b), from a shot on a V target approximately 1 cm square, also shows remote deposition, for an 80 ps pulse, with an asymmetric structure. The asymmetry was not reproducible, however the deposition was always greater at the edge of the spreading region, forming an irregular ring around the focal spot. The ring structure is more clear in Figure 4.02(c) for a 300 ps pulse on a large area target. For longer pulses, as in Figure 4.02(d), remote deposition, albeit not in a clear ring was also seen. Enhanced remote deposition at the target edge is clearly seen in Figure 4.02(e), the target for which was a 1 mm square of Cu supported on a thin fibre.

The spreading observed by the static pinhole camera shown in Figure 4.02 was time resolved using an X-ray streak camera. A streak record of K_α emission viewed at 10° to the target surface is shown in Figure 4.03 for a 1.3 nsec pulse. There is bright emission from the region of the focal spot at the bottom of the picture and clear evidence of sideways spreading away from the focal spot at a rate of $2.3 \pm 0.2 \times 10^8$ cm s^{-1}. Time resolution shows that the emission peaks at the edge of the region for a 1.3 ns pulse. Streak records of 80 ps experiments show a considerably

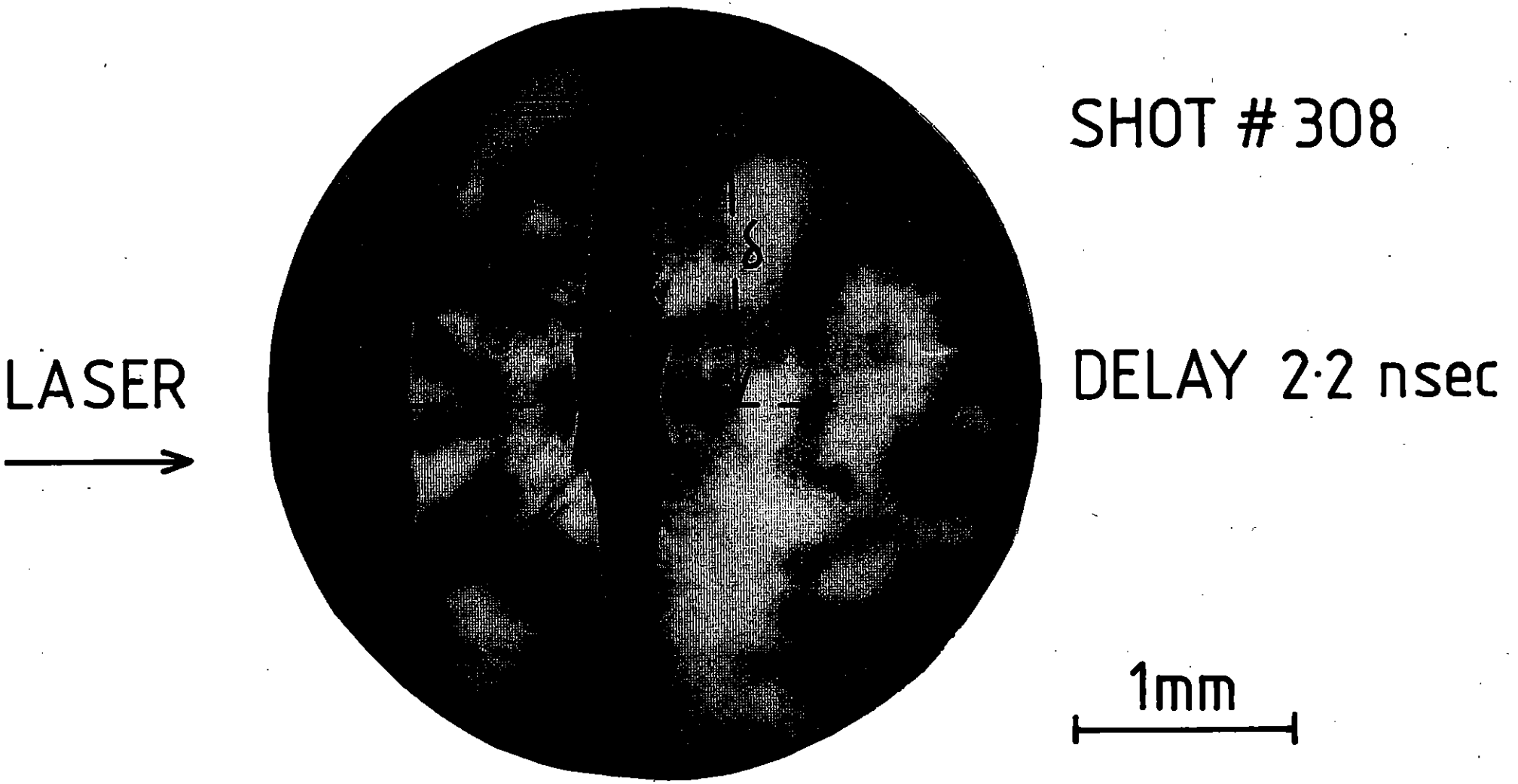

Figure 4.01 Optical shadowgram showing a 2μm thick, 500μm wide plastic foil strip 2.2 nsec after irradiation from the left by a 1.3μm laser pulse at an irradiance of 6×10^{15} W cm^{-2}. The rate of lateral energy spreading was obtained from streak photographs with the slit displaced a distance δ from the focus as shown.

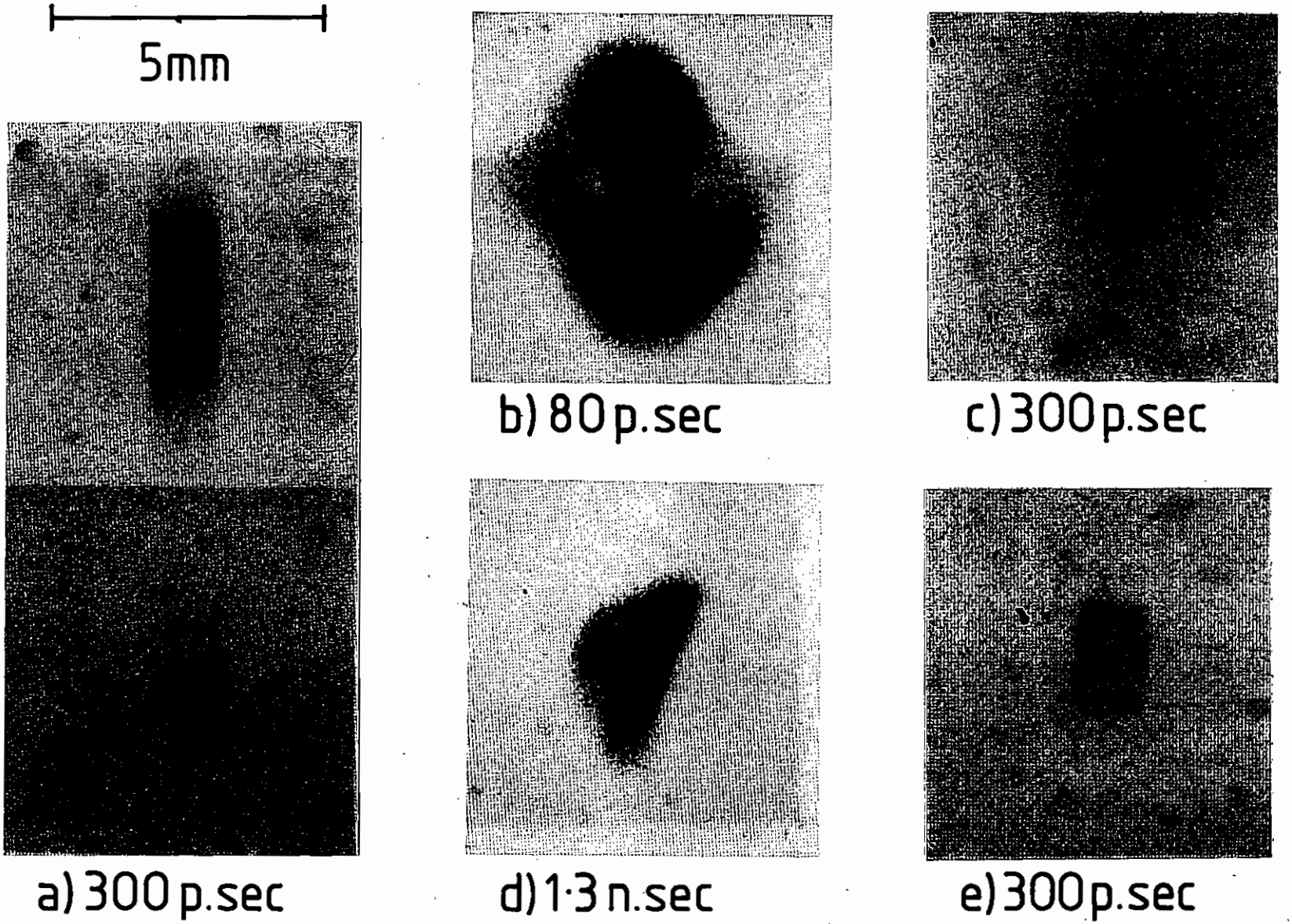

Figure 4.02 (a) A pair of X-ray pinhole camera images of a 1 mm wide V strip irradiated with a 1.3μm, 300 psec laser pulse focussed to 5 x 10^{15} W cm^{-2}. The upper and lower images were filtered by 12.5μm Ti and 25μm Sc respectively. Image (b) was for a 80 psec, 1.05μm laser pulse at 1.8 x 10^{16} W cm^{-2} onto V, filtered by 12.5μm Ti. Image (c) was for a 300 psec, 1.3μm laser pulse focussed to 6 x 10^{15} W cm^{2} onto Cu, and filtered by 11μm Cu. Image (d) was as (b) except that the pulse was 1.3 nsec long focussed to 2 x 10^{15} W cm^{-2}. For images (b), (c) and (d) the targets were large area. For (e) the target was a 1 mm square of Cu and conditions were as in (c). In all cases the targets were thick to fast electrons with an area density > 6 mgm cm^{-2}.

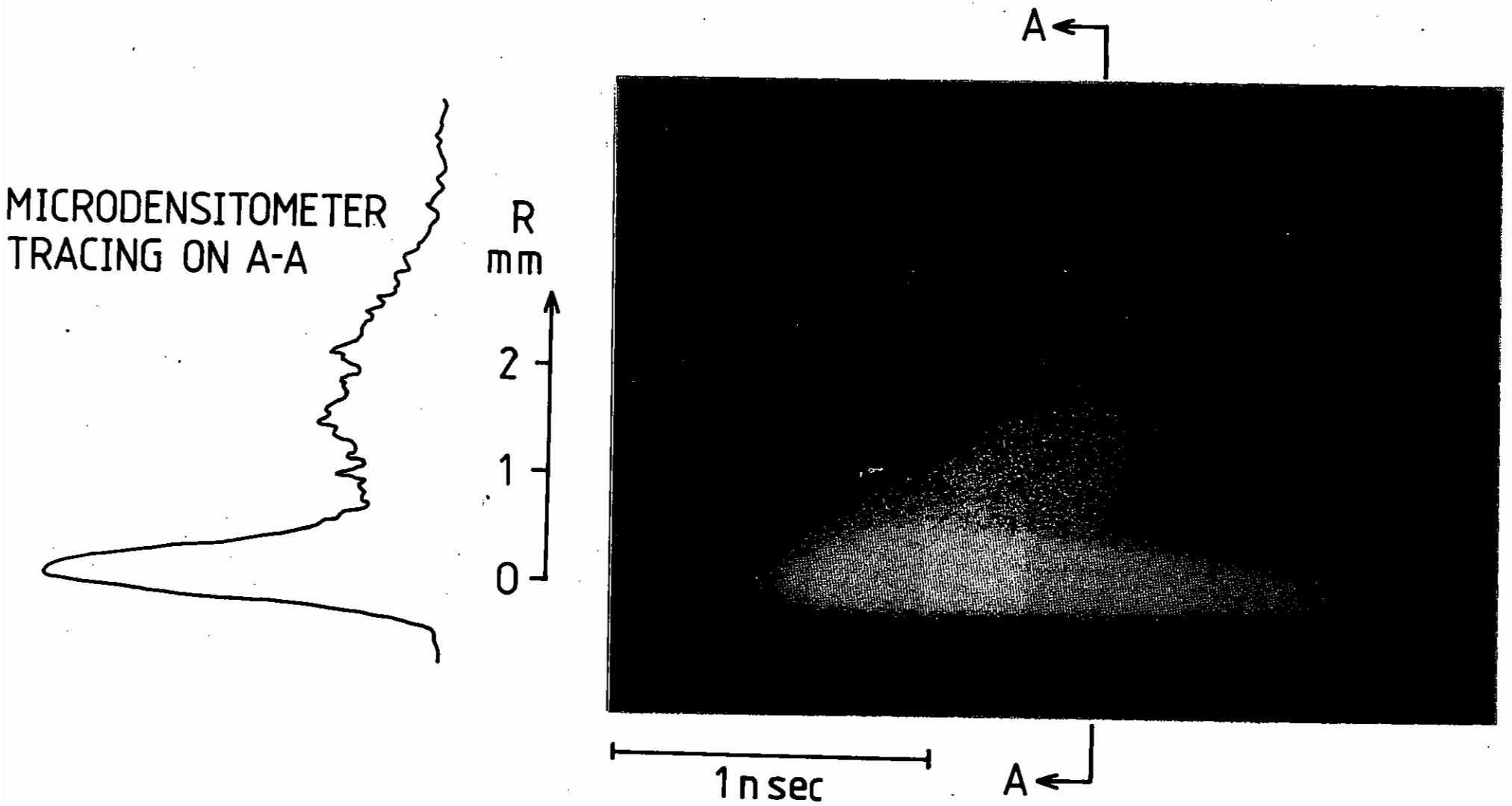

Figure 4.03 An X-ray streak record of the emission from a V target through a 12.5μm Ti K edge filter. The target, which was viewed obliquely, was irradiated at 2.6 x 10 W cm^{-2} with a 1.3 nsec, 1.05μm laser pulse. The bright emission at the bottom is the shadow of the 1 mm imaging slit, which was displaced such that only one side of the spread emission could be seen. The spot at the top left is an artefact.

higher spreading rate of $2.\cdot \pm 0.5 \times 10^9$ cm s^{-1}.

The time integrated measurements of K_α emission can be used to determine the total energy that fast electrons deposit into the target. Characteristic X-ray emission has the property that if E_o, the energy of the incident electron, is signficantly greater than the K ionisation threshold, E_{KI}, then the ratio of fast electron induced K_α emission to total energy deposited by fast electrons, $R(E_o)$, is almost constant (4.03). For a spectrum of fast electron energies (eg $f(E) = f_o \exp[-E/kT_h]$), $\bar{R}(T_h)$ can be computed. If $T_h \gg E_{KI}$ then $\bar{R}$ is insensitive to the exact form of the distribution function.

Experiments with various thicknesses of plastic coating over the fluor layer showed that 300 ps iodine laser pulses at 5×10^{15} W cm^{-2} the remote deposition is modelled by a distribution as above with $kT_h = 13 \pm 2$ keV. This observation completely rules out photoionisation as being a significant source of the emission since the drop in K_α yield with increasing plastic thickness is not consistent with the rather small attenuation by plastic of the greater than E_{KI} photon energies required to cause K-shell photoionisation. The total remote K_α yield was obtained from the X-ray pinhole images by integrating the exposure around the central pinhole shadow.

An alternative method was to use an edge to image, rather than a pinhole, such that the integration was automatically carried out to a large distance from the focal spot. The two techniques agreed with respect to the total K_α yield.

Values of the fractional remote energy deposition as shown in Table 4.01 are thus obtained. For the 80 ps and 1.3 ns experiments $\bar{R}$ was calculated using a value of T_h appropriate to the laser irradiance (4.04).

The local deposition was measured by an X-ray crystal spectrometer. For the 80 ps and 300 ps experiments the layered fluor target technique (4.03) was employed; for the 1.3 ns experiments there was a much lower local deposition so a single element target was used. The spectrum indicated a

bright source of K_α emission with fwhm $<$ 200 μm. This was attributed to local deposition beneath the focal spot. The fractional local depositions are shown in Table 4.01. The local energy deposition can be seen to drop with increasing pulse length.

In summary we have shown that lateral transport, which has previously been observed in 10.6 μm experiments, is energetically significant with shorter wavelengths, $\lambda \simeq 1$ μm. We find that up to 20% of the absorbed energy is deposited in an area several millimetres in diameter; a fraction which, for 300 ps and 1.3 ns pulses, exceeds that which enters the target under the focal spot. This remote energy deposition is over a depth in the target consistent with a fast electron distribution with $T_h \sim 10$ keV. The total fast electron energy deposition is broadly constant at $\sim$ 10% of the incident laser energy for all our experiments, however the balance between local and remote deposition depends on pulse length and, to a lesser extent, irradiance with longer pulses favouring remote deposition. It should be kept in mind that the numbers determined here represent a lower limit for lateral fast electron spreading as radiationless channels of energy dissipation (eg via fast ion generation) were not considered.

Estimates of space charge limitation show that the fast electron power flow ($\sim$ 10% of the incident laser power) must be through a neutralizing back-ground plasma rather than through the vacuum. The rapid formation of such a plasma cloud is in fact indicated by the emission of fast ions with velocities up to 7×10^8 cm s^{-1} as measured at $\lambda = 1.3$ μm in a preceding investigation (4.05).

There was irreproducible asymmetry in the remote deposition in all experiments, coupled with a tendency for deposition to be greater at the edge of the spreading region, leading to a ring-like structure. This could be explained by the presence of a large toroidal magnetic field channelling electrons to the edge of the plasma cloud.

The spreading observed with 80 ps pulses is inconsistent with the expansion of the fast ion cloud since the implied spreading rate (2×10^9 cm s^{-1}) is too great. It is probable that in the 80 ps

experiments a plasma layer is formed on the target surface by X-rays, a few very energetic fast electrons, laser light in the periphery of the focal spot or surface breakdown due to intense electric fields (4.06). The asymmetries and ring structure, further complicated by the enhanced deposition at the target edge (Figure 4.02(e)) make a quantitative model for our observations impossible at this stage.

4.3 Radial Transport

Much interest has recently been shown in the phenomenon of radial (lateral) transport - ie the transport of energy from within the focal spot to regions not directly heated by the laser beam. For example, the mass ablation rate measurements of Goldsack et al (4.07) made with plane targets could be made self-consistent only if it was assumed that a significant fraction (~10%) of the incident laser energy was deposited in an area much greater in size than the focal spot revealed by X-ray pinhole cameras filtered to about 1 keV, and that mass was ablated from that area.

In the experiment described in the previous section it was shown that with plane targets electrons travelling away from the focal spot generate K_α radiation up to 3 mm from the focal spot and that they carry about 10% of the incident energy.

In this section we report on a short experiment which was performed to verify the assumption that this remotely deposited energy causes ablation from an area much greater in size than the optical focal spot.

4.3.1 The Experimental Arrangement

The targets were either plane or cylindrical and consisted of a substrate onto which was deposited a spot of a material with a significantly different atomic weight (eg, plastic on gold, or vice versa) so that the emissions from the substrate could be differentiated from those from the deposited spot.

The laser pulse (1.3 ns FWHM, 50 J on target, λ = 1.05 μm) was tightly focused onto the centre of the spot. The ion emissions obtained with different sizes of spot were recorded with Faraday cups and a Thomson parabola ion analyser.

Several different combinations of substrate and spot materials were tried but it was found that gold spots on plastic (mylar) substrates gave the best Thomson parabola data. With such targets the very different relative atomic masses of the two materials rendered species differentiation straightforward. A typical set of parabolae is shown, enlarged ten-fold, in Figure 4.04. The data in this figure were obtained from a 500 μm diameter gold spot on mylar. The salient features to be noted are:

(i) This bright spot marks the origin of the parabolae. It is due to X-rays from the target.

(ii) The proton tracks lie on a well-defined parabola, the intensity of which decreases abruptly at the low-velocity end (farthest from the origin); this termination marks the edge of the sensitive area of the detector.

(iii) The tracks of gold ions occupy a broad band within which individual parabolae are not resolved. The maximum charge-state observed is Z ~ 50, whilst the minimum seen is about Z ~ 10. The maximum gold-ion velocity recorded is about 10^8 cm s^{-1}, whilst the minimum velocity seen is about 4×10^7 cm s^{-1}, although space-charge effects render determination of this velocity difficult.

(iv) Three distinct parabolae can be seen. These can be identified as being of Carbon 5+, Carbon 4+ and Carbon 3+.

It is the presence of these carbon parabolae which suggests that significant amounts of energy are lost from the focal spot. In the next section we shall show that most of the carbon emission came from around the focal spot and that a signficant amount of energy was transported a distance of as much as 3 mm from the focal spot.

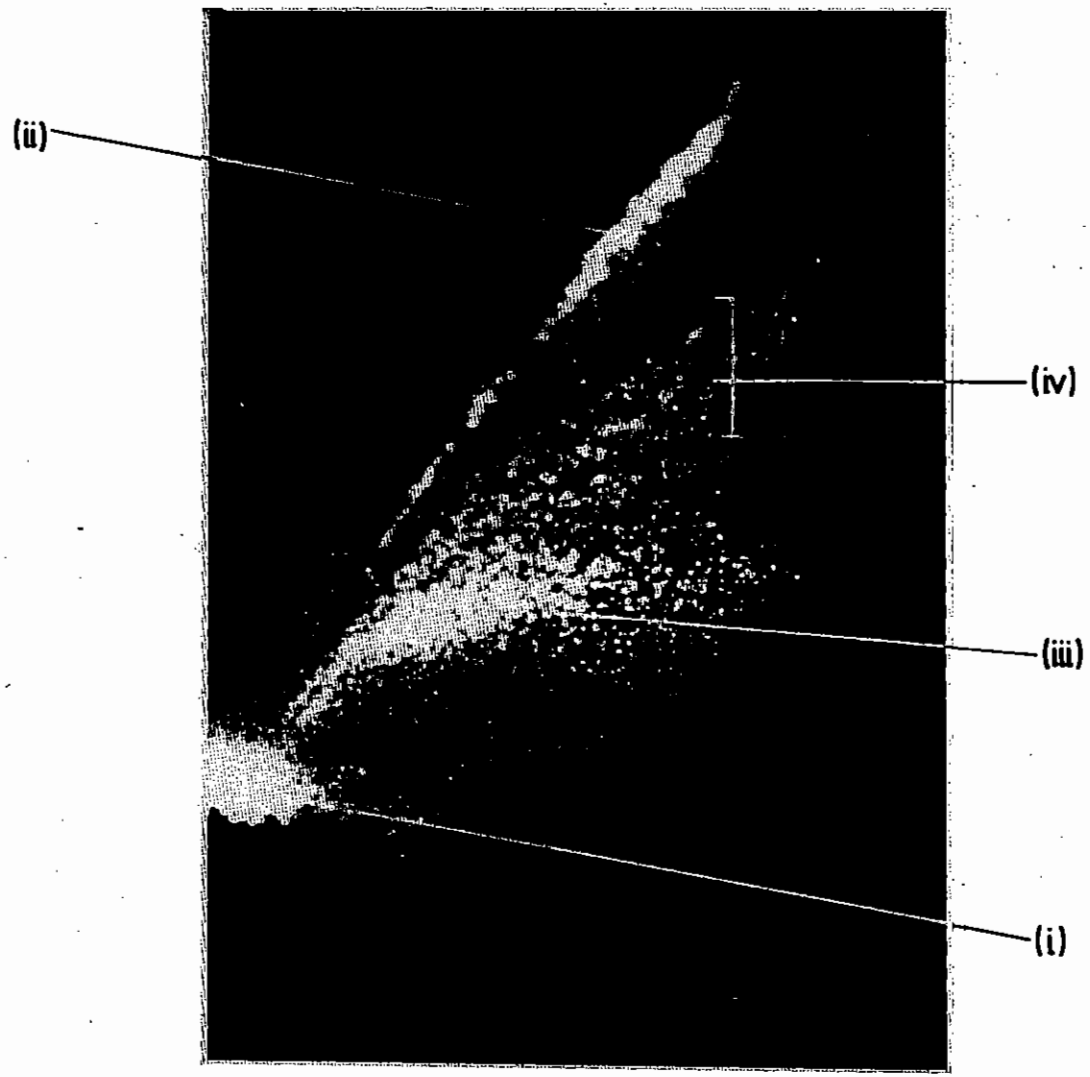

Figure 4.04 A typical set of parabolae obtained in the experiment. The target was a gold spot of 500μm diameter. The features are explained in the text.

4.3.2 The Origin of the Carbon Emission

The carbon ions described above could have come frome one or more of the following sources:

(i) The plastic substrate under the deposited spot,

(ii) hydrocarbon contamination upon the surface of the spot, or,

(iii) the plastic substrate around the deposited spot.

(i) There is no emission from under the deposited spot since the gold was too thick for the laser pulse to burn through it - the gold was 1.5 μm thick, corresponding to a ρl of 2.9 mg cm^{-2}. The mass ablation rate found in the experiment described in reference (4.07) varied as

$$\dot{m}_s \sim 10^5 I_{13}^{0.25} \qquad (1)$$

A 1 ns, 10^{13} W cm^{-2} pulse will thus burn through only 0.29 mg cm^{-2} of gold.

(ii) Emission of hydrocarbon contamination from the surface of the spot certainly does contribute to the observed ion signal. Figure 4.05 shows data recorded during this experiment for which the target was nominally pure vanadium. There is an obvious parabola caused by proton emission; the carbon emission is obscured by the vanadium parabolae.

This "background" hydrocarbon emission was recorded on all shots since the technique of heating the target to drive off surface contaminants (4.08) was not used during this experiment. Figure 4.06 shows data obtained from a target which was nominally pure gold. The contamination can be seen as a strong proton signal and a weak carbon signal. The carbon parabolae extend to a position corresponding to a velocity of approximately 2×10^8 cm s^{-1}. Since it is the spot-size dependence of this low-velocity cut-off which is investigated in this experiment this background emission limits the sensitivity of the technique.

Figure 4.05 Parabolae obtained from a vanadium target, showing a proton parabola. The carbon parabolae are masked by the vanadium parabolae.

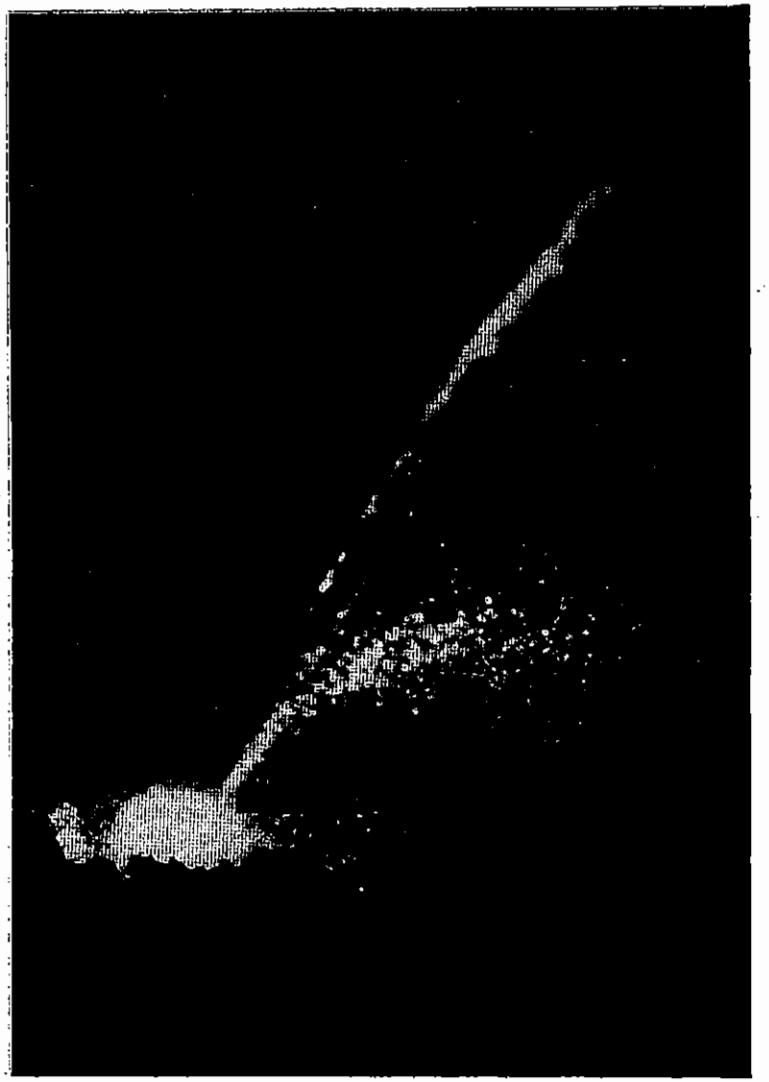

Figure 4.06 Parabolae obtained from a target that was nominally pure gold. Again hydrocarbon contamination can be seen.

Figure 4.07 As figure 4.04, but from a 2 mm gold spot. Note the low-velocity cut-off to the carbon emission(a).

Figure 4.08 As figure 4.04, but from a 5 mm gold spot.

(iii) Emission from around the deposited spot. Figures 4.04, 4.07 and 4.08 show data obtained with targets that consisted of 500 μm, 2 mm and 5 mm gold dots on mylar, respectively. It can be seen that whilst the hydrocarbon contamination was present on every target the low-velocity cut-off depends upon the size of the gold spot. To obtain a quantitative measure of this the films were scanned with a microdensitometer.

4.3.3 Data Reduction

The film was scanned on the microdensitometer and theoretical curves were fitted to them. The identiy of each significant peak, and its velocity, could then be determined.

The height of each peak (proportional to the film density) was then converted to a measure of the velocity spectrum through the relationship

$$I = 10^{yD/\gamma} \qquad (2)$$

where y is the peak height, D is the wedge calibration, γ is the film contrast which was assumed to be 0.8, and I is the deduced "brightness" of the parabola.

"I" was then multiplied by half the width of the peak (thus roughly taking into account the space-charge effects) to give a measure of the number of ions per unit area of film. This was converted to a velocity spectrum through:

$$\frac{dn}{dv} = \frac{dn}{dy}\,\frac{dy}{dv} \qquad (3)$$

$$y = \frac{Bzel}{AMv}\left(\frac{l}{z} + L\right) \qquad (4)$$

$$\frac{dn}{dv} = \frac{I}{V^2} \qquad (5)$$

Finally, log(dn/dv) was plotted as a function of ion velocity, and is shown in Figure 4.09.

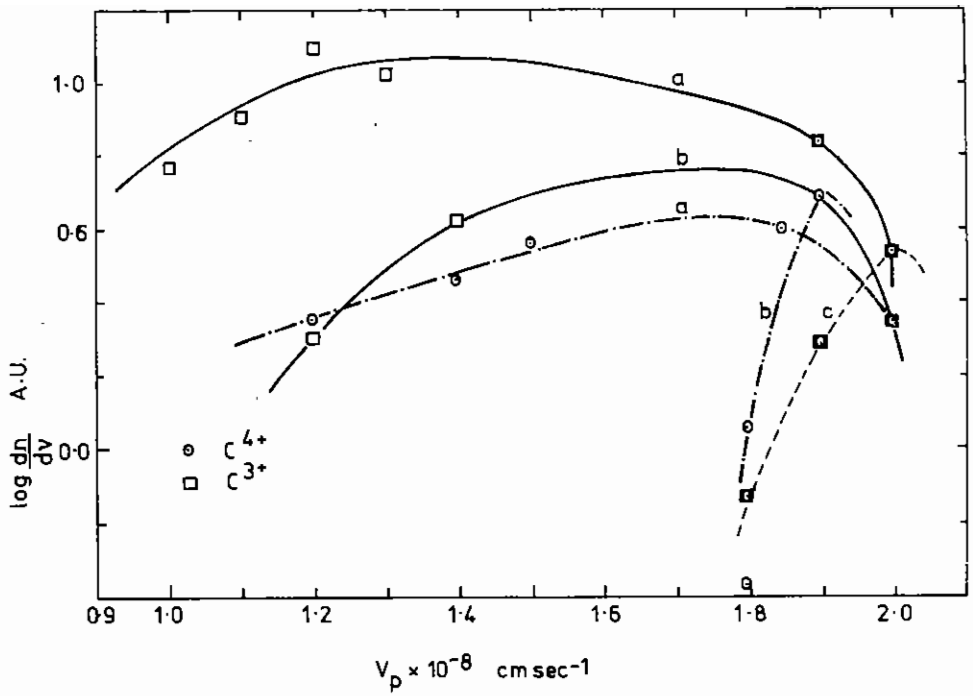

Figure 4.09 A plot of the velocity spectrum dn/dv from the C^{4+} and C^{3+}. Parabolae for (a) 500μm spot. (b) 2mm spot. (c) 5 mm spot.

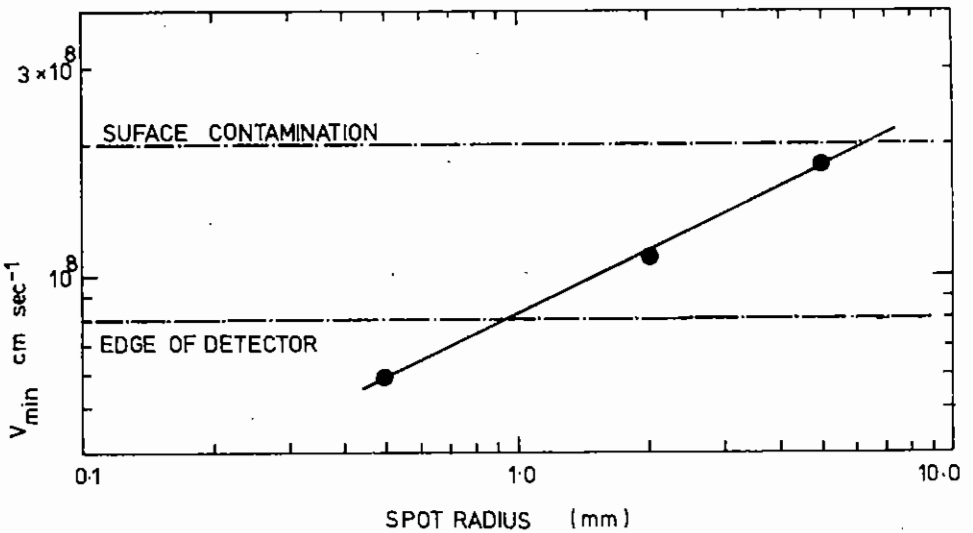

Figure 4.10 The minimum velocity of the C^{3+} ions plotted as a function of gold spot size.

It can be seen from this diagram that whilst the maximum observed carbon-ion velocity was about 2 x 10^8 cm s^{-1} (but note that, since the isovelocity lines are very close together at high velocities, a small error in the fitting of the parabolae can lead to a large error in the determination of high velocities), the minimum velocity observed increased as the spot size increased. This is shown more clearly in Figure 4.10 where the minimum velocity of the C 3+ ions (defined somwhat arbitrarily as the velocity at which dn/dv = 1 arbitrary unit) is plotted as a function of spot size.

It is apparent from this figure that there is a "sensitivity window" defined on the low-velocity side by the detector size and on the high-velocity side by the emission of hydrocarbon contamination. (The velocity seen in the 500 μm spot was obtained by extrapolation.)

The minimum velocity is observed to increase as

$$V_{min} \sim r_{spot}^{0.5} \qquad (6)$$

This means that the minimum energy of the carbon ions scales as the spot radius.

Since the optical densities of the carbon and hydrogen parabolae are similar to the optical density of the gold parabolae, significant numbers of carbon ions must have been accelerated to velocities of order 10^8 cm s^{-1}. (Since the device is not calibrated no quantitative measurement of the numbers involved could be made.) This means that substantial amounts of energy must have spread sideways.

These features are explained by assuming that with long pulses the fast electrons generate a fast-ion cloud which then expands at a velocity of about 2 x 10^8 cm s^{-1}. Fast electrons generated within this ion cloud are reflected at the cloud boundary and deposit their energy many millimetres form the optical focal spot, leading to emission of ions from this area. With short pulses, in contrast, the observed spreading velocity of 2 x 10^9 cm s^{-1} (see previous Section (4.2)) was too high to

be consistent with an expanding ion cloud. In this case it is probable that it is the fast electrons alone which are responsible for transporting the energy, and that they do so along the surface of the target in a plasma layer formed by X-rays or by the fast electrons themselves.

4.3.4 Interpretation of the Thomson Parabola Data

The ion-cloud model can be used to explain the observed radius-dependent minimum velocity seen in the Thomson parabola data, as well as the annular structure to the K_α emission (Section 4.2).

The fast electrons are generated around the critical-density surface. Initially some of them travel outwards, away from the target surface. In doing so they set up a self-consistent potential which pulls them back and causes the ion cloud to expand- the electrons are reflected at the sheath boundary. There is a "foot" to this sheath, caused by low-energy ion emission from the target surface (see Figure 4.11); this emission may be due to X-ray effects (the conversion efficiency for gold is high) or to fast electron effects.

At a later time (Figure 4.11(b)) the sheath has expanded and the foot has lengthened since a fast electron may have the trajectory shown. If an electron does have such a trajectory it will emerge from the end of the foot and set up a strong potential which will accelerate ions to high velocities. The potential reflects the electrons and some of them enter the target, generating K X-rays.

As the cloud expands the region of high potential also moves radially outwards fom the focal spot; the region of K_α emission is thus annular and the ion emission is such that ions emitted from the end of the foot (where the potential is strongest) are accelerated more than those emitted form the body of the foot. If the deposited spot is of such a size as to reach almost to the end of the foot then the ions emitted at the end of the foot - the high velocity ions - will be from the substrate, whereas ions emitted form the body of the foot - and therefore of lower energy - will be ions from the deposited spot.

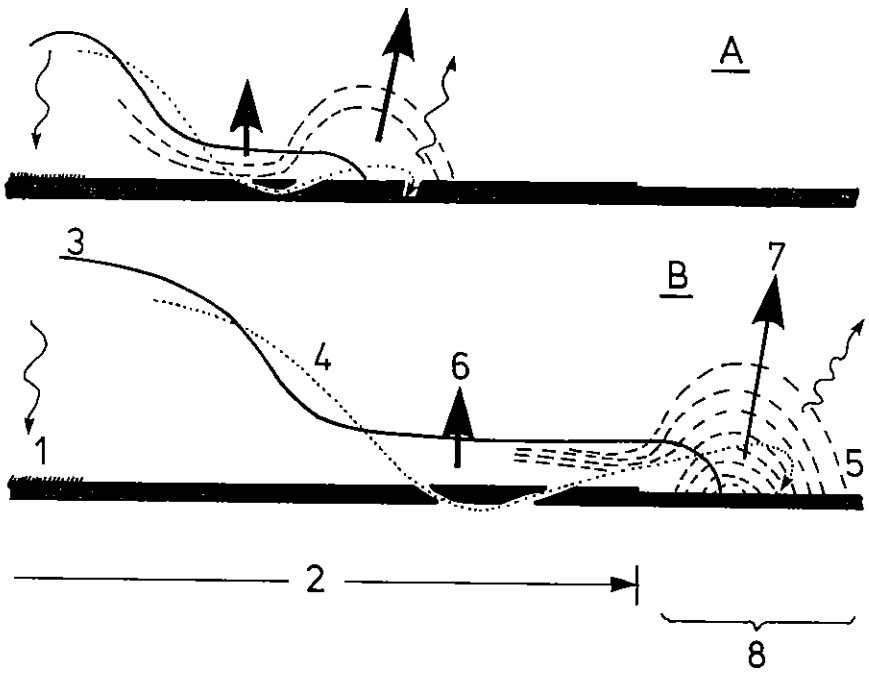

Figure 4.11 A diagramatic representation of the processes leading to ion emission from parts of the target a long way from the optical spot.

A) Early in the pulse
B) Later in the pulse.
1) Optical focal spot
2) Gold spot
3) Plasma front (Debye layer)
4) A fast electron trajectory
5) Hypothesised equipotentials
6) "Slower" ion emission
7) "Faster" ion emission
8) Annular K α emission.

4.3.5 Conclusions

It has been shown that ions are emitted from regions which are distant (~ 3 mm) from the focal spot, and that whilst the maximum energy of these ions is constant (to within the experimental error), the minimum energy of these ions is proportional to the size of the deposited spot. Finally, a mechanism which explains these, and other, observations has been suggested.

Many experiments which investigate phenomena that occur with spherical targets are performed with plane targets, since the rear of the target allows diagnostic access. It is clear from the results of this section that unless large (~ 1 mm) focal spots are used, such experiments may lead to erroneous conclusions.

T J Goldsack (Imperial College)

4.4 Thermal Smoothing in Ablatively Accelerated Targets

4.4.1 Experiments

To achieve a high density in laser driven compression, a spherical convergence with good symmetry is required. If there are no hydrodynamic instabilities the implosion symmetry depends on the symmetry of the driving pressure. This can be better than the symmetry of the irradiation because of sideways diffusion of energy from areas of high irradiance to areas of low irradiance in the region between the critical density and the ablation front.

A simple model suggests that the smoothing depends on D/λ_p where D is the separation of the absorption region and the ablation front and λ_p is the wavelength of the laser intensity modulation in the target plane. Numerical modelling (4.09) shows that in a steady state $D \propto (I\lambda^{3\cdot8})^{0\cdot7}$, where I is the incident irradiance and λ is the wavelength of the radiation. This would suggest that the smoothing also scales as $(I\lambda^{3\cdot8})^{0\cdot7}$.

Observations of improved smoothing as the irradiance increases have been made at a single wavelength using the technique of double colliding foils (4.10). Here we report the first direct comparison of thermal smoothing of laser beam modulations at wavelengths of 1.05 μm and 0.53 μm. The smoothing is measured by the more direct and novel technque of short pulse X-ray backlighting synchronous with a long pulse to accelerate the target. The measured smoothing varied as $I\lambda^{1.5}$. However comparison with a two-dimensional simulation indicates that an additional phenomenon, smoothing of the velocity modulation during a coasting phase, increases the perceived smoothing in this and previous measurements.

Experiments were performed using the Vulcan Nd glass laser at wavelengths of 1.05 μm and 0.53 μm (4.11). A 100 ps 1.05 μm oscillator pulse was split up and reconstructed to give a laser pulse of fwhm t_L = 430 ps and energy up to 60 J, and a 100 ps pulse to provide a backlighting pulse of X-rays. For 0.53 μm irradiation the beam was frequency doubled giving up to 30 J in 350 ps. The spatial fill factors of the beams were 0.5 and 0.6 for 0.53 μm and 1.05 μm irradiation respectively.

The near field of the incident laser beam was modulated by placing 20 mm wide strips of neutral density filter in the 100 mm diameter beam. The targets, 550 μm diameter 12.5 μm thick mylar discs, were placed either 400 μm or 250 μm from the focus of the f/1 lens. A modulation ratio of 4:1 and periods λ_p of 150 μm or 90 μm were measured from microdensitometer tracings of target equivalent plane photographs recorded on Polaroid type 57 film, as shown in Figure 4.12. The peak intensity in the target plane which was up to 3×10^{14} W cm^{-2}, was used to characterise the experiments. Lower peak intensities were achieved by decreasing the laser energy.

The short pulse backlighting beam was separately amplified to 40 J at 1.05 μm, and focused onto 0.1 μm thick Cu targets vacuum deposited onto 12.5 μm mylar substrates. The backlighting targets and the main target were normal to each other and separated by 0.5 mm, as shown in Figure 4.13. A pinhole camera looked edge on along the main target viewing the backlighting target through its 12.5 μm mylar substrate. The filtering on

the 5 μm/20 μm double pinhole was 12.5 μm mylar and 10 μm Be, giving a cut-off energy of 2.5 keV. The X-rays from the backlighting target were measured with a streak camera with similar filtering and were found to have a fwhm t_b of 100 ps.

When viewed edge on the 550 μm disc targets are optically thick to the 2.5 keV probing X-rays which have an attenuation length of 30 μm in cold mylar. Figure 4.14(a) shows an edge on shadowgram of an unirradiated disc target: the fwhm of the shadow of the disc is 15 μm which is consistent with the initial target thickness.

Backlit shadowgrams of accelerated targets are shown in Figures 4.14(b), 4.14(c) and 4.14(d). Experiments without backlighting showed that emission from the mylar targets was fainter than the backlighting emission in Figure 4.14(a), and was only present on the laser side of the target. The backlit shadowgrams, Figures 4.14(b) - 4.14(d), show a characteristic sharp edge on the laser side of the target, due to the unaccelerated outer ring of the 550 μm discs. The modulation in position of the rear of the target in Figure 4.14(b) - 4.14(d) correlates with the maxima and minima of the incident laser intensity profile.

The delay time t_d of the backlighting pulse was empirically adjusted so that the rear of the target moved a distance Z greater than the initial target thickness, and also so that the target remained opaque despite buckling and decompression. Consequently $t_d \sim (5 \pm 1)t_\ell$ for Figure 4.14 with 0.53 μm irradiation, and $t_d \sim (7 \pm 1)t_\ell$ for 1.05 μm irradiation. Under these conditions the smearing due to motion during the finite backlighting pulse was much less than Z, the distance moved.

The increase of smoothing with irradiance is clearly seen in Figure 4.14: there is a large modulation in the position Z of the rear of the target at low irradiance (Figure 4.14(b)) and very little target modulation at high irradiance Figure 4.14(d).

The variation in the position of the rear of the target was determined from measurements of microdensitometer tracings of each shot. The

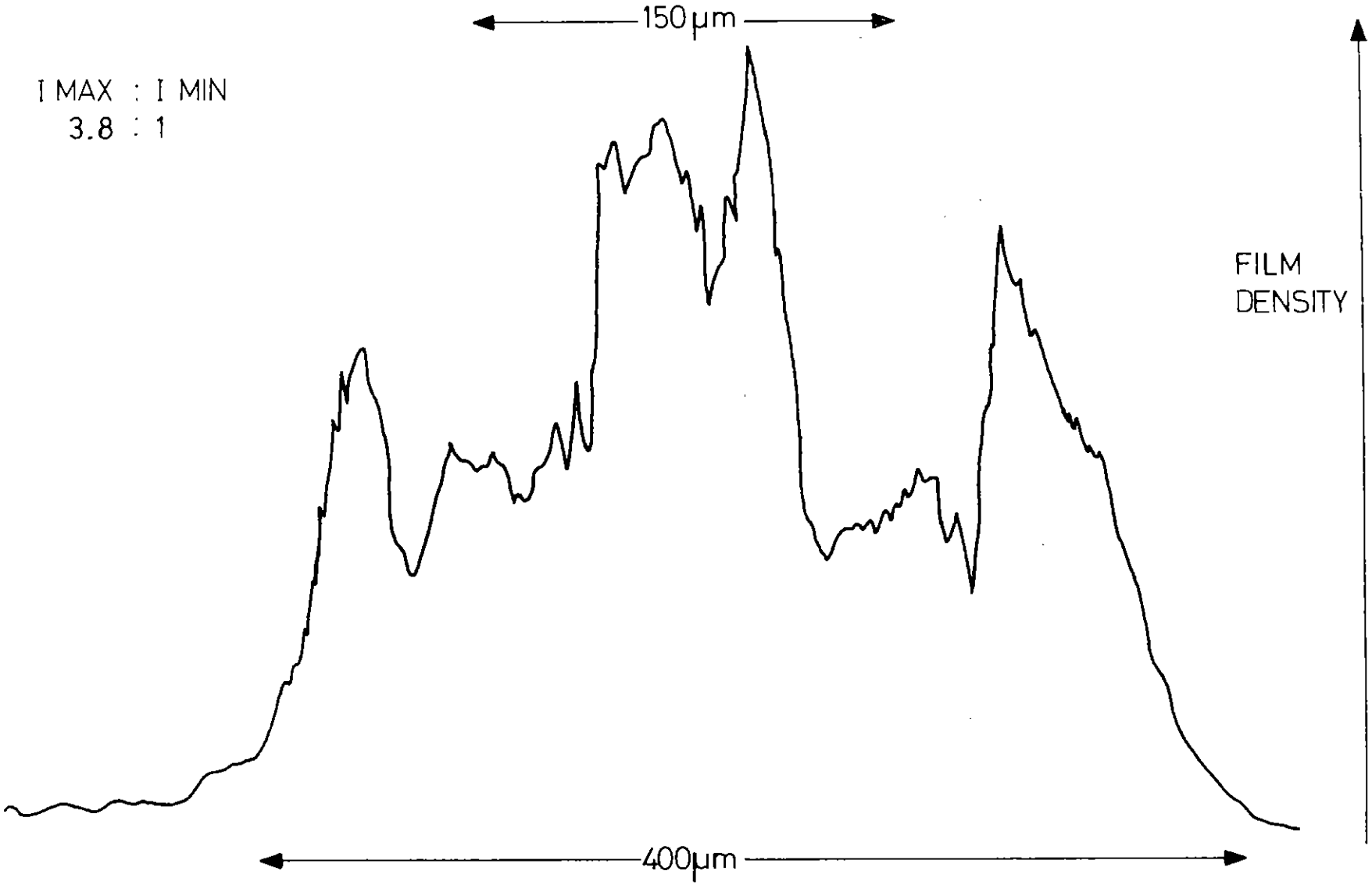

Figure 4.12 Densitometer tracing of target equivalent plane photograph showing a 4:1 modulation in intensity and an imposed modulation of period λ_p = 150μm.

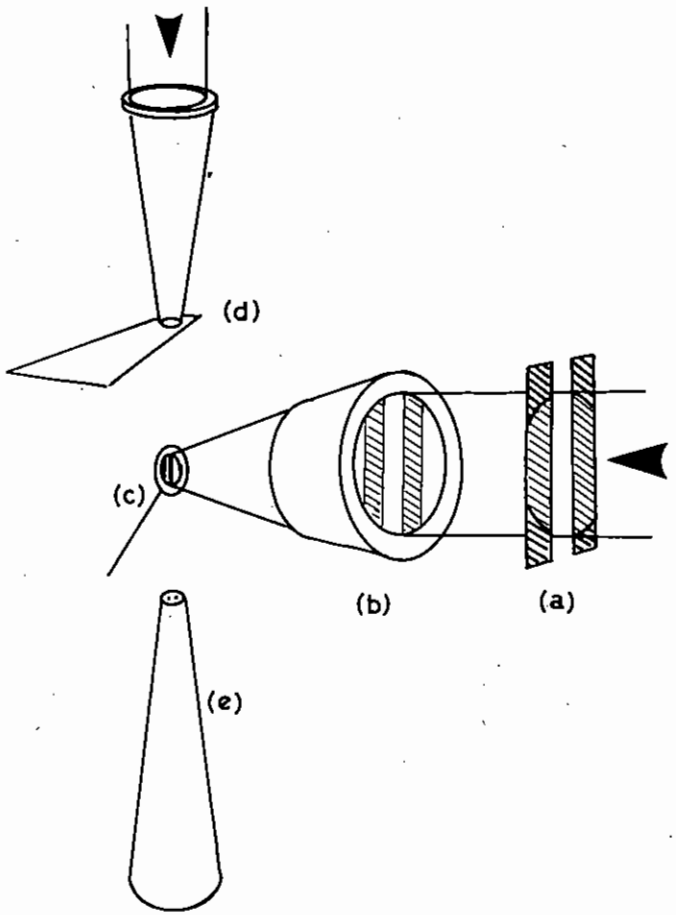

Figure 4.13 Experimental arrangement showing (a) beam modulation, (b) f/1 focussing lens, (c) microdisc target, (d) backlighting target and (e) recording pinhole camera.

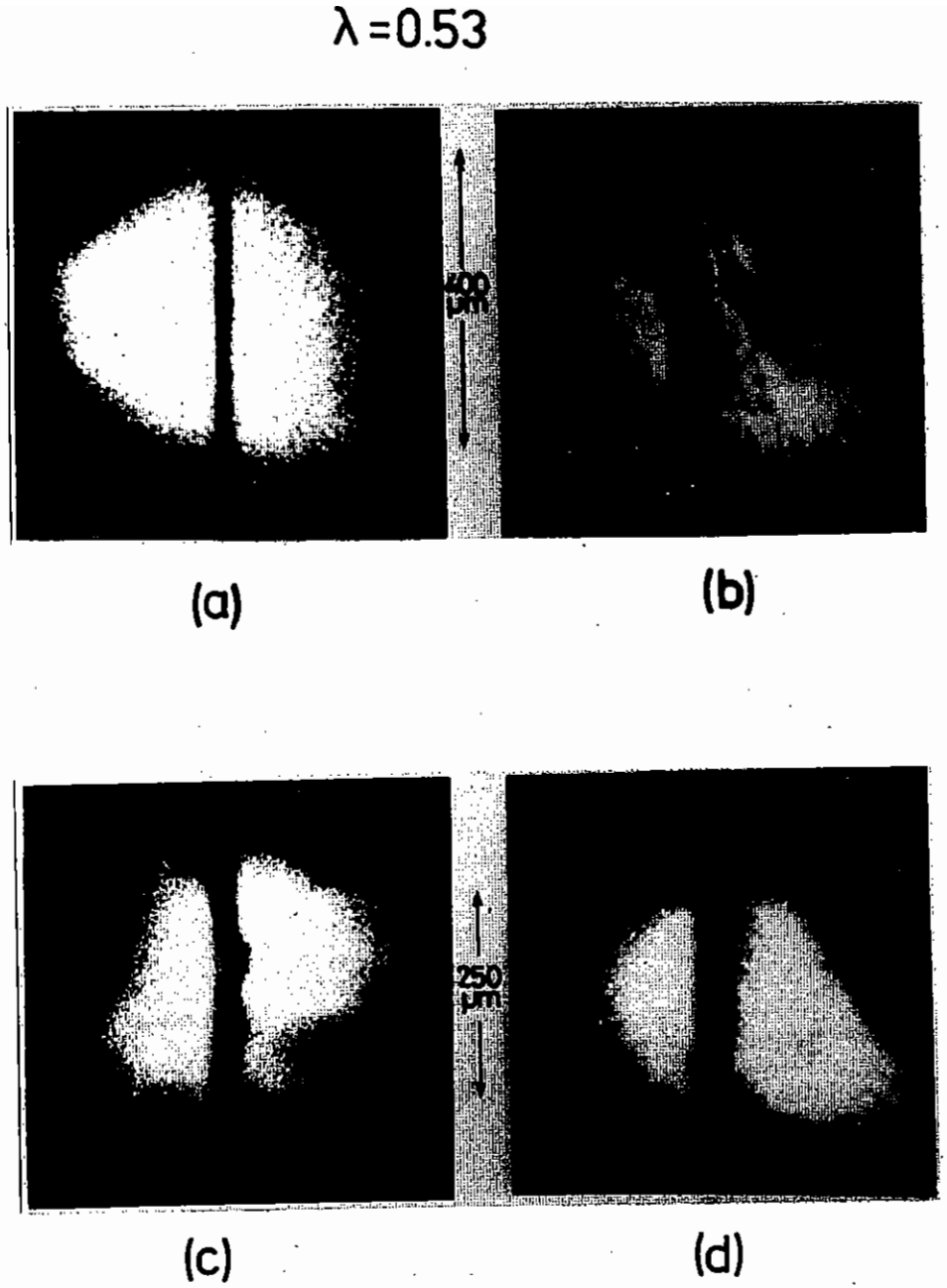

Figure 4.14 Shadowgrams of microdisc targets for a range of incident intensities. (a) Unirradiated mylar disc 550μm ϕ, 12.5μm thick. (b) Iinc = $3.4.10^{13}$ W cm^{-2}, Backlighting delay = 1.85 ns 150μm period on target, 400μm focal spot. Δ = 1.4 (c) Iinc = $9.2.10^{13}$ W cm^{-2}, Backlighting delay = 1.05 ns 90μm period on target, 250μm focal spot Δ = 0.3. (d) Iinc = $19.4.10^{-2}$, Backlighting delay = 1.05 ns 90μm period on target, 250μm focal spot Δ = 0.2.

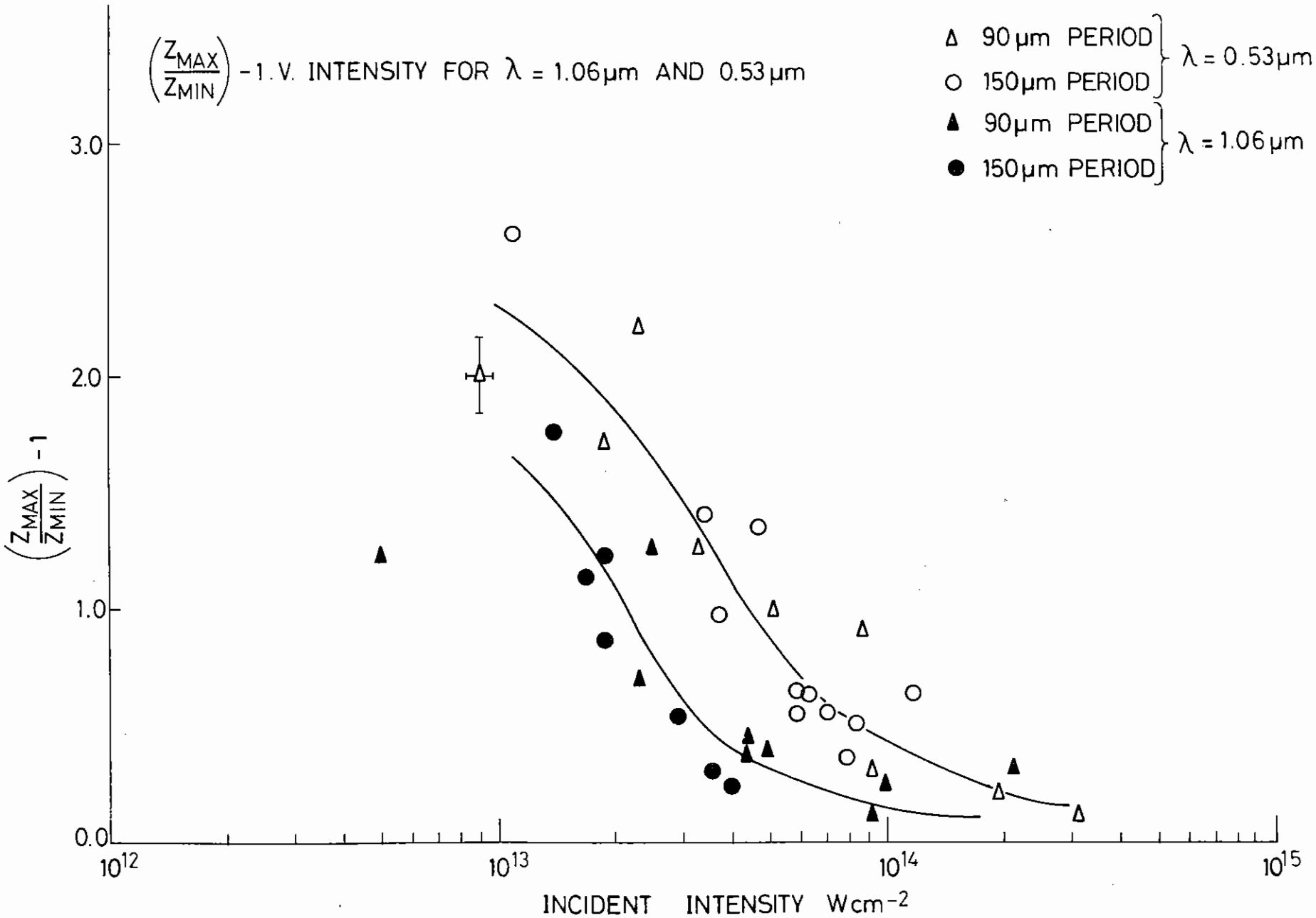

Figure 4.15 Δ versus incident intensity for 1.06 and 0.53μm light. Smoothing can be seen to improve - ie Δ decreases - for increased intensity and for longer wavelength light.

quantity Δ where

$$\Delta = \frac{\text{maximum Z}}{\text{minimum Z}} - 1$$

is plotted in Figure 4.15 as a function of the peak incident laser irradiance at constant defocus for both wavelengths. If there were no smoothing Δ would simply depend on the maximum and minimum pressure. For a 4:1 modulation in the irradiance and a scaling of the ablation pressure $p \propto I^{0.7}$ (4.07), the value of Δ would be 1.6. Thus Figure 4.15 shows that at low irradiance there is little smoothing, but the smoothing increases at higher irradiance and the smoothing is better for 1.05 μm than for 0.53 μm irradiation. From Figure 4.15 the smoothing is given by

$$I/\Delta = 0.5\ (I/10^{13}\ \text{W cm}^{-2})(\lambda/1\mu\text{m})^{1.5}$$

for $I \geq 2 \times 10^{13}$ W cm^{-2}.

There is some disagreement with the simple scaling of Gardner and Bodner which is $1/\Delta \propto I^{0.7}\lambda^{2.7}$. Simulations show that this results from decompression and transient effects in the experiment.

4.4.2 Simulations

Simulations using a two-dimensional Eulerian fluid code (4.12), illustrate the importance of decompressional effects during the coasting phase. The code was used in r - z geometry with periodic boundary conditions simulating the 4:1 intensity variation used in the experiment. The mesh spacing was 4 μm x 1 μm to describe accurately a period λ_p of 90 μm and the 12 μm foil thickness respectively. Absorption was by inverse Bremsstrahlung with any energy reaching critical density being deposited on the surrounding mesh points.

Results of the ratio of maximum to minimum pressure are shown in Figure 4.16 as a function of time. At a fixed time during the laser pulse $\left[\frac{P\text{max}}{P\text{min}} - 1\right]^{-1} \propto (I\lambda^2)^{0.67}$. During the course of the laser pulse, as the critical density surface moves outwards, the pressure modulation

decreases. This occurs more rapidly for 1.05 μm light because the lower value of critical density creates a larger scalelength. After the laser pulse the pressure becomes greater in the low intensity region as the pressure distribution relaxes (in an acoustic manner). This effect together with hydrodynamic flow from the back of the target results in an increased apparent smoothing of the target. The perfect gas equation of state causes the code to be inaccurate when decompression becomes significant, and prevents detailed comparison for $t_d > 1.8$ ns.

In conclusion, we have observed smoothing on the rear surface of an imposed intensity modulation, in an ablatively accelerated target with smoothing $I\lambda^{1.5}$. The importance of decompression effects to the interpretation of the experimental results is shown by 2-D code simulations which indicate that the smoothing might scale more strongly with wavelength than $\lambda^{1.5}$.

A J Cole, J D Kilkenny (Imperial College), P T Rumsby, M H Key and R G Evans (RAL)

4.5 An Analytical Model of Transient Thermal Smoothing

Recent discussion by Gardner and Bodner (4.09) of the effect of spatially inhomogenous irradiation on spherical implosions has focused attention on the need to obtain enough separation D between the absorption and ablation fronts in order that diffusive thermal smoothing should sufficiently reduce the pressure inhomogeneity. Specifically it has been argued that for diffusive heat flow the pressure variation $\Delta P/P$ is related to the irradiance variation $\Delta I/I = f$ by

$$\Delta P/P = f \exp(-2\pi D/L_p) \qquad (1)$$

where L_p is the spatial wavelength of the perturbations in irradiance.

It seems however that the exponential smoothing factor in equation (1) may considerably over estimate the smoothing because of the transient nature of the separation D.

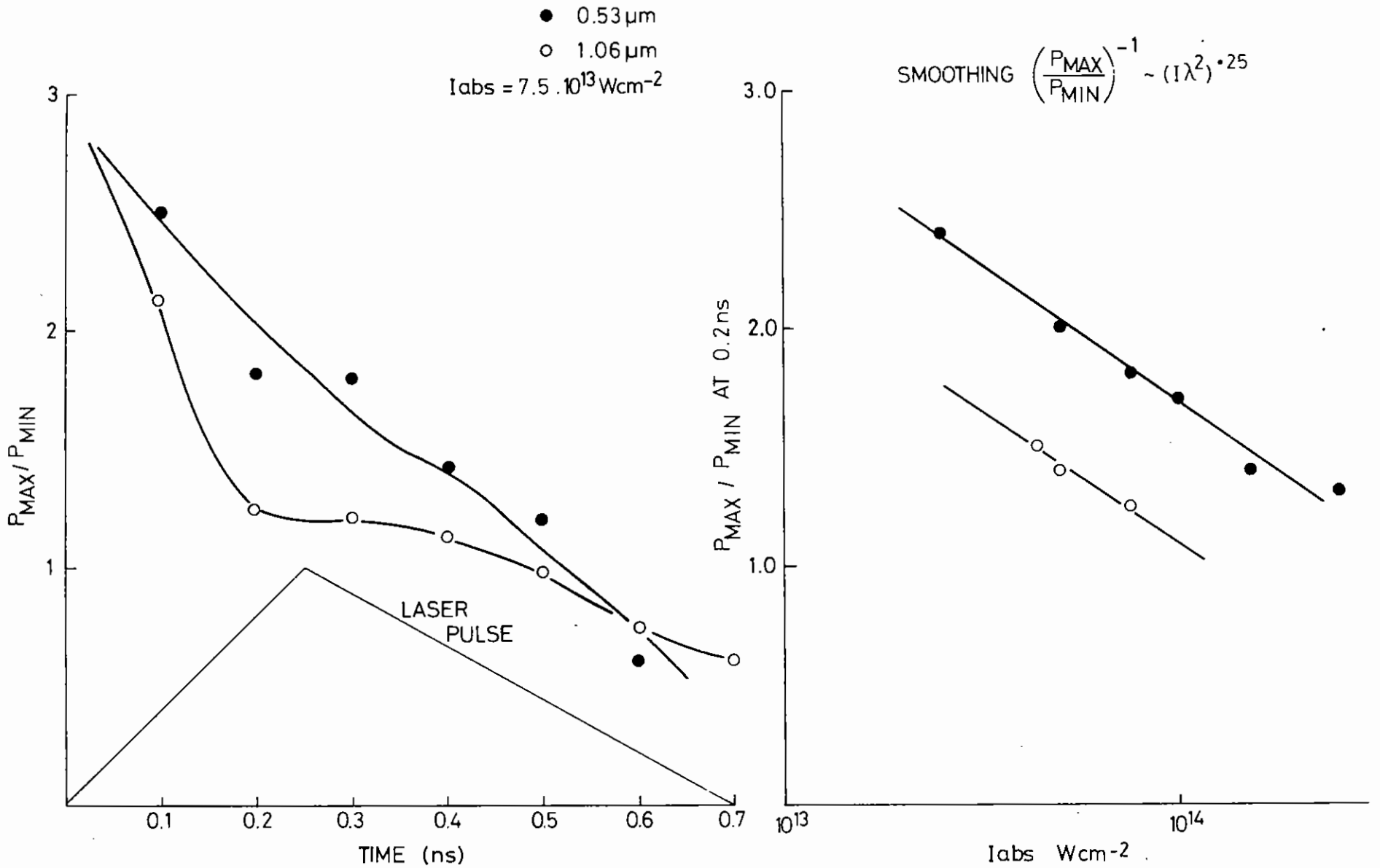

Figure 4.16 Ratio of maximum to minimum pressure as a function of time and P_{max}/P_{min} at time equal to 200 psec for a range of absorbed intensities.

Numerical calculations with a one dimensional hydrodynamic code MEDUSA (4.13) show that if a constant laser irradiance is applied at t = 0 the separation D is initially described by

$$D = v_s t \tag{2}$$

where v_s is the velocity of separation. This transient increase of D saturates at the steady state value, given by Gardner and Bodner in the form,

$$D_\infty/R = 0.14\left[(I/10^{13}\ \mathrm{W\ cm^{-2}})(\lambda/\mu m)^{3\cdot8}\right]^{0\cdot7}(R/1mm + 1)^{-1} \tag{3}$$

Thus in a typical ablative acceleration process by a laser pulse of duration τ we have,

$$\begin{aligned} D &= v_s t \qquad 0 < t < \varepsilon\tau \\ D &= D_\infty \qquad \varepsilon\tau < t < \tau \end{aligned} \tag{4}$$

where ε is the 'transient fraction' of the process.

The modulation of acceleration is

$$\ddot{x} \pm \Delta\ddot{x} \quad \text{where} \quad \Delta\ddot{x}/\ddot{x} = \Delta P/P$$

and $\Delta P/P$ is given by equation (1).

4.5.1 Transient Phase $0 < t < \varepsilon\tau$

Using $D = v_s t$ and integrating the equation of motion we have,

$$\ddot{x}(t) = \ddot{x}\left[t \pm (fL_p/2\pi v_s)(\exp(-2\pi v_s t/L_p)-1)\right]$$

so that when $\exp(-2\pi v_s t/L_p) \ll 1$,

$$\Delta\ddot{x}/\ddot{x} \approx fL_p/2\pi v_s t \tag{5}$$

similarly

$$x(t) = \ddot{x}\left[\frac{t^2}{2} \pm \left\{\left(\frac{fL_p}{2\pi v_s}\right)t + \left(\frac{fL_p}{2\pi v_s}\right)^2 (\exp(-2\pi v_s t/L_p)-1)\right\}\right]$$

so that as before

$$\Delta x/x \approx fL_p/\pi v_s t \tag{6}$$

The modulation in distance travelled in the transient and steady state limits respectively are,

$$\begin{aligned} &1 \pm fL_p/\pi v_s t \\ &1 \pm f\exp(-2\pi D/L_p) \end{aligned} \tag{7}$$

It follows that, for example, 10 fold smoothing requires

$$\begin{aligned} v_s t &= 3.2\ p \\ \text{or} \quad D_\infty &= 0.37\ p \end{aligned} \tag{8}$$

for the two cases respectively. The transient case clearly needs much greater critical to ablation surface separation and therefore much greater irradiance.

4.5.2 Steady State $\varepsilon\tau < t < \tau$

The distance travelled in this phase with constant acceleration and steady state smoothing is given by

$$x_2 \pm \Delta x_2 = \ddot{x}\left[\varepsilon\tau(1\pm\beta)(1-\varepsilon)\tau + \tfrac{1}{2}(1\pm\gamma)(1-\varepsilon)^2\tau^2\right] \tag{9}$$

where $\beta = fL_p/2\pi D_\infty$ and $\gamma = f\exp(-2\pi D_\infty/L_p)$ are the modulation of initial velocity and acceleration respectively.

Adding the modulation in distance travelled in the transient and steady

state phases respectively gives

$$\Delta x/x = (\Delta x_1+\Delta x_2)/(x_1+x_2) = \alpha\,\varepsilon^2 + 2\beta\,\varepsilon(1-\varepsilon) + \gamma(1-\varepsilon)^2 \qquad (10)$$

where $\alpha = fL_p/\pi D_\infty$ is the modulation in distance travelled in the transient phase.

Thus the resultant modulation in a mixed transient/steady state process, defined by the transient fraction ε, reduces to the transient limit α where $\varepsilon \to 0$, with the mixed term $2\beta(1-\varepsilon)\varepsilon$ dominating the intermediate case and to the steady state limit β where $\varepsilon \to 0$.

It is clear from equation (10) that, for smoothing to approach the steady state value, the transient phase must be a very small fraction of the process.

To estimate the duration of the transient phase the velocity v_s and the steady state separation D must be known.

The latter is given in equation (3) above while v_s can be estimated from the numerical calculations of Evans (4.13) discussed earlier. Table 4.02 shows values of v_s.

The velocity v_s is related to the ablation flow velocity v_a which in the Champman Jouguet approximation (sonic at critical density) is,

$$v_a = 4 \times 10^7 (\lambda/1\,\mu m)^{2/3}\ (I/10^{13}\ W\ cm^{-2})^{1/3}\ \ cm\ s^{-1} \qquad (11)$$

Normalising to $\lambda = 0.53\ \mu m$, $I = 10^{13}\ W\ cm^{-2}$ in Table 4.02 suggests that,

$$v_s \sim 9.1 \times 10^{-2}\ v_a \qquad (12)$$

Values calculated with this assumption are shown in Table 4.02 and give sufficient agreement with the numerically calculated values for use here.

	1.06 μm	0.53 μm	0.35 μm
10^{13}	3 (3.6)	2.2 (3.3)	2 (1.7)
10^{14}	8 (7.8)	5 (5.1)	2.2 (3.8)
10^{15}	26 (17)	12 (11)	8 (8.2)

TABLE 4.02

Velocity v_s in units of 10^6 cm s^{-1} for various irradiances in W cm^{-2} and laser wavelengths on targets with ionic charge Z = 10 and density $\rho = 2.5\ gcm^{-2}$ and radius 100 μm. Numbers in brackets are obtained from the approximate analytic expression in equation (12).

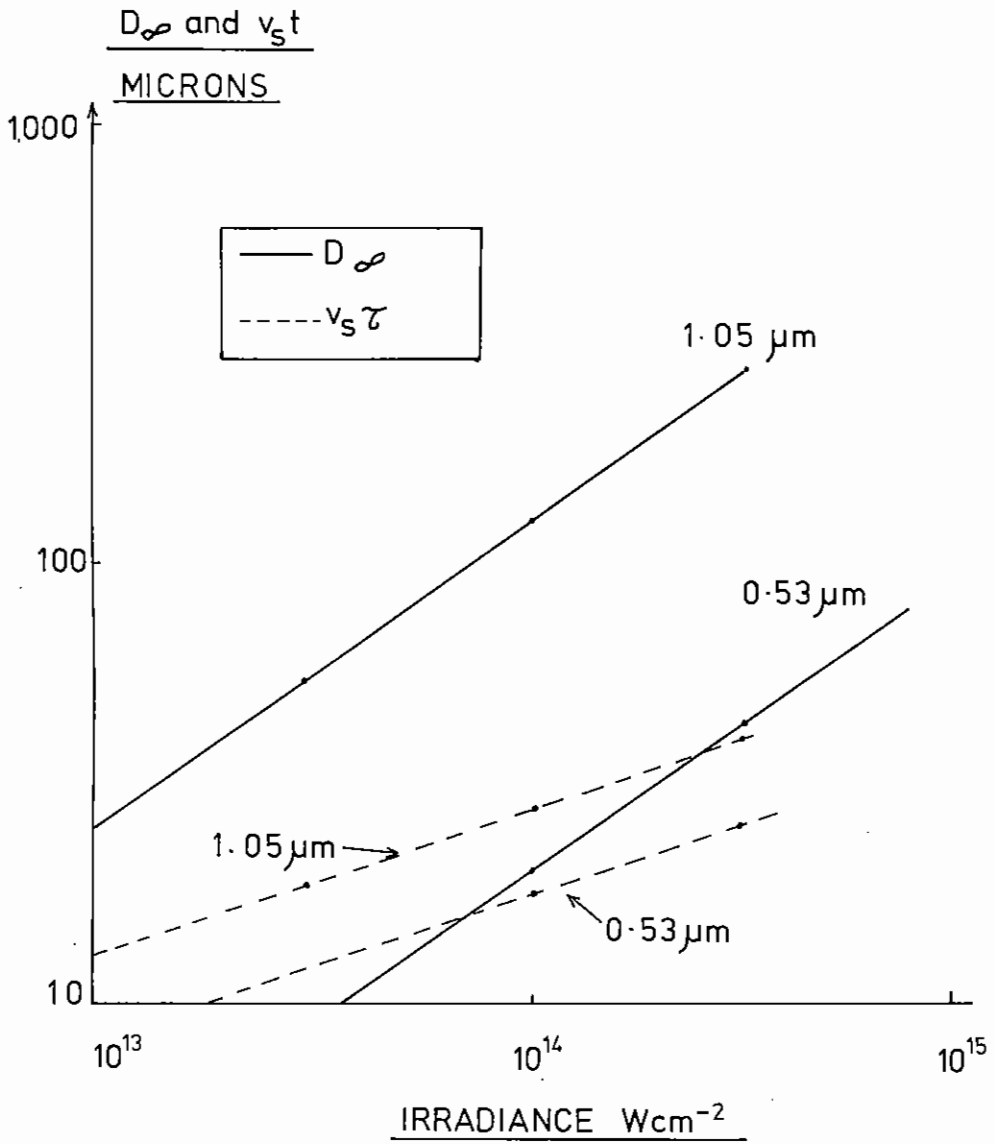

FIG 4·17

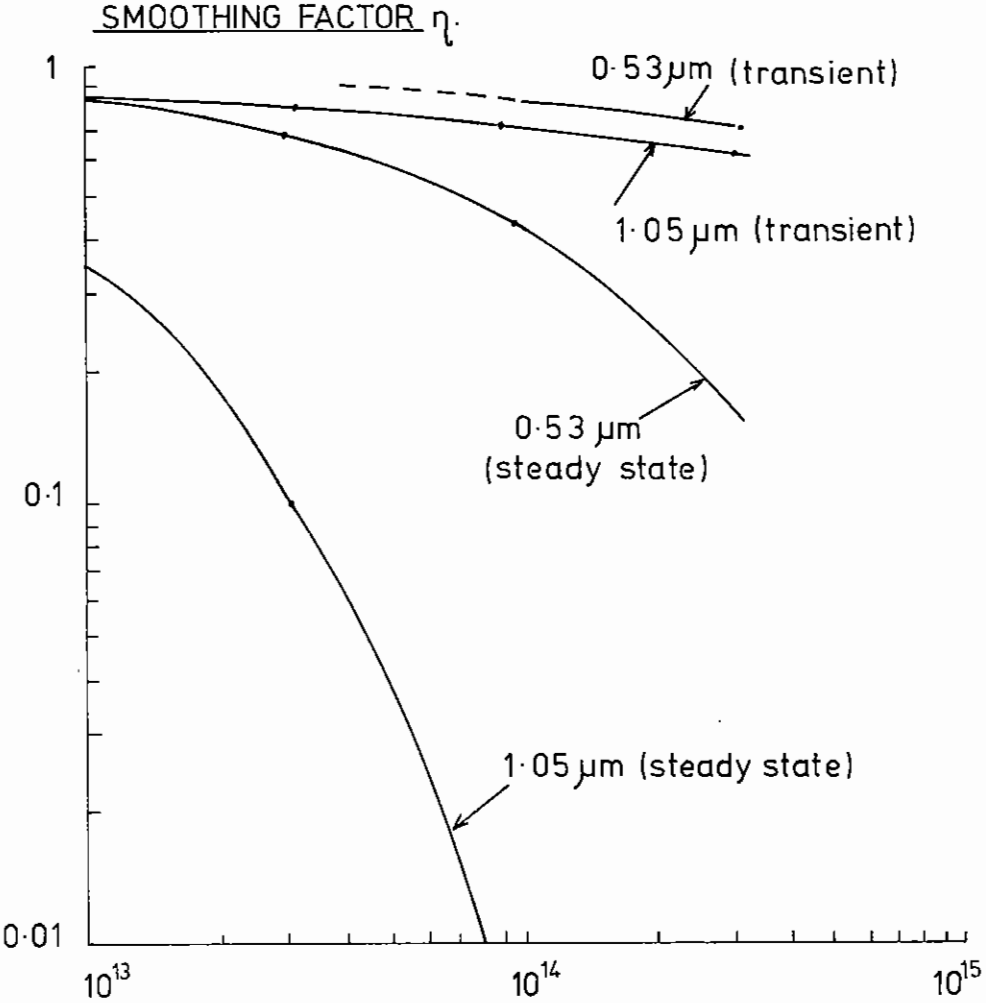

FIG 4·18

The thermal smoothing obtained in any specific case can now be estimated.

It is interesting to apply the argument to the experiment discussed in section 4.4 where the pulse duration is 350 ps, the spatial scale of the perturbations is 150 μm, the focal spot radius is 200 μm, λ = 1.05 μm or 0.53 μm and I is varied in the range 10^{13} to 2 x 10^{14} W cm^{-2}. Figure 4.17 shows D_∞ and $v_s t$ for the experimental situation and it is apparent that in the main $D_\infty > v_s t$ implying that the process is described by the transient model. Figure 4.18 shows the smoothing expressed as $(\Delta x/x)/(\Delta I/I)$ for the steady state limit and the transient limit. It is clear that while the steady state model predicts good smoothing in this experiment, consideration of the transient nature of the process shows relatively little smoothing is obtained. The experimental observation of smoothing 1 ns after the laser pulse can be understood in terms of a hydrodynamic process occuring during the 1 ns of unaccelerated motion as discussed in Section 4.4.

Comparison of this analytic approach with 2D fluid code calculations shows good enough agreement to make it a useful rapid aid to understanding thermal smoothing.

4.6 Interpretation of the Mass Ablation Rate of Laser Irradiated Spherical Targets in Terms of Heat Flux Limits

4.6.1 Introduction

When high intensity laser light is incident on solids, a high density plasma is formed which responds to its own pressure by flowing or ablating away from the solid. The rate at which mass is ablated and the ablation pressure are thus closely related quantities. The ablation pressure is of interest for laser fusion as it determines the dynamic response of targets. Moreover the mass ablation rate is dependent on energy transported inwards, principally by thermal conduction from the absorption region which is below critical density to the higher density ablation region. Accurate measurements of the mass ablation rate can therefore give values of the inward heat flux, as well as the ablation pressure.

Many measurements of the mass ablation rate have been made in recent years. Most of the early measurements (4.14, 4.15, 4.16) were from small focal-spot, single beam experiments at a laser wavelength of 1.06μm. The interpretation of the results of the experiments was usually with a one-dimensional simulation, leading to the conclusion that the heat flux was inhibited to a small fraction of the free-steaming limit (4.14) (4.16). More recently, results on the mass ablation rate have been obtained at different wavelengths (4.17, 4.18, 1.19), and substantially larger focal-spots (4.20) at lower irradiances.

Although plane-target measurements of the mass ablation rate are useful guides to the transport processes they are inevitably two-dimensional. This complicates the interpretation of experimental results since a two-dimensional simulation must be used to describe lateral transport of energy and two dimensional effects give rise to magnetic field generation.

The work presented here avoids the complication of lateral energy transport by using approximately symmetric irradiation of spherical targets. The transport of energy is thus predominantly radial, and the plasma is more adequately described by a one-dimensional simulation. The symmetry allows accurate measurements of the absorbed laser irradiance.

Results are presented for two wavelengths 1.05 μm and 0.53 μm. The mass ablation rate is measured by both x-ray streak spectroscopy and plasma particle diagnostics with good agreement. In contrast to most plane target measurements: (a) the mass ablation rate is found to scale strongly with absorbed irradiance and (b) a heat flux greater than 10% of the free streaming limit is inferred. Some plane target measurements (4.20), with large focal spots, achieve a similar scaling of the mass ablation rate with irradiance.

Section II of this paper describes the experimental arrangements and measurements. Section III describes the simulation, a test problem to establish its accuracy, and the post-processing of the simulation results for comparison with experimental data. In Section IV the comparison of

the simulations and experimental results is discussed. The conclusion is that the heat flux is greater than 10% of the free streaming limit. A low flux limit, e.g., 3%, disagrees with our results.

4.6.2 Experimental Arrangement

The experiments described here were performed using the six beam facility at the Science and Engineering Research Council's Central Laser Facility (4.11). Six synchronous laser beams were focused symmetrically by six f/1 lenses a distance 4 radii beyond the center of spherical targets. Wavelengths of 1.05 μm or 0.53 μm with pulse-lengths of 1.3 ns or 1.0 ns, respectively, were used.

The targets were glass spheres or empty glass shells with coatings of plastic and aluminium. The plastic and Al were vacuum deposited with thicknesses known to an accuracy of 10%. After being coated the targets were attached to 5 μm carbon support fibres for mounting in the target chamber. The background pressure in the chamber was less than 7×10^{-5} Torr.

Eight ion calorimeters were placed at various angles between the lenses. The closest angle to the centre lines of the laser beams allowed by the lens supports was 38°. The calorimeters consisted of pairs of tantalum discs, one exposed to the plasma, X-rays and scattered light, and the other exposed only to the scattered light. A differential temperature measurement thus gave the energy in the ions and X-rays. Sputtering data (4.21) show that the reflection coefficient for the plasma energy incident on the exposed disc is negligible. The variation in the energies measured by different detectors in the array was less than 20% for all of the shots described below, allowing calculation of the absorbed energy E_a from the average energy per steradian. The absorbed irradiance was given by $I_a = E_a/4\pi R^2\tau$ where $4\pi R^2$ is is the initial surface area of the target, and τ is the laser pulse length (full width half maximum).

A set of five Faraday cups 38 cm from the plasma was used to measure the ion velocity. A typical detector signal is shown in Figure 4.19,

illustrating the relatively narrow spread in velocity, which is 17% for the example shown. Values of the ion velocity v_i quoted below are the velocities corresponding to the peaks of the Faraday cup current. For the relatively narrow velocity distribution in this work, the mean velocity is less than 10% different from v_i.

The mass ablated from the targets was measured by the particle detectors. In essence this is given by

$$M = \frac{2E_a}{v_i^2} \qquad (1)$$

Allowance for the spread in velocity was made as discussed in reference (4.22), resulting in a small decrease from $2E_a/v^2{}_i$. In processing the Faraday cup signals ions of velocity less than 2×10^7 cm s^{-2} were neglected. In Figure 4.19, and from measurements taken with slower scans, it can be seen that there is negligible charge carried by ions slower than $v_i/2$.

A small correction was made to subtract the contribution of X-rays from the target from the measured E_a. This is most significant for the 0.53 μm experiments for which it was assumed that 15% of the absorbed energy was reradiated as X-rays. This value is an interpolation of data taken for Be and Ti targets (4.23). For the 1.05 μm data a 5% conversion to X-rays was assumed.

To calculate the specific mass ablation rate a time interval during which the mass M is ablated must be ascribed. As shown below the scaling of M and ($\dot{m}_s$) with the time average absorbed intensity I_a is approximately $I_a{}^{0.7}$. If the same scaling is assumed during the laser pulse, then the full width half maximum of the mass ablation rate will be the same as the fwhm of $(I_a(t))^{0.7}$. For the measured temporal shape of the 1.05 μm and 0.53 μm laser pulse this is $c\tau$ where $c = 1.1$ and τ is the fwhm of the laser power. The value of the specific mass ablation rate $\dot{m}_s$ is referenced to the initial surface area of the target and was then calculated from

$$\dot{m}_s = \frac{M}{4\pi R^2 c\tau}$$

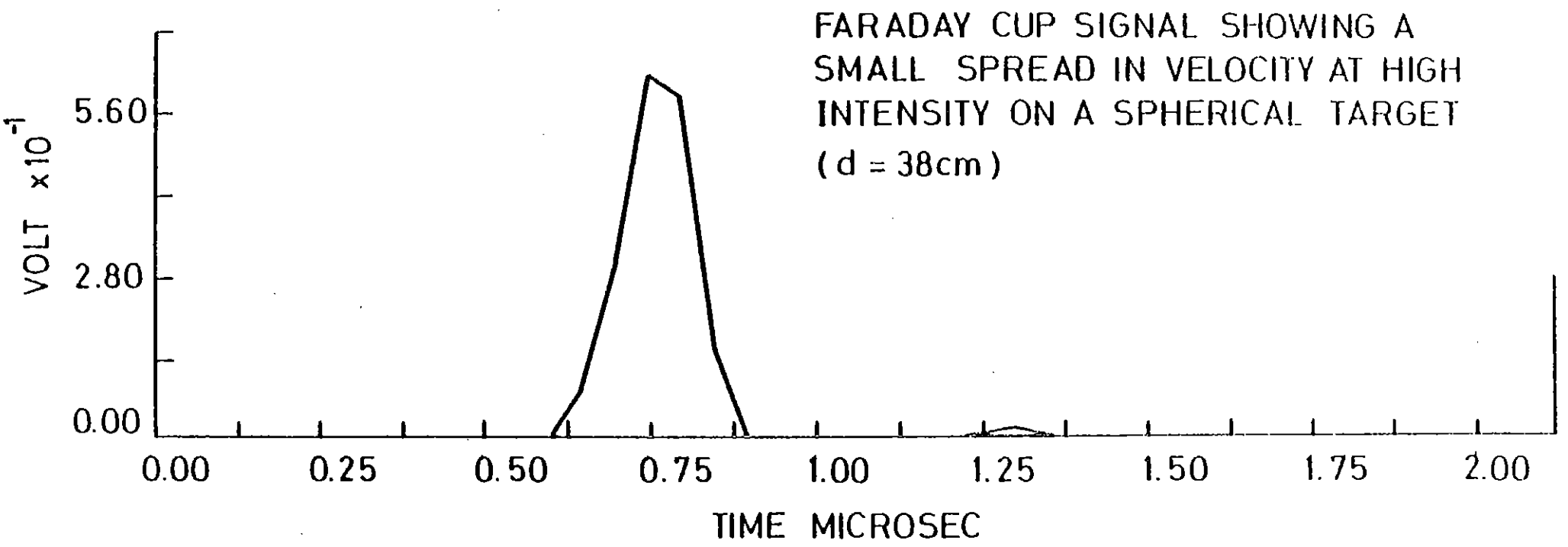

Figure 4.19 A typical Faraday cup signal, showing the small spread in velocity observed for spherical target irradiation.

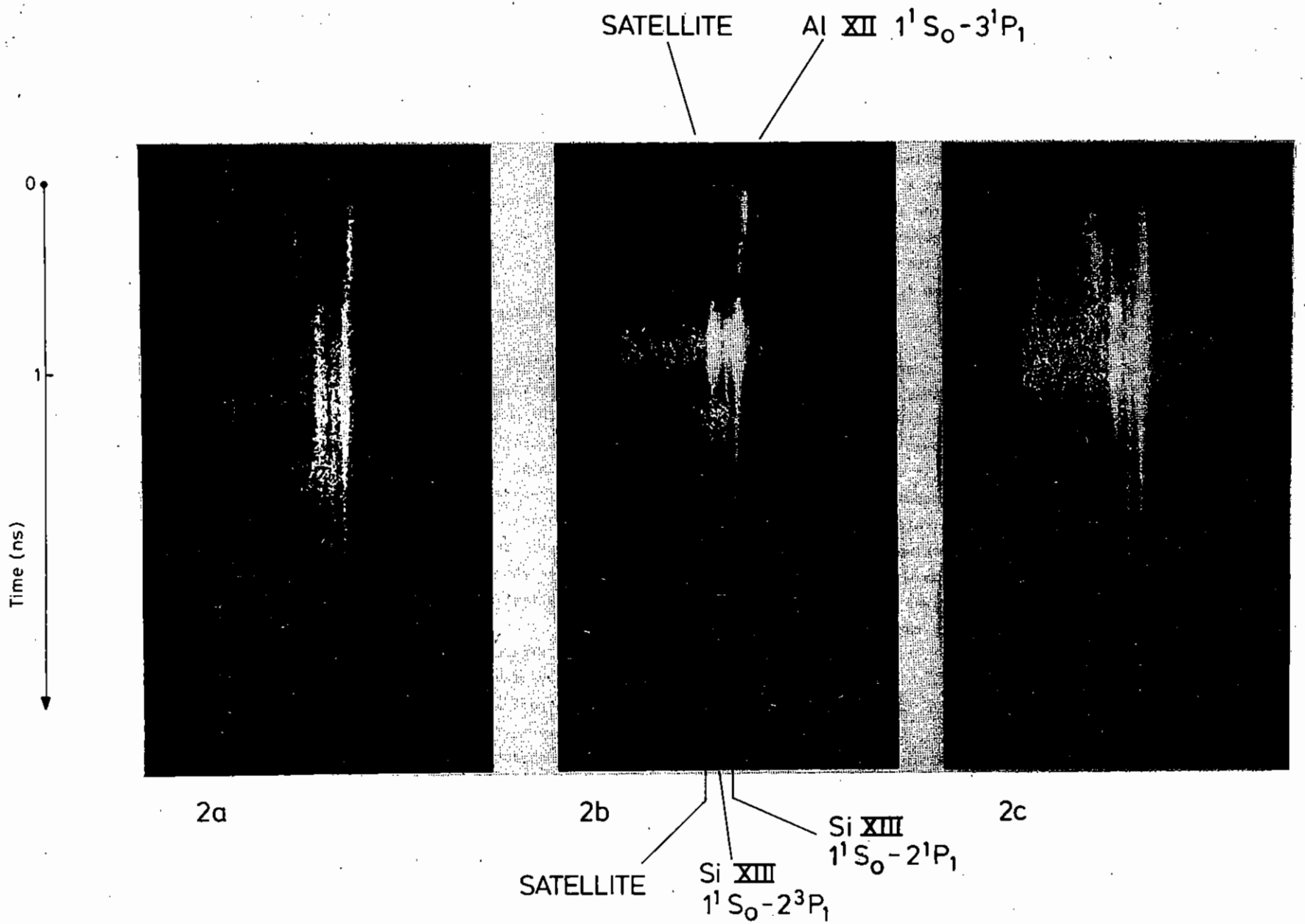

Figure 4.20 Examples of time resolved X-ray spectra of Al and plastic-coated glass targets irradiated at 0.53μm. (a) shows Al lines initially and a well defined delay for Si lines. (b) and (c) show precursor Si emission: on (b) this is resolved on the Si XIII $1^2S_0 - 2^1P_1$ line and its dielectronic satellites. The burn time τ_0 is taken from the start of the main Si emission. Note in (b) that the intensity of the Si precursor emission falls as the Al intensity falls.

For some very thin shell targets the mass recovered M was within 10% of the initial target. In such cases the data were discarded as the shell had been completely ablated away during the laser pulse.

The specific mass ablation rate was also determined from X-ray streak spectroscopy (4.24). A T&AP Bragg crystal was used with an X-ray streak camera of 50 psec time resolution, to observe helium-like emission lines from the Al and Si of the target coating. Figure 4.20 shows typical streaks. Initially the fiducial emission from the Al XII $1^1S_o - 3^1P_1$ and its dielectronic satellites is seen. In Figure 4.20(a) the intensity of these lines decreases as the Al ablates from the target; there then follows emission from the underlying Si at a time τ_b after the start of the Al emission.

One interesting feature of these streaks is the observation of a precursor to the main Si emission. Figure 4.20(a) shows this feature most clearly on the dielectronic satellites of Si XIII $1^1S_o - 2^1P_1$. A precursor is also seen on the I $^1S_o - 2\ ^1P_1$ transition, although the spectral coincidence to within 17 mÅ of the Al XIII $1\ ^1S_o - 3\ ^1P_1$ transition precludes the use of this line except for well resolved cases as in Figure 4.20(b). In measuring the mass ablation rates the precursor was ignored; the delay time τ_b was taken from the beginning of the Al dielectronic satellite to the beginning of the main Si dielectronic satellite. For Figures 4.20(b) and 4.20(c), τ_b was taken as 600 ps and 630 ps respectively. The specific mass ablation rate was calculated from these data assuming

$$\dot{m}_s = m_s\, c'/\tau_b \qquad (3)$$

where m_s is the areal density of the plastic and Al coating and c' is a small correction factor allowing for the time variation of the ablation rate (4.19).

Experiments were conducted with up to 40J of 0.53 μm radiation, or up to 200 J of 1.05 μm radiation, at the target. At 0.53 μm the absorbed irradiance was varied from 2×10^{12} W cm^{-2} to 9×10^{13} W cm^{-2}. At

1.05 μm the range of absorbed irradiance was from 3×10^{12} W cm^{-2} to 3×10^{13} W cm^{-2}. Examples of target details at either end of this range are shown in Table 4.03.

The variation v_i with I_a is shown in Figure 4.21(a) and Figure 4.21(b) for 0.53 μm and 1.05 μm respectively. The least squares fit to the data is

$$v_i = (4.29 \pm 0.07)10^7\ (I_a/10^{13}\ \text{W cm}^{-2})^{0.13 \pm 0.02}\ \text{cm sec}^{-1} \qquad (4)$$

$$v_i = (5.0 \pm 0.13)10^7\ (I_a/10^{13}\ \text{W cm}^{-2})^{0.18 \pm 0.04}\ \text{cm sec}^{-1} \qquad (5)$$

in the range 10^{12} W cm$^{-2} < I_a < 10^{14}$ W cm^{-2}

The values of the mass ablation rates as a function of I_a are plotted in Figure 4.22(a) and Figure 4.22(b) for 0.53 μm and 1.05 μm respectively. At 1.05 μm there were a limited number of shots with X-ray data particularly at high I_a. As can be seen at high I_a there is good agreement between the ion and the X-ray measurements of $\dot{m}_s$, with the X-ray measurements being higher by 30% in this range. The single X-ray measurement at low intensity, $I_a = 3 \times 10^{12}$ W cm^{-2} is discrepant, probably because of beam inhomogeneities or target imperfections on that single shot. It also appears that the values of $\dot{m}_s$ obtained with shells are slightly lower than the values obtained with solid targets.

From Figure 4.22(a) it appears that the data at low intensity scale more slowly with I_a than the data at high intensity. The limited number of data points precludes a definite conclusion, but the shaded areas in Figures 4.21(a), 4.22(a), 4.28(a) and 4.29(a) illustrate this possibility. In contrast the least squares fits are fits with single exponents. For both wavelengths there is a far greater range of data for the ion measurements. The least squares fit to the ion data values of $\dot{m}_s$ are

$$\dot{m}_s = (0.85 \pm 0.03)10^5\ (I_a/10^{13}\ \text{W cm}^{-2})^{0.72 \pm 0.03}\ \text{g cm}^{-2}\text{s}^{-1} \qquad (6)$$

and

$$\dot{m}_s = (0.81 \pm 0.03)10^5\ (I_a/10^{13}\ \text{W cm}^{-2})^{0.86 \pm 0.07}\ \text{g cm}^{-2}\text{s}^{-1} \qquad (7)$$

Shot, λ (μm)	Target				E_a J	I_a 10^{13} Wcm^{-2}	v_i 10^7 $cm\ sec^{-1}$	$\dot{m}_s$ 10^5 $gm\ cm^{-2}\ sec^{-1}$	M/Z
	R(μm)	ΔR μm							
		glass	plastic	Aluminium					
09090481 0.53	36	1.2	1.7	0.1	9.7	5.8	5.0	3.6	2.0
06060481 0.53	143	1.3	1.6	0.1	17.2	0.67	4.4	0.58	2.7
22010980 1.05	72	-	-	-	29.3	3.0	6.0	1.9	2.4
10010980 1.05	137	-	-	-	27.2	0.77	5.1	0.67	3.1

TABLE 4.03

Typical target and laser conditions and deduced ion quantities for 0.53 μm and 1.05 μm spherical experiments

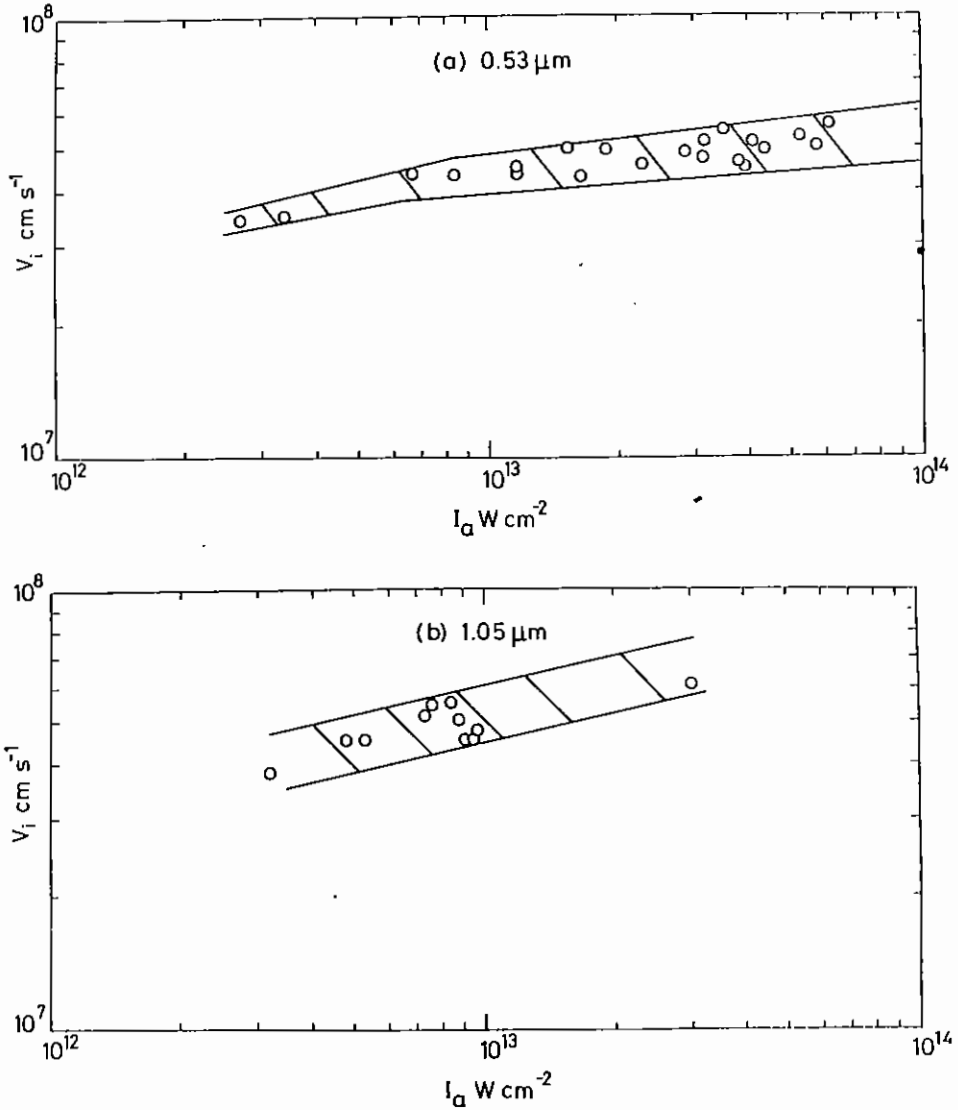

Figure 4.21 Peak ion velocity as a function of the absorbed irradiance at 0.53μm (a) and 1.05μm (b).

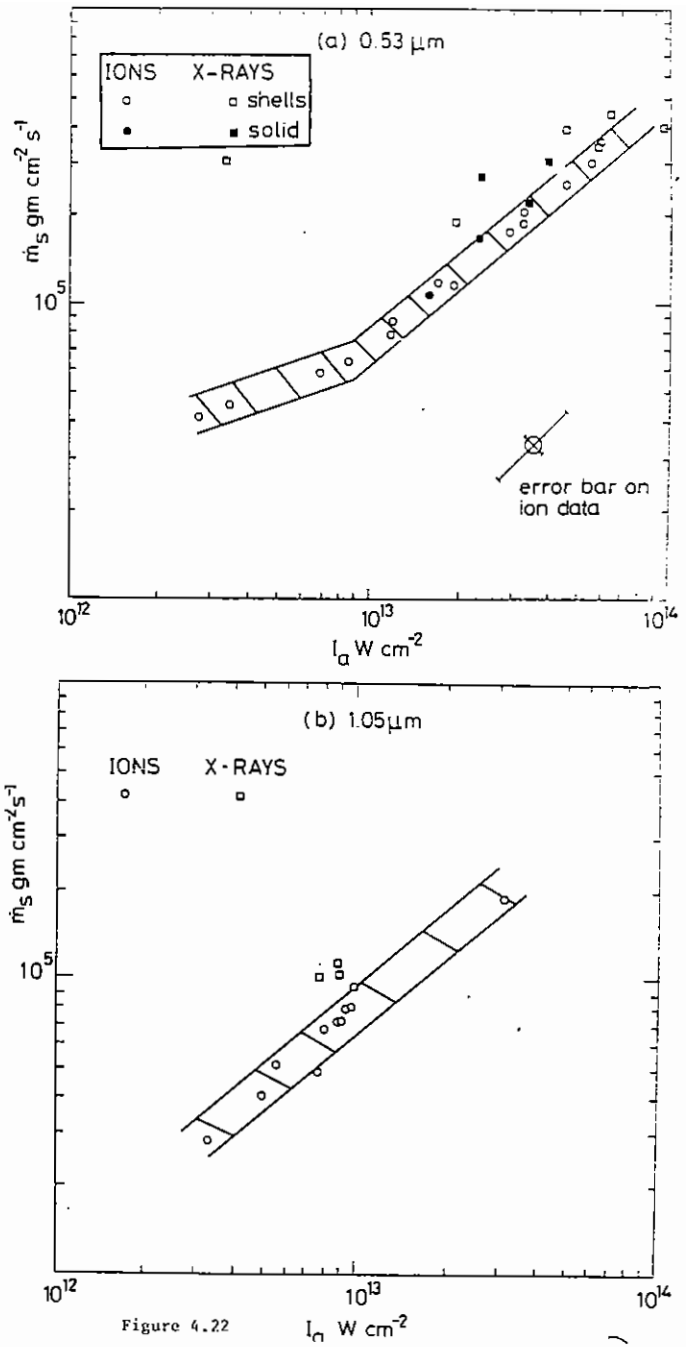

Figure 4.22

Specific mass ablation rates $\dot{m}_s$, for 0.53μm (a) and 1.05μm (b) irradiation, respectively, as a function of the absorbed irradiance I_a. A typical error bar, with a larger uncertainty at 45°, is shown. The bands represent a fit to the ion data.

for 0.53 μm and 1.05 μm respectively, with the smaller error for the former reflecting the better quality of the data.

The only other spherical mass ablation data known to us are 1.05 μm data at $I_a \sim 10^{13}$ W cm^{-2} for which the least squares fit is

$$\dot{m}_s = 0.7 \times 10^5 (I_a/10^{13} \text{ W cm}^{-2})^{0.7} \text{ g cm}^{-2}\text{s}^{-1} \quad (8)$$

showing fair agreement with our data. Our results show that there is a considerably more rapid increase of $\dot{m}_s$ with I_a for spherical targets than for plane targets (4.19). This is illustrated in Figure 4.23. where values of $\dot{m}_s$ from these spherical and other plane target data (4.19) are compared. In reference (4.19) it is argued that the plane target data underestimates $\dot{m}_s$ because of lateral loss of energy.

Even for 1.05 μm irradiation of plane targets with a larger focal spot (4.20) the specific mass ablation rate is

$$\dot{m}_s = 0.54 \times 10^5 (I_a/10^{13} \text{ W cm}^{-2})^{0.6} \text{ g cm}^{-2}\text{s}^{-1}$$

giving a lower mass ablation rate than for this spherical experiment.

The ratio of atomic mass to charge M/Z at the chamber wall was also obtained from the ion data (4.22). It ranged from 2 to 3 with no systematic dependence on I_a observed. Examples are given in Table 4.03, collumn 10. The relatively poor vacuum in the chamber, $\sim 7 \times 10^{-5}$ Torr, probably accounted for this variation although to first order this does not affect the measurement of the ablated mass.

Agreement between the X-ray and ion derived specific mass ablation rates indicates that fast electron driven ablation is not causing significant ablation after the laser pulse. Under conditions of fast electron driven ablation (4.26), ablation would occur for the time taken for the fast electron heated material to expand. This would be approximately equal to the depth of the preheated material (4.27) divided by the thermal velocity, and could be longer than the laser pulse length. Consequently

the use of τ, the laser pulse length in Equation (2) would overestimate the mass ablation rate. This is not a major effect since values of $\dot{m}_s$ derived from ion measurements are only slightly lower than those derived from X-ray measurements.

In deducing the ion mass ablation rates energy conservation is used. It can be seen from the above least square fits to $\dot{m}_s$ and v_i that

$$\tfrac{1}{2}\dot{m}_s \, v_i^2/I_a = 0.78(I_a/10^{13} \text{ W cm}^{-2})^{-0.02}$$

and

$$\tfrac{1}{2}\dot{m}_s \, v_i^2/I_a = 1.01(I_a/10^{13} \text{ W cm}^{-2})^{0.02}$$

for 0.53 μm and 1.05 μm respectively. For the 0.53 μm data 80% of the absorbed energy is in the ion flow, because of the assumption about X-ray conversion. For the 1.05 μm data energy conservation is demonstrated to within 20% over the range of I_a used. Exact conservation is not expected as v_i is the velocity of the peak current trace and there is a limited spread in ion velocities. The observed weak scaling is due to the spread in ion velocities changing with I_a.

However energy conservation is not implicit in the X-ray measurements of mass ablation rates. The agreement between the ion and X-ray measurements of mass ablation rates therefore demonstrates directly that the absorbed energy is recovered in the ablation flow.

4.6.3 Simulation

The well controlled experimental conditions provided by spherical symmetry allow an accurate comparison with a simple one-dimensional Lagrangian code that has been adapted from MEDUSA (4.28). The code has been checked against an analytic solution (4.29). Additionally the six beam focusing has been simulated by a three-dimensional ray tracing through the one-dimensional plasma to determine the energy deposition.

The code MEDUSA was used in spherical geometry with a zone spacing of approximately 3×10^{-6} gm cm^{-2}. The electron energy equation was

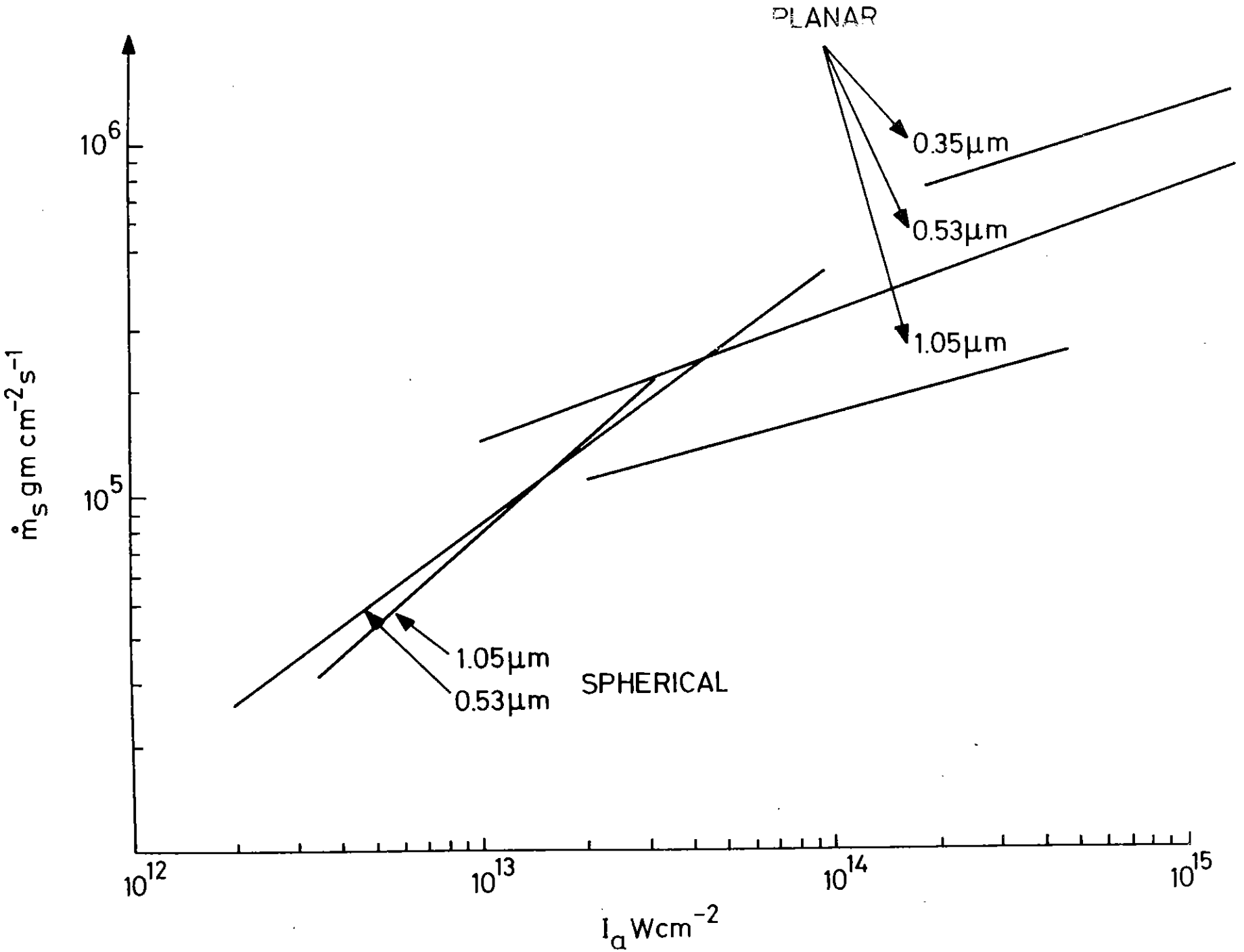

Figure 4.23 The specific mass ablation rate $\dot{m}_s$ as a function of absorbed irradiance I_a in spherical geometry and in plane geometry (4.19). Note the difference in the scaling.

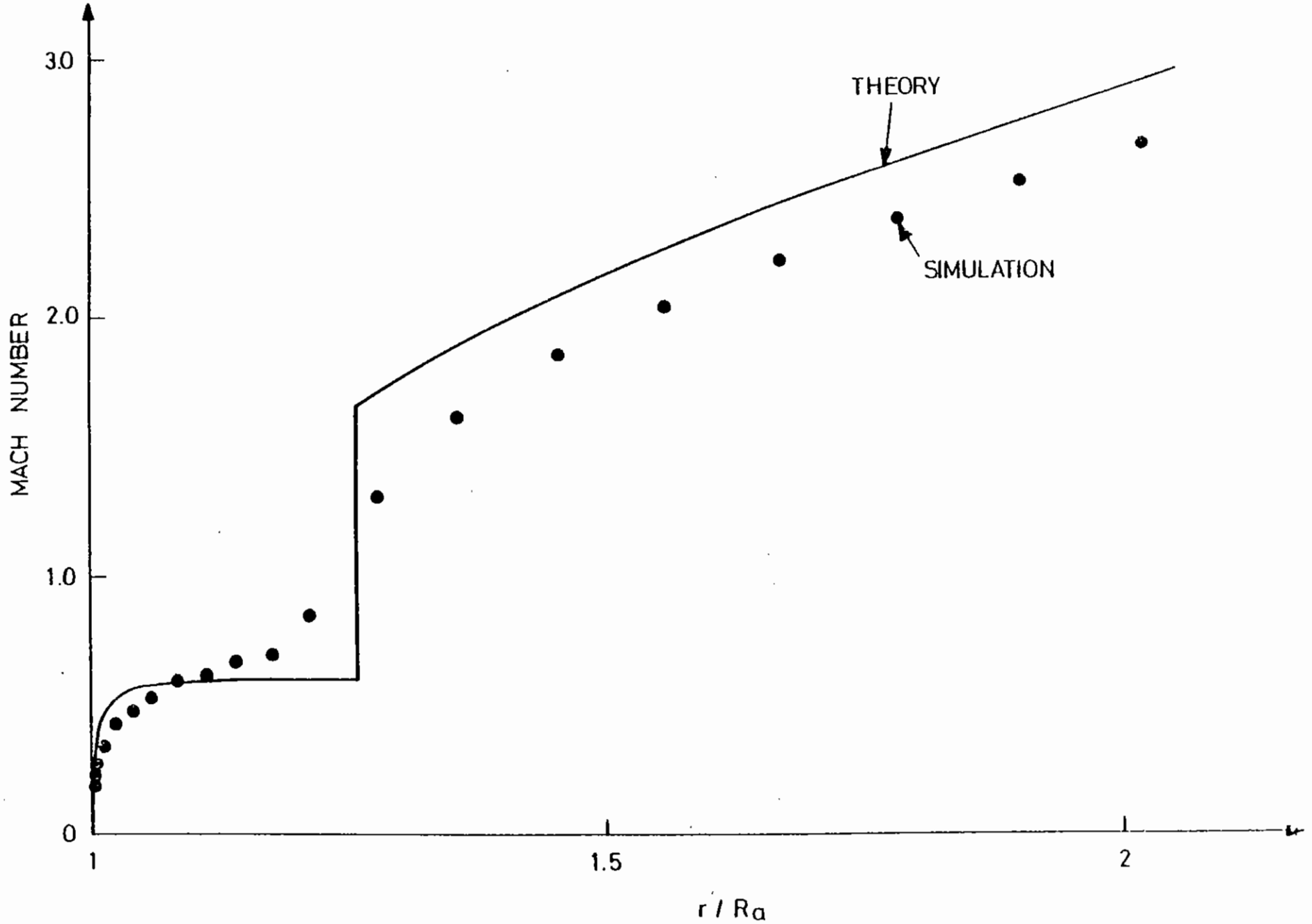

Figure 4.24 Isothermal Mach number as a function of radius normalised to the ablation radius R_a. The solid curve is the theoretical profile(4.29). Simulation matches theoretical condition: $\lambda = 1.05\mu m$, $I_a = 8.33 \times 10^{12}$ W cm^{-2} deposition only at critical, solid Al sphere radius 100μm, f = 0.03. Simulation results are shown 4 nsec after switching on the constant laser pulse.

TABLE 4.04 Comparison of observable from the simulation and from the analytic theory for the test case of Fig 4.24

Observable	Units	Analytic theory	Simulation
Temperature at critical density	K	5.4×10^6	$(4.9 \pm 0.1)10^6$
Radius at critical density	Ablation radius	1.21	1.26
Ablation pressure	Mbar	1.72	1.71 ± 0.02
Mass ablation rate	$gsec^{-1}$	81	93

differenced as suggested in Reference (4.29). The classical electron thermal conductivity K was used (4.30) with a sharp cut off flux limit, so that the heat flow q was given by

$$q = MIN(q_{cl}, fq_{fs})$$

where f is the heat flux limit, $q_{cl} = -KVT$ and $q_{fs} = nkT\left(\frac{kT}{m_e}\right)^{\frac{1}{2}}$.
It is well known that with deposition near to the critical density it is difficult to solve the hydrodynamic equations accurately because of the practical necessity of a relatively coarse zone in an ablating plasma (4.30). Therefore we have compared our code results with the analytic solution (4.29) to check that the numerical solution is accurate. For this purpose a simulation with energy deposition only at critical density and with the same zoning as used in the production runs discussed below was performed. The result is shown in Figure 4.24 and Table 4.04. Table 4.04 shows that values for the observables (discussed below) are in good agreement with the analytic theory. Figure 4.24 shows the Mach number as a function of radius, which agrees well with the analytic results.

The focusing conditions used in the experiment were empirically chosen to give spherically uniform X-ray emission. However, refraction of the non-radial rays and inverse Bremsstrahlung absorption leads to significant energy deposition well below critical density. To allow for this a three-dimensional ray trace was performed at each time step of the simulation. A set of rays representing a Gaussian beam of fill factor 0.5, focused 4 radii beyond the target centre by six F/1 lenses was traced through the spherically symmetric plasma. The energy deposition was calculated according to the corrected inverse Bremsstrahlung absorption coefficient (4.31) and resonance absorption (4.32). Resonance absorption was implemented for those rays which were reflected at the zone next to critical density. The fraction of the ray energy absorbed by tunnelling to critical density was taken from absorption fractions calculated for oblique incidence on a plane surface (4.32). However resonance absorption was insignificant compared with inverse Bremsstrahlung for the low values of $D\lambda^2$ in this work. The energy deposition as a function of r, θ, ϕ for six beams could then be calculated.

The most significant effect of the ray tracing was to deposit the energy at lower densities than without refraction. This is illustrated in Figure 4.25 where the power deposition at the end of a 1 ns, 0.53 μm simulation is shown at two angular positions compared with a simulation without refraction. Calculations including refraction show a 10% angular variation in the power deposition, which is in qualitative agreement with the experimental observation that this focusing condition led to uniform X-ray emission.

The relative invariance of power deposition with angle allows the use of the ray tracing energy deposition in the one dimensional hydrodynamic code. If $U(r, \theta, \phi)$ is the specific power deposition calculated by the ray tracing then a spherical average

$$U(r) = \frac{1}{4\pi} \int_0^{2\pi} \int_0^{\pi} U(r, \theta, \phi) \sin\theta \, d\theta \, d\phi$$

can be used as the power deposition in the hydrodynamic code. This average specific absorbed energy $U(r)$ was one of the results of the simulation. For comparison with the experiments an absorbed irradiance I_a was calculated with reference to the initial target surface area.

Simulations using energy deposition profiles calculated for selected angles instead of an average varied by at most 10% in the observables from simulations using the averaged deposition.

Simulations with and without refraction are compared in Table 4.05. For the simulation without refraction, rays were incident in a radial direction and were attenuated by inverse Bremsstrahlung up to the critical density where the remaining energy was deposited. As expected for similar deposited powers the mass ablation rates and ablation pressures are higher without refraction because of the higher average density of power deposition.

The observables were recovered from the simulations in the same way as in the experiment. Simulations were run for 5 nsec after the laser pulse. The plasma energy E_a was calcualted. A Faraday cup signal was

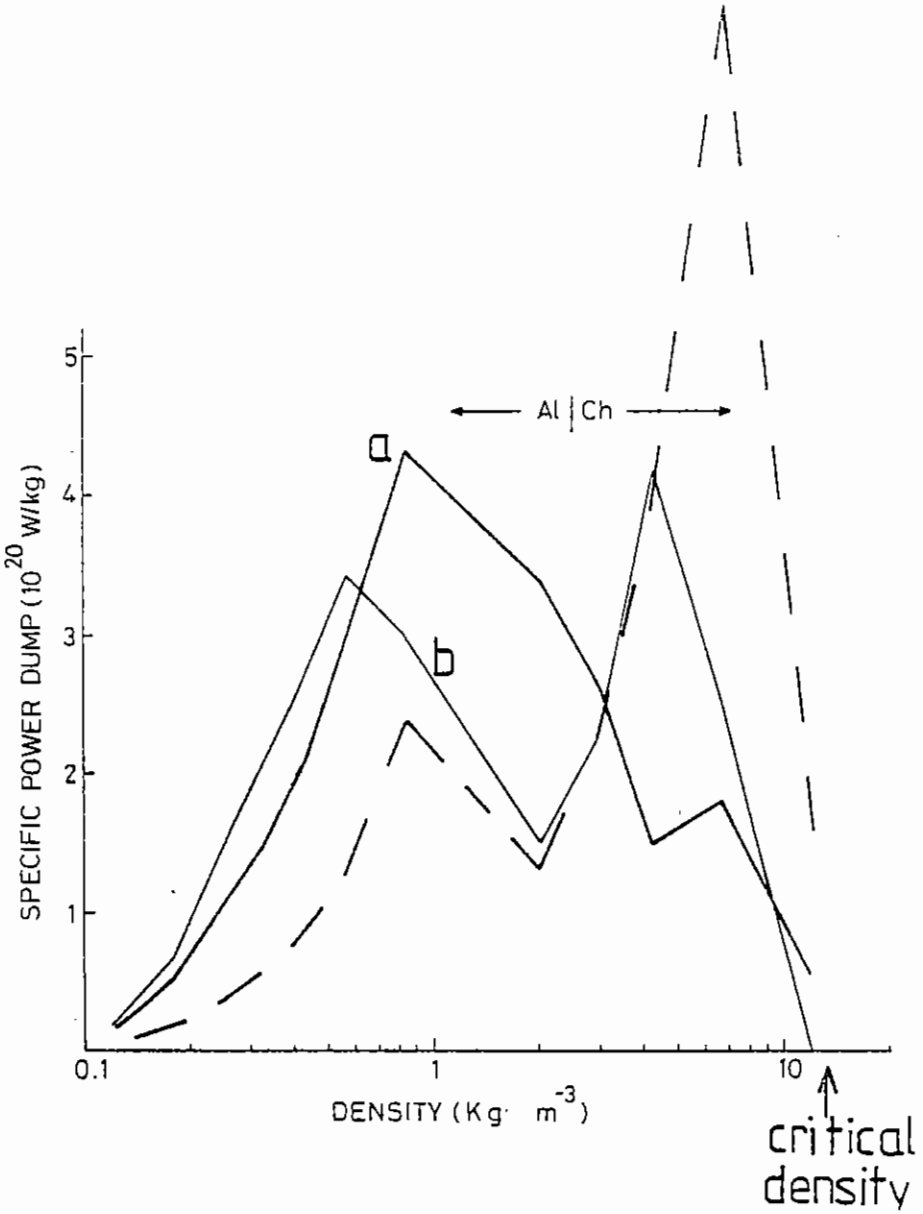

Figure 4.25 Power deposition versus density for an aluminium coated plastic target. The six f/1 laser beams are defocused 4 target radii beyond the centre of the target. Power deposition profiles are given for two points on the target.
(a) The centre of one of the beams. In spherical polar co-ordinates,
$\theta = 0, \phi = 0.$
(b) The point where three neighbouring beams overlay, eg
$\theta = \frac{\pi}{4}, \phi = \frac{\pi}{4}$. Critical density is 13 kg m^{-3}. A run with the same absorbed irradiance but without refraction is shown by the dashed line.

TABLE 4.05

	I_a W cm^{-2}	$\dot{m}_s$ gm cm^{-2} sec^{-1}	P_a (M bar)
Without refraction	$2.4 \quad 10^{13}$	$1.8 \quad 10^{5}$	5.0
With refraction	$2.2 \quad 10^{13}$	$1.2 \quad 10^{5}$	3.3

Comparison of macroscopic quantities from simulations with and without refraction. A pulse of 1 nsec for 0.53 μm irradiation is used.

reconstructed and analysed to give the velocity and hence mass of material travelling outwards at velocities greater than 2×10^7 cm sec^{-1}. The simulated specific mass ablation rate $\dot{m}_s$ was calculated as in Equation (2). The X-ray mass ablation rate was calculated form the Lagrangian motion of the T_e = 300 eV point. The ratio of the "X-ray mass ablation rate" to the integrated ion mass ablation rate is shown in Figure 4.26. For times longer than 0.5 ns there is good agreement between the two methods, and it should be noted that the experimental burn times τ were generally longer than 500 ps.

One notable feature of the targets was that the specific mass ablation rate depended on the atomic number of the target coating. The thin Al layer increased inverse Bremsstrahlung absorption in the low density plasma compared to a simple plastic coating, leading to a lower value of $\dot{m}_s$ for a given I_a. Increasing the thickness of the Al from 0.1 μm to 0.2 μm at an absorbed intensity of approximately 2×10^{13} W cm^{-2} reduced the mass ablation rate by 17% with a 10% flux limit, and 30% with a 3% flux limit. In general, dispensing with the 0.1 μm Al layer led to an increase in $\dot{m}_s$ for a given absorbed intensity at 10% flux limit and a 20% increase for a 3% flux limit.

The specific mass ablation rate and the ablation pressure are closely related. In plane geometry the quantities $\dot{m}_s = \rho v$ and $p + \rho v^2$ are spatial invariants for a steady state. Hence

$$P_a = \dot{m}_s v_i = (2\dot{m}_s I_a)^{\frac{1}{2}}$$

where v_I is the ion velocity when $p = 0$, ie at the wall of the target chamber.

In spherical geometry $4\pi r^2 \dot{m}_s$ is an invariant of the flow, so that $\dot{m}_s$ varies as $1/r^2$. The simulations show that the pressure drop occurs principally at the critical density surface and so approximately

$$P_a = \dot{m}_s^{cr} v_i$$

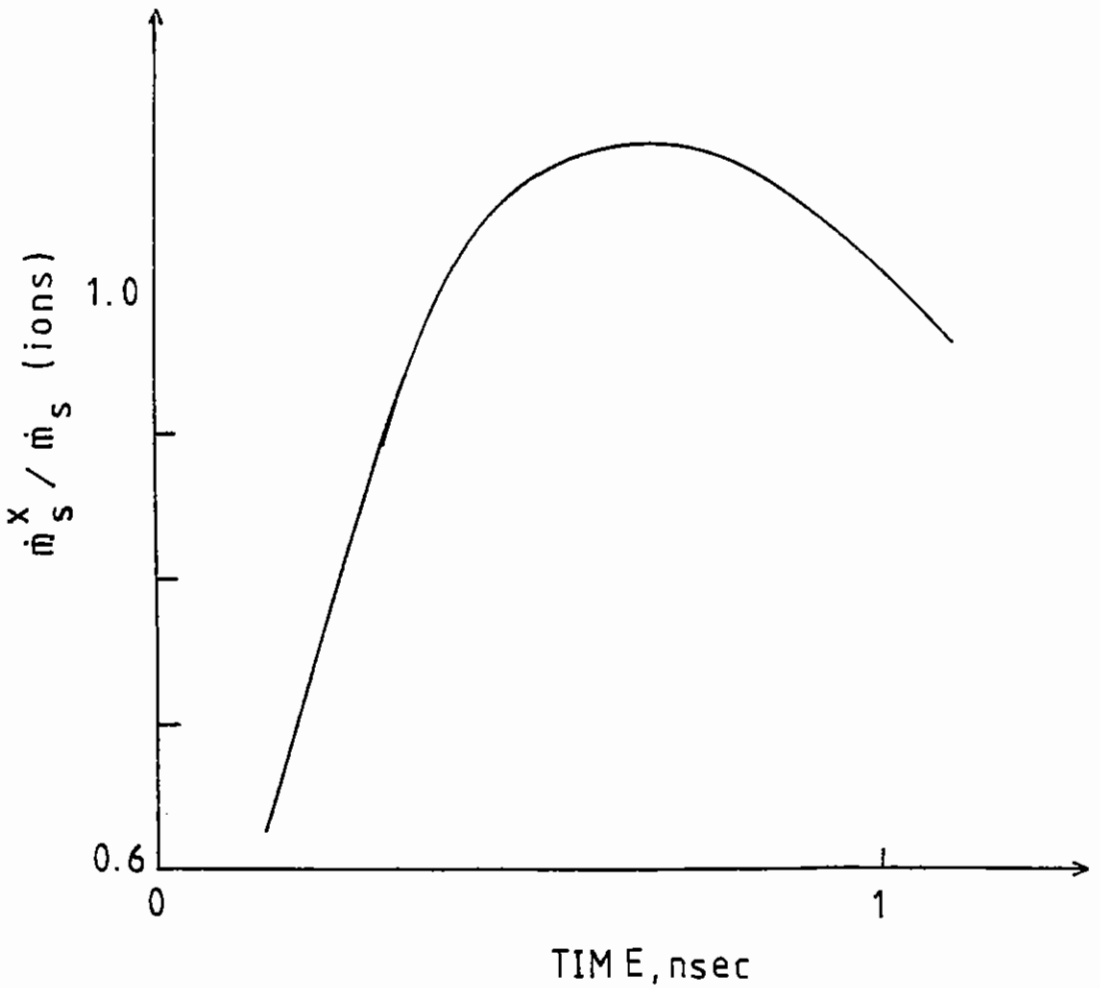

Figure 4.26 Comparison of the simulated specific mass ablation rates from X-ray streak spectroscopy $\dot{m}_s^x$ and the ion diagnostics $\dot{m}_s$. The value of $\dot{m}_s^x$ (t) is the average from 0 to t: $\dot{m}_s$ is averaged over the pulse.

where $\dot{m}_s^{cr}$, the specific mass ablation rate at the critical density surface, is generally less than $\dot{m}_s$, the specific mass ablation rate referenced to the initial radius of the target. From the simulations a correction factor

$$\gamma = \frac{\langle P_a \rangle}{\dot{m}_s v_i}$$

where $\langle P_a \rangle$ is the time averaged ablation pressure, can be calculated. This correction factor takes account of the separation of the critical density surface and the initial radius, and also the non local pressure gradient.

Values of γ from the simulation are shown in Figure 4.27. It is seen that is weak function of I_a and λ, allowing a measurement of ablation pressure from

$$P_a = \gamma \dot{m}_s v_i$$

4.6.4 Discussion

The experimental and theoretical values of velocity and specific mass ablation rate are compared in Figure 4.28 and Figure 4.29 respectively.

The experimental values are derived from the ion data. The laser power and target sizes in the simulations were changed in the same way as in the experiment. The targets has the same coatings in the simulation as in the experiment. Values of the flux limit shown are f = 0.01, f = 0.03 and f = 0.1 for λ = 0.53 μm and f = 0.03 and f = 0.1 for λ = 1.05 μm.

It is clear from Figures 4.28 and 4.29 that f = 0.03 gives too low a value of the specific mass ablation rate and too high a value of the plasma velocity. A flux limit of f = 0.1 gives better agreement for both of these observables, although at high intensities with both 0.53 μm and 1.05 μm radiation the simulation results differ from the experimental results. Increasing the flux limit above f = 0.1 does not give any further change in the value of the observables in the intensity range

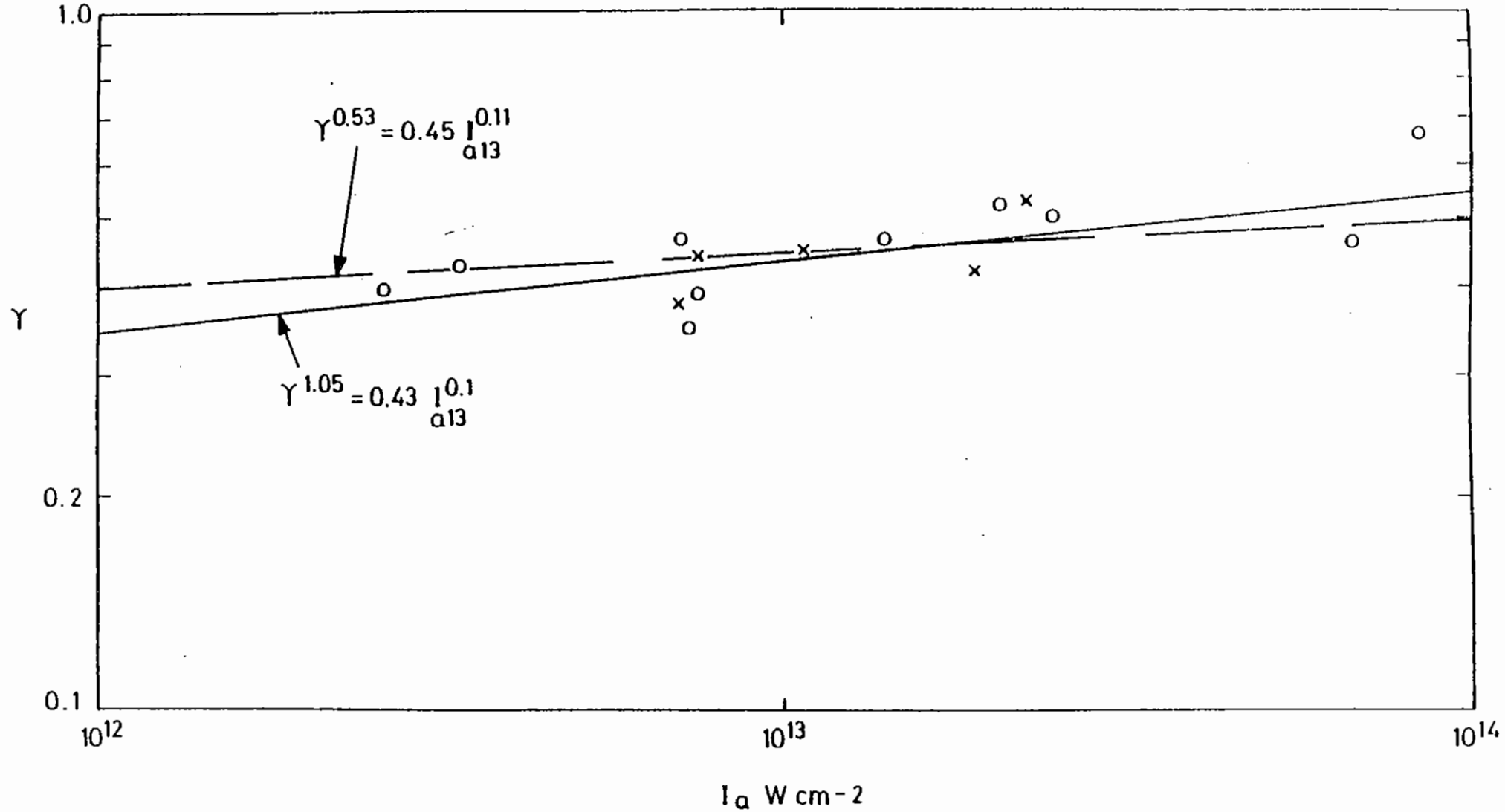

Figure 4.27 Values of the correction factor $\gamma = P_a/\dot{m}_s v_i$ from the simulation for 0.53μm, (0) and 1.05μm (x). Least squares fit to the simulation points are shown.

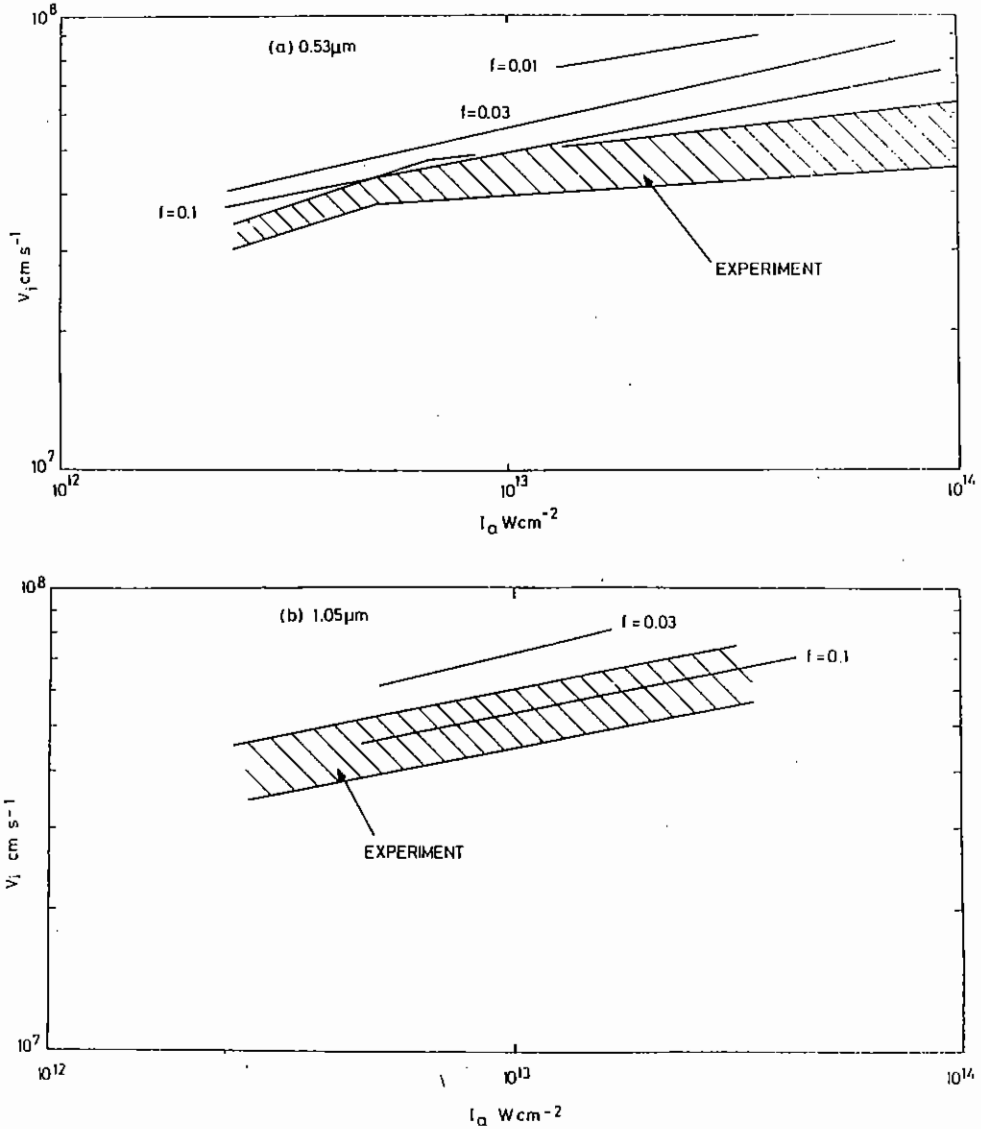

Figure 4.28 Comparison of experimental results, hatched area, and simulation results for the peak ion velocity at 0.53μm (a) and 1.05μm (b). Simulation results are shown for various values of the flux limit f.

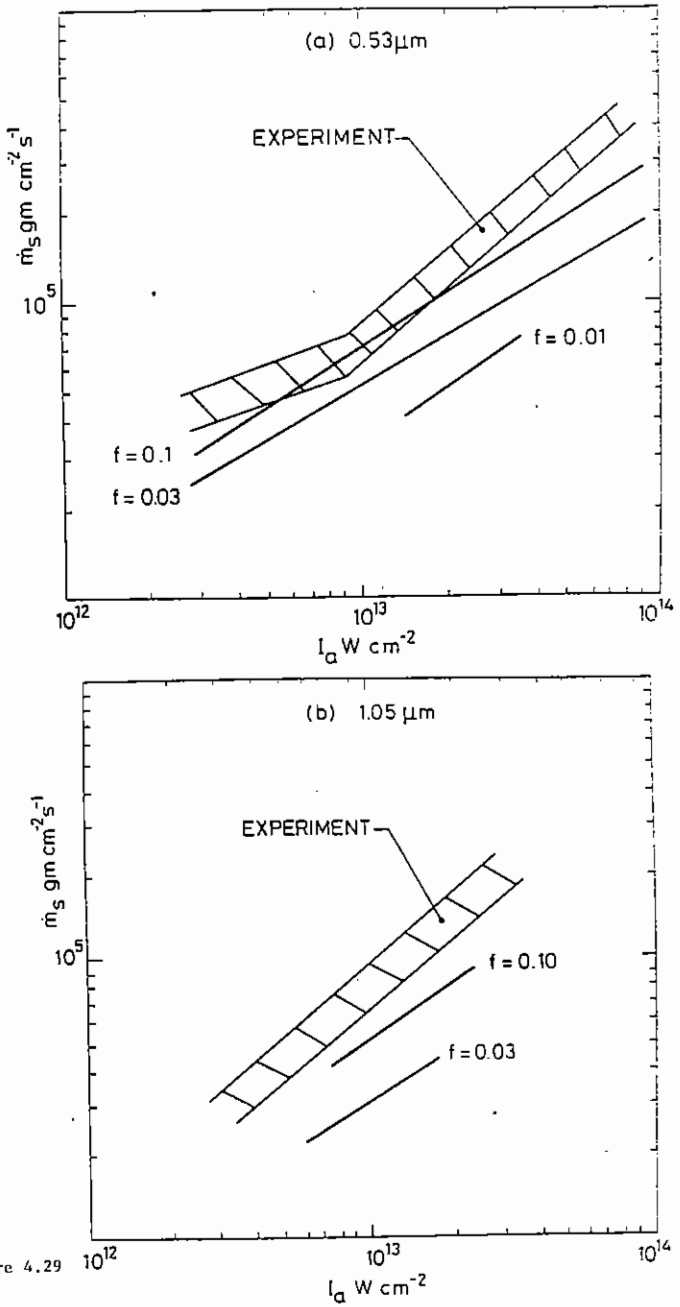

Figure 4.29

Comparison of experimental results, hatched area, and simulation results for the specific mass ablation rates at 0.53μm (a) and 1.05μm (b). Simulation results are shown for various values of the flux limit f. There is a 10% uncertainty in the simulation results. Flux limits higher than f = 0.10 have an insignificant effect on $\dot{m}_s$.

overlapping the experimental data. It is fortuitous that the simulations give similar values for f = 0.1 as an analytic theory (4.29), despite the fact that the latter assumes just an energy deposition at the critical density.

A flux limit of 0.1 is at variance with most although not all (4.33, 4.34) previous flux limit experiments. However in this experiment we can rule out several possible sources of error.

(1) Errors in the absolute calibration of the plasma calorimeters make little difference to the comparison between the values of $\dot{m}_s$ derived from ion data and the simulations. An error of a factor S in E_a will cause errors of the same amount in both $\dot{m}_s$ and I_a. But as $\dot{m}_s$ is approximately proportional to $I_a^{0.75}$ this would cause a much smaller discrepancy in the comparison with the simulation, namely $S^{0.25}$. This insensitivity to the calorimeter calibration arises from the use of the absorbed irradiance I_a and because the exponent of the scaling of $\dot{m}_s$ to I_a is close to unity.

A possible calibration error of 10% plus an error of 10% because of the albedo can be estimated for the calorimeters. An increase in E_a by 20% would decrease the difference between the X-ray and ion derived $\dot{m}_s$. However the ion derived values of $\dot{m}_s$ would increase with respect to the simulation by 5%. This is manifested by the error bars on Figure 4.22 being elliptical, with their major axis at 45° to the axes.

(2) For a similar reason, errors in focusing, and systematic errors because the calorimeters are all positioned between lenses, have little effect. If one beam is focused incorrectly the locally enhanced $\dot{m}_s$ will be approximately proportional to the enhanced local I_a. Shots with greater than 20% angular variation in E_a were rejected.

(3) Because of the spherical geometry there are no edge losses.

Nevertheless, the simulations with large heat fluxes give slightly higher values of $\dot{m}_s$ than the experimental results. There appears to be some

additional energy transport process which is enhancing the mass ablation rate in the experiment. At least three possible processes are omitted from the simulations:

(1) Fast electron preheat is neglected. For λ = 0.53 μm the highest $I_a\lambda^2$ is 2×10^{13} W cm^{-2}μm^2 and the highest $I_{inc}\lambda^2$ is 4×10^{13} W cm^{-2}μm^2. The fast electron temperature T_H would be (4.32) approximately 2 keV. At 1.05 μm the highest $I_a\lambda^2$ is 3×10^{13} W cm^{-2} μm^2 corresponding to $I_{inc}\lambda^2 = 2 \times 10^{14}$ W cm^{-2} μm^2 and T_H approximately 4 keV. Fast electrons at these low values of T_H would not be expected to have a major effect because of their short range, although it is conceivable that they could cause an increase of 20% in the mass ablation rate. The greater discrepancy at 1.05 μm, for which $I_{inc}\lambda^2$ is larger, favours this explanation.

(2) Similarly, radiative preheat would augment collisional transport and increase the specific mass ablation rate. Some evidence for this effect is seen in Figure 4.20, in the precursor X-ray emission. It is evident from the energy conservation discussion of Section 4.6.2 that it is correct to ignore this precursor emission in measuring $\dot{m}_s$, suggesting that the precursor arises from preheating or local burnthrough. In Figure 4.20(b) the intensity of the precursor emission drops as the intensity of the Al emission decreases. This suggests the possibility that the precursor is being caused by X-radiation from the ablating plasma.

The precursor emission could be evidence for burn through in a few spots because of filamentation of the laser beam and self-focusing in the plasma. In the case of local effects, the scaling of $\dot{m}_s$ with the local I_a should be as for plane data where lateral losses dominate , ie, $\alpha\ I_a^{0.3}$. In this case local enhancements of a factor of approximately 10 in the beam intensity would be needed to explain the precursor. No evidence for this was seen in X-ray emission pictures, and such local burn through would not be expected to switch off, as seen in Figure 4.20(b).

Simple estimates show that it is possible for significant radiative energy to be transmitted through the plastic, below its K edge, and be absorbed

in the surface of the underlying Si. However lack of detailed knowledge of the X-ray spectrum in this region precludes quantitative predictions at this stage.

(3) Beam inhomogeneities and self-focusing are neglected. Their effect (in locally increasing $\dot{m}_s$) can be neglected to first order as discussed above. However, the increase in $I\lambda^2$ would give rise to a greater T_H and more fast electrons.

The major conclusion from the comparison of experimental results and simulaitons is that there is large heat flux. A similar conclusion, that heat fluxes can exceed 10% of the free streaming limit, has been reached in some other experiments (4.33, 4.34). But in general this conclusion is in contrast to the conclusion of a low flux limit inferred by most other experiments. However our use of spherical geometry and particle diagnostics eliminates some common systematic errors such as lateral energy loss, magnetic field generation and the effect of different ionisation models.

Recent theoretical work supports the conclusion of a large heat flux. Two independent theoretical treatments of the heat flow in non-turbulent plasmas (4.35, 4,36) show that the heat flux can exceed 10% of the free streaming limit. There remains the possibility of a low flux limit being caused by turbulence. Direct experimental evidence for turbulent inhibition of heat flow has been obtained (4.37) in a plasma where the number of particles in a Debye sphere $n\lambda_D^3 \sim 10^2$. However in laser solid interation experiments, because $Z/n\lambda_D^3$ in the conduction region is higher it is hard to explain heat flux inhibition by ion acoustic turbulence (4.38). We can therefore conclude that the high heat fluxes we observe are in agreement with the most recent theoretical expectation.

The experimental results are used to derive values for this ablation pressure, from

$$P_a = \gamma \dot{m}_s v_i$$

in Figure 4.30. The least squares fits to the data are

$$P_a = (1.63 \pm 0.04)(I_a/10^{13}\ W\ cm^{-2})^{0.95 \pm 0.02} Mbar$$

and

$$P_a = (1.81 \pm 0.07)(I_a/10^{13}\ W\ cm^{-2})^{1.14 \pm 0.07} Mbar$$

for 0.53 μm and 1.05 μm respectively.

These pressures are probably lower limits on the ablation pressure in the experiments because of the low value of γ used. There is some evidence that the experimental results are not adequately represented by the one dimensional code. The disagreement of $\dot{m}_s$ at high I_a at 0.53 μm and the precursor emission are evidence of some physical process in addition to that included in the code. Additional processes, by transporting energy to higher density more quickly than in the simulation, would increase the ablation pressure. That is, the experimental γ factor may be higher than in the simulation. Analysis of implosion measurements of spherical experiments at 1.05 μm gives good agreement with the 1.05 μm pressures in this work (4.06). Preliminary analysis of implosion measurements at 0.53 μm indicates pressures a factor of 2 higher than the pressures in this work.

The pressures derived are similar for both 1.05 μm and 0.53 μm irradiation, in terms of the absorbed irradiance. However there are well known advantages of 0.53 μm irradiation over 1.05 μm irradiation, namely the higher absorptions and the lower fast electron temperature.

4.6.5 Conclusions

We have presented results on the mass ablation rates and ablation pressures where the spherical geometry has, for the first time, eliminated the possibility of lateral power loss. A comparison with simulation shows that under these conditions a low flux limit of f = 0.03 does not describe the experiment. A higher flux limit, f = 0.1 gives better agreement, although some extra energy transport process, probably radiation transport, increases the ablation rate above that predicted by simple

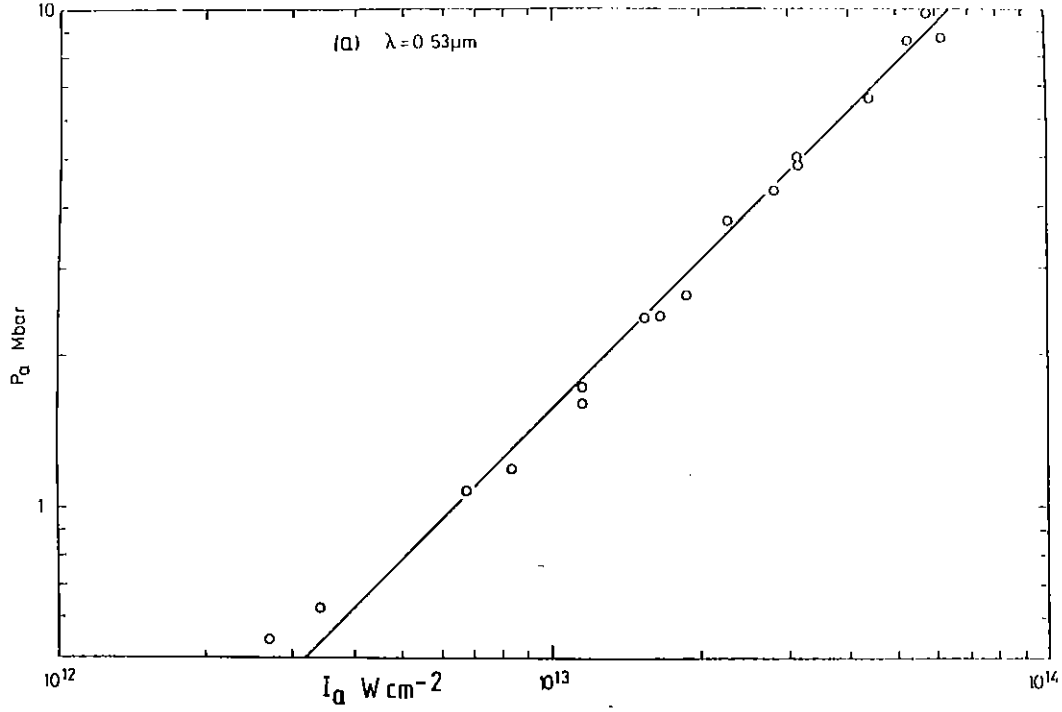

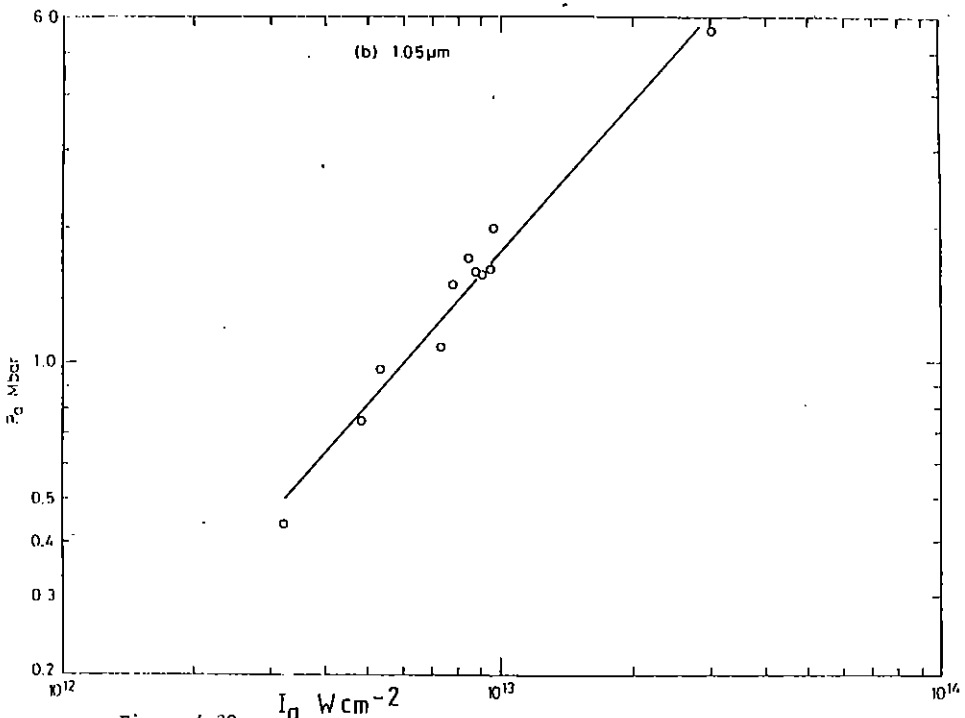

Figure 4.30

Experimental measurements of the ablation pressure from Pa = $\gamma \dot{m}_s v_i$ for 0.53μm (a) and 1.05μm (b). A least squares fit to the data is shown.

theory.

Values of ablation pressure are derived showing little difference between ablation pressure for 0.53 μm and 1.05 μm irradiation for the same absorbed irradiance but increased pressures at the same incident irradiance.

CHAPTER 4 REFERENCES

4.01 N A Ebrahim, C Joshi, D M Villeneuve, N H Burnett and M C Richardson, Phys Rev Lett, 43, 1995 (1979), P A Jaanimagi, N A Ebrahim, N H Burnett and C Joshi, Appl Phys Lett 38, 734 (1981)

4.02 R Decoste, J C Kieffer and H Pepin, Phys Rev Lett, 47, 35 (1981)

4.03 J D Hares, J D Kilkenny, M H Key and J G Lunney, Phys Rev Lett, 42, 1216 (1979)

4.04 D W Forslund, J M Kindel and K Lee, Phys Rev Lett, 39, 284 (1977)

4.05 G D Tsakiris, K Eidmann, R Petsch and R Sigel, Phys Rev Lett, 46, 1202 (1981)

4.06 R Fedosejevs, Yung-Lu Teng, R Sigel, K Eidmann and R Petsch, J Appl Phys, 52, 4186 (1981)

4.07 M H Key, W T Toner, T J Goldsack, J D Kilkenny, S A Veats, P F Cunningham and C L S Lewis, Submitted to Opt Comm (1982)

4.08 F Begay, T H Tan, J Hayden and J McLeod, J Phys D: Appl Phys, 13, L29 (1980)

4.09 J H Gardner and S E Bodner, Phys Rev Lett, 47, 1137 (1981)

4.10 S P Obenschein, J Grun, R H Ripin and E A McLean, Phys Rev Lett, 46, 1402 (1981)

4.11 I Ross, M S White, J E Boon, D Craddock, A R Damerell, R J Day, A F Gibson, P Gottfeldt, D J Nicholas and C J Reason, IEEE Quant Elec, QE-17, 1653 (1981)

4.12 G Pert, J Comp Phys, 43, 111 (1981)

4.13 R G Evans, private communication (1982)

B Yaakobi and T C Bristow, Phys Rev Lett, 38, 350 (1977); F C Young, R R Whitlock, R Decoste, B H Ripin, D J Nagel, J A Stamper J M McMahon and S E Bodner, Appl Phys Lett, 30, 45 (1977)

4.15 R C Malone, R L McCrory and R L Morse, Phys Rev Lett, 34, 721 (1975); J Murdoch, J D Kilkenny, D R Gray and W T Toner, Phys Fluids, 24, 2107 (1981); D R Gray, J D Kilkenny, J D Hares, S A Veats, R G Evans and W T Toner, "Laser Advances and Applications", Ed B S Wherrett, p211, J Wiley (1980)

4.16 A Zigler, H Zmora and J L Schwob, Phys Lett, 63A, 275 (1977)

4.17 F Amiranoff, R Fabbro, E Fabre, C Garban, J Virmont and M Weinfeld, Phys Rev Lett, 43, 522 (1979)

4.18 K Eidman, R Petsch, R Sigel, G Spindler, G Tsakiris and S Witkowski, Gordon Research Conf on Laser Interaction with Matter, Aug 1979; J C Kieffer, H Pepin, F Martin, R Decoste and P Church, BAPS, 24, 1105 (1979); K B Mitchell and R P Godwin, J Appl Phys, 49, 3851 (1978)

4.19 Rutherford Laboratory Annual Report to the Laser Facility Committee, RL-81-040 (1981); B Yaakobi, T Boehly, P Bourke, Y Conturie, R S Craxton, J Delettrez, J M Forsyth, R D Frankel, L M Goldman, R L McCrory, M C Richardson, W Seka, D Shvarts and J M Soures, Optics Comm, 39, 175 (1981)

4.20 J Grun, R Decoste, B H Ripin and J Gardner, Appl Phys Lett, 39, 545 (1981)

4.21 H Oechsner, Appl Phys, 8, 185 (1975)

4.22 T J Goldsack, J D Kilkenny and P T Rumsby, J Phys D: Appl Phys, 14, L47 (1981)

4.23 W C Mead, E M Campbell, K G Estabrook, R E Turner, W L Kruer, P H Y Lee, B Pruett, V C Rupert, R G Tirsell, G L Stradling, F Ze, C E Max and M D Rosen, Phys Rev Lett, 47, 1289 (1981)

4.24 M H Key, C L S Lewis, J G Lunney, A Moore and J M Ward, Phys Rev Lett, 44, 1669 (1980)

4.25 N G Basov, A A Erokhin, A S Shikanov, G C Sklizkov, Yu A Sakharenkov, S Denus, J Farny, W Mroz, J Wolowski and E Woryna, IPPLM Report No 37.80 (57) (S Kaliski Institute of Plasma and Laser Microfusion, Warsaw)

4.26 R E Kidder, Nucl Fusion, 14, 797 (1974); M H Key, "Laser Plasma Interactions" Eds R A Cairns and J J Sanderson, Publ SUSSP Publications, Edinburgh University (1979)

4.27 J D Hares, J D Kilkenny, M H Key and J G Lunney, Phys Rev Lett, 42, 1216 (1979)

4.28 J P Christiansen, D E T F Ashby and K V Roberts, Culham Report CLM R130

4.29 C E Max, F C McKee and W C Mead, Phys Fluids, 23, 1620 (1980)

4.30 L Spitzer and R Harm, Phys Rev, 89, 977 (1953)

4.31 T W Johnston and J M Dawson, Phys Fluids, 16, 722 (1973)

4.32 D W Forslund, J M Kindel, K Lee, E L Lindman and R L Morse, Phys Rev, A11, 679 (1975)

4.33 E S Wyndham, J D Kilkenny, H Chuaqui and A K L Dymoke-Bradshaw, Submitted to J Phys D (1982)

4.34 P A C Moore, J Phys D: Appl Phys, 14, 1429 (1980)

4.35 A R Bell, R G Evans and D J Nicholas, Phys Rev Lett, 46, 247 (1981)

4.36 D J Bond, BAPS, 26, 856 (1981); D J Bond, Phys Lett, 88A, 144 (1982)

4.37 D R Gray and J D Kilkenny, Plasma Phys, 22, 81 (1980)

4.38 W C Mead, CECAM Workshop on Transport of Fast Electrons in Laser Fusion Plasmas, CNRS, Universite Paris Sud (1979) and UCRL 85246

CHAPTER 5 ABLATIVE ACCELERATION AND COMPRESSION STUDIES

INDEX

CHAPTER EDITOR: P T Rumsby

CHAPTER 5 ABLATIVE ACCELERATION AND COMPRESSION STUDIES

5.1 Introduction

Compression experiments driven by both green and infra red beams have been carried out during the last year. Initial experiments with 6 green beam driven implosions were aimed at producing 2-D X-radiographs with good time resolution by utilizing a short pulse for X-ray backlighting syncronized not a long (stacked) pulse for the target drive. Results are presented in Section 5.2 which demonstrate the potential of short pulse X-ray backlighting for observing structure on the imploding shell and making measurements of the core density profile at peak compression.

Section 5.3 gives preliminary results from additional experiments carried out at λ=0.53μm at values of $I\lambda^2$ of about 10^{14} $Wcm^{-2}\mu m$ where ablation pressures are high but fast electron preheat is tolerable. X-ray and fusion reaction product emission was observed from the hot cores produced.

Direct observations of the growth of the Rayleigh-Taylor instability in accelerating lollipop targets are reported in Section 5.4 These results are encouraging as they suggest that the growth rate is comparable with 2-d computation and is a factor of a few below the classical rate.

Finally a few 2-D X-radiographic results have been obtained using the new syncronized short and long (smooth) pulse oscillators. These experiments (which are reported briefly in Section 5.5) were conducted in the infra red and indicate that somewhat higher compression ratios can be achieved at this wavelength compared to experiments conducted in the green.

5.2 Pulsed 2-D X-radiography and core density measurements of = 0.53 μm driven implosions

5.2.1 Introduction

X-ray backlighting techniques as a means to study imploding spherical shell targets have been developed at the CLF in recent years (5.01,5.02). Initial experiments with targets driven ablatively using six 1 nsec laser beams at wavelengths of 1 μm and 0.5 μm used ≃ 1 nsec duration X-ray backlighting source emission and absorption images were streaked in time (5.02,5.03). This technique allowed the trajectory of a section of the shell wall to be followed in time and the major conclusion was that, under the existing experimental conditions, the volume of the absorption zone at maximum compression was larger, by up to a factor x 10, than the volume predicted by 1-D hydrodynamic simulations. This observation indicated that the implosions were in some way degraded by either lack of implosion symmetry, Rayleigh Taylor instability or shell preheating and decompression. In this Section we describe developments of X-ray backlighting techniques to investigate the implosion degradation by pulsed 2-D absorption imaging of the target. Two techniques are described which allow 1) the 2-D structure of the shell to be observed at a preselected time in the implosion history and 2) the mass distribution of the target material to be determined, again at a given time during the implosion.

5.2.2 2-D pulsed X-radiography

The experimental arrangement is illustrated in Figure 5.01. Six orthogonal second harmonic laser beams (λ= 0.53 μm) irradiated a shell target while a seventh beam (λ= 1.05 μm) irradiated a thin backlighting target. X-rays transmitted through the backlighting target substrate were imaged onto Kodak No-Screen film using 5 and 20 μm diameter pinholes in a 10μm thick gold substrate. The solid angle subtended to the shell target from each pinhole is contained with the solid angle subtended to the backlighting source X-ray emitting region. The shell and backlighting target were separated by 800 μm and the pinhole camera had a x 4.3 magnification with an object distance of 10 cm. The camera resolution was

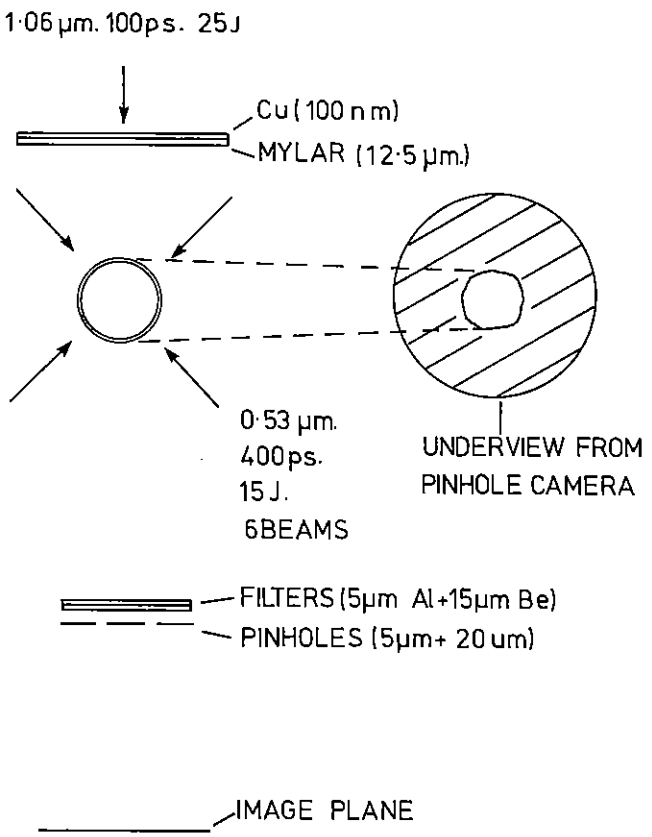

Figure 5.01 Schematic of experimental arrangement for 2-d pulsed X-radiography.

optimised (Fresnel number ≈ 1 for the smaller pinhole) for ≈ 1.5 keV X-ray photons. The static resolution of 6.5 μm, was estimated from a pulsed radiograph of an unirradiated shell (Figure 5.03(a)).

The shell driver beams were generated by pulse stacking a switched out 1.05 μm, 100 ps pulse from a mode-locked oscillator with subsequent amplification and conversion to second harmonic with KDP crystals. The backlighting beam was derived from the original laser pulse. Time-resolved braod band X-ray emission from various targets simultaneously irradiated with long and short pulses were recorded with an X-ray streak camera whose cathode was masked with a 200 μm mylar filtered slit giving 100 psec temporal resolution. Figure 5.02 shows a microdensitometer scan for a result from a gold target indicating the individual pulse durations and their relative time of arrival at the target.

The shell targets used in the experiment had typical parameters $\phi = 170$ μm, $\Delta r_{glass} \simeq 1$ μm, $\Delta r_{plastic} \approx 3$ μm. The laser delivered $\approx$15J in 500ps in the six $2\omega_o$ beams. The incident intensity on the target was typically 3×10^{13} W cm^{-2} (well below threshold for hot-electron effects). The six f/1 focusing lenses were focused 3.6 radii beyond the balloon centre. The backlighting target was 100 nm of copper coated on to a 5 μm aluminium substrate and was irradiated over $\approx$ 400 μm diameter area at an irradiance level of $\approx 10^{14}$ W cm^{-2}. The X-ray film sensitivity limited the degree of filtering possible. In the experiment the combined filtering effects (5 μm Al + 15 μm Be) limited the probe radiation to 1.5 keV. With this rather low X-ray energy the backlighting X-ray pulse was $\approx$250 ps in duration. Self emission from the glass shell was limited by the plastic coating.

Simulations for typical implosions in the experiment indicated implosion times of ≈ 2 nsec i.e. much longer than the drive pulse duration. Such implosions are referred to as "coasting implosions" as the shell moves inward at a constant velocity for a large fraction of the event time.

Pulsed radiography of the moving shell had a spatial resolution of ≈ 10 μm

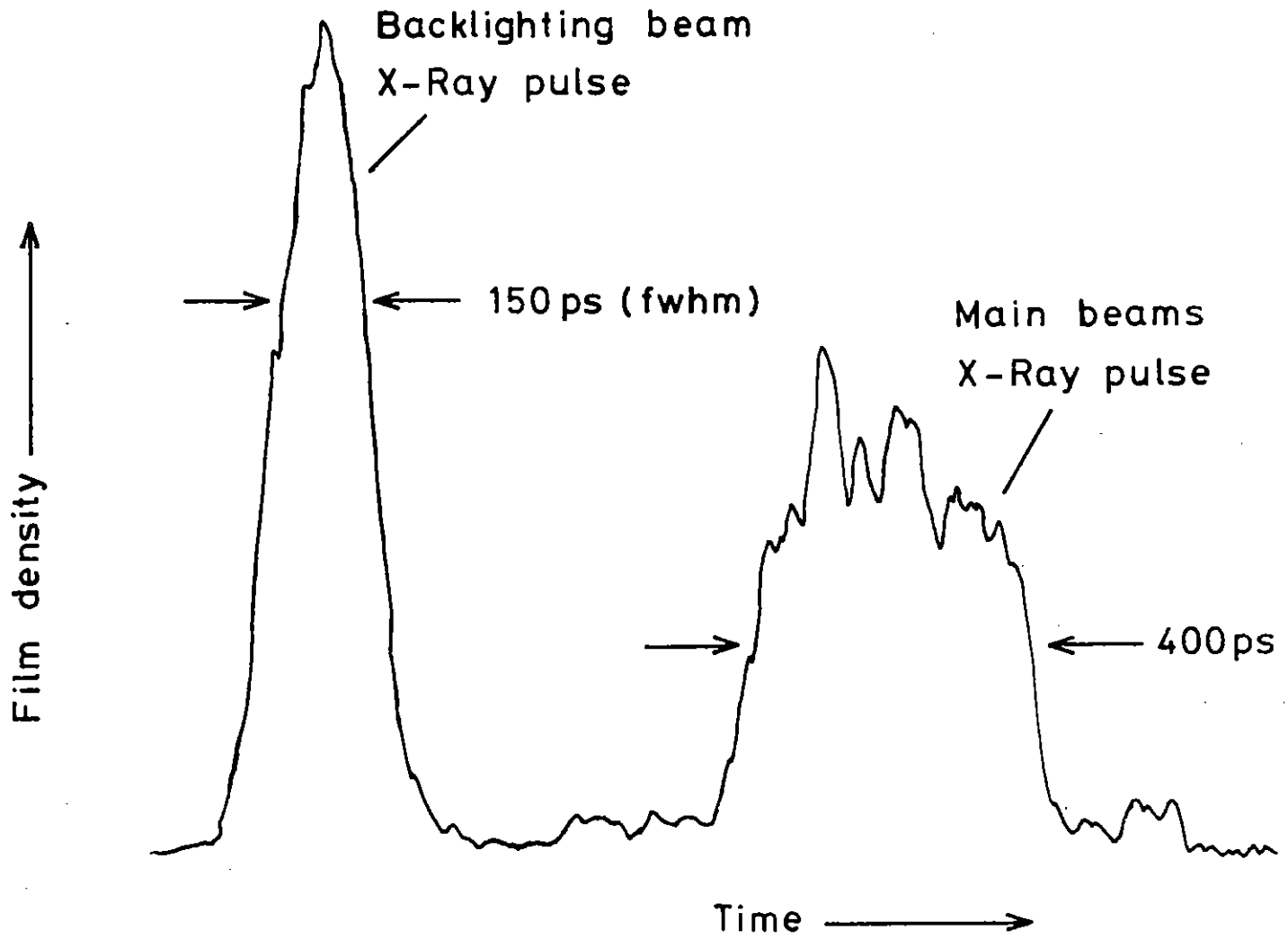

Figure 5.02 Time duration of X-ray backlighting pulse and main drive pulse measured using the X-ray streak camera.

Figure 5.03 X-radiographs of shell targets. Original target diameter shown. (a) Unirradiated glass shell, 5 μm pinhole. (b) imploding shell at τ = 2.45 ns, 5 μm pinhole.

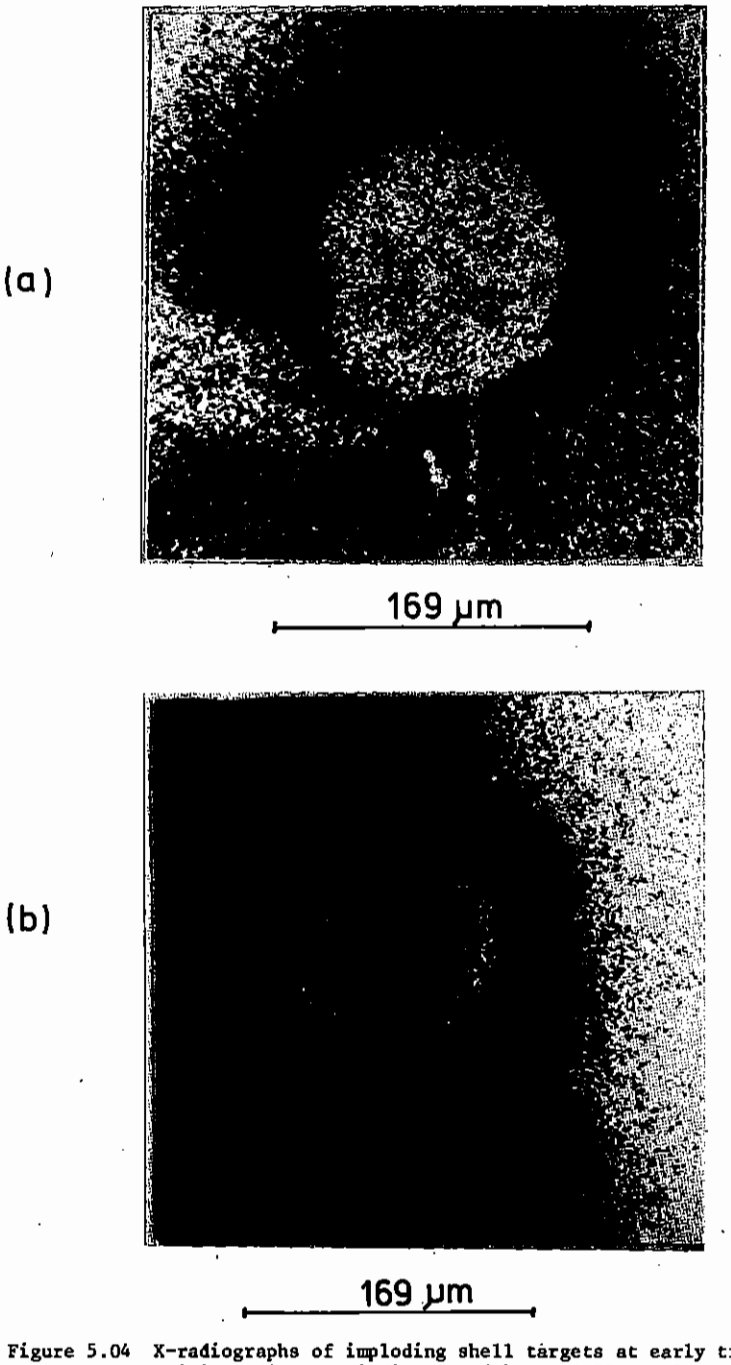

Figure 5.04 X-radiographs of imploding shell targets at early times. Original diameter indicated. (a) τ = 0.57 ns, 5 μm pinhole. (b) τ = 0.57 ns, 20 μm pinhole.

mainly limited by motional blurring during the frame time set by the back-lighting source duration.

The soft X-rays used in the experiment were adequate to map out the structural detail at the edges of imploding target material with 10 μm resolution. Three types of structural features were observed and these can be attributed to 1) gross beam energy imbalance giving rise to off-centre cores 2) illumination variation on a spatial scalelength of the order of the target radius giving rise to grossly mis-shapen cores and 3) non-uniform illumination on a spatial scalelength of tens of microns giving ragged edges to the core feature.

Figure 5.03(b) illustrates an off-centre absorption feature, defined by the shell self emission which in this case dominates the backlight. Figures 5.04 - 5.07 illustrate a sequence of pulsed radiographs taken as a function of backlighting delay time (relative to the peak of the driver pulse) using shell targets with approximately constant parameters. The absorption zone is clearly not perfectly symmetric and typical radii of the absorption zone were taken by averaging the maximum and minimum radii measured orthogonally. The outer edge of the absorption zone was defined as the point where the backlighting transmission dropped to 1/e. An absorption ring reflecting the shell structure was observed only in very early stage radiographs and only with the 20 μm pinhole (Figure 5.04(b)). Although the maximum delay time used was greater than the predicted implosion time no evidence was seen for a volumetric compression greater than about 20. This observation is consistent with our streaked shadowgraphy experiments (5.02,5.03). An attempt to illustrate the data graphically was made by calculating a normalised implosion time for each target and comparing it to a particular hydrodynamic simulation case.

The target parameters for a shot which showed a good implosion were taken for the reference case. The Medusa wall trajectory was compared with an analytic model solving $\dot{r} = \frac{K I^{0.8}(t)}{(\xi \rho \Delta r - \dot{m}(t) t)}$ .This indicated that the implosion time (τ_{imp}) corresponded to the time when $\frac{r(t)}{R_0} \approx 0.1$, where R_0 is the initial radius, Δr is the shell thickness, $I(t)$ is irradiance and m is mass ablation rate. Assuming this to hold for all

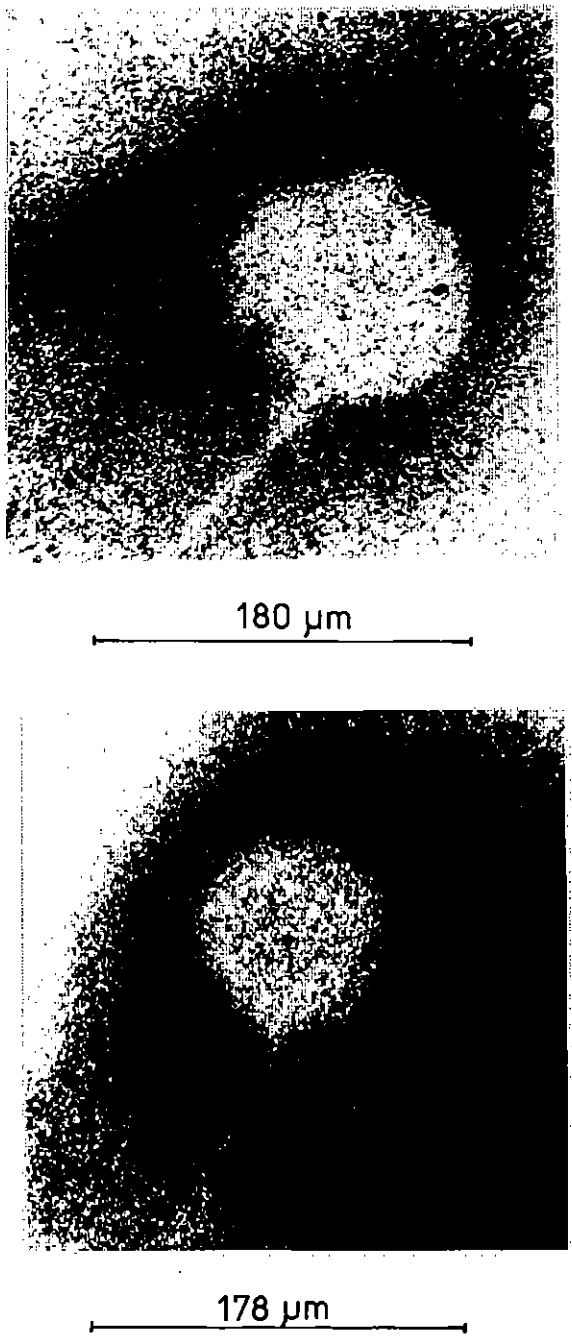

Figure 5.05 X-radiographs of imploding shell targets. Original diameter indicated. (a) τ = 1.02 ns, 5μm pinhole. (b) τ = 1.37 ns, 20μm pinhole.

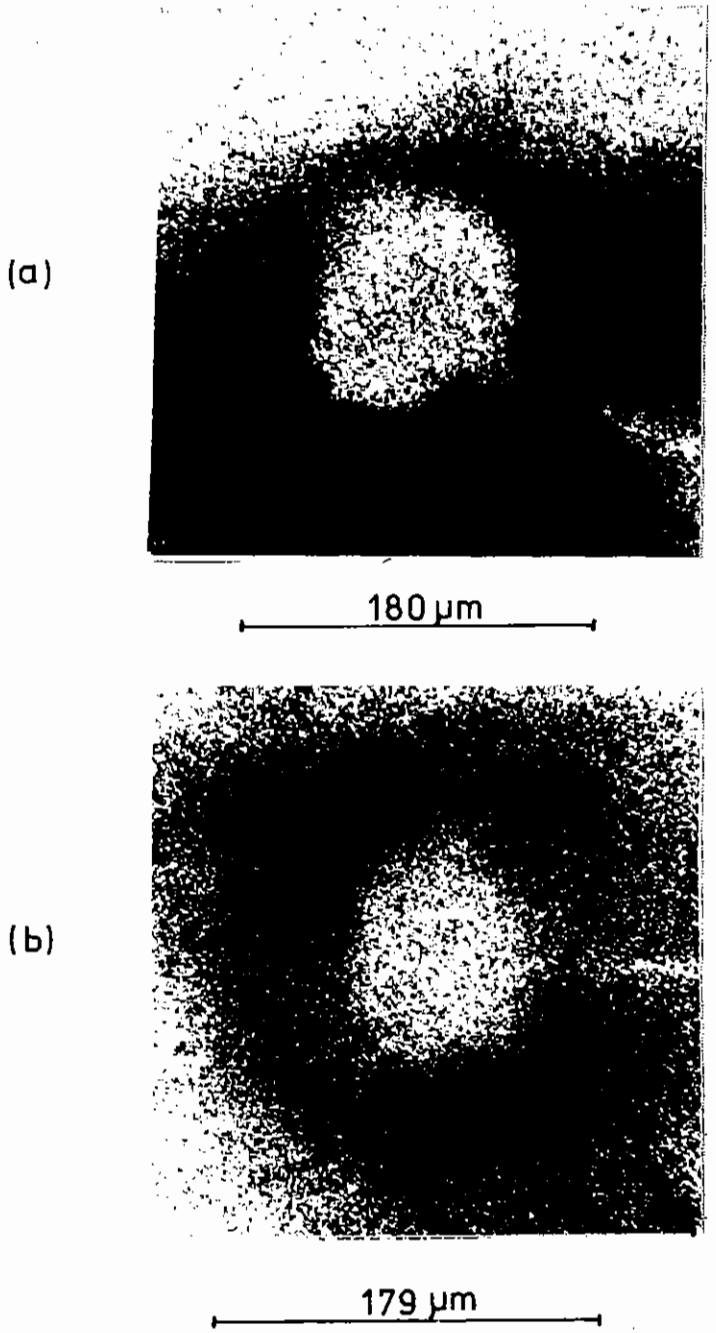

Figure 5.06 X-radiographs of imploding shell targets. Original diameters indicated. (a) τ = 2.05 ns, 20 μm pinhole. (b) τ = 2.05 ns 5 μm pinhole.

other targets the quantity $\tau_{B/L} \times \tau_{ref}$ was the calculated as the normalized implosion time where $\tau_{B/L}$ was the backlight delay and τ reference was the calculated implosion time for the reference case. For each shot the observed average core radius to initial radius $r(\tau_{B/L})/R_0$ was plotted against the normalised implosion time. The data is illustrated in Figure 5.08.

The poor quality of the implosions can (at least in part) be attributed to the conditions of illumination on the target surface. Figure. 5.09 shows a microdensitometer trace of the laser beam profile taken in an equivalent target plane and shows 2:1 modulation on a spatial scale of 30 - 40 μm. (The periodicity was largely due to poor A-R coatings on beam splitters at the time.) Figures 5.04(a) and 5.05(a) show a corresponding periodicity in the imploding target material and the scale lengths match well when spherical convergence up to the time of the radiograph is taken into account.

A more striking observation is shown in Figure 5.07(a). Here the fill factor of the target laser beams was increased at the same lens focusing conditions (i.e. $^{d}/_{R}$ = 3.6) causing increased irradiance at points of triple beam overlap. The radiograph shows a cubic-type core structure with the faces pointing to the direction of four triple overlap positions in the plane perpendicular to the camera axis. In 3-D the core has an octahedral shape since there are eight triple overlap points. The target irradiance (averaging over smaller scale structure) was estimated to be 1.7 times greater at overlap points compared to beam centre points.

Both observations (large and small scale structures) are broadly consistent with variations in irradiance on the target surface. For a constant acceleration the distance moved by the shell (x), the pressure applied (P) and the irradiance (I) giving rise to the ablation pressure are related by $x = A\,P = B\,I^{y}$ where A, B, y are constants, i.e. $\Delta x/x = \Delta I/I$. In the present observations $\Delta I/I \approx 2$ for small and large scale effects and $\Delta x/x = \frac{\Delta r}{R_0 - r} \approx 2$ where $r \pm \Delta r$ is the observed shell radius at a time close to the end of the laser pulses. Consideration of the secular growth of the perturbations during the post-pulse constant

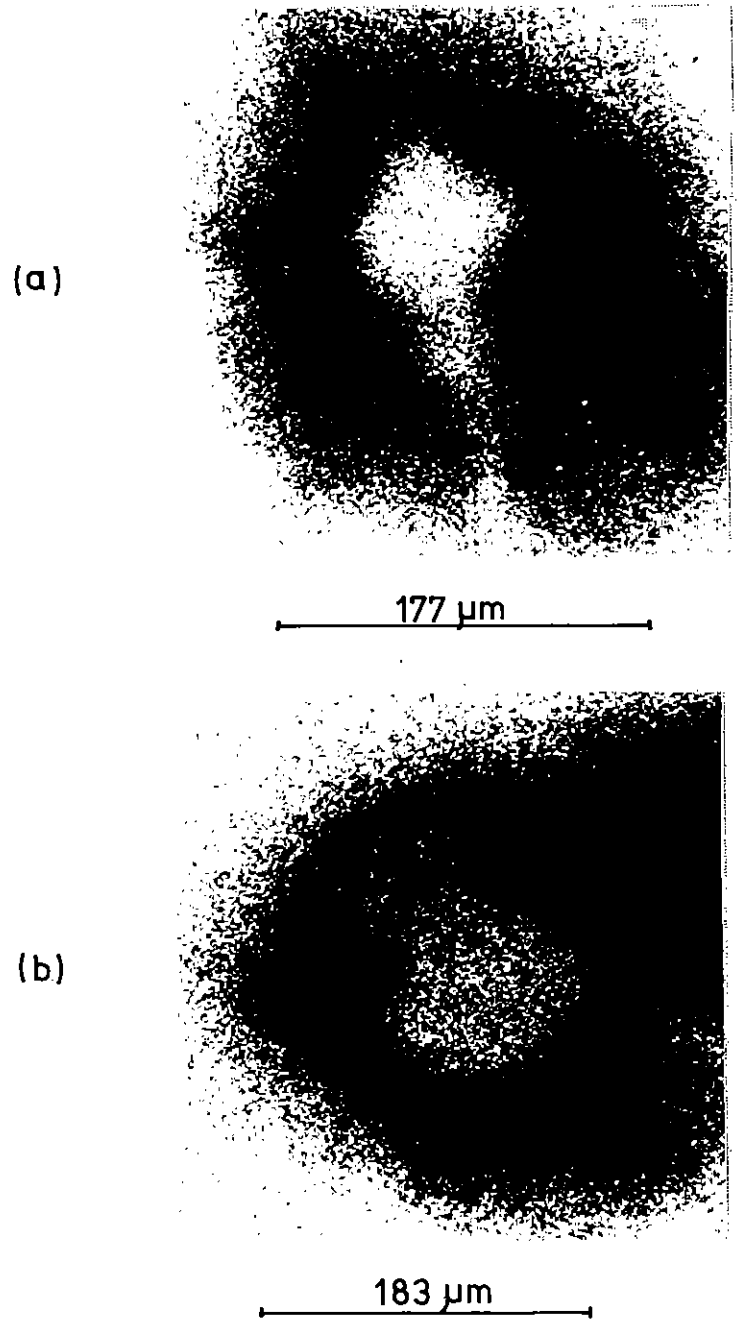

Figure 5.07 X-radiographs of imploding shell targets near peak compression. Original diameters indicated.(a) and (b) τ = 2.45 ns, 20 μm pinhole.

velocity shell movement indicates that the observed final core sizes $r \leq R_o/2$ is not surprising.

Thermal smoothing, whereby localised energy deposited at the critical density region may be diffusely redistributed through thermal conduction between critical and ablation surfaces may be a possible mechanism to improve such non-uniformities. It can be shown that for diffusive heat

flow situations pressure variations can be smoothed as

$$\Delta P/P = \Delta I/I \exp\left(-\frac{2\pi D}{L}\right)$$

where D is the steady state separation between critical and ablation layers and given by $D = 0.14 \left(I_{15} \lambda^{3.5}_{\mu m}\right)^{0.7} \frac{R}{R_{mm} + 1}$

L is the wavelength of irradiance perturbations on the target surface and R is the target radius. In the present experiment $I \simeq 3 \times 10^{13}$ Wcm^{-2}; $\lambda = 0.5$ μm, $R \approx 90$ μm and hence $D \approx 5$ μm. Hence in this case the thermal smoothing term $\exp(-\frac{2\pi D}{L})$ is only expected to be useful for perturbations of scale length $\lesssim 10$ μm (of the order of the experimental spatial resolution) and not expected to greatly influence the known experimental perturbations. Future experiments will be designed to investigate the parameter ranges where thermal smoothing effects can be observed.

5.2.3 Core density profile measurements by X-radiography

The experimental arrangement is illustrated in Figure 5.10. It differs from the previous experiment in that the backlighting plasma is viewed edge-on, minimising any hot-spot effects in the source distribution and increasing the line of sight source emission intensity. In addition the X-ray film is replaced by an X-ray streak camera operating in static mode as a sensitive active X-ray detector (X 100 over film).. This set-up allows harder filtering of the source emission and thus the ability to measure transmission through a greater ρr of absorbing material.

The backlighting target was 20nm of copper on mylar and was irradiated with a 100 ps, 1.06 μm, 20 J laser pulse. The shell targets were

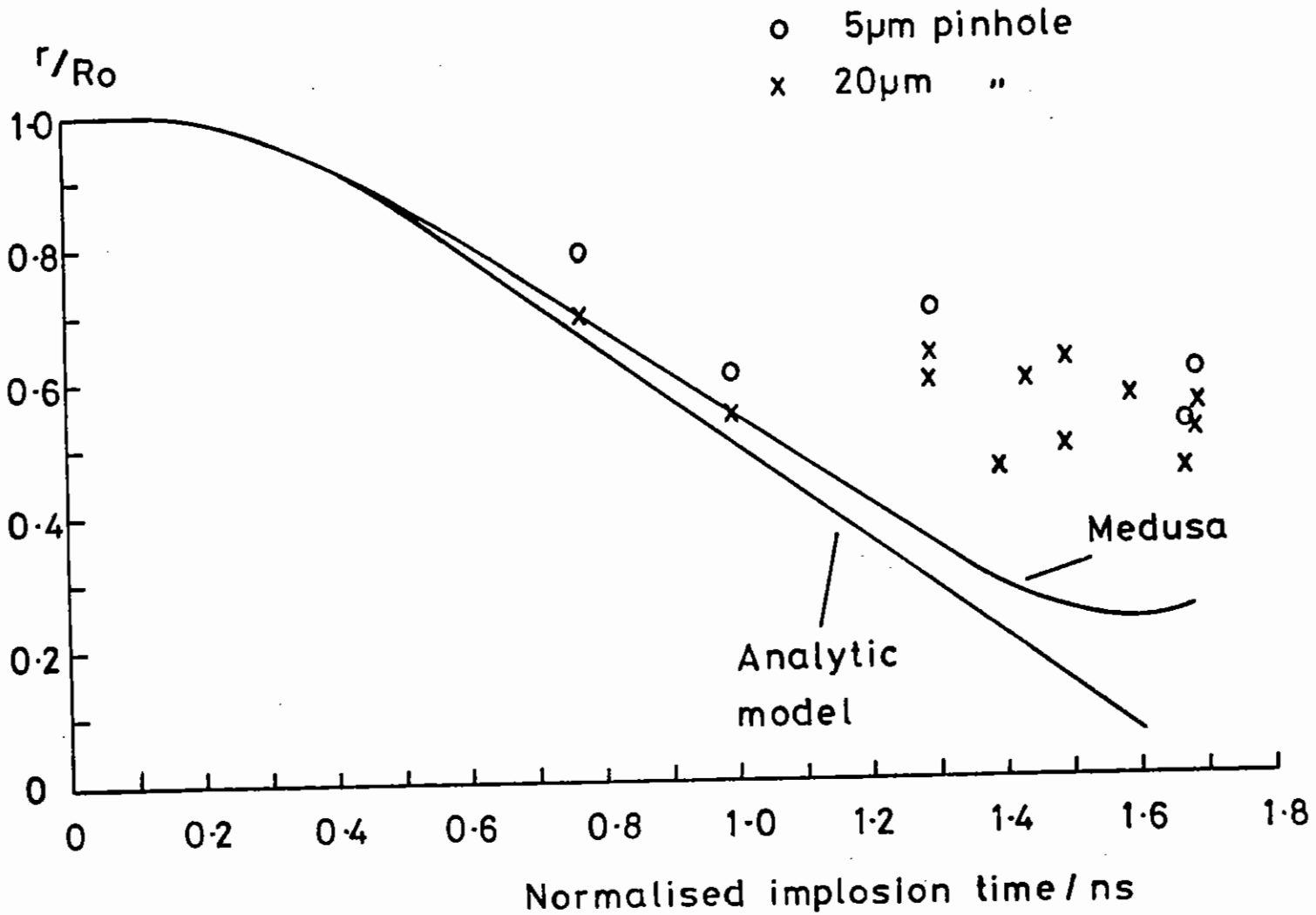

Figure 5.08 Comparison of implosion trajectories calculated from analytic model and Medusa code with experimental measurements.

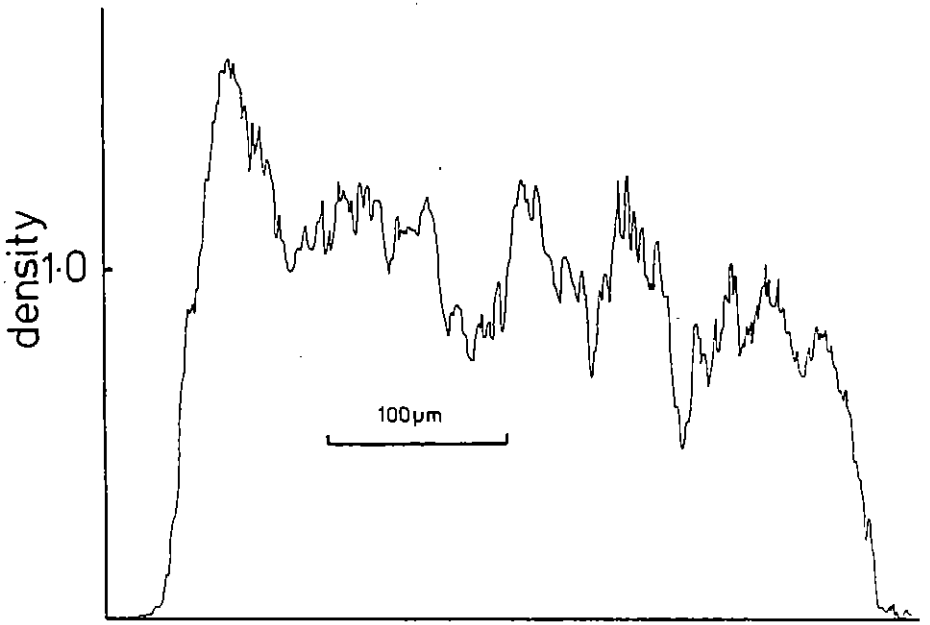

: Microdensitometer trace of the laser beam profile obtained from the equivalent plane monitor.

Figure 5.09 Microdensitometer trace of the laser beam profile obtained from the equivalent plane monitor camera.

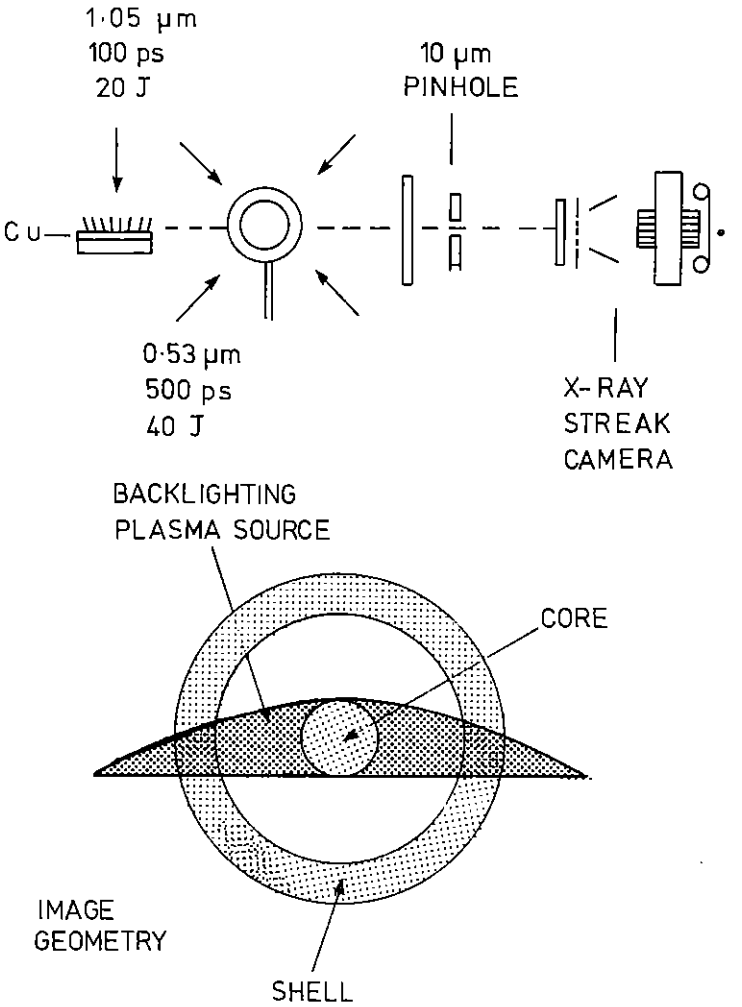

Figure 5.10 Schematic of experimental arrangement for core density measurements by X-radiography.

irradiated with ∿ 500 ps (stacked pulse), 0.53 μm pulses delivering a total of ∿ 40 J in six beams. This corresponded to ≤ 10^{14} W cm^{-2} irradiance level.

The 10 μm pinhole was filtered with 25 μm thick mylar and with the 15 μm. Be substate in the CsI X-ray photocathode the equivalent mylar thickness was 29 μm. The backlighting probe photon energy can be estimated as $E \approx (3\mu_1 \rho \times T)^{\frac{1}{4}}$ where E and the source plasma temperature T are in keV and μ_1 is the absorber mass attenuation coefficient at 1 keV (3×10^3 g^{-1} cm^2 for mylar). In the present case ρ = 1.37 and x = 29 μm giving E ≃ 2 keV for a typical source temperature ≈ 400 eV. The resonance line radiation from L-shell copper emissions lies at < 1.5 keV and is negligible here and, as in the above estimate of E, we asume the probe spectrum behaves as exp (-hν/KT) for hν > 1.5 keV. A consequence of this experimental set-up is that the imaged backlighting source is sausage-like as only continuum emission from the ablation region is imaged. (The backlighting pulse duration is also mainly dependent on the life-time of the hot ablation plasma i.e. ≈ 100 psec.) Thus proper 2-D pulsed radiography is not achieved but rather a slice of the shell target through its centre can be probed.

The set-up was calilbrated by radiographing a 140 μm diameter nylon fibre mounted orthogonal to the plane containing the backlighting target. The recorded opacity profile of this known mass distribution is shown in Figure 5.11(a). This was used to estimate the source plasma temperature. From measured film density and the H-D film curve the transmission of the fibre was plotted as a function of radius. An analytic fit to this curve was made by calculating the quantity

$$T(r) = \int \exp\left[-\frac{E}{T} + \frac{(\mu_1\rho)M^x}{E^3} + \frac{2(\mu_1\rho)_N (R^2 - r^2)^{\frac{1}{2}}}{E^3}\right] dE \Big/ \int \exp\left[-\frac{E}{T} + \frac{(\mu_1\rho)M^x}{E^3}\right] dE$$

where E and T are in keV and integration is over the range E = 0.5 - 10. Subscripts M, N refer to mylar and nylon, R is the fibre radius and $0 \leq r \leq R$. I_o is related to the background film density due to the integrated source radiation only. The computed function with r = 0 was fitted to the experimental curve at the minimum transmission point to determine T = 370 eV and the T(r) curve was matched at the T = 0.5 points to give the system

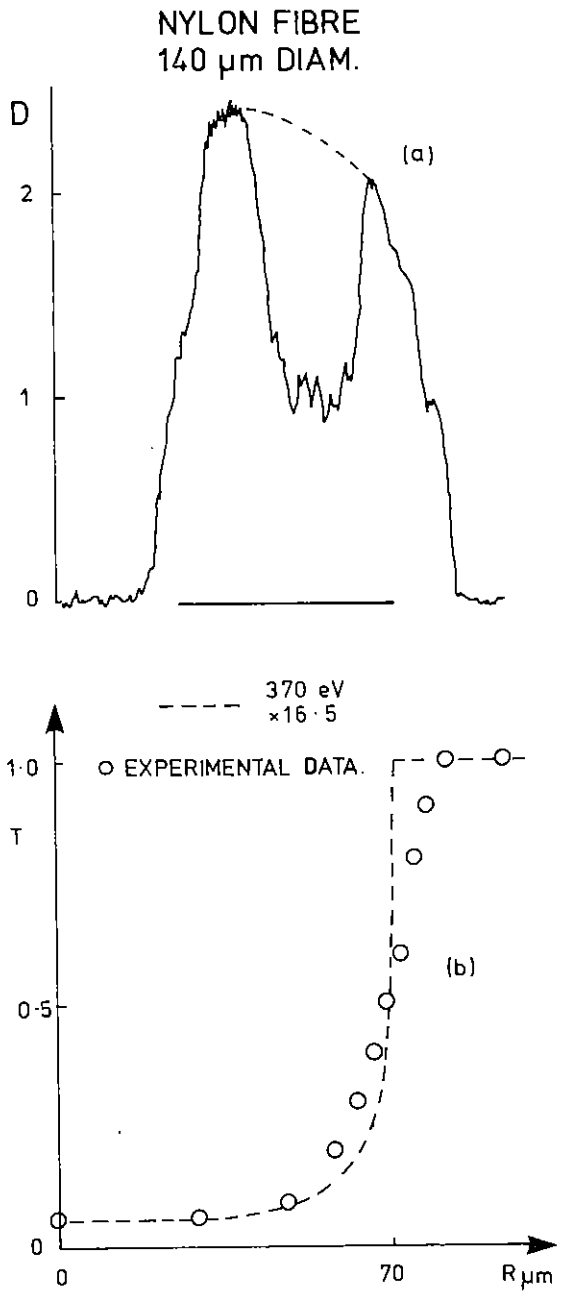

Figure 5.11 X-radiography of a nylon fibre. (a) Microdensitometer tracing of camera output. (b) Comparison of X-ray transmission profile for source temperature of 370 eV and x 16.5 magnification with experimental points.

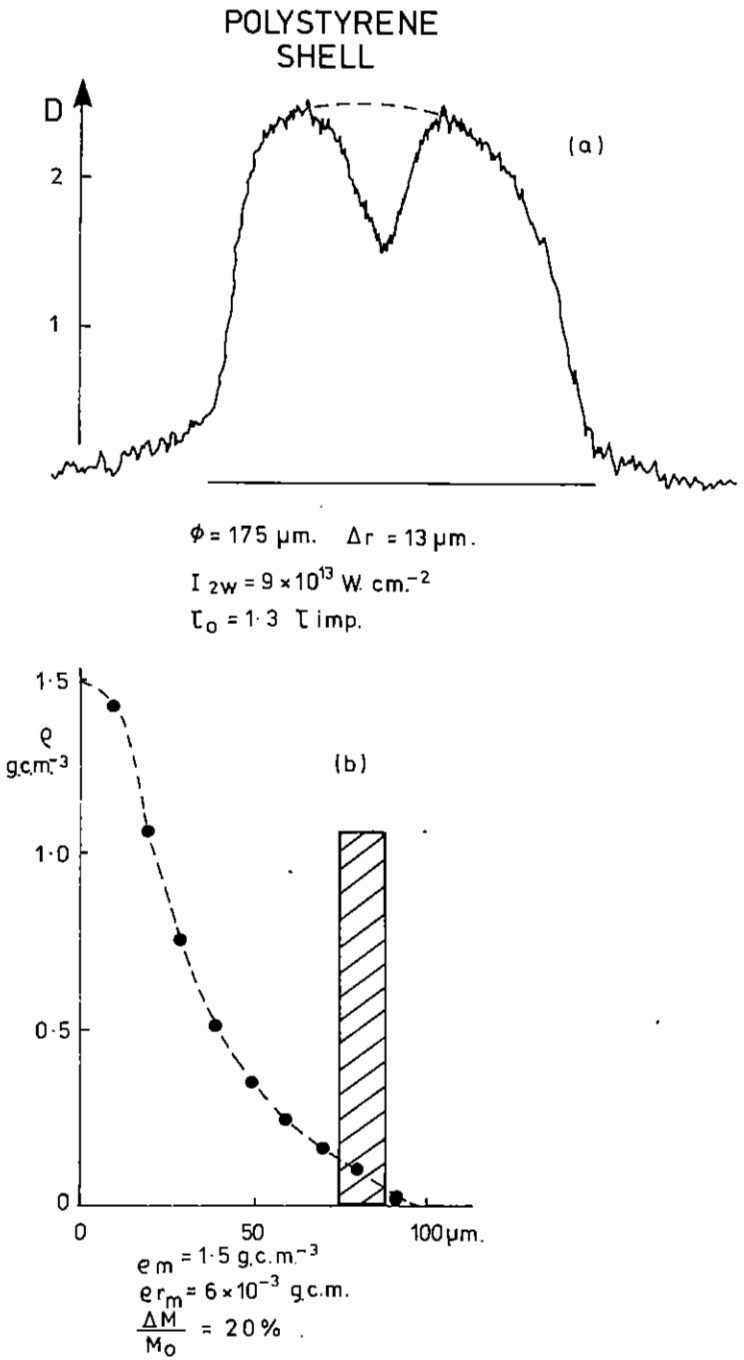

Figure 5.12 X-radiography of imploded shell. (a) Microdensitometer tracing of camera output. (b) Calculated core density profile. Original target wall position and thickness indicated.

magnification as shown in Figure 5.11(b). The magnification (X 16.5) agreed with the design value and the slight discrepancies between experimental points (open circles) and the analytic fit are consistent with the 10 μm spatial resolution not being convolved into the model.

A limited number of shell targets were imploded and radiographed with backlighting plasma conditions comparable to the calibration shot above i.e. $T_e \approx 370$ kV. Figure 5.12(a) shows the absorption feature from an empty, low aspect ratio polystyrene shell irradiated at $9 \times 10^{13} Wcm^{-2}$ and radiographed at a time 2.25 nsec into the implosion (with respect to the start of the drive pulse). It was estimated from analytic modelling and MEDUSA predictions that this was $\pm$ 20% of the target implosion time.

The observed transmission curve was again fitted by analytic modelling as in the last equation except that T = 0.37 keV and the magnification are now fixed and $(\mu_1\rho)_N$ becomes $(\mu_1\rho(r))_p$ for polystyrene. The fitting, using Abel inversion, determines the core density distribution $\rho(r)$ and is illustrated in Figure 5.12(b). The peak core density was $\approx$ 1.5 g cm^{-3} with a peak $\rho r = \int \rho(r)\, dr \approx 6 \times 10^{-3}$ g cm^{-2}. Improved beam quality, focusing conditions and higher irradiance in this experiment meant that thermal smoothing was more effective than in the previous discussion. A check on the modelling and Abel inversion procedure was made by integrating the total core mass, $\int 4\pi r^2 \rho(r)\, dr$. This indicated a mass loss of $\approx$ 20% which is consistent with previously measured mass ablation rate data at λ = 0.5 μm.

With sufficiently hard probe radiation the mass distribution in an imploding target can be measured as indicated in these preliminary experiments. Optimisation of filtering and source plasma temperature using the analytic expression for T(r) indicate that measurable transmission for $\rho r \approx 0.1$ is feasible with modest increase of the source temperature. The experiment described had a factor of X 30 sensitivity in hand.

Diagnosing plastic targets in this way relies on insufficient shell preheating to strip off the carbon K-electrons. Application of Saha's

equation indicates that this is not important for temperatures below 100 eV. The fractional abundance of carbon ions as a function of temperature for densities 1 and 5 g cm^{-3} are shown in Figure 5.13 as a function of temperature. Ground state statistical weights have been used with no ionisation depression and the electron density $n_e = \frac{\bar{Z}\epsilon}{2M_p Z}$ has been iterated to give self-consistent values of the average charge state Z.

It is interesting to note that the ion coupling parameter $\Gamma = 2{\cdot}3 \times 10^{-7}\ N^{1/3}\ T^{-1}.\ Z^2$, which is a measure of the ion-Coulomb interaction energy to the thermal energy is in the region $\Gamma = 1.2$ for these plasmas thus bringing them into the watershed region between ideal and non-ideal plasmas as shown in Figure 5.14.

C L S Lewis, P F Cunningham, M J Lamb (QUB)C Duncan (Oxford) M H Key, P T Rumsby C Hooker and S Knight (RAL), M Ward (QUB).

5.3 $\lambda = 0.53\ \mu m$ driven hot - ablative implosion experiments

5.3.1 Introduction

Compression experiments using 6 beam, 0.53 μm irradiation of targets at intensities of a few times 10^{14} W cm^{-2} were carried out. These experiments were successful in producing cores of high enough temperature to emit X-rays in the 2 keV region.

The concept of these experiments was to irradiate targets at a sufficiently high intensity to achieve ablation pressures in the 10 - 20 M Bar range yet keep fast election preheating to a tolerable level. Shock preheating of the target, (the magnitude of which is proportional to the ablation pressure) was the dominant preheat mechanism. For shock preheating followed by adabatic compression the final core gas density (ρ_f) is roughly constant and proportional to $r/\Delta r$, (the aspect ratio of the target) while the final core temperature (T_f) is proportional to the ablation pressure (Pa). Hence large values of ablation pressure should give rise to hot cores (Te >300eV) which emit X-rays and fusion reaction products. For example, for Pa = 20M Bar and $r/\Delta r = 10$, $\rho_f = 15$gm cm^{-3}

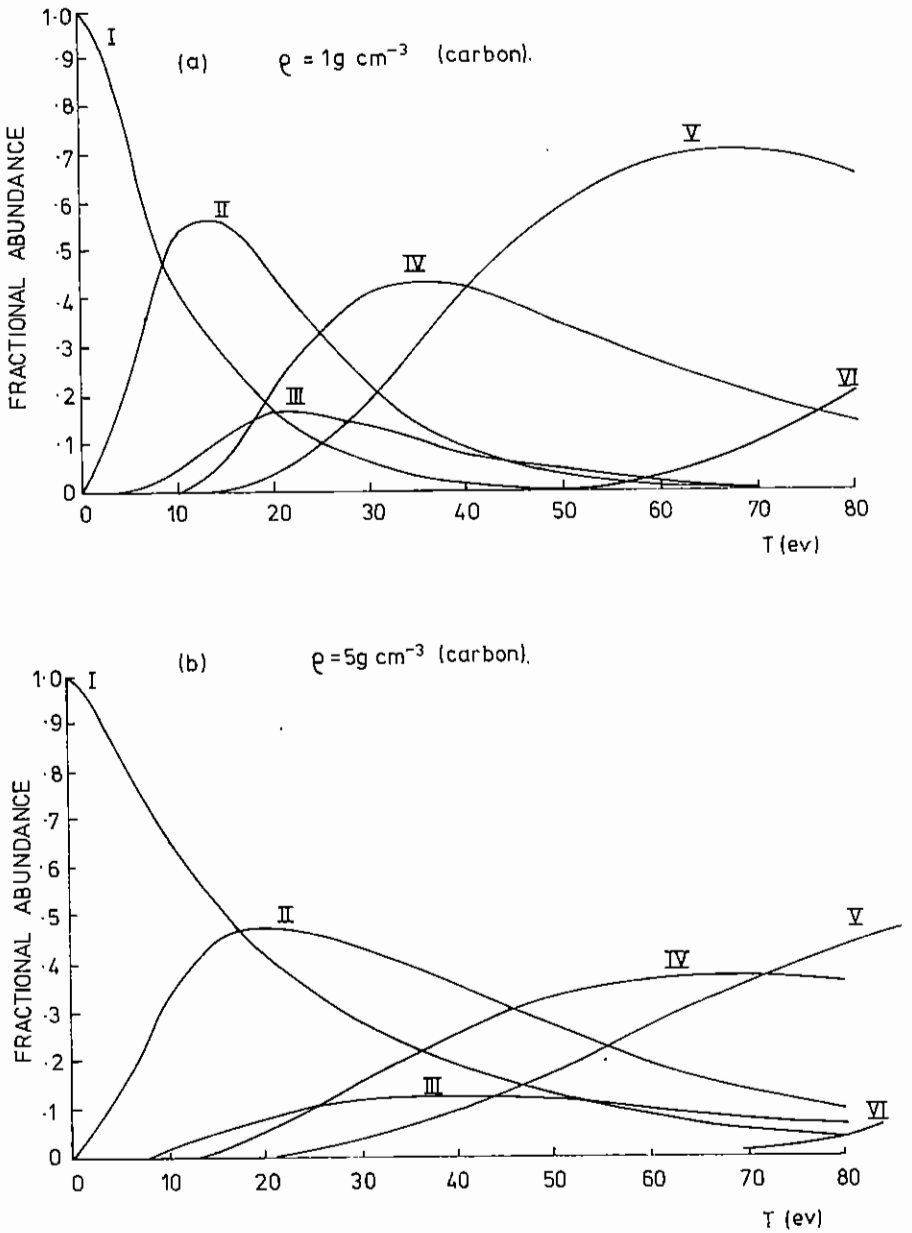

Figure 5.13 Temperature variation of the fractional abundance of various ionization stages for carbon. (a) ρ = 1 gm cm^{-3} (b) ρ = 5gm cm^{-3}

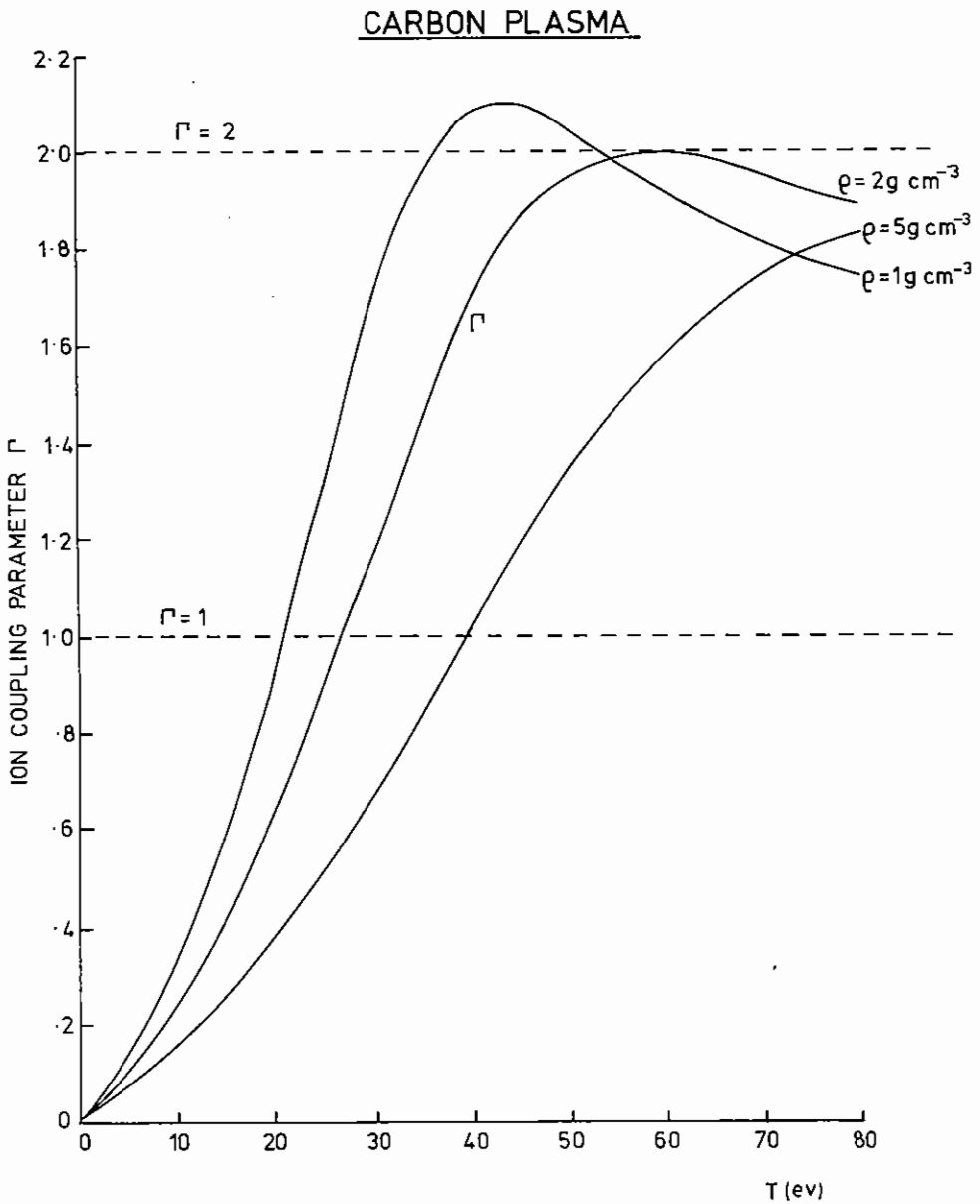

Figure 5.14 Ion coupling parameter variation with temperature for a carbon plasma of various densities.

and $T_f \approx 1$ keV.

The targets used were glass microballoons of approximately 120 μm diameter and 1 - 2 μm wall thickness, coated with approximately 1 μm of plastic for some shots. The gas fill was either 20 Bar DT (doped with Neon), 10 Bar Neon or 0.4 Bar argon. The analysis of the data obtained from these experiments is incomplete and will be reported later. However, some general observations from the diagnostics are given here.

5.3.2 Pinhole camera photographs

A pair of pinhole camera pictures is shown in Figure 5.15. The soft channel on the left shows a core of diameter about 20 μm giving a radial compression of 5 X from the initial 110 μm radius. In comparison the hard channel, which has a higher sensitivity shows little core emission. X-ray core temperatures of 220 ± 50 eV are consistent with this data.

The X-ray picture shows an absorption region around the core which is a self backlit absorption picture of the compressed glass, with the core emission superimposed. If all the residual target shell material is assumed to be situated in this opaque region this indicates densities of about 3 gm. cm^{-3} and ρr values of about 4 X 10^{-3} gm cm^{-2}.

Only thin targets with aspect ratios greater than about 20 gave rise to hot X-ray emitting cores contrary to expectations. This may well indicate that the adiabatic phase of the implosion is degraded (by some mechanism such as non uniform illumination or hydrodynamic instability) and that in order to produce a high enough core temperature additional preheating is required. In these experiments this would be due to X-radiation from the ablation plasma penetrating the thin shell walls. For lower aspect ratio thicker wall targets this radiative preheating would not be significant whereas for the thin walled targets it is estimated that radiative preheat of the fill gas was comparible with shock preheating.

Table 5.1

DATE	SHOT NO.	TARGET NO.	TEMPERATURES (ev)		
			C=700	C=350	C=175
2/12/81	5	2158	245	258	273
3/12/81	5	2162	300	318	337
	8	2159	261	276	292
4/12/81	6	2195	307	326	346
	8	2199	203	214	225
10/12/81	2	2200	279±40	295±40	312±40
	8	2205	230	242	255
	16	2203	209±15	220±15	232±15
	18	2212	211	222	234
14/12/81	1	2223	328±20	348±20	370±20
	3	2206	243	256	270
	4	2224	363±20	386±20	412±20
	6	2142	204	214	225
	8	2213	264	279	294
	9	2225	195	205	215

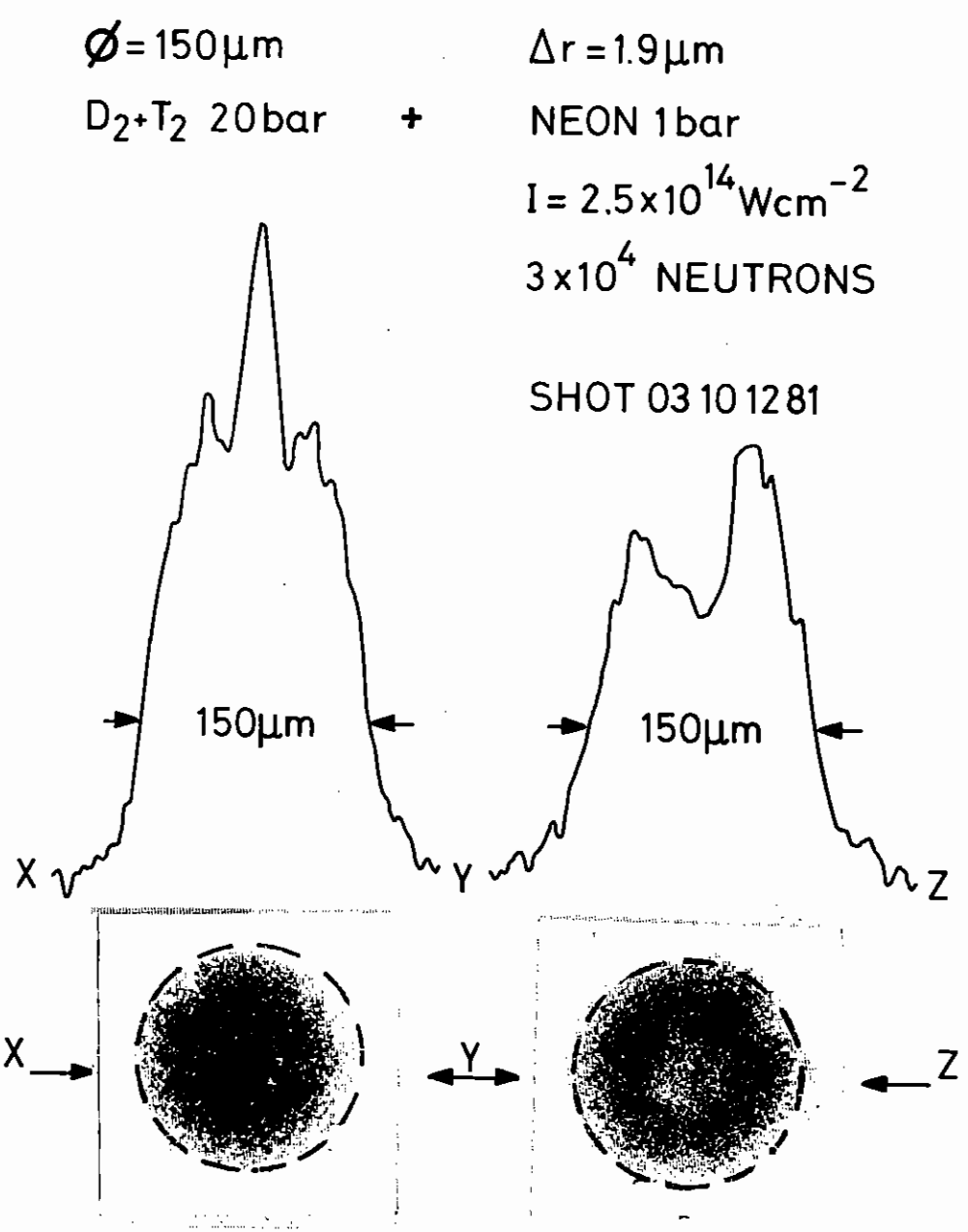

Figure 5.15 Soft and hard filtered X-ray pinhole camera photographs of a hot ablative implosion.

5.3.3 Neutron yields

A neutron scintillator detector indicated yields in the region 10^3 - 10^5. The corresponding ion temperatures were in agreement with the X-ray temperatures, namely 250 - 300 eV. The ion temperatures are tabulated in Table 5.01 for various assumed compression ratios, C.

5.3.4 α - Particle yields

A 2 x 1 cm foil of CR-39 was mounted at 60° with one end 15 mm from the imploding D-T filled microballoon as shown in Figure 5.16. The choice of angle was made both to ensure adequate projected track geometry and to use measurement of track dip (δ) and azimuth as additional identification criteria. This arrangement, which results in a variation of track dip angle down the plate ensured that α-tracks were always above the detection threshold. D and T knock-on ions, however, would lie above threshold only at the end of the plate nearest the microballoon (see section 1.7.7).

Exposed foils were etched for 3 h at 75°C in 6.25 N NaOH removing 5.9 μm of bulk surface. This etch time was chosen so that 3.5 MeV α-particle tracks were just etched to the end of their range. Additional foils exposed to Cf^{252} α-particles were included in the etch tank for calibration purposes.

Measurement of the size of background α-tracks that were inevitably present in the foils from the decay of Rn^{222} and daughter products naturally present in air were consistent in size with α-tracks on the calibration plastic. This indicated that the plastic had maintained its response characteristics despite the hostile background radiation environment close to the imploding microballoon and enabled measurement of Cf^{252} α-particle tracks to provide a calibrated V_T-R curve for the exposed foils.

All implosion shots where α-emission was detected yielded tracks considerably smaller in size than that expected from a 3.5 MeV α-particle and were visibly etched well beyond their range. This is illustrated in

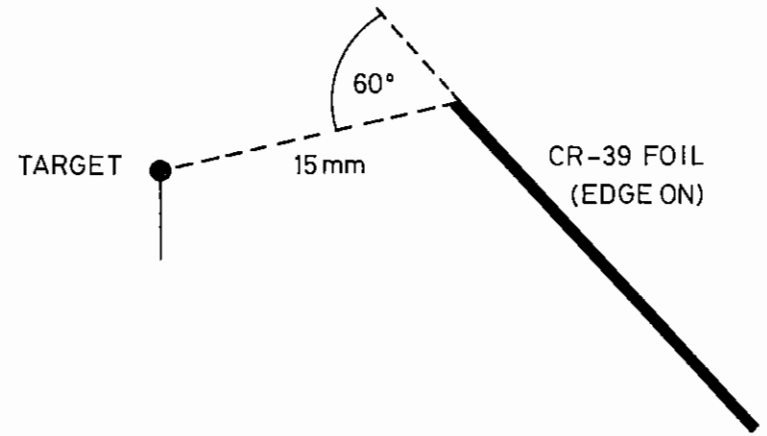

Figure 5.16 Schematic of CR-39 α-particle detector geometry.

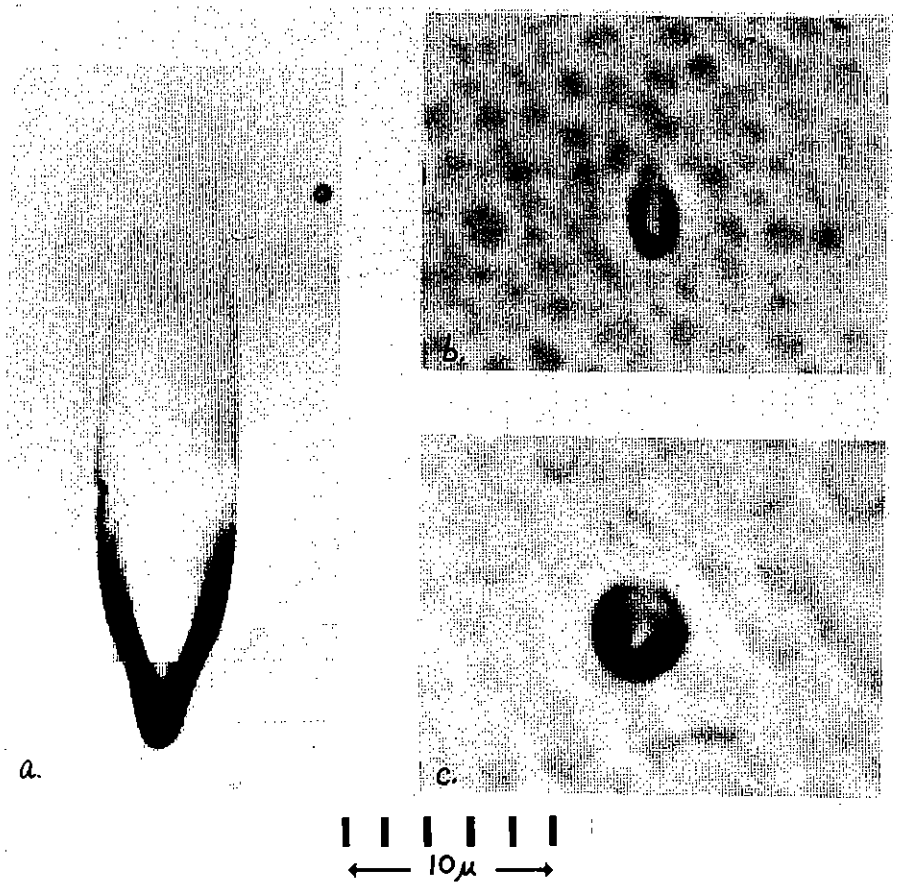

Figure 5.17 α-particle tracks in CR-39. (a) 5.55 MeV particle at dip angle of 38^0 (b) α-particle of 0.3 MeV energy from laser imploded DT filled target (c) Proton like particle assumed to be a fast ion.

Figure 5.17 which shows a photomicrograph of one of these tracks (b) alongside the track of a particle of range ∿ 40 μm(a). Detailed examination showed that the ranges of all tracks were < 4 μm corresponding to energies below 1 MeV. An analysis scheme was therefore developed specifically to determine the energy on these low range tracks.

Of 10 D-T filled target implosions showing neutron yields, 3 gave measurable α-tracks in the plastic. The resulting α-particle energy spectra for these are shown in Figure 5.18.

A feature of all the emissions is the down-shift of α-particle energy in escaping from the compressed fuel and pusher material. The energies are confined in the range ∿0.1 - 1 MeV in all cases. We estimate a low energy detection cut-off of 100 keV. Table 5.02 shows the corresponding 4π emission and neutron yield for each shot. The most important observation is that for most shots in which neutrons were produced, no α-particles were seen. When α-particles were observed their yield was much below (X 10) the neutron yield and the measured energies were very low. This immediately gives us an estimate of the density-thickness (ρR) product along the path from the target centre through the imploded shell or pusher to be ∿ 3×10^{-3} . The fact that some particles nevertheless have residual energies of up to 0.3 MeV indicates either spatial or temporal variations of ρR at around the time of yield.

Table 5.02

Shot no.	DIA(μm)	Wall thickness(μm)	Estimated 4π α-emission	Neutron yield
4 10/12/81	132	1.54	8.9×10^3	-
1 14/12/81	111	1.23	4.5×10^3	3.4×10^4
4 14/12/81	119	1.28	4.3×10^3	10^5

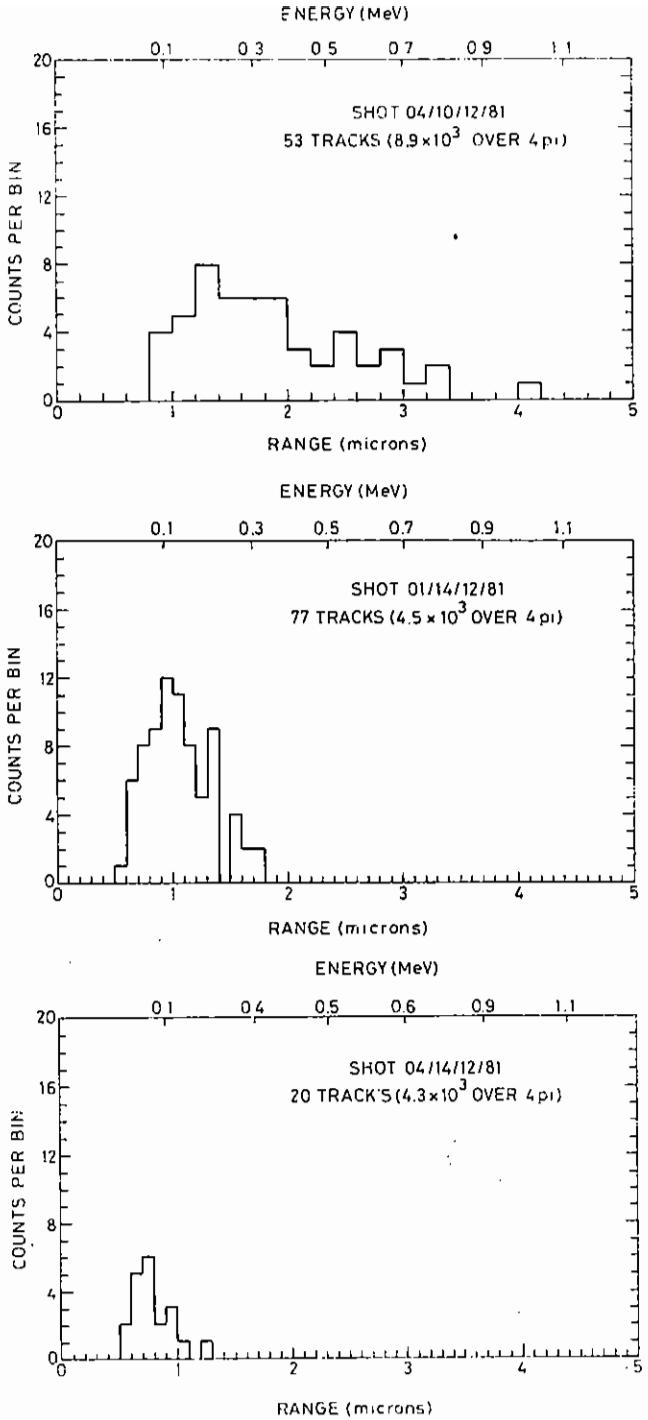

Figure 5.18 Energy spectra of α-particles escaping from imploded DT filled shells for three laser shots.

5.3.5 Space resolved X-ray spectroscopy

A space resolving crystal spectrometer measured the emission in the region 9 - 3.5A. Continuum core emission was observed on some shots. A typical spectrum is shown in Figure 5.19 showing Neon continuum from the core escaping through the silicon K window. Silicon absorption lines, due to the compressed glass are observed. A shifted silicon absorption edge is also evident indicating Li and He like silicon in the pusher. The slope of the continuum emission is consistent with an X-ray temperature of about 200 eV.

No argon line emission was seen from argon filled targets.

5.3.6 Time resolved X-ray emission

The Von Hamos curved crystal spectrometer (Section 1.7.1) was used to measure the time history of the implosions. A typical streak is shown in Figure 5.20 for a neon filled glass shell target.

The continuum burst corresponds to the time of peak compression. Figure 5.21 shows a streak for a target coated with plastic and 10nm of gold. In addition to the emission at peak compression a burst of continuum emission from the gold layer is also observed. From this type of shot implosion times of a few 100 ps were indicated.

5.3.7 Conclusions

Detailed analysis of the data has yet to be carried out but preliminary examination indicates that cores of a few 100 eV temperature and a few cm^{-3} density were produced for targets with aspect ratio greater than about 20. Compression ratios achieved were less than predicted by 1 - d modelling due possibly to non-uniform illumination or hydrodynamic instability. In order to achieve high enough core temperatures to compensate for the reduced adiabatic compression additional preheat must occur. For thin shell target ($Ar^{\sim}2\mu$) radiative preheat of the fill gas

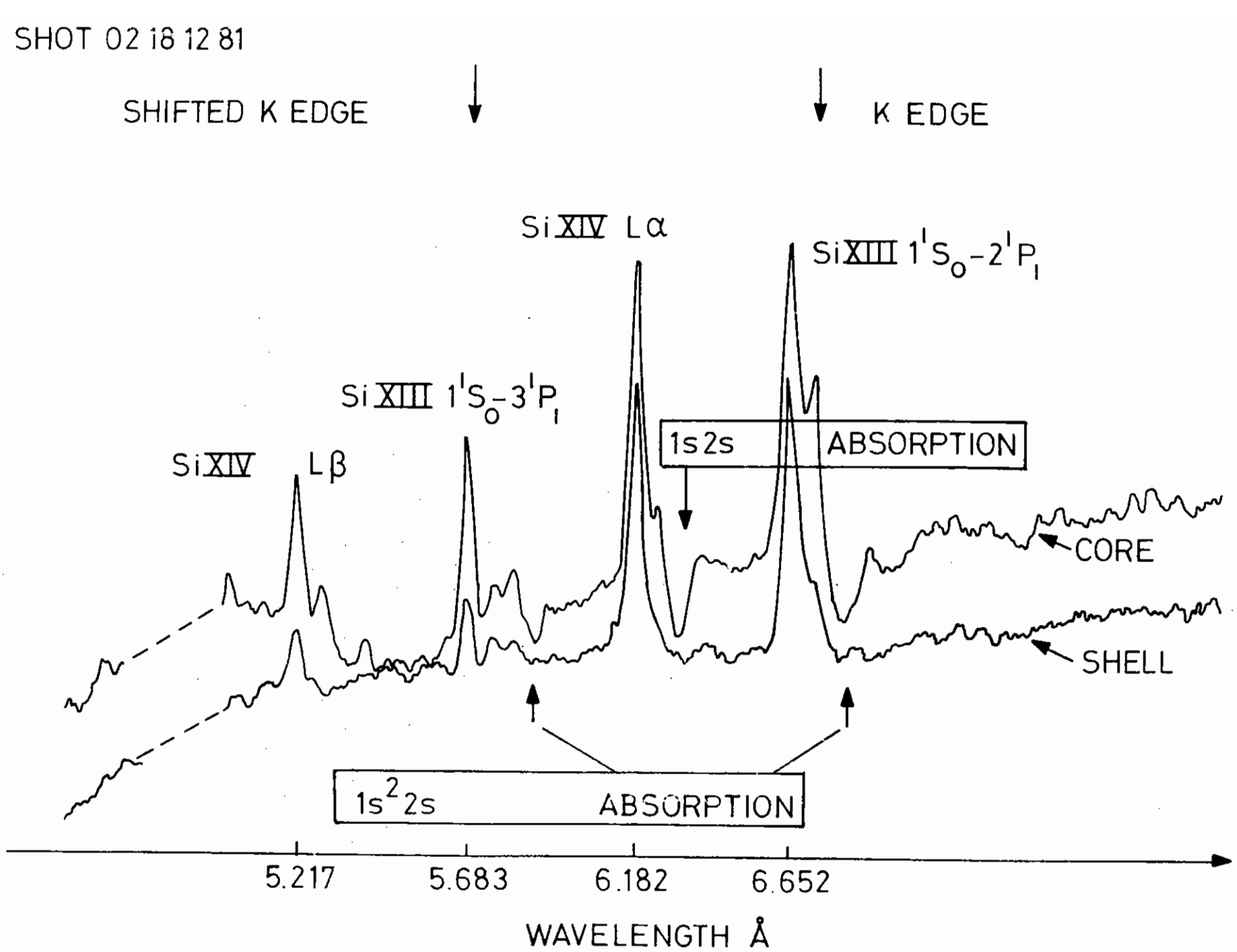

Figure 5.19 Time integrated space resolved X-ray spectrum from a neon filled glass shell target.

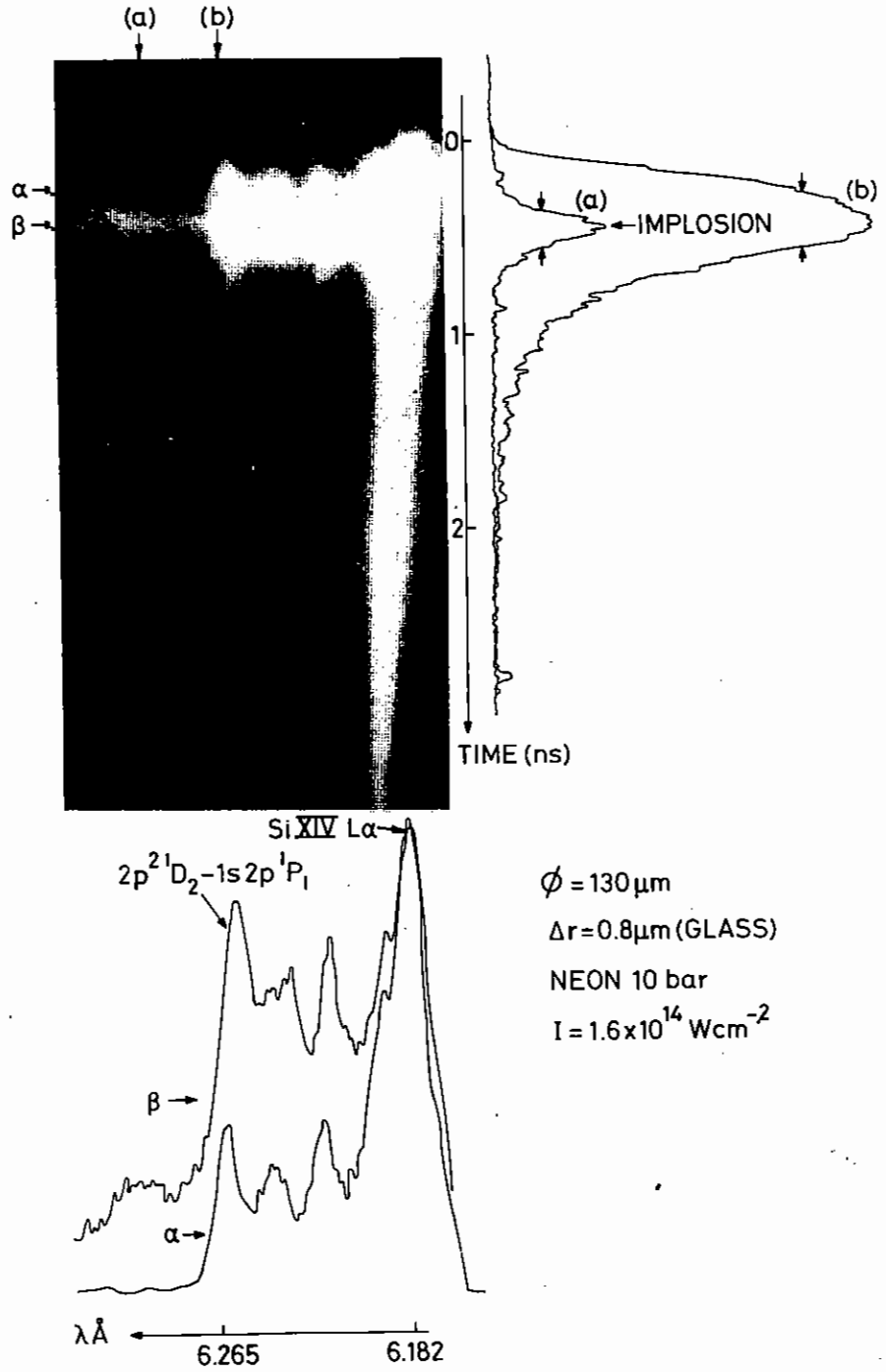

Figure 5.20 Time resolved X-ray spectrum from neon filled glass shell target.

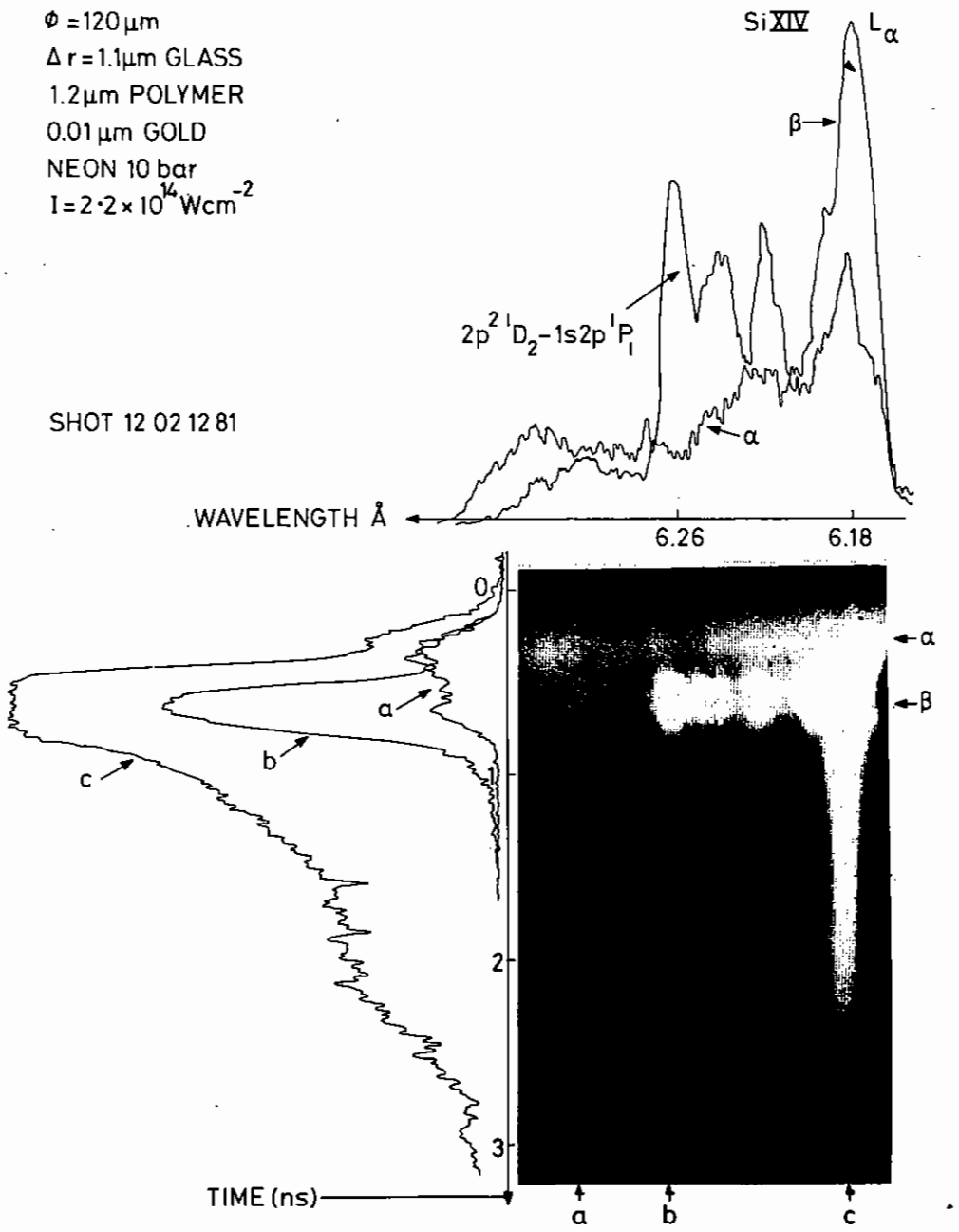

Figure 5.21 Time resolved X-ray spectrum from a neon filled glass shell target coated with 1.2 μm of plastic and 10nm of gold.

is comparable to the shock preheat.

J Kilkenny, B MacGowan (Imperial College) A Fews, D Henshaw (Bristol)
M Key, P Rumsby, C Hooker, S Knight, W T Toner and D Peplar (RAL)

5.4 Stability studies on Ablatively Accelerated Lollipop Targets

5.4.1 Introduction

The classical Rayleigh-Taylor (R-T) instability (5.04) is expected to occur in laser driven implosions where a dense shell is accelerated by lower density plasma formed by laser irradiation (5.05, 5.06,5.07).

Numerical simulations have predicted a growth rate $\gamma \approx 0.3\gamma c$ (where $\gamma c = (ka)^{\frac{1}{2}}$ is the classical growth rate for wave number k and acceleration a), and a peak growth rate for $k = 2\pi/\Delta r$ where Δr is the shell thickness. The peak instability growth exponent γt in implosions of a shell of radius R is then approximately $(R/\Delta r)^{\frac{1}{2}}$, implying an upper limit to shell aspect ratio $R/\Delta r$ and therefore a serious limitation on the implosion velocity obtainable with a given driving pressure (5.05).

We have made the first direct experimental observations of the instability in a laser accelerated target. The time-averaged growth of an imposed perturbation on a target has been measured to be $0.3 \pm 0.05 \times (ka)^{\frac{1}{2}}$ which is in closer agreement with numerical simulations than with the classical value.

5.4.2 Observation of R-T growth

The accelerated target was a plane aluminium disc of diameter 550 μm and thickness 3 μm, symmetrically irradiated with three of the six orthogonal 0.53 μm beams of the 6 beam compression facility (5.08). Each of the beams was focused with an f/1 lens at an angle of incidence of 56°, allowing the target normal direction to be used for diagnosis by streaked X-ray radiography.

To measure the acceleration of the targets they were positioned edge on and accelerated transversly across the field of view of an X-ray pinhole camera which had a 5 μm pinhole filtered with 3 μm of Al and 15 μm of Be. Images were recorded on an X-ray streak camera with 100 ps and 10 μm time and spatial resolution respectively. The three beams with 32J in total in 1.2 nsec were focused 250 μm beyond the targets, thus only illuminating and accelerating the central 300 μm of the target. The streaked X-ray emission is shown in Figure 5.22 where the accelerated central part of the target can be clearly seen moving away from the absorbing edge of the unaccelerated outer ring of target.

From knowledge of the laser irradiation time profile and independantly measured ablation pressure-irradiance scaling relationships (5.07) it was possible to determine the acceleration of the target as shown in Figure 5.22. This acceleration profile is compatible with the measured target trajectory also shown in Figure 5.22 and could be scaled to match the irradiance of the transmission measurement described below.

In order to observe the R-T instability the targets were turned to be facing away from the streak camera, and a different cluster of three beams was used to accelerate the target towards the camera. A more uniform illumination at approximately the same peak irradiance was used, by focusing 550 μm beyond the targets and increasing the laser energy to 87J on target. The R-T instability of the Al target was initiated by using a target with a corrugation of wavelength 20 μm and amplitude 0.5 μm.

Behind the Al disc targets a separate Cu target was irradiated by a fourth synchronous backlighting laser beam. This produced a plasma 500 μm across amd 100 μm high in the streak direction. In the spectral region of observation the X-ray emission from this target was several times brighter than that from the Al disc, and provided a source with which to make an X-ray absorption picture of the accelerated Al disc. The spectrum of the Cu backlighting target, measured with two crystal spectrometers, showed a peak at a wavelength of 10A (in I_λ) with a rapid fall at shorter wavelength. From the spectrum and the transmission of the filters the variation of the X-ray intensity reaching the streak camera with Al target

thickness was calculated, giving agreement with the 55% transmission observed through a 3 μm Al foil in a separate experiment. With this filtering 70% of the change in this spectrally integrated response with Al thickness was due to L shell absorption, the remaining change was due to K shell absorption in the Al. An X-ray streak photograph of the transmission of such an accelerated target is shown in Figure 5.23 with the corrugation parallel to the direction of streaking. Initially there is, as expected, no variation of transmission across the target, but as the instability grows, mass is redistributed and modulations in the transmission with a period of 20 μm can be seen. In control experiments, with no initial corrugation, no such regular modulation is observed.

The film density modulations evident in Figure 5.23 were converted to mass per unit area modulation by using the calculated variation of spectrally integrated transmission with Al thickness as described above. The amplitude of the modulation is shown in Figure 5.24 as a function of time, the errors representing the spread in the modulation amplitude of the 8 modulations evident at late time in Figure 5.23.

The average growth rate from Figure 5.24 is $1.6 \pm 0.5 \times 10^9$ sec^{-1}, with some evidence of saturation. The classical growth, taken from $(ka)^{\frac{1}{2}}$ and the acceleration scaled from the measurements shown in Figure 5.22, is also shown on Figure 5.24.

The classical growth is started, in Figure 5.24, at the onset of target motion with an initial amplitude determined by projecting back the slope of the experimental observations to zero time. This amplitude (corresponding to approximately 0.1 μm in target thickness) is of the order of what might be produced in the target manufacturing process. It can be seen that the observed growth rate is $0.3 \times (ka)^{\frac{1}{2}}$.

The experiment has been simulated using a 2-dimensional Eulerian fluid code (5.10). An absorbed irradiance of 2.0×10^{13} W cm^{-2} was used so that the distance the foil moved in the simulation matched the observed motion. A corrugated target as used in the experiment seeded the growth of an instability at the desired wavelength. The code predictions of

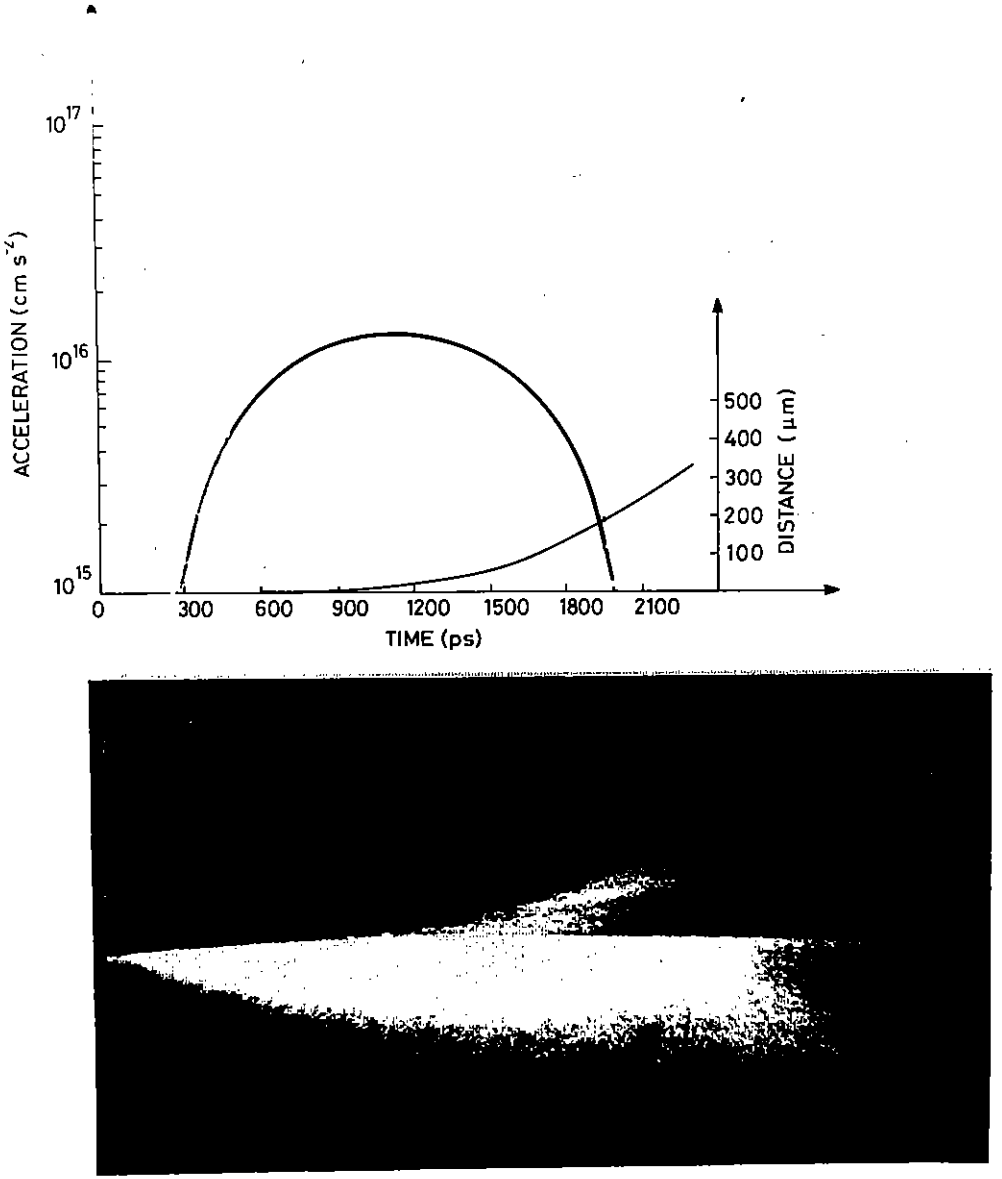

Figure 5.22 X-ray streak camera photograph of a laser accelerated microdisc target. The target is viewed edge on and is irradiated from below. The X-ray self emission of the accelerated material can be seen moving vertically away from the absorbing edge of unirradiated material. Also shown (above) is the target trajectory and the derived acceleration.

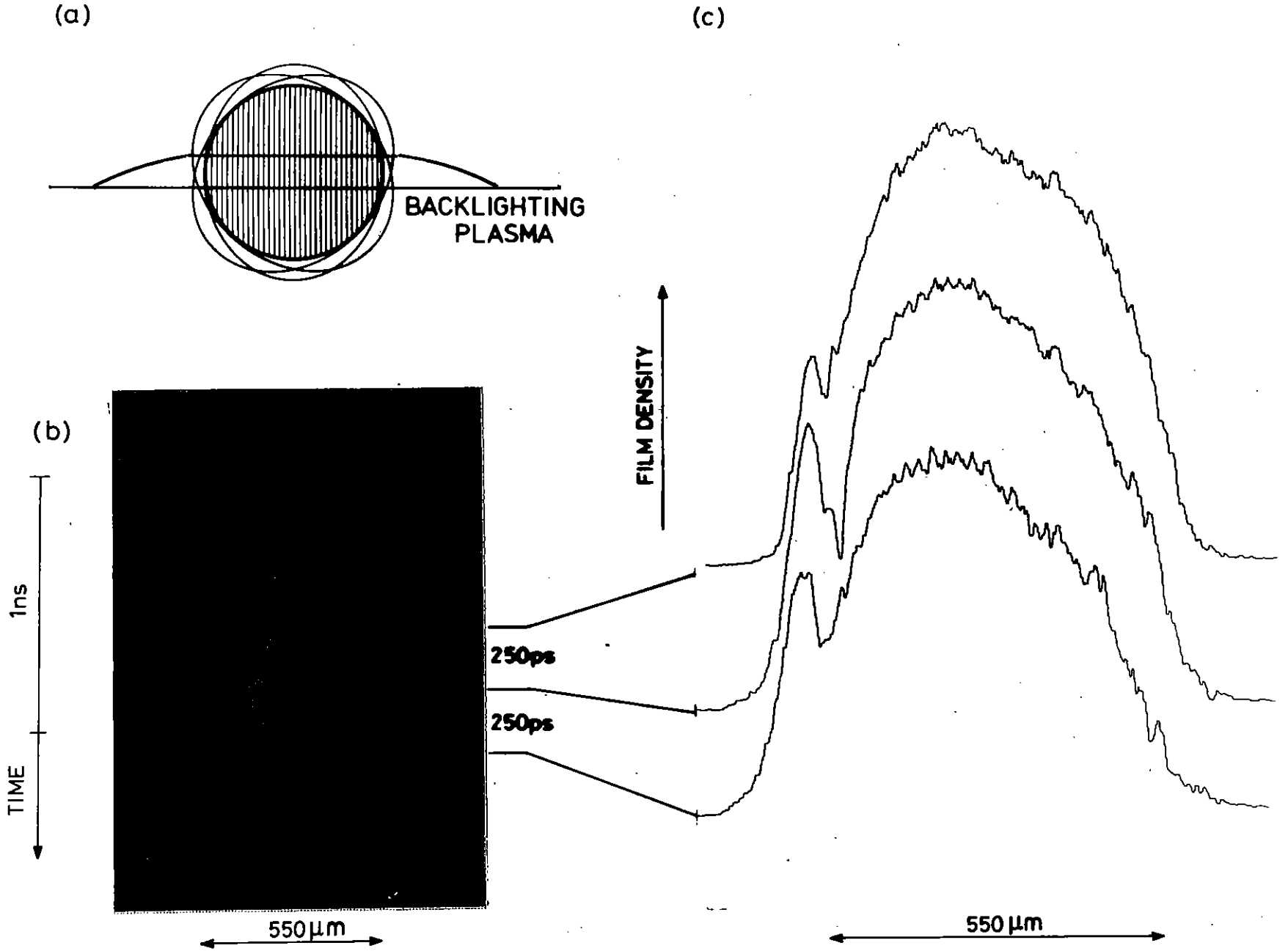

Figure 5.23 (a) Corrugated microdisc target illumination geometry showing location of backlighting plasma.

(b) X-ray streak photograph of backlighting emission through an irradiated microdisc target with 20 µm corrugation.

(c) Microdensitometer tracings of (b) at times 700, 950 ad 1200 psecs, showing increasing modulation with time.

growth in mass density modulations (after convolving with a pinhole response) are also shown in Figure 5.24.

The simulation predicts a slightly higher growth rate than is observed experimentally but of a similar amplitude. The code however starts from an initial mass modulation of zero which may be unrealistic. The analysis of the Al transmission assumes the cold X-ray mass attenuation coefficients, but the code values for the temperature and an LTE ionization equation shows that this produces a negligible error. The amount of mass ablated from the foil, estimated from independent measurements (5.09) is also shown in Figure 24. Several phenomena are omitted or modelled inaccurately in the simulation including radiation transport, equation of state, ion viscosity and magnetic field generation.

In conclusion, observations of the growth of area density modulations at a rate of 0.3 X $(ka)^{\frac{1}{2}}$ have been observed. It is encouraging for laser driven compression that the growth rate is reduced below the classical value as has been predicted by theory (5.10).

5.4.3 Other acceleration and stability observations

Target acceleration measurements similar to those described earlier were made on 5.0 μm thick mylar lollipop targets. Because of the small amount of self emmision produced by plastic a backlighting technique was used as described above. The target can be seen in absorption in Figure 5.25 as it moves across in front of the backlighting source. The estimated terminal velocity of the target is $1.8.10^7$ cms^{-1} in 0.9 ns and the derived ablation pressure is 14 Mbar for this shot.

A different method was also used to measure target motion. The short pulse backlighting technique (described in Sections 4.4 and 5.2) enabled 2-dimensional flash X-ray shadowgrams of accelerated lollipops to be obtained. Figure 5.26 shows a shadowgram of a 3 μm Al disc accelerated to $1.9.10^7$ cms^{-1} in 0.5 ns implying an ablation pressure of 30 Mb on this shot.

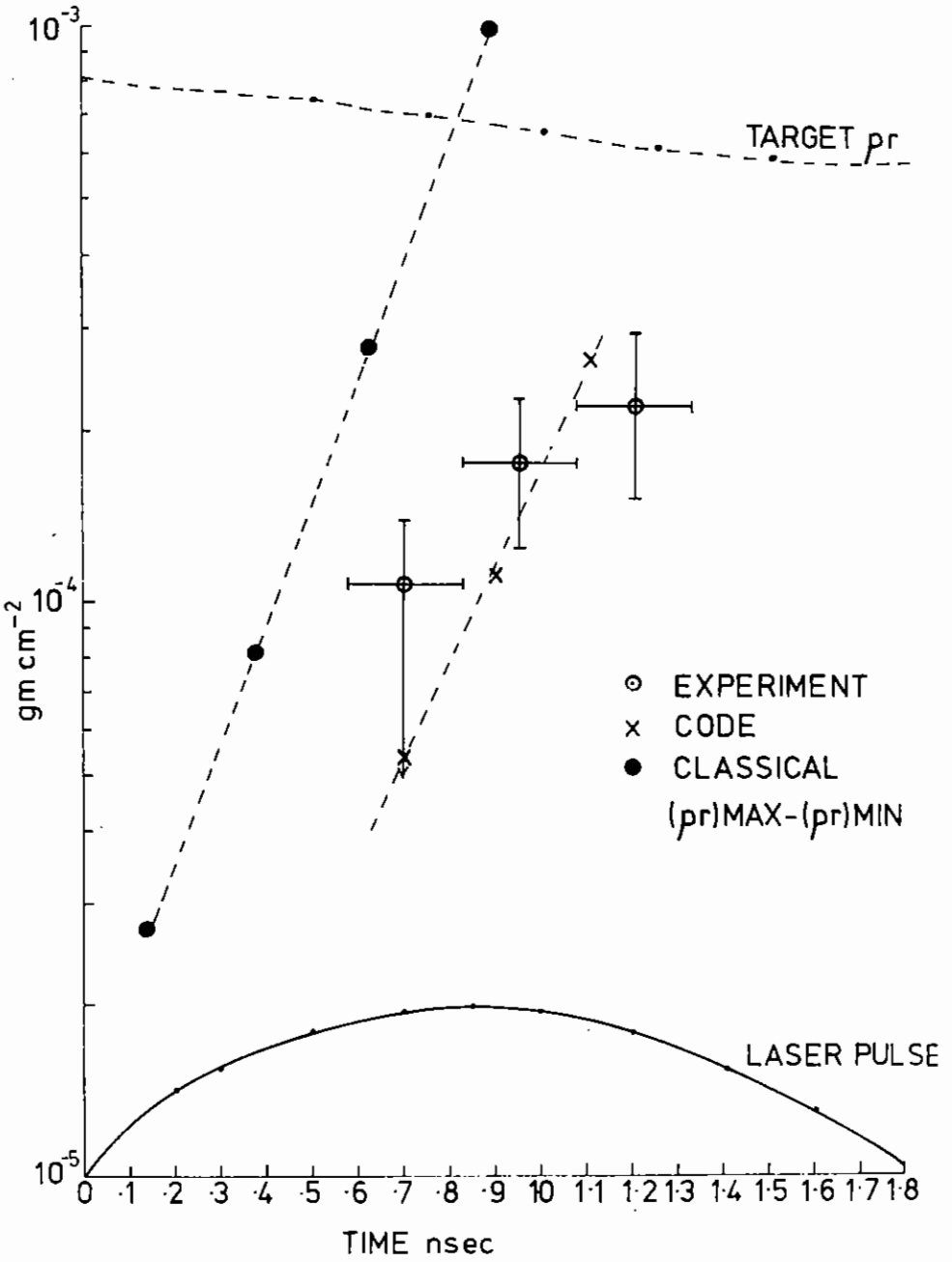

Figure 5.24 Graph of modulation in target areal density for the three experimental measurements in Fig 5.23 (c). Also shown are the results of 2-D fluid simulations and the modulation expected of a classically growing instability.

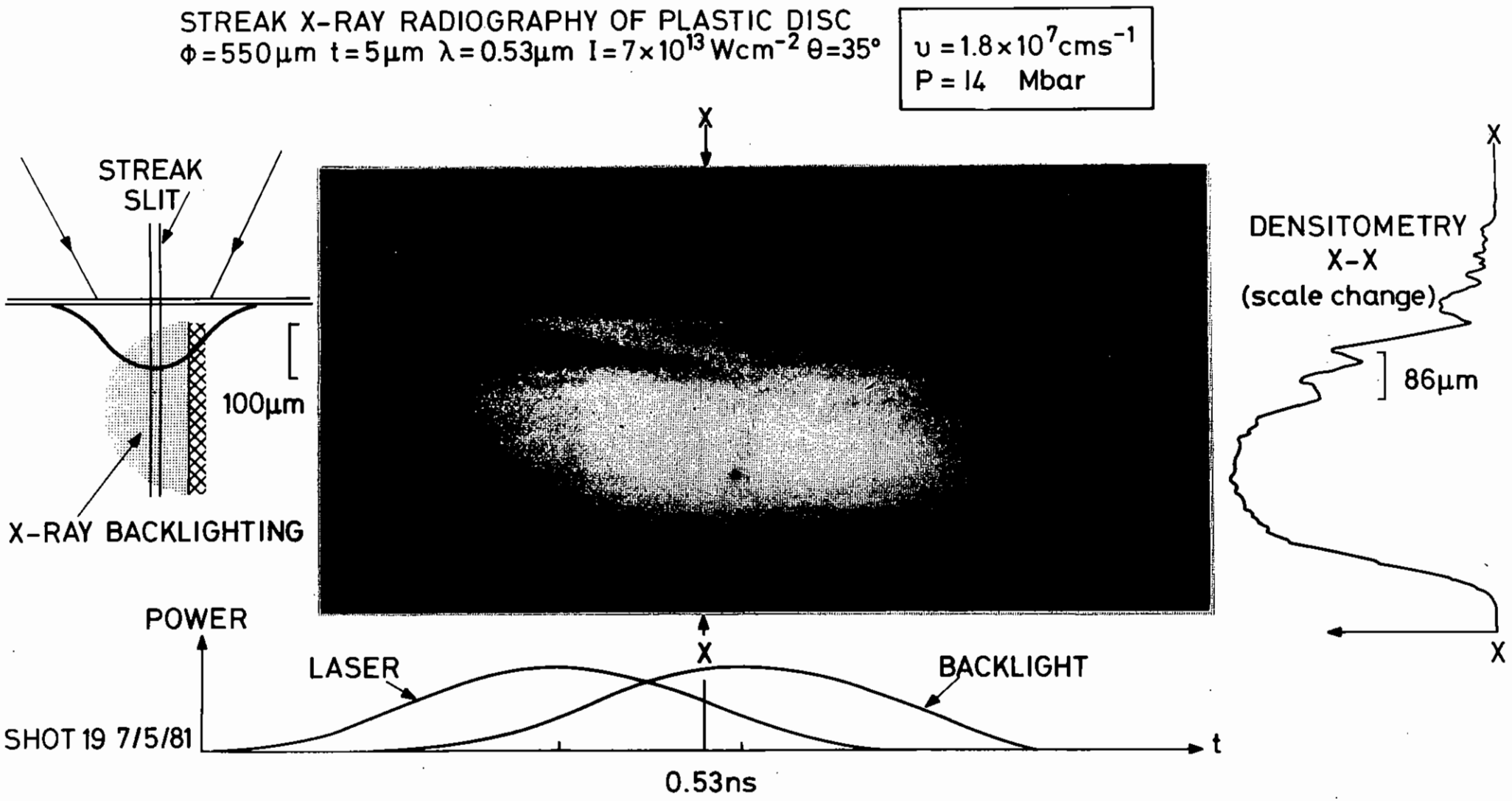

Figure 5.25 Streaked X-radiograph of accelerating plastic disc target.

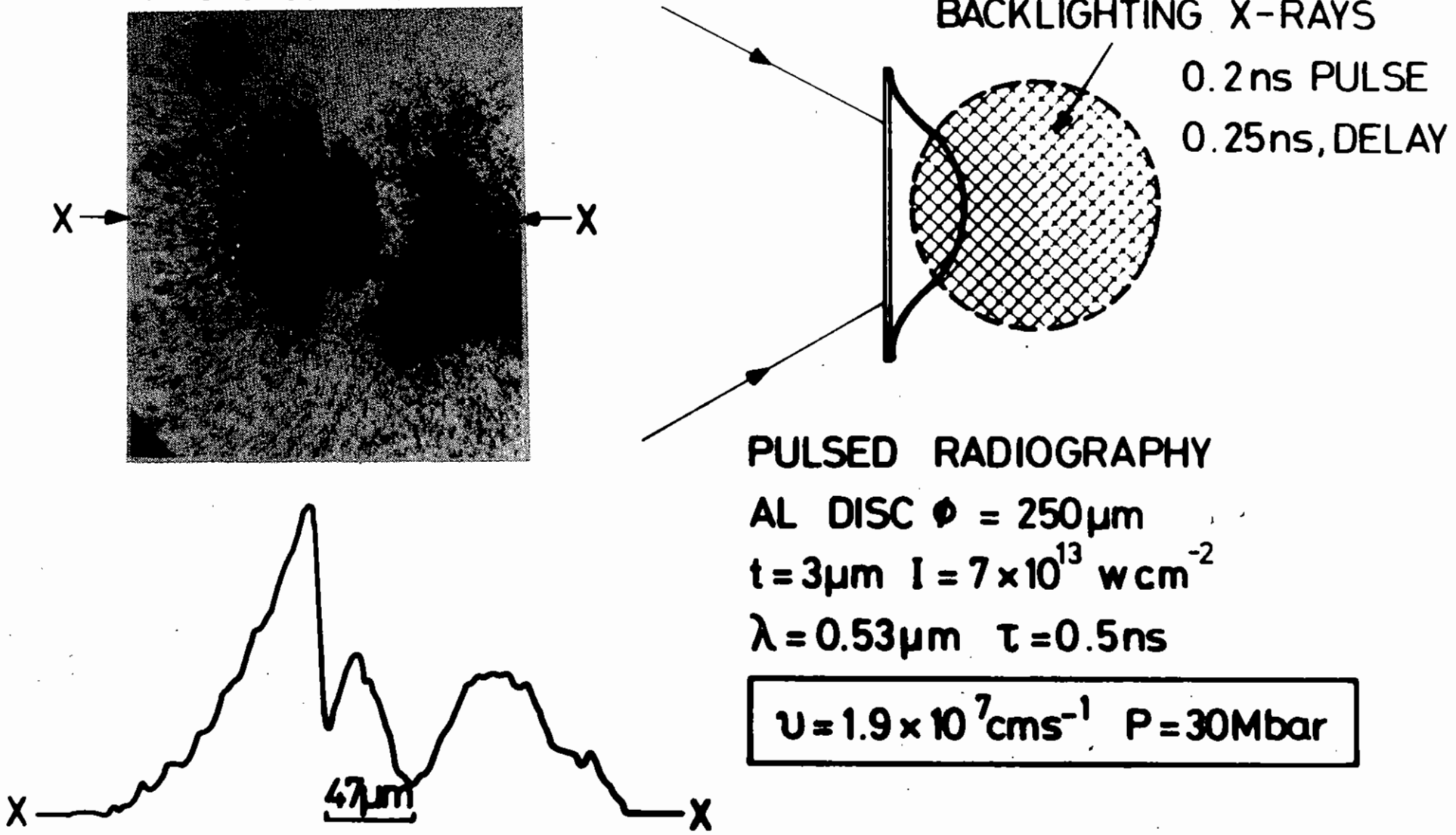

Figure 5.26 Pulsed 2-D X-radiograph of accelerating aluminium disc target.

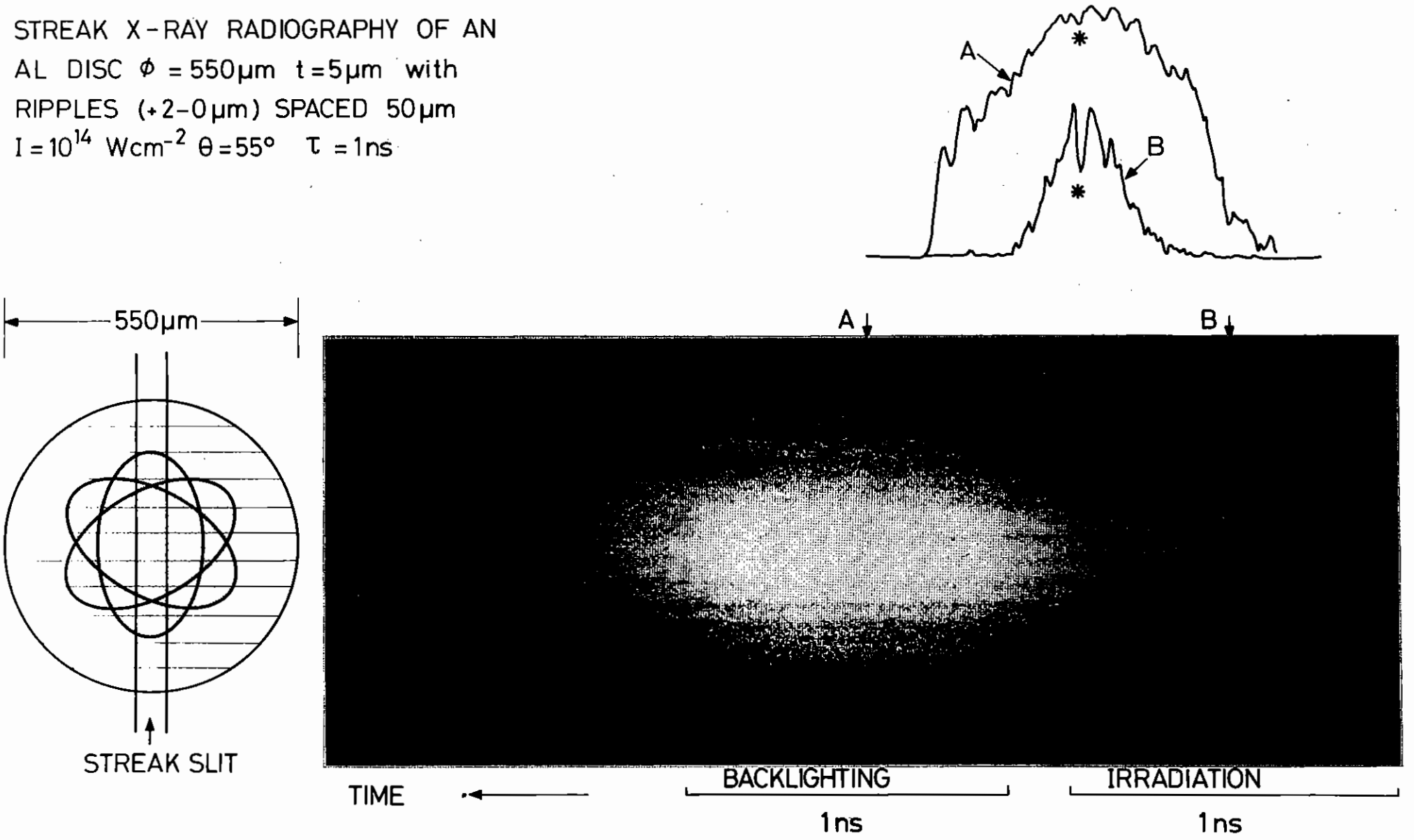

Figure 5.27 Streaked transmission X-radiograph of accelerating mass modulated aluminium disc target.

An attempt was also made to observe R-T growth in a mass modulated target. These were fabricated by coating through a mask onto a plain Al lollipop, stripes of extra material to a depth of 2 μm. An example of an X-ray streaked radiograph of such a target is shown in Figure 5.27. The mass modulation is clearly visible as a modulation in transmission through the target but no growth in the modulation amplitude is observed. This is probably due to the large wavelength of the perturbation (λp = 50 μm) and the lack of regularity in the perturbations, i.e. the wavenumber was not well defined.

A Cole, J Kilkenny (Imperial College), P Rumsby, M Key, C Hooker and S Knight (RAL)

5.5 Radiography of λ = 1.05 μm driven ablative implosions

Pulsed 2-D X-radiography experiments described in Section 5.2 relied on stacking a short pulse to generate a long target drive pulse synchronised to the initial short pulse used for backlighting. Preliminary experiments described here demonstrate a much improved technique whereby the synchronised oscillator system (described in Section 1.3.2) was used to generate 150 psec backlighting pulses synchronised to temporally smooth 1.2 nsec drive pulses.

The experiment, using this configuration for the first time, was similar to the study described in Section 5.2 where an X-ray streak camera was used as an active image recorder. The present experiment was carried out at 1.05 μm with typically 200J delivered to the target in six beams. Targets were low aspect ratio ($r/\Delta r \approx 6$-10) plastic coated glass shells and pure polystyrene shells. Typical targets had an initial diameter of 180 μm and were irradiated with an incident intensity of 1-3 X 10^{14} Wcm^{-2}. The experimental arrangement had the following measured parameters:- X-ray probe duration, 150 ps; X-ray probe energy, 2 keV; Spatial resolution, 12 μm; Overall magnification, X 20.

Figure 5.28 shows a radiograph of an imploding pure polystyrene shell taken 200 psec after the peak of the laser pulse. This shell had an initial diameter 180 μm, wall thickness 13.5 μm and was irradiated at 1.5 X 10^{14} Wcm^{-2}. Figure 5.29 shows the shell trajectory calculated from

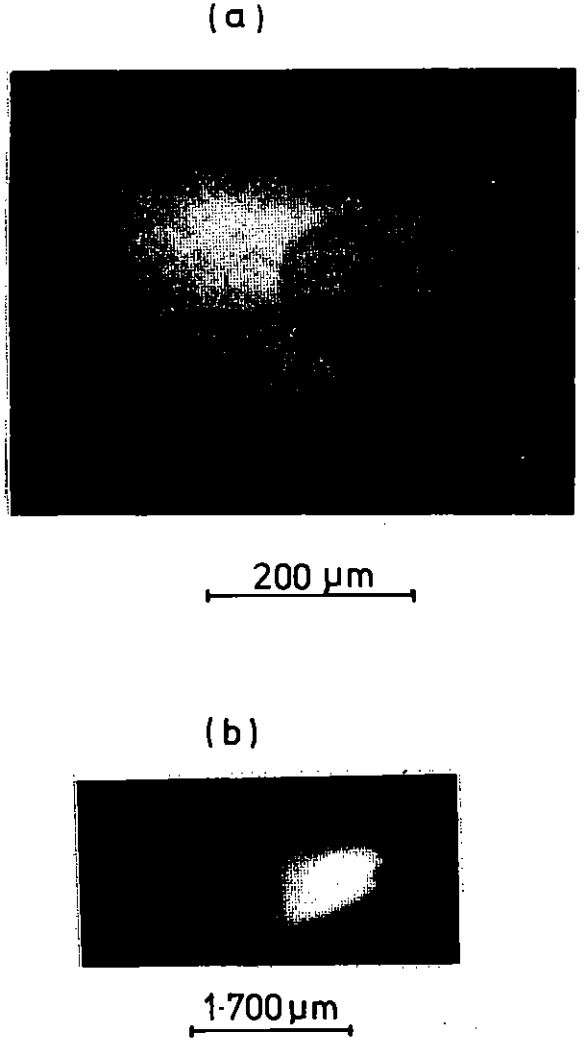

Figure 5.28 (a) Pulsed X-radiograph at 2 KeV, 200 ps after peak of main λ = 1.05 μm drive pulse. Initial target diameter indicated

(b) Pinhole camera photograph showing relative target self emission and X-ray backlighting source brightness at 1.5 KeV.

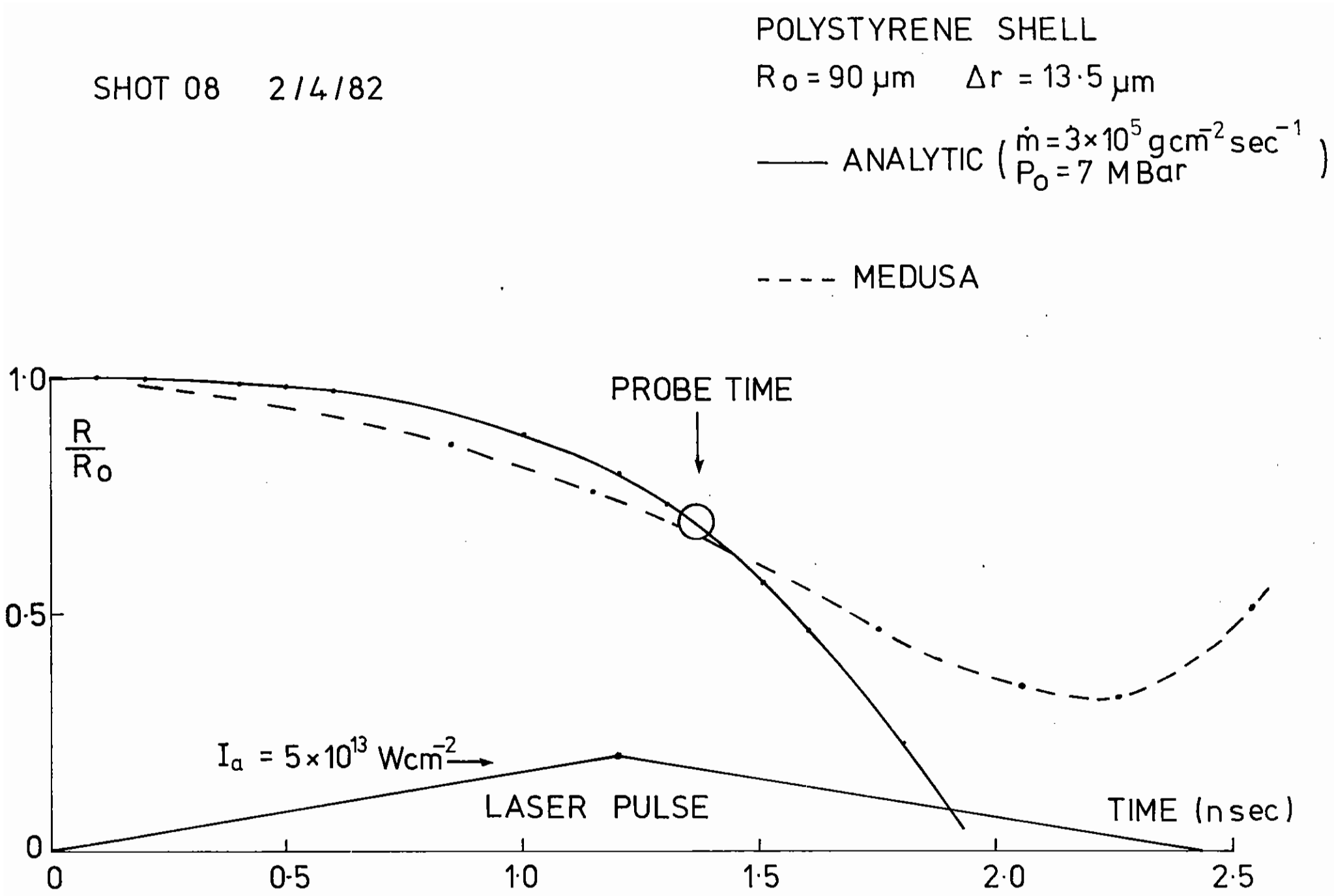

Figure 5.29 Comparison of calculated and computed implosion trajectories with experimental data for radiograph shown in Fig 5.28(a).

an analytic model taking the ablation pressure from earlier measurements (in this case 7 M Bar at the peak of the pulse). The circle represents the measured shell diameter from Figure 5.28 and also shown is the shell trajectory from a Medusa simulation.

Preliminary conclusions indicate that the quality of the implosions obtained at 1 μm, $I \sim 10^{14}$ Wcm^{-2} is better than obtained previously at 0.5 μm, $I \sim 10^{14} Wcm^{-2}$ and probably due to enhanced thermal smoothing. This is indicated by the well defined shell structure observed well into the implosion. Radiographs obtained closer to peak compression time with polystyrene shells were ill-defined, possibly due to excessive hot electron preheating (at $I\lambda^2 > 10^{14}$ $Wcm^{-2}\mu m^2$) causing the final core material to become transparent. Better defined core features observed with plastic coated glass shells indicated a volumetric compresion ≈ 30 with a core density ≈5 gcm^{-3}.

C Lewis, P Cunningham, M Lamb, S Saadat, P McCavana (Queens University, Belfast), M Key, P Rumsby, C Hooker and S Knight (RAL)

References

5.01 Key M H, Lewis C L S, Lunney J G, Moore A, Hall T A and Evans R G Phys. Rev. Lett 41, 1467, 1978

5.02 Key M H, Rumsby P T, Evans R G, Lewis C L S, Ward J M and Cooke R L Phys. Rev. Lett. 45, 1801, 1980

5.03 Rutherford Laboratory Annual Report to the Laser Facility Committee 1981. Section 5.2 RL-81-040(1981)

5.04 (1) Lord RAYLEIGH, Theory of Sound (Dover, New York 1945), 2nd 2nd ed., Vol.2; G.I. Taylor, Proc. Roy. Soc. (London), Ser.A 201, 192 (1930)

5.05 J.H. Nuckolls, L.Wood, A.Thiessen, G.Zimmerman, Nature 239, 139 (1972)

5.06 R.L. McCrory, L.Montieth, R.L.Morse and C.P. Verdon, Phys. Rev. Lett. 46, 336 (1981).

5.07 M.H.Emery, J.H.Gardner and J.P. Boris, Phys. Rev. Lett. 48 677 (1982)

5.08 I.Ross et al. J.Quantum Electronics QE-17,1653 (1981)

5.09 T.J.Goldsack, J.D. Kilkenny, B.J.MacGowan, S.A.Veats C.L.S. Cunningham, P.C.Lewis, M.H.Key, P.T.Rumsby, W.T.Toner Optics communications, in press 1982; also Annual Progress Report to Laser Facility Committee, RL-81-040

5.10 G.Pert, J.Comp. Phys. 43, 111 (1981)

CHAPTER 6 SPECTROSCOPY AND XUV LASERS

INDEX

CHAPTER EDITOR: I N Ross

CHAPTER 6 SPECTROSCOPY AND XUV LASERS

6.1 Introduction

The ongoing programme over the past year has reflected the increasing activities of the group in novel areas of X-ray and XUV spectroscopy. Classical grazing incidence and X-ray techniques have been developed to yield new diagnostic techniques, and to improve existing ones. In particular the time resolved spectra of pre-heated multi-layered targets opens a new field of interest not only for pre-heat diagnostic but also for the observation of line emissions from cold dense plasmas.

The more conventional line ratio diagnostic of plasma is open to interpretational difficulties when applied to laser produced plasmas. Careful theoretical analysis is necessary to reolve these difficulties. The development of appropriate conventional models to problems is an important aspect of the work of the group.

The use of laser produced plasmas as a source of lines from highly ionised species has formed a continuing part of the programme of the group since its inception. Further work in this area studying high level transitions in Li, Be, Na and Mg like ions was carried out with a view to diagnostic applications.

A new area of investigation opened this year with the preliminary experiment to study simultaneous electron-photon excitation of metastable helium states. Although the pilot experiment was not successful, it provided essential experience, which should allow more profitable investigations in the future.

Work on the carbon VI XUV laser scheme at 182 Å has proceeded during the year: the aim of this work being to try and resolve any differences between experiments at Hull and at the CLF. These experiments have been satisfactorily carried out, and improved alignment techniques developed. It is to be hoped that significant progress will occur in the coming year.

6.2 Carbon VI Experiment

6.2.1 Theory

Two major theoretical results have made a major impact on our understanding of the carbon fibre XUV laser system. These are the existence of incomplete fibre burn and the residual mass, and the generation of gain on impurities seeded in the fibre. In both cases numerical predictions have been observed in the experimental data obtained at Hull.

A detailed study of the interaction of line focused laser beams with carbon fibre targets is at present being carried out using the two dimensional hydro-codes MAGT and LAG2. The original aims of these calculations was to identify the impuritance of the pre-pulse and to estimate the plasma absorption. It was quickly realised that the behaviour was more subtle than had been initially appreciated. As outlined in last years report (6.21) the pre-pulse forms a hot tenuous plasma surrounding the entire fibre within which thermal conduction efficiently heats the fibre symmetrically provided the laser intensity is not too high that non-classical effects are significant. Under the conditions of the Hull experiments the heating is symmetric provided the fibre diameter is less than 6 μm; a result observed experimentally.

At the conclusion of the heating phase only a fraction of the fibre is observed to be heated in the model, unless the fibre diameter is less than 2.5 μm. Otherwise there remains a cold dense residual core. In the range of fibre diameters 2.5 - 6 μm, the mass of hot plasma is nearly constant. Since the residual core remains cold and dense, and therefore small, it plays practically no role in the expansion. The hot plasma therefore expands in a very similar fashion to a uniformly heated cylinder of the same mass, ie of initial diameter approximately 3 μm. This behaviour is observed experimentally. The weak diameter dependence of the experimental data is characteristic, and is clearly due to this effect. In addition we also observe that the data is in good agreement with the uniformly heated model for a fibre of 3 m diameter, confirming these predictions. The

absorption coefficient for a line fibre may be estimated at about 15% by comparing these experimental results with the model. These results have a useful practical significance, for fibres of narrow diameter are difficult to manufacture reproducibly and to handle. It appears, however, that the interaction smooths out variations due to fibre irreproducibility and departures from uniformity of the fibre itself.

Since the onset of gain in the expanding fibre is limited by the termination of trapping of the line L_α, any phenomenon which reduces the self-absorption of L_α can be expected to have a major effect on the gain due to the rapid decrease in density with time. Thus if the lasant is present only in small concentrations in a host, the host may provide the high electron density necessary for recombination, without the high lasant density giving rise to L_α trapping. There is, of course, a reduction of gain due to the low lasant density. On balance however these two effects cancel out, and gains of the same order of magnitude on H_α as in the host may be expected. We have modelled the case of nitrogen, oxygen, fluorine and neon impurities in carbon fibres and find peak gains at impurity levels not exceeding 20% as shown in the table below.

Element	N	O	F	Ne
Wavelength Å	133.8	102.4	80.9	65.5
Gain/cm	8.5	8.6	4.6	1.4

This effect has been observed in our carbon fibre experiments. The fibres contain nitrogen as an impurity though in variable amounts. In one plate an impurity concentration of about 10% nitrogen is estimated from the

line emission. A gain-length product of about 3 is measured in this case. This is a useful practical result, in principal greatly extending the range of the carbon fibre technique from 182 Å to 65 Å in wavelength, where it will join with the proposed aluminium foil scheme.

6.2.2 Carbon VI Experiment at Central Laser Facility

The experiments reported in the 1981 Annual Report (6.21) were designed to re-create experimental results obtained at Hull which showed gain on C VI Balmer α (6.22). Unfortunately, a number of problems, particularly with the GML5 spectrograph, produced inconclusive results which suggested very low energy coupling into the fibre. However, the calorimeter results which supported this view were felt to be unreliable because of the expected radial plasma expansion. In order to know the coupling accurately it is necessary to have some knowledge of the nature of the plasma expansion.

In view of these conclusions the last CVI experiment at the Central Laser Facility was devoted to resolving the question of what the coupling was, with a direct comparison experient being performed at Hull some months later.

The calorimeter which was used for these experiments consisted of an array of six pairs of thermocouple elements spaced 1 cm apart with each pair of elements connected directly to one input of a six channel chart recorder. Each channel was checked for sensitivity by shots on solid targets using a spot form and results were then normalized to one of the channels. It was expected that the signals from fibre targets would show a narrow peak which, together with the half width of the distribution, would allow estimates to be made of the energy coupling. It was hoped that measurements could be made with varying prepulse delay and also with second harmonic laser pulses but this proved to be rather ambitious and experiments had to be restricted to measurements at the fundamental laser wavelength. Initial problems with laser radiation being reflected off a pellicle directly onto the calorimeter array limited the variations which were possible in the prepulse delay. Results were obtained with a 10%

prepulse at either 1 ns or 2 ns delay.

The results obtained, with the calorimeter placed ∿ 21 cm from the target, below the lens, with a laser energy of 20 - 40 J in ∿ 80 ps produced coupling factors up to 8%. The focusing procedure (6.21), being very slow, greatly restricted the number of shots on target. Unfortunately, the low shot rate appears to be an unavoidable feature of this experiment since slight errors in focusing lend to considerably lower coupling. For example, using the target room CW YAG laser to align targets instead of the laser room YAG results in an unacceptably large error in the focus.

In common with previous CVI experiments at the Central Laser Facility pinhole camera pictures of the plasma were taken. These revealed a plasma length of ∿ 2 - 3 mm showing good uniformity (Figure 6.21). The length of the line focus, which was produced by a 500 cm concave cylindrical lens placed in front of an F/1.5 lens, determined from Polaroid burns was ∿ 3 mm. The fibres were generally not placed fully into the focus in order that the free end would be efficiently heated and not develop an absorbing region. The plasma was viewed axially with a one metre grazing incidence spectrograph (Astrophysics Research Unit, Culham) and spectra were obtained both from single and multiple shot exposures. The spectra were consistent with expectations but gain could not be inferred form them because no simultaneous measurements of spontaneous emission perpendicular to the axis were made. The resolution of the instrument was also insufficient to reveal the shape of the Hα doublet (6.21).

Electron temperatures were monitored with X-ray diodes and suggested ∿200 - 300 eV in good agreement with code calculations.

We conclude from these measurements that the focus was of good quality and that the fibre was positioned accurately within it. A peak coupling of ∿ 8% (ie 8% of the energy on target) seems to be attainable.

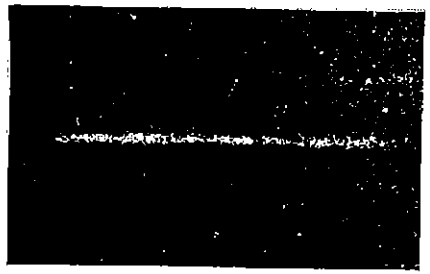

CARBON VI EXPERIMENT
X-RAY PINHOLE CAMERA PHOTOGRAPH

Figure 6.21 Line focus on 6μm carbon fibre, 35μm pinhole and 0.2μm aluminium fibre. Energy on target ≈ 5J/mm.

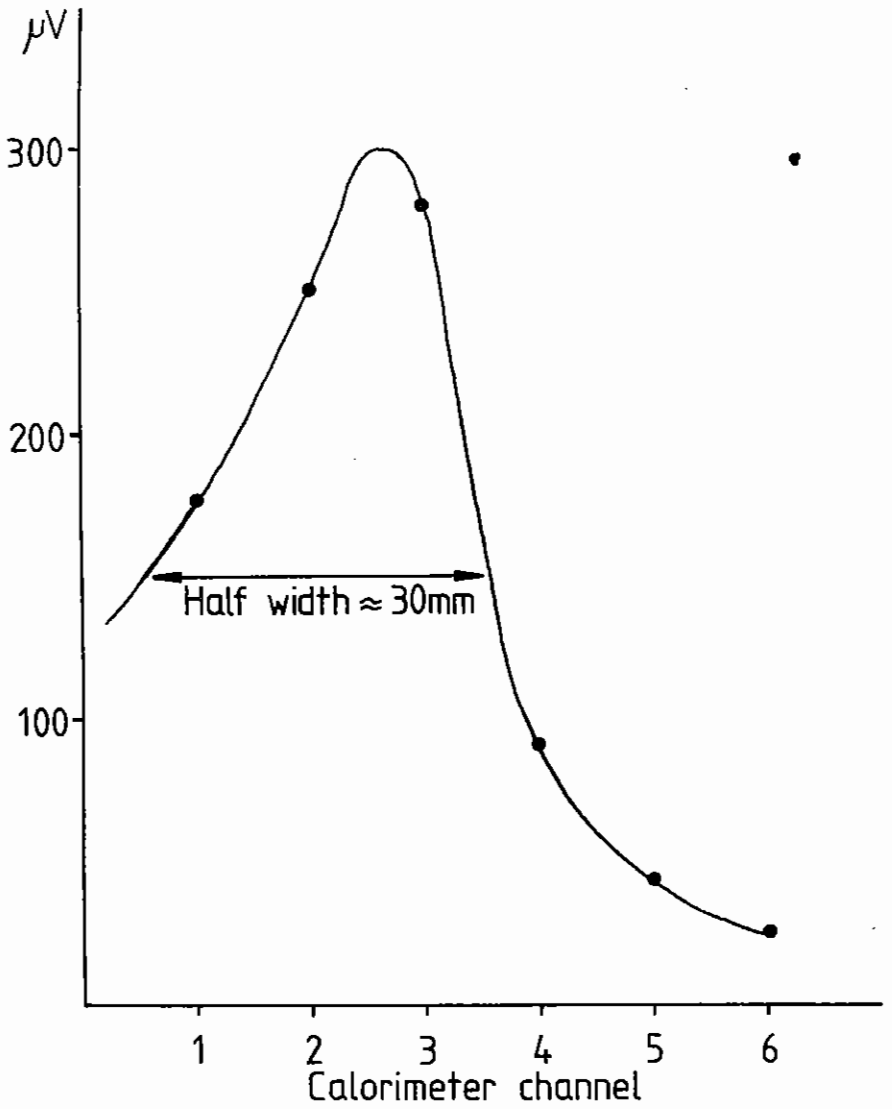

Figure 6.22 Signals recorded by the calorimeter array after normalization and correction for reflected light for a 7.8 J laser pulse on target. The coupling in this case is ∿ 9.4%. Channel 1 was closest to the free end of the fibre and the calorimeter was 5 cm from the target.

6.2.3 Carbon VI Experiment at Hull

In order to determine whether there is any basic difference between the experiments which have been done at the Central Laser Facility and at Hull a direct comparison has been made by measuring the coupling factor obtained at Hull.

In these experiments the focus is first defined by using low energy ocillator pulses to burn through thin coatings (∿ 200 Å) of indium deposited on glass slides. Using this technique it is possible to locate the focal position to within ∿10 - 20 m and this position is then referenced to graticules in orthogonal microscopes. The fibre can be placed relatively easily at the focus by means of a micropositioner with five degrees of freedom (three translation movements and two resticted rotation movements).

Other than the difference in the focusing technqiue the only differences between these experiments and those at the Central Laser Facility are a 20% prepulse preceeding the main pulse by ∿ 200 ps (in common with our earlier experiments) and a slightly shorter line lengths (∿2 mm, produced by a 200 cm concave cylindrical lens in front of an F/1 lens). The pulse length was initially 89 ps but will be changed to ∿170 ps for some later measurements.

Initial results were confused by severe reflections of laser radiation onto the calorimeter. These reflections, because the target chamber is very small, could not be entirely eliminated but their effects were reduced to an acceptable level by constructing a cone to limit the field of view of the calorimeter. Measurements made at ∿ 12.5 cm from the target (the furthest possible) proved inconclusive because the half width was not quite within the span of the calorimeter array. Moving the calorimeter sufficiently close without obstructing the focusing optics could only be achieved by putting the calorimeter directly beneath the target at a distance of 5 cm. Note that at this distance the effects of the inverse square law become quite noticeable and corrections have to be made to the signals from the edge elements. Results obtained in this

position typically produced peak signals of 200 - 400 μV with a half width between 15 mm and 35 mm depending on the peak. The peak coupling measured was 9.5% with a typical average being ∿ 7%. In calculating these values the channels were firstly calibrated by solid target shots with the calorimeter at ∿12.5 cm so that each element received almost identical signals. In addition several tests were done to determine the magnitude of the signals due to reflected laser light. These background measurements showed little consistency and so the highest signals obtained have been used to correct all the results. As a consequence of this the coupling quoted may be slightly low (possibly by ∿ 1%).

Figure 6.22 shows a typical result from a good laser shot and illustrates the very directional nature of the plasma expansion. The coupling in this case was ∿ 9.4% and the energy on target was ∿ 7.8 J in ∿ 80 ps.

Throughout these experiments problems with the focusing due to laser malfunction following modifications were encountered but these served to demonstrate that the calorimeter provides an excellent diagnostic for fibre experiments. An error of only ∿ 30 μm in the focus was seen to reduce the peak signals by almost an order of magnitude and illustrates once again that the major difficulty with this experient is achieving a good focus and accurate positioning.

Only one set of spectra was obtained in these experiments as a result of the focusing problems. Because the plates were multiple exposure and the energies from shot to shot varied considerably (∿4 J - 30 J) gain could not be inferred from the results.

6.2.4 Comparison of Results at Hull and the Central Laser Facility

The coupling factors measured at Hull and the Central Laser Facility are very similar and suggest that there is no basic difference between the experiments. A coupling factor 8 - 10% seems to be characteristic at the fundamental laser wavelength. It is also interesting that further, entirely independent, estimates of the coupling at Hull from space resolved experiments indicate a coupling of ∿ 10% when account is taken of

the incomplete burn-through of the fibre (6.23). The slightly higher value of the coupling in these experiments is thought to be due to two effects, firstly the earlier experiments were performed with polarisation at 45° to the fibre axis, allowing resonant absorption, whereas in the latter the polarisation was parallel to the fibre; and secondly due to the longer pulse length. It is planned to check these suggestions in the near future.

The delay between prepulse and main pulse appears to have little effect on the coupling over the range 200 ps - 2 ns which can be explained if the plasma 'blanket' formed by the prepulse is very slow moving (6.2.4). The prepulse fraction has not yet been investigated carefully but the fact that the preliminary results for 20% prepulse are similar to those for 10% prepulse suggests that it is not critical.

In the next scheduled experiment the coupling will be measured at the second harmonic wavelength. Axial and transverse viewing of the plasma by one metre grazing irradiance spectrographs is also planned for these experiments. If the coupling at the second harmonic should be found to be signficantly higher than the present coupling an experiment involving four green beam illumination of the target is envisaged, though alignment of the targets may then prove extremely difficult.

6.3 Trials for Experiment to Measure Simultaneous Electron-Photon Excitation of Metastable States in Helium

6.3.1 Introduction

The object of the experiment is to detect for the first time the laser assisted excitation of metastable Helium,

$$e + h\nu + He \rightarrow e' + He^{*}$$

and to measure the cross-section. The electron energy is just below the threshold of the direct reaction

$$e + He \rightarrow e' + He^{*}$$

We intend to make detailed measurements at relatively low irradiance ($\sim 10^{10}$ W cm^{-2}) using a high repetition rate low power laser (JK) and then to verify that the electron scattering cross-section is linear in the laser irradiance by repeating the experiment with VULCAN at $\sim 10^{12}$ W cm^{-2}. It may also be possible to study the photon wavelength dependence, perhaps using the UV radiation facility.

In 1981 the first tests of the method were made.

6.3.2 VULCAN Run

The experimental arrangement is shown in Figure 6.31. A pulsed electron beam with an energy of, for example, 19 eV and a photon beam from the laser intersect in the beam of He atoms from a gas jet. Atoms excited to the 19.8 eV metastable level are detected in the channeltron multiplier 55 mm from the interaction region. A 20 ns FWHM Q-switched pulse from the VULCAN laser was focused beyond the interaction region with a 1-metre lens to give a beam spot at the gas jet roughly 1 mm in diameter. Parasitic signals due to multiphoton processes in the background gas at 10^{-7} torr prevented any serious attempt to observe laser assisted scattering during this run. It is thought that they originated in the background gas at the minimum beam waist where the peak intensity could reach 10^{13} W cm^{-2}. Considerable progress was made in reducing these signals by enclosing the channeltron in a double shielded box with an entrance aperture screened from charged particles by biasing and deflecting fields. However, it proved impossible at the time to eliminate a prompt component we ascribe to ultraviolet photons. Owing to its very high impedence ($> 10^{9}\Omega$) and unitary construction the channeltron gain cannot be gated on in less than several milliseconds. In future runs a two element detector which can be gated will be used. It will also be advantageous to match the optics to produce an appropriately sized minimum waist at the interaction region so that the intensity is nowhere higher than it need be for the experiment itself. We found it possible to reproduce many of the features of the parasitic signals by directing the auxiliary JK laser at a solid object

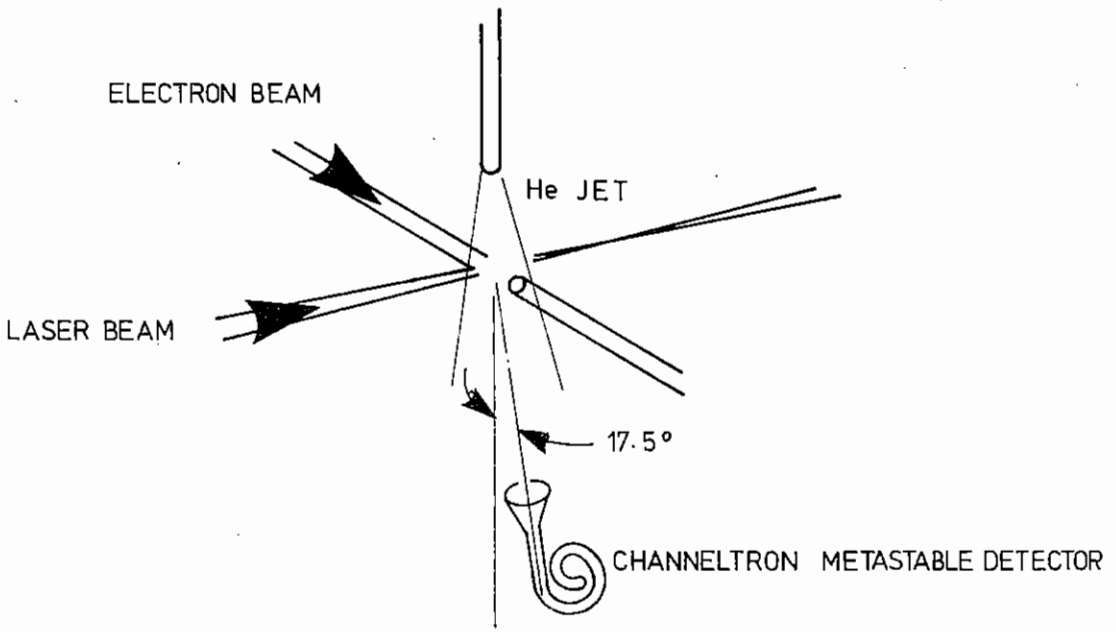

FIG. 6.31 LAYOUT OF EXPERIMENT

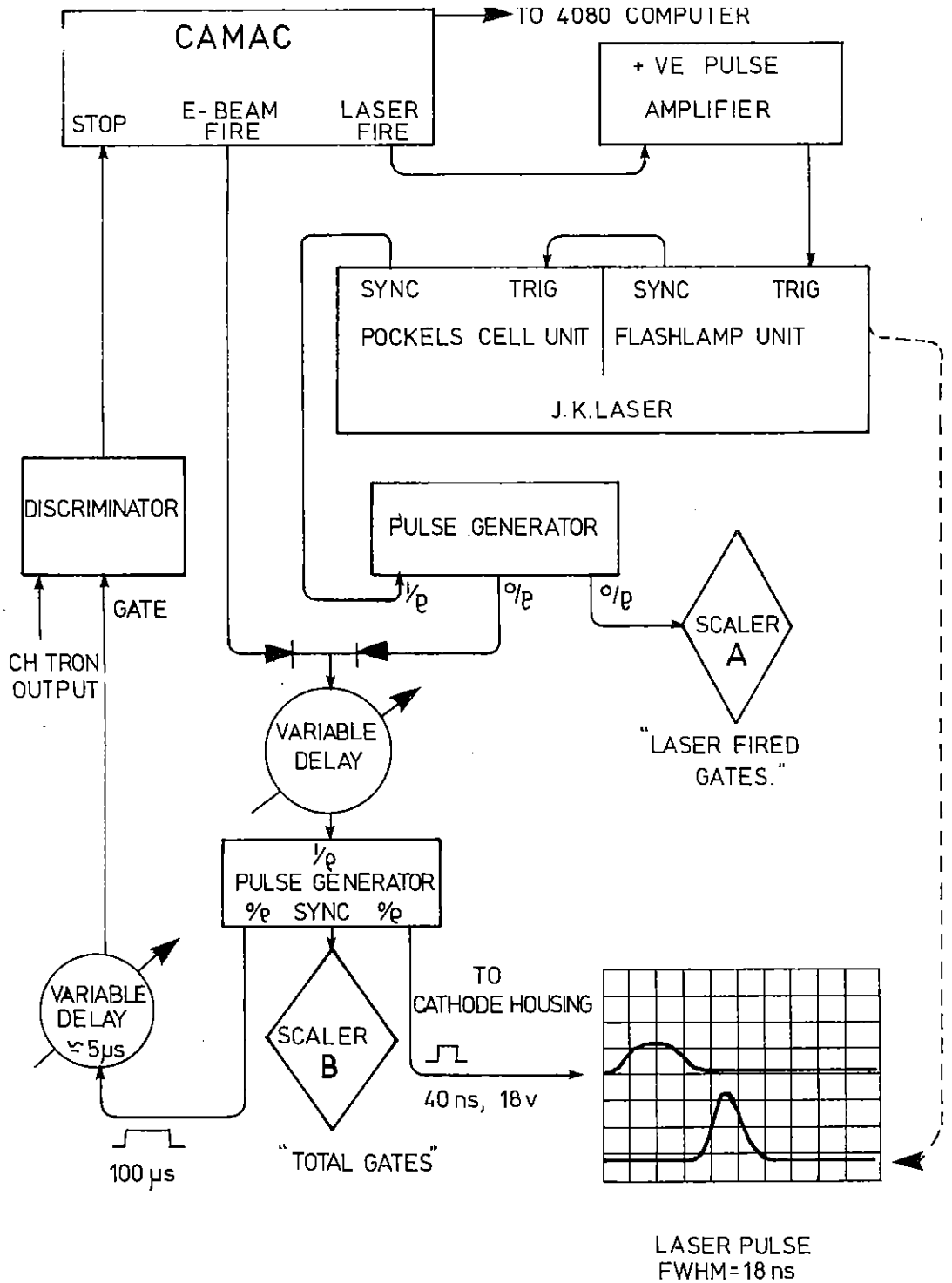

FIG. 6.32. SCHEMATIC DIAGRAM OF ELECTRONICS.

close to the interaction region so that tests of the improved system can be made off-line.

6.3.3 Low Power, High Repetition Rate Experiment

If as we expect the laser assisted electron scattering cross-section is proportional to the laser irradiance, then the total number of laser assisted events is proportional to the integrated laser energy passing through the interaction region during the experiment. The JK laser currently used for testing equipment at the CLF has an average power of 2 watts (peak power 6 Mwatts) and is thus capable of generating many more laser assisted events per hour than is VULCAN. However, the lower peak power results in a much smaller electron scattering cross-section and the experiment is much more sensitive to background due to the direct excitation of metastables by the high energy tail of the electron beam. A rather different approach is needed. The apparatus was modified so that "Laser On" shots at 20 pps could be interleaved with "Laser Off" shots at the same repetition rate and a sensitive difference experiment could be performed. The laser and electron beam firing signals were generated in a CAMAC unit interfaced to the CLF GEC 4080 computer which also logs the time of flight for each event. A schematic diagram of the electronics is given in Figure 6.32. It is possible to verify that any signal which is observed is real by repeating runs with a small ($\sim$ 20 ns) deliberate error in the timing of the electron beam relative to the laser pulse, or by introducing a small spatial error.

We anticipate the cross-section for laser assisted scattering of 19 eV electrons to be $\leqslant 10^{-3}$ of the cross-section for the direct scattering of 20.17 eV electrons and thus the feasibility of the experiment depends on the absence of any significant high energy tail to the electron beam. A high peak electron current is also needed in order to produce a significant number of events during the "Laser On" time of 1.7×10^{-8} seconds per pulse. We found that th eoriginal electron gun was unable to fulfil both conditions simultaneously. Figures 6.33(a) and 6.33(b) show the excitation curve at high and low current. On replacing the tungsten filament with LaB , a low work-function emitter, it was found possible

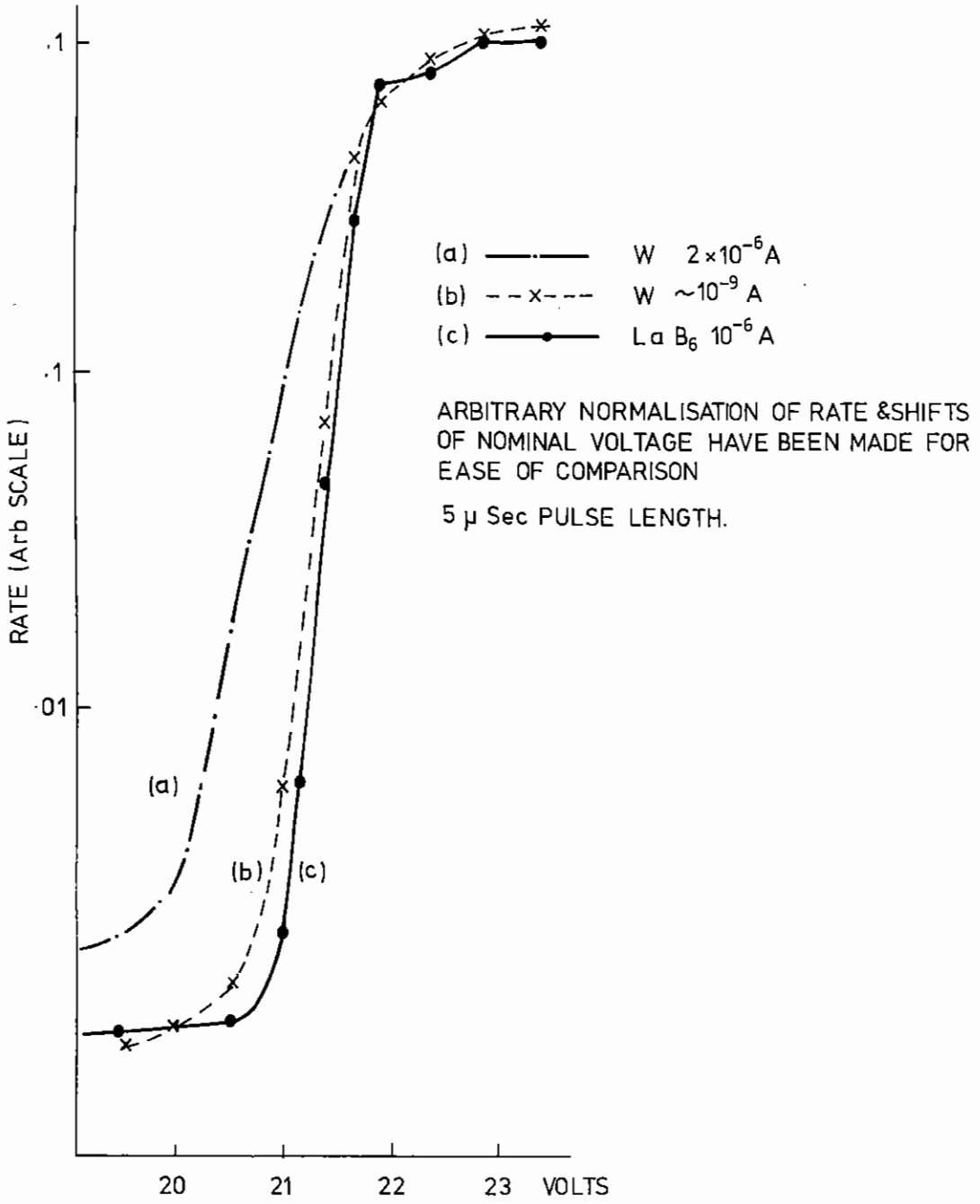

FIG. 6·33 COMPARISON OF W & La B_6 THRESHOLD CURVES.

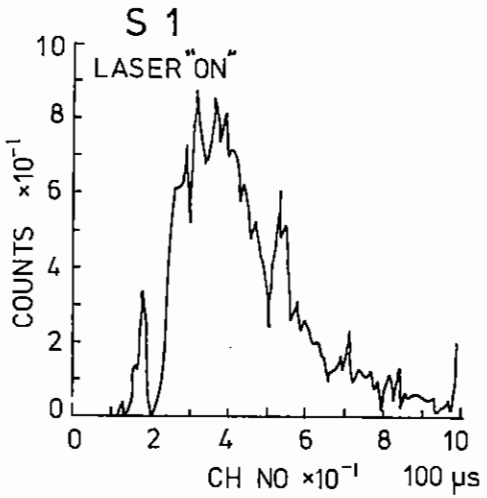

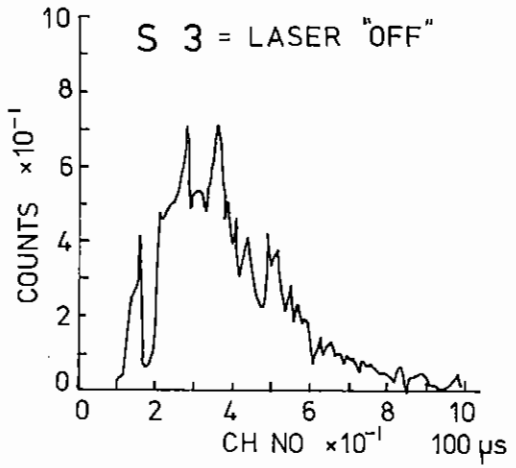

FIG. 6.34 LASER "ON" AND LASER "OFF" TIME OF FLIGHT SPECTRA.

(Figure 6.33(c)) to produce a suitably sharp threshold at high peak current during tests. However, the gun was now less stable and we were unable to complete the experiment in the time available. Metastable time-of-flight curves are shown in Figure 6.34. The envelope of the curves is what would be expected - approximately Maxwellian - but the fine structure is an artefact whose cause we have still to trace. When running on the plateau of the direct process excitation curve, above threshold we were able to demonstrate the absence of spurious systematic laser on/laser off effects down to the 2% level, within statistics, which is most encouraging. Some problems were still experienced when working on the steep part of the excitation curve but we are confident that they can be resolved by improving the stability of the electron gun. It would also be very advantageous to improve the output of the laser.

We intend to continue with the experiment later this year when the University College participants return from sabbatical leave. We believe it best to complete the low intensity experiment before resuming work on VULCAN so that we are able to carry out the high intensity experiment in the most advantageous conditions.

W R Newell, M Khakoo (University College, London), W T Toner and R Eason (RAL)

6.4 Time Resolved and Time Int grated Measurements of K-absorption Edge Structure in Preheated Material

6.4.1 Introduction

Previously K_α emission and hydrodynamic expansion have been used as diagnsotics of preheating in laser target irradiation experiments. Extracting the preheat level from the hydrodynamic behaviour of the target generally requires comparison with numerical simulations; also it is difficult to follow the hydrodynamic history due to the high densities to be probed. K_α emission has successfully been used to diagnose fast electron preheat (6.41) but problems of sensitivity have restricted this technique to high specific preheat levels and it is unable to diangose

shock preheating.

A new technique of preheat diagnosis has therefore been devised in which the spectral structure of the K absorption edge of the preheated material is used to infer preheat levels in the absorber. The method is in principle very sensitive as the more subtle features of K-shell X-ray absorption (eg EXAFS) are modified for very low absorber heating (6.42). This technique could offer a means of diagnosing the low preheat levels required for a Fermi degenerate adiabatic compression.

Several preliminary experiments have been performed and they divide naturally (and historically) into time integrated and time resolved measurements.

6.4.2 Time Integrated Experiments

The K absorption edge is a sudden jump in the X-ray mass attenuation coefficient of a given element for photon energies greater than the K-shell ionisation potential. The spectral position and structure of the edge are thus sensitive to local plasma conditions via their effect on the ionisation potentials. In this experiment the X-ray attenuation in an absorbing layer buried in a plane target was measured by recording plasma recombination continuum from the front of the target with a flat crystal spectrometer at the rear of the target, as shown in Figure 6.41(a). A second spectrometer at the front monitored the unattenuated continuum emission. During the 300 ps, 50 J Neodymium glass laser pulse the absorbing layer is preheated (in this case by fast electrons and radiation) so the spectrometer gives a time integrated record of the K absorption edge during the course of this preheating. With the target shown in Figure 6.41(a) Al recombination continuum was viewed through a KCl absorbing layer. The spectrometer, with a PET crystal, recorded emission in the region of both K edges. In order to accurately fix the position of the Cl edge a thin layer of KCl was included on the front of the target to provide Cl and K plasma lines in the region of the absorption edge. A typical spectrum from the rear spectrometer is shown in Figure 6.42 for which the incident irradiance was 10^{15} W cm^{-2}. The

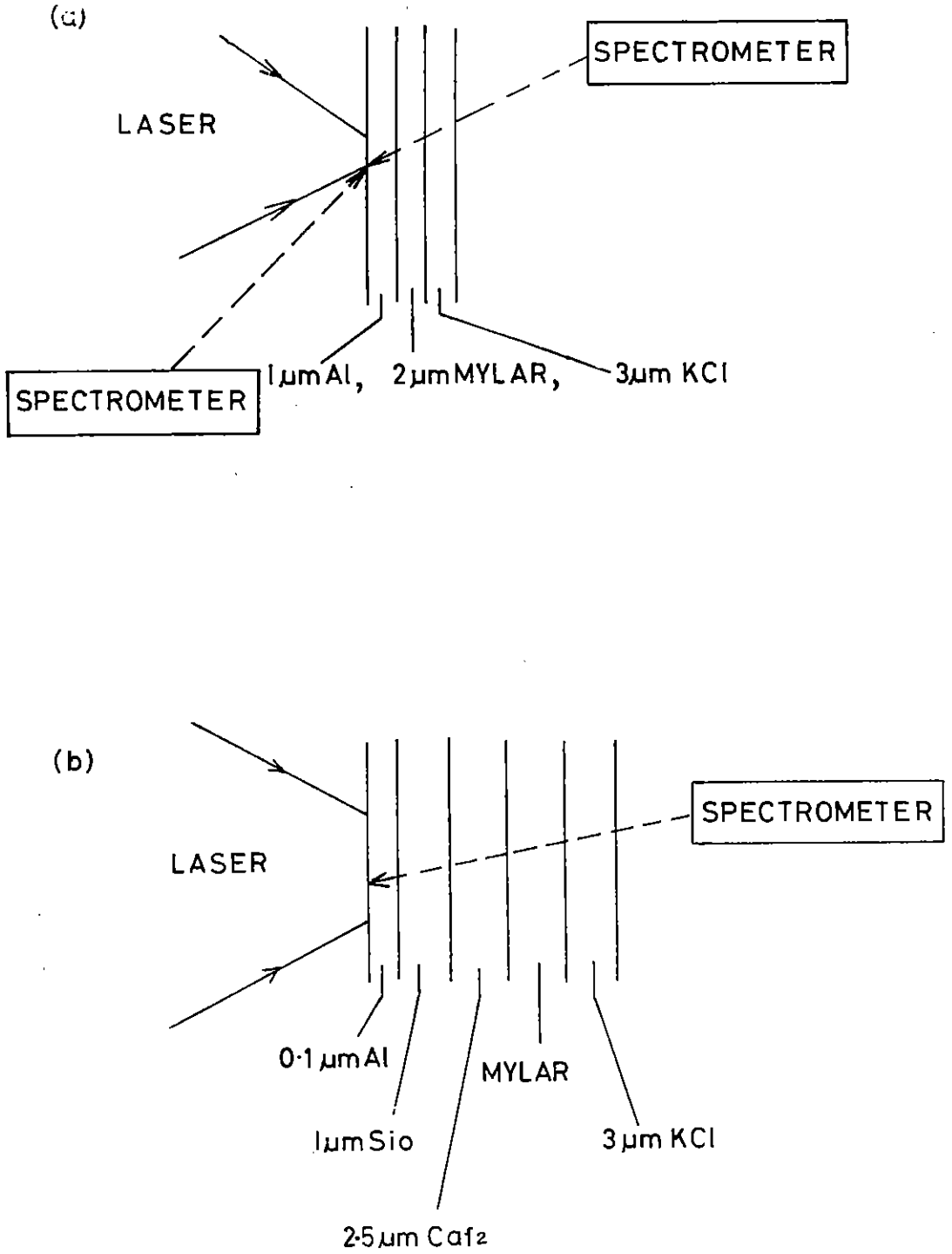

Figure 6.41 Geometry and targets for time integrated K edge measurements.

Cl and K Kabsorption edges are clearly visible together with Al, K and Cl plasma emission. Figure 6.43 shows an expanded tracing in the region of the Cl edge. The edge is $\sim$4 times broader than the spectral resolution of the spectrometer, which is indicated by the width of the Cl $1s^2$ - 1s2p line, but is not obviously shifted to higher energy. The position of the Cl edge in solid, cool KCl (being dependent on the compound (6.48)) and an upper limit for its spectral width were determined using a CW X-ray source and these are shown in Figure 6.43. During the course of the laser pulse the Cl absorption edge is broadened under the influence of preheating effects.

In another experiment similar targets, as illustrated in Figure 6.41(b) were irradiated with 100 ps, 20 ps Neodymium laser pulses at 2×10^{15} W cm^{-2}. For these conditions the fast electron preheat level is high (6.41) and a high stage of ionisation in the preheated material is to be expected. Two types of target were used, one with the abosrbing layer close to the irradiated surface and hence preheated a lot ($\sim 10^7$ J/gm) and one with a $\sim$1 mgm cm^{-2} of material between it and the surface, with a lower preheat ($\sim 10^6$ J/gm). Absorption spectra of the KCl layer were recorded using Al continuum emission for the two target types. These are illustrated in Figure 6.44. The spectrum from the target with a deeply buried absorber shows a well defined edge, although a spectral fix is not possible since Cl plasma emission is not present in the spectrum. The absorption edge with the other target type however is not clearly visible, presumably because the absorbing layer became highly ionised early on in the pulse. The obliteration of the edge under these conditions (which was seen on several different shots) makes it difficult to deduce anything more than that the absorber becomes highly ionised. The finite broadening in Figure 6.43 allows at least a crude analysis.

There are several mechansims affecting the K absorption edge which we will discuss and estimate their likely importance. Ionisation results in an increase in the K ionisation potential and hence K absorption threshold due to reduced screening of the inner shells. This shift is comparable to the current ionisation potential of the ion (6.43) (6.44). Another consequence of ionisation is the production of a high density plasma in

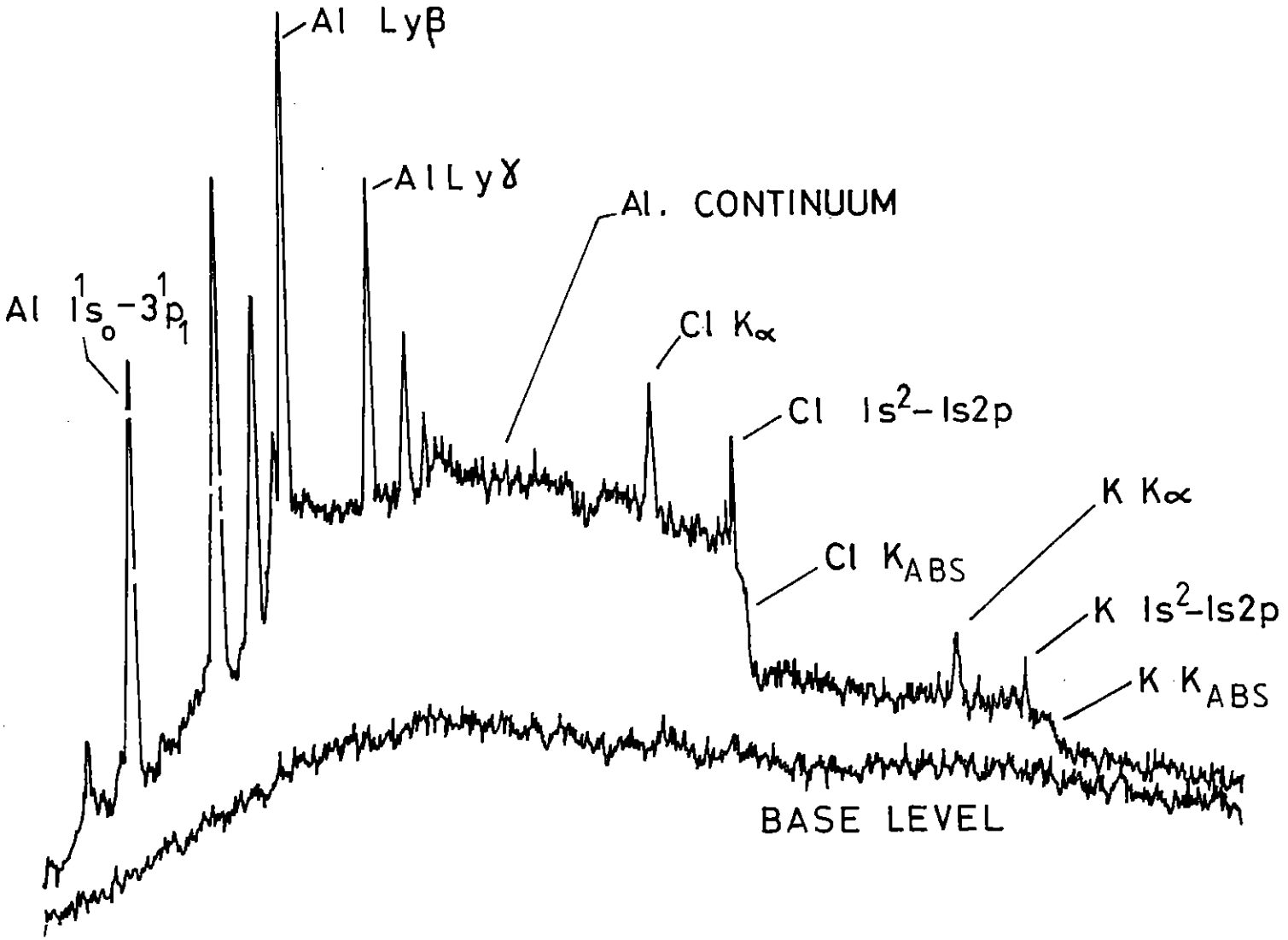

Figure 6.42 Typical spectrum from the rear of a K absorption target.

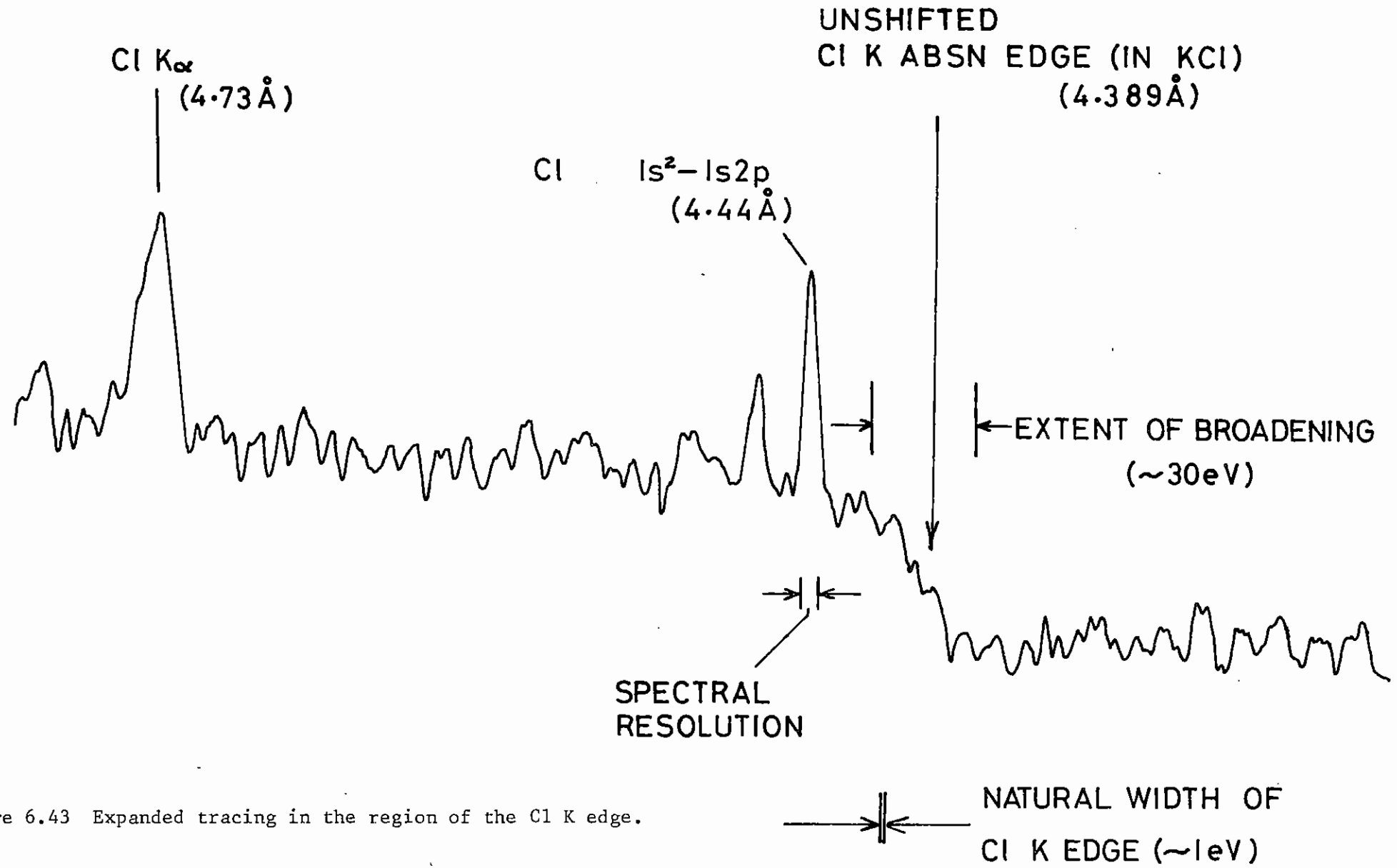

Figure 6.43 Expanded tracing in the region of the Cl K edge.

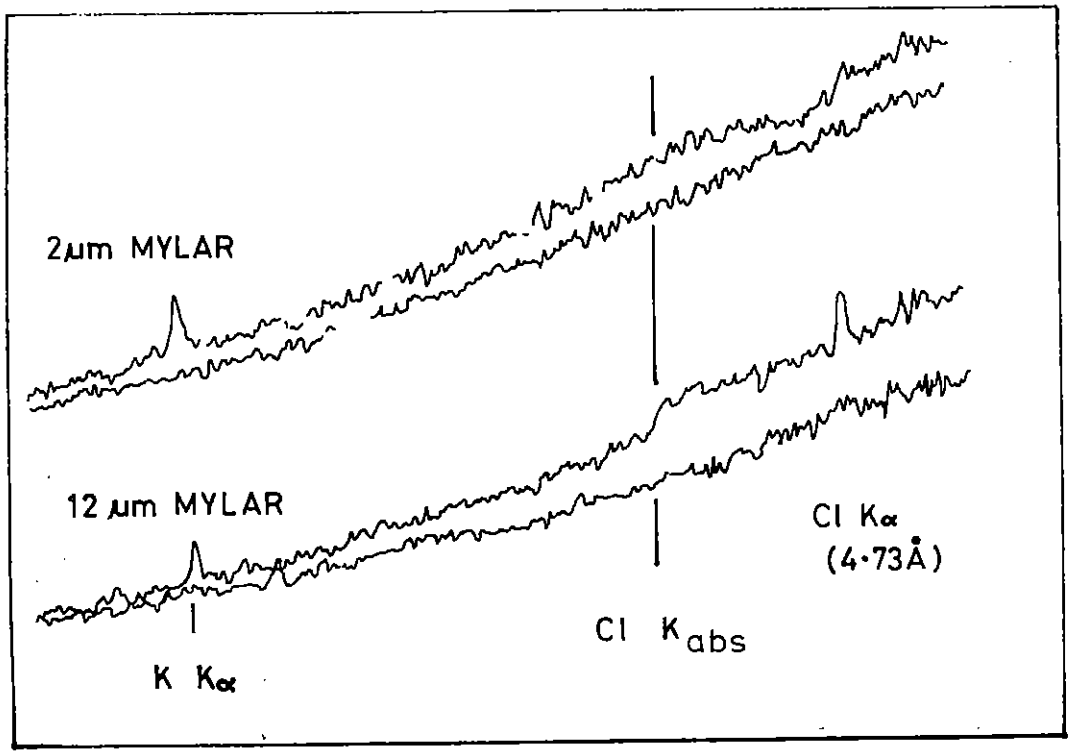

Figure 6.44 K absorption edge spectra for high and relatively low preheat levels.

which the ion is immersed. There may be a significant reduction in the ionisation potential due to the Debye depression (6.45). This depression may be further increased by the mechanism of the Inglis Teller limit in which vacant bound states close to the continuum are Stark broadened to the extent that they merge and effectively reduce the continuum energy level. A further result of screening of the absorber is the reduction of photoionisation cross-section, especially close to threshold, which may reduce the K edge jump ratio (6.46). Finally the appearance of Extended X-ray Absorption Fine Structure (6.42) arising from quantum mechanical interference during photoionisation, relies on an ordered structure in the absorbing material. Preheat will disorder the absorber and modify or inhibit EXAFS, the behaviour of which may be an extremely sensitive measure of preheat. Figure 6.45 gives a simple estimate of the magnitude of some of the above effects in the KCl absorber layer. For the relatively high preheat levels of the experiments EXAFS would not be expected however in the presence of shock preheating alone EXAFS could offer a diagnostic for preheat levels comparable to the heat of formation of an absorbing layer below which the absorber retains some ordered structure and this may be comparable to the Fermi energy content required for a Fermi degenerate adiatatic compression.

It can be seen from Figure 6.45 that the total shift is the difference between opposing and rather inadequately calculated effects. The shift observed from Figure 6.42 was < 10 eV, thus Figure 6.45 would suggest that the ionisation stage achieved in the absorber was < 2. We estimate the fast electron preheat level in the absorber to be 3×10^5 J/gm for these pulse conditions (300 ps, $I = 10^{10}$ W cm^{-2}) (6.41) (6.47) which would give an ionisation stage of approximately 6 and temperature of 45 eV using a simplified form of the Saha equations (4.68) which is in broad agreement with observations, although the high density and relatively cool absorber will have a very small Debye length making plasma parameters difficult to calculate.

In the absence of ionisation depression effects an ionisation stage of 6 would give rise to a shift of 120 eV, which is considerably larger than the observed shift. We conclude that the shift is reduced by ionisation

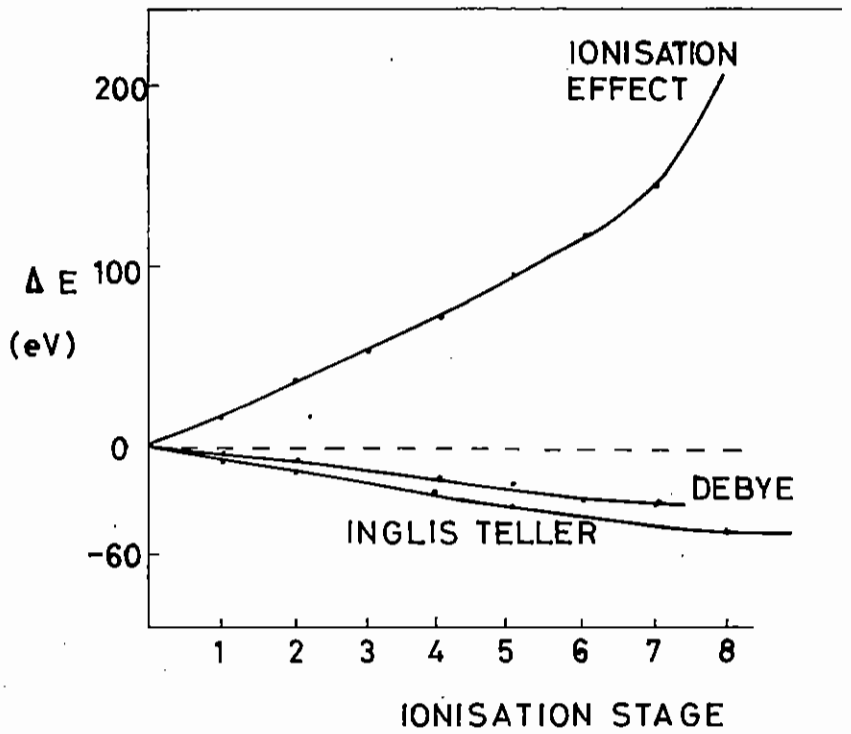

Figure 6.45 Relative importance of some of the shifting mechanisms calculated for the Cl K edge in solid KCl.

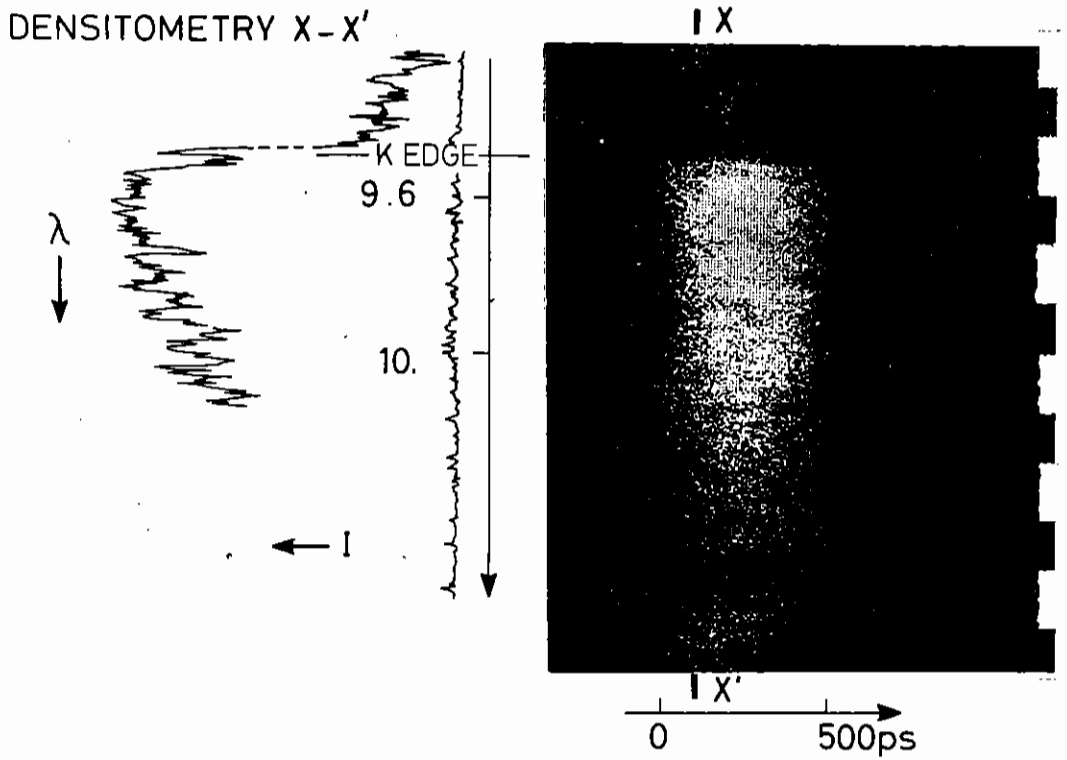

SHOT 03011281 $I = 2 \times 10^{15}$ Wcm^{-2}

SOLID Au, 2μm Mg ABSORBER DISTANT FROM FOCAL SPOT

Figure 6.46 Streaked Mg absorption spectrum with a cold absorber. Note the bound-bound absorption feature just below the K edge.

depression effects as mentioned above, or is obscured by uncertainties in the photoionisation cross-section in high density matter. Other absorption features, in particular $n = 1 \rightarrow 2$ transitions in highly ionised atoms (6.44) will further complicate the interpretation. These are discussed more fully in the next section.

6.4.3 Time Resolved Measurements

Absorption spectra have been taken before from laser produced plasmas using the hot highly emitting core of compression targets to 'backlight' the glass shell (6.49) (6.50). The spectra characterise a hot glass shell that is predominantly in the helium and lithium-like states of ionisation.

Here we report the first time-resolved X-ray absorption spectroscopy measurements of laser preheated solids. Absorber layers are buried at various depths from a laser produced plasma. Absorption lines, due to $n = 1 \rightarrow 2$ transitions in highly ionized material are seen early on in the laser pulse. The line widths are greater for the more highly ionized transitions. (The K edge appears to become a band with absorption just above the edge and a decrease well above the edge.) It is suggested that the mechanism responsible for preheat is radiation from the gold laser-plasma, and that the band of 'K' absorption is due to bound-bound transitions of highly ionized high density atoms.

A 0.53 μm, 500 ps, frequency-double Nd-glass laser pulse was incident on a range of flat layered targets. The beam was focused by an f/1 lens to a spot size of 35 μm ± 5 and by defocusing to a spot size of 47 ± 3 μm. The focal diameter was taken as being equal to the FWHM of an X-ray pinhole image recorded on Kodak No Screen film, using a 6 μm pinhole filtered by 5 μm Al. With incident laser energies of 14 ± 4 J the resulting intensities were $(3.0 \pm 0.9) \times 10^{15}$ W/cm^2 and $(1.6 \pm 0.5) \times 10^{15}$ W/cm^2.

Three types of targets were used, involving two different K edge absorbers. The first type consisted of 0.4 → 0.8 μm Au, 0.75 μm plastic, 0.5 or 1 μm NaCl, 0.75 μm Al; Na in NaCl being the absorber. The second

type consisted of 0.06 μm Au, 0.7 μm Mg, 0.75 μm Al, and the third type of target comprised 0.06 μm Au, 0.75 μm Al, 0.65, 0.7 or 0.8 μm Mg, the absorber being magnesium in the latter two cases. In each case the laser was incident on the gold side, which provided a bright continuum of X-rays for the absorption measurements. In addition, a fourth target consisting of an absorber of 2 μm Mg coated onto 2 μm Mylar held remote from a gold wire was used for calibration purposes.

The plane targets were tilted at 20° ± 5° to normal beam incidence and a time resolved absorption spectrum of the gold continuum through the absorber was obtained on an X-ray spectrometer positioned at 90° to incident laser beam. The length of absorber was then approximately the absorber thickness/sin 20°. The time resolution was 150 ps. The Bragg reflecting crystal on the streak camera was RAP (2d = 26.12 Å) giving a dispersion on the low density CsI photocathode of ∿ 0.1 Å/mm at the Mg and Na K edges.

The spectra were recorded on Ilford HP5 film with $\gamma = 1.1$. Densitometry of the films was carried out on a Joyce Loebl Mk III instrument.

Figure 6.46 shows the result obtained with a Mg absorber which was remote from the Au laser plasma. The K edge is pronounced, the jump ratio agreeing with calculated K jump ratio for cold material. The backlighting pulse of X-rays can be seen to last for 0.4 ns and is virtually a pure continuum. Some noise is evident on the continuum, but the absorption feature ∿ 4 eV below the K edge is probably due to a 1s - 2p transition in atomic Mg as has been observed for Na (6.51).

A high intensity laser shot is shown in Figure 6.47. Here the target has a Mg layer just beneath the Au, and the Mg XI (helium like) line complex can be seen in emission early in the laser pulse. Additionally absorption lines, between 9.9 and 9.6 Å can be seen. The Kα line of Mg is at 9.9 Å: the position of the spectrally shifted 1s - 2p transitions in ionized Mg has been calculated (6.44) and has been used to identify the absorption lines in Figure 6.47. Densitometry early in time, ie x - x', shows features corresponding to Mg IV to Mg VII. The line width is

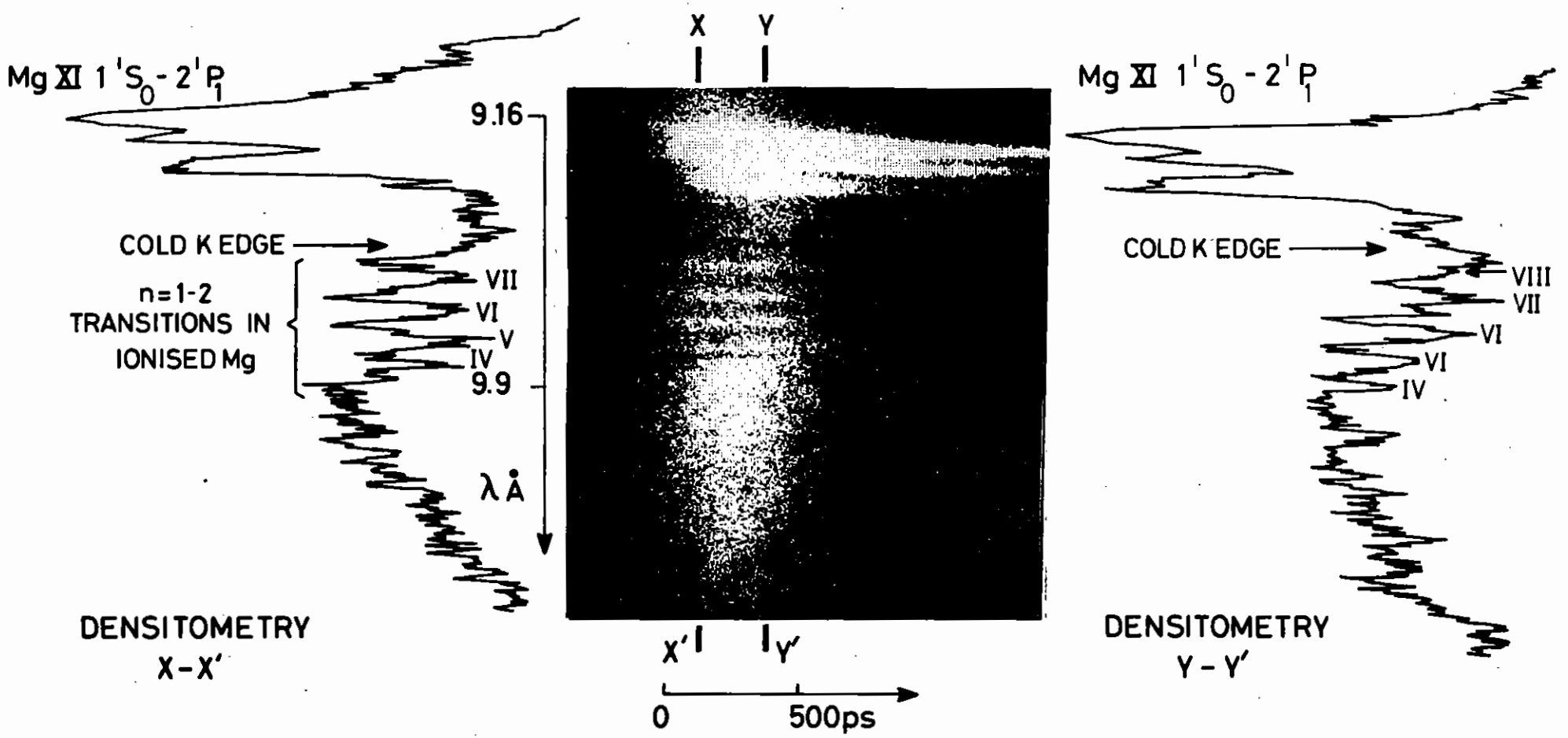

SHOT 01301181, $I = 2 \times 10^{15}$ Wcm^{-2}, $\lambda = 0.53\mu m$

0.06μm Au, 0.7μmMg., 0.75μm Al.

Figure 6.47 Streaked Mg absorption spectrum with a high intensity incident on the absorber showing strong $1s^2$-1s2p absorption features.

greater for the more highly ionized transition. There is an increase in the absorption at the position of the cold K edge, although this could be due to absorption by 1 - 2 transitions in states of ionisation higher than Mg VII.

The tracing at later time shows a decrease in the intensity ratio of the low state of ionisation to the high state of ionisation. The line width is narrower for the low state of ionisation.

The apparent opacity of the lines is between 1.1 and 0.4 at early time. Using the measured line width and assuming that the oscillator strengths of the various transitions that are all measured as one particular line, is 0.5, then the fractions of Mg atoms in states of ionisation Mg IV to Mg VII are approximately 0.5%, 0.7%, 1.0% and 1.5% repsectively. This assumed that the path length is 0.7 μm/sin 20°.

But is there a K edge? Figure 6.48 shows a lower irradiance shot where the absorbing Mg was deeper within the target. The Mg He-like lines only appear later in the pulse, allowing the absorption above the K edge to be seen more clearly than in Figure 6.47. At the position of the K edge there is an increase in the absorption, but only for 0.1 Å, after which the absorption falls, ie the absorption edge appears to be replaced by an absorption band.

A streak record with the Na absorber is shown in Figure 6.49. Here it is noticeable that the sodium helium-like line appears in absorption as soon as the gold continuum appears. Half way through the laser pulse the absorption line becomes an emission line, presumably because the layer of plastic ablates off in the middle of the focal spot.

The strength of the absorption features seen in Figures 6.47 to 6.49 implies that at least ∿1% of the atoms are in each of the states of ionisation Mg IV to VII. However, the targets will buckle because of acceleration during the laser pulse, thus increasing the grazing angle of observation through the target. This will decrease the viewing length through the target, thus the estimates of 1% per stage are probably low.

It is likely that on average a large fraction of the atoms are in high states of ionisation.

There is no striking dependence of the state of ionisation on time (except that noted for Figure 6.47). In contrast, models for the state of ionisation in a homogeneous plasma predict that one or two stages of ionisation will be dominant. Thus our observation implies a gradient in the state of ionisation across the absorbing layer. This in turn implies that fast electrons may not be responsible for the target heating. At this intensity the absorbing layer would be thin to fast electrons (with $T_H \sim 3$ keV) and consequent uniform heating would be expected. Radiative preheat however would penetrate the plastic and would predominantly heat the surface of the absorber.

With a high state of ionisation in the absorber foil, and a shock compression of say 4, the electron density could be $\sim 2 \times 10^{24}$ cm^{-3}, which would be sufficient to broaden the $1 \rightarrow 2$ transitions of Mg VIII and above to the band observed in Figure 6.48. The bound to free transition, corresponding to the K edge in cold material, would then be shifted to higher energy by either ionisation effects, or by degeneracy effects in the free electrons.

In conclusion we have seen rapid radiative preheat which produces a highly ionised plasma from solid material, with spectrally broadened $1 \rightarrow 2$ transitions. The K edge corresponding to bound-free transitions shifts to a much higher energy than for the cold material.

6.5 Ultraviolet Spectra and Spectral Line Widths between 300 Å and 975 Å

Spectra produced with the green laser beam were recorded with a one meter normal incidence spectrograph covering the spectral region between 300 and 975 Å. The green laser beam of power near 30 GW and pulse durations from 500 ps to 1 ns was focused with a 25 cm lens onto plane solid targets situated in a vacuum. Target materials used were carbon, sodium chloride, aluminium, silicon, phosphorus, potassium chloride, calcium, iron, lead

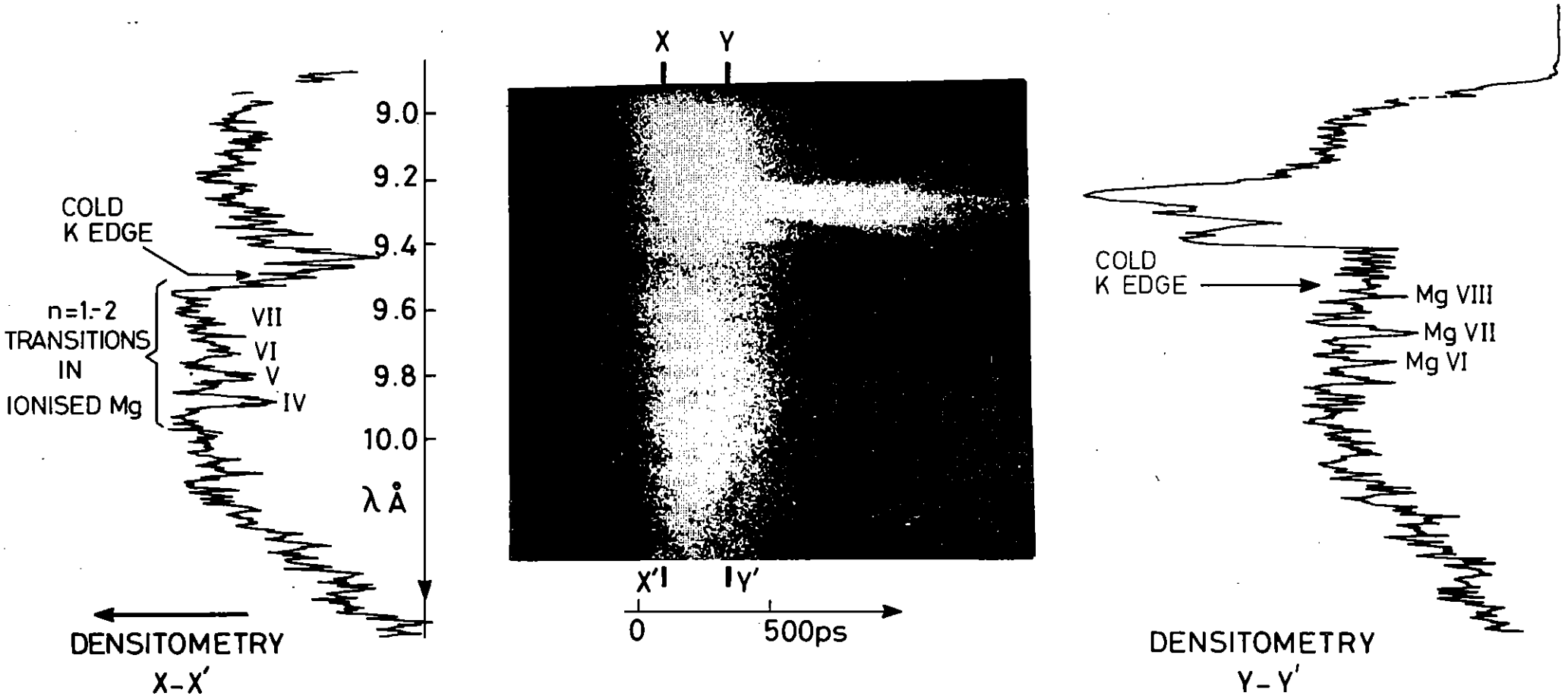

SHOT 01031281 $I = 3 \times 10^{14}$ Wcm^{-2}, $\lambda = 0.53\mu m$
0.08μm Au, 0.75μm Al, 0.7μm Mg.

Figure 6.48 Streaked Mg absorption spectrum with low intensity showing a band of 'K absorption'.

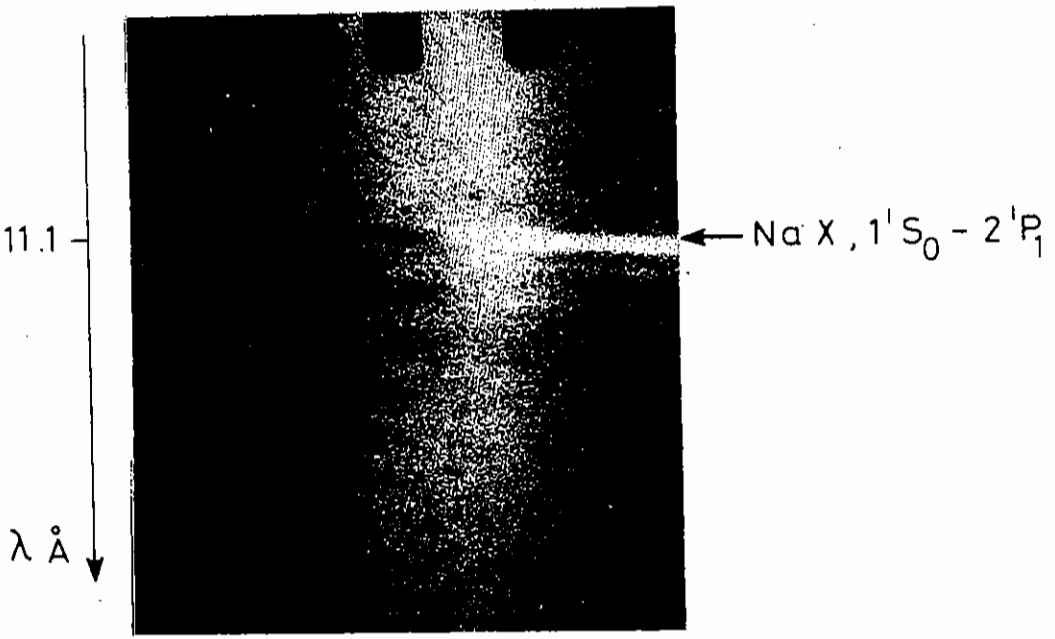

Figure 6.49 Na absorption spectrum at high intensity. Note that the Na X $1^1So - 2^1P$, appears in absorption immediately.

and rubidium and strontium carbonate.

The instrument (prepared by A Ridgeley) contained a 2400 line/mm concave grating blazed for 750 Å. The plate factor was 4.1 Å/mm and resolving power 0.1 Å with a 25 μm slit. Targets were placed at Sirks focus and at right angles to the slit so that spatially resolved spectra were recorded on the Ilford Q_z plates showing the spectral lines as a function of distance from the target. The instrument was capable of covering the range 300 - 2000 Å with different settings. For this experiment a setting for 365 - 975 Å was chosen with fainter records between 300 and 400 Å in the second order so that Li-, Be-, Na- and Mg-like spectra of interest for spectral line width measurements fell in the spectral range for some of the elements studied.

With the instrument in excellent focus fifteen well resolved spectrograms were recorded. The spectral resolution was more than adequate for easy measurement of spectral line widths which provided information on both Doppler and Stark broadening. Mass motion Doppler line widths are consistent with expansion velocities of around 2×10^7 cm per sec. Stark widths require more detailed analysis. Transitions between levels of high principal quantum number such as n = 3 - 4 and 5 - 6 in CVI result in emission lines with greater widths near the target surface than further away. In heavier elements transitions between levels of very high quantum number did not yield lines on the plates. Also absent were lines which require excitation from the $1s2s^3S$ He-I-like ions of sodium through to chloride. The very high plasma densities are responsible for depopulation of the ^3S level and further calculation regarding the population mechanism should give a lower limit for this density. Analysis of the spectrograms will also yield information for spectral line classification and this work is in progress. Spectra of lead taken with and without a lithium fluoride filter revealed the presence of a strong continuum close to the target with emission lines further away from the target surface. This could be used in future absorption experiments.

6.6 Highly Ionised Silicon Plasmas

6.6.1 Model Dependence of the Calculated Line Intensity Ratios

6.6.1(a) Introduction

The calculation of ionisation balance is of interest because line ratios are used as a diagnostic of plasma parameters. In a recent paper, Lunney and Seely (6.61) have proposed that the ratio $N(2s2p\ ^3P)A(2s2p\ ^3P;\ 1s2s\ ^3S) + N(2p^2\ ^3P)A(2p^2\ ^3P:\ 1s2p\ ^3P)/N(2p^2\ ^1D_2)A(2p^2\ ^1D;\ 1s2s\ ^1P_1)$ could be used as a density diagnostic for laser produced plasmas. While Vinogradov et al (6.62) have studied the dependence of the He-like resonance to intercombination line ratio

$$\alpha = N(2^1P_1)A(2^1P_1;\ 1^1S_0)/N(2^3P_1)A(2^3P_1;\ 1^1S_0)$$

on plasma density. However, as Weisheit et al (6.63) point out the analysis of the line ratios should still be corrected for opacity effects before experimental data is compared to theory. Uncertainties exist in these calculations for two principal reasons. Firstly, uncertainties exist in the collisional rates which are employed and, secondly, because of the restricted number of states and the restricted coupling between the states which are included in these calculations.

In this paper the results of calculations of ionisation balance in an Si-plasma are presented. These include higher level hydrogenic- and He-like states and a fuller modelling of the coupling between them than in previously reported results. Large discrepancies exist in the calculation of collision rates in the He-like ions. We investigate the effect of these differences on diagnostics by performing calculations using three different models for the collision rates, Vinogradov et al (6.62), Mewe (6.64) and Sampson and Park (6.65). The work by Weisheit et al (6.63) implied that the rates by Vinogradov et al (6.62) and Aglitski et al (6.66) are essentially the same as those of Sampson and Park's (6.65). This is not correct.

An outline of this paper is: Section 6.6.1(b) describes in detail the rate model: the states involved; the coupling between them; and, the solution of the resulting algebraic equations. Section 6.6.1(c) describes the collisional models which are used. Section 6.6.1(d) describes the results of the calculations of the line $N(2^1P_1)A(2^1P_1;\ 1^1S_0)/N(2^3P_1)A(2^3P_1;\ 1^1S_0)$ ratio, and the results for the dielectronic satellite lines and interprets the difference between these and previously reported results (6.61).

6.6.1(b) The Rate Model

The states which are being used in these calculations are shown in Figure 6.61. The errors due to the neglect of higher energy states were assessed by performing calculations with and without the n = 5 singly excited He-like state. This resulted in the fractional changes of order 10^{-3} in the populations of the states of interest, n = 2 and ground. The autionising rates and the energies of doubly excited states were taken from Vainshtein and Safronova (6.67), as were the radiative rates of the transitions of autoionising states to singly excited states.

The processes included are:

(i) For "bound-bound" transitions the radiative decay values which were not tabulated were obtained from the oscillator strength. The f-values can be expressed (6.74) as:

$$f = f_0 + \frac{1}{Z} f_1 + \frac{1}{Z^2} f_2 + \ldots \qquad (1)$$

where f_0 is the hydrogenic value and Z is the charge of the nucleus of the element. Using tabulated f-values for He and H we fit f against 1/z using the first two terms in the power series in Equation (1). We thus obtained values for Si XIII f-values for bound-bound transitions.

A number of models have been used for "Bound-bound" collision excitation rates; discussion of these has been deferred to the next section. The collision de-excitation rates are derived by employing the principle of detailed balance.

(ii) For "bound-free" transitions the collisional ionisation rates are taken from Seaton (6.68) and the 3-body recombination is calculated by the principle of detailed balance. The radiative recombination rates may be calculated from the photoionisation rates given by Ivanov (6.69) in an anologous manner.

(iii) For the case of transitions from the doubly excited levels to the next ionic ground state the rates, ie autoionisations, are taken from Vainshtein and Safronova (6.67) and the reverse process, electron capture, is again calculated using detailed balance (6.70).

(iv) Finally, for transitions between doubly excited states the radiative decay values are considered negligible and the collisional rates have been calculated by Sampson (6.71).

The rate equation of each state is of the following form:

$$- \sum_{i''<i} \left(n_{i''} \; R_{i''i} + C_{i''i} \right) \; + \; + n_i \left\{ \sum_{i''<i} \left[R_{ii''} + \left(\frac{n_{i''}}{n_i} \right)^* + C_{i''i} \right] + \sum_{i'>i} \left(R_{ii'} + C_{ii'} \right) \right\} - \; - n_i \sum_{i'>i} \left[R_{i'i} + \left(\frac{n_i}{n_{i'}} \right)^* C_{ii'} \right] \; = 0$$

where R_{jk} and C_{jk} are the radiative and collisional rates from state j to state k and an asterisk denotes the local thermodynamic equilibrium value.

The rate equation for the states shown in Figure 6.61 consitute a homogeneous set of n algebraic equations. We choose to solve for the ratio of each of the populations to the population of Li-like ground state. The equations then reduce to an inhomogeneous set of n - 1 equations. The solution of this large set of sparse linear equations is obtained using the method described by Duff (6.72). The method gives an efficient and very accurate solution but has the disadvantage of requiring large storage.

FIGURE 6.61

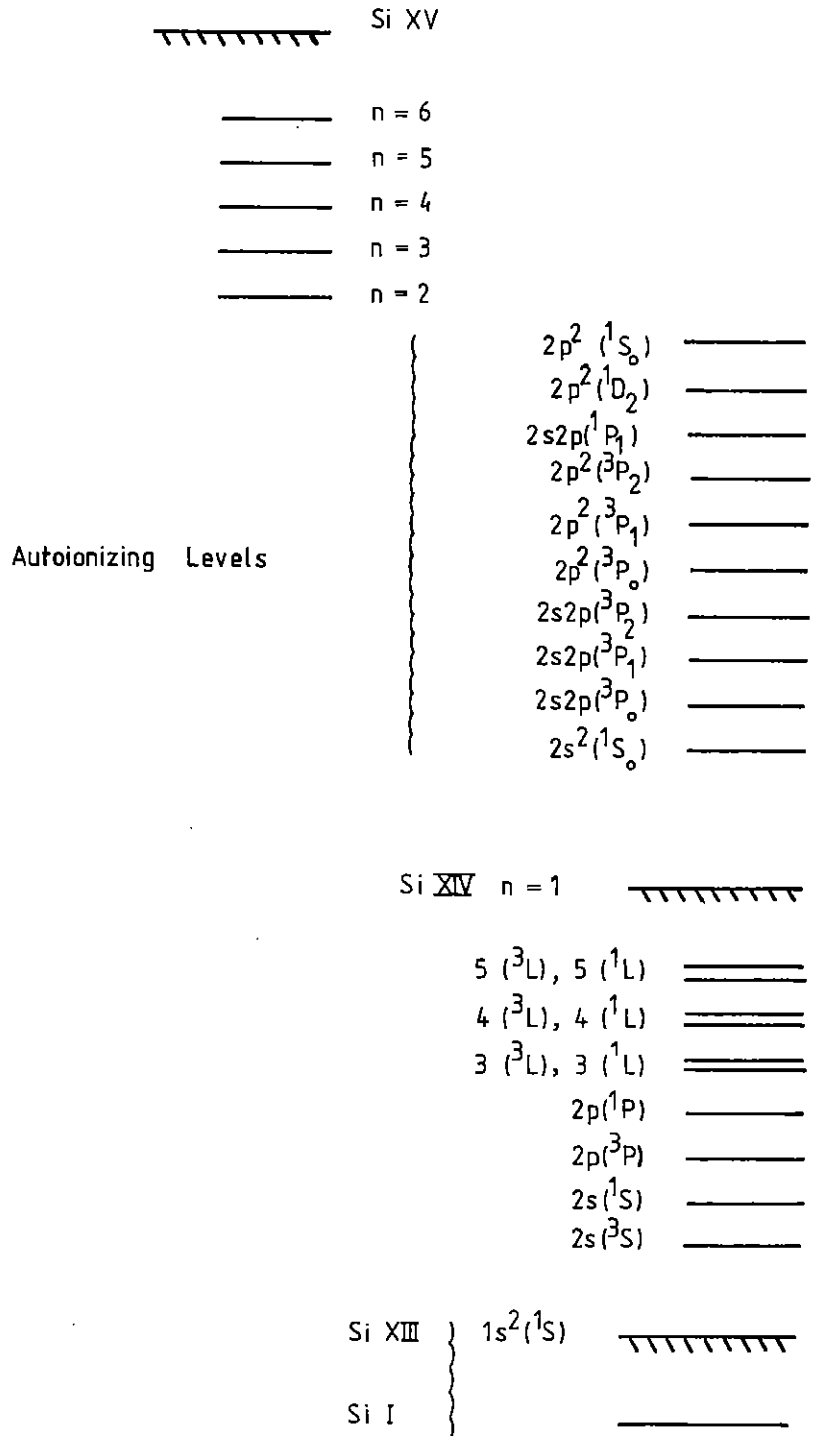

6.6.1(c) Calculation of the He-like inter-level Collision Rates

Although much effort has been put into calculating bound-bound collisional rates, for a Maxwellian electron distribution, the results of some calculations exhibit large differences between each other. It is thus important to understand the effect of uncertainties in these rates on our results. To this end we have performed calcuations using the results of three independent collisional rate models, ie those of Mewe (6.64), Vinogradov et al (6.62) and Sampson and Park (6.65). Because of the importance of these models to this work we give the collision rates from each below.

For an $i \rightarrow j$ transition between discrete levels Mewe (6.64) gives

$$C_{ij} = 1.7 \times 10^{-3} \times Te^{-1/2} \times E_{ij}^{-1} \times f_{ij} \times \bar{g}\,(y) \times 10^{-5040 \times Eij/Te}$$

where f_{ij} is the absorption oscillator strength of the transition for allowed transitions and for forbidden transitions we assume the f-value of the allowed transition to the level with the same quantum number. This allows the same fomula to be used for both allowed and forbidden transitions. E_{ij} is the excitation energy in eV, T_e is the electron temperature in ^{o}K, $y = E_{ij}/kT_e$, g(y) is the integrated gaunt factor given by Mewe(6.64) and is of the following form:

$$\bar{g}(y) = A + (By - Cy^2 + D)e^{y} E_1(y) - Cy$$

where $$E_1(y) = \int_1^{\infty} t^{-1} e^{-yt}\, dt$$

The values of the parameter A, B, C and D are given by Mewe (6.64). Some of these parameters have been recently revised by the same author (6.73), but these revisions do not affect the results here. Note that the use of the prescription for forbidden transitions is dubious since it is based on allowed transition oscillator strengths. We find below that these forbidden rates are not in agreement with other calculations.

For an $i \rightarrow j$ transition between discrete levels Vinogradov et al (6.62) gives:

$$C_{ij} = 10^{-8} \times \left[\frac{E_j}{E_i} \times \frac{R_y}{\Delta E_{ij}}\right]^{3/2} e^{-\beta} \times \frac{B_{ij}}{g_i} \times \frac{\phi(\beta)}{\beta + X_{ij}}$$

where E_i and E_j are the ionisation energies of levels i and j measured from the edge, $\Delta E_{ij} = E_j - E_i$, g_i is the statistical weight of level i, B and X are fitted parameters given in Vinogradov et al (6.62). R_y is the hydrogen ionisation energy and $\beta = \Delta E_{ij}/kT_e$

$\phi(\beta) = \beta^{1/2}\,(\beta+1)$ for transitions without change in spin.

$\phi(\beta) = \beta^{3/2}$ for transitions with change in spin.

For $i \rightarrow j$ transition between discrete levels Sampson and Park (6.65) gives:

$$\frac{C_{ij}}{\pi a_o^{\,2} N_e \bar{v}} = \frac{1}{\omega_i}\left(\frac{I_H}{KT_e}\right)\left\langle\Omega(i\rightarrow j)\right\rangle$$

where ω_i is the statistical weight of level i, a_o is the first Bohr radius of the hydrogen atom, I_H is the hydrogen ionisation energy, T_e is the electron temperature, N_e is the electron number density, $\Omega(i \rightarrow j)$ is the collision strength for an $i \rightarrow j$ transition, and

$$\bar{v} = \left(\frac{8kTe}{\pi m}\right)^{1/2}$$

$\left\langle\Omega(i\rightarrow j)\right\rangle$ is given by:

$$\left\langle\Omega(i\rightarrow j)\right\rangle \equiv \int_y^{\infty} d\left(\frac{E}{kTe}\right) e^{-E/kTe}\ \Omega(i\rightarrow j)$$

where y is the ratio of the excitation energy E to kT_e. The collision strengths corresponding to the various transitions in which we are interested are given by Sampson and Park (6.65).

The different dependencies of these rates on parameters such as the temperature is evident. Some important differences between the results of the three collision formulae are illustrated by Figures 6.67 and 6.68.

Figure 6.68 shows the large difference between the results of Mewe (6.64) and those of Vinogradov et al (6.62) and Sampson and Park (6.65) for the spin forbidden transition (2 P ; 1 S). Similar results have been found for all spin forbidden transitions (indicating the incorrectness of Mewe's formulation). Figure 6.67, which gives collision rates for the spin allowed transition (2 P ; 1 S), shows that the collision rates calculated from Sampson and Park (6.65) and Vinogradov et al (6.62) can vary as much as an order of magnitude at 100 eV and by a factor of two or more at temperatures of 800 eV.

Since the calculation of Mewe (6.64) is actually appropriate for allowed transitions the close agreement between the Mewe rates and the Sampson rates provides a verification of these two sets for the higher temperature region shown.

6.6.1(d) Results

6.6.1(d)(i) Effect of different collision rates on the $N(2^1P_1)A(2^1P_1;1^1S_0)/\ N(2^3P_1)A(2^3P_1;1^1S_0)$

Calculations of the He-like resonance to intercombination line ratio, ie

$$\alpha = N(2^1P_1)A(2^1P_1;1^1S_0)/N(2^3P_1)A(2^3P_1;1^1S_0)$$

have been performed using the model described in Section 6.6.1(b) and using each of the three collision rate formulae described in Section 6.6.1(c) for the collisional rates for "bound-bound" transitions.

Figures 6.62, 6.63 and 6.64 show the line ratios as a function of density for electron temperatures 100 eV, 400 eV and 800 eV respectively. Good agreement between results from different collisional models is found only for electron densities $\gtrsim 10^{23}$ cm^{-3}, where the limit of LTE is approached. At low densities the ratio of intensities is independent of the density and equal to the ratio of the excitation rates of the 2^1P and 2^3P levels by electron impact from the ground state. The relevant collision rates are those shown in Figure 6.67 and 6.68.

The density range of interest for "laser imploded microballoons" (6.61) is 10^{22} to 10^{24} cm^{-3}. In this range of densities the use of different collisional models can lead to order of magnitude errors in determining the density. The use of the set of rates by Sampson which is valid for both the allowed and forbidden rates should be seen as preferable.

6.6.1(d)(ii) Effect of Level Scheme on Dielectronic Satellite Ratios

The use of dielectronic satellite intensity ratios for diagnosing hot dense laser compressed plasmas have certain advantages. They are less susceptible to opacity effects than resonance lines. The satellite line emission is also more characteristic of the hot dense core region as it has been observed that it is only emitted briefly from the hottest plasma region.

The calculation of dielectronic satellite ratios given by Lunney and Seely (6.61) excludes collisional de-excitation from the doubly to singly excited states. These rates are comparable to the radiative rates for electron densities greater than 10^{22} cm^{-3}.

Figures (6.65) and (6.66) show the dielectronic satellite ratio as a function of density, for electron temperatures of 100 eV and 400 eV, calculated with and without collisional de-excitation from doubly to singly excited levels. From this it can be seen that errors can lead to orders of 20% to 30% over-estimate of the inferred density from the neglect of these rates.

At high densities the states are in LTE and the ratio is only dependent on temperature. At low densities the collisional downward rate is negligible compared with the radiative rate and the intensities depend only on the collisional upward rates.

6.6.1(e) Conclusions

Calculations using a rate equation model applicable to the study of high density $n_e \gtrsim 10^{19}$ cm^{-3} and high temperature $T_e \gtrsim 100$ eV plasmas have

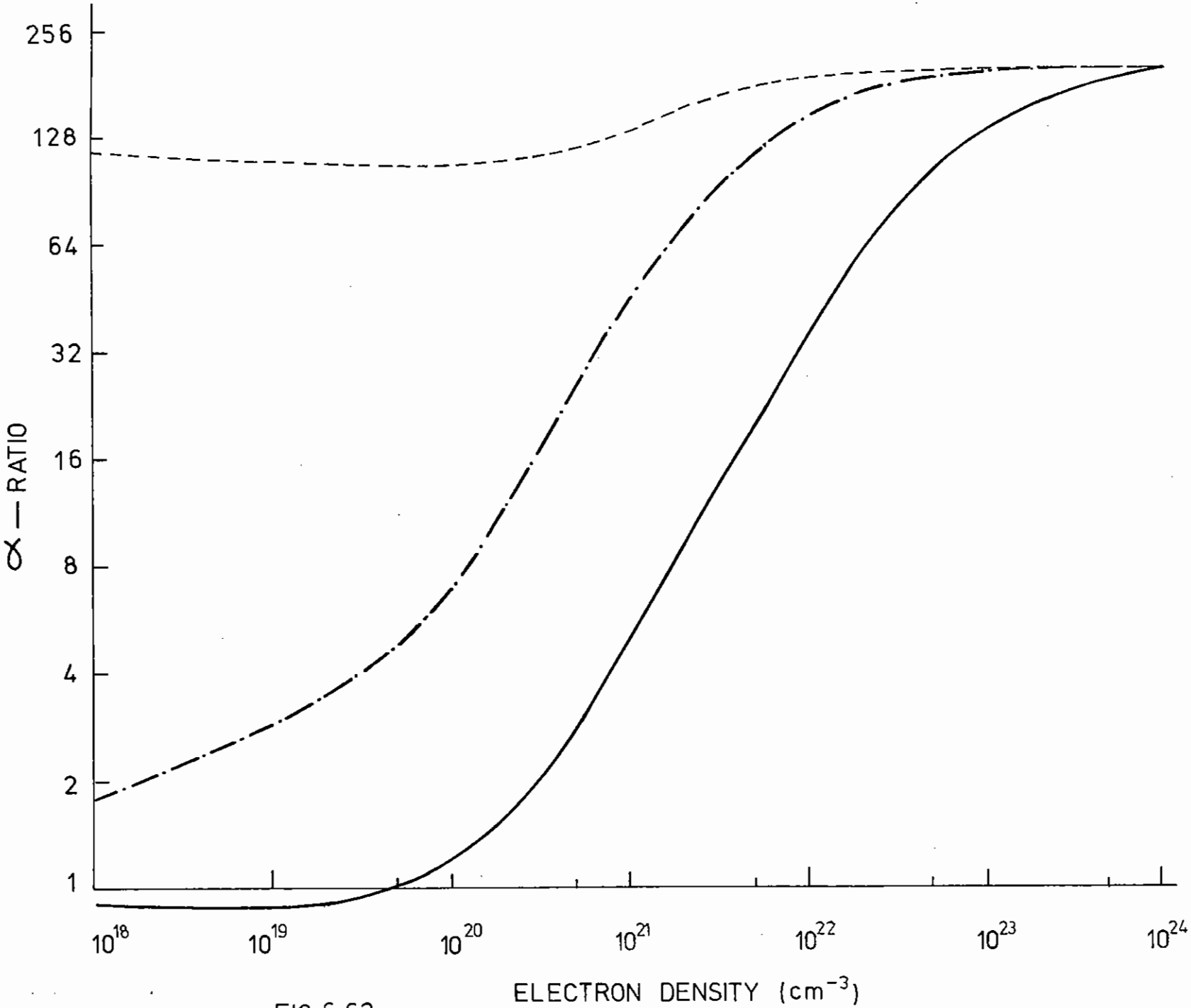
256
128
64
32
16
8
4
2
1
α — RATIO
10^18
10^19
10^20
10^21
10^22
10^23
10^24
ELECTRON DENSITY (cm^-3)

FIG. 6·62

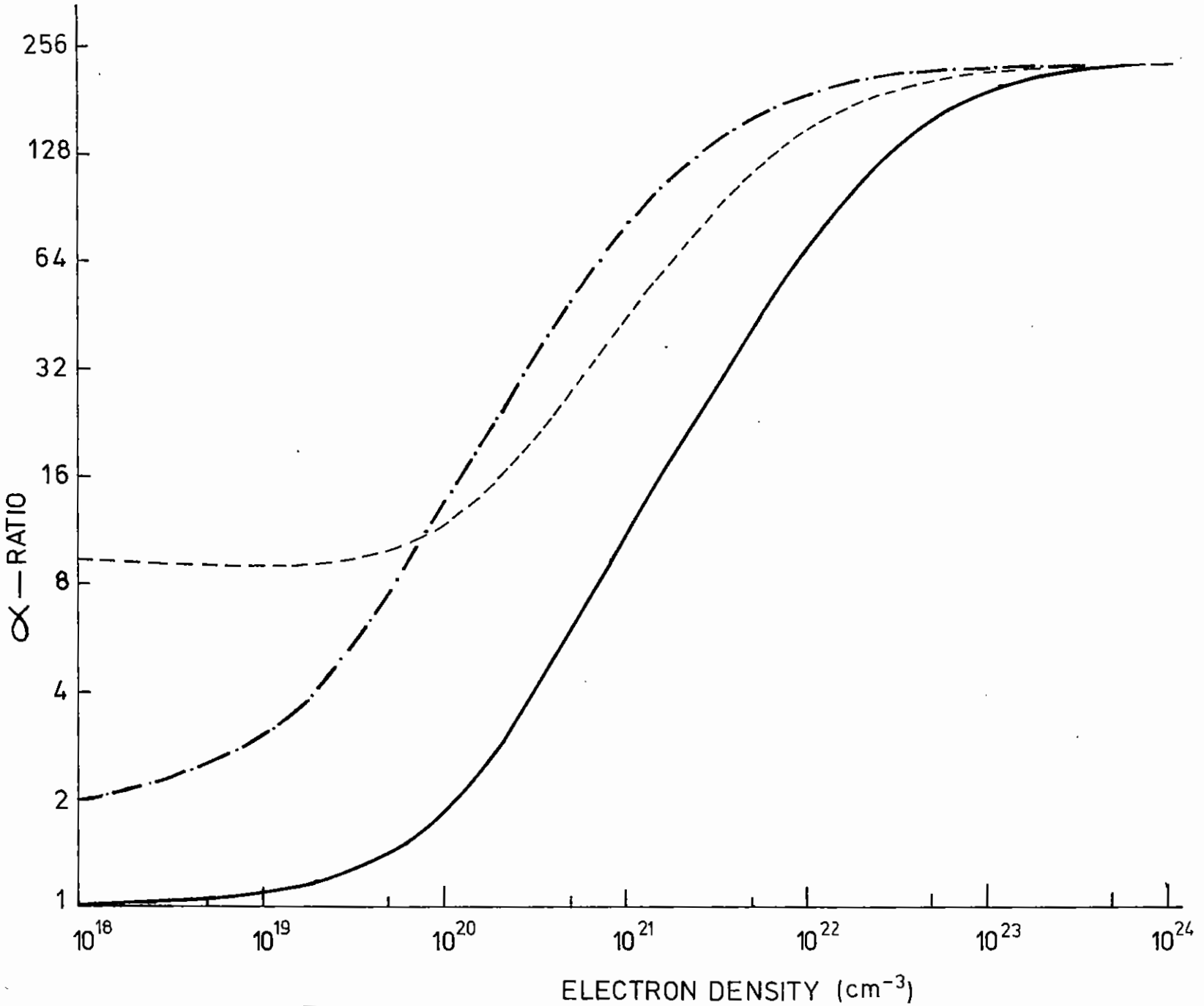
256
128
64
32
16
8
4
2
1
α — RATIO
10^18
10^19
10^20
10^21
10^22
10^23
10^24
ELECTRON DENSITY (cm^-3)

FIG. 6.63

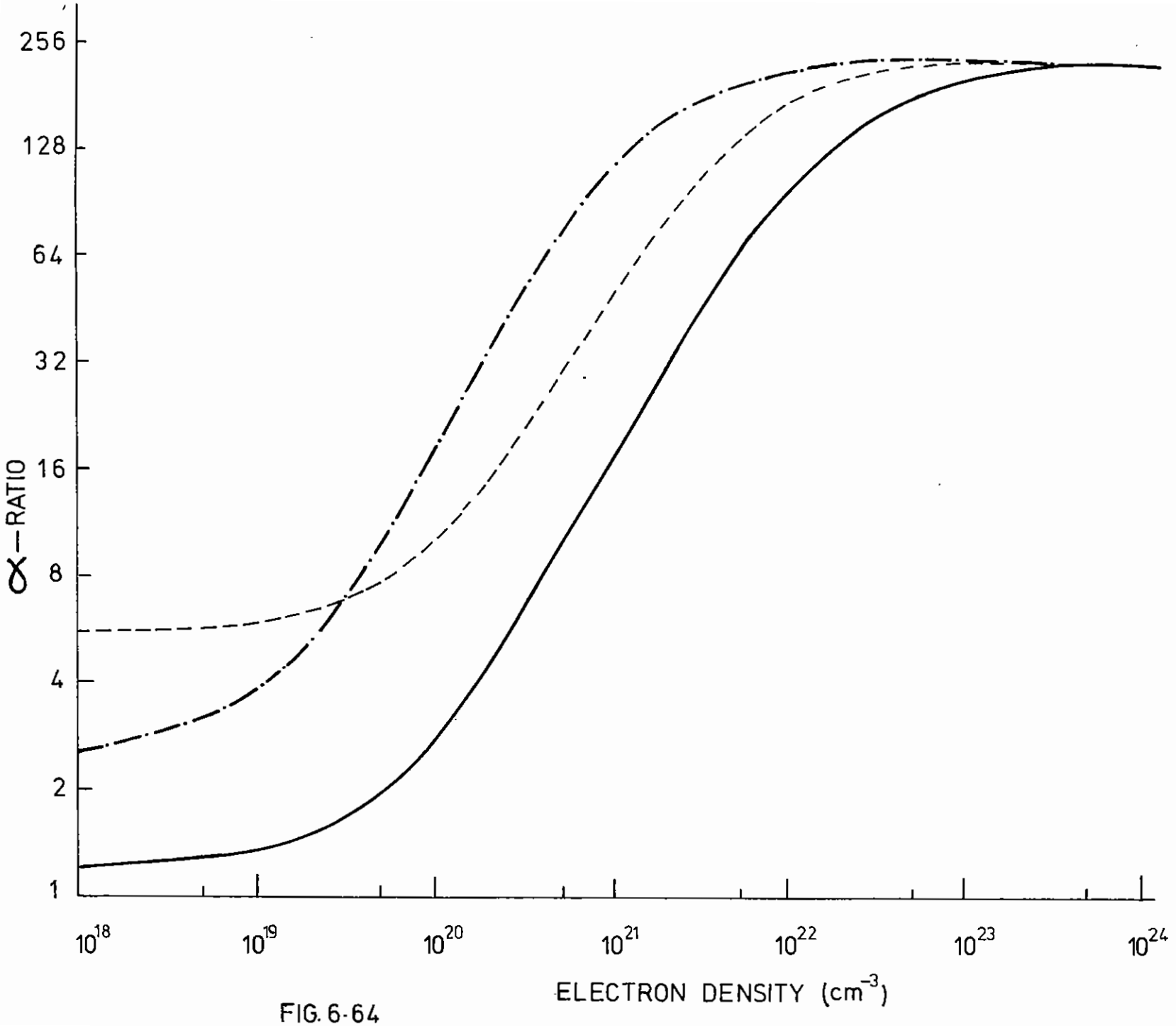
256
128
64
32
16
8
4
2
1
α — RATIO
10^{18}
10^{19}
10^{20}
10^{21}
10^{22}
10^{23}
10^{24}
ELECTRON DENSITY (cm^{-3})

FIG. 6·64

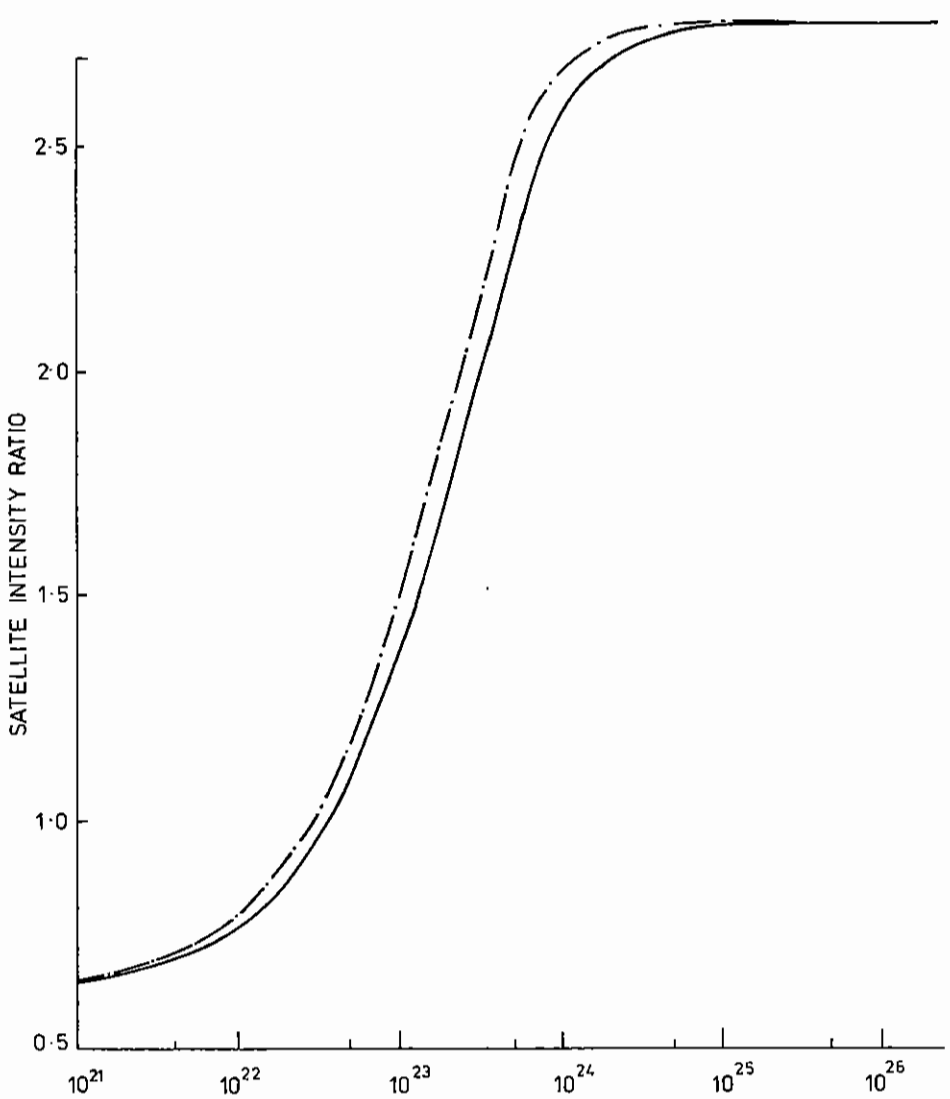

FIG. 6·65

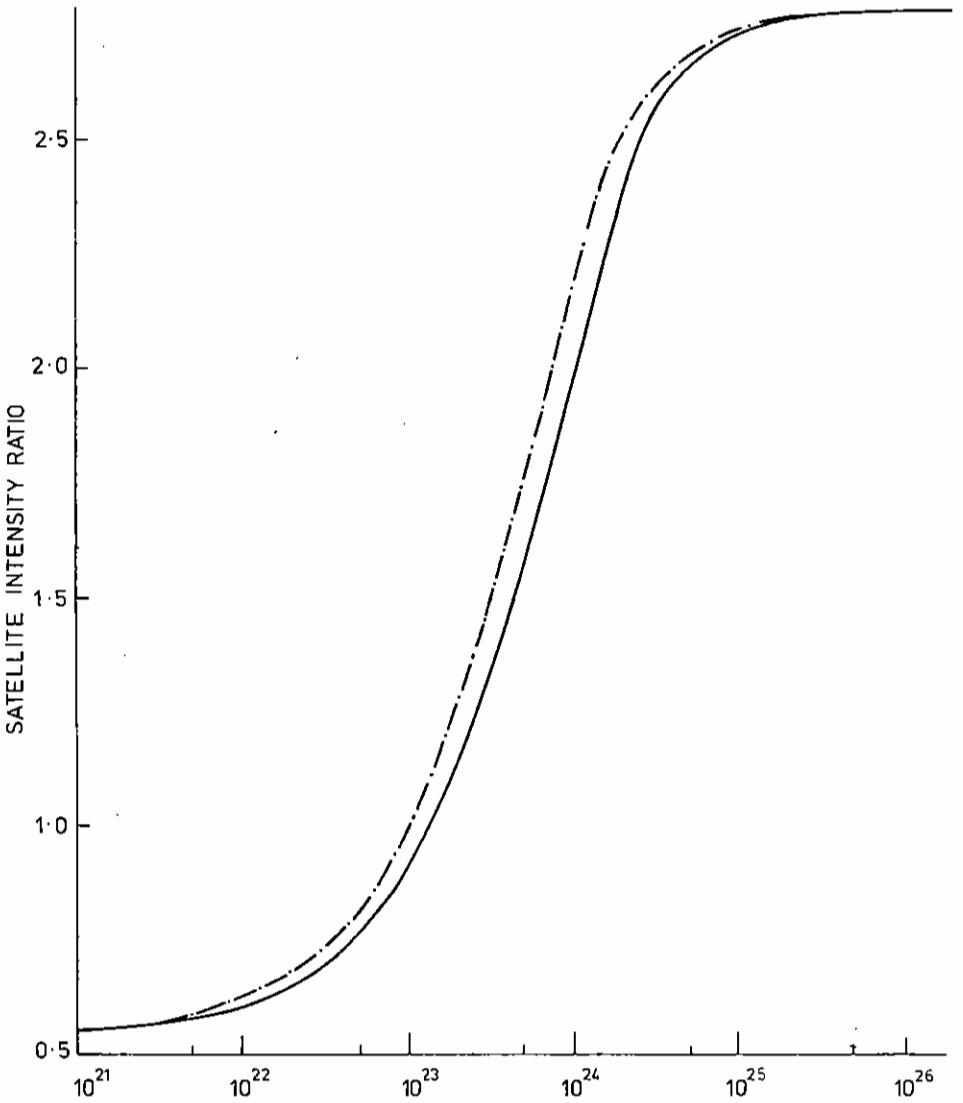

FIG. 6·66

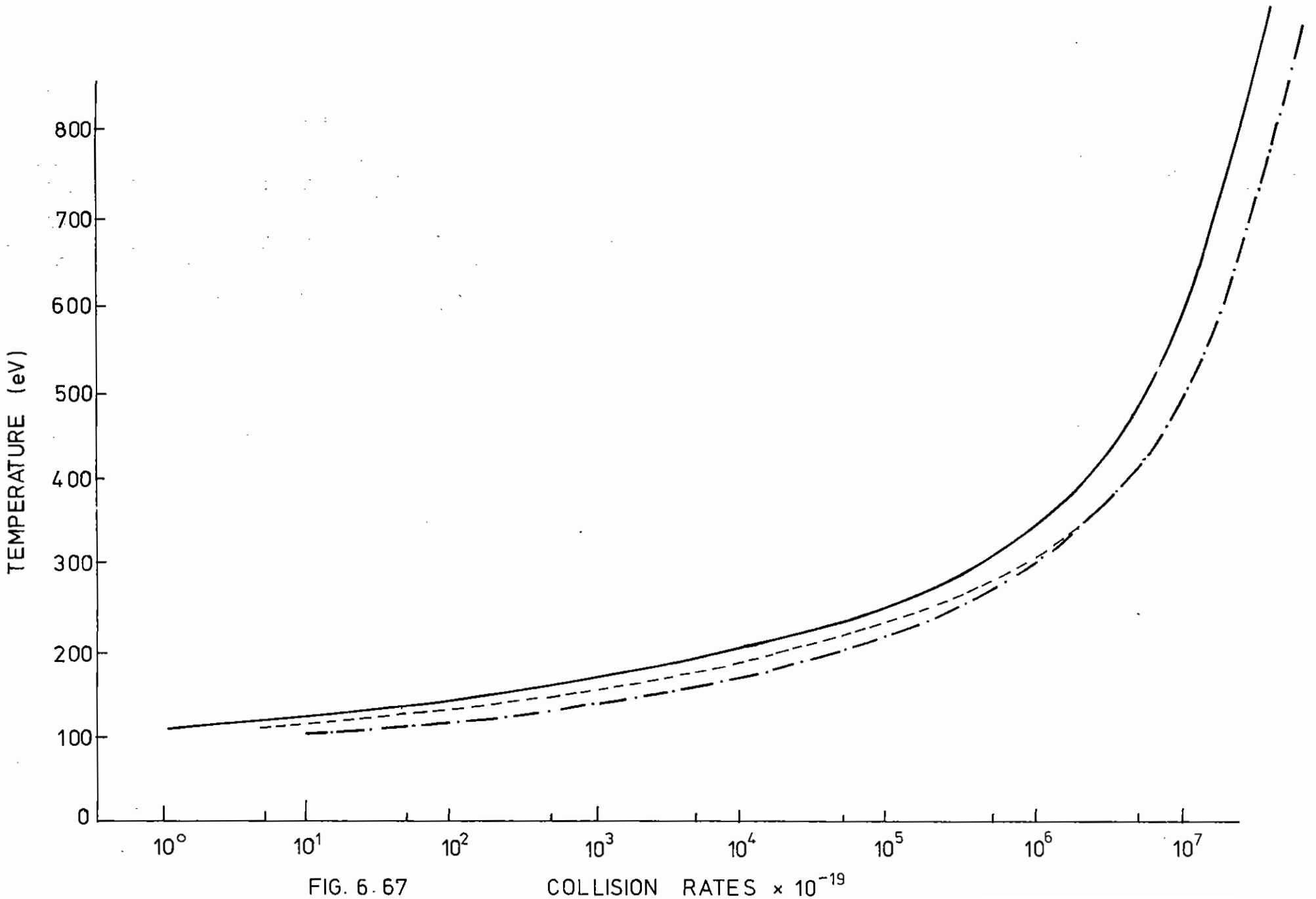
TEMPERATURE (eV)
800
700
600
500
400
300
200
100
0
10^0
10^1
10^2
10^3
10^4
10^5
10^6
10^7
COLLISION RATES × 10^{-19}

FIG. 6.67

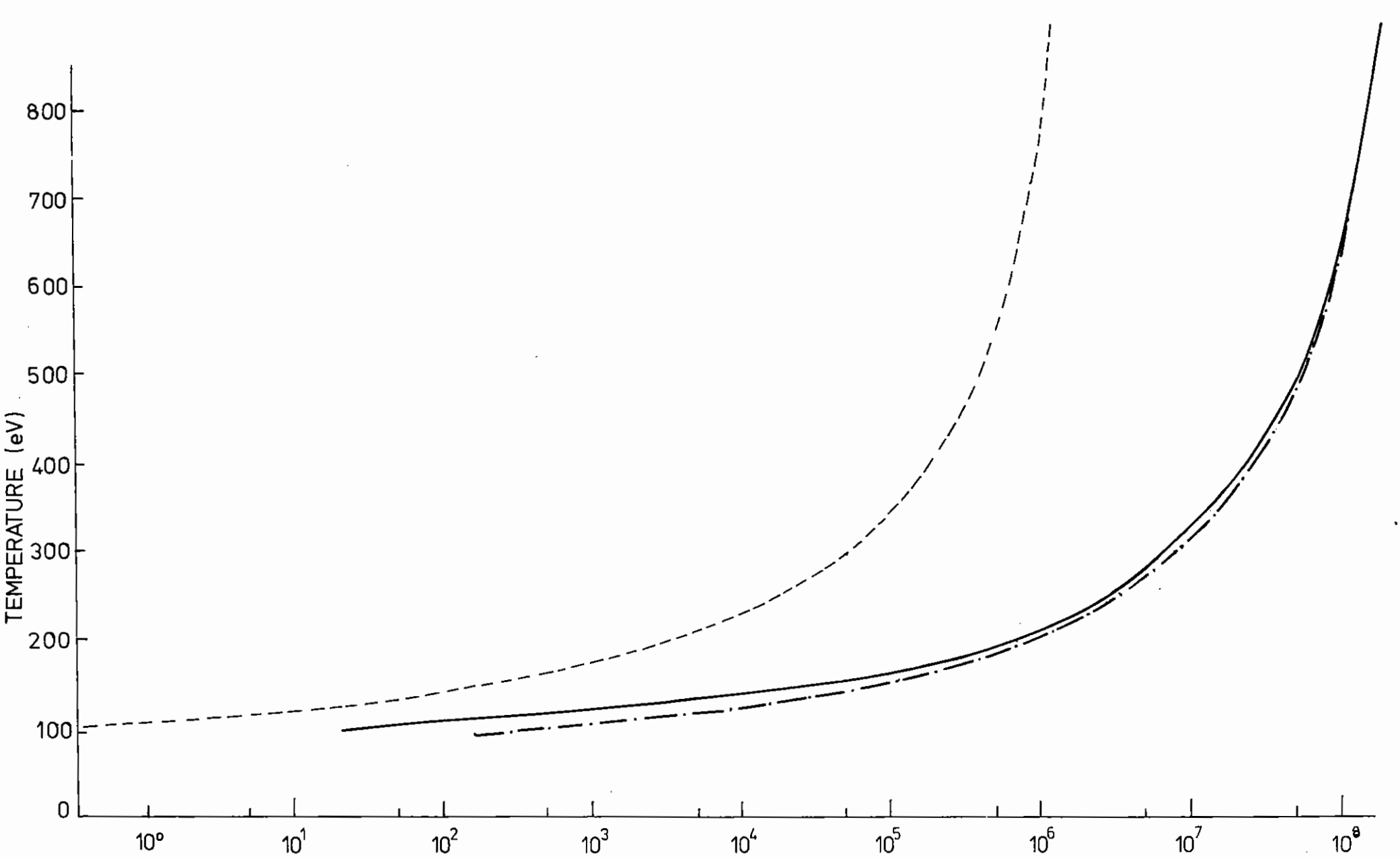
TEMPERATURE (eV)
800
700
600
500
400
300
200
100
0
10^0
10^1
10^2
10^3
10^4
10^5
10^6
10^7
10^8
COLLISION RATES $\times 10^{-20}$

FIG. 6.68

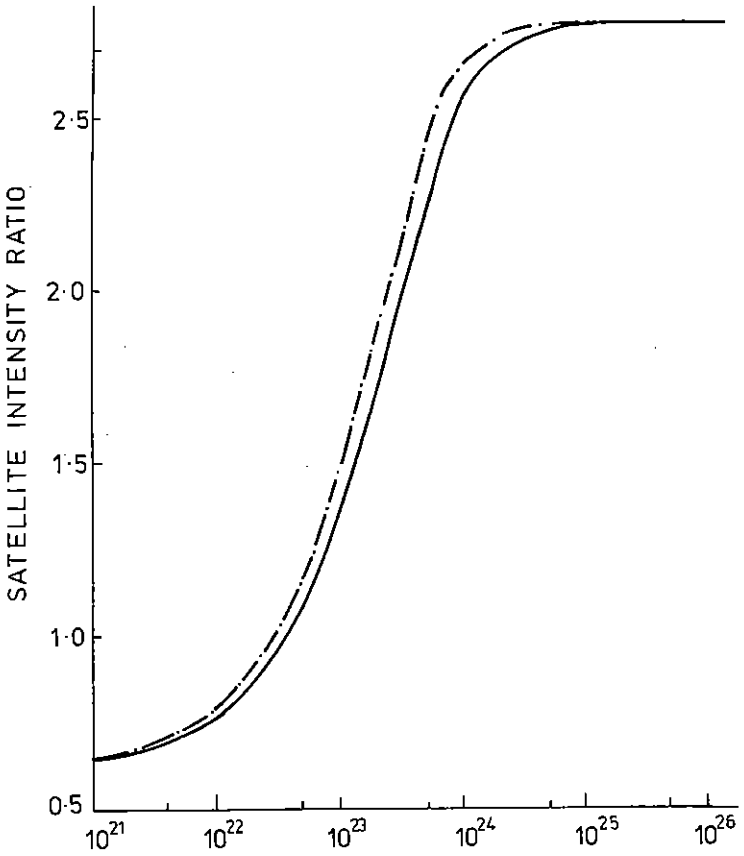

FIG. 6.69-THE SATELLITE LINE INTENSITY RATIO AS A FUNCTION OF DENSITY FOR A TEMPERATURE OF 100eV EXCLUDING (————) AND INCLUDING (—·—·—) COLLISIONAL DE-EXCITATION FROM DOUBLY TO SINGLY EXCITED HE-LIKE STATES.

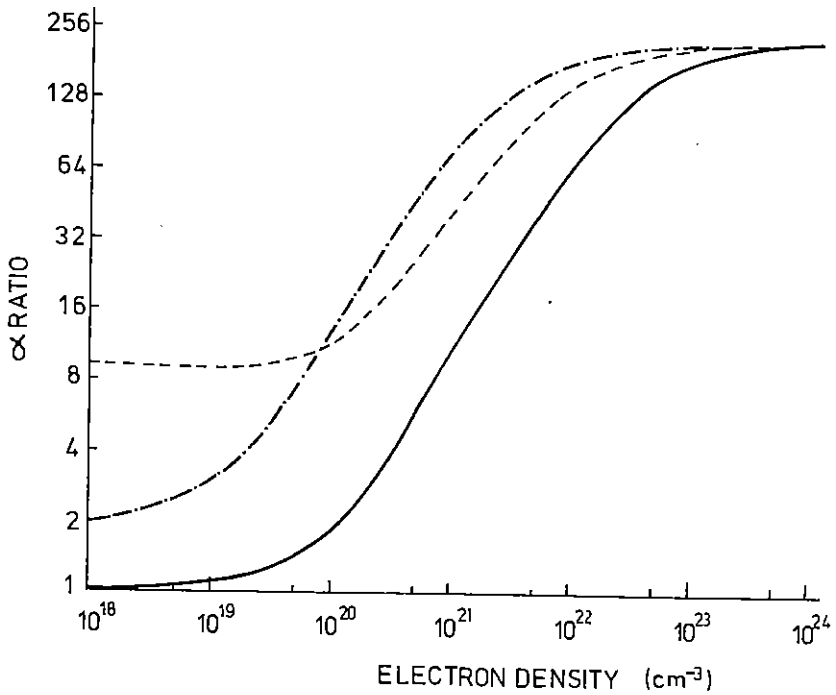

FIG. 6.70- THE VALUE OF THE RATIO ∝ AS A FUNCTION OF DENSITY FOR A TEMPERATURE OF 400 eV USING COLLISION RATES FROM MEWE (1972) (————), SAMPSON AND PARK (1974) (—·—·—) AND VINOGRADOV- ET AL. (1975). (— — —).

been used to examine the effects of different collision rates and of incomplete coupling between the levels which are used.

In the case of the dielectronic satellite ratio the neglect of the collisional de-excitation from autoionising to singly excited He-like levels has been shown to result in a significant error in the line ratio. This can explain the inconsistency between the diagnosed densities and experimental data which Lunney and Seely (6.61) explained by increased electron capture from the first excited state of the hydrogenic ion. However it should be noted that the original diagnostic predicts electron densities which are accurate to 30%.

The effect of using different models for collision rates was investigated by calculating the line ratio $(2\,^1P_1;\ 1\,^1S_0)/(2\,^3P_1;\ 1\,^1S_0)$ using the results of Mewe (6.64), Vinogradov et al (6.62) and Sampson and Park (6.65) for collision rates between singly excited He-like states. This shows that large differences in the line ration result using different collisional models, and emphasises the importance of accurate calculation of collision rates if meaningful spectroscopic diagnosis of plasmas is to be performed. As pointed out by Weisheit (6.63) the analysis of line ratios involving resonance lines has to include the effect of opacity. This does not alter the importance of accurate calculations of collision rates in the theoretical determination of line ratios.

6.6.2 Numerical Calculation of the Steady-State Ionisation Balance

A computational model has been developed to calculate the steady-state ionisation balance in a highly ionised plasma because line ratios are used as a diagnostic of plasma parameters.

In a recent paper by Lunney and Seely (6.61), the use of the dielectronic satellites ration

$$\frac{N(2_s2_p\,^3P)A(2_s2_p\,^3P;\,1_s2_s\,^3S)+N(2_p^{2}\,^3P)A(2_p^{2}\,^3P;\,1_s2_p\,^3P)}{N(2_p^{2}\,^1D_2)A(2_p^{2}\,^1D_2;\,1_s2_s\,^1P_1)}$$

has been proposed as a plasma density diagnostic and applied to results

from "laser imploded microballoons". In the model described in that paper the collisional de-excitation from autoionizing states to singly excited He-like states is not included. From Figure 6.69 it can be seen that errors of order 20% or 30% in the infrared density can be caused by the neglect of these rates.

Vinogradov et al (6.62) have described the use of the He-like resonance to intercombination line ratio

$$\alpha = \frac{N(2^1P_1)\ A(2^1P_1;\ 1^1S_0)}{N(2^3P_1)\ A(2^3P_1;\ 1^1S_0)}$$

as a density diagnostic. Calculations of this line ratio have been performed using three independent collisional rate models, ie those of Mewe(6.64), Vinogradov et al (6.62) and Sampson and Parks (6.65). Figure 6.70 shows the α-line ratio calculated using each of the three collision-rate models mentioned above, as a function of density at T_e = 400 eV, At $n_e \gtrsim 10^{23}$ cm^{-3} the LTE limit is approached and the three results agree. At low densities the α-line ratio depends only on the ratio of the excitation rates of the 2^1P and 2^3P levels by electron impact from the ground state. At the density range of interest for "laser imploded microballoons" the use of different collisional models can lead to order of magnitude errors in determining the density.

In summary, in the regime of interest for laser produced and laser compressed plasmas (10^{19} - 10^{24} cm^{-3} and T $\geqslant$ 100 eV) two effects were found to be of importance in determining accurately the plasma parameters:

(i) The collisional de-excitation from autoionising to singly excited He-like states and

(ii) The collisional model used to calculate rates between singly excited He-like states.

The programme includes Li-like ground and first excited states, He-like

and H-like states with n ≤ 6 and the He-like and Li-like autoionising states which are coupled between them with all the appropriate processes. Temperature, density and atomic number are inserted as data and at the present the code runs for Si and Al.

T A Stavrakas and R W Lee (Imperial College)

REFERENCES CHAPTER 6

6.21 Rutherford Laboratory Annual Report to the Laser Facility Committee, RL-81-040 (1981)

6.22 D Jacoby, G J Pert, S A Ramsden, L D Shorrock and G J Tallents, Opt Commun37, 193 (1981)

6.23 G J Pert and L D Shorrock, to be published in Proc of Fifth Nat Quant Elect Conf, J Wiley

6.24 G J Pert, Phys Trans A 300, 621 (1981)

6.41 J D Hares, J D Kilkenny, M H Key and J G Lunney, Phys Rev Lett 42, 1216 (1979)

6.42 P Eisenberger and B M Kincaid, Science 4349, 1441 (1978)

6.43 Rutherford Laboratory Annual Report to the Laser Facility Committee, RL-79-036

6.44 L L House, Astrophys J Suppl 18, 21 (1969)

6.45 J C Strewart, K D Pyatt, Astrophys J 144, 1203 (1966)

6.46 G J Hatton, N F Lane and J C Weisheit, J Phys B 24, 4879 (1981)

6.47 J D Hares and J D Kilkenny, J Appl Phys 52, 6420 (1981)

6.48 Ya B Zel'dovich and Yu P Raiser, 'Physics of shock waves and high temperature hydrodynamic phenomena', p201, Academic Press (1966)

6.49 A Hauer, ' Spectral Line Shapes', Ed B Wende and W de Gruyter, Berlin 1981, also LA-UR80-1660

6.50 Osaka Annual Report 1981, p47

6.51 R E La Villa, Phys Rev A19, 1999 (1979), also M V Tuiller, D Laporte and J M Esteva, 'Physics of Atoms and Molecules', Ed D J Fabian, p427, Plenum, New York 1981

6.61 J Lunney and J Seely, Phys Rev Lett 46, 5, 342 (1981)

6.62 A Vinogradov, I Skobelev and E Yukov, Sov J Quant Electron 5, 6, 630 (1975)

6.63 J Weisheit, JQSRT 16, 659 (1976)

6.64 R Mewe, Astron and Astrophys 20, 215 (1972)

6.65 D Sampson and A PArks, Astrophys J Suppl 28, 263, 323 (1974)

6.66 E Aglitski, V Boilko, A Vinogradov and F Yukov, Sov J Quant Electron 4, 3, 322 (1974)

6.67 L Vainshtein and U Safronova, Atomic Data and Nuclear Data Tables 21, 49 (1978)

6.68 M J Seaton, Phys Soc 79, 1106 (1962)

6.69 V Ivanov, 'Transfer of Radiation in Spectral Lines', NBS Special Publication, 385 (1973)

6.70 V Jacobs and J Davis, NRL Mem Rep 3641 (1978)

6.71 D Sampson, Private communication (1980)

6.72 I Duff, AERE Report R.8730 (1976)

6.73 R Mewe, J Schrijver adn J Sylwester, Astron & Astrophys 87, 55 (1980)

6.74 W L Wiese, H W Smith and B M Milesm 'Atomic Transition Probabilities', Vol II, Sodium through Calcium, NSRDS, Natural Bur Standards, 22, page X (1969)

CHAPTER 7 THEORY AND COMPUTATION

INDEX

CHAPTER EDITOR: A R Bell

CHAPTER 7 THEORY AND COMPUTATION

7.1 Introduction

During the last year most aspects of laser-plasma interactions have been studied, with particular emphasis on processes that have relevance to the experimental programme. This interaction with the experimental work is important, not only for the interpretation of present data and phenomena, but also for identifying scaling laws and making predictions that will influence the future experiments. With the present considerations of a major up-grade of the laser it is important that the theory can help to identify the characteristics required of the new laser.

Among the topics closely related to exeriment is that of non-linear thermal transport. This country has established a lead in this area and in the related area of heat flow instabilities, represented by the work reported here and last year. The CECAM International Workshop on the Flux Limiter and Heat Flow Instabilities at Orsay, 13 September - 2 October 1981, had over 20 participants from the U.S., France, Japan and included 5 from the U.K. This was a most successful workshop covering both non-linear heat flow and also examining in detail three electromagnetic instabilities associated with heat flow. A report on this will appear soon.

A present trend is to examine thermal conduction and thermal smoothing. Related to this is the problem of light filamentation through self-focusing, and the degree of residual asymmetry that could trigger off a Rayleigh-Taylor instability. Magnetic fields, which are spontaneously created, are relevant here, as well as in the heat flow instabilities. The theory of the parametric process in the laser-plasma interaction itself has also been extended during the year to include the effect of such a magnetic field.

M G Haines (Imperial)

7.2 Laser Compression Studies

7.2.1 Fluid Code Development

The major effort over the past year has been directed towards the development of a satisfactory form of quasi-Lagrangian rezoning for multidimensional Eulerian codes using a time varying orthogonal mesh. A versatile stable scheme has been identified and has been incorporated into new versions of MAGT and POLLUX using non-uniform meshes. A new rapid solution of the ionisation equilibrium equations has been tested and implemented into an earlier version of MAGT. Minor improvements to the two dimensional Lagrangian code LAG2 have been made.

Quasi-Lagrangian Rezoning

One of the principal difficulties in modeling laser produced plasmas from solid targets is the large range in density which a typical fluid element undergoes during its flow. In the initial phase of the interaction the flow has a developing structure, but at later times may have a steady state structure, but with large density variations. The initial flow phase is clearly well modelled by a Lagrangian code, but the later steady structure is more suited to an Eulerian description. The object of quasi-Lagrangian rezoning is to develop a nearly Lagrangian mode (but with some slip to maintain an orthogonal mesh) whilst the mesh is less than some appropriate boundary limit, and be Eulerian henceforth.

As reported last year (7.01) we initially used the method proposed by Craxton and McCrory (7.02), in which the grid is moved according to a subsidiary Lagrangian mesh. Whilst this proved satisfactory during the Lagrangian phase, the transition to an Eulerian mesh by the introduction of a mesh boundary gave continual trouble, which could not be satisfactorily resolved. The simpler method of rezoning according to the line centres-of-mass velocity used by Boris (7.03) and Anderson (7.04) was adopted.

In designing such a code we may require the usual conditions of good

behaviour namely consistency, conservation and positivity. Since the latter two ensure general boundedness, such a scheme is stable in the sense that the growth of perturbations is bounded. Clearly, however, for good behaviour the perturbation should not grow at all. We therefore add linear (von Neumann) and odd-even stability to our requirements.

It is shown quite generally that a code can be consistent and conservative only if it is defined with respect to cell-centred grid on which the mesh points are defined and the cell boundaries are placed mid-way between the cell boundaries. Most Lagrangian codes are defined on a mesh centred grid, on which the cell boundaries are defined and the mesh points are placed at the cell centres: they are never strongly conservative. In contrast Eulerian codes are usually defined on a cell-centred grid.

It is a well known result that simple one-dimensional Lagrangian codes on cell-centred grids are linearly unstable. Since the one-dimensional case of our quasi-Lagrangian scheme can be expected to reduce to this form, this must be avoided. A simple solution is to introduce the intermediate time pressure. Thus let

$$\gamma_i = \rho_i^n \; C_i^{n2} \; / \; p_i^n$$

where p_i^n, ρ_i^n, C_i^n are the pressure, density and sound speed at time step n in cell i, then

$$p_i^{n+\frac{1}{2}} = p_i^n \begin{cases} 1 - \frac{1}{4}\gamma_i(u_{i+1}^n - u_{i-1}^n)Dt/\Delta z_i^n & u_{i+1}^n < u_{i-1}^n \\ 1 \; / \; (1+\frac{1}{4}\gamma_i(u_{i+1}^n - u_{i-1}^n)Dt/\Delta z_i^n) & u_{i+1}^n > u_{i-1}^n \end{cases}$$

where u_i^n, and Δz_i^n are the flow velocity and cell width in cell i respectively. The linear stable one dimensional form is therefore:

$$u_i^{n+1} = u_i^n - p_i^{n+\frac{1}{2}}/\rho_i^n \Delta z_i^n$$

$$\Delta z_i^{n+1} = \Delta z_i^n + \tfrac{1}{4}\,(u_{i+1}^{n+1} + u_{i+1}^n - u_{i-1}^{n+1} - u_{i-1}^n)\; Dt$$

$$\rho_i^{n+1} = \rho_i^n \; \Delta z_i^n / \Delta z_i^{n+1}$$

$$\varepsilon_i^{n+1} = \varepsilon_i^n - p_i^{n+\frac{1}{2}} \; (\Delta z_i^{n+1} - \Delta z_i^n)/(\rho_i^n \Delta z_i^n)$$

This scheme is strongly conservative in energy (as well as mass and momentum) and subject to an appropriate time step constraint is positivity maintaining.

We may also remark that due to the use of advanced pressure the scheme is second order.

The above hydrodynamic algorithm in its multi-dimensional form is clearly an appropriate base for the required quasi-Lagrangian scheme. The complete algorithm takes the form of a Lagrangian advance followed by rezoning back on to the new mesh. The latter procedure is just equivalent to advection, and is accomplished by a suitable mesh routine. In an extensive series of trials the SHASTA scheme with flux corrected transport (7.05) was found to be particularly satisfactory. Indeed in this form a fully Lagrangian one-dimensional routine with no artificial viscosity was found to be well-behaved.

In order to avoid the Courant-Friedrichs-Lewy time step trap described in ref. (7.02) a simple grid slip was found extremely appropriate. Thus in one dimension the grid points are moved not with the fluid velocity u_i but according to

$$Dz_i = u_i Dt / \left[1 - \mathrm{XMin}\left(0, \frac{(u_i - u_{i-1})Dt}{\Delta z'_{i-\frac{1}{2}}}, \frac{(u_{i+1} - u_i)Dt}{\Delta z'_{i+\frac{1}{2}}}\right)\right]$$

where $\Delta z'_{i+\frac{1}{2}}$ is the distance between the cell centres i and $(i+\frac{1}{2})$.

A more detailed study of these schemes will be presented in a forthcoming report.

Calculation of Ionisation Equilibria

In order to preserve the conservation law properties of multi-celled fluid codes, the natural thermodynamic variables are density, ρ, and specific internal energy, ε, rather than temperature, T, which is more appropriate to a free energy description of the equation of state. If the medium is an ionising gas the thermodynamic state of the electrons is described by its ionisation and energy balances. These take the form

$$\frac{q_i}{q_{i+1}} = r_i + r_i' Z \tag{1}$$

$$Z = \sum_{i=1}^{N} i q_i \tag{2}$$

and

$$\varepsilon = E_v + \frac{3}{2} z k T_e \tag{3}$$

where $E_v = \sum_{i=1}^{N} V'_i q_i$ (4)

is the total ionisation energy. The population q_i, of the various ionisation stages vary rapidly with the electron temperature T_e, through the rate coefficients $r_i(T_e)$ and $r_i'(T_e)$, and satisfy

$$\sum_{i=0}^{N} q_i = 1 \tag{5}$$

The energies V_i' are the net energy required to form an ion of species i and are related to the ionisation energies V_i through:

$$V'_i = V'_{i-1} + V_{i-1} \tag{6}$$

We require a rapid and efficient method of solving this set of equations for Z and T_e. Since $r_i(T_e)$ and $r_i'(T_e)$ are complicated functions of T_e it is preferable to solve for Z as a function of T_e, and then iterate to find T_e. Given a guess (old) value of Z we may easily solve (1) and (5) to find the set, q_i, for

$$q_i = 1/\left[X_i + Y_i - 1 \right] \tag{7}$$

where the sets

$$\begin{aligned} X_i &= 1 + R_i X_{i-1} \quad : \quad X_1 = 1 \\ Y_i &= 1 + Y_{i+1}/R_{i+1} : \quad Y_N = 1 \end{aligned} \tag{8}$$

are obtained recursively and

$$R_i = r_i + r_i' Z \tag{9}$$

Hence from (2) we find a new value of Z.

A rapid iteration for Z is obtained by noting that Z_{new} is a positive monotonically decreasing function of Z_{old}. Thus writing $Z_{old} = X$ and $Z_{new} = y$ we require the solution to

$$y = f(x) \quad : \quad y = x \tag{10}$$

Given two sets of values (x_o, y_o) and (x_1, y_1) and noting the behaviour of f(x) we may find a new best solution to (7) by considering a rectangular hyperbola through these two points. The next interation for Z is given by the intersection of this hyperbola with the line (x = y), i.e.

$$X^2 = (X_o X_1 + y_o u_1)(x_1 y_o - x_o y_1)/(x_1^2 - x_o^2 - y_o^2 + y_1^2) \tag{11}$$

In numerical tests this form converged much more rapidly than the Newton-Raphson iteration which is based on a straight line through the known points. In order to start the iteration an initial starting value based on coronal equilibrium (Z=0) is used. We may also remark on the need for bounds on the elements (X_i, Y_i).

Some care is also required in the outer iteration for T_e, due to the rapidly varying nature of Z with T_e at low temperatures. For this purpose we have found it appropriate to use bounded values of T_e within which the iteration is performed. In this case we seek the solution of:

$$F(T_e) = \varepsilon = (E_V(T_e) + \frac{3}{2} Z(T_e) k T_e) \tag{12}$$

which, for practical values of r_i and r'_i, is a monotonically decreasing function T_e. Given two values of T_e, T_o and T_1, and the corresponding values F_o and F_1, the next best value of T_e is

$$T = (F_1 T_o - F_o T_1)/(F_1 - F_o) \tag{13}$$

(far from equality $T = \sqrt{(T_o T_1)}$ may be appropriate)
If $T_o < T_1$ then $T_o < T < T_1$, thus choosing (F_o, T_o) and (F_1, T_1) to be lower and upper bounds respectively by adjusting T_o or

T_1 after each iteration by:

if $F > 0$: $T_o \rightarrow T$ or if $F<0$: $T_1 \rightarrow T$ (14)

the convergence of the iteration may be markedly improved. Suitable initial values of the bounds are:

$$T_o > \text{Max}\left[T_{1t}, (\varepsilon - V_N')/(\tfrac{3}{2}(N-1))\right]$$

$$T_1 < \text{Max}\left[V_o, 2/3\ \varepsilon\right] \quad (15)$$

where T_{1t} is an appropriate absolute lower bound.

G J Pert and A J Bennett (Hull)

7.2.2 Rayleigh - Taylor Instabilities

The achievement of inertially confined thermonuclear fusion in laser driven pellets requires that a hollow shell be symmetrically imploded to less than one tenth of its initial radius in order to generate the high densities needed for significant thermonuclear burn (7.06). The use of a hollow rather than solid pellet reduces the peak power requirement from the laser which decreases as the ratio of shell radius to thickness, $\alpha = R/\Delta R$, is increased. Unfortunately the hollow shell targets are hydrodynamically unstable in the ablation region where the pressure and density gradients are of opposite sign, ie. $\nabla p.\nabla\rho < 0$. The instability in this region is similar to the classical Rayleigh Taylor (R-T) instability of two incompressible fluids (7.07) but is complicated by the finite density and temperature scale lengths, heat conduction, compressibility and flow of the ablating material. Various analytic approximations have been made to estimate the growth rates (7.08, 7.09), and numerical simulations using both Eulerian and Lagrangian formulations have also been employed (7.10 - 7.12).

The simulation data consistently show growth rates α reduced by a factor of two or three below the classical growth rate for an Attwood number of unity $\gamma = \sqrt{ka}$; where k is the wave number and a the effective acceleration.

There is a qualitative difference between the results of McCrory et al (7.11) and those of Emery et al regarding the appearance of a Kelvin - Helmholtz (K-H) type of instability as evidenced by a broadening of the tips of the R-T "spikes" as they fall into the less dense medium. We describe here the results of simulations performed with an Eulerian code which show that the appearance of the "Kelvin-Helmholtz" features is dependent on the initial conditions of the problem and indeed cast some doubt as to whether it is indeed a Kelvin Helmhdtz instability. Our results agree well with both Emery et al and McCrory et al for the rather dissimilar cases that they considered.

The simulations are performed using an Eulerian code "POLLUX", described in Section 7.2.1 and ref 7.13.

In performing the simulations it is necessary to "seed" the instability by introducing a perturbation into the target mass distribution or the laser irradiance or by introducing a divergence free velocity perturbation in the fluid flow. The advantage of this latter method is that a form for the velocity perturbation may be taken which approximates to the eigen - function of the instability. Exponential growth is then seen almost immediately whereas if the mass distribution is perturbed it is necessary to wait until the non-growing components of the perturbation have been overtaken by the unstable modes.

Since one of the aims of this work is to make a quantitative estimate of the break up of a target due to Rayleigh-Taylor instabilities we have chosen to perturb the initial mass distribution despite the disadvantages outlined above. The overriding benefit is that immediate comparison can be made with targets actually used for laser acceleration and implosion experiments. The initial conditions of the simulation are shown in Figure 7.01, a flat foil of thickness 2.5 μm is irradiated from the right of the Figure with a uniform intensity of 2×10^{13} W cm^{-2} of laser light at a wavelength $\lambda = 0.53$ μm. The target is "corrugated" as shown with a square wave of amplitude 0.125 μm and wavelength $\lambda_L = 2.5$ μm deliberately chosen to approximate the most damaging mode. The simulation mesh is 5 μm by 10 μm and is made up of 50 x 80 intervals.

Figure 7.02 shows a sequence of density contours at later times, at 100 ps the foil has undergone shock compression and appears much thinner, at 200 ps the Rayleigh-Taylor growth is appearing on the surface of the foil facing the laser while the back face appears relatively flat. At 300 ps the instability appears as the characteristic "bubble and spike" with the spikes pointing towards the laser and the K-H effects appearing as a "mushroom" like broadening of the tips of the spikes.

Since the initial perturbation is a square wave it is natural that the spatial harmonics of the perturbation wavelength also appear in the instability. These higher frequency perturbations, still several computational cells in size, are clearly seen in Figure 7.02. In the classical R-T instability the growth rate increases with decreasing wavelength but in the ablation instability the finite gradient scale lengths and thermal conduction effects act to stabilise the instability at short wavelengths.

Simulations have also been performed for foils of similar initial mass distribution but with the laser irradiance increased to 10^{14} W cm^{-2} and 5×10^{14} W cm^{-2}, still at a laser wavelength of 0.53 μm. For the simple incompressible Rayleigh-Taylor instability with a constant acceleration the integrated growth exponent $\int \gamma dt = \sqrt{4\pi z/\lambda_L}$ depends only on z. Thus it is a sensible comparison to show the simulation results for different irradiances at the same distance travelled. In order to keep the ablated mass fraction constant at a constant distance travelled we have increased the initial mass density to compensate. In Figure 7.03 and Figure 7.04 we show the comparison of the three irradiances at distances of about 9.5 μm and 11 μm respectively. Clearly the spatial growth rate is somewhat reduced at the increased irradiance. There are two notable features in the simulations, firstly the high spatial frequencies appearing at 2×10^{13} W cm^{-2} are progressively reduced at higher irradiances and secondly the Kelvin Helmholtz "mushroom" features also diminish as the irradiance is increased.

Our simulations at 2×10^{13} W cm^{-2} are qualitatively similar to those of Emery et al at 10^{13} W cm^{-2} with prominent K-H features, while at

5×10^{14} W cm^{-2} our results are in good agreement with the McCrory et al simulations at 10^{15} W cm^{-2}. It is tempting to attribute the disappearance of the Kelvin-Helmholtz features to the increased plasma temperature at the higher irradiances. As well as increasing the thermal conductivity this will change the gradient scale lengths and hence the Richardson number (7.14).

However the K-H features are also removed at an irradiance of 2.10^{13} W cm^{-2} if the form of the initial perturbation is changed. In Figure 7.05 we show the result of a sinusoidal rather than square wave initial modulation of the target surface. Although still not an eigen mode of the R-T instability the content of the higher spatial harmonics is reduced and the density profiles show no evidence of K-H growth. In Figure 7.06 we show the result of irradiating a flat target with a laser whose intensity varies with radius as $I = I_0 (1 + 0.2 \sin (r/2.5\ \mu m))$. The R-T instability is then seeded by the vorticity generated by the differential shock velocity in the solid, and again there is no evidence of K-H growth.

We propose two possible explanations of the behaviour of the "Kelvin-Helmholtz" features.

(i) The effect is not due to Kelvin Helmholtz instability but is the result of vorticity being generated at high spatial frequencies due to the form of the initial perturbation. This vorticity is advected into the spikes by the fluid flow and appears eventually as a broadening of the tips.

(ii) The effect is a manifestation of K-H instability but the gradients, and hence the Richardson number are changed by the presence or absence of high spatial frequencies in the initial perturbation.

It may be possible to distinguish these by careful analysis of more

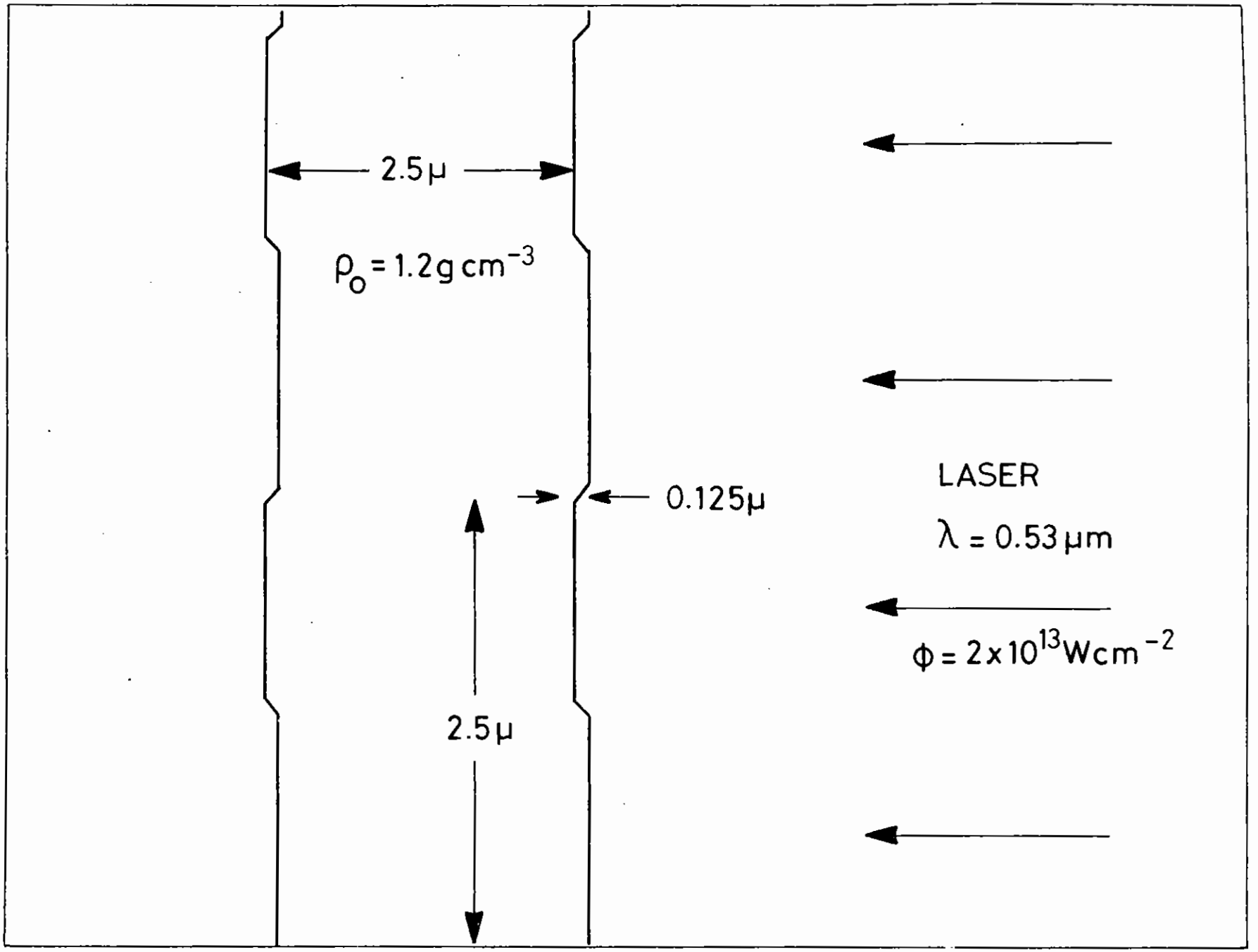

Figure 7.01 Initial conditions for the Rayleigh-Taylor simulations

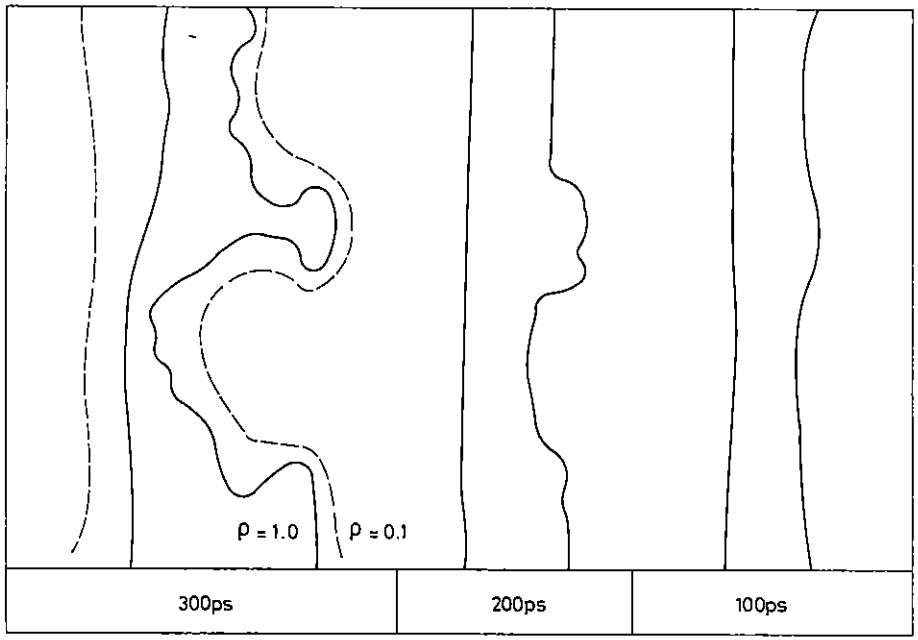

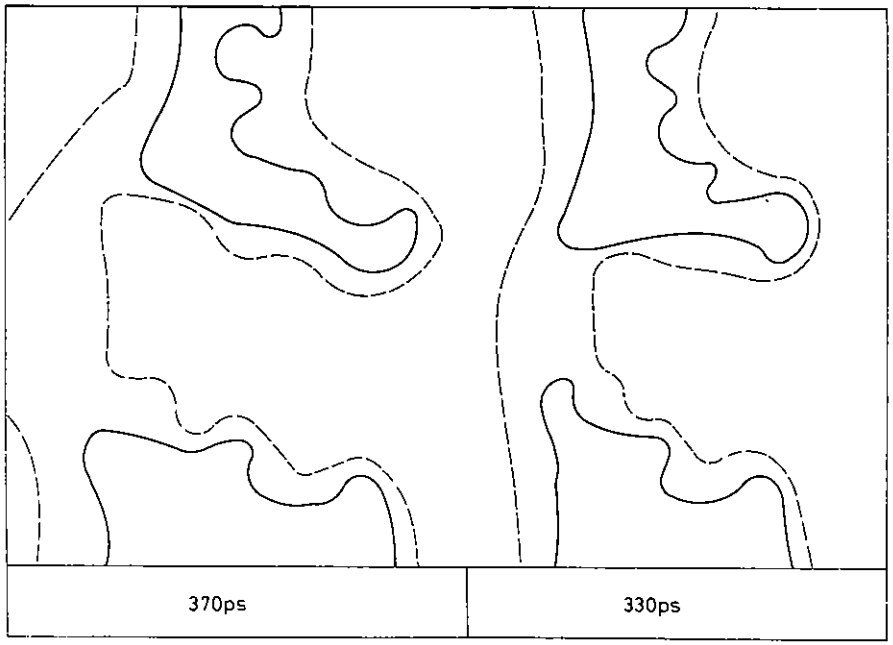

Figure 7.02 Evolution of density contours

simulations but the effect certainly does not originate in the numerical methods employed.

R G Evans (RAL) and G J Pert (Hull)

7.2.3 Scaling Laws for Implosions with Thermal Smoothing

It has been shown in earlier work that approximate analytical models of ablative implosions can give useful insight into the scaling of the compressed plasma parameters with laser and target variables. In particular Ahlborn, Key and Bell (7.15) have discussed ablative implosions in which constant laser power drives single spherical shell targets. The scaling behaviour under the constraints of constant aspect ratio $r/\Delta r$ (for hydrodynamic stability) and constant ratio of preheating by hot electrons to preheating by shocks (for ablative dynamics) were considered.

Recently it has become clear that the spatial variation of ablation pressure resulting from spatially inhomogeneous irradiation is a serious problem for directly driven implosions. Gardner and Bodner (7.16) have discussed the steady state thermal smoothing of pressure variations arising from diffusion between the absorption and ablation surfaces and Key (Ibid 4.5) has considered smoothing under transient conditions as the absorption to critical surface separation develops.

Lindl (7.17) has pointed out that a required degree of thermal smoothing can be introduced as a constraint on the scaling of ablative implosions. In particular he has analysed the requirements for implosions with simultaneously specified

(a) absorbed energy

(b) implosion momentum flux density ρv^2

(c) thermal smoothing of irradiance perturbations.

The present work will;

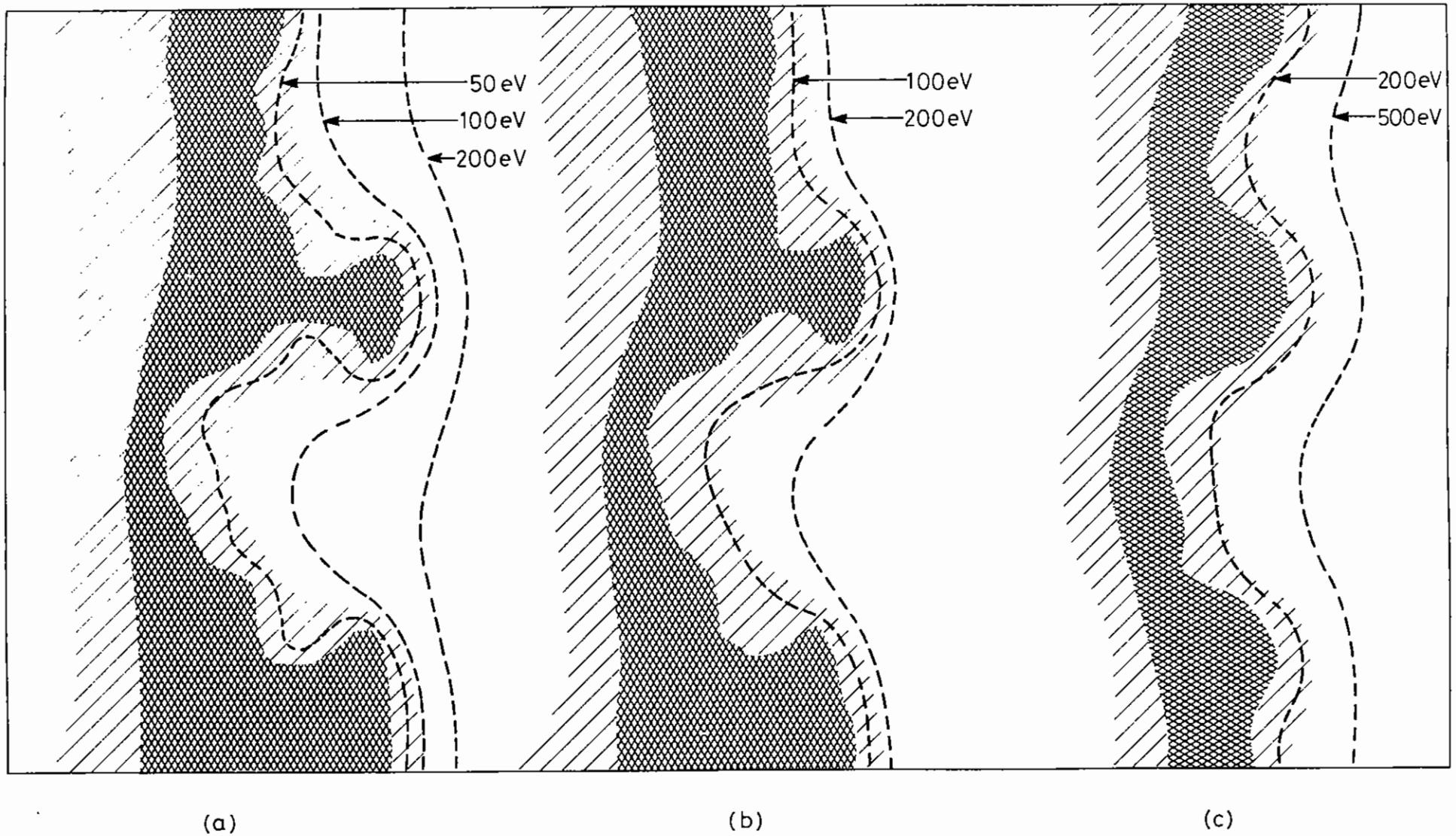

Figure 7.03 Comparison of simulations at (a) 2×10^{13} W cm^{-2} (b) 10^{14} W cm^{-2} (c) 5×10^{14} W cm^{-2}, at Z $\simeq$ 9μm.

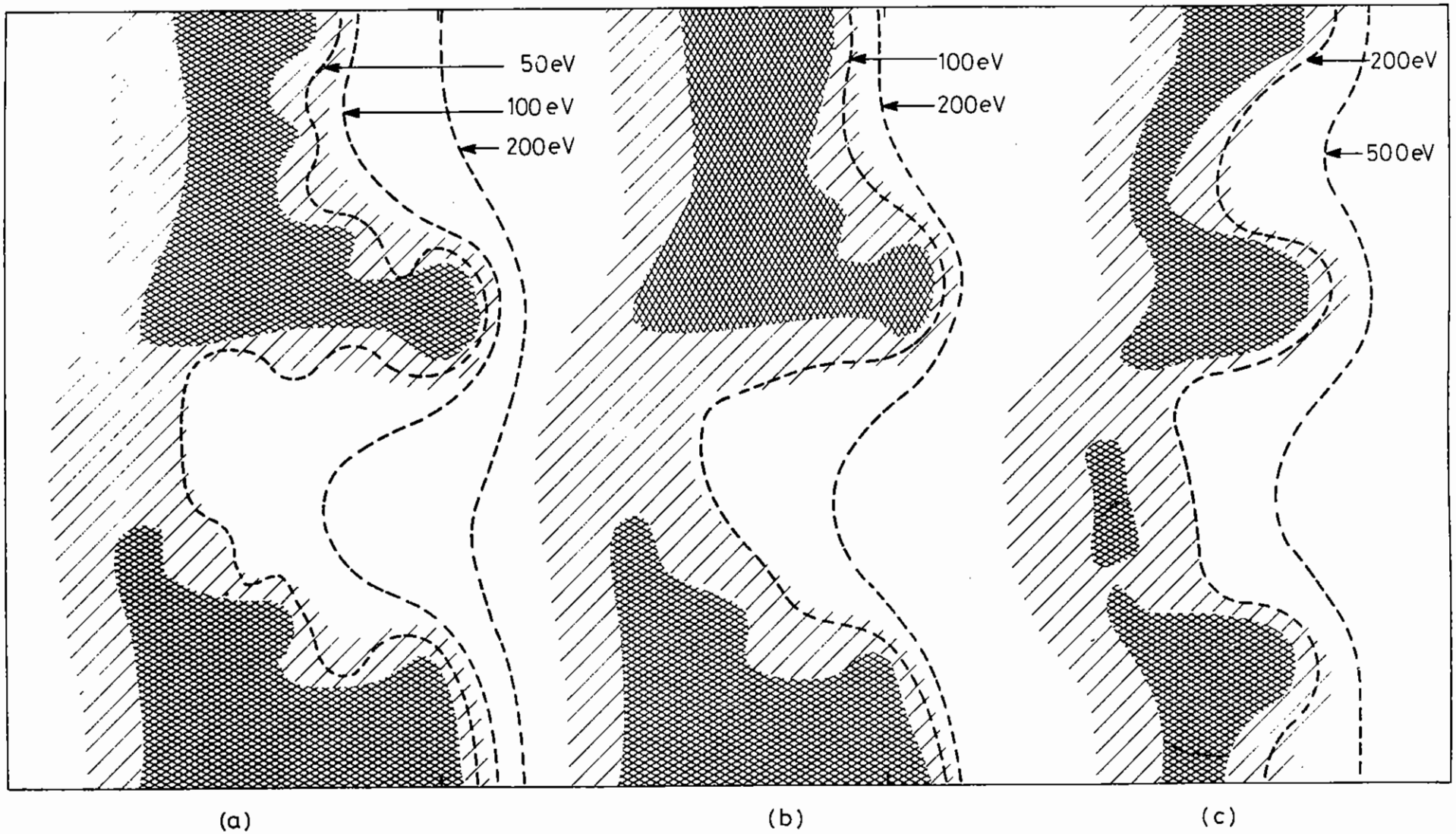

Figure 7.04 As figure 7.03 but at Z ≈ 11μm.

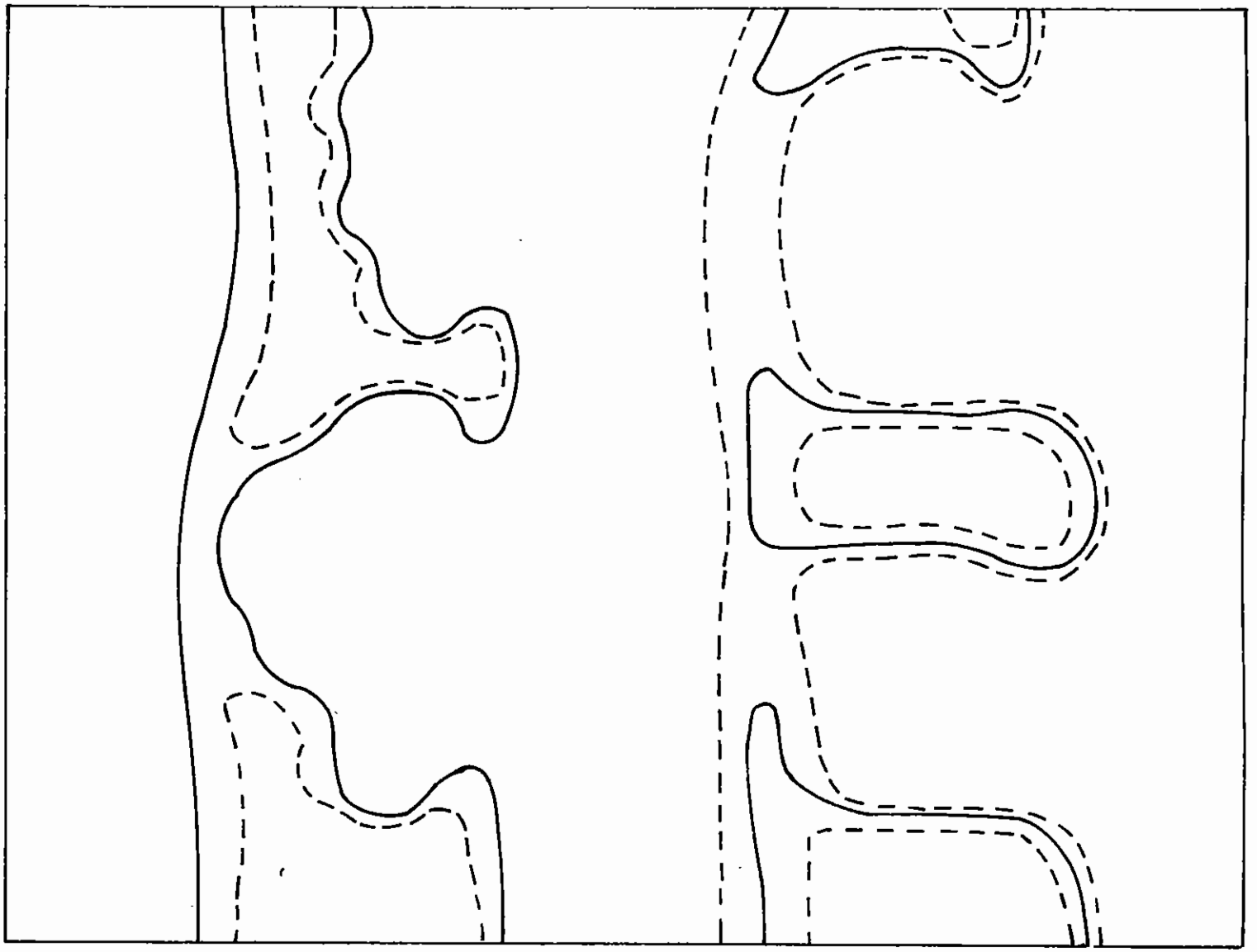

Figure 7.05 Comparison of density contours for step function initial modulation of target and sine wave modulation.

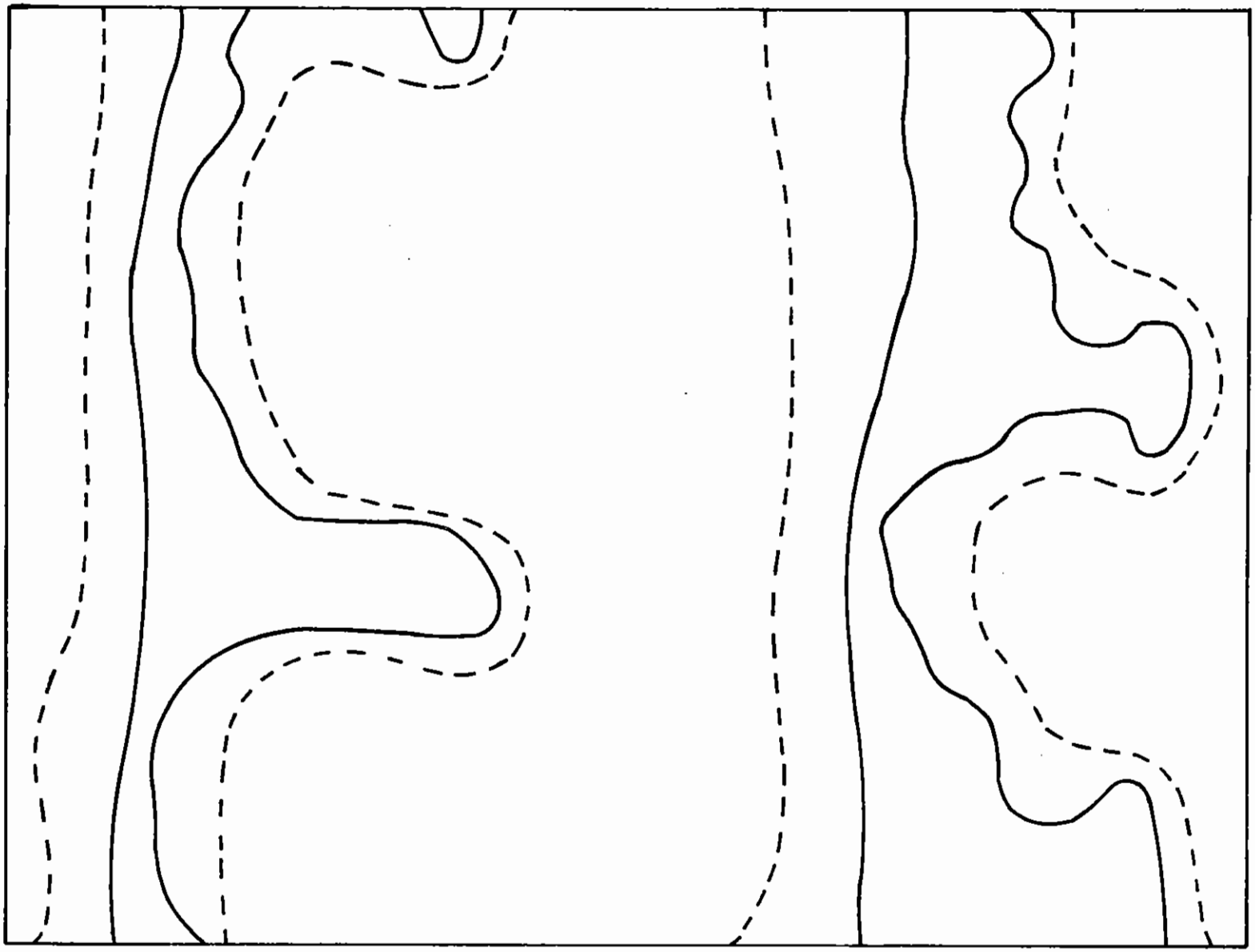

Figure 7.06 Comparison of Rayleigh-Taylor instability driven by spatially modulated laser beam and by modulated target.

(a) summarise Lindl's arguments

(b) examine how they are changed by using a better description of the steady state separation D of absorption and ablation surfaces, viz Gardner and Bodner's results (7.16),

(c) consider the effect of the effect of the transient phase of development of D on the thermal smoothing in implosions,

(d) examine an alternative formulation of the constraints on implosions in which thermal smoothing, hot electron preheating and ρv^2 are specified.

7.2.3(a) Summary of Lindl's Model

Steady state thermal smoothing is assumed viz

$$\Delta P/P = (\Delta I/I) \exp(-2\pi D/L_p) \quad (1)$$

where L_p is the spatial scale of perturbations and D the steady state absorption/ablation surface separation.

Max, McKee and Mead's (7.18) formulation of steady state ablation is used to give

$$r_c/R = 1.24\ (I_{13}\lambda_\mu^{3.45})^{0.11}\ (ZR_{mm})^{-0.08} \quad (2)$$

for the critical surface radius r_c relative to the target radius R, with $I_{13} = I/10^{13}$ W cm^{-2}, $\lambda_\mu = \lambda/1$ μm and $R_{mm} = R/1$ mm. The same analysis gives the ablation pressure

$$P = 1.9 \times 10^{12}\ I_{13}^{0.57}\lambda_\mu^{-0.99}(ZR_{mm})^{0.07}\ \text{dynes cm}^{-2} \quad (3)$$

The largest values of L_p of interest are those associated with the illumination geometry (viz $L_p/R = 1.57$, 1.11 or 0.73 for 6, 12 and 20 beams illumination). Thus $L_p/R \simeq 1$ is a typical case and for 10 fold

attenuation of pressure variations $r_c/R = 1.3$ from equation (1) so that equation (2) gives,

$$1.3 = 1.24\ (I_{13}\lambda_\mu^{3.45})^{0.11}\ (ZR_{mm})^{-0.08} \quad (4)$$

as the first constraint in the model.

Secondly it is assumed that implosions must achieve a specific value of momentum flux density ρv^2. A simple model for a shell with constant acceleration (7.15) shows that,

$$\rho v^2 = \frac{4}{3} P\ (R/\Delta R) = 10^{15}\ \text{g cm}^{-1}\ \text{sec}^{-2} \quad (5)$$

for $v = 2.2 \times 10^7$ cm s^{-1} and $\rho = 2$ g cm^{-3}.

Thirdly Lindl assumed a constant absorbed laser energy $E = 4\pi R^2 I\tau$ where τ, the implosion time is $[(4/3)\rho R\Delta R/p]^{\frac{1}{2}}$ so that where $E_{KJ} = E/1$ kJ

$$2.1 \times 10^2\ I^2\ R^5\ \rho\Delta R P^{-1} = E_{KJ}^2 \quad (6)$$

and from (5) and (6) with $\rho = 2$ g cm^{-3}

$$R_{mm} = 0.51\ I_{13}^{-1/3}\ E_{kj}^{1/3} \quad (7)$$

Elimination of variables then yields,

$$I_{13} = 1.9\ E_{KJ}^{0.2}\ \lambda \quad (8)$$

$$R_{mm} = 0.38\ E_{KJ}^{1/3}\ \lambda_\mu^{0.85} \quad (9)$$

$$\Delta R_{mm} = 3.3 \times 10^{-3}\ E_{KJ}^{1/3}\ \lambda_\mu^{-2.37} \quad (10)$$

$$R/\Delta R = 115\ \lambda_\mu^{0.22} \quad (11)$$

Equations (8-11) summarise the wavelength scaling implications of Lindl's model. It is clear that shorter wavelengths allow thicker shells of lower aspect ratio which may be expected to be more hydrodynamically stable, with no penalty in the thermal smoothing which has been held constant. It

is interesting to see how the requirement for smoothing compares with the requirement for insignificant hot electron preheating discussed in (7.15) which can be expressed as

$$I_{13} \leq 1.4\ \lambda_\mu^{-2}\ (\Delta R/1\mu m)^{1.1} \qquad (12)$$

or with the value of Δr in equation (8).

$$I_{13} \leq 5.2 \times \lambda_\mu^{-4.6}\ E_{KJ}^{0.37}$$

so that the ratio η of the upperbound irradiance permitted by preheat to the lower bound required for smoothing is

$$\eta = 2.7\ \lambda_\mu^{-2.1}\ E_{KJ}^{0.17} \qquad (13)$$

showing that as the wavelength is reduced the ratio increases giving improved possibilities for thermal smoothing.

7.2.3(b) Lindl's Model with a better description of Steady State Thermal Smoothing

The numerical calculations of Gardner and Bodner give for the absorption to ablation front separation D,

$$D/R = 0.14\ (I_{13}\ \lambda_\mu^{3.8})^{0.7}\ /(Rmm + 1) \qquad (14)$$

and for the pressure P,

$$P = 2 \times 10^{12}\ (I_{13}\lambda_\mu^{-0.25}\ R_{mm}^{0.18})^{0.7} \qquad (15)$$

Since these calculations have a more complete physical model than the analytical solution of Max, McKee and Mead they are probably more reliable where major differences exist. The irradiance scaling of the separation D is one such difference emphasised in Table 7.01.

Table 7.01

I Wcm^{-2}	r_c/R	$1 + D/R = r_c/R$
10^{12}	0.87	1.01
10^{13}	1.12	1.07
10^{14}	1.45	1.35
10^{15}	1.86	2.76
	Eq 2	Eq 14

Note that $r_c/R < 1$ is physically impossible but implied by the MMM scaling at $I = 10^{12}$ W cm^{-2}. The previous smoothing criterion now becomes

$$D/R = 0.3 = 0.14\ (I_{13}\lambda_\mu^{3.8})^{0.7}/(R_{mm} + 1) \qquad (16)$$

while equations (5), (6) and (7) give the constraint on the implosion for constant ρv^2 and constant absorbed energy as before.

Elimination of variables using now equation (15) for the pressure in place of equation (3) gives

$$I_{13} = 3\lambda_\mu^{-3.8}\ (1 + I_{13}^{-1/3}0.51E_{KJ}^{1/3}) \approx 3\lambda_\mu^{-3.8} \qquad (17)$$

$$R_{mm} = 0.36\ E_{KJ}^{1/3}\ \lambda^{1.27} \qquad (18)$$

$$\Delta R_{mm} = 1.3\ 10^{-3}E_{KJ}^{0.5}\ \lambda_\mu^{-2.21} \qquad (19)$$

$$R/\Delta R = 277\ E_{KJ}^{0.17}\ \lambda_\mu^{3.5} \qquad (20)$$

and from (12) and (19) the constraint for no hot electron preheating is

$$I_{13} < 1.9\ E_{KJ}^{0.55}\ \lambda_\mu^{-4.4} \qquad (21)$$

with the ratio η of maximum permissable to minimum required irradiance from equations (21) and (17)

$$\eta = 0.63\ \lambda_\mu^{-0.6}\ E_{KJ}^{0.55} \qquad (22)$$

Equations (17-22) may be compared with Equations (8-13) to assess the effect of using Gardner and Bodner's calculations of absorption to ablation front separation rather than Max, McKee and Mead. The general effect is to make it less easy to exceed the irradiance required for smoothing while remaining below that giving hot electron preheating and to require less stable higher aspect ratio shells. The qualitative conclusion that shorter wavelengths permit thicker more stable shells and

have a greater ratio η of the upper bound and low bound irradiances remain unchanged.

7.2.3(c) The Transient Phase of Thermal Smoothing in Implosions

It is shown in section 4.5 ibid that thermal smoothing can be analysed in terms of a transient phase and a steady state phase with the duration of the transient phase given by

$$\tau_s = D_\infty/V_s \qquad (23)$$

where D_∞ is the steady state separation of the absorption and ablation surfaces and v_s the velocity of separation.

With expressions for D_∞ from equation (14) and for v_s from equation (12) in section 4.5 it follows that

$$\tau_s = 4.7 \times 10^{-9}\ I_{13}^{0.37}\ \lambda_\mu^{2}\ R_{mm}/(R_{mm} + 1) \qquad (24)$$

The implosion time τ_i is readily expressed in terms of the ablation pressure P in the form

$$\tau_i = \left[(4/3)\ R_\rho \Delta R/P\right]^{1/2} \qquad (25)$$

and with equation (15) for P the ratio τ_s/τ_i becomes

$$\tau_s/\tau_i = 3.2 \times 10^{-2}(I_{13}\lambda_\mu^{3.8})^{0.72}(R/_\rho\Delta R)^{0.5}\lambda_\mu^{-0.84}R_{mm}^{0.12}(1 + R_{mm})^{-1} \qquad (26)$$

This shows that $\tau_s/\tau_i \not< 1$ in most cases of interest. For example the optimised implosions described by equations (17-20) above have from equation (3)

$$\tau_s/\tau_i = 0.94\ \lambda_\mu^{0.73}\ E_{KJ}^{-0.13}\ (1 + 0.36\ E_{KJ}^{0.33}\ \lambda_\mu^{1.27})^{-1} \qquad (27)$$

which clearly implies a predominantly transient situation with a greater proportion of steady state as λ is decreased.

The optimisation assumed a criterion for tenfold smoothing of perturbations of scale $L_p = R$, viz $D \simeq 0.3\ R$ but the actual smoothing would be much reduced by the transient phase of the process (see equation (10) in section 4.5 where $\epsilon = \tau_s/\tau_i$ and τ_s/τ_i is now given by equation (27) above). Eg, for $\lambda = 0.53\ \mu m$, $E = 1$ kJ, we have $\epsilon = 0.5$, and the smoothing factor is 0.5 rather than 0.1 for perturbations with $L_p \simeq R$. Tenfold smoothing would be obtained in the above example for perturbations on a smaller scale $L_p \simeq 0.2\ R$.

This suggests that it may not be possible to obtain good thermal smoothing for perturbations with scale length $L_p \simeq R$ arising from multi-beam illumination and that the illumination itself may have to be uniform while smaller scale perturbations due to inhomogeneities within laser beams may be adequately smoothed.

The wavelength scaling of thermal smoothing is different in the transient and steady state limits, ie $I\lambda^2$ and $I\lambda^{3.8}$ respectively from equations (3) and (19) + (12) in section 4.5.

The attenuation of pressure inhomogeneity for a given irradiation inhomogeneity defines a smoothing factor $\delta = (\Delta P/P)/(\Delta I/I)$. In an implosion where ϵ is given by equation (26) and the smoothing is dominated by the transient terms in equation (10) of Section 4.5 ibid we have

$$\delta = \epsilon\ L/\pi\ D_\infty \simeq L/(\pi\ v_s \tau) \qquad (28)$$

where τ is the implosion time and L is the wavelength of the irradiance perturbation. It follows from equations (14) and (26) that

$$\delta \simeq 0.1\ (L/R)\ (R/\rho\Delta R)^{1/2}\ \lambda_\mu^{-0.8}\ I_{13}^{0.02}\ R_{mm}^{0.06} \qquad (29)$$

It therefore seems that the smoothing may be essentially independent of the irradiance and target size but linear in (L/R). The wavelength dependence $\lambda^{-0.8}$ suggests that less smoothing is obtained for shorter wavelengths. Since higher pressure is available ($P \propto \lambda^{-2}$ at constant $I\lambda^2$) the aspect ratio could be scaled as $R/\Delta R \propto \lambda^{1.6}$ giving wavelength

independent smoothing. The implosion velocity is then $v \propto \lambda^{-0.2}$, which is also almost independent of wavelength. This analysis suggests that thermal smoothing is another factor in addition to Rayleigh Taylor instability mitigating in favour of low aspect ratio. It also follows that the advantage of short wavelengths may be the possibility of achieving a given level of smoothing and implosion velocity with a thicker shell having greater stability and preheat screening albeit using more laser energy $E \propto \lambda^{-2}$ for a target of fixed size.

7.2.3(d) An Alternative Set of Constraints on Implosions

A useful extension of the above discussion was pointed out by R Evans (7.19). The constraints on implosions can be defined as:

- constant thermal smoothing
- constant ρv^2
- constant hot electron preheating

If the first two are taken to be the same as discussed in section 7.2.3(b) above we have equation (4) for constant steady state smoothing and equation (5) for constant ρv^2.

The preheating has been estimated by Ahlborn, Key and Bell (7.15) and a criterion for tolerable preheating (less than shock preheating) has been defined which can be approximately expressed as a shell thickness R given by,

$$\rho\Delta R \simeq 9(\rho l)_h \qquad (30)$$

where the hot electron preheating range $(\rho l)_h$ is given by,

$$(\rho l)_h = 2 \times 10^{-5}\ (I_{13}\lambda_\mu^2)^{0.9}\ \ g\ cm^{-2} \qquad (31)$$

Using equations (5) and (7) with equation (15) for the pressure and equations (30) and (31) above for the preheating it follows that

$$I_{13} \simeq 3\,\lambda_\mu^{-3.8} \tag{32}$$

$$\Delta R\,\mu \simeq 2.5\,\lambda_\mu^{-1.6} \tag{33}$$

$$R\,\mu \simeq 860\,\lambda_\mu^{1.2} \tag{34}$$

$$R/\Delta R \simeq 340\,\lambda_\mu \tag{35}$$

$$E_{KJ} \simeq 14\,\lambda_\mu^{-0.2} \tag{36}$$

$$\tau_i/1\text{ns} \simeq 5.2\,\lambda_\mu^{1.2} \tag{37}$$

It is interesting to note that the energy is almost constant so that this set of constraints is similar to that obtained in section 7.2.3 (b) where the energy was specified as constant. The new consideration is that the absolute magnitude of the energy is defined. The absolute magnitude of E scales as the cube of the ratio of $(\rho\ell)_h$ to $\rho\Delta R$ assumed in equation (30) which fixes the size of the target, since other constraints fix the aspect ratio. This high sensitivity means that the absolute value of E depends critically on the exact criterion adopted for the preheating and suggests that a better formulation of the problem than was used to obtain equation (30) should be adopted. It is clear however that preheating tends to require a relatively large scale experiment for low adiabat compressions, though not by any means as large as is required for laser fusion.

M H Key (RAL)

7.2.4 Thermal and Thermomagnetic Instabilities

It is generally accepted that megagauss magnetic fields may considerably affect thermal conduction and hydrodynamic processes in a laser-produced plasma. Such fields have been experimentally observed (7.20-7.22) and are sometimes associated with the formation of filamentary structures along the plasma flow (7.23-7.24).

Many mechanisms exist, such as thermal (7.25) and thermomagnetic (7.26-7.29) instabilities, to account for the occurence of the above effects. These instabilities have so far been investigated only under very special conditions (for a homogeneous plasma or with no hot electron effects). Here we report on the results obtained for a more complete model, consisting of counter-streaming currents of collisional cold and collisionless hot electrons in an inhomogeneous plasma background (with fixed ions). Conditions of charge neutrality and zero net current (in the steady state) are imposed, and it is assumed that the cold fluid may be described by classical transport theory (using Braginskii's coefficients) (7.31).

An algebraic dispersion relation was derived for perturbations in a direction perpendicular to the zero order heat flow. From it we were able to identify two distinct instability regimes, depending upon the magnitude of χ_m/χ_t ($\sim 0.05\,c^2/\omega_p^2\,\lambda_{mfp}^2$), χ_m and χ_t being the magnetic and thermal diffusivities respectively, ω_p the electron plasma frequency, and λ_{mfp} the electron mean-free-path.

For $\lambda_m/\lambda_t \gg 1$ (eg 0.3 keV, solid densities and $Z \sim 10$) the Ohmically driven 'thermal instability' due to M G Haines (7.25) becomes the most important destabilizing mechanism. Its growth rate and optimum wavelength are approximately given by $2\upsilon(m_e/m_i)$ and $10(m_i/m_e)^{\frac{1}{2}}\lambda_{mfp}$ respectively, provided the instability criterion $T_e/T_i > (3/2)$ is satisfied. Here, υ is the electron-ion collision rate, m_e/m_i the electron-ion mass ratio, and T_e/T_i the electron-ion temperature ratio. Also under the same conditions, the 'radiation cooling instability' recently proposed by R G Evans (7.30) has the effect of enhancing the above growth rate and decreasing the optimum wavelength, whenever

$\mu < (3/2)$ (where μ is the temperature exponent of the radiation cooling rate). This was earlier shown by Haines (7.25) for the special case of Bremsstrahlung.

If on the other hand $\chi_m/\chi_t \ll 1$, as would be the case for medium Z plasmas at around critical densities and kilovolt temperatures, another class of instabilities becomes important. These we put under the general heading of 'thermomagnetic instabilities' since they arise basically as a result of the Righi-Leduc heat flux (ie the $\underline{B} \times \nabla T_e$ component of the heat flux). Their growth rates are of the order of $(T_e/m_e)^{\frac{1}{2}} \lambda_{mfp} |\nabla T_e/T_e|$ with optimum wavelengths slightly less than the temperature scale length $|T_e/\nabla T_e|$. Usually, however, instability only occurs for plasmas in which $\nabla n_e \cdot \nabla T_e > 0$. Inclusion of ion motion relaxes this condition somewhat.

Still for the case of $\chi_m/\chi_t \gg 1$ we discovered another type of instability which arises from the fact that the cold electron return current is streaming in an inhomogeneous plasma background. This time the linearized $\underline{B} \times \underline{j}_e$ component of the thermoelectric heat flux will act in the opposite sense to the Righi-Leduc heat flux whenever $\nabla n_e \cdot \nabla T_e < 0$, and cause destabilization if $|\nabla T_e/T_e| < |\nabla n_e/n_e|$. Such a configuration is possible between the critical and ablation surfaces of a laser driven target. The optimum growth rate for this instability is given by $\gamma \sim (T_e/m_e)^{\frac{1}{2}} (n_h/n_e)^{\frac{1}{3}} |\nabla n_e/n_e|$ (where n_h is the hot electron number density).

Both 'thermal instability' (with radiation cooling effects), as well as the above thermoelectric instability may give rise to filamentary structures in high Z materials, such as those recently reported by O Willi (7.32). Further investigation is under way for the possible interactions of such instabilities with the Rayleigh-Taylor mode.

M G Haines and E M Epperlein (Imperial College)

7.2.5 Morphology of Magnetic Fields in Long Pulse Experiments

Recent experiments (7.33 - 7.35) have established the structure of magnetic fields generated by irradiating plane aluminium targets with

1.06 μm light together with the modifications produced in the plasma density profile by these fields. Experiments were carried out in two distinct regimes - short pulse (100 ps) high irradiance (10^{16} W cm^{-2}) and long pulse ($\sim$ 1 ns) with irradiances in the range 10^{13} - 10^{14} W cm^{-2}.

The model we have used to describe the evolution of the magnetic field is a simplified version of that given by Braginskii (7.31). In view of the fact that the time scales over which the magnetic field evolves (ie 100 ps - 1 ns, depending on the regime) are shorter than characteristic convection and diffusion times we have neglected the hydromagnetic terms in the Braginskii equation. We retain the thermoelectric source ($\nabla N \times \nabla T$) term together with the Hall term and that describing the thermal force. In view of the structure of the field observed in the experiments which showed clearly that the peak field occurred well away from the critical density surface we have also chosen to neglect the radiation pressure source term on the grounds that the contribution from this will not be dominant at densities below about 0.5 N_c, where N_c is the critical density. Using this reduced equation to describe the evolution of the field combined with the continuity and momentum equations we have obtained results for the structure of both the magnetic field and the electron density in short pulse and long pulse experiments.

Figure 7.07 shows magnetic field profiles plotted as functions of the axial distance Z from the target surface in short pulse experiments (7.37). The continuous curve is the measured profile. The other curves are drawn using data form the numerical experiments at the position of maximum field and correspond to two different gaussian temperature profiles. The temperature profile has to be modelled, unlike the density profile which is measured independently; the dashed curve corresponds to a half-width of 15 μm and the dotted curve to one of 20 μm. The agreement as far as the magnitude and spatial position of the peak magnetic field and the overall structure of the profiles is seen to be satisfactory.

Results from the long pulse simulations are shown in Figure 7.08 and 7.09. Figure 7.08 plots the self-generated magnetic field as a function of R and Z. In the high density (low Z) region fields of about 1 MG are generated which compare with measured values of about 1.5 MG. At lower densities,

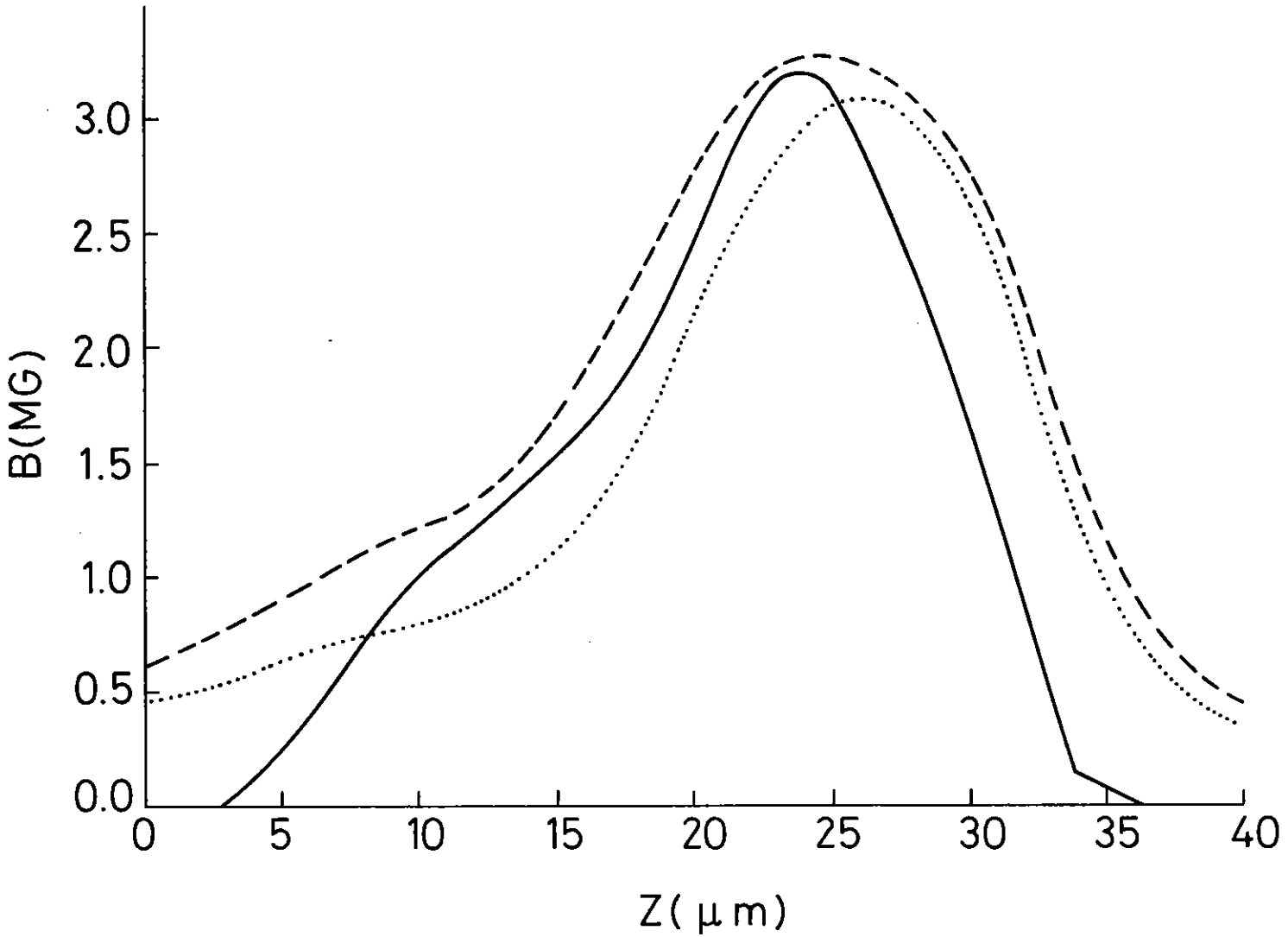

Figure 7.07 Magnetic field profiles plotted as functions of the axial distance Z from the target surface in short pulse experiments. The continuous curve is the measured profile. The other curves are drawn using data from numerical experiments at the position of maximum field and correspond to two different gaussian temperature profiles.

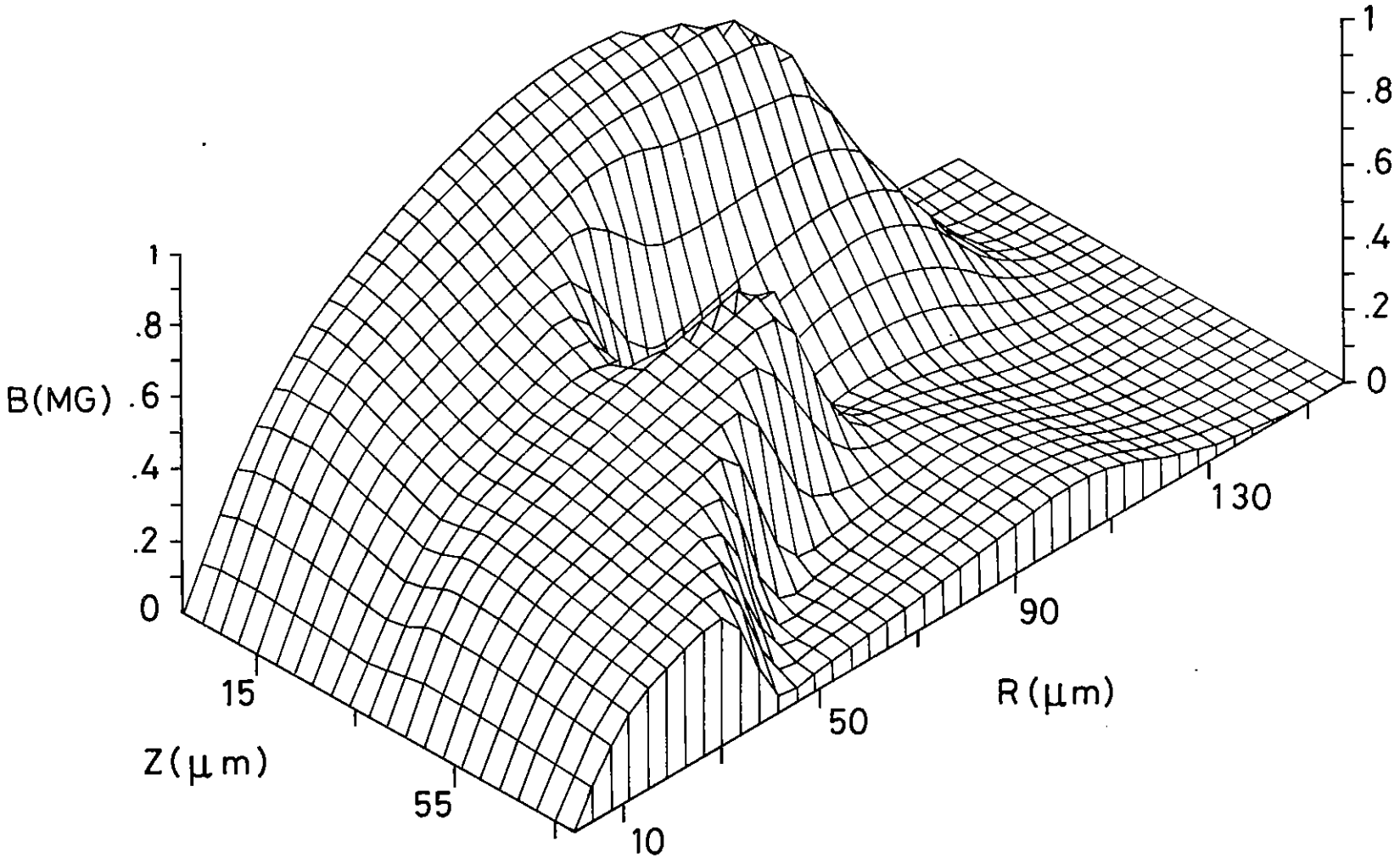

Figure 7.08 Self-generated magnetic field as a function of R and Z for a long pulse simulation.

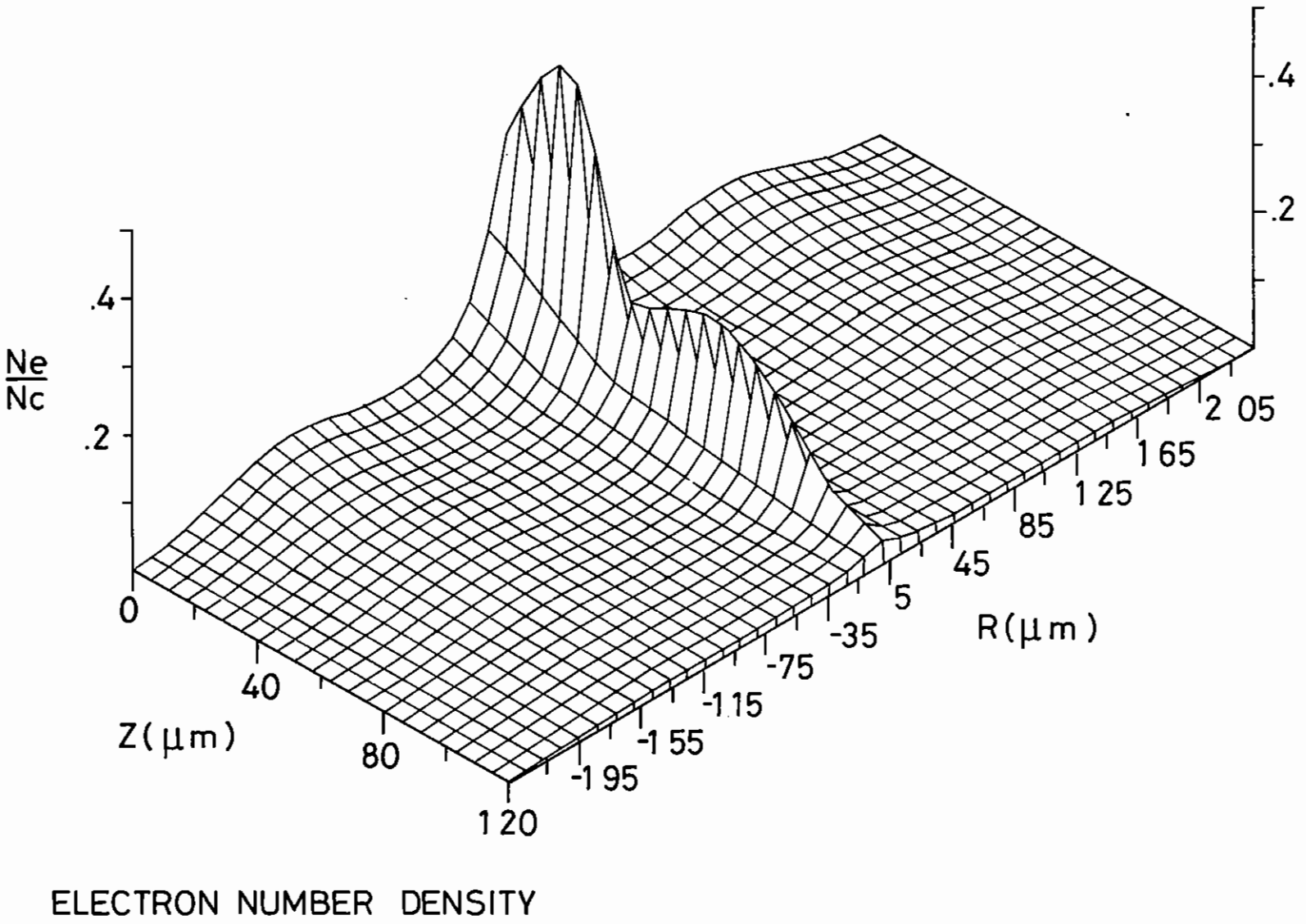

Figure 7.09 Density as a function of R and Z for a long pulse simulation.

in the region Z ∿ 35 μm, the field shows a minimum as a function of Z for values of R just outside the focal spot radius (R ∿ 50 μm), a feature which is reproduced in the measured field profiles (7.35).

Figure 7.09 plots the density profile from the numerical experiment showing the highly localized enhancement along the laser axis (R = 0), together with a bimodal structure in the axial direction with peaks around Z = 20 μm and Z = 60 μm. A similar structure appears in the measured density profiles for planar targets (7.35).

T J M Boyd and D Cooke (Bangor)

7.3 Laser Plasma Interactions

7.3.1 Raman and Two Plasmon Decay Instabilities in Magnetized Plasmas

The presence of strong magnetic fields generated by the irradiation of plane targets with laser light suggests that there may be observable effects in parametric processes occurring in the coronal plasma. The effects of a constant and uniform magnetic field $\underline{B}_c$ on stimulated Raman scattering and two-plasmon decay have been studied in the region of the quarter critical density where both processes occur.

A general fully electromagnetic dispersion relation has been derived from the fluid equations, valid for any plasma density, pump power and magnetic field, $\underline{B}_c$, and has been applied to examine the decay of a pump extraordinary wave into an upper hybrid wave and either a scattered extraordinary wave (stimulated Raman scattering) or another upper hybrid mode (two-plasmon decay). We have been interested first and foremost in the region near to quarter-critical where both SRS and TPD occur. This is a complex region, rich in physical effects, the details of which are only represented accurately by the electromagnetic dispersion relation.

We have solved the full electromagnetic dispersion relation numerically and find that in general the maximum growth rates of both the SRS and TPD instabilities are increased by the magnetic field. Typical results are plotted in Figure 7.10 and 7.11 showing growth rates versus k_x of the upper hybrid wave with frequencies normalized to ω_o^{-1}, wave vectors to

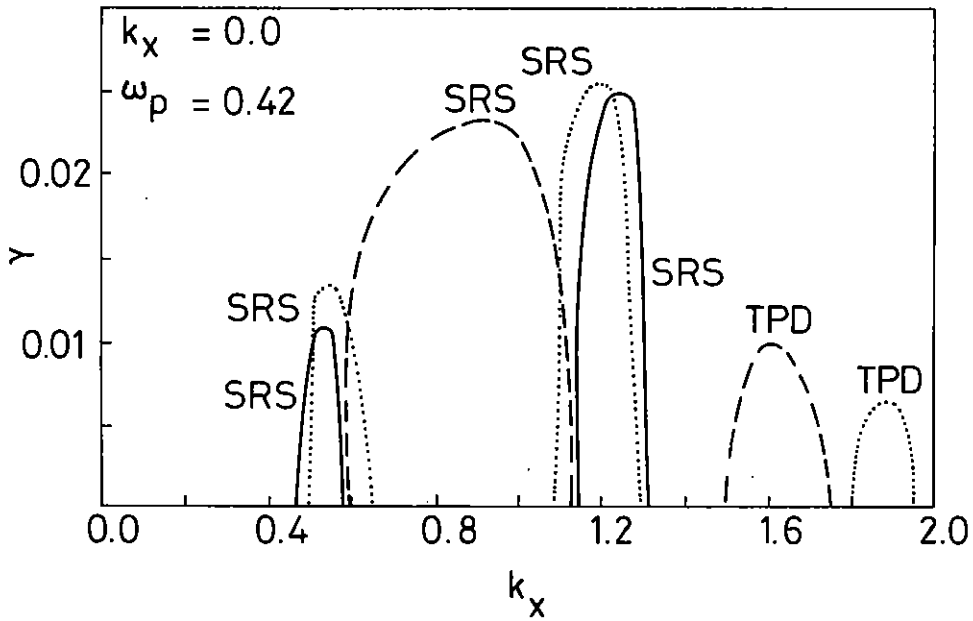

Figure 7.10 Growth rates vs. k_x for stimulated Raman scattering (SRS) and two-plasmon decay (TPD).

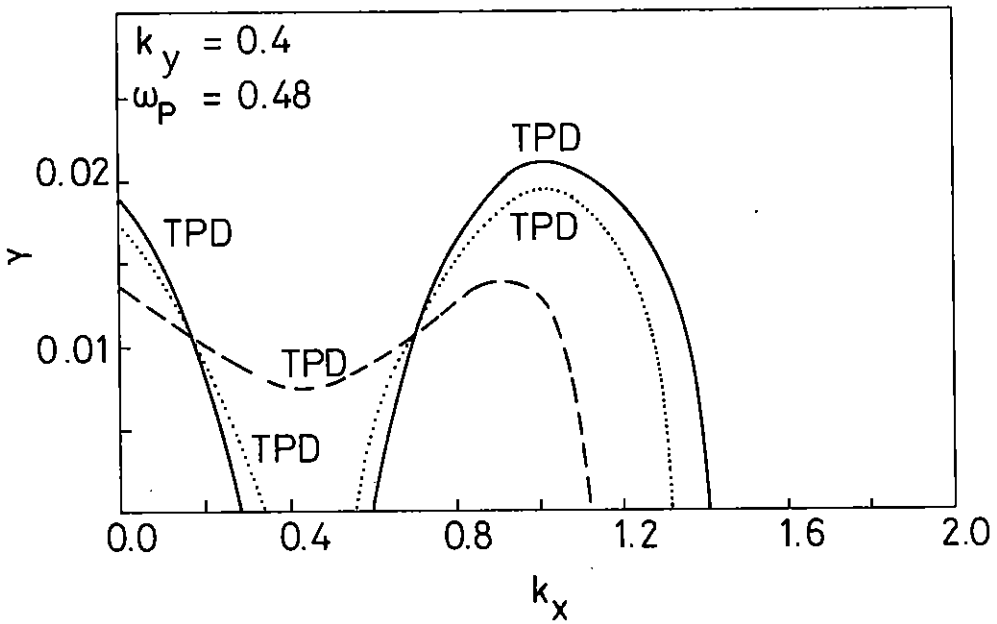

Figure 7.11 Growth rates vs. k_x for two-plasmon decay (TPD).

ω_o/c and speeds to V_e/c where V_e is the electron thermal speed. In the figures solid lines represent $\Omega_c = 0$, dotted lines $\Omega_c = 0.1$ and broken lines $\Omega_c = 0.2$ (Ω_c is the cyclotron frequency). In all cases $V_e = 0.1$ and $v_o = 0.1$.

Consider first stimulated Raman scattering. In an unmagnetized plasma the growth rate near $n_c/4$ is $\gamma = \omega_p v_o k k_{x-}/2k_-$, where $k = |\underline{k}_- - \underline{k}_o|$. For $k_y = 0$ the reflection point (at which forward ($k_{x-} < 0$) and backscattered ($k_{x-} > 0$) waves are indistinguishable) occurs at $\omega_p^2 = (1/4) - (9/8)\, V_e$. At lower densities forward and backscattered waves separate (Figure 7.10). For sidescatter ($k_y \neq 0$), as k_y increases the maximum density at which Raman occurs decreases correspondingly and we find Raman scattering limited to $k_y < 1/\sqrt{2}$.

The presence of a magnetic field induces changes in the frequency and growth rates of the instability. The frequency shifts can be deduced from phase matching conditions, and for the Raman process the shift (induced at the reflection point of the extraordinary wave, with $k_y = 0$) due to the magnetic field is given by $\omega_1 = \frac{1}{2} + (9/8)V_e^2 - \Omega_c/4$ (see Section 7.3.2). The frequency shift is particularly relevant when one considers that it happens at the reflection point where absolute instability occurs. The location of the reflection point is pushed to lower densities by the magnetic field as can be seen in Figure 7.10.

Consider now the two-plasmon instability. In an unmagnetized plasma the growth rate is given by $\gamma = \omega_p V_o k_o k_y K/2kk_-$, and occurs at a maximum density $\omega_p^2 \sim (1/4) - 6V_e^2(k_y^2 + k_o^2/4)$ when $K^2 = k_y^2 + k_o^2/4$ as shown in Figure 7.11.

At lower densities phase matching occurs at higher k_x and results in reduced growth. Note that while Raman scattering grows faster for small k_y, two-plasmon decay quickly dominates for $k_y \gtrsim 0.4$. Note too that two-plasmon decay can occur in one dimension in a magnetized plasma, driven by the electrostatic component of the extraordinary wave. The frequency shift induced by the magnetic field is given by $\omega_1 = \frac{1}{2} + k_o K[3V_e^2 + \omega_p^2 \Omega_c^2/k_1^2 k_2^2]$. The magnetic field, therefore, serves to increase the shift of both products from $\frac{1}{2}$, symmetry being

preserved (see Section 7.3.2).

Finally, we have compared the results of our fluid calculations (Figures 7.10 and 7.11) with those obtained from a kinetic treatment of the problem. In so doing, we restrict ourselves to backscatter and use an electrostatic approximation on the upper hybrid wave. This restriction invalidates our results close to the $n_c/4$ region where the phase velocity of the upper hybrid wave is large. The frequency shifts discussed above (and in Section 7.3.2) arise out of electromagnetic corrections to the dispersion relation for the upper hybrid wave and are obviously not present in our kinetic calculation.

In the kinetic theory there exists a competition between the magnetic effects and the plasma temperature. The presence of the magnetic field can serve to increase the Raman growth rates while the plasma temperature acts to reduce them. If the plasma is relatively hot there results a net reduction in the growth rates as is evident in Figure 7.12.

T J M Boyd, H C Barr, L R T Gardner and R Rankin (Bangor)

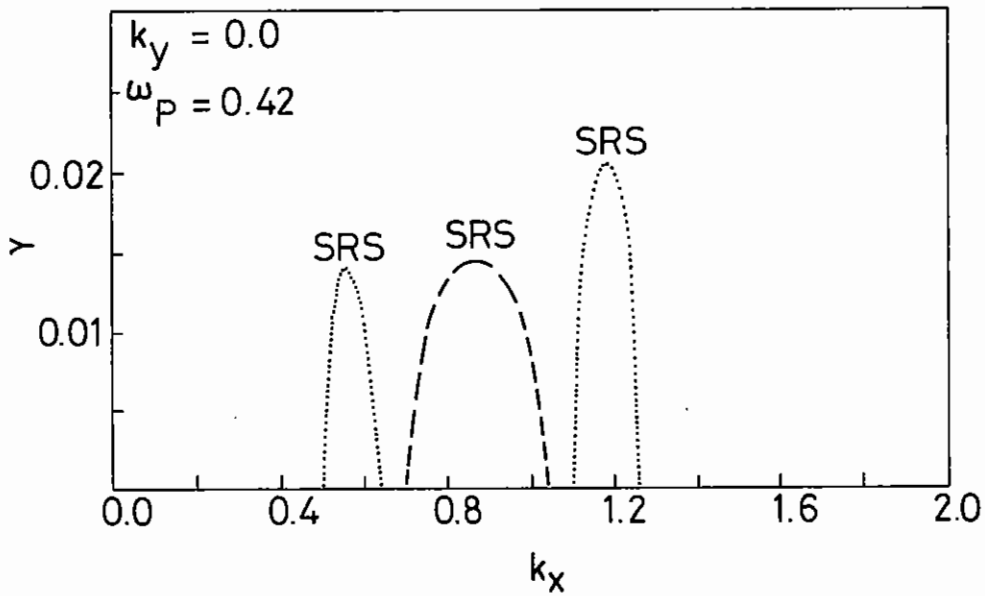

Figure 7.12 Growth rates vs. k_x for stimulated Raman scattering (SRS).

7.3.2 Raman Shifts Induced by Magnetic Fields

Recent experiments have established the presence of very large, if highly localized, magnetic fields in plasmas created by the irradiation of solid targets by high intensity lasers. In particular, strong magnetic fields in the megagauss range have been seen from large plane targets (7.33). The experimental results show that the thermoelectrically generated field at the edge of the focal spot rises from zero at the refractive cut-off to about 600 kG at the critical density and increases steadily to just over 3 MG at 0.2 N_c before dropping steeply to zero around 0.1 N_c. The main conclusion from this work is that the strongest fields are to be found in the low-density coronal plasma.

The existence of fields of this magnitude in the neighbourhood of the quarter-critical density suggests that there may be observable effects due

to their presence in laser-plasma interactions in that region. Parametric processes in laser-produced plasmas in which strong magnetic fields are present have not been widely studied. Since these fields are generated in the main by the so-called $\nabla N \times \nabla T$ source and the principal density gradient is aligned along the laser direction, one should properly consider the geometry in which the incident radiation propagates across the magnetic field.

In two recent papers Grebogi and Liu (7.39-7.40) have considered stimulated Raman scattering and the parametric decay of an extraordinary electromagnetic wave into two upper hybrid plasmons. However neither is adequate to deal with the effects of a self-generated magnetic field in a laser produced plasma. In the work on stimulated Raman scattering for example it is assumed that the frequency of the upper hybrid wave is very much less than that of the pump or the scattered extraordinary mode. This has the consequence that their treatment is only valid in the underdense plasma away from the quarter-critical density. The upper hybrid wave is treated electrostatically ie the phase velocity is very much less than the velocity of light.

Elsewhere (see Section 7.3.1) we have examined in detail the effect of a magnetic field on the two plasmon decay and Raman instabilities. The aim here is to indicate that self generated magnetic fields can induce observable frequency shifts in both instabilities, which can exceed the expected thermal shifts.

Assume that the self generated magnetic field is $\underline{B} = B\hat{\underline{z}}$ and that the laser radiation is an extraordinary wave with frequency ω_o, wave number $\underline{k}_o = k_o\hat{\underline{x}}$, electric field $\underline{E}_o \perp \underline{B}$ and magnetic field $\underline{B}_o \parallel \underline{B}$. Consider the decay of this pump wave into an upper hybrid wave (ω_1, $\underline{k}_1$) and either a second upper hybrid wave (corresponding to the two plasmon decay) or an extraordinary wave (corresponding to stimulated Raman scattering) (ω_2, $\underline{k}_2$) such that $\omega_o = \omega_1 + \omega_2$, $\underline{k}_o = \underline{k}_1 + \underline{k}_2$. Our attention is primarily confined to scattering/decay in the plane perpendicular to $\underline{B}$. Assume for convenience that all frequencies are normalized to ω_o, all velocities to the speed of light c and all wave numbers to ω_o/c. The dispersion relation of extraordinary waves (+ sign) and upper hybrid waves (- sign) is

$$\omega^2 = \omega_p^2 + \tfrac{1}{2}(k^2 + 3k^2V_e^2 + \Omega^2) \pm \left[\tfrac{1}{4}(k^2 - 3k^2 V_e^2 - \Omega^2) + \omega_p^2\,\Omega^2\right] \qquad (1)$$

where $\omega_p^2 = 4\pi n_o e^2/m$, $\Omega = eB/mc$.

When $\Omega \ll \omega_p$ and $k^2 \gg \Omega\,\omega_p$, the dispersion relation for extraordinary waves is

$$\omega^2 = \omega_p^2 + k^2 + \Omega^2\left(\frac{\omega_p^2}{k^2}\right) . \qquad (2)$$

Near quarter critical density the laser radiation is accurately described by (2). Then the upper hybrid dispersion relation is

$$\omega^2 = \omega_p^2 + 3k^2 V_e^2 + \Omega^2\left(1 - \frac{\omega_p^2}{k^2}\right) \qquad (3)$$

This is purely electrostatic only when $\omega_p \ll k$ ie in the very underdense plasma. Near quarter critical density, the phase velocity of the decay wave approaches the speed of light and this electromagnetic correction must be included. When $k^2 \ll 2\,\Omega\,\omega_p$, then $\omega^2 \simeq \omega_p^2 \pm \omega_p\Omega$ or

$$\omega \simeq \omega_p \pm \frac{\Omega}{2} . \qquad (4)$$

Consider the Raman backscatter ($\underline{k}_1 \parallel \underline{k}_2 \parallel \underline{k}_o$) at the reflection point of the scattered wave ($\underline{k}_2 = 0$) where we can expect absolute instability. Then, from (4), $\omega_2 = \omega_p + \frac{\Omega}{2}$ while the upper hybrid wave satisfies (3), whence, to lowest order

$$\omega_2 \simeq \tfrac{1}{2} - \frac{9V_e^2}{8} + \frac{\Omega}{4} \qquad (5)$$

assuming $k^2 \simeq 3/4$ near quarter critical density. Thus the expected thermal red shift $9V_e^2/8$ can be reversed by the magnetic field. For example, in a plasma with temperature $V_e = 0.05$ we would need a field of 1.1 megagauss for a Neodymium laser or 0.11 megagauss for a CO_2 laser to nullify the thermal red shift.

Figure 7.13 plots the frequency shift in (5) versus Ω/ω_o. Also plotted are results from a simulation using the particle code EMPIRE, though these may not be compared directly with the theoretically predicted shifts in that the simulation uses an inhomogeneous plasma and, for low values of

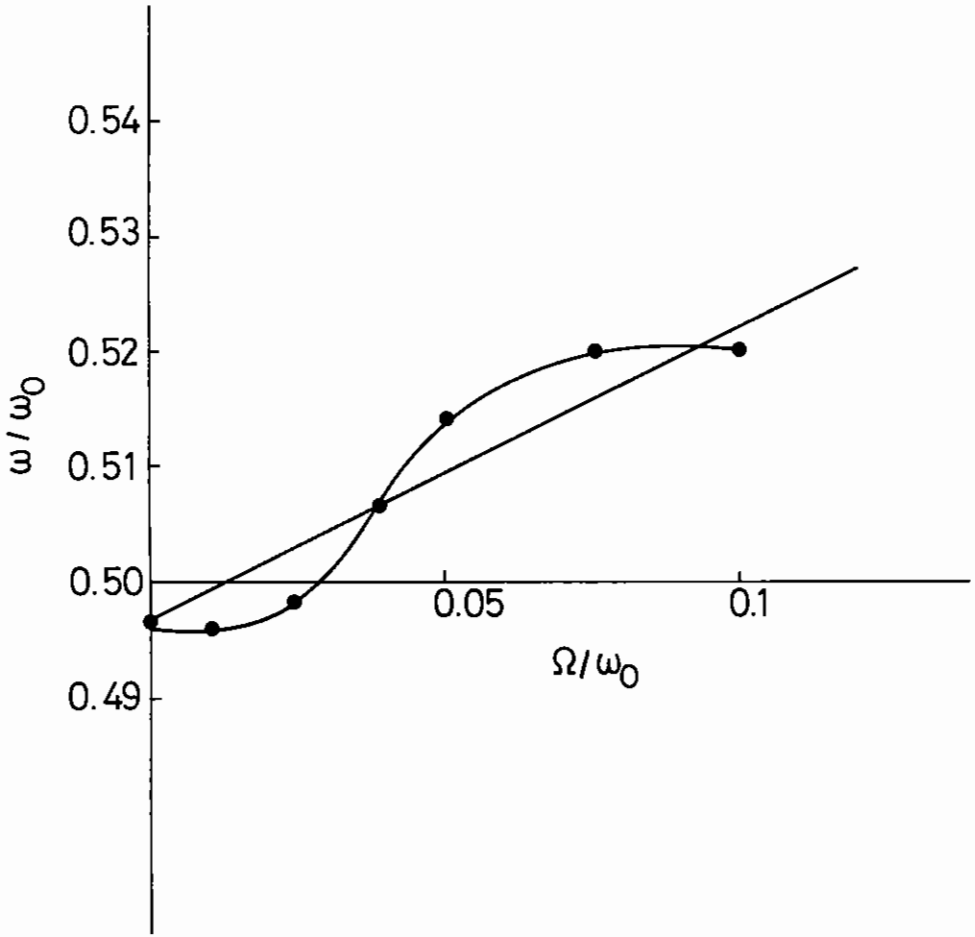

Figure 7.13 The effect of magnetic field strength on the frequency of backscattered radiation (solid line, theoretical predictions; • results from simulations).

Ω/ω_o, shows significant electron heating together with some level of magnetic field generation.

Frequency shifts have been measured in a variety of laser-target experiments. Further work on the relative contributions of thermal shifts to those due to self-generated magnetic fields is continuing.

In the absence of a magnetic field we expect to see predominantly s-polarized emission arising from absolute instability at the reflection point of the scattered wave (on account of the coupling coefficient being proportional to $\underline{E}_o \cdot \underline{E}_2$). Thus, for p-polarized emission from the reflection point of the scattered wave $\underline{E}_o \cdot \underline{E}_2 = 0$ whence we have no growth. However, the electrostatic component of the laser (extraordinary) wave induced by the magnetic field can now drive such p-polarized emission. It may be possible to observe such emission shifted to the red by at most $\Delta\omega = \frac{\Omega}{4} - \frac{9V_e^2}{8}$. For s-polarized emission we have absolute instability, in the absence of a magnetic field, when $\underline{k}_2 \,||\, \underline{B}_o$, $\underline{E}_2 \,||\, \underline{E}_o$ and $\underline{B}_2 \,||\, \underline{k}_o$. Add to this a DC magnetic field $\underline{B} \,||\, \underline{B}_o$ and the scattered wave is propagating along the DC magnetic field. It becomes therefore either a left or right circularly polarized electromagnetic wave whose dispersion relation is

$$k_2^2 - \omega_2^2 + \omega_p^2 = \pm \frac{\Omega\, \omega^2}{\omega_2 \pm \Omega p} \quad . \tag{6}$$

If $\omega_2 >> \Omega$

$$\omega_2^2 \simeq \omega_p^2 + k_2^2 \pm \frac{\Omega\, \omega^2}{(\omega_p^2\, k_2^2)^{\frac{1}{2}}}$$

$$\simeq \omega_p^2 \pm \Omega\omega_p + k_2^2 \quad (k_2^2 << \omega_p)$$

or $$\omega_2 \gtrsim \omega_p \pm \frac{\Omega}{2} + \frac{k_2^2}{2\omega_p} \tag{7}$$

The dispersion relation for upper hybrid waves with a small component of wave number along B (ie $\underline{k}_1 = k_1(\sin\theta, 0, \cos\theta), \theta \simeq \pi/2$) is

$$\omega_1^2 = \omega_p^2 + 3k_1^2 V_e^2 + \Omega^2 \left(1 - \frac{\omega_p^2}{k_2^2}\right) \sin^2\theta \tag{8}$$

Phase matching yields, to lowest order,

$$\omega_2 \simeq \tfrac{1}{2} \pm \frac{\Omega}{4} + \frac{k_2^2}{2} - \frac{9V_e^2}{8} \qquad (9)$$

in contrast to the p-polarized case ($\underline{k}_2 \| \underline{B}$) where one root (− sign) represented an upper hybrid wave which could not, of course, be directly observed. We now have the possibility of decay into both a right circularly polarized and a left circularly polarized electromagnetic wave both of which should be observable. The magnetic field shifts of each are opposite to one another whence a doublet structure in the emission would be expected in the emission with a peak separation $\Omega/2$ providing a useful diagnostic for the local magnetic field near quarter critical density. In fact, in experiments at the Rutherford Laboratory where $\omega_o/2$ emission was observed in long pulse experiments using 1 μm, 0.5 μm, 0.3 μm radiation just such a structure has been observed. The splitting of 100 Å in the 1 μm experiments would imply a field of about one megagauss. Although we have yet to evaluate the growth rates for this polarization, since the Raman emission is predominantly s-polarized, we would not expect the imposition of weak magnetic fields ($\Omega << \omega_p$) to radically alter this picture although there will be some differential between the two wings of the doublet.

Finally looking at the two plasmon decay instability, if we assume that both decay products are accurately described by (3), phase matching yields

$$\omega_1 = \tfrac{1}{2} + k_o K\left(3V_e^2 + \frac{\omega_p^2 \Omega^2}{k_1^2 k_2^2}\right) \qquad (10)$$

where $K = k_{x1} - \frac{k_o}{2}$. The magnetic field thus increases in magnitude the shift from 1/2 of both decay products. This shift can exceed the thermal shift for large enough magnetic fields or cool enough plasmas.

H C Barr, T J M Boyd and G A Gardner (Bangor)

7.3.3 Effect of Magnetic Field on Backscattering Instabilities

We have investigated nonlinear scattering of laser radiation in the presence of a self-generated magnetic field, in particular the decay of the incident wave into a backscattered wave and ion or electron Bernstein modes. The dispersion relation is derived, following the procedure of

Tripathi, Grebogi and Liu (7.41), for scattering in a plane perpendicular to the magnetic field, which is assumed to be at right angles to the incident radiation. The scattered radiation, which is at a frequency well above the cyclotron frequency is taken to be described by the cold-plasma dispersion relation, while the Vlasov equation is used to describe the plasma modes.

The incident wave, with frequency and wavenumber (ω_o, $\underline{k}_o$), is taken to decay to a Bernstein mode (ω, k) and a scattered electromagnetic wave ($\omega_1 = \omega_o - \omega$, $\underline{k}_1 = \underline{k}_o - \underline{k}$). The equation for the electrostatic Bernstein mode is given by Poisson's equation

$$\varepsilon_{e,i} \nabla^2\phi = 4\pi e (n_e^{NL} - n_i^{NL}) \qquad (1)$$

where $\varepsilon_{e,i}$ is the linear dispersion function for the electron or ion Bernstein modes, as appropriate. The driving term on the right hand side contains the nonlinear electron and ion density perturbations generated by the interaction of the pump and backscattered modes. For the electron modes the ion density perturbation can be neglected, while both species must, of course, be taken into account when dealing with the ion modes.

The equation for the scattered wave is, from Maxwell's equations

$$\nabla^2 \underline{E}_1 - \nabla(\nabla.\underline{E}_1) + \frac{\omega^2}{c^2} \underline{\underline{\varepsilon}}.\underline{E} = -\frac{4\pi i\omega_1}{c^2} \underline{J}_1^{NL}, \qquad (2)$$

where $\underline{J}_1^{NL}$ is the nonlinear low frequency current density arising from the beating of the pump and backscattered waves and $\underline{\underline{\varepsilon}}$ is the dielectric tensor. If a constant pump amplitude is assumed, then (1) and (2) give the usual type of coupled equations describing the growth of a parametric instability.

It is, of course, necessary to find the nonlinear charge and current densities on the right-hand sides of (1) and (2) in terms of the wave amplitudes. This has been done, with a kinetic theory approach using the Vlasov equation and following, in outline the procedure of reference (7.41). The detailed calculations and resulting expressions are rather cumbersome

and will not be repeated here, details being available in references (7.42) and (7.43). The result is that (1) and (2) are brought to the form

$$\varepsilon_{e,i}\ \phi = B E_{l\perp} \qquad (3)$$

$$\underline{\underline{D}}_l \cdot \underline{E}_l = \underline{\alpha}\ \phi \qquad (4)$$

with B and α proportional to the pump wave amplitude. The electromagnetic wave propagation is assumed to be adequately described by cold plasma theory, so that $\underline{\underline{D}}_l$ is the usual cold plasma dispersion tensor. Eliminating ϕ and $\underline{E}_l$ from (3) and (4) gives the dispersion relation which determines the growth rate of the parametric decay to electron or ion Bernstein modes. This work extends the fluid theory of Grebogi and Liu (7.39) to the kinetic regime which is appropriate to some laser-plasma interaction processes.

To illustrate the theory we have calculated growth rates for decay to the first few electron and ion Bernstein modes for a plasma temperature of 4 keV, a magnetic field of 2 MG and a plasma density of 1/25 critical density. The growth rate does not vary much for the first few modes and is (in sec^{-1}) around $2 \times 10^{14} v_o/v_e$ for the electron modes and $2 \times 10^{12}\ v_o/v_e$ for the ion modes, v_o being the amplitude of the oscillation electron velocity in the incident wave which is taken to be at the frequency of a Nd laser.

S Ram and R A Cairns (St Andrews)

7.3.4 The Use of the Finite Element Method in Electrostatic Particle Codes

In this new application the finite element method is used within a two dimensional electrostatic particle code to study problems concerned with wave-wave and wave-particle interactions in plasma physics.

In particle codes the problem domain is divided into cells and charged particles, selected with velocities obtained from a prescribed Maxwellian

distribution, are shared amongst them in such a way as to produce a plasma with a prescribed number density and frequency. A random or uniform spatial distribution of particles often results in a noisy plasma which may be at levels high enough to prevent the study of particular phenomena. Quiet start techniques have been used to reduce the noise to acceptable levels. The electrostatic fields arising from the charged particle distribution are derivable from a potential function which is governed by Poisson's equation. In most cases it is desired to simulate an infinite plasma so we have initially incorporated doubly periodic boundary conditions into the code.

When the finite element method is used the cells mentioned above are identified with finite elements. Nodal variables are the values of the potential function, ϕ and Poisson's equation is replaced by its functional analogue. For any particular element the functional χ^e to be minimised for the nodal values of the potential ϕ^e is

$$\chi^e = \tfrac{1}{2}\, \underset{\sim}{\phi}^{e^T} k^e\, \underset{\sim}{\phi}^e + \underset{\sim}{\phi}^{e^T} \underset{\sim}{F}_e$$

where k^e has its usual form for Poisson's equation in terms of the element shape functions $\underset{\sim}{N}$ and $\underset{\sim}{F}_e$ is determined from the distribution of charged particles over the element. After assembling contributions from all elements and minimising the resulting functional with respect to all the nodal values we obtain a set of linear equations which are solved for the nodal values of the potential. The electric fields are then obtained by differentiation eg

$$E_x = -\frac{\partial \underset{\sim}{N}}{\partial x}\, \underset{\sim}{\phi}^e \quad , \quad E_y = -\frac{\partial \underset{\sim}{N}}{\partial y}\, \underset{\sim}{\phi}^e \ .$$

The equations of motion for each of the charged particles are now integrated and their new velocities and coordinates computed. The finite difference scheme used is time centred, second order accurate and time reversible.

When the code is run, at each time step the assembled (force) vector $\underline{F}$ is determined from the particle distribution, the functional equation is solved for the potential from which the electric fields are obtained and the particles are then pushed. This procedure is repeated several thousand times so that through observation of the motion of the particles and the evolution of the state variables the processes excited within the plasma may be studied.

An initial version of the code has been written and has been used as a test bed for various element configurations. Code parameters, eg collision and heating times, are being determined and compared with corresponding results for conventional finite difference codes.

T J M Boyd, G A Gardner and L R T Gardner (Bangor)

7.3.5 Simulations of Optical Filamentation

7.3.5(a) Steady State Simulation

Interest in the phenomenon of filamentation or self-focusing of laser light in plasmas has been renewed recently with the observation (7.44) of filamentary or jet-like structures in laser irradiated plasmas at irradiances of $\sim 10^{13}$ W cm^{-2}.

Self-focusing arises because plasma is expelled from regions of high laser intensity either by the ponderomotive force of the electromagnetic wave or by local heating followed by flow towards the state of uniform pressure. The depression of plasma density along the lines of highest laser intensity produces a converging lens and further enhances the laser intensity.
This process is offset by spreading of the beam due to diffraction and thermal conduction smoothing of the hot spots.

Analytic approximations to these processes (7.45) have been used to obtain thresholds and growth rates for both ponderomotive and thermal self-focusing. The analytic models assume a Gaussian cross-section of the

beam throughout the self-focusing process and clearly this is most unlikely in practice. Numerical calculations of self-focusing have been performed and show in specific cases the appearance of phenomena similar to "spherical aberration" in the self-focusing process and the consequent appearance of a ring-like structure in the self-focused beam.

We have extended the numerical calcualtions to a variety of initial conditions including the mutual interactions of two filaments and also computed the self-focusing in a non-uniform plasma. The aberrations in the self-focusing process give rise to a bifurcation of single filaments and to a merging of multiple filaments.

The Wave Equation

The equation for electromagnetic waves propagating in a medium of dielectric constant ϵ is

$$\nabla^2 \underline{E} - \underline{\nabla}\ (\underline{\nabla}.\underline{E}) = \frac{1}{c^2}\ \frac{\epsilon\ \partial^2 \underline{E}}{\partial\ t^2} \qquad (1)$$

The term $(\underline{\nabla}.\underline{E})$ may be neglected if the material contains no inhomogeneity in the direction of $\underline{E}$. Strictly speaking this means that we should consider normal incidence of laser light on plasma slabs and consider filaments to form as sheets infinitely extended in the direction of $\underline{E}$. This will be true for the calcalations in plane geometry, but we will also assume that $\underline{\nabla}(\underline{\nabla}.\underline{E})$ is small in our calculations of cylindrically symmetric filaments. Thus for laser light of frequency ω

$$\nabla^2 \underline{E} + \frac{\omega^2}{c^2}\ \epsilon\ \underline{E} = 0 \qquad (2)$$

A solution of equation (2) for a cylindrically symmetric beam propagating in the Z - direction is

$$\underline{E} = \underline{A}\ (r,z)\ \exp\ (i(\omega t + \frac{\omega}{c} \int_0^Z n_o dZ)) \qquad (3)$$

$$n_o = \epsilon o^{1/2}(Z)$$

where n_o and ε_o are the refractive index and the dielectric constant of the unperturbed plasma respectively and $\underline{A}$ is a slowly varying amplitude. Substituting equation (3) in equation (2) and neglecting the term d^2A/dZ^2 , which implies that the characteristic distance in the Z - direction of the intensity variation is much larger than the wavelength , we obtain the usual paraxial wave equation:

$$2i\omega\, \varepsilon o^{1/4} \frac{d}{dZ} (\varepsilon_o^{1/4} A) + \frac{1}{r}\frac{dA}{dr} + \frac{d^2A}{dr^2} + \frac{\omega^2}{c^2} (\varepsilon - \varepsilon o)\, \underline{A} = 0 \qquad (4)$$

where ε_o is the dielectric constant of the plasma with the non-linearity. In order to solve this equation numerically we discretise the problem on a mesh 25 cells in the r direction and 50 cells in the z direction and use a second order accurate Crank Nicholson differencing scheme. Absorption is taken into account by writing the refractive index of the plasma in the complex form

$$n_o = k_1 + ik_2$$

which gives

$$\underline{E} = \underline{A} \exp\left(\frac{-\omega}{c}\int k_2 dz\right) \exp\left(i(\omega t + \frac{\omega}{c}\int k_1 dz)\right) \qquad (5)$$

However, for simplicity, we do not change the plasma temperature, except as implied by the non-linear index.

The dielectric constant of the plasma in the presence of a high intensity laser beam may be written

$$\varepsilon = \varepsilon_o + \varepsilon_2 - i\varepsilon_i$$

where ε_2 is the non-linear part of the dielectric constant, and is given by

$$\varepsilon_2 = \frac{\omega_p^2}{\omega^2} \left[1 - \exp(-(\alpha\, EE^*))\right]$$

where α EE* is of the order of the ratio of the field pressure to the

plasma thermal pressure ie

$$\alpha EE^* \sim \frac{I/2c}{2n_e KT_e}$$

where n_e, T_e are electron density and temperature respectively and I is the beam intensity. We choose T_e = 500 eV throughout.

Solving the wave equation in plane geometry is useful to understand the behaviour of multiple perturbations in the laser beam which the axial singularity prevents us studying realistically in cylindrical geometry. We will describe the qualitative features of the simulation results and their dependence on the width and the strength of the perturbation, and the plasma density, and show how the numerical solutions of the wave equation lead to very complex behaviour of the filaments.

In Figure 7.14(a) a Gaussian beam with width of 8.3 μm (FWHM) and a peak intensity of 2.7 x 10^{14} W/cm^2 superimposed on a uniform background intensity of 3 x 10^{13} W/cm^2, is incident on a uniform plasma of density 0.2 n_c and length of 500 μm. As the beam propagates through the plasma, it suffers self-focusing and reaches a minimum width of 2.2 μm at z_f = 250 μm, where the peak intensity on the axis reaches 8.5 x 10^{14} W/cm^2. Beyond z = 250 μm the beam starts to defocus. In Figure 7.14(b) the peak intensity of the initial perturbation is 4.5 x 10^{14} W/cm^2, and the width is the same as in Figure 7.14(a). The self-focusing length has decreased to Z_f = 98 μm. (In analytical approximations $Z_f \propto (P/P_{cr}-1)^{-1/2}$ where P is the beam power and P_{cr} is the critical power.) The minimum width of the distribution was 2.2 μm (as in Figure 7.14(a)) and the peak intensity reached 1.5 x 10^{15} W/cm^2.

However, in this case, when the filament begins to defocus the distribution splits into two and starts to form two filaments, with widths of 3.2 μm (FWHM) at z = 370 μm and peak intensities of 4.6 x 10^{14} W/cm^2. We then repeated the computation of the case of Figure 7.14(b) but artificially switched off the non-linear terms beyond the first focusing region, at z = 98 μm. The result is shown in Figure 7.14(c), where the split again occurred but since there is no non-linearity beyond z = 98 μm,

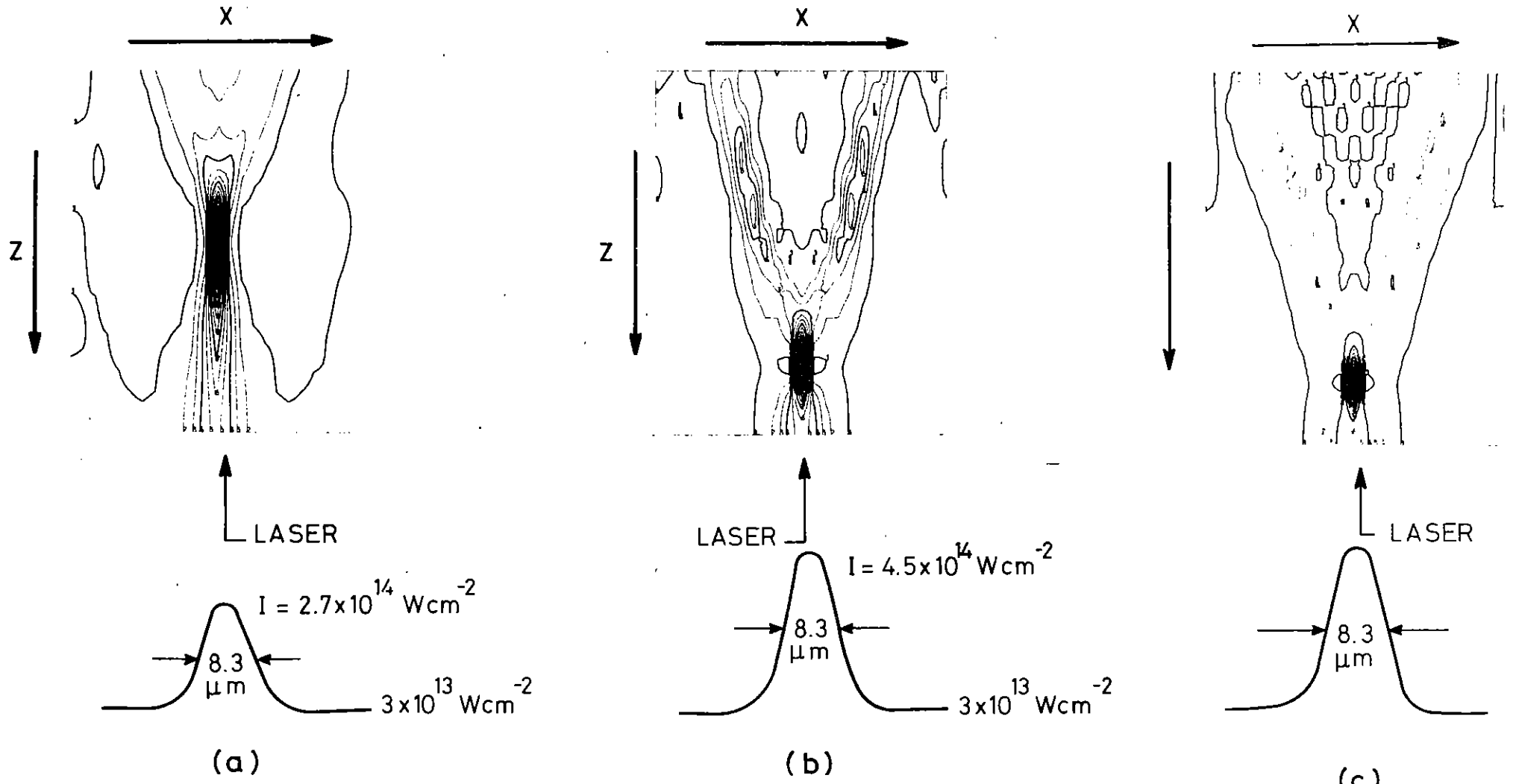

Figure 7.14 Propagation of Gaussian beams superimposed on a uniform background intensity of 3×10^{13} W cm^{-2}. In (c) the non-linear terms are artificially switched off beyond the first focusing region.

the branches do not themselves suffer self-focusing. The split is therefore due to the aberration effects produced during the first self focusing. In the present simulations the effective lens produced by the non-linearity in the region before the first focus is very far from ideal. Marburger and Dawes (7.46) argue that such effects can be produced by a non-linear index which saturates at high intensity. Akhmanov et al (7.47) studied analytically the self-focusing of light in a non-linear medium, and also found that strong aberrations occur. We therefore conclude that the complex phenomena which follow the formation of a filament are due in the first instance to the linear propagation of wave front aberrations generated earlier. From Figures 7.14(a) and 7.14(b) we can conclude that there is a threshold value of the intensity at the focusing region for the beam to split, but the exact value will depend on the size and form of the initial beam modulation.

In Figure 7.15, we show the result of taking two Gaussian perturbations on a uniform background. The ratio between the peaks and the background is $\sim$ 15 and the plasma density is 0.2 n_c. The width of each peak is 3.3 μm (FWHM), and the distance between them was varied. At first each beam diverges which implies that the width of the distribution is less than the critical value 2Xmin required for the self-focusing to exceed the spreading of the beam by diffraction (7.45). As the beam width becomes larger than 2Xmin they start to focus.

During the diverging stage, the two distributions begin to overlap, and this influences the development of the filaments. As the distance between the two peaks is decreased the two distributions begin to interact during the defocusing state. For distances of 12 μm and less between the peaks, the two distributions merge together and form one filament as we see in Figure 7.15. When the plasma density is increased the self-focusing length decreases and the simulation shows further stages of interaction between filaments. Figure 7.16 is a typical example of a cascade of self-focused filaments generated by a double humped beam incident on a plasma of 0.3 n_c. The introduction of a density gradient along the direction of propagation does not produce any significant qualitative changes.

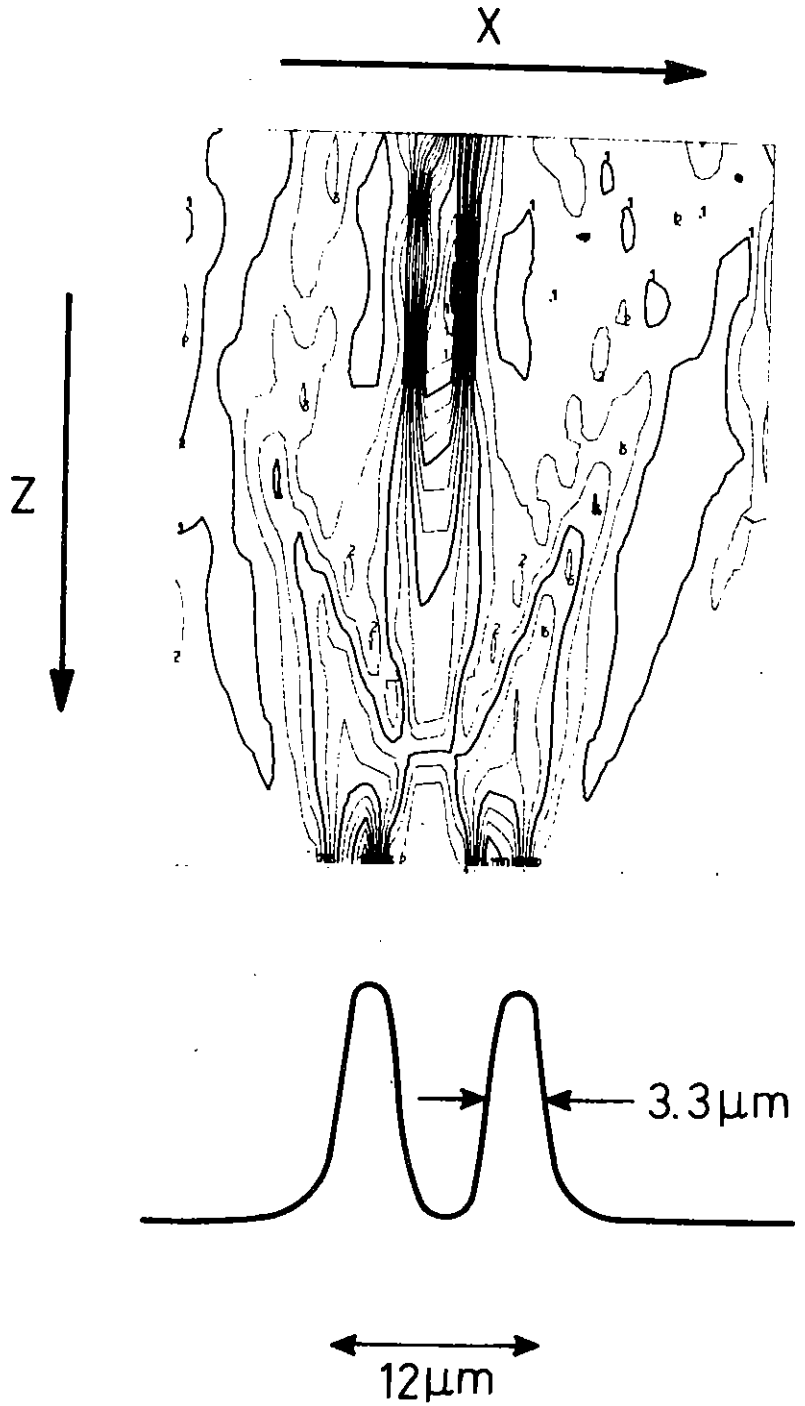

Figure 7.15 Propagation of a double Gaussian intensity variation.

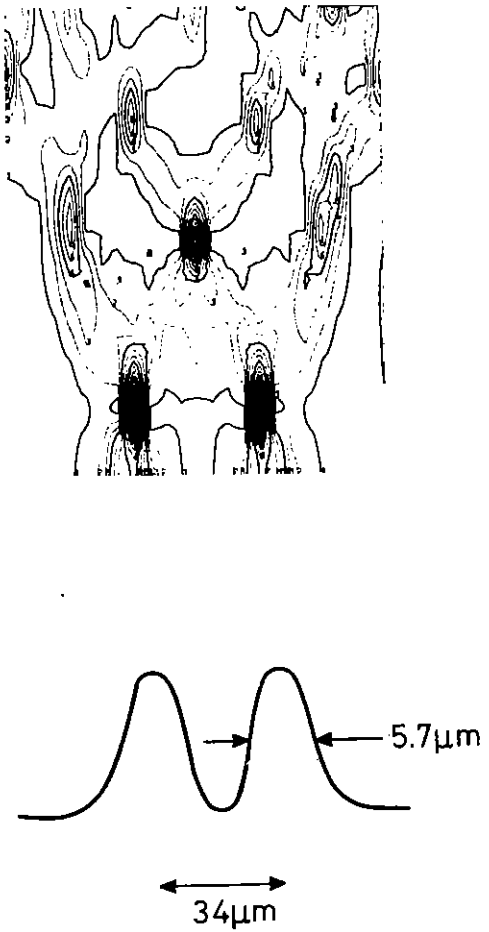

Figure 7.16 Cascade of filaments resulting from a double-humped intensity variation.

Results similar to the plane geometry cases were obtained when the analysis was repeated for cylindrical geometry. Figure 7.17 shows the self-focusing of a cylindrical beam in a 0.2 n_c plasma, together with a plot of the intensity along the axis.

In analytical approximations, the beam should retain its gaussian shape throughout and after self-focusing should return to its original intensity. It is quite clear that this does not happen in the simulation. Nevertheless, there is agreement to within 10% between the simulation and the analytical model of Sodha et al (7.44) for the distance to the first focus of a filament.

7.3.5(b) Hydrodynamic Simulation

To test whether the similar effects can be observed in a hydrodynamic plasma, a 2-D Eulerian hydrodynamic code in cylindrical geometry originally written by G J Pert (7.13) was modified to include the ponderomotive force.

The paraxial wave equation was solved numerically for each time step and the ponderomotive force in the R and Z direction was calculated at each cell and included in the equation of motion. The hydrodynamic simulation then includes both ponderomotive and thermal force pressures. Our ability to investigate some of the complex structures observed in the model was restricted by the long computation time required for each run, some two hours on the CRAY 1 machine.

In the simulation, a Gaussian beam with a diameter of 24 μm at half maximum intensity, simulating a hot spot, was assumed to propagate through a plasma of 100 μm length, 30 μm in diameter. The initial plasma density was changed in steps from 0.01 n_c up to a solid density in 100 μm. The laser beam was incident normal to the plasma surface and absorption was assumed to occur only via inverse Bremsstrahlung of the incident wave, up to the critical density. The laser pulse was simulated by a step-like function with a rise time of 150 ps and a plateau intensity of 4×10^{14} W/cm^2. In order to allow the plasma to form a natural density

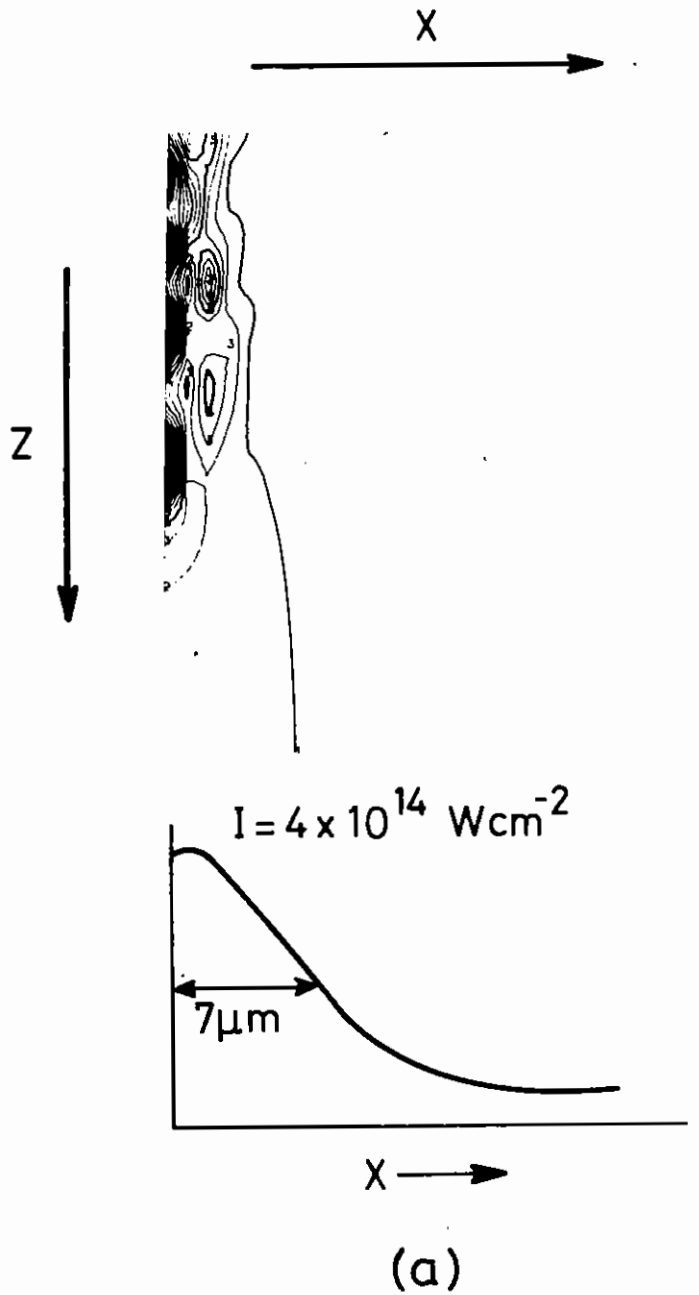

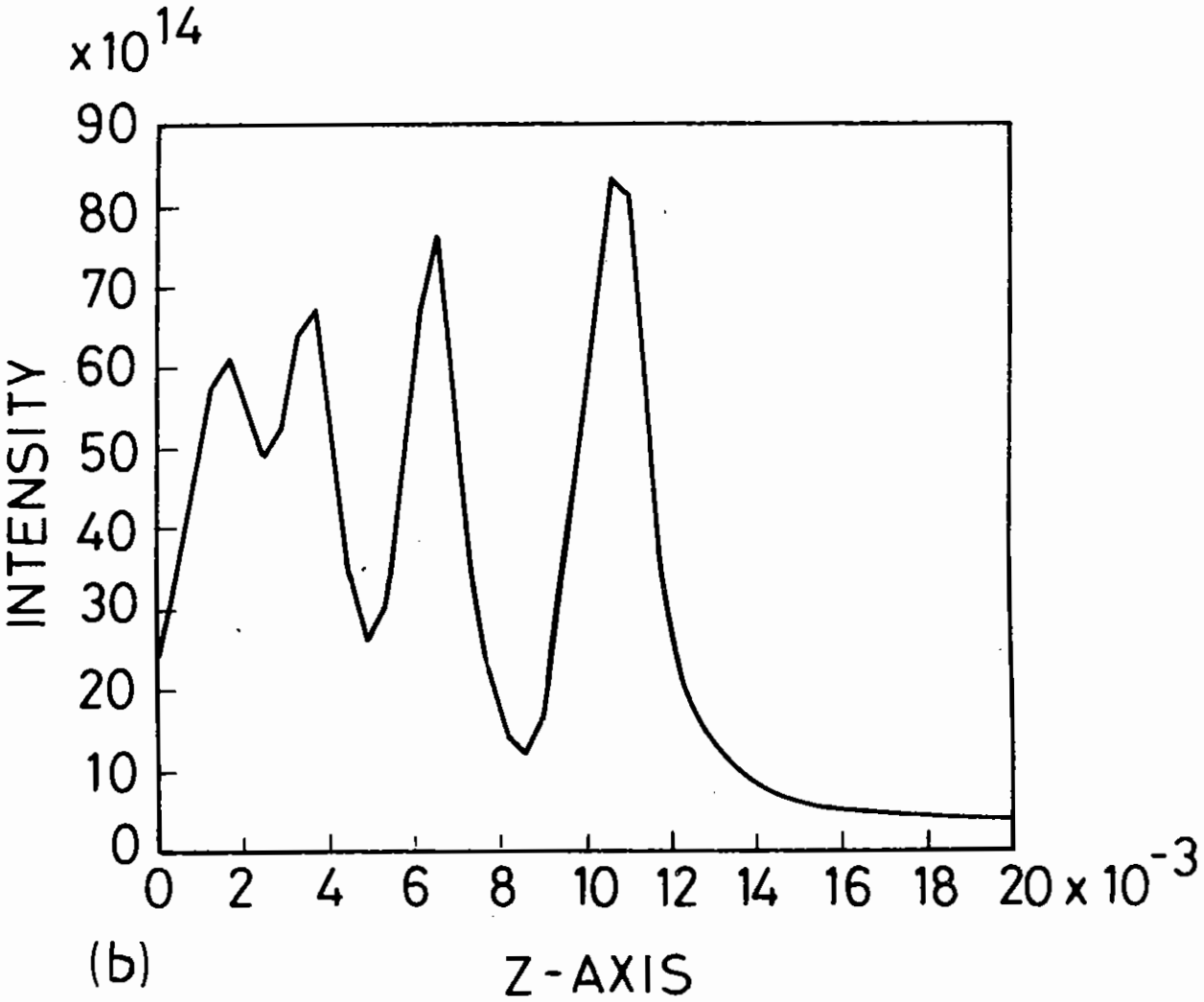

Figure 7.17 Self-focusing of a cylindrical beam. (b) is a plot of intensity along the axis.

gradient, no ponderomotive force effect was included during the first 50 ps of the laser pulse.

It was found that in the time interval between t = 60 ps and t = 120 ps the plasma density gradient changed from 12 μm to 22 μm, and prior to t = 120 ps no observable effects of the ponderomotive force were detected. However, at a time $t \geq 120$ ps after the beginning of the laser pulse, a density cavity on the axis of symmetry and other, complex, plasma structures started to form.

Plasma Features at t = 140 ps

At this time the initial beam intensity on the axis of symmetry was 3.9×10^{14} W/cm^2. Figure 7.18 shows the plasma density distribution in the R and Z - directions. A density cavity can be seen on the axis of symmetry. The beam intensity within the cavity increases along the direction of propagation due to self-focusing; the ponderomotive force also increases and plasma is expelled in the R - direction. In association with the cavity formation on the axis of symmetry, density ripples are formed in the R - direction. Some of these density ripples break the beam up into a number of ring beams whose intensity increases along the direction of propagation as a result of self-focusing, and they merge together. Hence, more plasma will be expelled in the R - direction. Ring beams close to the axis of symmetry converge on the axis in a short Z - interval. Figure 7.19 shows the density, the temperature and the intensity distributions along the Z - axis at R = 0. The second peak is the result of a ring beam converging on the axis of symmetry. The large density peak seen in Figure 7.19 may be the result of plasma subjected to large ponderomotive force from all directions. The intensity distribution in the R - direction, for all values of Z, is a mirror image of the density distribution.

Plasma Features at t = 160 ps

At this time the initial beam intensity on the axis of symmetry is 4×10^{14} W/cm^2. A density cavity on the axis of symmetry already exists.

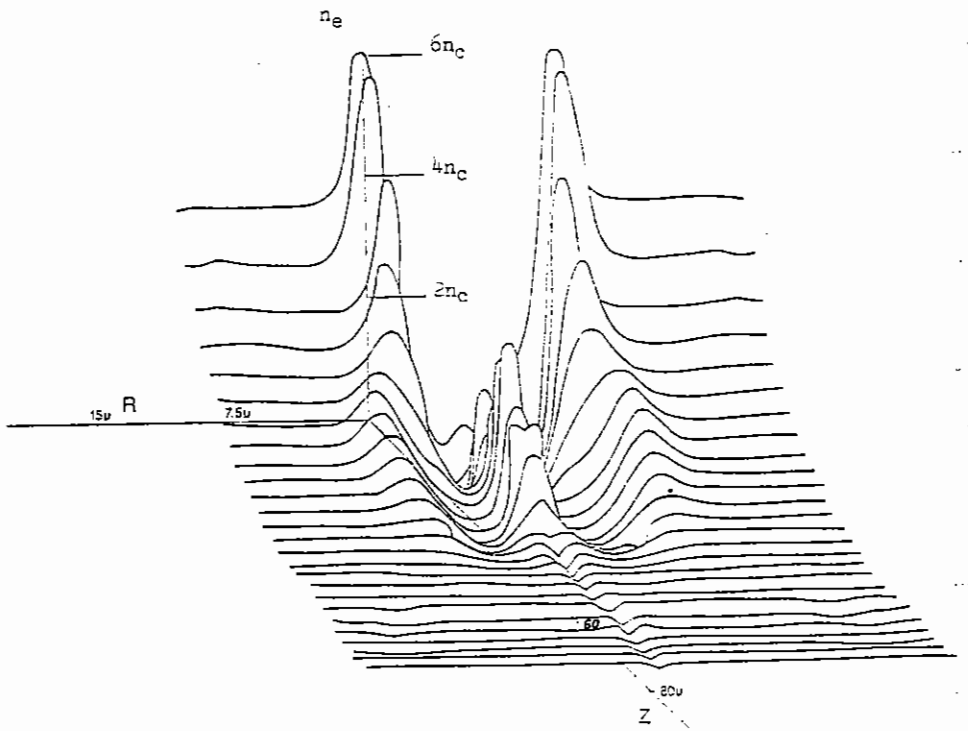

Figure 7.18 Plasma density distributions in R and Z directions at time t = 140 psec.

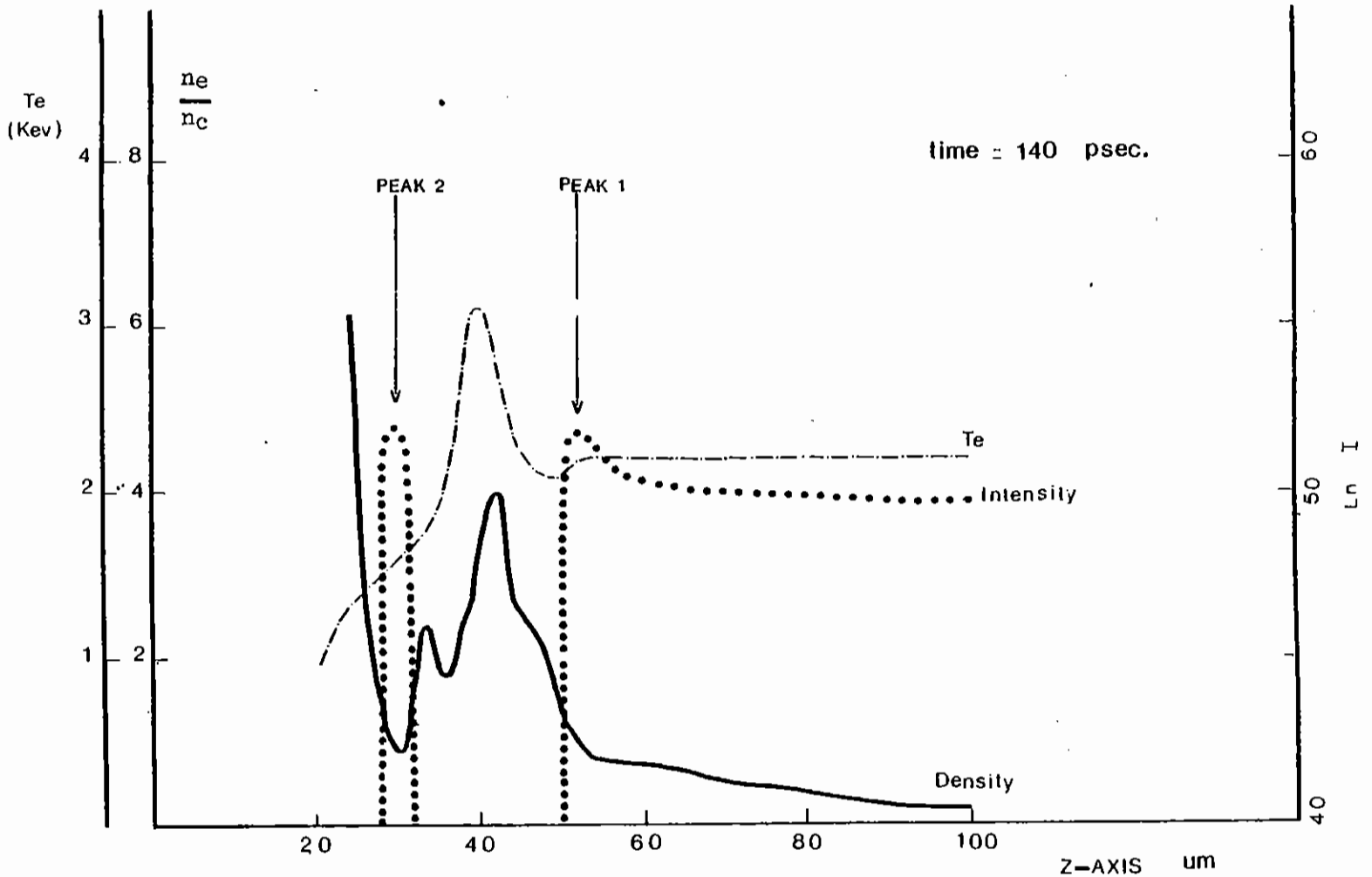

Figure 7.19 Density, temperature and intensity distributions along the Z axis at R=0 and time t=140 psec.

This enhances the focusing of the central part of the beam and more plasma is expelled radially. Within the cavity the central part of the beam has a bouncing focusing region. Figure 7.20 shows the density along the Z - axis at R = 0. The Z - component of the ponderomotive force slows down the expansion of the plasma near the density peak, and the R - component of the force causes the outwardly expanding low density plasma to move away from the axis, so that it does not fill the central cavity. The density ripples in the R - direction formed earlier in time will break up the beam again and form rings of high intensity and low density. Figure 7.21 shows the density distribution in the R and Z - directions.

The region from the boundary at Z = 100 μm to Z $\sim$ 42 μm contains the central cavity and a high intensity ring beam. The intensity within the cavity and in the ring beam increases as we move into the plasma, as a result of which the plasma density between the cavity and the ring beam increases and plasma flows in the Z - direction. The presence of this high density annulus slows down the convergence of the ring beam on to the axis of symmetry.

The central cavity ceases to exist just beyond the focus of the axial part of the beam. The ring beam propagates beyond the cavity region and moves towards the axis of symmetry almost surrounding the density peak. At the bottom end of the ring beam, the locally absorbed energy together with the ponderomotive force in the R and Z - directions may cause the plasma to flow into the density peak. This flow together with the high ponderomotive force around the density peak may be producing an adiabatic compression, hence increasing both the temperature and the density within the peak. If the pulse is switched off after this time or the initial beam intensity is decreased, then the thermal pressure within the peak could form a jet like structure flowing out in the Z - direction.

Since the complex, small scale length, structures in the simulation might be expected to produce a thermoelectric magnetic field, growth rates were calculated at t = 120, 140 and 160 ps for each cell and estimates of the nett field were made. Growth rates as high as 2 MGauss/ps were obtained. However, except in the vicinity of the density spike, the thermal pressure

was much in excess of the magnetic. We may therefore suppose the simulation to be realistic except near the spike.

In the hydro code the first focus occurs after a path of 35 μm in the underdense plasma (Figure 7.20) to be compared with analytical results for uniform plasmas varying smoothly from 250 μm for the conditions corresponding to the plasma boundary to around 20 μm for the conditions just beyond the focus.

It was not possible to make an exact comparison of the hydro code with the steady state simulations of 7.3.5(a). However we note that the basic assumption governing the behaviour of the non-linear index in the steady state model - that the actual plasma density is a mirror image of the intensity - is well borne out by the hydro model. This is shown clearly in Figure 7.22 where the variation of density and intensity across the beam is shown.

S Sartang (Westfield), W T Toner and R G Evans (RAL)

7.3.6 Wavelength Dependence of Light Filamentation

In laser plasmas, many mechanisms have been proposed to account for self-focusing, (7.44,7.48 and 7.49) the essential nature of which depends on the change of refractive index of the plasma with electron concentration, decreasing from unity to zero at the critical density. Two effects appear to dominate the plasma motion under the influence of an intense electro-magnetic wave and give rise to local density perturbations: the ponderomotive force (7.50,7.51) proportional to $\nabla\langle E^2\rangle$, where $\langle E\rangle$ is the time-average electric field and local heating (7.52) through non-uniform energy deposition followed by a net flow of plasma towards a state of uniform pressure.

In the present model the filament is described in terms of a EM wave whose initial distribution is Gaussian in both space and time. The time-dependent wave equation is adopted in the paraxial approximation.

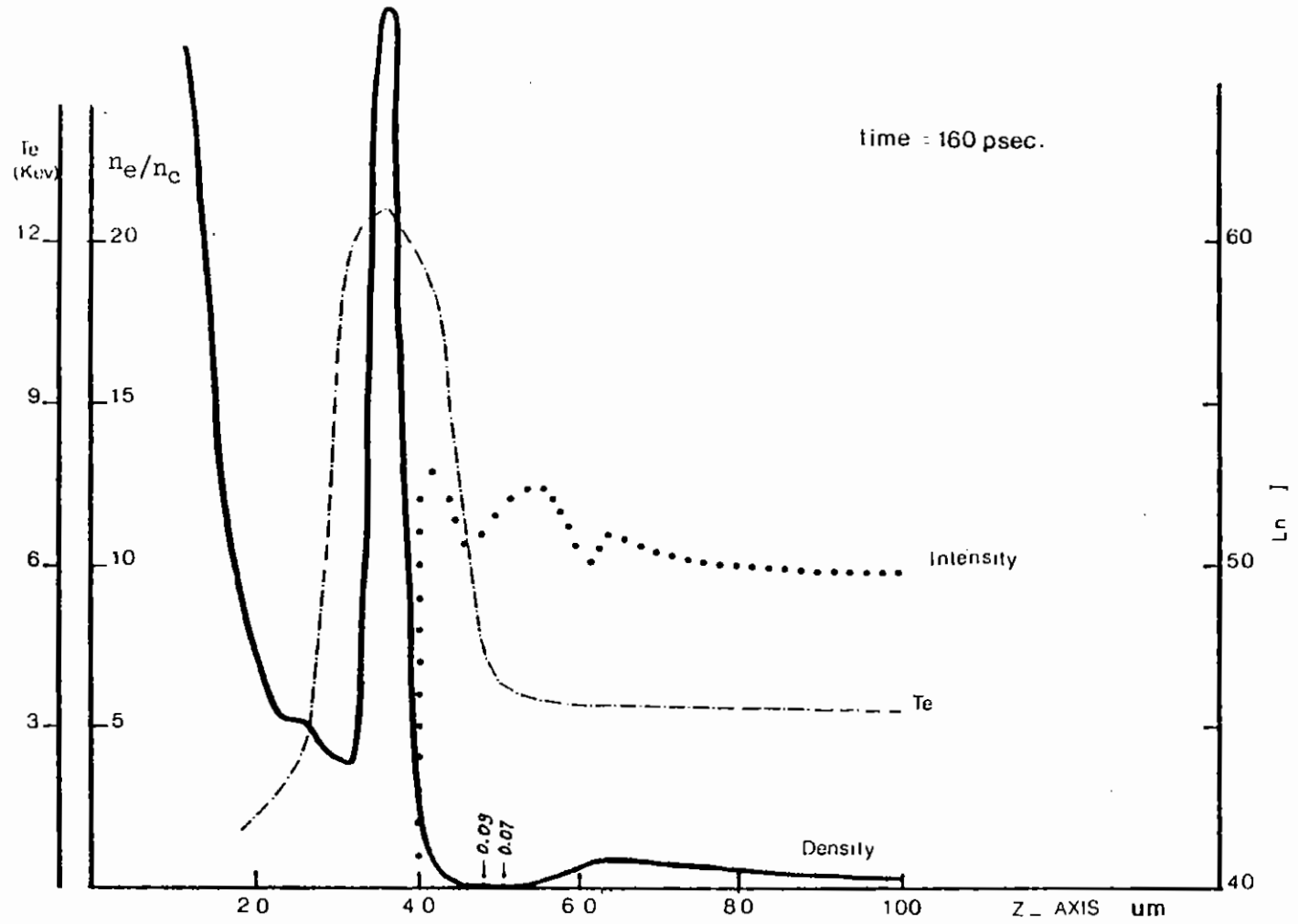

Figure 7.20 Density, temperature and intensity distributions along the Z axis at R=0 and time t=160 psec.

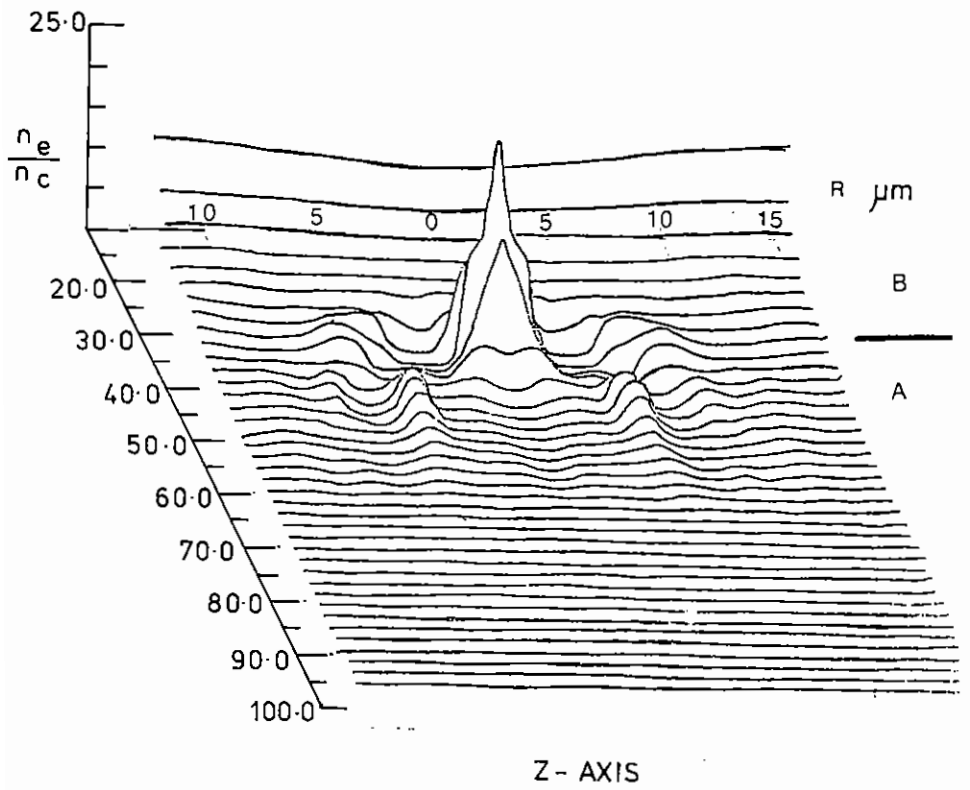

Figure 7.21 Plasma density distributions in Z and R directions at time t = 160 psec.

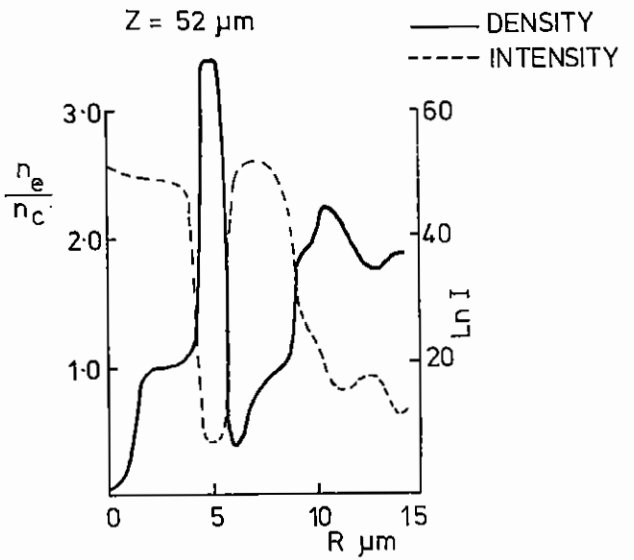

Figure 7.22 The intensity and density distributions in the R direction at time t = 160 psec.

A two-fluid model is assumed for the plasma which is considered to be composed of ions, charge + Ze, mass M and of electrons, charge - e and mass m. The neutral plasma density condition is $N_e = ZN_I$ where N_e and N_i are the average electron and ion densities. Defining the rate of momentum change for the plasma (7.55) as

$$\rho \frac{du}{dt} = N_e m \frac{d\bar{V}e}{dt} + N_i M \frac{d\bar{V}i}{dt}$$

where $\bar{V}_e$ and $\bar{V}_i$ are the electron and ion speeds, the momentum equation takes the form

$$\rho \frac{du}{dt} \simeq \tfrac{1}{4} (\varepsilon' - \varepsilon_0) \nabla \langle E^2 \rangle - \nabla P_p \qquad (1)$$

when P_p is the total pressure for both electrons and ions. The energy conservation equations for the electrons and ions are

$$\rho C_{v\alpha} \frac{\partial T\alpha}{\partial t} + \nabla \xi_\alpha \, u + \rho \nabla .u + \nabla q = E(r,t) \pm K_\alpha , \alpha = e,i \qquad (2)$$

where K is the rate of energy exchange between electrons and ions, q is the thermal energy flux, $q = - fK\nabla T$, K the classical Spitzer electron thermal conductivity and f an adjustable constant, normally set between 0.03 and 0.1(7.56). ξ is the internal specific energy and $C_v = \frac{1}{\rho} \frac{\partial \xi}{\partial t}$ the specific heat. The rate of heating due to the laser beam, represented by $\dot{E}(r,t)$ is due to inverse-bremsstrahlung absorption so that the dispersion relation takes the form,

$$\varepsilon' = 1 - \left(\frac{\omega_p^2}{\omega_o^2 + \nu^2} \right) - \frac{i\nu}{\omega_o} \left(\frac{\omega_p^2}{\omega_o^2 + \nu^2} \right)$$

where ε' is the complex permittivity, ω_o is the laser light frequency, $\omega_p^2 = e^2 N_e / \varepsilon_o m \, [1 + Z(m/M)]$ is the plasma frequency and $\nu = 4.2 \times 10^{-5} \, Z \, N_e / T_e^{3/2}$ is the electron-ion collision frequency. Here T_e is expressed in keV.

The phase shift $\delta\phi$ in the laser light due to a density dependent refractive index can be written as

$$\delta\phi = \frac{2\pi e^2}{m\omega_o c} \left(1 - \frac{4\pi e^2 N_e}{m \omega_o^2} \right)^{-1/2} \delta N_e$$

However, additional phase-shifts arise from this treatment. In the expression for the electrical current density J there is an additional term due to the local contribution to the plasma motion caused by the laser beam: a longitudinal component $J_z \alpha E^2$ and a transverse component $J_\perp \alpha - 2i \, F \, E^2 \nabla_\perp \phi$ where F is the Fresnel number ($= \pi r_p / \lambda L$), λ the laser light wavelength, L the local density scale length $(1/n)\nabla n$ and r_p the initial Gaussian radius of the beam. This latter component is associated with intensity dependent radial variations of phase. When $\partial\phi/\partial r > 0$ self-induced focusing dominates the diffraction spread and, locally, the beam converges.

The system of equations describing the plasma and the laser beam are integrated numerically (7.57) under the assumption of cylindrical symmetry. In order to ensure stability and sufficient resolution in the numerical schemes, re-zoning methods are adopted.

This model has been used to study a number of problems associated with the wavelength dependence of light filamentation. As a comparative example, the growth of a single filament, at a laser wavelength of 1 μm is followed in a low Z plasma (Z = 10) with $T_e \sim 500$eV and $I/I_{th} = 10$, I_{th} being the threshold intensity. The filament is described initially by means of a Gaussian distribution in space and time with $r_p = 12.0$ μm, $\tau_p = 75$ ps and $I(0) = 2 \times 10^{14}$ W/cm^2 for $\lambda = 1054$ nm. An initial electron density $N_e = 0.25 N_c$ is taken, $v_{osc} (= eE_o/m\omega_o) = 0.01c$ and an arbitary initial phase angle. Figure 7.23 shows the normalised intensity distribution across the filament near the focus at six successive time intervals during the filamentary pulse. Marked oscillations in intensity appear across the beam which is increasingly focused with time. The oscillating break-up of the beam into smaller filamentary structures and the 25-fold enhancement in intensity near the centre is a highly localised effect depending critically on the relative magnitudes of the net focusing and diffracting terms. The light is diffracted both inwards and outwards and can locally enhance the filamentary region. In this simulation the beam reaches a

first focus at an axial distance z = 180 μm. After passing through the focus it diverges and then reconverges again in a succession of tighter foci the pattern gradually increasing in intensity and moving, in time, towards the axis. This phemonena of successive foci has been observed previously (7.53) and displayed graphically in recent numerical simulations (7.54). Extremely high peak intensities ∿30I(0) can be seen near the axis over regions of the order of a free - space wavelength. Other filamentary structures develop in time and, as the simulation is followed beyond the first focus, these 'beat' with each other in increasing complexity. The estimated gain - length for the process, based on this model is ∿ 220 $cm.^{-1}$.

A detailed study of the time dependent energy flow near the focal region shows that just prior to the focus, the local group velocity ($\partial\omega/\partial k$) exceeds the local phase velocity of the beam, temporal distortion of the pulse occurs and what amounts to an optical shock is formed. In fact a succession of these shock waves are formed and propagate coherently. These would have a significant effect on the stability of an imploding microballoon should they occur near the ablation region. An estimate of the pulse distortion can be obtained by comparing the interval between successive radial beam profiles shown in Figure 7.23.

The results obtained above are compared with another simulation carried out at the second harmonic, wavelength λ = 527 nm. Again $I(0) = 2 \times 10^{14}$ W/cm^2 and in general conditions are maintained such that the problem can be reasonably scaled. Figure 7.24 show the radial beam profiles just after the first focus at z = 310 μm. The radial beam profile demonstrates the effects of wavelength scaling with much finer structure appearing on the beam. The intense on-axis structure is accompanied by several filaments developing radially, including one well developed structure.

Of central importance to the understanding of the quantitative behaviour of filamentation is the relative magnitude of the thermal kinetic pressure to the pondermotive force. Using equation (1) this ratio can be written as,

$$\Gamma = \left| \int_0^{\tau} \frac{d}{d\tau} \nabla P_p \, d\tau \right| \Big/ (\nabla \langle E \rangle^2)$$

The integration is carried out temporally over the local time co-ordinate τ of the pulse whilst spatially over a time equivalent to the filament acoustic transit time $[c_s (\omega/c)]^{-1}$. Monitoring Γ enables the dominant physical process to be identified. For example, at λ = 1054 nm, the thermal processes dominate the growth of the filament to a region around the first focus. However at this wavelength small scale effects are not smoothed out in a relatively collisionless plasma Figure 7.23. The main filament is dominated by intense local structures but these do not carry a large fraction of the energy. In the simulation carried out for green light, that is the second harmonic, there is a considerable narrowing of the filament waist and a reduction in the intensity of the small-scale spatial frequencies, Figure 7.24.

The final simulation described is carried out at the third harmonic wave-length blue light with λ = 351 nm. Again the starting intensity $I(0) = 2 \times 10^{14}$ W/cm^2 and an initial Gaussian filament profile in both space and time (r_p = 12.0 μm, τ_p = 75 ps). Figure 7.25 shows the radial intensity profile near the position of the first focus z = 468 nm. As with previous simulations there are small scale length, high intensity structures, but in addition the whole beam waist has also narrowed down to ∿5 μm; in other words there is whole beam self-focusing. The previous simulation with green light appears to indicate this trend, but it shows up quite clearly with the blue light. The plasma, at this wavelength is highly collisional, small-scale structures in the filament are smoothed out and thermal self-focusing dominates (Γ > 10).

Thus, whilst at λ = 1054 nm there are high intensity filaments, they contain little of the total energy of the filament. At λ = 351 nm however the intensity spikes are suppressed and whole beam self-focusing dominates the filamentation process.

There is some evidence, from recent experiments carried out at this laboratory(7.58), that seems to support these findings. Optical probing experiments at 1054 nm display intense small-scale filamentary features

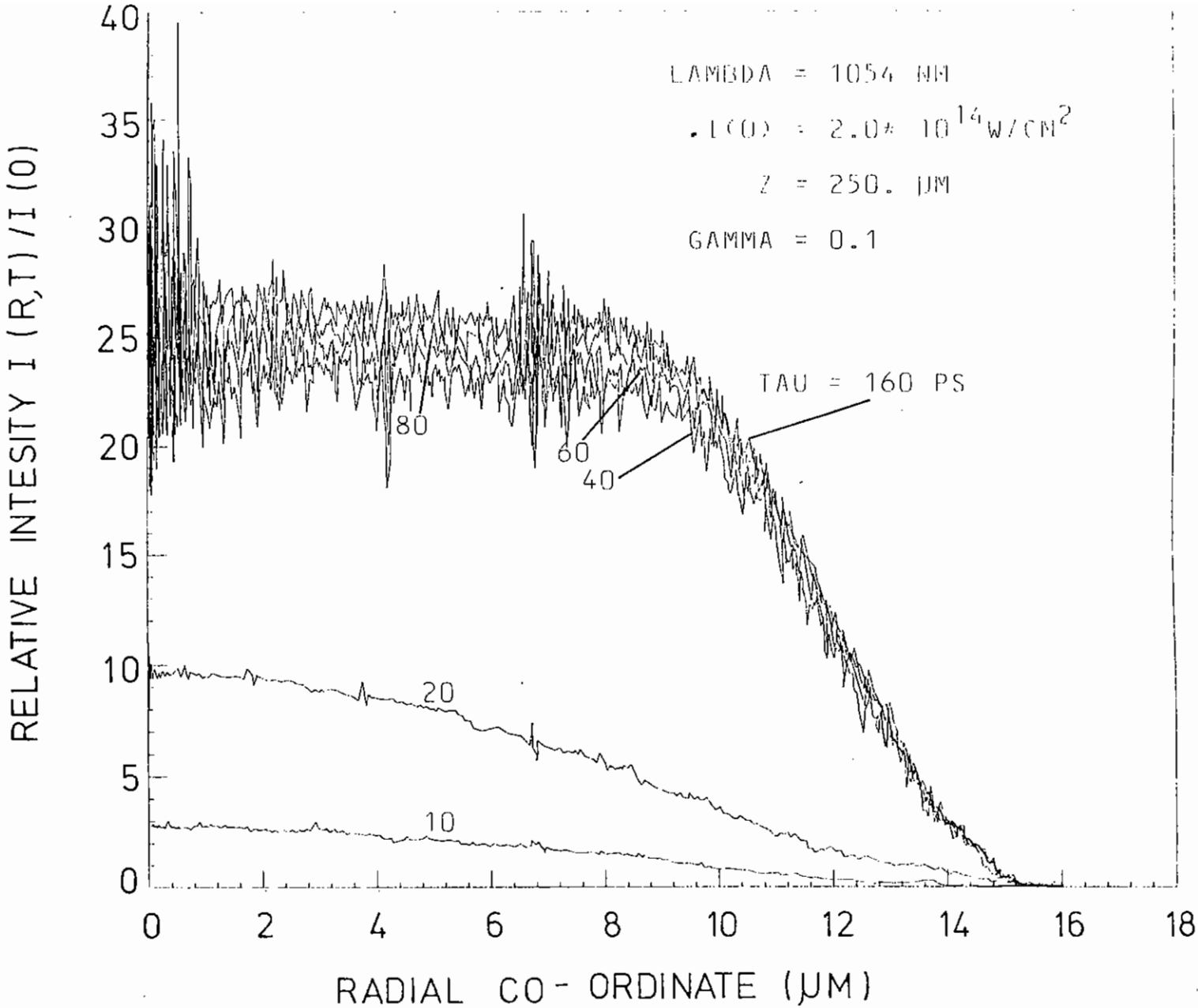

Figure 7.23 Radial intensity profiles across the filament at λ = 1054 nm. Six profiles are shown at various time intervals, tau, within the pulse up to the peak at τ = 160 ps. Note the bunching of the profiles at later times indicating pulse compression.

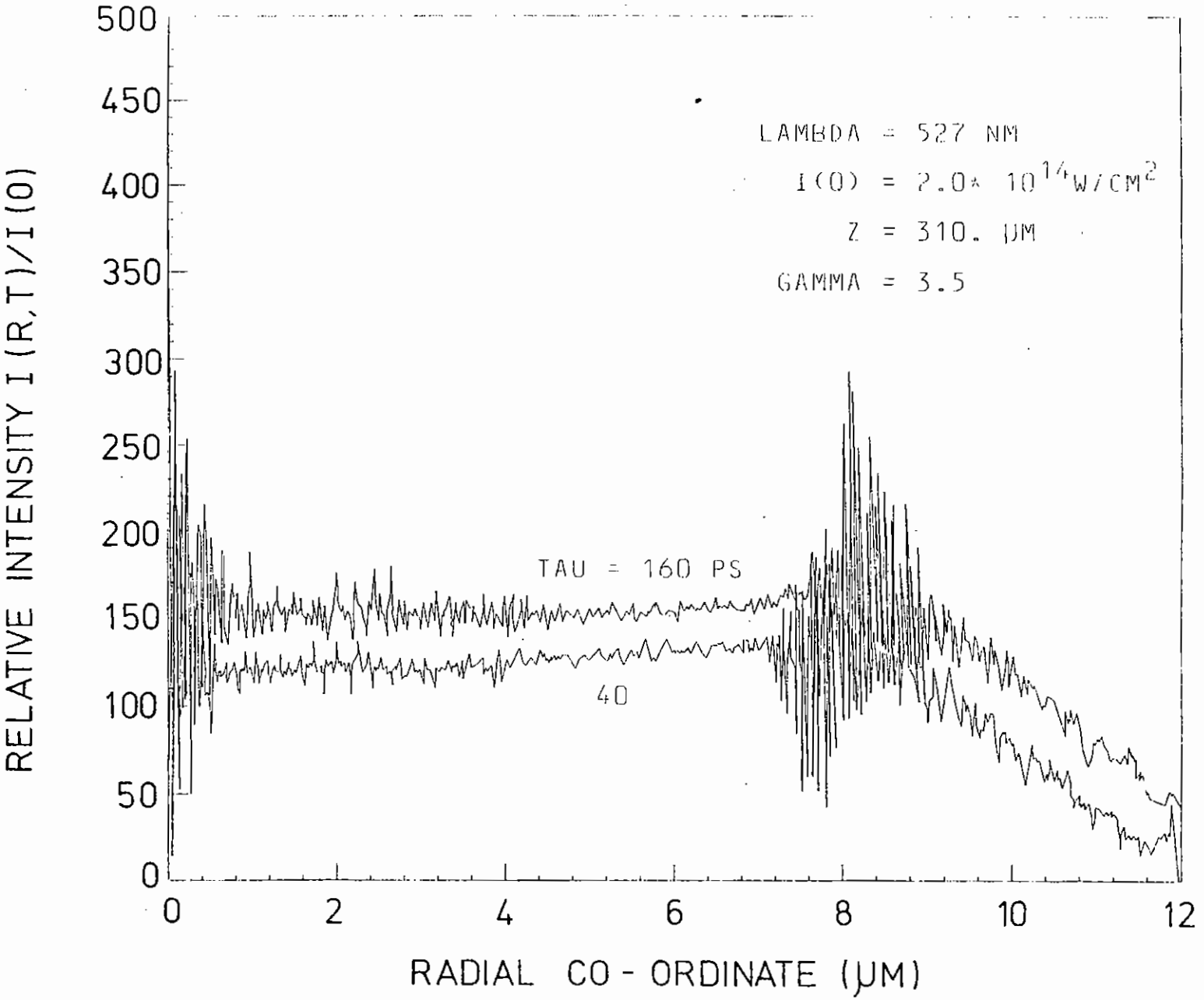

Figure 7.24 Radial intensity profiles in green light at λ = 527 nm.

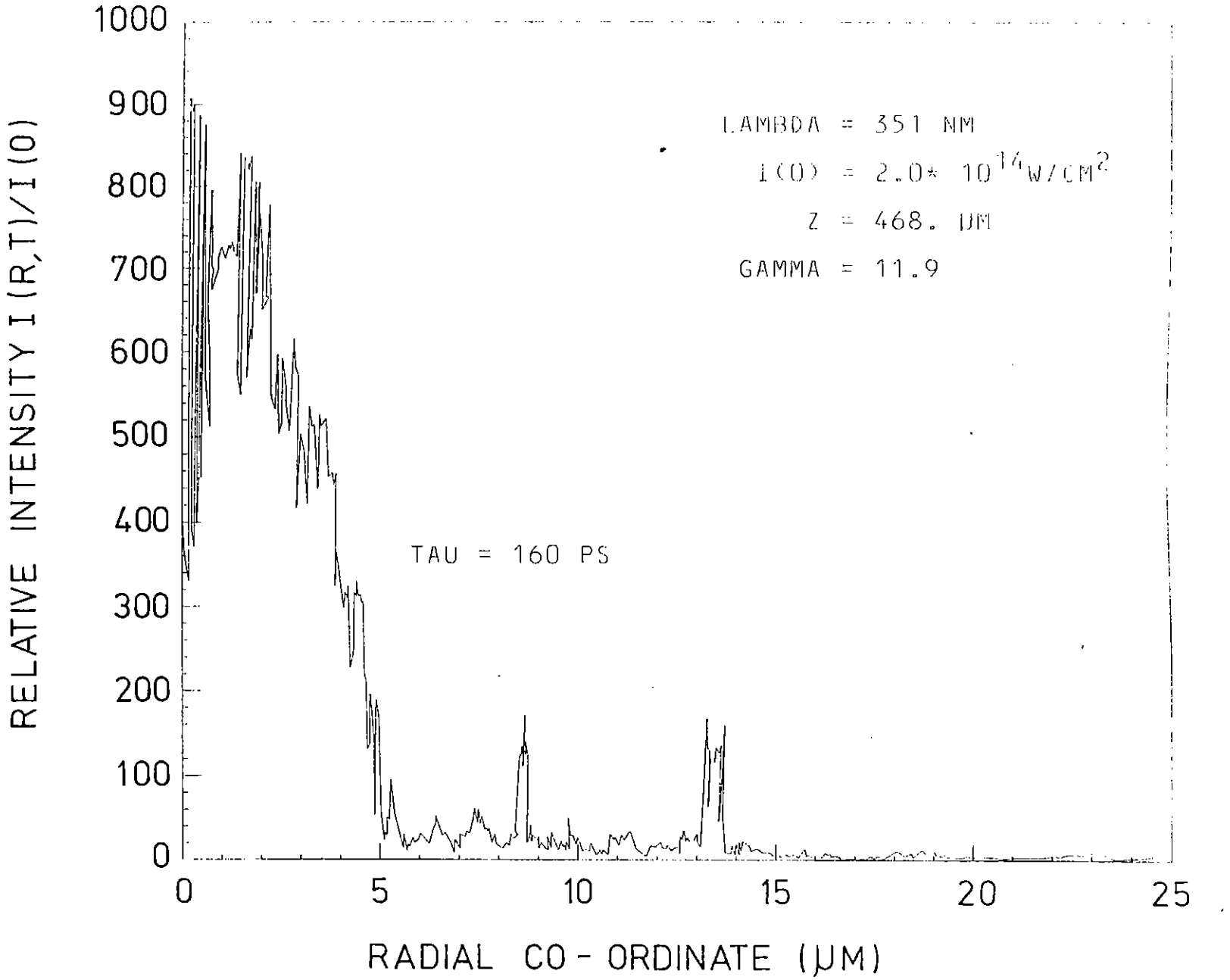

Figure 7.25 Radial intensity profile for blue light at λ = 351 nm. The radial width of the filament has decreased to ~ 5μm denoting whole beam self-focusing. There is also a marked absence of high spatial frequencies due to collisional smoothing.

whilst at 351 nm more uniform features with strong x-ray emission are observed indicating whole beam self-focusing with large-scale concentration of energy.

D J Nicholas (RAL)

7.4 Transport Processes

7.4.1 Effects of Anisotropic Scattering on Non-linear Steady State Heat Flow

Non-linear steady state heat flow in a plasma is studied using a multi - (total) energy group, discrete ordinate code. The electric field needed to impose quasi-neutrality is treated self-consistently. The angular mesh is chosen to follow the trajectories of the collisionless electrons and thus avoid the need for angular redistribution of particles. The linear characteristic method is then used to integrate spatially along these trajectories. An adaptation of the Alcouffe Diffusion Synthetic method is used to accelerate convergence of the inner (source) - iteration. The iteration scheme is described in (7.59, 7.60).

Results (7.61) for a non-current carrying, homogeneous, Lorentz plasma between two 'plates' differing in temperature by a factor of two show that:

(i) There is no single value of 'f', the flux inhibition factor, given by

$$q = f\, nkT \left(\frac{kT}{m_e}\right)^{1/2}$$

which fits the whole range ($0.01 \leqslant D/\lambda \leqslant 160$) of collisionality studied (D is the separation of the 'plates' and the λ is the electron mean-free-path defined by

$$\lambda = \frac{2kT_{av}}{4\pi ne^4} \quad \frac{\bar{i}}{Z \ln \Lambda}$$

(ii) For $20 < D/\lambda < 100$, the appropriate value of f is ~ 0.2, which is in general agreement with recent experimental results (7.62) indicating a

high flux limit of about 15%.

These numerical results use ten total-energy groups and assume that the electrons are scattered isotropically. The sensitivity of these results to the latter assumption is currently being investigated.

The Fokker-Planck operator for eleastic scattering is

$$\frac{\partial f}{\partial t}\ (x,\ \mu,\ E)\Big|_c = \frac{\alpha}{v^4}\ \frac{\partial}{\partial \mu}\ (1-\mu^2)\ \frac{\partial}{\partial \mu}\ f\ (x,\ \mu,\ E) \qquad (1)$$

where α is a constant depending on the density and charge number.

A systematic approximation to treat the non-isotropic part of the electron distribution may be done by expanding $f(x, \mu, E)$ in a Legendre series to some finite order:

$$f\ (x,\mu,E) = \sum_{l=0}^{M-1} \left(\frac{2l+1}{2}\right)\ P_l\ (\mu)\ \ f^l\ (x,E) \qquad (2)$$

Making use of equation (2) and the identity

$$\frac{\partial}{\partial \mu}\ (1-\mu^2)\ \frac{\partial}{\partial \mu}\ P_l\ (\mu) = -l(l+1)\ P_l\ (\mu) \qquad (3)$$

equation (1) may be rearranged in the 'extended transport approximation' (7.63):

$$\frac{\partial f}{\partial t}\ (x,\mu,E)\Big|_c = \sum_{l=0}^{M-1}\ \frac{\alpha}{v^4}\ \frac{2l+1}{2}\left[(M-l)M-(l+1)l\right] f^l(x,E)P_l(\mu) - \frac{\alpha}{v^4}M(M-1)f(x,\mu,E) \qquad (4)$$

Isotropic scattering is obtained by taking M = 2. This corresponds to the 'transport approximation' frequently used in neutron transport. From equation (2) it can be seen that this is a good approximation for a near isotropic electron distribution. Deviation from near isotropicity of the distribution function may be approximated by including higher moments of the Legendre expansion.

Preliminary studies using M = 3 indicated that the above results are not sensitive to this extra term. The code is presently being modified to study the effect with M = 5.

T H Kho and D J Bond (Imp Coll)

7.4.2 Heat flow in a propagating temperature gradient

This work is intended to study heat flow in a plasma under conditions of steady and relatively steep temperature gradients, when the energy transport is between collision-free and collision-dominated behaviour. Following earlier work by Bell **et** al (7.56, 7.64) in which a numerical solution of the Fokker-Planck equation was developed, it was decided to set up a steady temperature profile by introducing propagation of the heat front; the work of Bell et al never established a steady heat flow. The results obtained show that a steady, propagating temperature profile was achieved and that the shape of the temperature variation was different from that predicted by a collision-dominated theory, i.e. significant departures from Spitzer-like thermal conduction were observed.

In order to establish a steady heat front one must somehow balance the forward heat diffusion; Bond et al (7.65) have introduced fixed temperature boundaries to achieve this. Here, the heat front propagates into cooler plasma so that convection of cold plasma into the front balances the forward heat diffusion. This is achieved as follows:

A one dimensional slab of plasma at temperature T_o occupies the region $0< x < d$ at time $t<0$. For times $t\geq 0$ the plasma in the region $0 < x < X_o+ut$ is supplied with sufficient energy to maintain the temperature at $T_1=2T_o$; u is the constant velocity at which the top of the front propagates and X_o is a small offset. The front propagation speed u is comparable with the ion acoustic speed (C_s) in the plasma, where $C_s^2 = kT_e/(1836m_e)$ and m_e is the electron mass. There are no density gradients in the plasma and ion motion is suppressed; there is no energy exchange between electrons and ions but electrons are scattered by the ions and do experience the self consistent electric fields due to

local charge separation. Three different values of Z and two different propagation velocities have been used. It is instructive to see how heat/flow is related to local temperature in a steady heatfront as this not only demonstrates a way of checking the numerical computations but also gives useful insight to the problem. If a steady profile is achieved, then the energy absorbed per unit volume, per unit time on the front, dQ/dx, is given by:

$$\frac{dQ}{dX} = \frac{3}{2}\, nku\frac{dT}{dX}$$

This is essentially a constant volume heat flow equation in the rest frame of the temperature profile, the factor $\frac{3}{2}$ reflecting the neglect of ion motion and associated work; if hydrodynamic work were to be included, the factor $\frac{3}{2}$ would be replaced by $\frac{5}{2}$. This equation can be formally integrated between some point x on the front and some remote point in the unheated plasma where $T=T_o$ and the local heat flow is zero. Then:

$$Q(x) = \frac{3}{2} nku\,(T(x) - T_o)$$

This expression can be rearranged into two forms which will be useful:

$$\frac{Q(x)}{\frac{3}{2}nkT(x)u} = \left(1 - \frac{To}{T(x)}\right) \qquad (1)$$

$$\frac{Q(x)}{Qf(x)} = \frac{3}{2}\,\frac{u}{(kT(x)/m)^{1/2}}\left(1 - \frac{To}{T(x)}\right) \qquad (2)$$

where $Q_f(x) = nkT\sqrt{kT/m_e}$ is the local free-streaming heat flux. Equation (1) will be used later in assessing the degree to which a steady profile has been achieved. Equation (2), which compares the actual local heat flow to the local free-streaming value reveals three interesting points.

(i) Because no reference has been made to a thermal conductivity, the equation contains local information but provides no way of determining the overall spatial variation of either the heat flow or the temperature. The role of the important variable Z, the ionic charge, is associated

with this unrevealed spatial variation; Z does not appear explicitly in the equation. It should be noted also that equation (2) is general and in no way excludes the Spitzer model (7.66).

(ii) The temperature of the cooler plasma, T_o, enters the expressions and sets an upper limit to Q/Q_f.

(iii) A second constraint on the maximum Q/Q_f is provided by the propagation speed, u, on which Q/Q_f depends linearly. For constant u, the maximum Q/Q_f would arise when $T = 3T_o$. In this work $T < 2T_o$ which restricts the peak value of Q/Q_f to $\sim 5 \times 10^{-2}$ for 'u' approximately one and a half times the ion acoustic speed in the heated plasma.

The Fokker-Planck code developed by Bell et al. (7.56, 7.64) has been modified to allow heat front propagation and has been run for long enough to establish a steady temperature profile. Equation (1) was derived for a source-free, steady heat-front so one test that conditions in the front are steady is to plot both sides of equation (1) as a function of distance using data from the computations. (The temperature and heat flux at any point is obtained by suitable integrations over the local velocity distribution function). Figure 7.26 shows the results for Z=4, u=1.52 times the ion acoustic speed in the heated plasma (c_s), after 100, 500 and 1000 mean angular scattering times. The solid lines are the right hand side of equation (1): the horizontal start of each line section is just inside the heated region where equation (1) is not valid, but the downward slope is the region of interest on the heat front. The discrete points are the left hand side of equation (1). It is evident from this plot that a steady state profile was evolving and was virtually established in the last case shown. This particular plot is a sensitive test of how steady conditions are. A less sensitive demonstration is provided by plotting the maximum heat flow on the front as a function of time. Reference to equation (2) and previous discussion suggests that an upper limit can be placed on the steady value that this should have and reveals a simple dependence on the propagation velocity, u. Figure 7.27 shows a plot of $(Q/Q_f)_{max}$ against time, indicating how the limiting

value is reached: data are presented for Z = 10 and Z = 4 with u equal to 1.52 c_s and also for Z = 4 with u equal to 1.14 c_s. For lower Z, the steady conditions are approached more quickly because of the more efficient scattering. The time scale of Figure 7.27 extends over a range of approximately 1000 angular scattering times for an electron with thermal energy in the heated plasma. A further test of the steadiness of front propagation is provided by comparing both T(x) and Q(x) at two different but 'late' times in the computations. Careful comparison of the curves
in Figure 7.28 shows that, consistent with the two previous checks, a steady, propagating heat front has been established.

In the steady profiles one can examine how Q/Q_f is related to the local normalized temperature gradient scale-length, L/λ. Initially there are changes with time, but the heat flux settles down as the temperature profile becomes steady. The chief point of interest here, for the smaller values of L/λ (steepest gradients) is how great a departure there is from the prediction of a Spitzer conductivity approach; see the log-log plots in Figure 7.29. In Figure 7.29 the leftmost points are on the steepest portion of the steady heat front; for u = 1.52 C_s the heat flux is only 55% of the value given by Spitzer for the same gradient whereas with u = 1.14C_s the heat flux is only 47% of the equivalent Spitzer value. It should be emphasized that these figures are dependent upon the propagation speed, u, the atomic number, Z, and the cooler plasma temperature, T_o, and can not be reconciled by simple reference to a 'flux limit'. The effect of increasing Z is to steepen the maximum gradients; this is not well demonstrated in Figure 7.29 but computations (to be reported more fully later) with Z = 400 indicate comparable values of Q/Q_f but with L/λ decreased by a factor of three or so, suggesting a departure from Spitzer of about an order of magnitude. It is again pointed out that these computations are intended to study the spatial variation of heat flow and temperature in a semi-collisional plasma, where one would not expect Spitzer conductivities to be valid.

This work has examined heat flow through a steady temperature profile in a plasma for the simplified case in which ion motions and density gradients

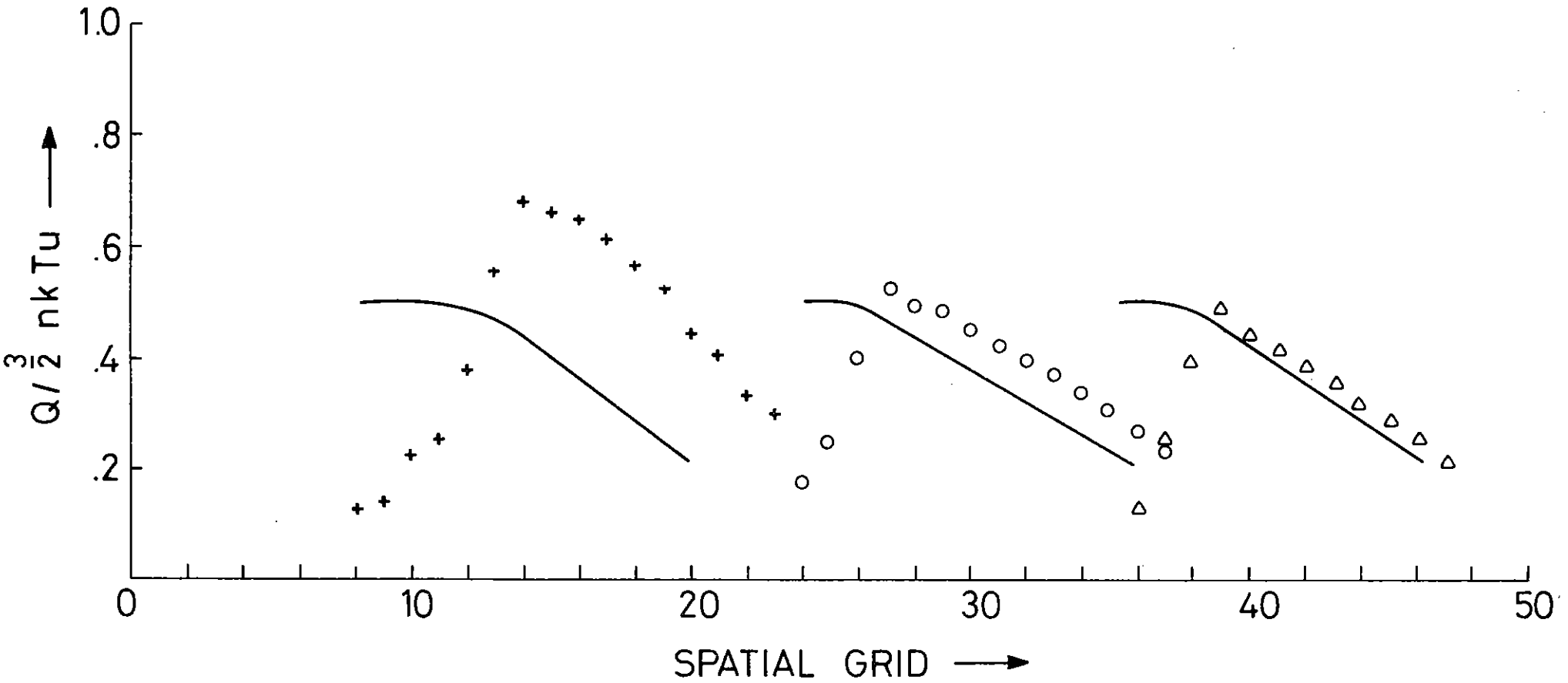

Figure 7.26 A comparison of 'calculated' and 'computed' values of the ratio $Q/(\frac{3}{2}$ nkTu). Solid lines are from the RHS of equation (1); points are from the LHS. The downward sloping regions are on the heat front which is propagating from left to right at constant velocity (u) equal to 1.52 times the ion acoustic speed in the heated plasma (the computational grid on which the data are presented is not linear in real space). Z=4. Data presented after 100(+), 500 (o) and 1000 (Δ) mean angular scattering times.

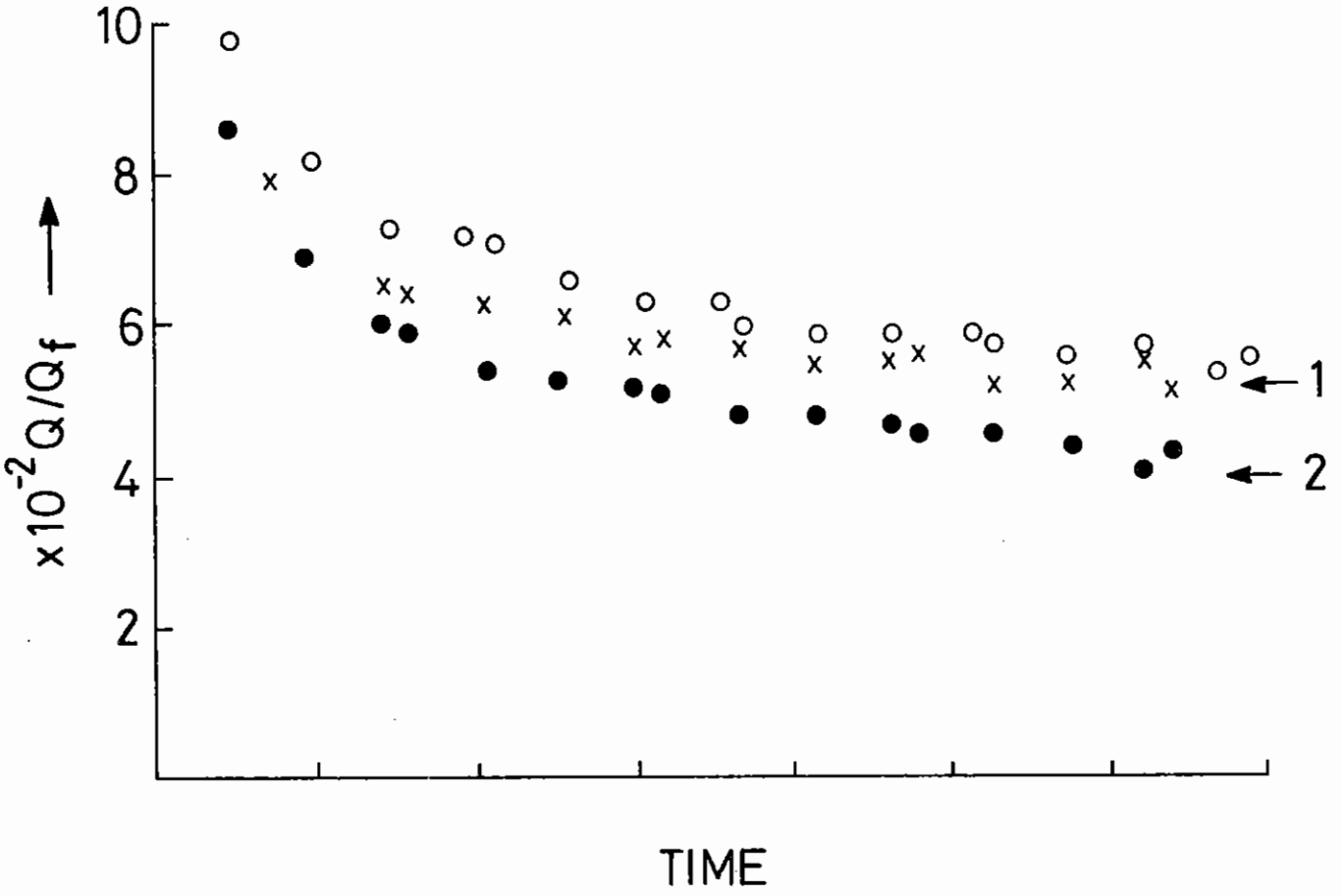

Figure 7.27 The maximum value of Q/Q_f on the heat front as a function of time:
o Z=10, $u=1.52c_s$
x Z=4, $u=1.52c_s$
• Z=4, $u=1.14c_s$
The maximum value expected in the steady state is calculated from equation (2) and is marked by arrow 1 for o and x, and by arrow 2 for •.

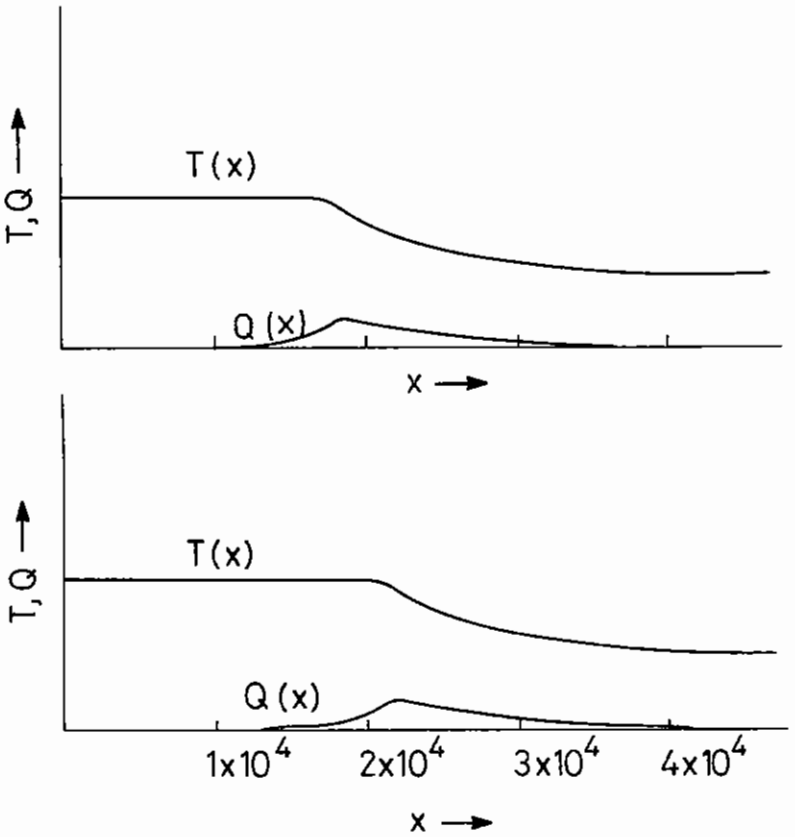

Figure 7.28 Plots of spatial variation of temperature T(x), and heat flux Q(x), after approx 1000 mean scattering times at two different times separated by 70 scattering times. Z=10, $u=1.52c_s$.

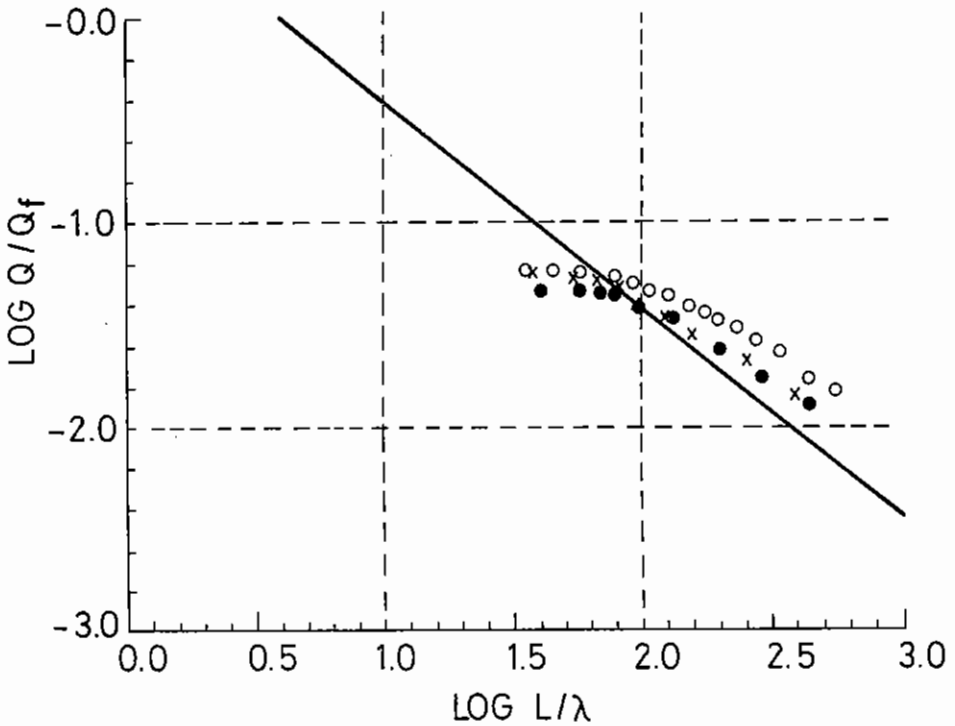

Figure 7.29 Log-log plots of the normalised heat flux Q/Q_f against the locally normalised temperature gradient scalelength, L/λ_s. Only data points along the indirectly heated heat front ($x>x_0+ut$) are shown.
- o Z=10, $u=1.52c_s$
- x Z=4, $u=1.52c_s$
- • Z=4, $u=1.14c_s$

are suppressed. The Fokker-Planck equation has been used to examine the relationship between heat flow and temperature gradient-scale length for semi-collisional conditions and has shown that the concept of a local thermal conductivity may not always be useful even under steady conditions; a similar conclusion was reached by Bell et al (7.56).

N St J Braithwaite (Oxford), A R Bell (RAL)

7.4.3 Electron Energy Transport in Ion Waves

The heat flow at any point in a plasma is determined by the state of the surrounding plasma over a distance of many mean free paths, and hence the conductivity depends on the specific context in which it is calculated (7.56,7.67-7.72). We consider heat flow in the context of ion waves in which the scalelengths can be of the order of an electron mean free path and the density profiles move at around the sound speed. In the limit of large wavelengths/ion sound waves become fully collisional and therefore adiabatic since thermal conduction is then negligible. In the small wavelength limit thermal conduction is very strong giving isothermal ion acoustic waves. At wavelengths between 1 and 1000 times the electron mean free path the waves are intermediate between collisional sound waves and collisionless ion acoustic waves. A 1KeV electron in a Z=10 plasma with an electron density of 10^{22} electrons cm^{-3} has a mean free path of about 0.2μm and so this intermediate regime is appropriate for laser-produced plasmas.

We assume that the ions are cold ($T_i \ll T_e$) and we consider a Lorentz (high Z) plasma so that angular scattering of electrons by ions is the only significant collision process. The Fokker-Planck equation for the electron distribution function in a rest frame moving at velocity u(x,t) is

$$\frac{\partial f}{\partial t} + v_x\frac{\partial f}{\partial x} + \frac{eE}{m_e}\frac{\partial f}{\partial v_x} + u\frac{\partial f}{\partial x} - \frac{\partial u}{\partial x}v_x\frac{\partial f}{\partial v_x} - \frac{\partial u}{\partial t}\frac{\partial f}{\partial v_x} - \frac{u\partial u}{\partial x}\frac{\partial f}{\partial v_x} = \frac{D}{2v^3}\frac{\partial}{\partial\mu}\left[(1-\mu^2)\frac{\partial f}{\partial\mu}\right] \quad (1)$$

where $\mu = \frac{v_x}{v}$ and $D = 4\pi n_e m_e^{-2} e^4 Z \ln\Lambda$

u(x,t) is set equal to the cold ion velocity at position x and hence f is

the electron distribution function seen in a frame moving with the ions. We treat f as a zeroth order isotropic Maxwellian plus a perturbation which we expand as a sum of Legendre polynomials in μ. We also impose an $\exp i(kx+\omega t)$ variation in space and time. The Fokker-Planck equation then separates into an infinite set of equations. It can be shown that only the first two terms in the Legendre expansion and consequently the first two equations of the series are needed. Equations for ion momentum and energy conservation and charge neutrality complete the set of equations which can then be solved for the dispersion relation

$$\left(\frac{v_p}{v_a}\right)^2 = \frac{\eta}{9}J_6 - \frac{i}{9}\frac{J_9^2}{J_7} \quad (2)$$

where

$$J_n = \left(\frac{2}{\pi}\right)^{1/2}\int_0^\infty \frac{x^n e^{-\frac{1}{2}x^2}}{\eta - ix^5}\,dx$$

$v_p = \omega/k$

$v_a^2 = v_t^2 Z m_e/m_i$

$\eta = 3Dw/(k^2 v_t^5)$

and $v_t^2 = k_B T_e/m_e$

Figure 7.30 is a graph of the real and imaginary parts of the frequency as a function of $(k\lambda_s)^{-1}$, where $\lambda_s = 9v_t^4/D$ is the mean free path of an electron with energy $3m_e v_t^2/2$. The wavenumber k is scaled by the ionic charge to mass ratio Z/A. The dispersion relation derived from the Spitzer conductivity (7.73) instead of the Fokker-Planck equation is given for comparison in Figure 7.30In the collisionless limit $v_p = v_a$ and the solution for an isothermal ion acoustic wave is recovered. In the collisional limit $v_p = (5/3)^{\frac{1}{2}}v_a$ as expected for an adiabatic sound wave. The damping rate reaches a maximum of about $0.05\mathrm{Re}(\omega)$. The damping is mainly caused by those electrons with velocities of approximately $v_t(k\lambda_s)^{-1/5}$. Since the velocity of these electrons is such a weak function of k, diffusive damping is strong over a larger range of k than is found by linearising the fluid equations and the Spitzer-Harm

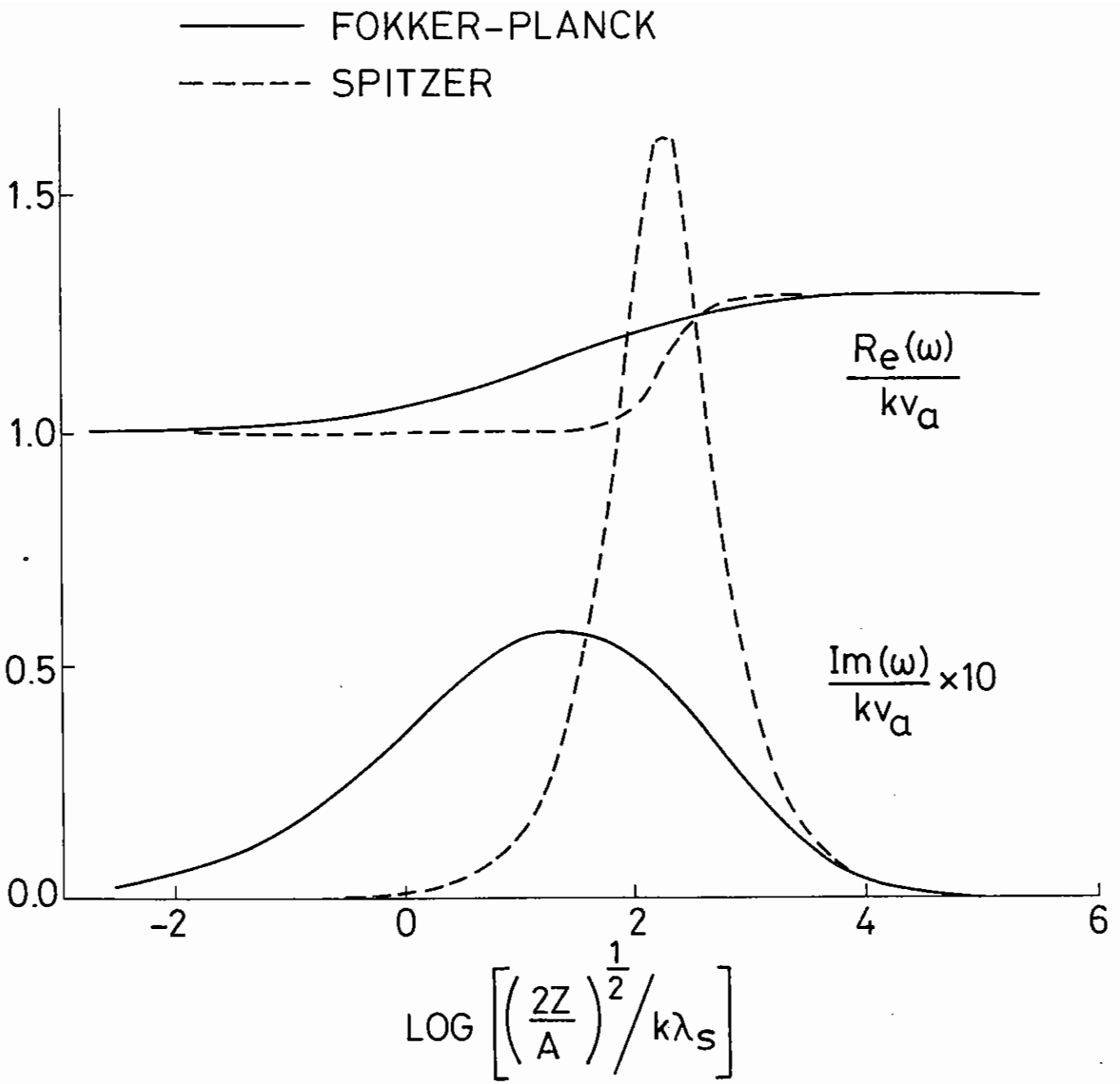

Figure 7.30 Dispersion relation for ion waves. The imaginary part is plotted on a scale which is 10 times larger than that used for the real part.

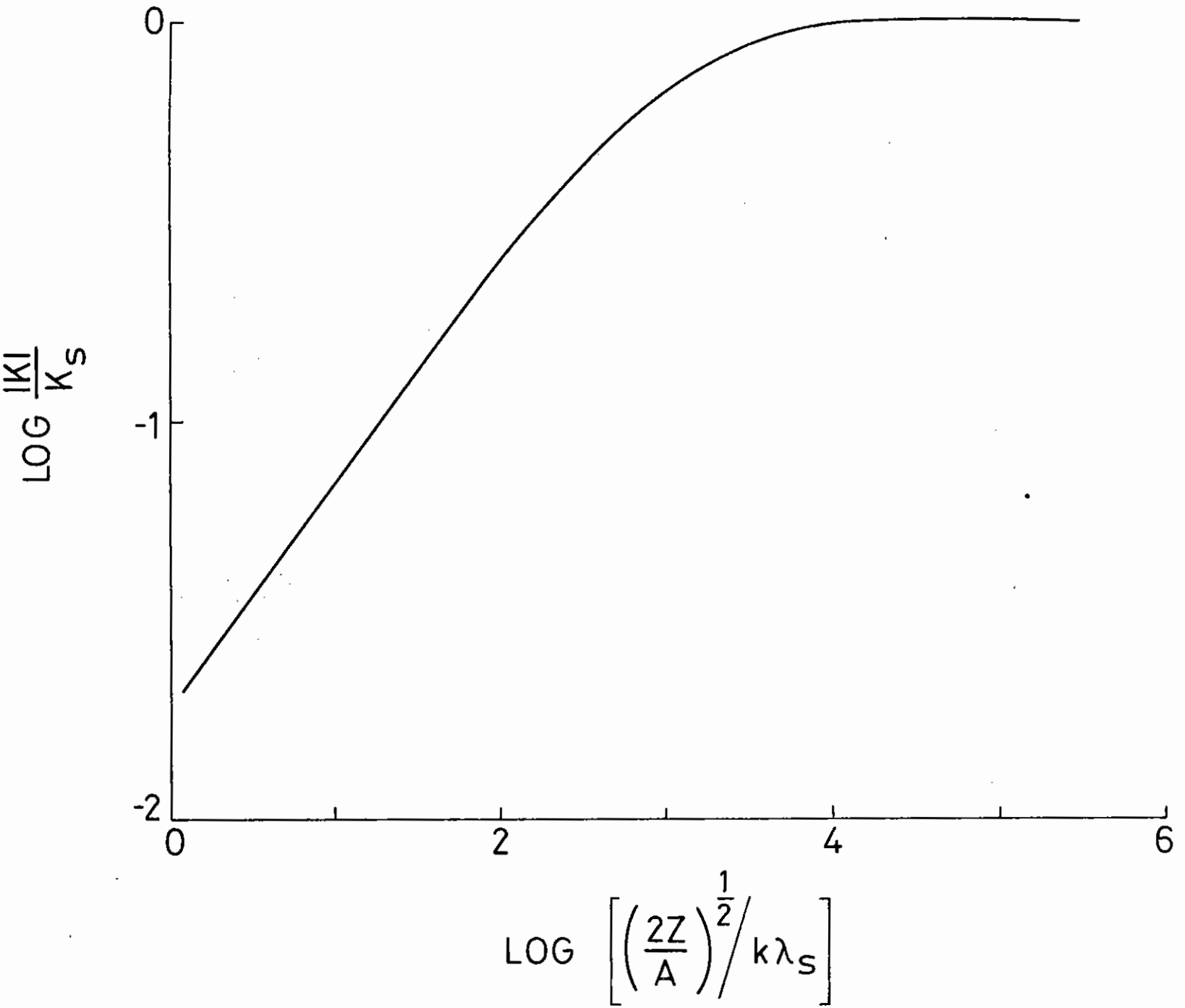

Figure 7.31 Absolute value of the conductivity compared with the Spitzer-Harm conductivity.

conductivity.

The perturbed electron distribution is derived neglecting terms of order $(Zm_e/m_i)^{\frac{1}{2}}$ for those electrons which are predominantly collisionless, and we therefore expect errors of this magnitude in the dispersion relation which might be comparable with the calculated damping rate. The main effect of the neglect of these terms is the omission of electron Landau damping. For a plasma with 2Z/A=1, the collisionless value of the Landau damping rate (7.74) is approximately 20 percent of the maximum damping rate due to electron diffusion as calculated here. The damping rate calculated here is probably dominant when $(k\lambda_s)^{-1}$ is greater than one, but at shorter wavelengths it is progressively less accurate due to the neglect of Landau damping. At longer wavelengths the plasma becomes increasingly collisional, the approximate treatment of collisionless electrons is less important, and Landau damping is less strong.

Expressions can be deduced for the heat flow Q carried by the electrons and the perturbed electron temperature T_1, and a complex conductivity defined as

$$K(k) = \frac{-Q}{\sqrt{k_B}T_1} = \frac{3}{2}\, n_e\, \frac{v_p}{k}\, \frac{J_{11} - J_9^2/J_7}{nJ_6 - iJ_9^2/J_7 - 9} \qquad (3)$$

In the collisional limit K(k) tends to the Spitzer conductivity K_S. Figure 7.31 is a plot of $|K(k)|/K_S$ as a function of $1/(k\lambda_s)$. The conductivity is very close to the Spitzer-Harm limit for small k but the Spitzer-Harm approximation begins seriously to break down when $1/(k\lambda_s)$ =1000. It should be noted that this is not a saturation effect since it is independent of the magnitude of the perturbation, and should be distinguished from the breakdown of the Spitzer-Harm conductivity when the electron distribution function becomes negative as discussed elsewhere (7.56) reduced conductivity calculated here is caused by the ability of electrons with velocity greater than $(D\omega/k^2)^{1/5}$ to diffuse across a distance 1/k in times less than $1/\omega$. These electrons are more nearly isotropic than they would be for a temperature gradient with the same magnitude extending over larger distances. Consequently their mean

velocity is low and they carry a reduced energy flow.

The heat flow in an ion wave with wavenumber k can be written in the form

$$\frac{Q(k)}{Qf} = \frac{5v_a^2-3v_p^2}{2v_a^2}\, \frac{n_{e1}}{n_e}\, \frac{v_p}{v_t} = \frac{5v_a^2-3v_p^2}{2v_p^2-2v_a^2}\, \frac{T_1}{T_0}\, \frac{v_p}{v_t} \qquad (4)$$

where Q_f is the 'free-streaming' heat flow defined as $Q_f=n_e m_e v_t^3$, and n_{e_1}/n_e and T_1/T_o are the amplitudes of the density and temperature perturbations respectively. Q/Q_f is plotted in Figure 7.32 where it can be seen that, as $k\to\infty$, Q/Q_f appproaches an upper limit $Q_{max} = (n_{e_1}/n_e)(v_p/v_t)$. If, instead of solving the linearised Fokker-Planck equation, it is assumed that the Spitzer-Harm conductivity is correct, the same upper limit is found but the temperature gradients accompanying this energy flow are much smaller.

Equation (3) gives the conductivity for ion waves as a function of spatial frequency and we would like to compute the response to a general temperature profile. The heat flow at any point in a plasma in which motions can be treated as linear ion waves can be obtained by Fourier analysing the temperature gradient, multiplying each mode by its conductivity and transforming back from transform space. However, we can also obtain the solution by convolving L(x), the Fourier transform of the conductivity K(k), with the temperature gradient $k_B\nabla T(x)$. The function L(x) is different for each of the two directions the waves can travel. L(x) for waves travelling in the +x direction is plotted in Figure 7.33. If the direction of wave propagation is reversed the function L(x) should also be reversed.

A R Bell (RAL)

7.4.4 Radiation Transport

The transport of photons within a laser produced plasma is in general an extremely difficult problem since the plasma is transient and has large gradients of temperature, density and velocity. The hot regions of the plasma are usually not in LTE and may not even be in collisional -

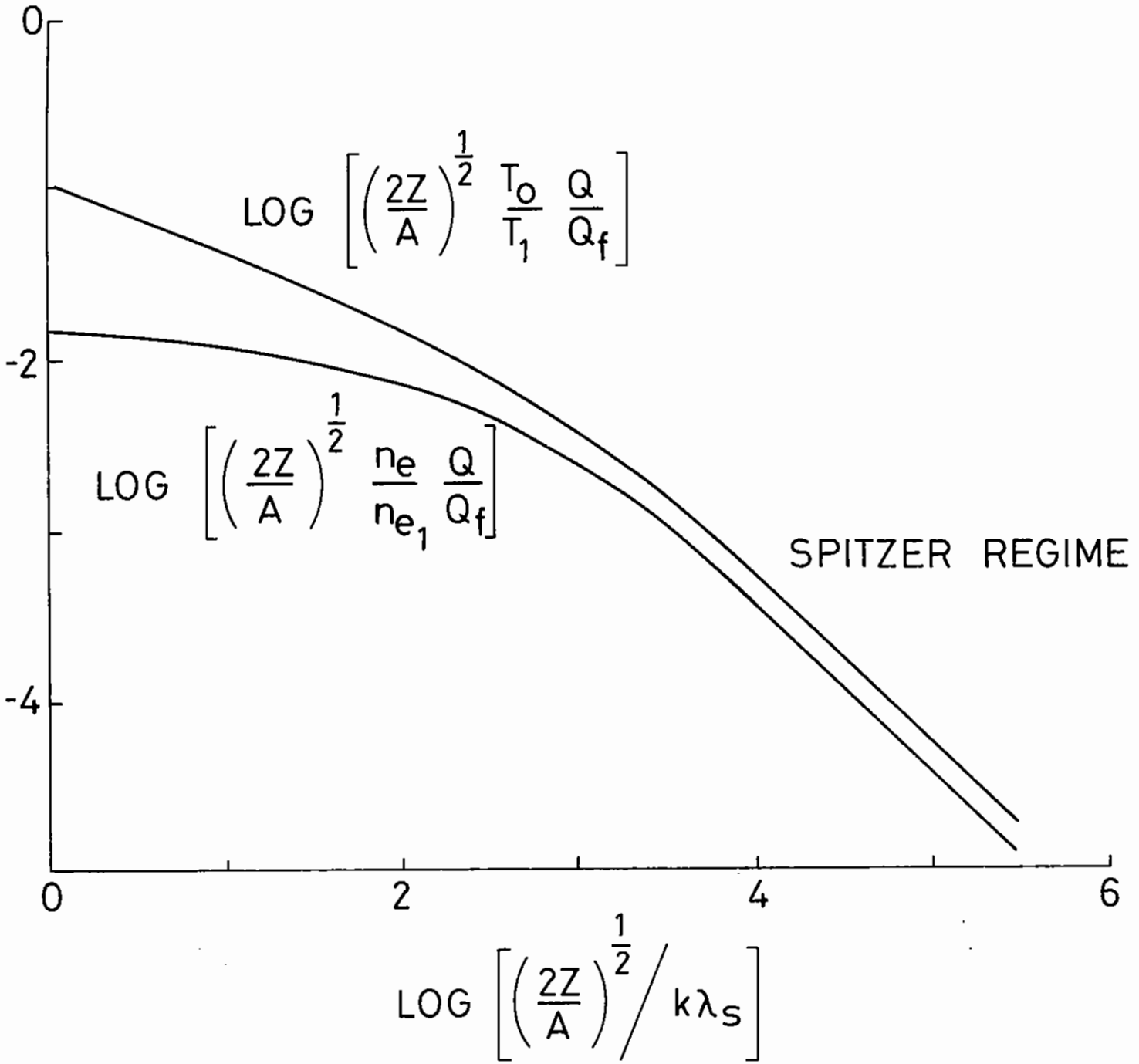

Figure 7.32 Heat flow relative to the free-streaming limit Q_f as a function of wavelength.

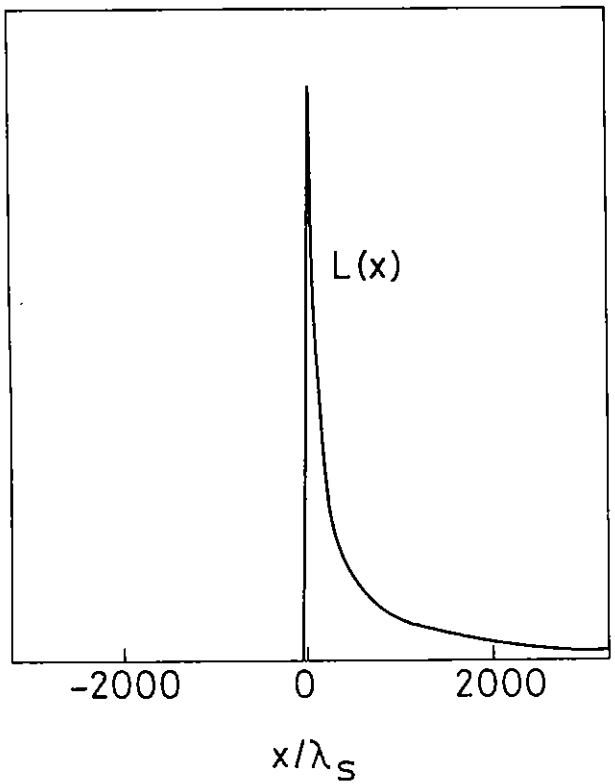

Figure 7.33 Convolution function L(x) used to derive the heat flow for a propagating ion wave. L(x) has been smoothed with a Gaussian function with half-width of approximately $30\lambda_s$. In this figure 2Z/A=1.

radiative equilibrium so that the calculation of photon emission and absorption rates is itself a very complex problem.

There are two very distinct reasons for calculating radiation transport in laser produced plasmas, each arising from the desire to perform numerical simulations of the plasma behaviour and to predict observeable quantities. In the very gross sense the X-ray photons are responsible for the transport of energy throughout the plasma, radiating energy away from the hot regions and heating the cool plasma ahead of the thermal conduction front. On a much more detailed scale the X-ray line spectrum, including line profiles and dielectronic satellite lines is a very rich source of diagnostic information and it is invaluable to be able to calculate emitted spectra including the effects of inhomogeneity and opacity for comparison with experiment.

The model presented here is suitable only for the treatment of gross energy balance since a number of approximations are made to reduce the computational expense. As in all numerical representations of radiation transport the photons at each space-time point are split into a number N_g of energy groups defined by the boundary frequencies $\nu_g \rightarrow \nu_{g+1}$. The simplest method of handling the transport equation is to use the diffusion approximation but for photons this can lead to serious errors. It is usual to apply a flux limit to the diffusive flux $J_\nu = -D_\nu \nabla I_\nu$ by a suitable modification to the diffusion coefficient D_ν, and this removes most of the non-physical results of diffusion theory. However the diffusion approximation requires that particles are scattered in angle much more rapidly than they are absorbed. An important aspect of laser heated targets is the transport of photons from the hot ablation plasma ($T_e \geq 10^3$eV) through a "cold" shell of material ($T_e \leq$ 10eV) see Figure 7.34. In this case the scattering of photons is negligible and there is an approximately exponential fall off of the photon intensity. On the other hand the steady state solution to the diffusion equation for the same problem yields a Gaussian solution which obviously cannot match an exponential. The diffusion theory is at its worst when the individual computational zones of the problem are less than a photon mean free path

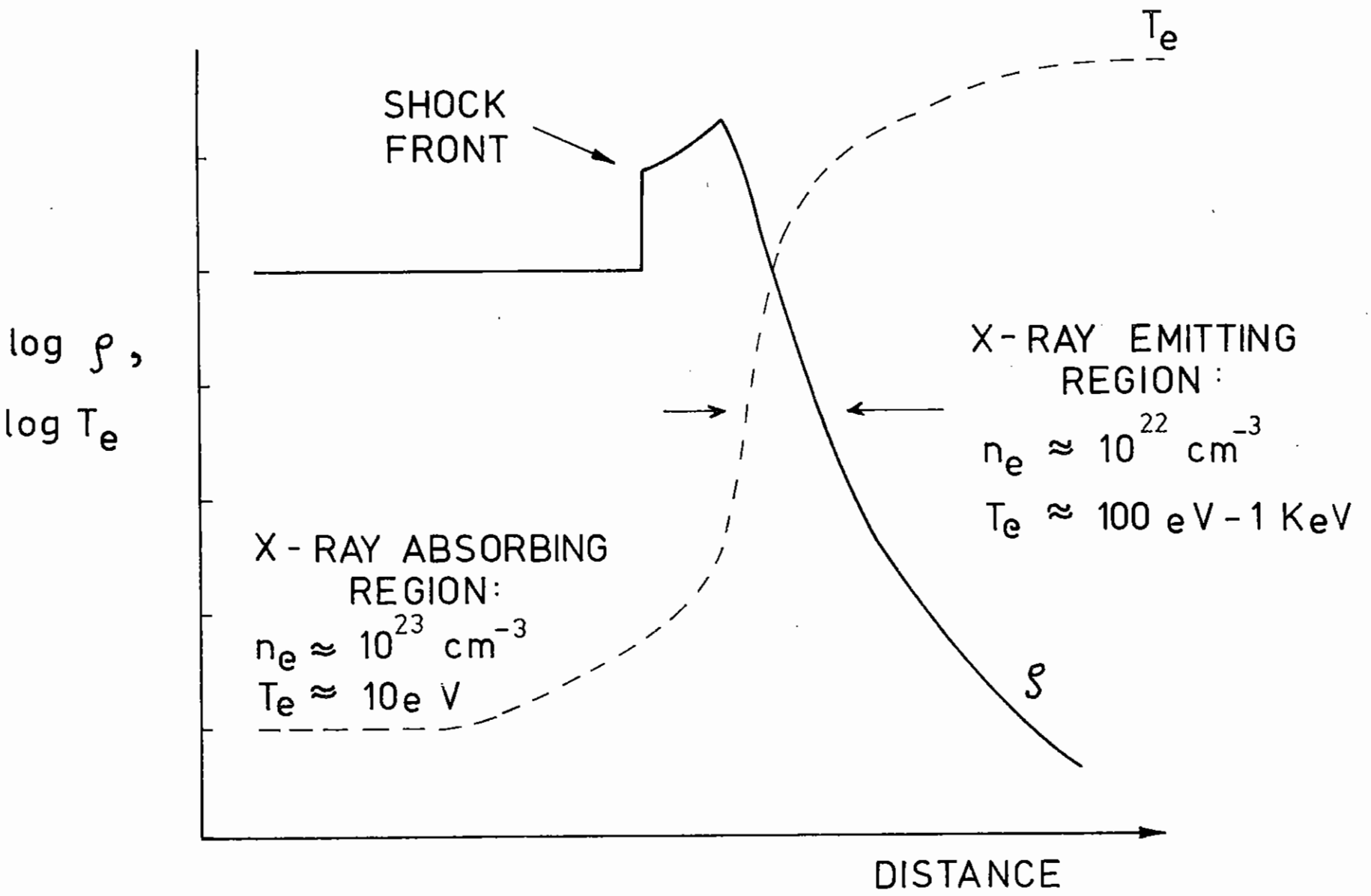

Figure 7.34 Schematic representation of the emitting and absorbing regions in a laser heated target.

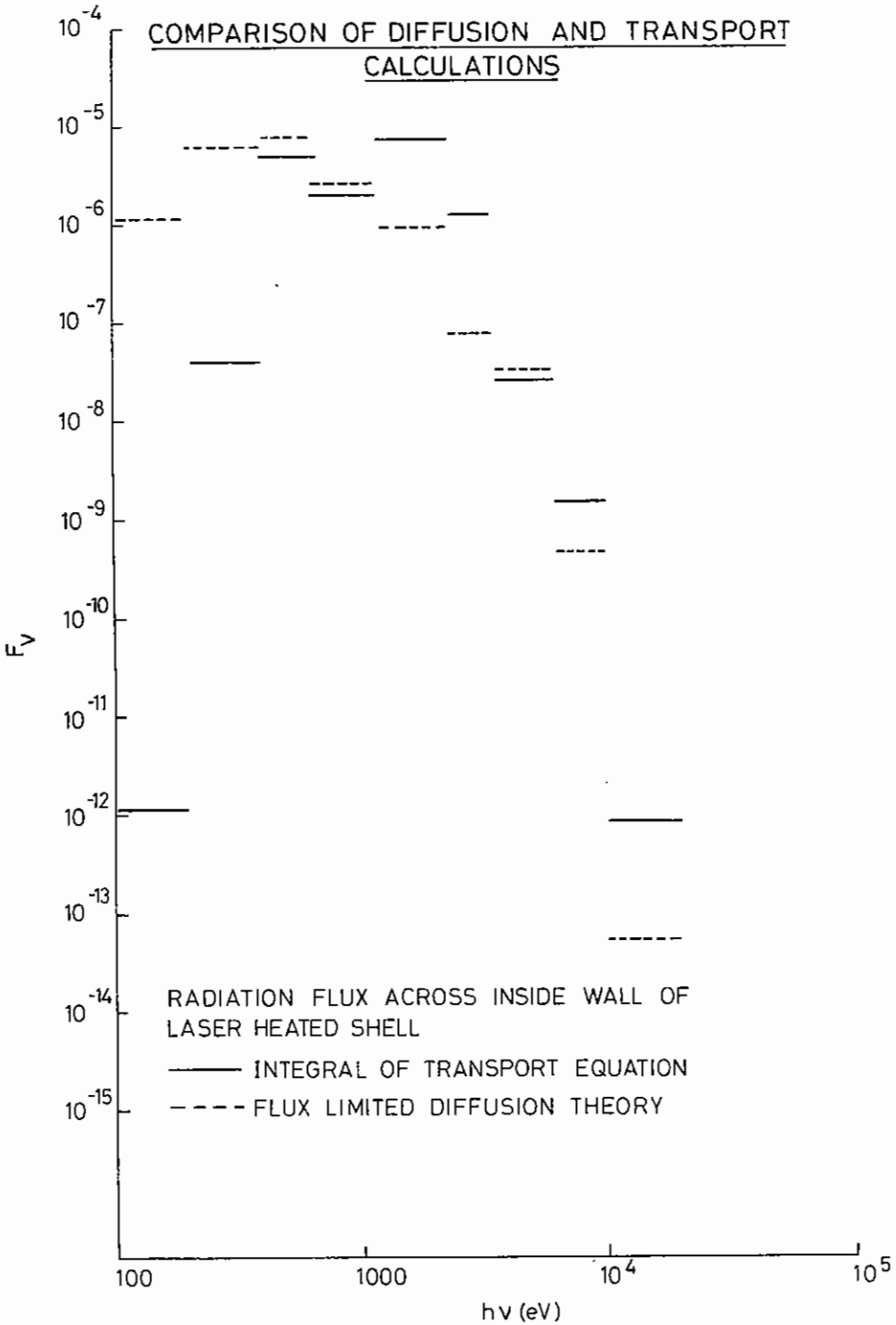

Figure 7.35 Comparison of diffusion and transport calculations for the X-ray flux on the inside of a glass shell target.

(so that the flux limit is not involved) but the whole shell is many times the mean free path. An error of several orders of magnitude in the radiation preheat is then possible. A comparison of diffusive and transport calculations is shown in Figure 7.35 where an error of six orders of magnitude is seen for the lowest energy group.

A better solution to the transport equation is obtained by direct integration of the steady state equation along several lines of sight. For the case of spherically symmetric targets an integration along just

two lines of sight yields a useful approximation if suitable corrections are made as shown below.

The numerical implementation of the model is eased considerably if two further simplifying assumptions are made.

a) The emission and absorption rates are functions only of the local thermodynamic properties of the plasma.

b) Photons are not scattered from one energy group to another.

Taken together these permit tables of source functions and opacities to be precalculated for any material of interest rather than being calculated in step with the hydrodynamics. It is however then necessary to pay careful attention to the integration of the equation of transfer so that radiation fluxes never exceed the black body flux. Since the purpose of the radiation transport model is to calculate energy transport we must also ensure that energy is strictly conserved in the numerical calculations.

We see from Figure 7.34 that the emitting region of the plasma is at a relatively low density and is far removed from the conditions of LTE (local thermodynamic equilibrium). While a full collisional radiative calculation would be appropriate we can usefully approximate this region by the coronal calculations of Summers and McWhirter(7.75). On the other hand the absorbing plasma is relatively cold and dense and approximately

in LTE. The absorption of this region may conveniently be calculated from an LTE model which is described later.

Integration of the Radiation Transfer Equation

It is required to integrate the radiation transport equation

$$\frac{\partial}{\partial r} J_\nu + K_\nu J_\nu = S_\nu \qquad (1)$$

for several discrete frequency groups (ν_{g-1}-ν_g) as part of the coupled radiation - hydrodynamic calculation for laser heated targets. The

accuracy of the solution depends on the number of lines of sight which are included in the integration. For a simple spherically symmetric hydrodynamic model it is possible to get a useful approximation by calculating just two sight lines.

The geometry of the computational mesh is based on the MEDUSA code (7.76) which has a Lagrangian (i.e. co-moving) computational mesh. Cell central quantities are subscripted L, mesh centred quantities are subscripted J and the element of plasma in the simulation is one steradian. The radii of each of the mesh points is R(J) and it is convenient to define the mesh area as S(J) = R(J)*R(J) and cell thickness DR(L) = R(J+1)-R(J).

We define F1(J) and F2(J) to be the inward and outward directed fluxes in one frequency group across the mesh lines so that F1(J)/S(J) is the flux per unit area. The flux incident on the outer boundary of the plasma is zero i.e. F1 (NJP1) = 0.0 so that this is the logical point to begin integrating the equations.

The finite difference implementation of equation
(1) then gives on the inward integration

$$F1(J) = F1(J+1)e^{-\tau} + SG(L) \qquad (2)$$

where $\tau = K_g \times DR$ and SG is the integral of the source function in cell L. If the flux F1 is assumed to originate from an isotropic source then equation (2) must be modified to prevent an infinite flux per unit area at the origin. Clearly the transmission across the cell is modified by the surface area ratio so that

$$F1(J) = F(J+1)e^{-\tau} \frac{S(J)}{S(J+1)} + SG(L) \qquad (3)$$

The inward flux which does not pass through S(J) is in fact converted into outward flux F2(J+1) so this term $G(J) = F1(J+1) \times \left(1 - \frac{S(J)}{S(J+1)}\right)$ is

stored for use on the outward integration.

In the low density emitting plasma we wish to calculate SG(L) from the Summers and McWhirter emission functions while in the optically thick limit we wish F1(J) to tend to $B_g \times S(J)$ where $B_g = \int_{\nu_{g-1}}^{\nu_g} B_\nu \, d\nu$ is the black body flux density.

If we divide equation (3) by S(J) and take a uniform optically thick plasma, then

$$B_g = B_g e^{-\tau} + \frac{SG(L)}{S(J)}$$

In order to preserve the correct black body limit it is clear that we must have

$$\frac{SG(L)}{S(J)} = B_g(1 - e^{-\tau}) \qquad (4)$$

This is the normal integrated form of the source function in the LTE limit and the only problem is that SG must pass over correctly into the low density limit.

For small values of τ we have

$$SG(L) = B_g K_g DR \qquad (5)$$

which shows that $B_g \times K_g$ can be identified with the volume emission rate W_g provided that K_g is defined correctly. In the low density limit we must have $K_g = W_g/B_g$ where W_g is the Summers - McWhirter

coronal emission rate while at high densities Kg is given by the LTE tables. Since K_g in the low density region scales as the square of the density while K_g in LTE scales approximately linearly with density we wish to use always the smaller of the two quantities. This is conveniently done by taking the harmonic mean of the LTE and coronal calculations. With K_g calculated in this way equations (4) and (5) now give the correct limiting behaviour in LTE and also for optically thin coronal emission.

The outward fluxes F2(J) are calculated similarly by beginning with F2(1) = 0 and integrating outwards.

$$F2(J+1) = F2(J)e^{-\tau} + SG(L) + G(J)$$

This time there is no geometric loss in the flux transferred across the

cell but the flux transferred from F1 to F2 in the inward integration must be added. In order to conserve particles in the optically thin limit SG must be calculated from

$$\frac{SG\ (L)}{S(J+1)} = B_g\ (1 - e^{-\tau})$$

At the outer boundary F2(NJP1) represents the net loss of energy from the plasma and is stored for printing out when appropriate.

It is possible to define an effective radiation temperature T_r by means of the equation

$$\sigma\ T_r^4 = \sum_{g=1}^{NG} \left[\frac{F1_g(J) + F2_g(J)}{S(J)}\right]$$

The radiation pressure $P_R = \frac{1}{3} U_R$ where U_R is the radiation energy density is formally added to the plasma pressure in calculating the fluid acceleration but in practice it is usually found to be negligible.

The Coronal Source Function

Summers and Mc Whirter have calculated the total radiative power loss of several elements using the low density coronal approximation. The total

power loss W is given by $W = R(Z,T_e)n_e n_i$ and is approximately proportional to the square of the density. Unfortunately the spectral distribution is not given so the radiation is assumed to be distributed as a grey body at the local electron temperature i.e.

$$S_g = R\ n_e\ n_i\ \frac{\int_{\nu_{g-1}}^{\nu_g} B_\nu(T_e)\ d\nu}{\int_0^\infty B_\nu(T_e)\ d\nu}$$

The LTE opacity calculations

The LTE model is based on a code PLASMA kindly made available by Dr A.Pritzker. The code uses a set of Slater screening parameters to calculate the excitation and ionisation energies of each ionisation state of the element of interest. For each temperature and density point a Saha - Boltzmann calculation of the level populations is made and the bound-free absorption at each absorption edge is calculated using scaled hydrogenic cross-sections.

Above the K-edge the opacity is assumed to scale as ν^{-3} but below the K - edge a ν^{-2} scaling is used to agree with measured X-ray absorption coefficients. Finally the bound-free and free-free absorption cross-sections are integrated over an arbitrary number of frequency groups.

The Slater model gives excellent results for K and L-shell electrons but outer shell energies are very inaccurate. As a result, the opacities generated are excellent for $Z \lesssim 26$, but unreliable for very high Z. Since high Z materials always ionise until the next ionisation potential is of the order of the electron thermal energy, the model is to some extent self-correcting and opacity tables have been generated for high Z materials although they need to be treated with some caution.

In Figure 7.36 we show the computed group mean opacities for Si and for Au together with the measured data for the cold materials. Agreement is excellent for Si, and also for the other moderate Z materials which have been calculated (C,O,Ne). The computed data for Au are two large at low

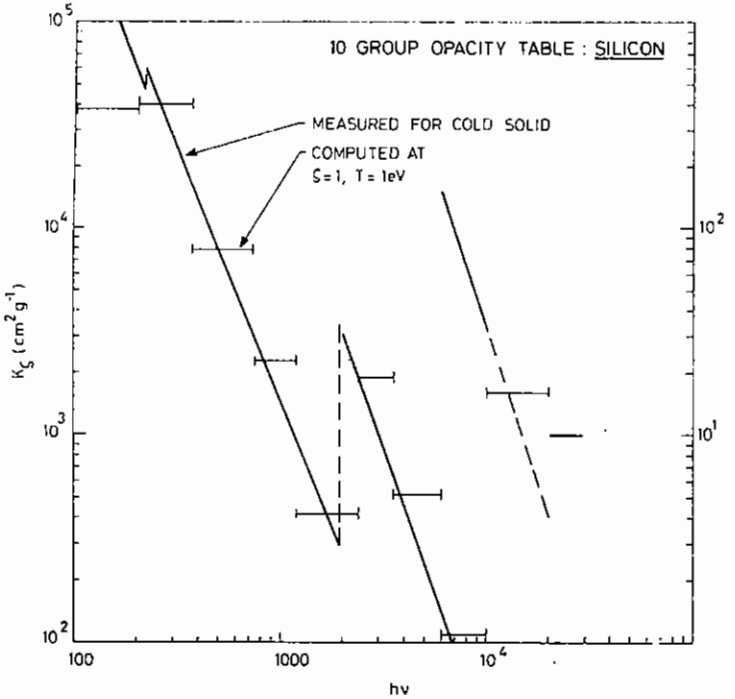

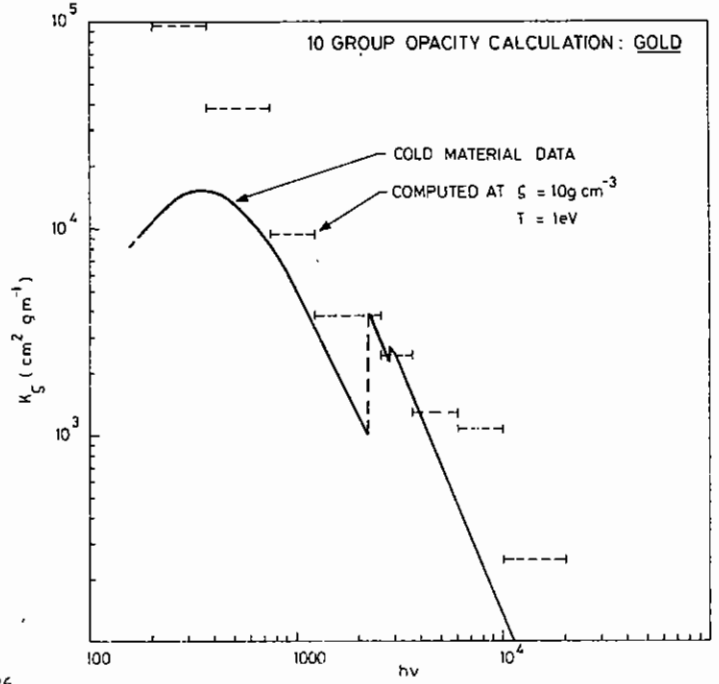

Figure 7.36

Multi-group opacity calculations for (a) silicon and (b) gold. The horizontal bars are the group mean opacities and the full lines the measured cold material opacities.

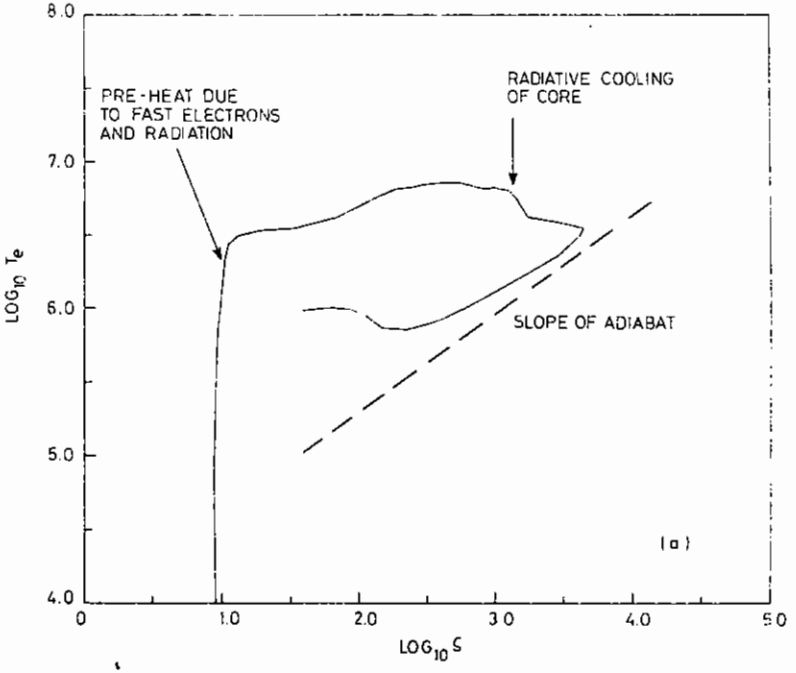

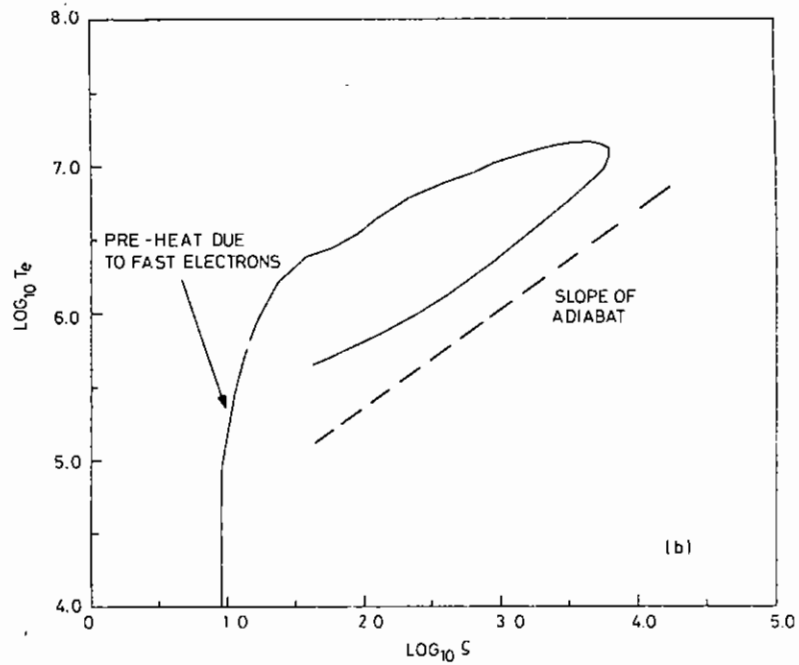

Figure 7.37 Thermodynamic (ρ,T) trajectories of a fuel element with (a) and without (b) radiation transport.

photon energies but in part at least this is due to the "cold" temperature of 10eV used in the computation.

Results from the model

The model has been used to calculate the radiative preheating effects in glass microballoon compression experiments. In Figure 7.37 we show the (ρ,T) trajectory of an element of the fill gas calculated with and without radiation transport. The effective preheat temperatures are several tens of eV and the resulting degradation of the compression is clear.

R G Evans (RAL)

7.4.5 Opacity Calculations for Radiation Transport

A new model for the calculation of radiation cross-sections of high Z materials is being developed based on the Thomas-Fermi model for an atom. The energy levels in the atom are calculated by dividing the density of states into energy bands and then calculating the average energy of these bands. The K shell energy is therefore given by the average energy of the lowest energy band containing two states worth of phase space, while the L shell energy is given by the average energy
of the band containing the next 8 states worth of phase space, etc.

An attempt is then made to estimate possible variations in energy levels due to some atoms having more or less electrons in each level compared with the average atom. To estimate these variations the effect caused by the removal of one electron from each level in turn on the energies of all the other levels is calculated. This is done by calculating the charge distribution of the removal electron and therefore its perturbation on the potential of the atom. Iteration is then used to calculate the atom's new electron distribution in a new self consistent potential. Using this new potential the energies of the levels of the perturbed atom can be found.

To calculate the widths of the energy levels an estimate must be made of the variation of the occupancy of each level. The variance in occupation

of each level however can easily be found from the occupation of the level and thus the widths of the energy levels can be calculated.

At present knowing the energies, widths and occupancies of the levels, Kramers formula is used to estimate the bound-free and bound-bound terms in the cross-section. The degree of ionisation is also easily found from the T-F model so the free-free radiation term can be calculated. Two examples of total cross-sections calculated for gold at 1 keV and at 0.1 and 1.0 times solid densities are shown in Figures 7.38 and 7.39 respectively.

Improvements are at present being made to both the calculation of the bound-free and bound-bound cross-sections using experimental data and oscillator strength function.

T D Beynon, E H Smith (Birmingham)

7.4.6 Optimisation of mesh resolution in Medua using a treadmill rezoner

The one dimensional Lagrargian simulation code MEDUSA (7.76) has been modified to allow greater resolution of short scale length density and temperature gradients. Provision of a finer zoned region around critical density leads to a better representation of heat flux saturation.

A fine zoned mesh can be applied by starting the simulation with more zones packed closely together. Although the treatment of the temperature equation in Medusa is implicit, imposing few constraints on the timestep size, the Navier - Stokes equation is differenced explicitly. The timestep is therefore limited by the C.F.L. condition

$$\Delta t < \frac{\Delta r}{V_s} = \Delta r\sqrt{\frac{\rho}{\gamma p}}$$

where V_s is the sound speed in the plasma and Δr is the zone size at that time. For any zone its density is proportional to the reciprocal of Δr.

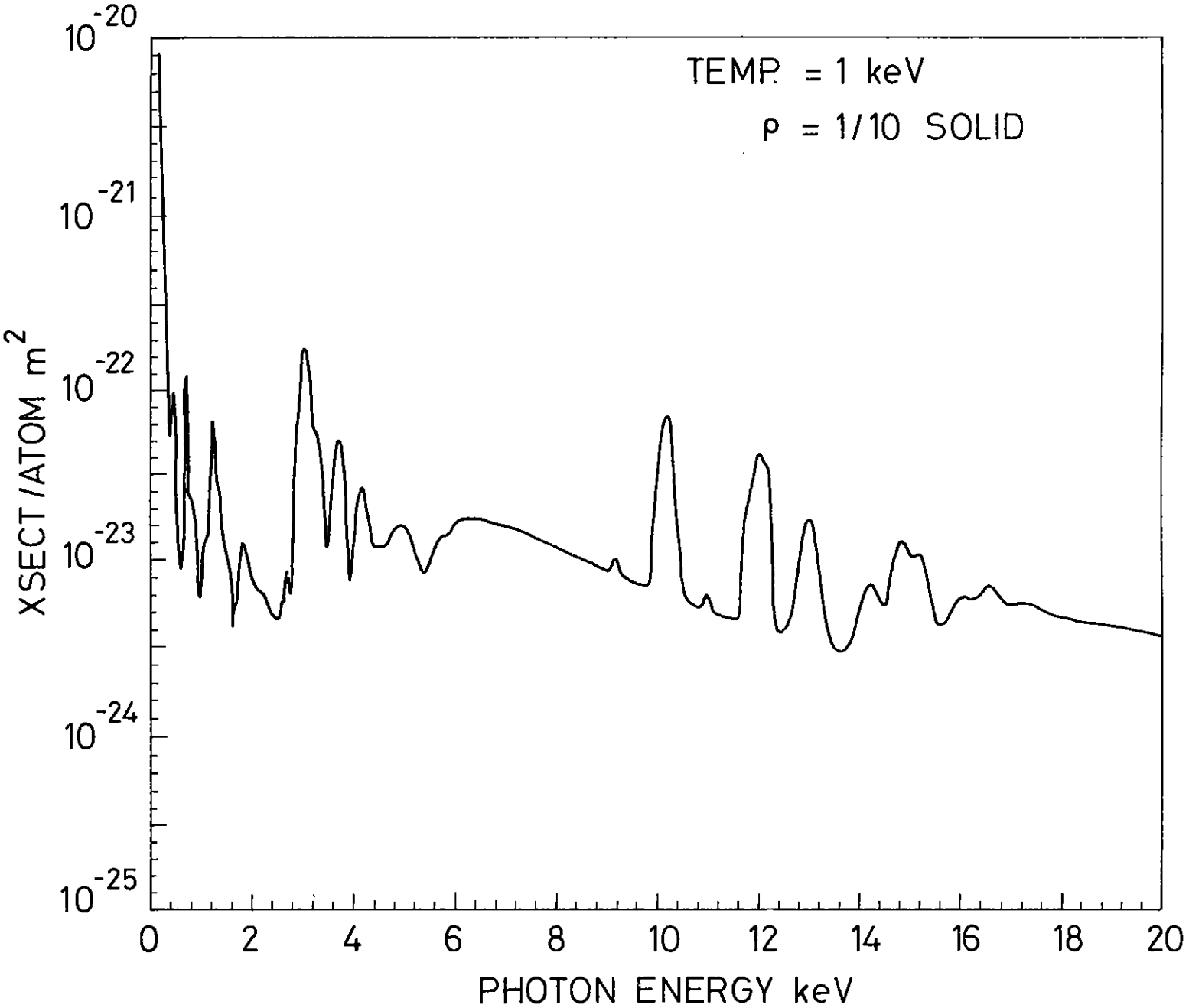

Figure 7.38 Cross-sections calculated for gold at 1 KeV and 0.1 times solid density.

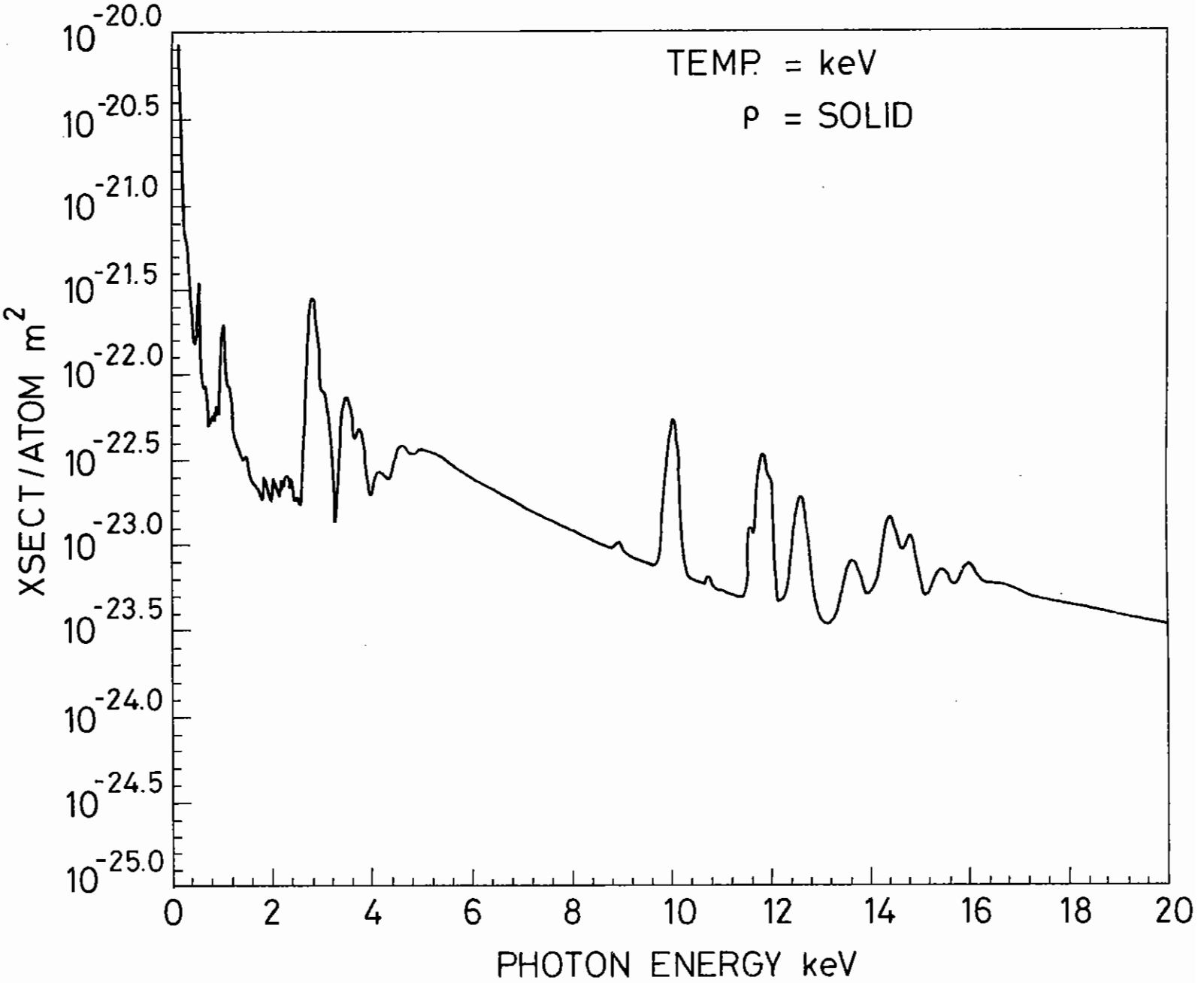

Figure 7.39 Cross-sections calculated for gold at 1 KeV and solid density.

The C.F.L. condition can be rewritten as

$$\Delta t \sim (\Delta r/\gamma P)^{\frac{1}{2}}$$

Producing a finer mesh by globally reducing the zone sizes Δr, reduces the permitted time step and increases the required computer time.

The zones which impose the greatest restriction on Δt, in a laser plasma simulation, are on the high density side of the ablation front. Here, in the solid target surface, Δr is small and the pressure P large. Small zones can be used without limiting the timestep if they are created by splitting up larger zones as they leave the target surface. The zones are split as they are ablated from the target and by the time they flow into the critical density region a reduction of up to 8 in the zone mass will be achieved. To avoid having the number of cells increasing as the simulation progresses, the zones are merged back together on reaching the low density side of critical where scale lengths are longer and a coarse mesh can be used. The action of splitting zones at high density and merging them at low density is performed by a treadmill rezoner (7.77).

Simulations using a fine zoned outer mesh with no attempt at rezoning have been done using zones of line density 3 10^{-6} g cm^{-2}, smaller zones than this meant an excessive use of computer time. Using a treadmill rezoner, cells of less than 10^{-6} gcm^{-2} could be used for the same test problem with a reduction by a factor of 6 in required computer time. The minimum zone size that is usable with the rezoner is set when the internal energy of the cell becomes comparable with the heat flowing through it in one timestep. When this happens the timestep must be reduced and the code slowed down as a result.

B J MacGowan (Imperial College)

CHAPTER 7 REFERENCES

7.01 Rutherford Laboratory Annual Report to the Central Laser Facility, RL81-040, p7.03 (1981)

7.02 R S Craxton and R L McCrory, J Comp Phys 33, 432 (1979)

7.03 J P Boris and D L Book, Methods of Comp Phys 16, 85 (1976)

7.04 D V Anderson, J Comp Phys 17, 246 (1975)

7.05 J P Boris and D L Book, J Comp Phys 11, 38 (1973)

7.06 R E Kidder, Nucl Fusion 16, 3 (1976)

7.07 S Chandrasekhar, Hydrodynamic and Hydromagnetic Stability, Oxford University Press, Chap 10 (1961)

7.08 S E Bodner, Phys Rev Lett 33, 761 (1974)

7.09 E Ott and D A Russell, Phys Rev Lett 41, 15 (1978)

7.10 J Lindl and W C Mead, Phys Rev Lett 34, 1273 (1975)

7.11 R L McCrory, L Montierth, R L Morse and C Verdun, Phys Rev Lett 46, 336 (1981)

7.12 M H Emery, J H Gardner and J P Boris, Phys Rev Lett 48, 677 (1982)

7.13 G J Pert, J Comp Phys 43, 111 (1976)

7.14 S Chandrasekhar, Hydrodynamic and Hydromagnetic Stability, Oxford University Press, Chap 11 (1961)

7.15 B Ahlborn, M H Key and A R Bell, Phys Fluids 25, 541 (1982)

7.16 J M Gardner and S E Bodner Phys Rev Lett 47, 1137 (1981)

7.17 J D Lindl, presented at 15th ECLIM, Schliersee, Febury 1982

7.18 C E Max, C F McKee and W C Mead, Phys Fluids 23, 1620 (1980)

7.19 R G Evans, private communication

7.20 J A Stamper, K Papadopoulos, R N Sudan, S O Dean and E A McClean, Phys Rev Lett 26, 1012 (1971)

7.21 J A Stamper and B H Ripin, Phys Rev Lett 34, 138 (1975)

7.22 O Willi, P T Rumsby and C Duncan, Opt Comm 37, 40 (1981)

7.23 O Willi and P T Rumsby, Opt Comm 37, 45 (1981)

7.24 M J Herbst et al, NRL Memorandum Report 4437 (1981)

7.25 M G Haines, Phys Rev Lett 47, 917 (1981)

7.26 D A Tidman and R A Shanny, Phys Fluids 17, 1207 (1974)

7.27 A Hirao and M Ogasawara, J Phys Soc Japan 50, 668 (1981)

7.28 A Z Doginov and V A Urpin, Sov Phys JETP 50, 912 (1979)

7.29 E M Epperlein, G J Pert and D G Colombant, CECAM Report (1981)

7.30 R G Evans, J Phys D 14, L173 (1981)

7.31 S I Braginskii, Reviews of Plasma Phys, ed M A Leontovich (Consultants Bureau, New York) 1, 125 (1965)

7.32 O Willi, presented at 15th ECLIM, Schliersee, February 1982

7.33 A Raven, P T Rumsby, J A Stamper, O Willi, R ILlingworth and R Thareja, Appl Phys Lett 35, 526 1979)

7.34 A Raven and O Willi, Phys Rev Lett 43, 278 (1979)

7.35 C Duncan, W D Luckin, O Willi and P T Rumsby, CLF Report RL-81-40, Section 4.6.1 (1981)

7.36 S I Braginskii, Reviews of Plasma Phys 1, 205 (1966)

7.37 T J M Boyd, D Cooke and G J Humphreys-Jones, Phys Lett A 88, 140 (1982)

7.38 O Willi, A Raven and P T Rumsby, Phys Lett A 71, 435 (1979)

7.39 C Grebogi and C S Liu, Phys Fluids 23 1330 (1980)

7.40 C Grebogi and C S Liu, J PlasmaPhys 23, 147 (1980)

7.41 V K Tripathi, C Grebogi and C S Liu, Phys Fluids 22, 301 (1979)

7.42 S Ram, 'Nonlinear scattering from electron Bernstein modes in a plasma', Plasma Phys, to be published

7.43 S Ram, 'Nonlinear scattering from ion Bernstein modes in a plasma', submitted for publication

7.44 M S Sodha, A K Ghatak and V K Tripathi, Progress in Optics 13, 169 (1976)

7.45 D Anderson and M Bonnedal, Phys Fluids 22, 105 (1979)

7.46 J H Marburger and E Dawes, Phys Rev Lett 21, 556 (1968)

7.47 S A Akhamanov, A P Sukhorukov and R W Khokhlov, Sov Phys JETP 23, 1025 (1966)

7.48 H Hora, Phys Fluids 12, 182 (1969)

7.49 M S Sodha, J Phys Edn (India) 1, 13 (1973)

7.50 P Kaw, G Schmidt and T Wilcox, Phys Fluids 16, 1522 (1973)

7.51 C E Max, Phys Fluids 19, 74 (1976)

7.52 L C Steinhauer and H G Ahlstrom, Phys Fluids 13, 1103 (1970)

7.53 P L Kelley, Phys Rev Lett 15, 1005 (1965)

7.54 B F Lasinski and A B Langdon, Livermore Laser Program Annual Report for 1979, p3.47

7.55 J W Shearer and J L Eddlemen, Phys Fluids 16, 1753 (1973)

7.56 A R Bell, R G Evans and D J Nicholas, Phys Rev Lett 46, 243 (1981)

7.57 D J Nicholas, RAL Report RL-82-021 (1982)

7.58 O Willi, P T Rumsby, Z Q Lin and S Sartang, CLF Annual Report RL-81-040 (1981)

7.59 D J Bond, J Phys A, in press

7.60 D J Bond, T H Kho and M G Haines, Plasma Phys, in press

7.61 D J Bond, Phys Lett A 88, 144 (1982)

7.62 E S Wyndham et al, submitted to J Phys D

7.63 Wienke, Los Alamos Report LA-UR 81-1489

7.64 A R Bell, R G Evans and D J Nicholas, RAL Report RL-80-091 (1980)

7.65 T H Kho and D J Bond, Section 7.4.1 of this report

7.66 L Spitzer, Physics of Ionised Gases, Publ Interscience (1956)

7.67 R J Mason, Phys Rev Lett 47, 652 (1981)

7.68 D R Gray and J D Kilkenny, Plasma Phys 22, 81 (1980)

7.69 D Shvarts, J Delettrez, R L McCrory and C P Verdon, Phys Rev Lett 47, 247 (1981)

7.70 D J Bond, J Phys D 14, L43 (1981)

7.71 M H Shirazian and L C Steinhauer, Phys Fluids 24, 843 (1981)

7.72 S A Khan and T D Rognlien, Phys Fluids 24, 1442 (1981)

7.73 L Spitzer and R Harm, Phys Rev 89, 977 (1953)

7.74 N A Krall and A W Trivelpiece, Principles of Plasma Physics, p389, Publ McGraw-Hill (1973)

7.75 H P Summers and R W P McWhirter, J Phys B 12, 2387 (1979)

7.76 D E T F Ashby, J P Christiansen and K V Roberts, Comp Phys Comm 7, 271 (1974)

7.77 D Tanner, KMS Annual Report for 1979

APPENDIX

CENTRAL LASER FACILITY PUBLICATIONS 1981/82

RESEARCH PAPERS

B Ahlborn, M H Key and A R Bell
An analytic model for laser driven ablative implosion of spherical shell targets
Phys Fluids, 25, 541 (1982)

B Ahlborn and M H Key
Scaling laws for laser driven exploding pusher targets
Plasma Phys 23, 435 (1981)

H C Barr and T J M Boyd
Saturation levels of heat flux and fast electron driven ion acoustic wave turbulence
Phys Rev A24 (1981)

H C Barr, T J M Boyd and L R T Gardner
Raman and two plasmon decay instabilities in a magnetized plasma
Phys Fluids 25, (1982) (in press)

A R Bell
Electron energy transport in ion waves and its relevance to laser-produced plasmas
Phys Fluids (in press)

N St J Braithwaite, A Montes and L M Wickens
Some comments on thermal flux inhibition in laser produced plasmas
Plasma Phys 23, 713 (1981)

D J Bond, J D Hares and J D Kilkenny
A measurement of the reduction of the range of fast electrons from laser irradiated targets due to density structure in low density gold substrates
Plasma Phys 24, 91 (1982)

T J M Boyd and H C Barr
Ion turbulence and thermal transport in laser fusion plasmas
Plasma Physics (in press)

R A Cairns
The intensity and angular dependence of second harmonic emission from a laser produced plasma
Plasma Physics 23, 705 (1981)

R A Cairns
Time dependence and saturation of Brillouin backscatter
Plasma Physics 24, 109 (1982)

R G Caro and M C Gower
Phase conjugation of a KrF laser
Optics Lett 6, 557 (1981)

R G Caro and M C Gower
Amplified phase conjugate reflection of KrF laser radiation
Appl Phys Lett 39, 855 (1981)

R G Caro, M C Gower and C E Webb
A high spectral intensity narrow line width KrF laser
J Phys D: Appl Phys (in press)

R W Eason, R C Greenhow and J A D Matthew
Modelling of picosecond pump and probe photobleaching experiments on fast saturable absorbers
IEEE J Quant Elec 17, 95 (1981)

C B Edwards, J M Gallego and H S Reehal
Pulsed XeCl laser annealing of ZnS.Mn thin films
Appl Phys Lett (Feb 1982)

C B Edwards, F O'Neill and M J Shaw
Absorption and gain measurements in the KrF laser medium at high pump rates
Appl Phys Lett 38, 843 (1981)

J Elezar, W T Toner and E R Wooding
Backscattered radiation at /2 from Nd laser plasma interactions
Plasma Phys 23, 813 (1981)

R G Evans
Radiation cooling instabilities in laser heated plasmas
J Phys D: Appl Phys 14, L173 (1981)

R G Evans, A R Bell and B MacGowan
Numerical studies of laser driven ablation
J Phys D: Appl Phys (in press)

R G Evans, A J Bennett and G J Pert
2D fluid simulations of non-uniformly irradiated targets for inertial fusion J Phys D (in press)

A F Gibson
Lasers for compression and fusion
Comtemp Phys (in press)

T J Goldsack et al
Evidence for large heat fluxes from the mass ablation rate of laser irradiated targets
Phys Fluids (in press)

T J Goldsack, J D Kilkenny and P T Rumsby
Determination of mass ablation rates and ablation pressures on spherical targets by ion emission
J Phys D: Appl Phys 14, L47 (1981)

T J Goldsack et al
The variation of mass ablation rate with laser wavelength and target geometry
Opt Comm (in press)

M C Gower
KrF laser-induced breakdown of gases
Opt Comm 36, 43 (1981)

M C Gower, S Rolt and C E Webb
Direct measurement of photoabsorption cross-sections; application of UV photolysis of OCS_e and Se_2 + CO
J Phys D: Appl Phys 15, (1982)

M C Gower and C B Edwards
Gain and absorption measurements in a discharge excited KrF laser
Opt Comm 40, 369 (1982)

M G Haines
Thermal instability and magnetic field generation by large heat flow in a plasma, especially under laser-fusion conditions
Phys Rev Lett 47, 917 (1981)

J D Hares
A simple CW X-ray source for laser plasma X-ray diagnostic alignment
J Phys E: Sci Instrum (in press)

J D Hares and J D Kilkenny
A demonstration of the decrease of fast electron preheat from laser produced plasma with increasing pulse length
J Appl Phys 52, 6420 (1981)

D Jacoby, G J Pert, S A Ramsden, L D Shorrock and G J Tallents
Observation of gain in a possible extreme ultra violet lasing system
Opt Comm 37, 193 (1981)

R Illingworth and R K Thareja
Generalised coefficients for Abel inversion
J Phys E: Sci Instrum 14, 147 (1981)

M H Key
Lasers and the physics of high energy density
Physics Bulletin 33, 95 (1982)

M H Key
Interactions of intense laser radiation with matter
Phil Trans Roy Soc A300, 599 (1981)

J D Kilkenny, S Veats, A Shalom and R W Lee
Emission line shapes from laser compressed plasmas
"Spectral Line Shapes", editor B Werde, Pub, Walter de Gruyler & Co, Berlin (1981)

Z Q Lin, O Willi and P T Rumsby
Evidence for beam self-focusing in the corona of laser irradiated spherical targets
J Phys D: Appl Phys 14, L35 (1981)

M Martin, C Fotakis, R J Donovan and M J Shaw
Optical pumping and collisional quenching of I_2 ($D^1 \pi_u$)
Nuovo Cimento 63B, 300 (1981)

E McGoldrick and S M L Sim
Time resolved studies of 3/2 ω_o harmonic emission from laser produced plasma Opt Comm 39, 172 (1981)

A Montes and O Willi
Self consistent variation of the critical density scale length due to the ponderomotive force
Plasma Phys (in press)

J Murdoch, J D Kilkenny, D R Gray and W T Toner
Time resolved measurements of the laser burn-through of thin foils
Phys Fluids 24, 2107 (1981)

D J Nicholas
Diffraction propagation of a light beam through a high power laser system
Optica Acta 29, 325 (1982)

D J Nicholas and J E Boon
Production of an aspheric surface for an f/1 lens by a CNC machine
Proc Soc Photo Inst Eng 235, 92 (1980)

D J Nicholas and I N Ross
Beam propogation studies in high power laser systems
Proc Soc Photo Inst Eng 236, 243 (1980)

G J Pert
Efficient integration of the time dependent collisional-radiative equations
J Comp Phys 39, 251 (1981)

G J Pert
Physical constraints in numerical calculations of diffusion
J Comp Phys 41, 20 (1981)

G J Pert
Algorithms for the self-consistent generation of magnetic fields in plasmas
J Comp Phys 43, 111 (1981)

S Ram
Nonlinear scattering from electron Bernstein modes in a plasma
Plasma Phys (in press)

A Raven, H Azechi, T Yamanaka and C Yamanaka
Stability of ablatively accelerated thin foils
Phys Rev Lett 47, 1049 (1981)

A Raven, H Azechi, M Nakai, T Matsuo, T Yamanaka and C Yamanaka
A comparison of ablative acceleration measurements
Appl Phys Lett (submitted)

I N Ross et al
VULCAN - a versatile high power glass laser for multiuser experiments
IEEE J Quan Elec 17, 1653 (1981)

J F Seely and J G Lunney
Digital enhancement of the argon dielectronic satellite spectrum from a laser-imploded microballoon
Opt Comm 41, 43 (1982)

O Willi, P T Rumsby and S Sartang
Optical probe observations of non-uniformities in laser produced plasmas
IEEE J Quant Elec 17, 1909 (1981)

O Willi, P T Rumsby, C Hooker, A Raven and Z Q Lin
Observations of instabilities in the corona of laser produced plasmas
Opt Comm 41, 110 (1982)

T K Yee and M C Gower
Diagrammatical analysis of laser-switched collision processes
IEEE J Quant Elec (in press)

CONFERENCE PAPERS TO BE PUBLISHED

Proc of the 5th Nat Quant Elec Conf. J Wiley and Sons (to be published)

Gain and Absorption measurements in discharge pumped rare gas halide lasers

H S Reehal, J M Gallego, C B Thomas and C B Edwards XeCl laser annealing of ZnS

D A Pepler, J Szechi and W T Toner
Multi-wavelength target irradiation system at the SERC Central Laser Facility

M H Key
Progress in laser plasma interactions

M C Gower and T K Yee
Diagrammatical analysis of laser switched collision processes

M C Gower and R G Caro
Phase conjugation of a KrF laser

D Craddock, C B Edwards, F S Gilbert, F O'Neill, D J Nicholas, P Rockett and M J Shaw
Development of pulsed E-beam systems for large volume high power KrF lasers
Proc 3rd IEEE Int Pulsed Power Conf, Albuquerque (1981)

D Craddock, C B Edwards, F S Gilbert, F O'Neill, D J Nicholas and M J Shaw
Development of pulsed E-beam systems for large volume high power KrF lasers
Proc 4th Int Top Conf on High Power Electron and Ion Beam Research and Technology, Palaiseau (1981)

M Khakoo, W R Newell, W T Toner, R W Eason
Conf Proc of IX Summer School on Quantum Optics, Cetnieno, Poland
Acta Physica Polonica (1981)

E R Wooding, J Elazar and N Sayed
The 2 spectrum in laser plasma interaction
Proc 10th European Conf on Controlled Fusion and Plasma Physics, Moscow (1981)